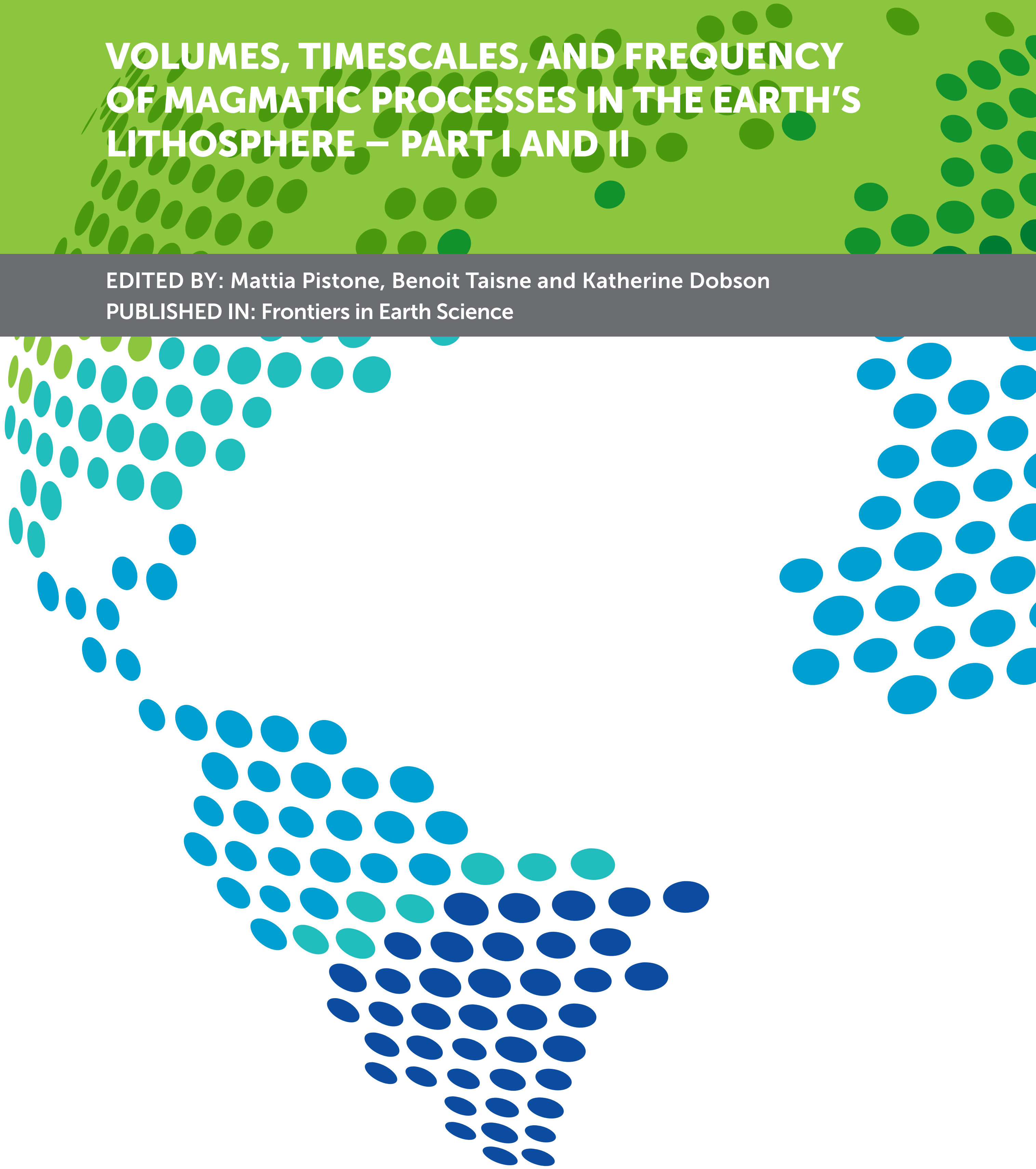

VOLUMES, TIMESCALES, AND FREQUENCY OF MAGMATIC PROCESSES IN THE EARTH'S LITHOSPHERE – PART I AND II

EDITED BY: Mattia Pistone, Benoit Taisne and Katherine Dobson

PUBLISHED IN: Frontiers in Earth Science

frontiers Research Topics

ISSN 1664-8714
ISBN 978-2-88963-777-5
DOI 10.3389/978-2-88963-777-5

About Frontiers

Frontiers is more than just an open-access publisher of scholarly articles: it is a pioneering approach to the world of academia, radically improving the way scholarly research is managed. The grand vision of Frontiers is a world where all people have an equal opportunity to seek, share and generate knowledge. Frontiers provides immediate and permanent online open access to all its publications, but this alone is not enough to realize our grand goals.

Frontiers Journal Series

The Frontiers Journal Series is a multi-tier and interdisciplinary set of open-access, online journals, promising a paradigm shift from the current review, selection and dissemination processes in academic publishing. All Frontiers journals are driven by researchers for researchers; therefore, they constitute a service to the scholarly community. At the same time, the Frontiers Journal Series operates on a revolutionary invention, the tiered publishing system, initially addressing specific communities of scholars, and gradually climbing up to broader public understanding, thus serving the interests of the lay society, too.

Dedication to Quality

Each Frontiers article is a landmark of the highest quality, thanks to genuinely collaborative interactions between authors and review editors, who include some of the world's best academicians. Research must be certified by peers before entering a stream of knowledge that may eventually reach the public - and shape society; therefore, Frontiers only applies the most rigorous and unbiased reviews.
Frontiers revolutionizes research publishing by freely delivering the most outstanding research, evaluated with no bias from both the academic and social point of view. By applying the most advanced information technologies, Frontiers is catapulting scholarly publishing into a new generation.

What are Frontiers Research Topics?

Frontiers Research Topics are very popular trademarks of the Frontiers Journals Series: they are collections of at least ten articles, all centered on a particular subject. With their unique mix of varied contributions from Original Research to Review Articles, Frontiers Research Topics unify the most influential researchers, the latest key findings and historical advances in a hot research area! Find out more on how to host your own Frontiers Research Topic or contribute to one as an author by contacting the Frontiers Editorial Office: researchtopics@frontiersin.org

VOLUMES, TIMESCALES, AND FREQUENCY OF MAGMATIC PROCESSES IN THE EARTH'S LITHOSPHERE – PART I AND II

Topic Editors:
Mattia Pistone, University of Georgia, United States
Benoit Taisne, Nanyang Technological University, Singapore
Katherine Dobson, University of Strathclyde, United Kingdom

Citation: Pistone, M., Taisne, B., Dobson, K., eds. (2020). Volumes, Timescales, and Frequency of Magmatic Processes in the Earth's Lithosphere – Part I and II. Lausanne: Frontiers Media SA. doi: 10.3389/978-2-88963-777-5

Table of Contents

05 ***Editorial: Volumes, Timescales, and Frequency of Magmatic Processes in the Earth's Lithosphere***
Mattia Pistone, Benoît Taisne and Katherine J. Dobson

09 ***Seismicity Associated With the Formation of a New Island in the Southern Red Sea***
Jade H. W. Eyles, Finnigan Illsley-Kemp, Derek Keir, Joël Ruch and Sigurjón Jónsson

19 ***Nonlinear Moment-Tensor Inversion of Repetitive Long-Periods Events Recorded at Pacaya Volcano, Guatemala***
Federica Lanza and Gregory P. Waite

35 ***Isotopic and Petrologic Investigation, and a Thermomechanical Model of Genesis of Large-Volume Rhyolites in Arc Environments: Karymshina Volcanic Complex, Kamchatka, Russia***
Ilya N. Bindeman, Vladimir L. Leonov, Dylan P. Colón, Aleksey N. Rogozin, Niccole Shipley, Brian Jicha, Matthew W. Loewen and Taras V. Gerya

62 ***360 Intrusions in a Miniature Volcano: Birth, Growth, and Evolution of an Analog Edifice***
Allan Derrien and Benoit Taisne

78 ***Burial-Related Compaction Modifies Intrusion-Induced Forced Folds: Implications for Reconciling Roof Uplift Mechanisms Using Seismic Reflection Data***
Craig Magee, Murray Hoggett, Christopher A.-L. Jackson and Stephen M. Jones

94 ***Magma Transfer Processes in the NE Japan Arc: Insights From Crustal Ambient Noise Tomography Combined With Volcanic Eruption Records***
Georg F. Zellmer, Kai-Xun Chen, Yuancheng Gung, Ban-Yuan Kuo and Takeyoshi Yoshida

102 ***Bayesian Markov-Chain Monte Carlo Inversion of Low-Temperature Thermochronology Around Two 8 – 10 m Wide Columbia River Flood Basalt Dikes***
Leif Karlstrom, Kendra E. Murray and Peter W. Reiners

121 ***Deep Magma Storage Revealed by Multi-Method Elemental Mapping of Clinopyroxene Megacrysts at Stromboli Volcano***
Teresa Ubide, John Caulfield, Claire Brandt, Yannick Bussweiler, Silvio Mollo, Flavio Di Stefano, Manuela Nazzari and Piergiorgio Scarlato

144 ***Evidence for Cyclical Fractional Crystallization, Recharge, and Assimilation in Basalts of the Kimama Drill Core, Central Snake River Plain, Idaho: 5.5-Million-Years of Petrogenesis in a Mid-crustal Sill Complex***
Katherine E. Potter, John W. Shervais, Eric H. Christiansen and Scott K. Vetter

161 ***Magmatic Densities Control Erupted Volumes in Icelandic Volcanic Systems***
Margaret Hartley and John Maclennan

170 ***A NanoSIMS Investigation on Timescales Recorded in Volcanic Quartz From the Silicic Chon Aike Province (Patagonia)***
Susanne Seitz, Benita Putlitz, Lukas Baumgartner, Anders Meibom, Stéphane Escrig and Anne-Sophie Bouvier

189 ***Unraveling the Physics of the Yellowstone Magmatic System Using Geodynamic Simulations***
Georg S. Reuber, Boris J. P. Kaus, Anton A. Popov and Tobias S. Baumann

frontiers in Earth Science

EDITORIAL
published: 16 April 2020
doi: 10.3389/feart.2020.00118

Editorial: Volumes, Timescales, and Frequency of Magmatic Processes in the Earth's Lithosphere

Mattia Pistone[1]*, *Benoît Taisne*[2] and *Katherine J. Dobson*[3]

[1] Department of Geology, University of Georgia, Athens, GA, United States, [2] Earth Observatory of Singapore, Nanyang Technological University, Singapore, Singapore, [3] Department of Civil and Environmental Engineering, University of Strathclyde, Glasgow, United Kingdom

Keywords: magmatic processes, earth's lithosphere, volumes, timescales, frequency

Editorial on the Research Topic

Volumes, Timescales, and Frequency of Magmatic Processes in the Earth's Lithosphere

Heat, mass, and fluid transfer processes related to the formation and growth of the continental crust along convergent and divergent plate boundaries, and the formation, modification, and recycling of the continental crust are key research themes in the solid Earth Science community. Establishing the link between magma generation, transport, emplacement, and eruption can therefore significantly improve our understanding of crust-forming processes associated with plate tectonics, and, particularly, help determining the architecture, and composition of the Earth's lithosphere.

One of the Earth's characteristic processes is chemical differentiation, forming a SiO_2-rich continental crust that is continuously shaped and reworked throughout Wilson cycles. The continental crust covers 41% of Earth's surface (Cogley, 1984) and sits at higher elevation compared to the oceanic crust that tends to be largely subducted. The SiO_2-rich rocks that dominate the upper portions of Earth's crust are unique in the Solar System (e.g., Taylor, 1989) and are ultimately linked to the presence of liquid water on Earth (Bowen, 1928; Campbell and Taylor, 1985). But when, where and for how long magmas are stored within the Earth's lithosphere and how they contribute to its chemical, physical, and thermal architecture remain important challenges in geosciences.

The presence of magmatic bodies in the crust have been confirmed through a wide range of geophysical investigations; however, the volume, geometry, mechanics, chemical signatures, and evolution of these bodies remain poorly constrained. Establishing the link between magma generation, transport, emplacement, and eruption is therefore essential to significantly improve our understanding of crust-forming processes associated with plate tectonics, and help determine the Earth's lithosphere architecture, composition, and dynamics. In this cross-disciplinary Research Topic, contributions aim to answer such fundamental questions.

OPEN ACCESS

Edited and reviewed by:
Valerio Acocella,
Roma Tre University, Italy

****Correspondence:***
Mattia Pistone
Mattia.Pistone@uga.edu

Specialty section:
This article was submitted to
Volcanology,
a section of the journal
Frontiers in Earth Science

Received: *13 March 2020*
Accepted: *27 March 2020*
Published: *16 April 2020*

Citation:
Pistone M, Taisne B and Dobson KJ (2020) Editorial: Volumes, Timescales, and Frequency of Magmatic Processes in the Earth's Lithosphere. Front. Earth Sci. 8:118. doi: 10.3389/feart.2020.00118

HOW DO WE DETECT VOLUMES AND GEOMETRY OF MAGMATIC BODIES AT DEPTH AND THEIR ERUPTIVE PRODUCTS?

In recent decades, advances in geophysical techniques that image the structure of magma plumbing systems have allowed identification of zones of melt accumulation, crystal mush development, and magma transport (e.g., Magee et al., 2018). Combining these geophysical observations with petrological and geochemical data allows the development of entire magma plumbing systems to be understood. Reuber et al. (2018) employ lithospheric-scale three-dimensional visco-elasto-plastic geodynamic models and a joint modeling gravity inversion approach to test the influence of chamber connectivity, rheology of the lithosphere, and the effective density of the magma chambers on the dynamics of the system and amplitude of surface uplift. By application of their numerical approach to Yellowstone's magmatic system, one of the largest magmatic systems on Earth, they validate their approach against processes that are observable using the present-day geophysical spatial resolution (Vasco et al., 2007; Smith et al., 2009).

The structure of upper crustal magma plumbing systems controls the distribution of volcanism and influences tectonic processes. Specifically, space for shallow-level sills and laccoliths is commonly generated by bending and uplift of overlying rock and sediment ("roof-uplift" mechanics). The surface expression of forced folds captured by seismic reflection images can be used to constrain both elastic and inelastic mechanics and related geometries of the intruding magma bodies in the shallow Earth's crust. Magee et al. use seismic-based observations to evaluate the elastic and inelastic deformations that accommodated magmatic intrusions. Using geological and geophysical information from the Resolution-1 borehole offshore eastern New Zealand, the authors show that post-emplacement, burial-related compaction processes can modify initial fold amplitude and intrusion thickness. Magee et al. thereby provide a methodology that can account for post-emplacement, burial-related compaction signature, and enable more accurate estimation of the intrusive magma body thickness in two-dimensional seismic reflection profiles.

HOW CAN WE QUANTIFY CHEMICAL, MECHANICAL, AND THERMAL PROCESSES THAT INFLUENCE MAGMA TRANSPORT AND ERUPTION EVENTS?

Geophysical, petrological, and geochemical methods are generally applied across a range of different spatial and temporal scales, and to different tectonic settings to evaluate the chemical, mechanical, and thermal processes that govern magma transport and eruption at active volcanoes. Zellmer et al. show the possibilities provided by better integration between these methodologies, when constraining the role of the crustal thermo-mechanical properties on magma transport. By studying the long debated processes controlling the relative proportion of intrusive to extrusive volumes of arc magmas along subduction zones (Crisp, 1984; White et al., 2006), Zellmer et al. use published ambient noise tomography data from the NE sector of the Japanese arc system, to propose that plutons/magma reservoirs (bodies characterized by low shear velocities) are found beneath most of the active volcanoes exhibiting caldera-forming eruptions, and represent a hotter and more ductile crustal response to intrusive activity that hinders magma transport to the surface along most of the arc. The approach also identifies mechanisms to explain the behavior of Zao volcano, which has erupted more frequently and produced greater tephra volume than any other volcano along the Japanese arc in the last 2,000 years. At Zao volcano, Zellmer et al. propose that frequent low-volume volcanism is fed by dikes that traverse the relatively cool and brittle arc crust. This dichotomy of volcanic activity highlights how physical and thermal heterogeneity of the arc crustal system influences volcanic style, frequency, and volumetric output at the surface.

Linking seismicity to magma dynamics at depth preceding volcanic eruption events is the target of Lanza and Waite. By stacking of thousands of repetitive explosion-related long-period (LP) events at Pacaya volcano, Guatemala (October-November 2013), and using non-linear waveform inversion, Lanza and Waite re-construct the associated non-linear moment-tensor, to characterize seismicity along a tensile crack, dipping ∼40° to the east. This allows them to infer that the N-S elongate geometry of the volcano conduit remains consistent throughout most of the edifice. The authors show how decoding seismic signals produced by volcanoes is crucial windows to magmatic systems and the complex interactions between gas, liquid, and solid along magma pathways.

The extent to which the physical properties of magma (e.g., density and viscosity) exert a fundamental control on their transport and eruptibility is the focus of Hartley and Maclennan (2018). Studying exposed lava flows of known age and volume from Iceland's Northern Volcanic Zone, the authors directly relate erupted volumes to magmatic physical properties. They identify that over 85% of the total volume of erupted magma was close to a density and viscosity minimum coincident with the nucleation of plagioclase in the basalt. This petrological window favors a high buoyancy of the magmas with respect to the upper crustal rocks. While primitive basalts and olivine-phyric picrites with densities higher than upper crustal rocks demonstrate that any density filter must be leaky, Hartley and Maclennan (2018) show that this is facilitated by the generation of overpressure in magma chambers in the lower crust and uppermost mantle.

Moving to shallowest levels of the magmatic system, understanding shallow magma transfer, volcanic edifice growth, and interaction between edifice stress state and magma transfer remains challenging from routine seismology and geodesy monitoring techniques. Derrien and Taisne show laboratory-based analog experiments that reproduced the mechanics of volcanic edifice birth and growth in an analog elasticity-dominated material. By monitoring the evolution of the stress field within and around the volcano edifice, the authors show that cyclic eruptive patterns alternating between eruptive and intrusive phases contribute to the formation of the initial volcanic edifice and to the subsequent edifice growth radial compressive stress build-up and release that act to localize the stress field to shallow level. Derrien and Taisne demonstrate these experiments can be used as a proxy for long-term stress perturbations in volcanic edifices and can provide understanding of edifice morphology during successive eruptive activity stages.

Finally, Eyles et al. present seismic data from Eritrea, Yemen, and Saudi Arabia which, when integrated with interferometric synthetic aperture radar data (Xu et al., 2015), identifies the propagation and inflation of a ∼12 km-long dike, emplaced parallel to the overall strike of the Red Sea as the earthquake focal mechanisms observed on 12th and 13th December 2011, which were then followed by the subaerial eruption witnessed by Yemeni fishermen on 18th December 2011, and the formation of a new volcano in mid-ocean ridge system at Sholan Island, Read Sea.

HOW DO WE DECIPHER THE RECORD PRESERVED IN MINERALS, GLASSES, AND ROCK TEXTURES TO CONSTRAIN THE TIMESCALES AND DYNAMICS OF MAGMATIC PROCESSES AT DEPTH?

Textural, petrological and chemical forensic approaches are critical in the interrogation of igneous rocks, and in determining the processes through which they formed. As elsewhere in this volume, we highlight the additional insight that can be gained by combining approaches, or linking traditional and more novel methods.

Seitz et al. (2018) use nanoscale secondary ion mass spectrometry, coupled to compared quartz zonation, Ti-in-quartz thermometry, and diffusion chronometry to assess eruption timescales for coeval rhyolitic crystal-rich and crystal-poor magmas from the Jurassic Chon Aike Province in Patagonia (Argentina). The data support rapid melt extraction and eruption in < 10 years in the crystal-poor systems. It also supports rapid (< 3 years) and violent eruption within the crystal mushes, but only after long storage in a reservoir affected by continuous thermal fluctuation. Critically, the authors show that the mobilization and eruption of both crystal-rich and crystal-poor magmas can occur over the same short timescales.

Also, working in silica-rich volcanism, Bindeman et al. use a combination of Ar-Ar dating, isotopic analysis, petrological, and thermomechanical modeling to investigate the genesis of voluminous eruptible rhyolites leading to caldera-forming eruptions. By exploring the diversity of compositional flavors found at the Karymshina caldera, which is the largest silicic system of the Kamchatka Peninsula (eastern Russia), the authors capture the magmatic diversity arising from fractional differentiation of mantle-derived basalts and assimilation of mafic crust produced during basalt magmatism. The time-integrated isotopic analysis reveal that the generation of these "super-rhyolites" required increasing magma differentiation and that the spikes of rhyolitic magmatism were likely driven by delamination of cumulates and lithospheric mantle after 4 million years of crustal thickening.

Similar insight can be achieved by applying multiple methods to mafic magmatism. Ubide et al. provide a very detailed textural and geochemical analysis using laser ablation time-of-flight mass spectrometry and clinopyroxene-melt thermobarometric and hygrometric calibrations to accurately track the depth, temperature, and water content of the shoshonite magmas from Stromboli volcano (Italy). They found that the volcanic system of Stromboli was originally dominated by protracted periods of magma replenishment and convection, punctuated by rapid megacryst evacuation and eruption upon arrival of more mafic magma (days to weeks). Since the inception of current steady-state activity, the melts from injections triggering eruptions have become appreciably more mafic, suggesting that intrusion of primitive magma may be a key driver of the modern eruption's dynamics at Stromboli.

Karlstrom et al. tackle a very different challenge, and use thermochronological methods to probe the mechanics of flood basalt emplacement and the tempo of individual eruptions, targeting two exhumed dikes from the Columbia River Flood Basalt province in northeast Oregon, USA (e.g., Ho and Cashman, 1997; Camp et al., 2017). Using apatite and zircon (U-Th)/He thermochronology, thermal modeling of melt-fraction temperature relationships for the intruding magma and a Bayesian Markov-Chain Monte Carlo inverse modeling framework, Karlstrom et al. interrogate partly and un-reset ages (i.e., crystallization age of host pluton) and reset ages (i.e., exact timing of dike emplacement), to define distinct emplacement histories for the two magma bodies. The inverse modeling shows that while one dyke was fed continuously over 1–6 years, the other had a shorter thermal lifespan with an unsteady heating rate suggestive of low magma flows. The authors highlight the power of Bayesian inversion methods to quantify magmatic processes that have hitherto been challenging to constrain.

Finally, Potter et al. (2018) showcase a time-integrated petrological and geochemical investigation of basalts from the Kimama borehole in the Snake River Plain of central Idaho, USA (Shervais et al., 2011, 2012, 2013). This rock core links eruptive processes to the construction of mafic intrusions and highlights the cyclic variations in basalt composition caused by temporal chemical heterogeneity related to fractional crystallization and assimilation of previously-intruded mafic sills over 5.5-million-year history. Through detailed logging of distinct lava flows representing single eruptive episodes and flow groups, the time-integrated chemical variation can be constrained. Potter et al. (2018) propose that this evolution is related to source heterogeneity, magma processing during physical, and chemical evolution of the layered intrusions, and varying degrees of assimilation of gabbroic to ferrodioritic sills at shallow to intermediate depths over short periods of time.

CONCLUDING REMARKS

Understanding the volume and timescales of magmatic processes, and the controls on the evolution of magmatic systems have become key challenges in twenty-first century geoscience. In this introduction, we have highlighted how cross-disciplinary approach that fosters the collaboration of scientists of different expertise can constrain new insight into the physical and chemical properties of magmatic systems, from both single to repetitive events, and across a wide range of both spatial and temporal scales.

The original multidisciplinary research presented here has been driven by the need to correlate magmatic processes across the storage system, with volcanic eruptions at surface, and the associated geological hazards. The papers presented in this Research Topic all address the complexities necessitated by a three-dimensional and time-integrated (4D) view of magmatic systems. These contributions indeed offer new perspectives on how magmas evolve, how they feed active volcanoes, and how to link volcanism and plutonism within this "top-to-bottom" approach of observing and decoding surface processes to monitor deep processes in the Earth's interior.

AUTHOR CONTRIBUTIONS

MP drafted the first version of the manuscript. All authors contributed to the final version of the manuscript.

ACKNOWLEDGMENTS

We are grateful for the support of Frontiers in Earth Science in producing this Research Topic as ebook, for the efforts of reviewers in improving the content of each contribution, and to Ursula Rabar, Andrea Lazenby, and Emily Legge for professional and efficient editorial support. We thank Olivier Bachmann (ETH-Zurich) as Guest Editor of Part I of this Research Topic and Valerio Acocella (University of Roma Tre) as Editor-in-Chief for editorial handling of Part I and II of this Research Topic. MP acknowledges the support of the SNF Ambizione Fellowship (grant PZ00P2_168166). BT acknowledges support by the National Research Foundation Singapore and the Singapore Ministry of Education under the Research Centers of Excellence Initiative. This work comprises Earth Observatory of Singapore contribution. KD acknowledges the support of the Natural Environment Research Council Fellowship (Grants NE/M018687/1 and NE/M018687/2).

REFERENCES

Bowen, N. L. (1928). *Evolution of the Igneous Rocks*. Princeton, NJ: Princeton University Press.

Camp, V. E., Reidel, S. P., Ross, M. E., Brown, R. J., and Self, S. (2017). Fieldtrip guide to the vents, dikes, stratigraphy, and structure of the Columbia river basalt group, eastern oregon and southeastern Washington. *Sci. Invest. Rep.* 5022, 1–88. doi: 10.3133/sir20175022N

Campbell, I. H., and Taylor, S. R. (1985). No water, no granites – no oceans, no continents. *Geophys. Res. Lett.* 10, 1061–1064. doi: 10.1029/GL010i011p01061

Cogley, C. G. (1984). Continental margins and the extent and number of the continents. *Rev. Geophys.* 22, 101–122. doi: 10.1029/RG022i002p00101

Crisp, J. A. (1984). Rates of magma emplacement and volcanic output. *J. Volcanol. Geother. Res.* 20, 177–211. doi: 10.1016/0377-0273(84)90039-8

Hartley, M., and Maclennan, J. (2018). Magmatic densities control erupted volumes in icelandic volcanic systems. *Front. Earth Sci.* 6:29. doi: 10.3389/feart.2018.00029

Ho, A. M., and Cashman, K. V. (1997). Temperature constraints on the Ginkgo flow of the Columbia River Basalt Group. *Geology* 25, 403–406. doi: 10.1130/0091-7613(1997)025<0403:TCOTGF>2.3.CO;2

Magee, C., Stevenson, C. T. E., Ebmeier, S. K., Keir, D., Hammond, J. O. S., Gottsmann, J. H., et al. (2018). Magma plumbing systems: a geophysical perspective. *J. Pet.* 59, 1217–1251. doi: 10.1093/petrology/egy064

Potter, K. E., Shervais, J. W., Christiansen, E. H., and Vetter, S. K. (2018). Evidence for cyclical fractional crystallization, recharge, and assimilation in basalts of the kimama drill core, Central Snake River Plain, Idaho: 5.5-million-years of petrogenesis in a mid-crustal sill complex. *Front. Earth Sci.* 6:10. doi: 10.3389/feart.2018.00010

Reuber, G. S., Kaus, B. J. P., Popov, A. A., and Baumann, T. S. (2018). Unraveling the physics of the yellowstone magmatic system using geodynamic simulations. *Front. Earth Sci.* 6:117. doi: 10.3389/feart.2018.00117

Seitz, S., Putlitz, B., Baumgartner, L., Meibom, A., Escrig, S., and Bouvier, A.-S. (2018). A NanoSIMS investigation on timescales recorded in volcanic quartz from the silicic chon aike province (Patagonia). *Front. Earth Sci.* 6:95. doi: 10.3389/feart.2018.00095

Shervais, J. W., Evans, J. P., Christiansen, E. H., Schmitt, D. R., Kessler, J. A., Potter, K. E., et al. (2011). Project hotspot: the Snake river scientific drilling project. *Geotherm. Resourc. Council Transac.* 35, 995–1003.

Shervais, J. W., Nielson, D. L., Evans, J. P., Christensen, E. J., Morgan, L., Shanks, W. C., et al. (2012). Hotspot: the Snake River geothermal drilling project – initial report. *Geotherm. Resourc. Council Transac.* 36, 767–772.

Shervais, J. W., Schmidt, D. R., Nielson, D., Evans, J. P., Christiansen, E. H., Morgan, L., et al. (2013). First results from HOTSPOT: the Snake river plain scientific drilling project, Idaho, USA. *Sci. Drill.* 15, 36–45. doi: 10.5194/sd-15-36-2013

Smith, R. B., Jordan, M., Steinberger, B., Puskas, C. M., Farrell, J., Waite, G. P., et al. (2009). Geodynamics of the yellowstone hotspot and mantle plume: seismic and GPS imaging, kinematics, and mantle flow. *J. Volcanol. Geother. Res.* 188, 26–56. doi: 10.1016/j.jvolgeores.2009.08.020

Taylor, S. R. (1989). Growth of planetary crusts. *Tectonophys* 161, 147–156. doi: 10.1016/0040-1951(89)90151-0

Vasco, D., Puskas, C., Smith, R., and Meertens, C. (2007). Crustal deformation and source models of the Yellowstone volcanic field from geodetic data. *J. Geophys. Res. Solid Earth* 112:B07402. doi: 10.1029/2006JB004641

White, S. M., Crisp, J. A., and Spera, F. J. (2006). Long-term volumetric eruption rates and magma budgets. *Geochem. Geophys. Geosyst.* 7:Q03010. doi: 10.1029/2005GC001002

Xu, W., Ruch, J., and Jónsson, S. (2015). Birth of two volcanic islands in the southern Red Sea. *Nat. Commun.* 6:7104. doi: 10.1038/ncomms8104

Conflict of Interest: The authors declare that the research was conducted in the absence of any commercial or financial relationships that could be construed as a potential conflict of interest.

frontiers
in Earth Science

ORIGINAL RESEARCH
published: 24 September 2018
doi: 10.3389/feart.2018.00141

Seismicity Associated With the Formation of a New Island in the Southern Red Sea

Jade H. W. Eyles[1,2], Finnigan Illsley-Kemp[1,3], Derek Keir[1,4]*, Joël Ruch[5,6] and Sigurjón Jónsson[6]

[1] Ocean and Earth Science, University of Southampton, Southampton, United Kingdom, [2] School of Environmental Sciences, University of East Anglia, Norwich, United Kingdom, [3] School of Geography, Environment and Earth Sciences, Victoria University of Wellington, Wellington, New Zealand, [4] Dipartimento di Scienze della Terra, Universita degli Studi di Firenze, Florence, Italy, [5] Department of Earth Sciences, University of Geneva, Geneva, Switzerland, [6] Physical Science and Engineering Division, King Abdullah University of Science and Technology, Thuwal, Saudi Arabia

OPEN ACCESS

Edited by:
Benoit Taisne,
Nanyang Technological University,
Singapore

Reviewed by:
Luca De Siena,
University of Aberdeen,
United Kingdom
Eisuke Fujita,
National Research Institute for Earth
Science and Disaster Prevention,
Japan

***Correspondence:**
Derek Keir
d.keir@soton.ac.uk

Specialty section:
This article was submitted to
Volcanology,
a section of the journal
Frontiers in Earth Science

Received: 04 June 2018
Accepted: 05 September 2018
Published: 24 September 2018

Citation:
Eyles JHW, Illsley-Kemp F, Keir D,
Ruch J and Jónsson S (2018)
Seismicity Associated With
the Formation of a New Island
in the Southern Red Sea.
Front. Earth Sci. 6:141.
doi: 10.3389/feart.2018.00141

Volcanic eruptions at mid-ocean ridges are rarely witnessed due to their inaccessibility, and are therefore poorly understood. Shallow waters in the Red Sea allow the study of ocean ridge related volcanism observed close to sea level. On the 18th December 2011, Yemeni fishermen witnessed a volcanic eruption in the Southern Red Sea that led to the formation of Sholan Island. Previous research efforts to constrain the dynamics of the intrusion and subsequent eruption relied primarily on interferometric synthetic aperture radar (InSAR) methods, data for which were relatively sparse. Our study integrates InSAR analysis with seismic data from Eritrea, Yemen, and Saudi Arabia to provide additional insights into the transport of magma in the crust that fed the eruption. Twenty-three earthquakes of magnitude 2.1–3.9 were located using the Oct-tree sampling algorithm. The earthquakes propagated southeastward from near Sholan Island, mainly between December 12th and December 13th. The seismicity is interpreted as being induced by emplacement of a ∼12 km-long dike. Earthquake focal mechanisms are primarily normal faulting and suggest the seismicity was caused through a combination of dike propagation and inflation. We combine these observations with new deformation modeling to constrain the location and orientation of the dike. The best-fit dike orientation that satisfies both geodetic and seismic data is NNW-SSE, parallel to the overall strike of the Red Sea. Further, the timing of the seismicity suggests the volcanic activity began as a submarine eruption on the 13th December, which became a subaerial eruption on the 18th December when the island emerged from the beneath the sea. The new intrusion and eruption along the ridge suggests seafloor spreading is active in this region.

Keywords: Red Sea, mid-ocean ridge, dike, seismicity, InSAR, eruption

INTRODUCTION

Magma motion through the crust can induce earthquakes, the analysis of which is a useful tool to understand when, where, and how magma is transported. The understanding of magma intrusion and volcanism is key for understanding dynamic processes that occur at divergent boundaries (e.g., Ebinger et al., 2013; Pagli et al., 2015; Ruch et al., 2016; Wilcock et al., 2016). However, the understanding of the extensional processes at submarine ocean ridges in space and time is limited by the difficulty associated with observing seismicity and ground deformation in the deep oceans (e.g., Soule et al., 2007; Carey et al., 2018). Over the past 20 years, the Southern Red Sea has experienced six seismic swarms interpreted to be related to magma intrusions (Xu et al., 2015). The Southern Red Sea has a large proportion of shallow waters, which provide a rare opportunity to study volcanic eruptions that occur above sea level (**Figure 1**). Three sub-aerial volcanic eruptions have occurred in the last decade: on Jebel at Tair island (2007) and two eruptions resulting in the formation of Sholan Island (2011) and Jadid Island (2013) (Jónsson and Xu, 2015). All the islands lie on the rift axis of the Southern Red Sea. The eruptions of Jebel at Tair and Jadid lasted 8 and 2 months, respectively, and followed short duration (days) low magnitude ($M > 4$) seismic swarms thought to be caused by the intrusion of magma through the crust to the Earth's surface (Xu et al., 2015). The eruption of Jebel at Tair was subaerial, while the first half of the Jadid eruption was submarine (Xu et al., 2015).

The eruption of Sholan Island occurred between Haycock and Rugged islands in the Zubair Archipelago and was first witnessed by Yemeni fishermen on the 18th December 2011 (**Figure 2**). The eruption started as submarine activity before erupting as a surtseyan eruption, and lasted until the 12th January 2012 (Jónsson and Xu, 2015). A SO_2 anomaly was first recorded on the 19th December from the Ozone Monitoring Instrument (OMI) taken on NASA's EOS-AURA satellite; maximum SO_2 values reached 2.06 DU. The newly formed island joined ten pre-existing volcanic islands known as the Zubair Archipelago (**Figure 2**); the island consisted primarily of hydromagmatic deposits reaching a maximum of 0.25 km^2 (Xu et al., 2015). The Sholan eruption was soon followed by the eruption and formation of Jadid Island in September 2013, situated between Saddle and Saba Islands (**Figure 2**). The eruption at Jadid lasted for 54 days and the island reached a maximum size of $\sim$0.68 km^2 (Xu et al., 2015). Optical imagery taken from the Sentinel-2 satellites shows that Sholan and Jadid island are still visible today.

Xu et al. (2015) used interferometric synthetic aperture radar (InSAR) to measure centimeter-scale ground deformation during the eruption of Sholan and Jadid islands, and modeled dikes to account for the observed deformation. For the Sholan eruption one interferogram from 13th October 2011 to the 15th December 2012 was used for interpretation; 1.5 and 3 cm of deformation were observed on Saba and Zubair islands, respectively. In addition, optical imagery on the 23rd December 2011 showed the eruption coming from a short N-S fissure as well as a new fracture system orientated NW-SE on Haycock Island (Xu et al., 2015). Accounting for this widespread deformation, Xu et al. (2015) modeled a 1.5 m thick, 10-km-long, north-south orientated feeder dike under Sholan Island responsible for this eruption. For the 2013 Jadid eruption, two interferograms were obtained showing several continuous deformation fringes on Saba and Zubair island; a 1 m thick, 12 km long, NNW-SSE oriented dike was modeled (**Figure 2**).

Preceding the Sholan eruption, three distinct seismic swarms occurred in April, June, and August 2011 and the Yemeni seismological network detected two earthquakes of magnitude 3.7 and 3.9 on the 13th December 2011, taken from the International Seismic Catalogue (ISC). In this study we investigate the temporal and spatial variability in seismic activity prior to the eruption of Sholan Island. Analysis of seismic data from local seismic networks in Eritrea, Yemen, and Saudi Arabia allows us to locate earthquakes surrounding the island which were not recorded by the ISC. The increased number of earthquakes that we detect, coupled with improved relative earthquake locations, allows us to place constraints on the location, timescales and direction of intrusion that fed the eruption. In addition, we use the seismic results to guide new deformation models created from InSAR data. Our data of land-based stations positioned relatively close to an ocean ridge place rare constraints on a seafloor-spreading episode and provide additional insights into the rifting mechanics of the Southern Red Sea.

Tectonic Setting

The Red Sea formed due to the divergence of the Nubian and Arabian plates (Bosworth et al., 2005). Extension and rifting started 25 Ma, the emplacement of dikes throughout the Red Sea begun 24 Ma which was associated with increased volcanism in the region (Bosworth et al., 2005). Rifting of the Red Sea then continued in episodic periods, with seafloor spreading initiating 5 Ma (Bosworth et al., 2005). Magnetic anomalies between 16 and 19^{o}N display five symmetrical magnetic stripes that are interpreted to have begun 3 Ma (Bonatti, 1985; Almalki et al., 2016). Further north, magnetic anomalies become discontinuous before disappearing. This has led some authors to propose that spreading is confined to the Southern Red Sea (Bonatti, 1985), whereas other authors suggest that spreading is evident throughout the Red Sea with the southern end being further evolved (Schettino et al., 2016).

South of 17°N, GPS measurements show the locus of extension splits into two branches: the continuation of the Red Sea ridge in the east, and the Danakil depression to the west (McClusky et al., 2010; **Figure 1**). The bifurcation of the rift into the Danakil depression is thought to have begun 9 Ma (Le Pichon and Gaulier, 1988). The rate of extension increases from 15 mm/year at 16°N to 20 mm/year in the south (13°N), with extension predominantly ENE-WSW (McClusky et al., 2010). GPS velocities show that north of 16^{o}N lateral extension is fully accommodated by the Red Sea ridge, whereas south of 13°N lateral extension is accommodated purely in the Danakil depression (McClusky et al., 2010). Together these account for the total relative plate motion of the Arabian and Nubian plates. The termination of the Southern Red Sea rift is unclear due to conflicted data; bathymetry and gravity data suggests the termination at 14°N, whereas magnetic stripes are only recorded until 15.5°N (Almalki et al., 2016). This suggests a gradual change in spreading from the Red Sea ridge to the Danakil block; extension in the Red Sea ridge decreases to the south, whereas

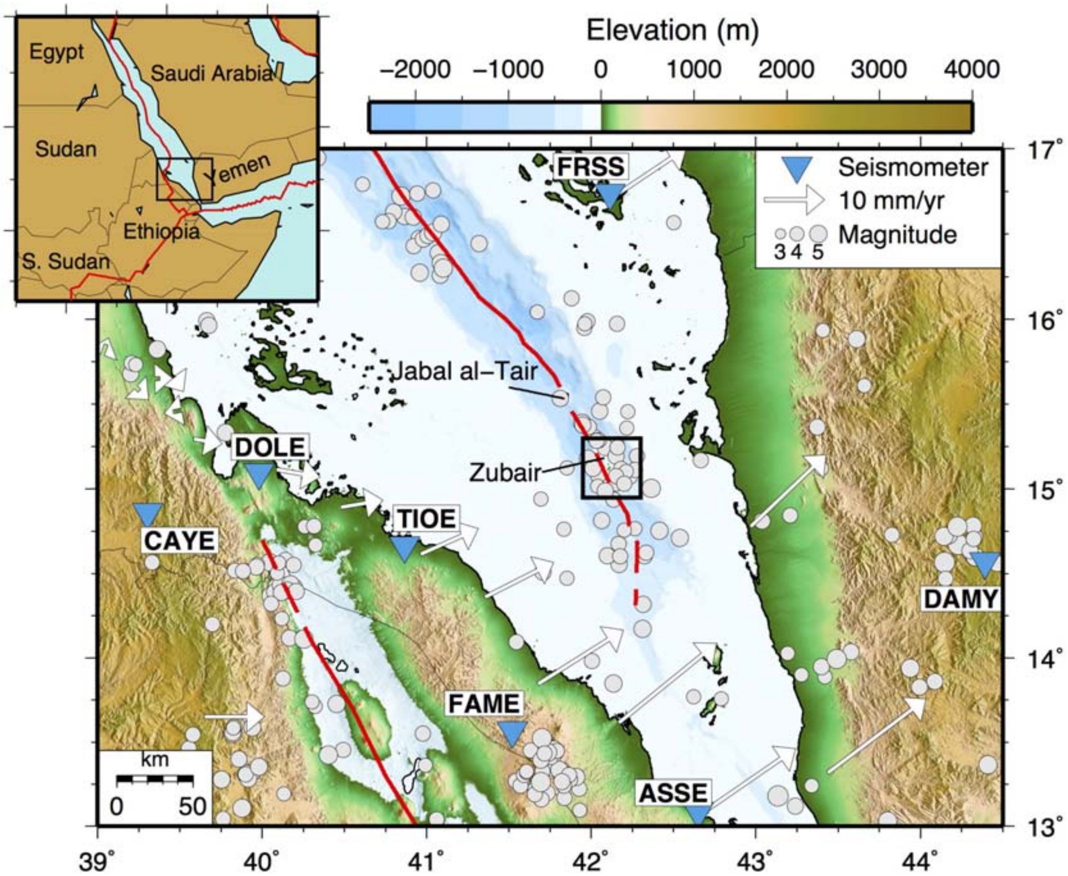

FIGURE 1 | Topographic map of the Southern Red Sea. Gray circles show the NEIC earthquake catalog locations from 1950 to present, red lines denote the axis of extension in the Red Sea and Danakil Depression. GPS measurements taken from McClusky et al. (2010) with respect to the Nubian plate. Black box denotes the Zubair archipelago.

extension gradually increases to the south in the Danakil depression resulting in overlapping ridges in the region 14.5–15.5°N.

The Zubair archipelago (at 15–15.2°N) is a 25 km by 10 km shallow platform [<100 m below sea level (bsl)] orientated parallel to the Red Sea ridge; it consists of ∼10 volcanic islands situated along the central axis of the Red Sea (Jónsson and Xu, 2015). The islands follow a general NW-SE orientation and consist of basaltic tuff, conglomerate, and lava (Jónsson and Xu, 2015). Prior to volcanic activity at the Zubair islands, two known eruptions at Saddle island in 1824 and 1846 are reported, leaving a century of quiescence (Jónsson and Xu, 2015). Over the past few decades the region has seen increased activity. A major rifting event with the intrusion of 14 dykes, and 4 eruptions occurred during 2005–2010 along the Manda Hararo rift segment in Afar (e.g., Wright et al., 2006; Barnie et al., 2016). This was coincident with the eruptions of Jebel at Tair island in 2007 (Xu and Jónsson, 2014) and Alu-Dalafilla in 2008 (Pagli et al., 2012), and followed by the eruptions of Erta Ale in 2010 (Field et al., 2012), Nabro in 2011 (Hamlyn et al., 2014; Goitom et al., 2015), and also increased volcanic activity of the western Gulf of Aden (Ahmed et al., 2016) and of the Zubair Archipelago (Jónsson and Xu, 2015).

DATA AND METHODS

We used seven broadband seismometers in Eritrea, Yemen, and Saudi Arabia (**Figure 1**). A Butterworth band pass filter was applied to the data to only allow frequencies between 1 and 10 Hz for the stations in Eritrea, and 1–8 Hz for the Yemen and Saudi Arabia stations due to a higher level of noise. Earthquakes were manually picked for both P and S waves, and events with a minimum of four arrival times at three stations were located with NonLinLoc, using the Oct-Tree Sampling Algorithm (Lomax et al., 2000). Due to the large distance between stations and earthquakes, the depth of events cannot be reliably constrained, and we therefore fix the depth of earthquakes to 5 km. This is well within the ∼10 km thick crust. We compared locations for depths from 1 to 9 km, which can be seen in **Supplementary Figure 1**. The variance in locations for latitude and longitude were low, showing that constraining the depth to 5 km has minimal overall effect on the location (**Supplementary Table 1**). For our final locations, we used a two-dimensional velocity model based on controlled source experiments (Berckhemer et al., 1975; Egloff et al., 1991). This took into account the shallow low velocity mantle recorded at the rift axis, and the deepening of the Moho

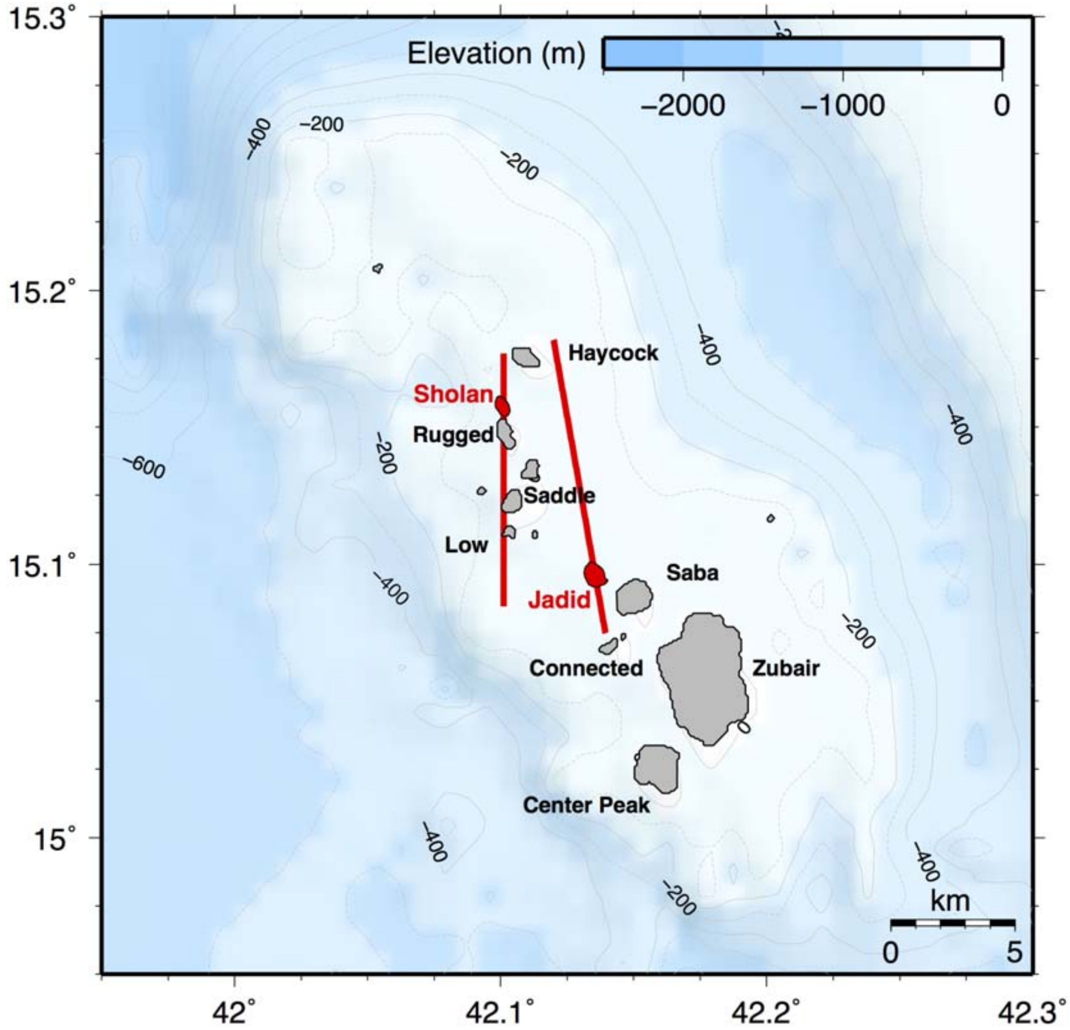

FIGURE 2 | The Zubair archipelago in the Southern Red Sea. Sholan and Jadid Island, erupted in 2011 and 2013, respectively, are shown in red. Proposed dike locations from Xu et al. (2015) are shown as red lines.

along the rift flanks to a maximum depth of 25 km. A constant sediment thickness of 2 km was used across the profile. A variety of velocity models were input into NonLinLoc to see how the overall location of earthquakes varied for different models. A comparison of the locations achieved using the 1D model (**Supplementary Figure 2**) with those achieved with the final 2D model (**Supplementary Figure 3**) used for this study show similar locations for the earthquakes. The 1D model produced more scattered locations, but the relative distribution of earthquakes in both space and time is similar to the extent that our overall interpretation would remain unchanged.

Magnitudes are calculated by measuring the maximum peak-to-peak amplitude and using the local magnitude scale of Illsley-Kemp et al. (2017). Seismic moment release (M_o) is determined using empirical relationships between M_L, m_b, and M_o (e.g., Kanamori, 1977; Hanks and Kanamori, 1979; Scordilis, 2006). Focal mechanisms were further calculated using P-wave polarities and the software FocMec (Snoke, 2003).

RESULTS

Using arrival times from a minimum of 3 and up to 7 seismic stations, we locate 28 individual earthquakes in NonLinLoc in the vicinity of the islands from the 5th December 2011 to the 12th January 2012. Latitude and longitude errors were calculated in NonLinLoc; these are statistical errors based on the probability density function of each earthquake's location (**Supplementary Figure 3**). Five additional earthquakes were removed due to having error bars larger than 5 km, leaving 23 earthquakes that were used for final analysis that define a broadly NW-SE trend (**Figure 3**). Further information on the earthquakes location, errors and statistics can be found in **Supplementary Table 1**. The main seismic events are focused within the Zubair archipelago and occurred during the 12th and 13th December with just two events after this time period (**Figure 4**). The first earthquakes, on the 12th December occur to the north of Sholan island, beneath Haycock island, and then migrate southeast to Saba island with

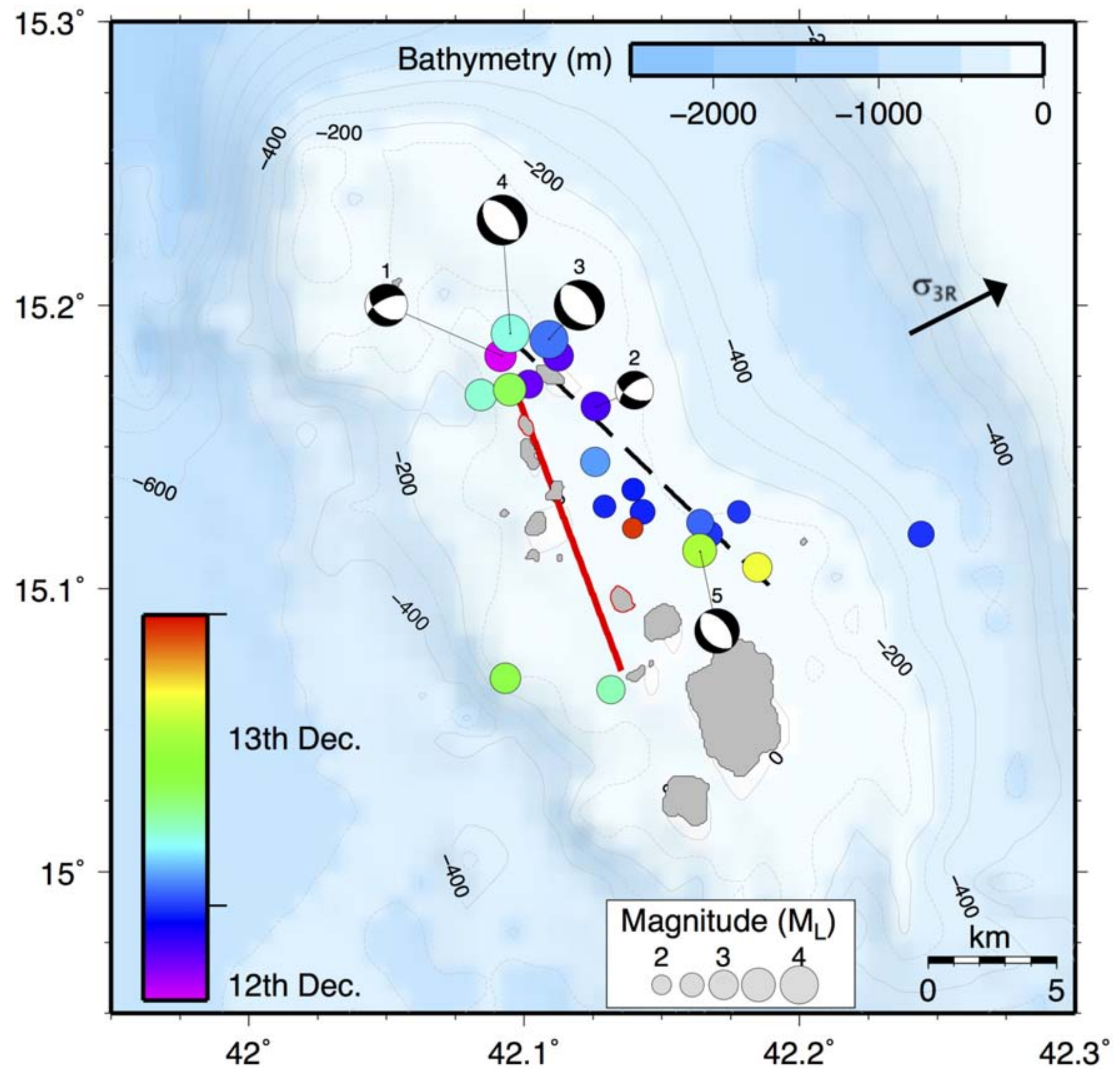

FIGURE 3 | The Sholan seismic sequence with earthquakes colored by time. Focal mechanisms show three normal faulting and two strike-slip faulting events. The black dashed line denotes the inferred dike location taken from earthquake hypocenters only; the red line denotes the final dike location taken from combining ground deformation and earthquake hypocenters.

time (**Figure 3**). The computed errors in horizontal earthquake location are within ±5 km. The PDF scatter clouds produced by NonLinLoc can be seen in **Figure 3**.

The calculated local magnitudes (M_L) vary from 2.1 to 3.9, with the majority of earthquakes ranging from 2.5 to 3.5 (**Figure 4**). No temporal trend in M_L with time can be seen over the 12th–13th December. However, a cluster of low magnitude events is observed at the end of the 12th December. Larger magnitudes are observed north of the island with M_L 2–3 earthquakes further south (**Figure 3**). Cumulative seismic moment calculated over December shows the majority of the energy release occurring on the 12th–13th December, in agreement with the number of events. A gradual increase in energy release to 19×10^{14} Nm is observed over the 12th and 13th December, with little additional energy from the two events on the 16th and 27th (**Figure 4**). Due to quality of data, only five focal mechanisms were adequately constrained (**Table 1** and **Figure 3**). The solutions show a combination of normal fault and strike-slip fault plane solutions (**Figure 3**).

TABLE 1 | Focal plane solutions of five events on 12th–13th December 2011.

ID	DATE	TIME	LAT.	LONG.	MAG.	STRIKE	DIP	RAKE
1	12/12/11	16:59:27	15.182	42.092	3.27	127.4	44.9	−35.3
2	12/12/11	20:45:20	15.164	42.126	2.99	117.0	54.9	−36.3
3	13/12/11	01:22:12	15.188	42.109	3.92	323.5	50.1	−86.1
4	13/12/11	05:01:49	15.190	42.095	3.92	322.1	50.1	−86.1
5	13/12/11	13:02:31	15.113	42.164	3.47	322.1	50.1	−86.7

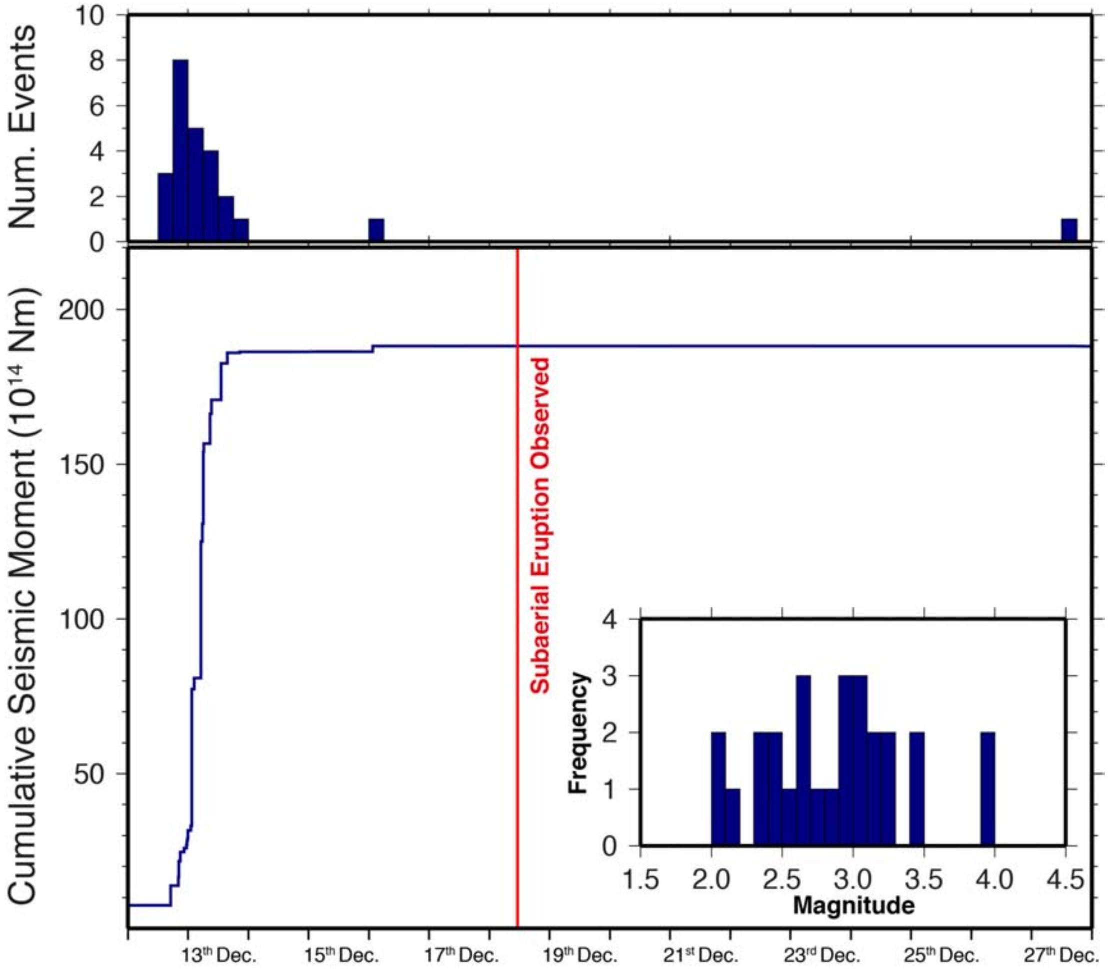

FIGURE 4 | Cumulative seismic moment release and number of events over December 2011 for the Sholan seismic sequence. Inset: histogram displaying the range of magnitudes for events in December 2011. Red line denotes the start of the subaerial eruption.

DISCUSSION

The locations of 23 earthquakes in the Zubair Archipelago shows a clustering of events that follow a NW-SE trend. The variation of event locations with time shows a progression toward the south originating from near Sholan island, with larger magnitude events occurring at either end of the sequence. Earthquakes are commonly induced at the leading edge of a propagating dike due to concentration of extensional stresses (e.g., Roman and Cashman, 2006). We therefore interpret southwards migration of hypocenters on the 12th–13th December as suggesting movement of the dike away from Sholan island. Subsequent earthquakes later on the 13th December, after the initial movement, show hypocenters located at either end of the dike migration pattern. These earthquakes are consistent with the pattern of seismicity at the edges of the final position of the dike once it has reached its full length (**Figure 3**). No spatial or temporal pattern is observed with magnitude during the time frame studied. Using the range of magnitudes calculated, it is suggested that no events under M_L 2 would be recorded. The lack of recorded earthquakes with magnitudes less than 2 is likely due to the distance of the seismic stations from the located hypocenters, which varies from 140 to 300 km. Analysis of seismic moment release shows that the majority of energy release occurred over a 24-h period from the 12th–13th December. This supports results found for the main dike propagation event.

The focal plane solutions show two focal mechanisms (1, 2) which occur on the 12th December in the early stages of dike propagation (**Figure 3**). Both these events display a large component of strike-slip deformation, with p-axes oriented 70° from the regional maximum horizontal compressive stress (σ_{1R}). These two earthquakes are best explained by a model proposed by Roman (2005), which suggests that earthquakes within the walls around a dike growing in width will have p-axes near perpendicular to σ_{1R}. We therefore infer that dike propagation is accompanied by dike inflation, likely behind the propagating tip of the dike. The remaining three focal mechanisms (3, 4, 5) occur on the 13th December, once the dike propagation has largely ceased (**Figure 3**). All three events are located near the tips of the proposed dike location, two near Sholan island and one near Jadid (**Figure 3**). The location and normal mechanism with extension parallel to the regional minimum compressive stress (σ_3) is consistent with that expected to be caused by induced stress changes near the dike tips, which promotes normal faulting (e.g., Rubin and Gillard, 1998; Roman and Cashman, 2006).

Xu et al. (2015) proposed a north-south orientation of the feeder dike for the Sholan eruption and a NW-SE feeder dike for the 2013 Jadid eruption (**Figure 2**). With the Sholan eruption, their north-south strike was based partly on the short (∼300 m) north-south oriented eruptive fissure and north-south co-diking cracks seen in an optical satellite image from the early phase of the eruption (23 December, 2011). In addition, the modeled ground deformation caused by a N-S striking dike is not inconsistent with the observed ground deformation data. However, the earthquake epicenters found in our study suggests the feeder dike for the Sholan eruption is more likely to strike sub-parallel to the Red Sea rift.

In order to reconcile the observed ground deformation pattern, eruption and ground fracturing locations, and the seismicity we used rectangular dislocations in an elastic halfspace to model the dike opening, and calculated the expected surface deformation from several different possible dike locations. For the models we use a dike depth of 0–5 km, vertical dip, and thickness of 0.5 m. We show the modeled ground deformation patterns from Xu et al. (2015) (**Figure 5A**), from interpretation of the dike position based solely on seismicity (**Figure 5B**), and from a combination of seismicity and the constraints used in Xu et al. (2015; **Figure 5C**). This shows that the calculated deformation pattern on Saba and Zubair islands, where the InSAR observations of Xu et al. (2015) provide key information, is strongly controlled by the location of the SE end of the modeled dike. When the SE end of the dike is NE of Saba and Zubair islands, as constrained from seismicity only (**Figure 5B**), the predicted deformation pattern is inconsistent with the InSAR observations. We thus modified the location of the modeled dike for it to pass through Sholan Island and changed the strike from NW-SE to NNW-SSE such that the SE end is west of Saba and Zubair islands (**Figure 5C**). This modeled dike location agrees with the observed deformation fringes on Saba and Zubair islands, and better reflects the orientation of the seismic cluster. The shift in dike position from that based solely on seismicity, to that based on seismicity and geodesy, are within the error bars of the earthquake locations.

In order to understand the migration of the earthquakes with time, a projection was taken along the length of the inferred dike and compared with the hypocenters of the earthquakes (**Figure 6**). Here we can clearly see that the southward dike propagation occurs between 17:00 on the 12th December and 02:00 on the 13th December, and by varying isotachs (lines of constant speed) we estimate that the dike propagated at a rate of 0.32 ms^{-1}. This compares with a dike propagation event seen at Bárðarbunga in August 2014 which had dike propagation rates of up to 0.83 m/s (Sigmundsson et al., 2015). Propagation rates of 0.2–0.6 km/s was also observed during dike intrusions of both the Krafla and Dabbahu spreading episode (Brandsdottir and Einarsson, 1979; Einarsson, 1991; Keir et al., 2009; Wright et al., 2012). Once the dike had ceased propagating the seismic activity was limited to either end of the dike, near Sholan and Jadid islands.

The cessation of the dike to the south is likely due to the dike reaching a stress barrier such as caused by a topographic load (Urbani et al., 2018), layering in the bedrock (Rivalta et al., 2015), or due to the exhaustion of the magma supply. Topographic loads alter the surrounding stress field, making it difficult for subsurface magma to propagate upslope (Rivalta et al., 2015; Urbani et al., 2018). Similarly, bedrock heterogeneity can result in strong contrasts in elastic parameters, stopping the dike (Rivalta et al., 2015). Due to the eruption occurring several days after the seismic activity, we suggest that the cessation of the dike is not due to magma exhaustion, and instead a result of reaching a stress

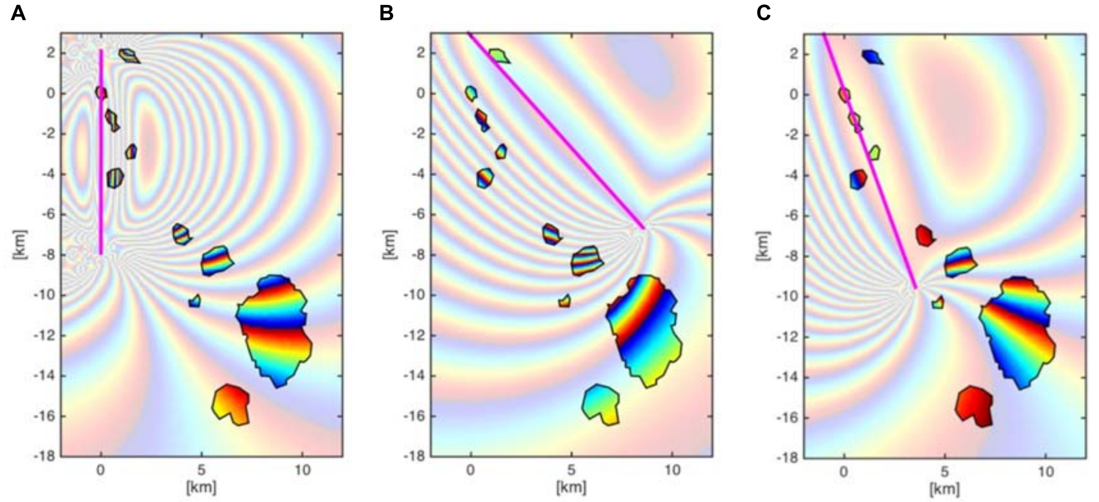

FIGURE 5 | Interferograms produced by modeling the ground deformation pattern using different dike locations. **(A)** Original dike location produced by Xu et al. (2015). **(B)** Dike location interpreted purely from earthquake hypocenters. **(C)** Dike location that satisfies seismicity and geodesy data.

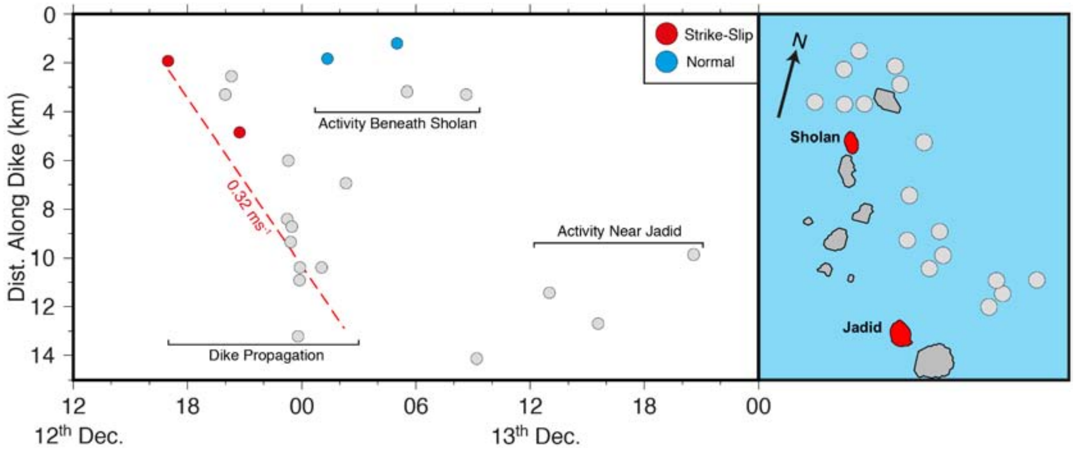

FIGURE 6 | The Sholan seismic sequence projected along the length of the proposed dike. The dike propagation phase is clearly seen with activity at either end of the dike continuing once propagation has ceased. The red dashed line shows the 0.32 ms^{-1} isotach indicating the speed of dike propagation.

barrier, resulting in the eruption occurring at the beginning of the dike.

Little seismicity is recorded after the 13th December, with only one further earthquake recorded prior to the first observation of the subaerial eruption on the 18th December. We suggest that the eruption began as a submarine eruption on the 13th December once the dike had ceased propagating to the south. We interpret this sequence of events using insights from subaerial fissure eruptions in Afar (Belachew et al., 2011; Barnie et al., 2016), where eruptions typically began within hours of the termination of dike propagation. Water depths around Sholan island are less than 100 m, and we therefore suggest that the submarine eruption continued for 5 days, causing the volcanic edifice to increase in height such that on the 18th December it reached the surface and was observed by the Yemeni fishermen. As well as this direct observation of the subaerial eruption, an SO_2 anomaly was also observed on the 19th December. SO_2 is highly soluble in water (Butterfield et al., 2011) and anomalies are typically not observed at submarine eruptions (Barrancos et al., 2012). The lack of an SO_2 anomaly until the eruption became subaerial on the 18th December is therefore consistent with a submarine eruption between the 13th and 18th December. An alternative explanation is that the seismic activity recorded over the 12th and 13th December occurred during an initial dike intrusion that fractured the crust but failed to reach the surface. A second pulse of magma through the already formed conduit, potentially on the 16th December due to an additional earthquake on this date, resulted in the magma erupting at the surface, initiating the submarine eruption and reaching sea level on the 18th December.

There is uncertainty in the nature of the Red Sea ridge between 15.5 and 14.5°N. A lack of magnetic anomalies suggests an absence in seafloor spreading in this region, however, bathymetry data suggest the ridge continues to 14.5°N (Almalki et al., 2016). The revised dike position that we propose is somewhat similar is position and orientation to that constrained for the Jadid eruption (**Figure 2**), and suggests that both dikes were likely intruded along the same rift segment. The modeled dike thicknesses of 0.5 m for Sholan, and 1 m for Jadid are in line with the average 0.5–1.5 m dike thickness most commonly seen at mid-ocean ridges (Qin and Buck, 2008), and also consistent with the hypothesis that they are part of a multi-intrusion spreading episode (Qin and Buck, 2008). The body of evidence suggests that the Zubair archipelago is an active spreading segment with dikes intruding parallel to the trend of the Red Sea, and that the Red Sea ridge is actively accommodating extension at the southern end via spreading episodes similar to those seen at mid-ocean ridges.

CONCLUSION

We analyse a swarm of earthquakes in the Red Sea at 15–15.2°N and 42–42.3°E, associated with a subaerial volcanic eruption starting on the 18th December 2011 that resulted in the formation of Sholan Island. Intense earthquake activity on the 12th December forms a NW-SE trending cluster with the time evolution of seismicity showing a southward migration over a day period. The rapid migration of earthquakes, coupled with earthquakes focused at the lateral tips of the cluster after migration stops strongly suggests the earthquakes are caused by an intrusion that fed the eruption, broadly consistent with surface deformation patterns best modeled using the presence of a dike. The seismicity migration suggests that the dike propagated at speeds of 0.32 ms^{-1} and was approximately 12 km in length. Analysis of focal mechanisms suggests that the seismicity in the early stages of dike propagation was caused by stresses around the expanding dike. Once, propagation had halted seismicity is dominated by normal faulting suggesting dike-induced extension. We interpret dike position and a NNW-SEE orientation based on tested forward models of ground deformation pattern based on both geodetic and the new seismicity data. Observations from other dike intrusions in Afar, coupled with high solubility of SO_2 in water, suggest that a submarine eruption may have begun on the 13th December once the dike had ceased propagating. The intrusion of the dike parallel to the orientation of the Red Sea suggests seafloor spreading is still active in this region, with the increased seismicity and magmatic activity likely related to a spreading event.

AUTHOR CONTRIBUTIONS

JE conducted seismology analysis, and led the interpretation and writing of the paper. FI-K contributed to seismology analysis, interpretation, and writing the paper. DK contributed to project design, interpretation, and writing the paper. JR contributed to the project design, interpretation, and writing the paper. SJ conducted the InSAR analysis and related modeling, and contributed to interpretation and writing the paper.

FUNDING

FI-K was funded through NERC studentship NE/L002531/1 and a grant to GSNOCS from Roy Franklin O.B.E and the ECLIPSE Program funded by the New Zealand Ministry of Business, Innovation and Employment. DK was supported by NERC grant NE/L013932, and grant number OSR-2015-CRG4-2643 from King Abdullah University of Science and Technology. JE was supported by NERC studentship NE/L002582/1.

ACKNOWLEDGMENTS

We acknowledge the support of Martin Mai (KAUST) in facilitating acquisition of data from Farasan Island from the Saudi Geological Survey, who are also thanked. The remaining data was downloaded from the IRIS-DMC. We thank the reviewers EF and LDS, editor BT, and chief editor Valerio Acocella for constructive reviews.

SUPPLEMENTARY MATERIAL

The Supplementary Material for this article can be found online at: https://www.frontiersin.org/articles/10.3389/feart.2018.00141/full#supplementary-material

REFERENCES

Ahmed, A., Doubre, C., Leroy, S., Kassim, M., Keir, D., Abayazid, A., et al. (2016). Seafloor spreading event in western Gulf of Aden during the November 2010 - March 2011 period captured by regional seismic networks: evidence for diking events and interactions with a nascent transform zone. *Geophys. J. Int.* 205, 1244–1266. doi: 10.1093/gji/ggw068

Almalki, K. A., Betts, P. G., and Ailleres, L. (2016). Incipient seafloor spreading segments: insights from the Red Sea. *Geophys. Res. Lett.* 43, 2709–2715. doi: 10.1002/2016GL068069

Barnie, T. D., Keir, D., Hamling, I., Hofmann, B., Belachew, M., Carn, S., et al. (2016). A multidisciplinary study of the final episode of the Manda Hararo dike sequence, Ethiopia, and implications for trends in volcanism during the rifting cycle. *Geol. Soc. Special Publ.* 420, 149–163. doi: 10.1144/SP420.6

Barrancos, J., Padilla, G., Padron, E., Hernández, P., Calvo, D., Marquez, A., et al. (2012). Estimated CO_2, SO_2 and H_2S emission to the atmosphere from the 2011 El Hierro submarine eruption (Canary Islands) on the basis of helicopter gas surveys. *Geophys. Res. Abstr.* 14:12345.

Belachew, M., Ebinger, C., Cote, D., Keir, D., Rowland, J., Hammond, J., et al. (2011). Comparison of dike intrusions in an incipient seafloor- spreading segment in Afar, Ethiopia: seismicity perspectives. *J. Geophys. Res.* 116:B06405. doi: 10.1029/2010JB007908

Berckhemer, H., Baier, B., Bartlesen, H., Behle, A., Burkhardt, H., Gebrande, H., et al. (1975). "Deep seismic soundings in the Afar region and on the highland of Ethiopia," in *Afar Depression of Ethiopia*, eds A. Pilger and A. R ösler (Stuttgart: Schweizerbart), 89–107.

Bonatti, E. (1985). Punctiform initiation of seafloor spreading in the Red Sea during transition from a continental to an oceanic rift. *Nature* 316, 33–37. doi: 10.1038/316033a0

Bosworth, W., Huchon, P., and McClay, K. (2005). The Red Sea and Gulf of Aden basins. *J. Afr. Earth Sci.* 43, 334–378. doi: 10.1016/j.jafrearsci.2005.07.020

Brandsdottir, B., and Einarsson, P. (1979). Seismic activity associated with the september 1977 deflation of the krafla central volcano in northeastern ice- land. *J. Volcanol. Geothermal Res.* 6, 197–212. doi: 10.1016/0377-0273(79)90001-5

Butterfield, D. A., Nakamura, K. I., Takano, B., Lilley, M. D., Lupton, J. E., Resing, J. A., et al. (2011). High SO_2 flux, sulfur accumulation, and gas fractionation at an erupting submarine volcano. *Geology* 39, 803–806. doi: 10.1130/G31901.1

Carey, R., Soule, S. A., Manga, M., White, J. D., McPhie, J., Wysoczanski, R., et al. (2018). The largest deep-ocean silicic volcanic eruption of the past century. *Sci. Adv.* 4:e1701121. doi: 10.1126/sciadv.1701121

Ebinger, C. J., van Wijk, J., and Keir, D. (2013). The time scales of continental rifting: implications for global processes. *Geol. Soc. Am. Special Papers* 500, 371–396. doi: 10.1130/2013.2500(11)

Egloff, F., Rihm, R., Makris, J., Izzeldin, Y., Bobsien, M., Meier, K., et al. (1991). Contrasting structural styles of the eastern and western margins of the southern Red Sea: the 1988 SONNE experiment. *Tectonophysics* 198, 329–353. doi: 10.1016/0040-1951(91)90159-P

Einarsson, P. (1991). "The Krafla rifting episode 1975–1989," in *Nattura Myvatns (The Nature of Lake Myvatn)*, eds A. Gardarsson and A. Einarsson (Reykjavic: Icelandic Nature Science Society), 97–139.

Field, L., Barnie, T., Blundy, J., Brooker, R. A., Keir, D., Lewi, E., et al. (2012). Integrated field, satellite and petrological observations of the November 2010 eruption of Erta Ale. *Bull. Volc.* 74, 2251–2271. doi: 10.1007/s00445-012-0660-7

Goitom, B., Oppenheimer, C., Hammond, J. O. S., Grandin, R., Barnie, T., Donovan, A., et al. (2015). First recorded eruption of Nabro volcano, Eritrea, 2011. *Bull. Volc.* 77:85. doi: 10.1007/s00445-015-0966-3

Hamlyn, J. E., Keir, D., Wright, T. J., Neuberg, J. W., Goitom, B., Hammond, J. O. S., et al. (2014). Seismicity and subsidence following the 2011 Nabro eruption, Eritrea: insights into the plumbing system of an off-rift volcano. *J. Geophys. Res.* 119, 8267–8282. doi: 10.1002/2014JB011395

Hanks, T. C., and Kanamori, H. (1979). A moment magnitude scale. *J. Geophys. Res.* 84, 2348–2350. doi: 10.1029/JB084iB05p02348

Illsley-Kemp, F., Keir, D., Bull, J. M., Ayele, A., Hammond, J. O., Kendall, J.-M., et al. (2017). Local earthquake magnitude scale and b-value for the Danakil region of northern Afar. *Bull. Seis. Soc. Am.* 107, 521–531. doi: 10.1785/0120150253

Jónsson, S., and Xu, W. (2015). *Volcanic Eruptions in the Southern Red Sea During 2007-2013. The Red Sea*. Berlin: Springer, 175–186. doi: 10.1007/978-3-662-45201-1_10

Kanamori, H. (1977). The energy release in great earthquakes. *J. Geophys. Res.* 82, 2981–2987. doi: 10.1029/JB082i020p02981

Keir, D., Hamling, I. J., Ayele, A., Calais, E., Ebinger, C., Wright, T. J., et al. (2009). Evidence for focused magmatic accretion at segment centers from lateral dike injections captured beneath the Red Sea rift in Afar. *Geology* 37, 59–62. doi: 10.1130/G25147A.1

Le Pichon, X. T., and Gaulier, J.-M. (1988). The rotation of Arabia and the levant fault system. *Tectonophysics* 153, 271–294. doi: 10.1016/0040-1951(88)90020-0

Lomax, A., Virieux, J., Volant, P., and Berge-Thierry, C. (2000). "Probabilistic earth- quake location in 3D and layered models," in *Advances in Seismic Event*

Location, eds C. H. Thurber and N. Rabinowitz (Berlin: Springer), 101–134. doi: 10.1007/978-94-015-9536-0_5

McClusky, S., Reilinger, R., Ogubazghi, G., Amleson, A., Healeb, B., Vernant, P., et al. (2010). Kinematics of the southern Red Sea-Afar Triple Junction and implications for plate dynamics. *Geophys. Res. Lett.* 37:L05301. doi: 10.1029/2009GL041127

Pagli, C., Mazzarini, F., Keir, D., Rivalta, E., and Rooney, T. O. (2015). Introduction: anatomy of rifting: tectonics and magmatism in continental rifts, oceanic spreading centers, and transforms. *Geosphere* 11, 1256–1261. doi: 10.1130/GES01082.1

Pagli, C., Wright, T. J., Ebinger, C. J., Yun, S.-H., Cann, J. R., Barnie, T., et al. (2012). Shallow axial magma chamber at the slow-spreading Erta Ale Ridge. *Nat. Geosci.* 5, 284–288. doi: 10.1038/ngeo1414

Qin, R., and Buck, W. R. (2008). Why meter-wide dikes at oceanic spreading centres? *Earth Planet. Sci. Lett.* 265, 466–474. doi: 10.1016/j.epsl.2007.10.044

Rivalta, E., Taisne, B., Bunger, A., and Katz, R. (2015). A review of mechanical models of dike propagation: schools of thought, results and future directions. *Tectonophysics* 638, 1–42. doi: 10.1016/j.tecto.2014.10.003

Roman, D. C. (2005). Numerical models of volcanotectonic earthquake triggering on non-ideally oriented faults. *Geophys. Res. Lett.* 32:4. doi: 10.1029/2004GL021549

Roman, D. C., and Cashman, K. V. (2006). The origin of volcano-tectonic earthquake swarms. *Geology* 34, 457–460. doi: 10.1130/G22269.1

Rubin, A. M., and Gillard, D. (1998). Dike-induced earthquakes: theoretical considerations. *J. Geophys. Res.* 103, 10017–10030. doi: 10.1029/97JB03514

Ruch, J., Wang, T., Xu, W., Hensch, M., and Jónsson, S. (2016). Oblique rift opening revealed by reoccurring magma injection in central Iceland. *Nat. Commun.* 7:12352. doi: 10.1038/ncomms12352

Schettino, A., Macchiavelli, C., Pierantoni, P. P., Zanoni, D., and Rasul, N. (2016). Recent kinematics of the tectonic plates surrounding the Red Sea and Gulf of Aden. *Geophys. J. Int.* 207, 457–480. doi: 10.1093/gji/ggw280

Scordilis, E. M. (2006). Empirical global relations converting Ms and mb to moment magnitude. *J. Seismol.* 10, 225–236. doi: 10.1007/s10950-006-9012-4

Sigmundsson, F., Hooper, A., Hreinsdóttir, S., Vogfjörd, K. S., Ófeigsson, B. G., Heimisson, E. R., et al. (2015). Segmented lateral dyke growth in a rifting event at Bararbunga volcanic system. *Icel. Nat.* 517, 191–195. doi: 10.1038/nature14111

Snoke, J. A. (2003). FOCMEC: focal mechanism determinations. *Int. Handb. Earthq. Eng. Seismol.* 85, 1629–1630. doi: 10.1016/S0074-6142(03)80291-7

Soule, S. A., Fornari, D. J., Perfit, M. R., and Rubin, K. H. (2007). New insights into mid-ocean ridge volcanic processes from the 2005-2006 eruption of the East Pacific Rise, 9 46 N-9 56 N. *Geology* 35, 1079–1082. doi: 10.1130/G23924A.1

Urbani, S., Acocella, V., Rivalta, E., and Corbi, F. (2018). Propagation and arrest of dikes under topography: models applied to the 2014 Bardarbunga (Iceland) rifting event. *Geophys. Res. Lett.* 44, 6692–6701. doi: 10.1002/2017GL073130

Wilcock, W. S., Tolstoy, M., Waldhauser, F., Garcia, C., Tan, Y. J., Bohnenstiehl, D. R., et al. (2016). Seismic constraints on caldera dynamics from the 2015 axial seamount eruption. *Science* 354, 1395–1399. doi: 10.1126/science.aah5563

Wright, T., Ebinger, C., Biggs, J., Ayele, A., Yirgu, G., Keir, D., et al. (2006). Magma-maintained rift segmentation at continental rupture in the 2005 Afar dyking episode. *Nature* 442, 291–294. doi: 10.1038/nature04978

Wright, T. J., Sigmundsson, F., Pagli, C., Belachew, M., Hamling, I. J., Brandsdóttir, B., et al. (2012). Geophysical constraints on the dynamics of spreading centres from rifting episodes on land. *Nat. Geosci.* 5, 242–250. doi: 10.1038/ngeo1428

Xu, W., and Jónsson, S. (2014). The 2007-8 volcanic eruption on Jebel at Tair island (Red Sea), observed by satellite radar and optical images. *Bull. Volc.* 76, 795–808. doi: 10.1007/s00445-014-0795-9

Xu, W., Ruch, J., and Jónsson, S. (2015). Birth of two volcanic islands in the southern Red Sea. *Nat. Commun.* 6:7104. doi: 10.1038/ncomms8104

Conflict of Interest Statement: The authors declare that the research was conducted in the absence of any commercial or financial relationships that could be construed as a potential conflict of interest.

frontiers in Earth Science

ORIGINAL RESEARCH
published: 25 September 2018
doi: 10.3389/feart.2018.00139

Nonlinear Moment-Tensor Inversion of Repetitive Long-Periods Events Recorded at Pacaya Volcano, Guatemala

Federica Lanza[1,2]* *and Gregory P. Waite*[1]

[1] *Department of Geological and Mining Engineering and Sciences, Michigan Technological University, Houghton, MI, United States,* [2] *Department of Geoscience, University of Wisconsin-Madison, Madison, WI, United States*

Detailed models of low-frequency seismicity at volcanoes provide insights into conduit structure and dynamics of magmatic systems. Many active volcanoes produce repetitive seismic events, but these are often too small to model on their own. Here we examine thousands of repetitive explosion-related long-period (LP) events from Pacaya volcano, Guatemala, that were recorded during a temporary installation of four broadband seismic stations from October to November 2013. As most of the LP events are buried in background tremor, we used a matched filter from the higher signal-noise infrasound expression from these events. We derive a representative seismic signal from the phase-weighted stack of 8,587 of these events, and invert for a source moment tensor. To address the limitations posed by the number of stations of the local network, we employ a nonlinear waveform inversion that uses a grid search for source type to obtain a quantitative measure of the source mechanism reliability. With only four stations, Pacaya represents a case of limited observational data, where a quantitative description of moment-tensor uncertainty is needed before any interpretation is to be attempted. Results point to a shallow source mechanism somewhat like a tension crack, dipping ∼40° to the east, consistent with the dominant E-W motion in the seismic records. The uncertainties determined from the nonlinear inversion are not insignificant, but clearly constrain the mechanism to be a source dominated by isotropic components. The N-S orientation of the modeled crack is parallel to surface features and the dominant dikes modeled in numerous geodetic studies, suggesting the conduit may be elongated N-S throughout most of its path through the edifice. Our study demonstrates that by stacking thousands of small LP events they can be modeled to build understanding about conduit structure.

Keywords: long-period event, phase-weighted stacking, waveform inversion, source processes, Pacaya volcano

Edited by:
Benoit Taisne,
Nanyang Technological University, Singapore

Reviewed by:
Yosuke Aoki,
The University of Tokyo, Japan
Cynthia J. Ebinger,
Tulane University, United States

***Correspondence:**
Federica Lanza
flanza@wisc.edu

Specialty section:
This article was submitted to Volcanology, a section of the journal Frontiers in Earth Science

Received: *13 June 2018*
Accepted: *04 September 2018*
Published: *25 September 2018*

Citation:
Lanza F and Waite GP (2018) Nonlinear Moment-Tensor Inversion of Repetitive Long-Periods Events Recorded at Pacaya Volcano, Guatemala. Front. Earth Sci. 6:139. doi: 10.3389/feart.2018.00139

INTRODUCTION

Seismic signals produced by volcanoes can be seen as windows to magmatic systems and the complex interactions between gas, liquid, and solid along magma pathways (Chouet, 1996). Their origin can be related to fluid transport phenomena as well as shear failure along conduit walls. Models of these pathways, processes, and geometries can be extrapolated by retrieving the source mechanisms of the seismic events occurring beneath volcanoes. In particular, the analysis of low-frequency events, which include tremor, long-period (LP, 0.5–2 Hz) and very-long-period (VLP, 0.01–0.5 Hz) signals, has been a powerful tool to discern information on the physical processes connected to eruption activity. Seismic sources in volcanoes can be kinematically described using the moment tensor and single force representation of the source (Aki and Richards, 2002). This is a symmetric second-order tensor which allows to describe mechanisms such as slip across a fracture plane or opening/closing of a crack. For example, the passage of fluids into a crack will cause it to expand and act as seismic source with an isotropic (dilatational) component. Magma movement between conduits can therefore be represented through volumetric source components in the moment tensor. Single forces are also commonly considered in volcanic source due to the mass advection processes that can accompany eruptions. Source geometries and mechanisms for LPs and VLPs are obtained with full-waveform moment-tensor inversion. This technique has been used successfully at numerous active volcanoes around the world (Chouet and Matoza, 2013).

Pacaya volcano (14.381°N, 90.601°W) is a 2552 m high composite stratovolcano located about 30 km SSW of Guatemala City, in the Central American Volcanic Arc (**Figure 1**). Pacaya is a complex of multiple basaltic cones that have been active for at least several thousand years (Rose et al., 2013). The current eruptive phase began in 1961, building the modern Mackenney cone upon the site of the massive flank failure of an ancestral cone 600–1,500 years ago (Kitamura and Matías, 1995). This vent has produced persistent degassing and intermittent strombolian-type eruptions. Basaltic lava flows have been erupted from the summit and vents as far as 2.5 km from the Mackenney cone (Rose et al., 2013). The most voluminous recent explosive eruption occurred 27 May 2010, accompanied by formation of an elongated depression extending 600 m NNW of the summit (**Figure 1**). Geodetic modeling suggests both largescale flank motion and dike intrusion are responsible for the E-W extension of the Mackenney cone and the N-S orientation of vents and surface deformation features (Schaefer et al., 2017; Wnuk and Wauthier, 2017).

Beginning in January 2013, the volcano entered a new period of increased activity taking place mainly at the Mackenney cone and characterized by more continuous and energetic strombolian eruptions, ash eruptions and lava flows often accompanied by strong seismic tremor as reported by INSIVUMEH (Instituto Nacional de Sismologìa, Vulcanologìa, Meterologìa and Hidrologìa). Tremor was not only recorded by the INSIVUMEH seismic network, but it was also felt by the population of the nearby villages (Gustavo Chigna, pers. comm.). This new unrest prompted the installation of a local network to augment the single permanent station located ∼1 km from the Mackenney cone (PCG—**Figure 1**) with the aim of monitoring and investigating the seismic activity.

This study focuses on modeling the source mechanism of thousands of small LP events associated with weak strombolian explosions at the summit vent of Pacaya volcano. The persistent volcanic activity and the proximity of numerous villages are just two factors that motivate us to better understand the magmatic processes and structure of this very active volcano. Due to the limited number of stations available for the seismic experiment, we employ a recently developed nonlinear moment-tensor inversion approach (Waite and Lanza, 2016; Lanza and Waite, 2018), which adds a more thorough quantitative evaluation of source mechanism reliability. The study of Lanza and Waite (2018) provides a framework for evaluating moment-tensor solutions for a variety of hypothetical seismic networks and seismic source types. The procedure involves a grid search over all possible moment-tensor types and orientations at the best-fit centroid location and the results provide a range of acceptable models that fit the data. The present study is the first to thoroughly investigate the source processes of Pacaya's shallow LP seismicity.

DATA ACQUISITION AND PROCESSING

Temporary Seismic Network

We conducted a seismic experiment at Pacaya volcano during October-November 2013 to study the continuous tremor-like signals and the explosions occurring at the summit crater. Three Guralp CMG-ESPC 3-component broadband seismometers (60s corner period) and one Guralp CMG-40T sensor (30s corner period) were installed around the central vent at distances between 0.6 and 1.5 km from the crater (**Figure 1**).

Two of these stations (P01 and P02) were also outfitted with 3-element, equilateral triangular infrasound arrays, with ∼30 m between elements. Data were recorded on Reftek 130 digitizers operating in continuous mode at 125 samples per second and equipped with Global Positioning Systems (GPS) timing. Concerns about vandalism and theft discouraged us from deploying solar panels; therefore, the experiment ran for about 10 days from 31 October through 10 November. The single permanent station (PCG) from the local network operating at the time has an uncalibrated short-period sensor so the data from that station could not be incorporated into the study.

Visual Observations

During the installation of the temporary seismic network, about ∼3 h of video recordings using a SONY HD video camera were acquired. Camera clock was calibrated by hand, referencing hand-held GPS units. The recordings show the occurrence of frequent small strombolian explosions and puffing of gas from the cinder /spatter cones inside the summit vent (Mackenney cone, **Figure 2A**).

LP Events

During the 10 days the temporary network was operative, the infrasound network recorded thousands of impulsive events with an inter-event time of about 1–2 s. Because the events were more clear in the infrasound than the seismic, we used one of these events as a template and performed waveform cross-correlation to search for similar events within the acoustic record. Cross-correlation is carried out on filtered data bandpassed between 0.5 and 10 Hz. By applying this time-domain matched filter approach, we were able to identify hundreds of events that

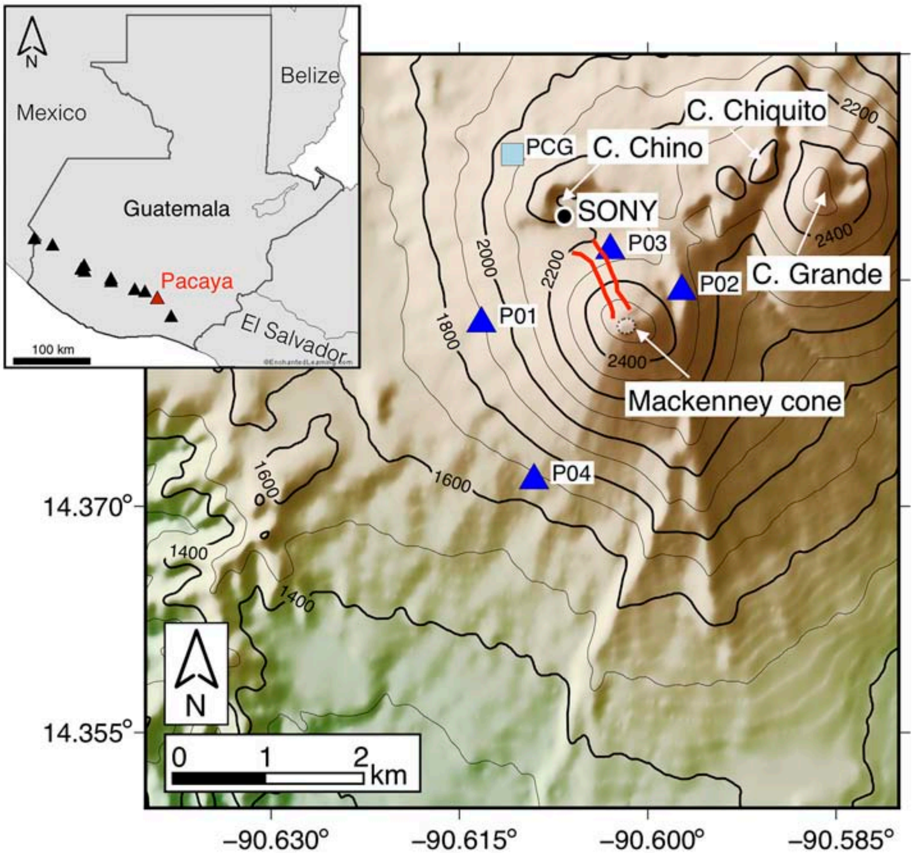

FIGURE 1 | Map of Pacaya volcano showing the location of the seismic stations used in this study (blue triangles). The single permanent station of the local network, PCG, is shown by the light blue square. The black circle indicates the position of the portable SONY video camera used during the field campaign. Red lines indicate the linear depression that developed during the May 27, 2010 eruption. Contour interval is 100 m. The box in the upper left corner shows the position of Pacaya volcano in Guatemala with respect to the Central American Volcanic Arc volcanoes marked as black triangles.

correlated with the template with a cross-correlation coefficient of 0.9 or higher, which were stacked to create a new template (Shearer, 1994; Richardson and Waite, 2013). To improve the signal-to-noise (S/N) ratio of the template, we then ran this new template through the dataset again with a cross-correlation cut off of 0.8. In this way, we identified more than 80,000 events over a 10-day long period from 31 October to 11 November 2013 (**Figure 2B**). This infrasound catalog was then used to extract the corresponding waveforms from seismic data. This revealed the presence of a repetitive seismic signal (LP event type) associated with the acoustic emissions that was not clearly visible above the background tremor and/or other noise sources (**Figure 3**). With the term association we here refer to those LP events that are happening at the same time of the infrasound pulses and that have a cross-correlation > 0.8. These amount to 32,908 events in the same 10-day time period.

While the infrasound data helped to identify the associated seismic event, the seismic data had minor time shifts when aligned with the times of the infrasound events. While the seismic velocity structure was presumably stable over the course of the deployment, variations in wind velocity and air temperature may have produced small variations in the sound speed profile between the vent and our array. In order to overcome this, we cross-correlated one channel of the seismic data at each station to determine time shifts that would improve the alignment. These shifts were on the order of 0.1 s.

We reduced the number of events from 32,908 to 8,587 by considering only those events that have a S/N ratio greater than 1.2 on the east component of station P02 (**Figure 3A**). We then followed the phase-weighted stacking approach (Schimmel and Paulssen, 1997; Thurber et al., 2014), which resulted in waveforms with an improved signal to noise ratio when compared to the linear stacks. Although the phase-weighted stack is slightly lower in amplitude, the pre- or post-event noise is much lower (**Figure 3B**).

One additional challenge in obtaining a representative stacked seismic event resulted from the somewhat discontinuous nature of the seismic data. Because the stations were not all contemporaneously operational, simply stacking waveforms to obtain a waveform that would synthesize the response from all four stations would produce a stack with disproportionally low amplitudes for those stations with fewer events. We employed

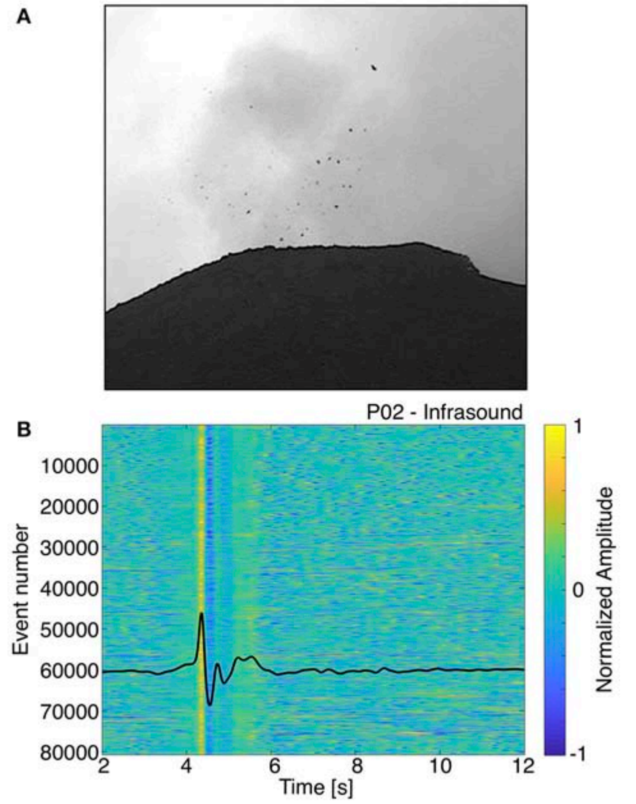

FIGURE 2 | (A) Single frame from a video-recording of one small explosion at the crater recorded on November 3, 2013. The video camera was positioned on Cerro Chino at about 1 km NNW of the Mackenney cone (see black circle in **Figure 1**). **(B)** Waveforms of 80,701 events on the infrasonic record over a 10-day long period from 31 October to 11 November 2013, normalized to the maximum absolute amplitude. Plotted in black is the stacked infrasound template event used in the matched filter approach.

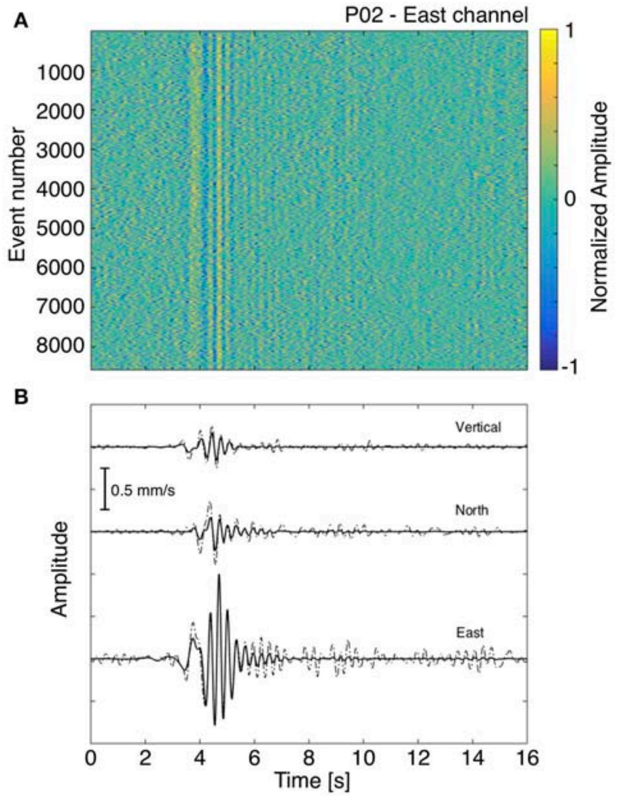

FIGURE 3 | (A) Waveforms of 8,587 seismic events with S/N greater than 1.2 observed on station P02 (east channel) over the same 10-day long period used for the infrasound detections. Waveforms are normalized to the maximum absolute amplitude. **(B)** Stacked seismograms for all three-components at station P02. Both linear time-domain (dashed lines) and phase-weighted stacks (bold lines) are shown.

a method described by Richardson and Waite (2013) to assure correct amplitudes in the stacks. As station P02 was running concurrently with all the other stations, we used it to tie events recorded by different stations and to compare amplitudes. Since the east component is consistently the highest amplitude component for P02, we used it as the reference channel. For each of the other stations, we generated temporary stacked seismograms of P02 east that included only the events recorded by the station of interest (i.e., **Figures 4A–C**, bottom row, panel 1). We then calculated the ratio of the stack for a particular component to that of the P02 east component stack for the same subset of events (**Figures 4A–C**, bottom row, panel 2). In this way, all the channels were converted from stacked amplitudes to amplitudes proportional to the east component of P02 (**Figures 4A–C**, bottom row, panel 3). All stacked amplitudes were then converted back to true amplitudes proportional to one of the largest observed LP events seen at P02 through simple multiplication of each trace by the maximum velocity amplitude of P02 for that event.

At the two closest stations, P02 and P03, the main part of the signal lasts 2.5–3 s. The coda, a significant component of which is likely due to scattering, continues for more than 10 s. Interestingly the largest amplitudes at these closest stations, which are ∼600 m east and 500 m north of the summit vent, respectively, are on the east component. This is also the case at P01, which lies 1200 m west of the source. While the dominant E-W signal is not so clear on station P04, 1500 m SW of the summit, it is evidence of a significant E-W feature of the source-time process.

We prepared the stacked waveforms for the full-waveform inversion by band-pass filtering 0.5–2 Hz with a zero-phase Butterworth filter. The data were also downsampled from 125 samples per seconds (sps) to 50 sps, trimmed, and multiplied by a cosine tapered window centered on the highest amplitudes. Last, we transformed the data into the frequency domain.

LP INVERSION

Full-Waveform Inversion Procedure

We followed an inversion approach that is similar to other studies (see e.g., Auger et al., 2006; Waite et al., 2008; Dawson et al., 2011; Richardson and Waite, 2013) where the inversion is performed in the frequency domain to reduce the computation time and

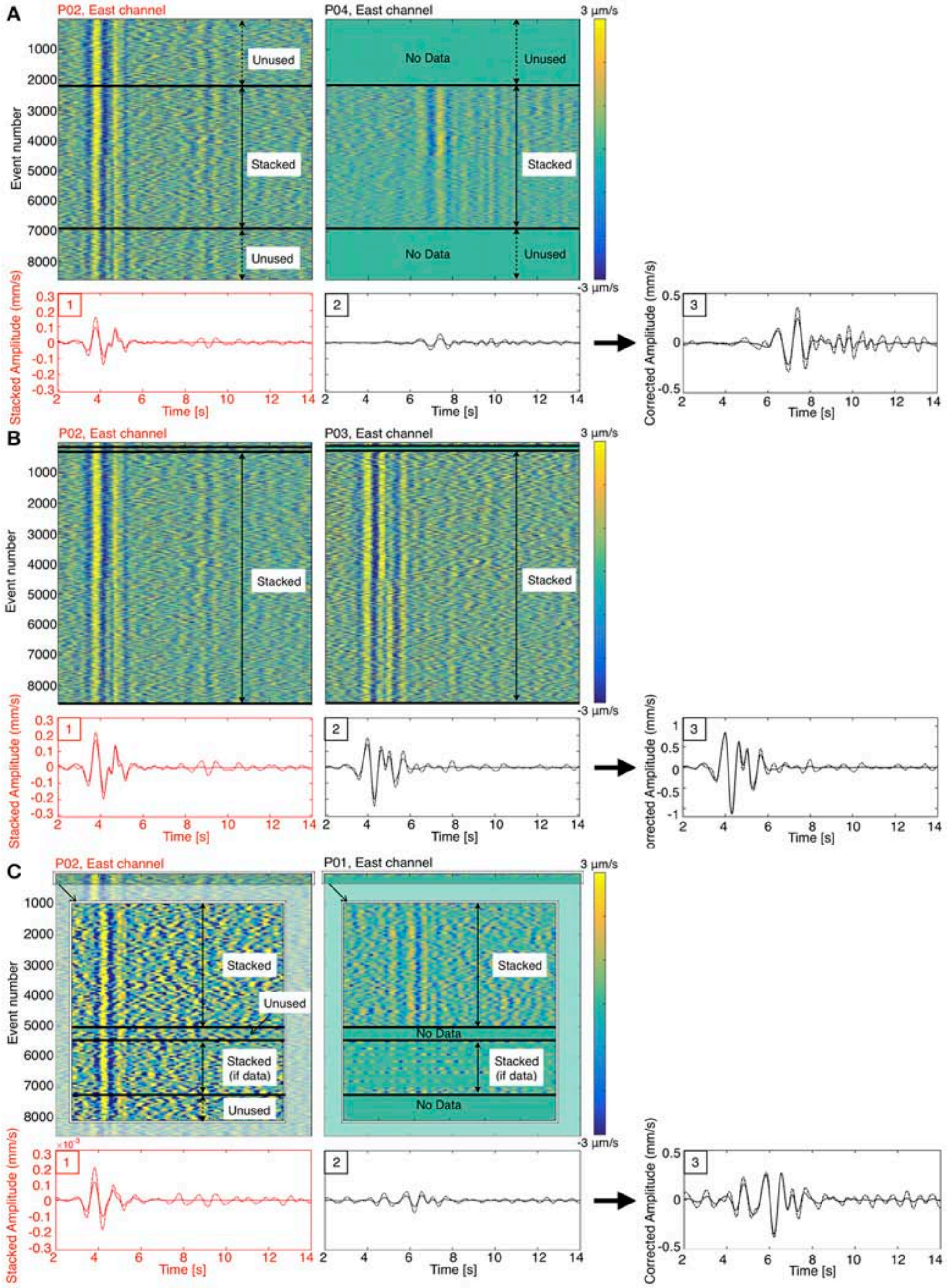

FIGURE 4 | Stacking procedure for east components of P02 and P04 **(A),** P02 and P03 **(B),** P02 and P01 **(C).** P02 is the reference station used for normalization. **(A)** top row: waveforms of events recorded at P02 and at P04; black lines indicate the stacking interval used for P04. Waveforms are bandpass filtered between 0.5 and 2.0 Hz, and amplitudes are scaled appropriately to the color bar. Bottom row, panel 1: we show in red the phase-weighted (solid line) and linear (dashed line) stacks for P02 over the stacking interval of P04. Bottom row, panel 2: we show in black the phase-weighted (solid line) and linear (dashed line) stacks for P04. In panel 3, we show the phase-weighted and linear stacks of the east component waveform for P04 with amplitude normalized by the maximum absolute amplitude of the P02 stack over the stacking interval station P04. **(B)** and **(C)** same as **(A)** but for stations P03 and P01 respectively.

permit a grid search over a large volume. With this approach, we solved for the full spectra of the bandpass filtered (0.5–2 Hz) seismograms and invert at each frequency separately. In terms of the classic least-squares inversion equation, $\mathbf{d} = \mathbf{Gm}$, $\mathbf{d}$ represents the vector of complex spectra for a single frequency for all the data channels, $\mathbf{G}$ represents the matrix of Green's functions for that frequency, and **m** represents the spectral component of the corresponding source components (e.g., six moment-tensor components). After inverting for each frequency, the source-time functions for the model components are computed from their inverse Fourier transforms.

This procedure is performed at thousands of points within the three-dimensional (3D) model of the volcano, allowing to scan the model space for location. In this paper, the inversion is initially unconstrained, meaning that the inversion is performed for different combinations of the nine free parameters (six moment-tensor components and three single forces) with no constraint on the source-time functions. In some cases, this leads to an unrealistic and uninterpretable set of time histories for the source components, but this is quantified through the similarity of the waveforms. The moment tensor is comprised of force couples, but because mass advection processes can also produce single forces on the Earth, it's important to consider the single forces as parameters to invert for in source inversions of volcanic signals. Examples for which the single forces have been used to explain the seismic signals recorded at volcanoes include Asama volcano, where the results of the waveform analyses of 5 explosion earthquakes indicated that a vertical single force dominated the force system at the source region (Ohminato et al., 2006); lateral ejection of material at Mount St. Helens in 1980 was also attributed to a single force system (Kanamori and Given, 1982), and LPs recorded at Villarica volcano were related to a single force resulting from a bursting bubble in the lava lake and the responsive drag force of the lava sloshing to fill in the void produced by the gas emissions (Richardson and Waite, 2013).

We here adopt the term MT+F to describe unconstrained inversions that include all nine free parameters; the term MT indicates unconstrained inversions that only include six moment-tensor components; and the term F here stands for unconstrained inversions performed using only single forces. In a second step, "constrained" inversions at the best-fit centroid obtained from the unconstrained inversions are performed as part of the nonlinear inversion procedure which involves a grid search over all possible moment-tensor types and orientations.

For both unconstrained and constrained inversions, synthetic Green's functions were computed with the 3D finite-difference method of Ohminato and Chouet (1997). We used a cosine smoothing function to synthetize the Green's functions and assure stability. This wavelet has a time constant period of 1 s (1 Hz) to approximate the peak frequency of the LP events recorded at Pacaya volcano. The Green's functions convolved with the cosine function represent the elementary source-time functions used in the inversion. We used a model that includes the 3D topography of Pacaya, derived from a digital elevation map (DEM) from 2006 with a resolution of 10 m. The model domain is centered on the active summit crater of the volcano (Mackenney cone), and it has lateral dimensions of 4 by 4 km and a vertical extent of 3.5 km. This yields a model with 401 × 401 × 351 nodes spaced 10 m apart. All station locations were rounded to the nearest node, and topography was resampled to match the correct node grid. The node spacing satisfies the criterion of minimum number of grids per wavelength of 25 established through a trial-and-error approach by Ohminato and Chouet (1997) to insure a stable computation. The model is also wide enough to minimize edge reflections of the boundaries while including all the stations. To find the best location for each of the point sources, we conducted a grid search over a volume of 740 × 740 × 500 m centered on the summit vent at a spacing of 20 m. In order to reduce the number of calculations required to derive the Green's functions, we followed Chouet et al. (2005), and used the reciprocal relation (Aki and Richards, 2002) between source and receiver in which each station is treated as a point source and each potential source as a receiver.

Nonlinear Inversion Procedure

As described in Waite and Lanza (2016) and Lanza and Waite (2018) we explore the uncertainty in the source type through a grid search over all possible moment-tensor types and orientations. In this nonlinear inversion, the single forces are kept as free parameters when they are included.

The search over source types is determined using the fundamental lune source-type definition of Tape and Tape (2012). Similar to a Hudson-type plot (Hudson et al., 1989), the lune maps the distribution of all possible moment-tensor source types onto a surface. Source types are defined by two parameters, the spherical coordinates γ and δ, which are defined by the ratios of the moment-tensor eigenvalues. The longitude parameter, γ, ranges from -30° to 30°, and it is defined as:

$$\gamma \ = arctan\left(\frac{-\,L_1 +\ 2L_2\ -\ L_3}{\sqrt{3}\ (L_1\ -\ L_3)}\right) \tag{1}$$

where L_1, L_2, and L_3 are the eigenvalues of each point of the source-time function.

The latitude parameter, δ, ranges from -90° to 90°, and it is derived from the co-latitude parameter, β, for which:

$$\beta \ = arccos\left(\frac{L_1 +\ L_2 +\ L_3}{\sqrt{3}\ ||\Lambda||}\right) \quad with$$

$$||\Lambda|| = \sqrt{{L_1}^2 + {L_2}^2 + {L_3}^2} \tag{2}$$

$$\delta = 90^\circ\ -\ \beta \tag{3}$$

where L_1, L_2, and L_3 are the eigenvalues of each point of the source-time function. The latitude δ is zero for deviatoric patterns, and both δ and γ are zero for double couple mechanisms.

The search over the γ and δ uses the surface spline method described in Tape and Tape (2012), which effectively reduces the number of points required to evenly sample the distribution over an evenly spaced grid. We evaluate the full range of γ and δ and the full lune are shown for the real data. However, for the synthetic tests, because we didn't use time-shifts, we show only the upper half of the lune which is in this case simply the opposite sign of the lower half (e.g., net positive isotropic versus net negative isotropic).

In addition to exploring the full source-type space, the range of possible orientations for each source is also examined. To do this, we rotate the moment tensor at 10° intervals using a sequence of three rotations about the initial coordinate system of the moment tensor. Complete sampling of the symmetric tensor orientations requires exploring three rotations: a full 360° range about one axis, for example, the z axis; a range from 0 to 180° of dip of z to z'; and finally, 90° of rotation about the new, rotated z' axis (Goldstein et al., 2002; Waite and Lanza, 2016). The 10° interval was chosen for computational reasons after having assessed, through multiple tests with finer intervals, that although there are small changes in the misfit values, there were no significant changes in the pattern of misfits. This involves 5832 combinations of rotation angles combined with 223 γ-δ pairs, for a total of 1,300,536 trial moment-tensor solutions.

For each individual moment source-type in the gridded lune we invert for the source-time function that provides the best fit to the data by fixing the moment tensor and fitting the best source-time function. We refer to Waite and Lanza (2016) for the details of the inversion approach.

Evaluation of the Inversion Results

The overall selection of the best solution was based on a weighted squared error between the observed and modeled data described as E_2 (Ohminato et al., 1998; Chouet et al., 2003):

$$E_2 = \frac{1}{N_r}\sum_{n=1}^{N_r} \frac{\sum_1^{N_r}\sum_{p=1}^{N_s}\left(u_n^0\left(p\,\Delta\,t\right) - u_n^s\left(p\,\Delta\,t\right)\right)^2}{\sum_1^{N_r}\sum_{p=1}^{N_s}\left(u_n^0\left(p\,\Delta\,t\right)\right)^2} \tag{4}$$

where $u_n^0\left(pt\right)$ is the pth sample of the nth data trace, $u_n^s\left(pt\right)$ is the pth sample of the nth synthetic trace, N_s is the number of samples in each trace, and N_r is the number of three-component receivers. Here the squared error is normalized by station, so that stations with varying amplitude contribute equally to the error. We adopt E_2 error as it accounts for stations from all distances equally; with just four stations we felt it more important to find a well-balanced of fit on all receivers, rather than favoring only the nearest stations with the largest amplitude arrivals. The use of misfit information here is not only employed to define uncertainty on the source centroid as a result of the unconstrained inversions, but also to examine the uncertainty in the moment-tensor type.

For the unconstrained inversion results, the influence of the number of free parameters in each source model was evaluated by calculating the Akaike's information criterion (AIC; Akaike, 1974), expressed as:

$$AIC = N_t N_s ln E_2 + 2 N_m N_f \tag{5}$$

where E_2 is the squared error from equation (4), N_m is the number of source mechanisms, and N_f is the number of frequencies in the passband of interest. In general, the use of more free parameters is considered justified when both the squared error and AIC are reduced.

Evaluation of the Velocity Model

We considered a homogeneous velocity model with P-wave velocity of 978 m/s, S-wave velocity of 565 m/s and density of 1750 kg/m^3. These values are based on the mean of the first 5 layers (first 130 m in depth) of the shear-wave velocity model of Lanza et al. (2016), which was derived from Love and Rayleigh dispersion curves. While this homogenous model is not ideal, we did not have a detailed 3D model available. In order to evaluate how the limitations in the velocity model influence the solution, we performed synthetic tests that use a smooth 1D model. The 1D model follows the topography and is composed of 2 layers followed by a half space. The first layer extends until 100 m depth and we assigned P-velocity of 866 m/s, so that it will be lower than the homogeneous model in which V_P is set to 978 m/s. This choice is functional to test the presence of a low velocity layer, which is very common in volcanic areas. The second layer extends until 530 m, which is the maximum depth reached by the S- wave velocity model of Lanza et al. (2016). This layer has a P-velocity of 1.66 km/s obtained by averaging the V_P velocities of Lanza et al. (2016)'s model for layers encompassing the same depths. A P-wave velocity of 3.05 km/s was assigned to the half space. The S wave speed is fixed at $Vp/\sqrt{3}$. For each layer, the density was calculated averaging by depth the density values derived from the model of Lanza et al. (2016), so that the first layer has a density of 1.99 g/cm^3, the second layer of 2.24 g/cm^3, and the half space of 2.56 g/cm^3.

For the synthetic tests, we computed synthetic Green's functions in both homogeneous and 1D models for a vertical crack input model striking 80° E with dipole magnitude ratios of [3, 1, 1] ($\gamma = -30°$, $\delta = 60.5°$). Synthetic tests involving different source types (from double couple to isotropic sources) were also carried out in a parallel study that focused on the assessment of network performances for moment-tensor studies of long-period events at volcanoes, in which one of the network array considered mirrored the one deployed at Pacaya volcano (Lanza and Waite, 2018). To synthesize a realistic set of seismograms, the Green's functions calculated for the input source model were convolved with a portion of the M_{xx} component of the source-time function obtained from the unconstrained inversion of data (see section Inversion Results). Synthetics were computed for (1) an input location situated 260 m directly beneath the highest point in the topographical model of Pacaya volcano, at 2330 m a. s. l. where all source points are below topography in order to minimize possible edge effects in the Green's functions; (2) an input location situated 100 m beneath the crater, in order to consider a case of a very shallow source. Both locations are chosen to be directly beneath the active summit vent based on the initial hypothesis that the close association of seismic and infrasound events, tied by visual observations, is related to a source located below the summit vent. To simulate noisy traces in real data, white noise bandpass filtered in the LP band was added to the final synthetic waveforms. Noise amplitude was calculated using the average of the root mean squared of the synthetic signal amplitudes from the four stations. In this way, the noise amplitude was constant across the network.

We modeled synthetic data through both the homogeneous and the smooth 1D model at the two chosen depths. For all cases, we inverted the synthetic waveforms using the Green's functions generated for the homogeneous velocity model in an effort to simulate modeling real data with Green's functions from a homogeneous model. While inversions of synthetic data computed in the homogenous model were very good, the moment-tensor source-time functions from the 1D model synthetics have a shift in the source type from the initial

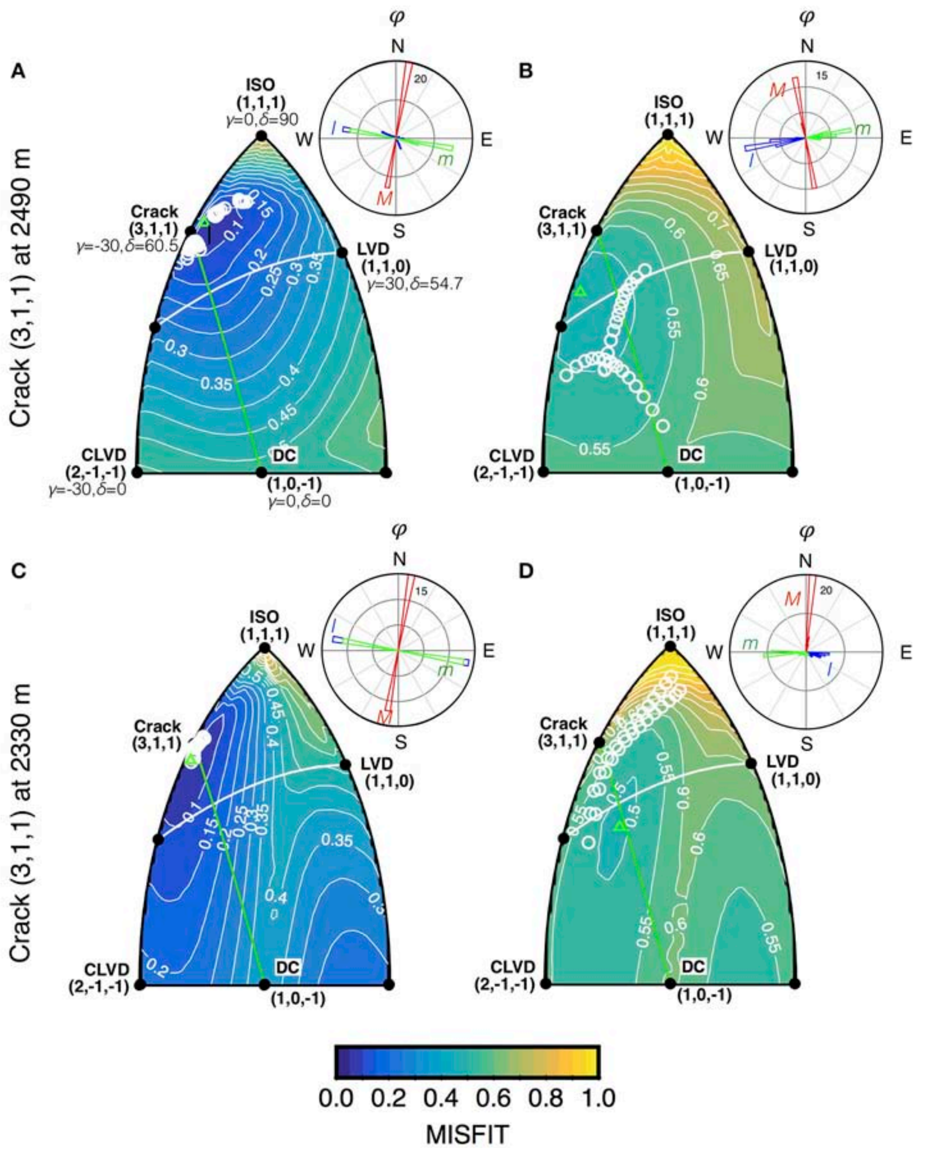

FIGURE 5 | Misfit by fixed moment tensor solution, plotted together with the point-by-point eigenvalue decomposition of the moment-tensor solution for the unconstrained inversion as white circles for a crack input source model located at 2490 m, and 2330 m a.s.l. The green triangles indicate the γ-δ pairs with the minimum misfit. **(A)** Solution for synthetic data generated with a homogeneous velocity model. **(B)** Solution for synthetic data generated with a 1D velocity model. **(C)** and **(D)** same as **(A)** and **(B)** but for an input source located at 2330 m a.s.l. Rose diagrams show the orientations of the maximum, intermediate and minimum eigenvectors for the unconstrained inversion solutions.

input crack model toward a linear-vector dipole (LVD) source mechanism, with a much broader γ and δ distribution (**Figure 5**). The values of E_2 are higher with respect to the misfits obtained with the homogenous model. Since the lune plots do not give the orientation of the source, we plotted the eigenvectors of the best fit moment tensors in the top left corners of **Figure 5** as rose diagrams of the azimuth ϕ. The original orientation is recovered well in the homogeneous case (**Figures 5A,C**), while it presents some deviations from the original input orientation for the solution obtained with the 1D smooth velocity model (**Figures 5B,D**) for both depths considered. These tests confirm an expected degradation of the accuracy of the solution related to the incorrect velocity model (Bean et al., 2008) and shallow depth (Trovato et al., 2016). However, even with an incorrect velocity, which usually constitutes one of the major unknowns in source modeling studies, we can constrain the reconstructed source mechanism to a region of the lune that includes source types similar to the input source model.

INVERSION RESULTS

Unconstrained Inversion Results

Data were first inverted in the 0.5–2 Hz band without constraining the solution in any way. We prefer this method for

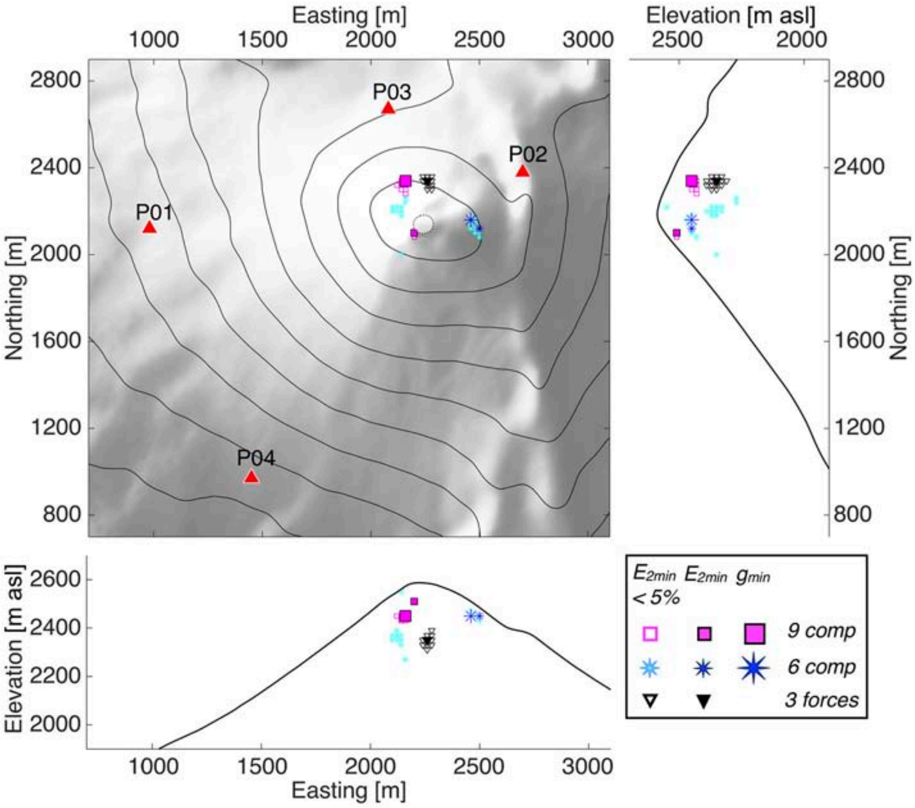

FIGURE 6 | Locations of best-fit source centroids for minimum misfit (E_{2min}), for all solutions within 5% of the minimum misfit ($E_{2min} < 5$ %), and when both source-time function stability and minimum misfit are considered (g_{min}). Locations for all three unconstrained inversion trials are shown. Contour interval is 100 m. Red triangles indicate the broadband network position.

searching over possible source centroid locations. We solved for three types of source models: single forces alone (F); moment-tensor components alone (MT); and a combination of both single forces and moment components (MT+F). We then use several approaches for evaluating the best model from these inversion results as has been done in prior work (e.g., Matoza et al., 2015).

Generally, source locations for all of the unconstrained inversion trials (F, MT, and MT+F) are displaced from the summit; they are either to the north for the F, MT+F and a local minimum of solutions for the MT, or to the east for the global minimum solution for the MT inversion. All reveal a shallow source location ranging from 20 to 240 m below the highest topographical point (**Figure 6**). Given the close association between the seismic and the infrasound signal associated with these events we are confident that the true LP source is shallow and just below the vent.

The error in centroid location is primarily attributed to the homogeneous model used in the inversion, but the uncertainties seen in the hypocenter location can be a result of a combination of errors in the velocity model and station distribution. And even though the first arrivals are difficult to time accurately, it is clear from the signal travel time move-out that the LP source must be located within the upper cone.

The best-fit model, based on both the residual error estimates and AIC, is the one that includes a combination of six moment-tensor components and three single forces (MT+F), as seen in **Table 1.** However, the choice of the best source model has to consider not only an assessment of the overall misfits, but also an evaluation of whether the model is geologically reasonable. We explore interpretations of the single forces in terms of other observations of the events and previous work to determine if they are reasonable, or more likely a result of an artifact, such as unmodeled structure in the edifice.

Because no constraints on the source type were used in these inversions, the model source-time function components can be inconsistent over time, resulting in a difficult to interpret, geologically unreasonable model. For source nodes having E_2 within 5% of the minimum, we calculated the consistency of the source-time function over its duration using the standard deviations of the ratios of the eigenvalues. This measurement is expressed by a statistic called gamma by Matoza et al. (2015), and g by Waite and Lanza (2016) to avoid possible confusion with the previously defined moment-tensor lune longitude. The parameter g is obtained by calculating the square root of the sum of the squared standard deviations of the ratios of the minimum to maximum and intermediate to maximum eigenvalues for each time in the source history (also equation 6 in Matoza et al., 2015):

$$g = \left[\sigma^2\left(3\frac{\alpha_1}{\alpha_3}\right) + \sigma^2\left(3\frac{\alpha_2}{\alpha_3}\right)\right]^{\frac{1}{2}} \tag{6}$$

where σ is the standard deviation, and α_1, α_2, α_3 are the minimum, intermediate, and maximum moment-tensor eigenvalues, respectively. The standard deviations provide a measure of the consistency of the source-time function over its duration, so we seek a solution that both minimized the misfit (low E_2) and has a consistent set of moment-tensor components (low g).

We computed the ratio of eigenvalues at each point in the source-time function having amplitude greater than 60% of the maximum to reduce the influence of noise in low-amplitudes. For both the MT and MT+F models, the solution with the lowest value of g within these error volumes is very similar to the source-time function at the minimum E_2, both in terms of the misfit and the moment tensor. The best-fit source centroids for minimum misfit, together with the g_{min} best-fit locations, and all the solutions within 5% of the minimum misfit, are shown in **Figure 6.**

We note that although the absolute value of g is a function of the moment-tensor eigenvalue ratios assumed in the calculation, this assumption does not significantly influence the identification of the solution with the lowest value for g. For example, Waite and Lanza (2016), based on *a priori* information, used moment-tensor eigenvalue ratios of 2:1:1 for examining g values for a source-time function of a VLP signal recorded at Fuego volcano. They also considered different ratios and found that although the values for g vary, there was no difference in which solutions had the lowest g. Based on those results, we simply assumed ratios of 1:1:1 in our computations for g. We computed a similar statistic for the case of single forces only which is based only on the consistency of the single-force source-time functions, but we do not report this here to avoid unnecessary complexity when comparing to the moment components. In summary, for the MT and MT+F models, both solutions with minimum E_2 and those with minimum g have moment-tensor source-time functions that are consistent throughout the time history of the source.

Based on the model fits ($E_2 = 0.531$), and the AIC (AIC $= -2353.1$), we first discard the force-only solution. In addition to fact that it has the worst fit, which is partially due to the smaller number of parameters used in the inversion, the single forces only inversion source-time function components are not in phase, indicating that the mechanism is not stable in time (see **Figure S2**). The largest force is in the east-west direction, which is consistent with the large east-west component on the nearest stations. But the overall poor fit to the data suggests this is not a reasonable model for this stacked event (**Figure S1**).

We next consider the subtle differences between the MT and the MT+F solutions. Both have a moment tensor somewhat like a dipping crack with similar solutions for both the minimum E_{2min} and minimum g_{min} solutions. The E_{2min} misfits are 0.323 and 0.140 for MT and MT+F, respectively (**Table 1**). The model synthetic fits to the data are quite good and match the large amplitudes on the east components much better than the single

TABLE 1 | Unconstrained inversion results.

Inverted parameters	E_{2min} solutions						g_{min} solutions				
	E-W position relative to summit [m]	N-S position relative to summit [m]	Depth below topography [m]	E_2	AIC	Eigenvalue ratios	E-W position relative to summit [m]	N-S position relative to summit [m]	Depth below topography [m]	g	Eigenvalue ratios
MT+F	40 W	60 S	60	0.140	−7471.8	1, 0.35, 0.45	80 W	180 N	20	0.016	1, 0.37, 0.43
MT	260 E	40 S	40	0.323	−3871.4	1, 0.20, 0.35	220 E	0	40	0.014	1, 0.23, 0.30
F	20 E	180 N	120	0.531	−2353.1						

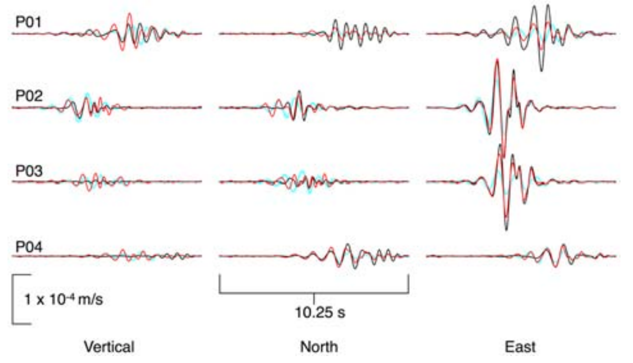

FIGURE 7 | Waveform fits for the representative LP event obtained from the phase-weighted stacks of 8,587 repeating events. Fits are for the E_{2min} solution for the 6- components unconstrained inversion. Red lines indicate unconstrained -inversion synthetics, cyan lines are best-fitting constrained inversion synthetics, and black lines represent observed velocity waveforms.

force model does. For brevity, we focus on results from the E_{2min} MT model, but include results from the MT+F inversions and the g_{min} MT model in the supplementary materials (**Figures S3–S6**). For reasons described below, we favor the model that does not include single forces. **Figure 7** shows the data (black) along with the modeled waveforms for the MT E_{2min} solutions. The unconstrained inversion synthetics, shown in red, generally fit the data fairly well. The synthetics from the fixed tensor solution, shown in cyan and described in the following section, have greater misfits, as expected for models with fewer free parameters. A similar plot for the MT+F model is shown in **Figure S3**.

The source-time functions for both the unconstrained and constrained MT inversion are shown in **Figure 8A**. We used the general formulation convention with M_{xx} oriented East, M_{yy} North, and M_{zz} Up. Note how the dipole components M_{xx} and M_{zz} are in phase, even for the unconstrained inversions, and dominate the source-time function.

The source-time function of the unconstrained MT inversion is further analyzed through point-by-point eigenvector decomposition. We use only points with amplitude of at least 60% of the peak amplitude to assure stability. **Figure 9** shows the statistics of the eigenvectors through rose diagrams of the azimuth ϕ, and inclination angle ϑ, measured from the vertical. For each point of the source-time history, we calculated the longitude γ and the latitude δ of the fundamental lune and the ratios of minimum and intermediate eigenvalues to the largest, whose median values are reported in **Table 1**. The eigenvector analysis and the point-by-point γ-δ pairs define a fairly constrained solution in the region that includes sources from a tension crack (white circles in **Figure 8B**) dipping ~40° to the east ($\phi = -6.4°$).

Although the network includes only four stations, they are well distributed. The solution behaves consistently through time, in agreement with the finding by Lanza and Waite (2018) that the azimuthal coverage has an important influence in the stability of the source-time function compared to factors such as the number of stations used in the inversion.

Constrained Inversion Results

The source-time functions derived from the unconstrained inversion were further investigated through constrained inversions for source type. Again, we focus on results for the MT inversion, but include results from the MT+F inversions in the **supplementary materials**. **Figure 8B** shows the misfits at each moment-tensor type for the lowest misfit tensor orientation. That is, each point in the lune plot represents the lowest misfit value for all moment-tensor orientations with the particular γ - δ pair. The misfits for the constrained inversion results are much larger than those of the unconstrained inversions, ranging from values of 0.64 to 0.84, with respect to the minimum value of 0.32 obtained from the unconstrained inversion. This is not unexpected given that there is essentially one model parameter in the constrained inversions, compared to six independent model parameters for the unconstrained inversions. The nonlinear inversion suggests a slightly larger area of possible source mechanisms types; however the region surrounding 5% above the minimum occupies an area in which all the eigenvalues are the same sign. Uncertainties of the moment tensor for each component and cross-components trade-off in the moment tensors within this area are explored by calculating the ratios of each moment components with the moment components of the best fitting solution (red triangle in **Figure 8B**). As shown in **Figure S7**, the cross-components M_{xy} and M_{yz} components are poorly constrained compared to the other components which, instead, show a tighter range of variation.

The ratio of eigenvalues (0.20, 0.42, 1) from the nonlinear inversion points to a source not precisely like a known theoretical source. It is somewhat like a theoretical tensile crack in a Poisson solid (1, 1, 3) in which the largest eigenvalue is perpendicular to the crack, but with less symmetry in the in-plane deformation. This is explored further below.

The constrained inversions for the MT+F inversions (**Figures S4, S5**) have much lower misfit values but appear to be completely unconstrained. While the best-fit mechanisms are very close to the mechanisms determined from the unconstrained inversions for MT+F, the area of acceptably low misfit covers most of the lune. We attribute this result to the lack of constraint on the single forces. For nearly any mechanism type, the combination of the three unconstrained single force model parameters and one moment tensor model parameter can fit the data reasonably well. So, in this model, the use of the full lune is not as illustrative of model fit.

DISCUSSION

The LP events we recorded at Pacaya volcano in 2013 are associated with small explosive outgassing events at the summit. With a scalar seismic moment of about $4x10^{10}$ Nm, these events release about as much energy as a Mw 1 earthquake. The fact that this same source was activated as often as every 1–2 s, with larger, clearer signals about every 15 s during our short deployment, suggests this dominant style of activity is important to understand. We rely on the infrasound record of these events, along with our visual observations of puffing and weak

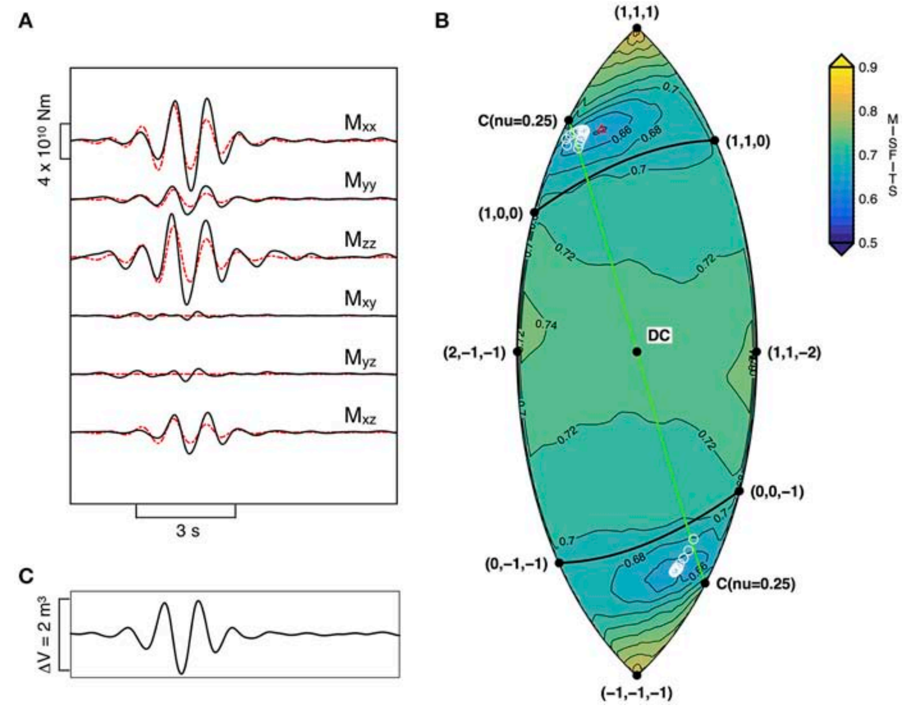

FIGURE 8 | (A) Source-time function from the MT unconstrained inversion (black line), and for the E_{2min} solution from the constrained inversion (dashed red line). **(B)** Misfit by fixed moment-tensor solution, plotted together with the γ-δ distribution for the unconstrained inversion (white circles), and with the γ-δ pair for the constrained inversion (red triangle). **(C)** Estimated volume change for the source-time function of the MT solution.

explosions, to inform our interpretation of the seismic moment tensor and help constrain the models. Given the association of the seismic LP with the infrasound source we attribute the LPs to strombolian bubble-burst events. Here we interpret the seismic source models to provide some constraints on the process involved in these explosions and on the conduit structure just below the vent.

The ascent of a bubble, and the flow of magma down and around it should produce a reaction force in the Earth. Assuming a nearly vertical conduit, we should expect to see a nearly vertical single force together with a moment tensor that models some associated conduit deformation. This has been seen in laboratory experiments (James et al., 2009) and in data from other volcanoes. One excellent example is the Kilauea VLP source model of Chouet et al. (2010). They modeled VLP events as resulting from the ascent, expansion, and burst of a large slug of gas. They interpreted the presence of a dominant vertical single force as a result of an upward force on the Earth induced by the approaching of the slug to the surface and consequent pressure decrease and conduit deflation below the slug. The magnitudes of the vertical forces were consistent with slug masses of 10^4 to 10^6 kg.

In another study involving a bubble ascent mechanism, Richardson and Waite (2013) found that a dipping single force model provided the best-fit to repetitive LPs associated with strombolian explosions at Villarrica volcano. In that case, the E-W oriented particle motions at all azimuths were attributed to near horizontal viscous forces associated with a structural feature in the upper conduit. The moment-tensor components were not required by the data.

In the case of Pacaya, the single forces involved in the source process might be too small to model. We estimate the mass of bubbles that produce the small strombolian explosions we observe as LP events assuming a monopole source in which the mass emission as a function of time, $q\,(t)$, can be estimated as (Lighthill, 1978; Firstov and Kravchenko, 1996):

$$q\,(t) = 2\pi r \int p\left(t - \frac{r}{c}\right) dt \tag{7}$$

where r is distance from the source, c is the speed of sound (∼340 m/s) and p represents the excess pressure time series. This approach was extended by Johnson and Miller (2014) to ensure zero net pressure over a finite window around the recorded event. We then calculated the mass of gas from discrete infrasound events using the integral of mass emission rate. These events, which have amplitudes between 1 and 3 Pa at our closest sensors, are up to about 500 kg. These values are similar to those Dalton et al. (2010) estimated from records of Pacaya in 2008), a time period in which the style of summit activity was very similar to the 2013 activity. They found repeated events characteristic of strombolian explosions with peak amplitudes ranging from 0.17 to 2.61 Pa at about twice the distance of our array in 2013 (∼1 km) and estimated masses of 12 to 962 kg.

The vertical single forces in the MT+F inversions have amplitudes on the order of 5-10 x10^9 N. When we compare the amplitudes of the modeled single forces to prior work on bubble ascent, we find they are orders of magnitude too large. Using the empirical scaling relation of James et al. (2009), in which the magnitude of the upward force is proportional to the square root of the slug mass, and the magnitude of our vertical single force of nearly 1.0 GN, we estimated a slug mass of up to 10^8 kg. Even considering the uncertainties associated with our mass estimates, we should not expect to be five orders of magnitude in error.

Any single force associated with the ascent of these bubbles must be many orders of magnitude smaller than what we find with our MT+F inversion. The inversion results, therefore might be unreliable due to the small number of stations (12 channels) we model. In a study of synthetic sources, Lanza and Waite (2018) found that there is a strong trade-off between single forces and moment tensor components when they are in phase. Further they found that inverting for single forces can increase the discrepancy between the modeled and input moment tensors. A similar study by Trovato et al. (2016) also points to challenges with MT+F inversions. While the source process we model here may involve mass advection or another process that would lead to a single force, the actual forces are likely much too small to be reliably modeled.

We therefore attribute the most reasonable data fit to a 6-component (MT) mechanism. The best-fitting source for the MT inversion when both source-time function stability and minimum misfit are considered is found ∼200 m to the ESE of the summit of the Mackenney cone at 2450 m above sea level, corresponding to about 40 m below the highest node in the topographical model in this location (**Figure 6**). While the model epicenter is displaced from the active vent, the shallow depth is consistent with the related infrasound and observed explosions and the epicentral error is likely a result of inaccuracies in the velocity model.

An important challenge of this work is that we are working with a small number of stations. We can clearly identify a dominant LP event but questioned how reliably we could resolve the source mechanism. Synthetic tests described in Lanza and Waite (2018) have shown that a complete azimuthal coverage, with a maximum gap of about 130°, is desired for a higher resolution of the retrieved source-time function. They also stated that azimuthal coverage has a larger influence on network performances over the number of stations used. However, for sources with a large isotropic component, four stations were deemed to be the limit of acceptable performances as with a lower number of stations the source mechanisms are unconstrained. Therefore, the case study of Pacaya where LP events were recorded by a network of only four stations with a fairly good azimuthal coverage should provide a reasonable model of the source mechanism.

As shown by additional synthetic tests described in this study, an unknown velocity model can introduce a further degradation of the solution. Although the source-time function is constrained to a region in which sources have a large isotropic component, the range of source-type shown in **Figure 8** could reflect the effect of a scarcity of stations and of an incorrect velocity model.

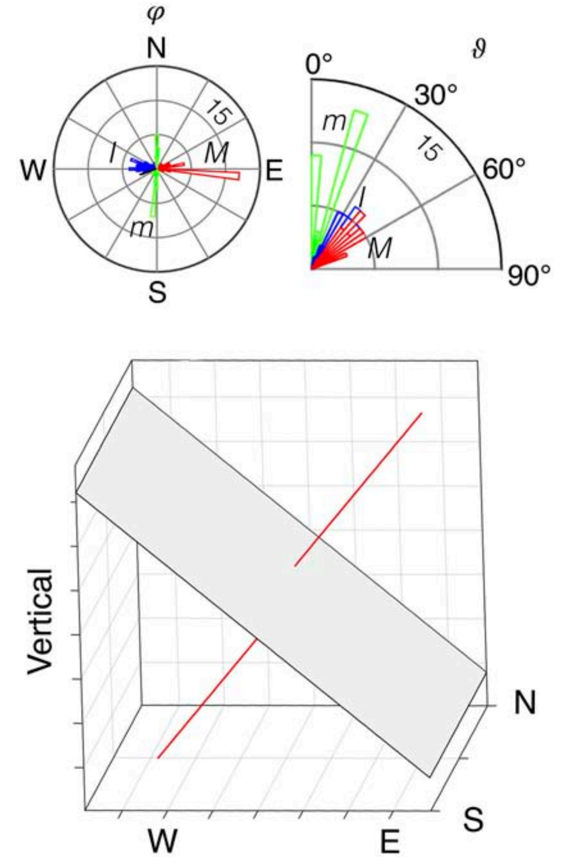

FIGURE 9 | Eigenvector statistic for the unconstrained MT inversion solution. The smallest (*m*), intermediate (*I*), and largest (*M*) eigenvectors are shown by green, blue, and red bins, respectively. ϕ is the azimuth, measured clockwise from north and ϑ is the inclination angle, measured from the vertical. The orientation of the crack plane and its normal (maximum eigenvector) are also shown in the xyz coordinate system.

With that in mind, we find that both the constrained and unconstrained inversions point to a source mechanism somewhat like a tension crack but with less symmetry. The nonlinear inversions indicate a range of possible solutions could fit the data reasonably well. The magnitude of the derived moment tensor is around 4 x 10^{10} Nm. This is comparable to moment-tensor solutions obtained for low-amplitude LPs at other volcanoes. At Mount St. Helens, Matoza et al. (2015) inverted small LP events and found a moment tensor with amplitudes on the order of 10^{10} Nm. Small LP events have been also imaged at Popocatepetl, Mexico, and showed moment-tensor components of similar order of magnitude (Arciniega-Ceballos et al., 2012). In both cases the low-amplitude LP events were related to shallow crack mechanisms and interpreted as hydrothermally driven fractures. At Pacaya, while the source mechanism is not precisely a theoretical crack, we can interpret it as a source that is dominated by volume change, consistent with a repetitive source that is associated with bubble bursts. We estimate the volume change in the source-time function from the amplitude

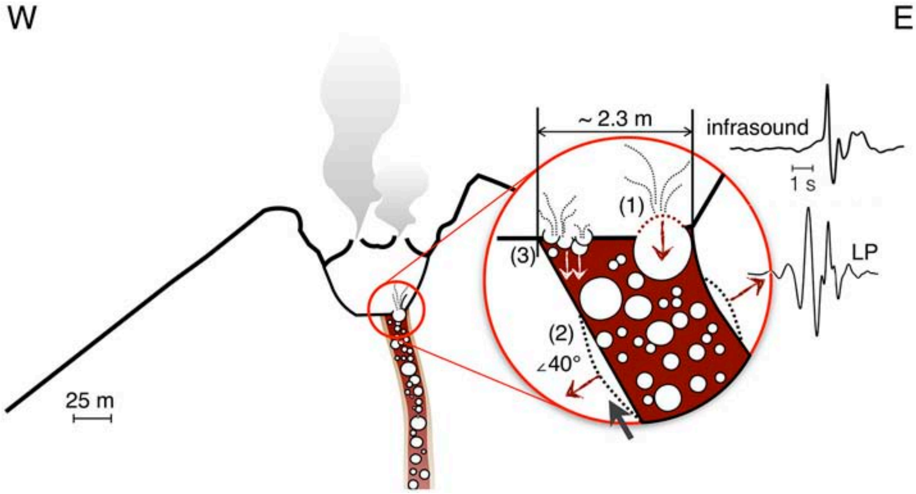

FIGURE 10 | Schematic of the proposed interpretations of the source-time function of the small long-period events recorded at Pacaya: (1) LPs seen as a manifestation of the reaction force to the expansion and ejection of the bubbles; (2) LPs seen as originating from the movement of the bubbles through an inclined crack that inflates and deflates as a result of the passage of fluids; (3) LPs seen as the results of bubbles that act as a volumetric source exploding at the surface with a sudden release in pressure.

$(\lambda + 2\mu)\Delta V$, assuming $\nu = 1/4$ ($\lambda = \mu$) as the source-time function occupies a region along the arc with $\nu = 1/4$ in the fundamental lune (**Figure 8C**). We use a shear modulus for the crack wall rock of 10 GPa following Lyons and Waite's (2011) study at Fuego volcano. The calculated volume change is ~ 2 m^3. This value reflects the representative average event obtained from the stacked waveforms, and it is reasonable for the size of the events recorded. We used the relationship between excess pressure and volume change in a penny-shaped crack (equation 11 from Chouet et al., 2010) to estimate the crack width as ~2.3 m. We envision the crack not as an isolated feature, but as a component of the shallow conduit that responds to the passage of these bubbles.

A schematic of the proposed physical interpretation of the source of these small shallow long-period events is shown in **Figure 10**. As gas slugs rise toward the surface, they expand and burst, creating an initial positive infrasonic pulse followed by a negative pulse. This generates the infrasound signal which was also observed in 2008 by Dalton et al. (2010). Both LPs and the acoustic waves show compressional first motions, with LP signals preceding the infrasound by ~ 1 s. The time delay is compatible with a source that simultaneously causes both the seismic and infrasound, given an airwave travel time of nearly 2 s and seismic travel time of under a second. One possibility is that the LPs are a manifestation of the reaction force to the expansion and ejection of the slugs (or bubbles). While the coupling of this source could possibly explain the dipping crack-like moment tensor, a simple calculation of the vertical force associated with bubble expansion (Gerst et al., 2013) indicates that it is perhaps 6 orders of magnitude smaller than would be required to explain the seismic moment of the LP.

A second explanation is that the non-destructive LP events originate from the movement of the slugs (or bubbles) through a N-S oriented, dipping crack that inflates and deflates as a result of the passage of fluids; when the slugs (bubbles) reach the lava free surface, they burst creating the infrasound signals. Given the short delay between the seismic and infrasound arrivals, the LP crack source must be very close to the surface, but this mechanism is compatible with timing of infrasound and seismic arrivals and the observations of E-W particle motions at stations west, north, and east of the summit.

Another possible explanation to the source dominated by isotropic components obtained by our inversion could involve the presence of bubbles that act as a volumetric source exploding at the surface with the sudden release in pressure. Distortions in the wavefield caused by propagation through the near-vertical walls of the conduit could explain why the mechanism is not calculated as perfectly isotropic.

In the broader context of the Mackenney cone and the recent eruptive history, the N-S orientation of the seismic source is consistent with both shallow and somewhat deeper features. The NNW oriented depression that developed during the 2010 eruption, shares a similar orientation. Flank vents, both north and south of the summit vent, have formed since the 2010 eruption. Modeling of InSAR data collected in from 2012-2014 points to the repeated opening of a NNW oriented dike within the upper 400 m of Mackenney cone (Wnuk and Wauthier, 2017). The Mackenney cone itself is built upon the scarp of a prehistoric flank collapse to the WSW and recent largescale motion of that flank has been in roughly the same direction (Schaefer et al., 2017). The conduit just below the vent, as modeled by the shallow LP seismicity, shares this dominant N-S direction imparted by deeper structures.

CONCLUDING REMARKS

We investigated the source mechanism and geometry of a class of LP events that includes thousands of small, repetitive, events that are associated with weak strombolian explosions at the summit vent of Pacaya volcano, Guatemala. LP events were recorded in October-November 2013 by four broadband stations located around the summit. Tremor-like seismic signals dominate the records at Pacaya during much of the deployment, but we find that the tremor is comprised in part by many small events, closely spaced in time. By employing the less noisy infrasound records to identify discrete events, we generate a representative LP event that we model with full waveform inversion.

Uncertainty in the velocity model and the small number of stations employed in the inversion allow for a certain degree of ambiguity in the source location, but we can clearly demonstrate that this event involves volume change in the source process. Our modeling demonstrates that the LP events reflect a shallow crack-like mechanism most likely related to bubble-bursting events at the summit. The N-S orientation of the model crack is consistent with aligned surficial features including vents and the NNW oriented depression that formed during the May 2010 explosive eruption. Similarly, dikes modeled geodetically have a N-S orientation such that the conduit must be elongated N-S throughout the edifice. Our study of 10 days of seismic data represents only a snapshot of the dynamic recent history of Pacaya volcano, but the combined seismic-infrasound approach provides constraints on the magmatic processes within the shallow conduit and the relationship between conduit structure and the overall structure of the Mackenney cone.

DATA AVAILABILITY

Data collected during the 2013 experiment are available through the IRIS Data Management Center. The facilities of the IRIS Consortium are supported by the National Science Foundation under Cooperative Agreement EAR-0552316 and by the Department of Energy National Nuclear Security Administration. The phase-weighted stacking code was provided by D. Mikesell.

AUTHOR CONTRIBUTIONS

FL took part in the seismic network installation, performed initial data processing for the temporary array, carried out the full waveform moment-tensor inversion, and wrote the first draft of the manuscript. GPW supervised all the work, advised FL on data processing, contributed to the development of the nonlinear inversion methodology, and provided revisions for/edited the manuscript. All authors read and approved the submitted manuscript.

FUNDING

This work has been supported by the National Science Foundation Career Award No. 1053794 entitled Eruption Dynamics From Low-Frequency Volcano-Seismic Signals.

ACKNOWLEDGMENTS

We thank J. Richardson for his guidance and fieldwork support. We are grateful to Parque Nacional Volcán de Pacaya and INSIVUMEH for allowing access and permission to install seismometers. We also thank two reviewers and Chief Editor Valerio Acocella for their useful comments which resulted in this improved version of the original manuscript.

SUPPLEMENTARY MATERIAL

The Supplementary Material for this article can be found online at: https://www.frontiersin.org/articles/10.3389/feart.2018.00139/full#supplementary-material

REFERENCES

Akaike, H. (1974). A new look at the statistical model identification. *IEEE Trans. Automat. Control* 19, 716–723. doi: 10.1109/TAC.1974.1100705

Aki, K., and Richards, P. G. (2002). *Quantitative seismology,* 2nd Edn. Sausalito, CA: University Science Books.

Arciniega-Ceballos, A., Dawson, P. B., and and Chouet, B. A. (2012). Long period seismic source characterization at Popocatépetl volcano, Mexico, Geophys. *Res. Lett.* 39:L20307. doi: 10.1029/2012GL053494

Auger, E., D'Auria, L., Martini, M., Chouet, B. A., and Dawson P,B. (2006). Real-time monitoring and massive inversion of source parameters of very long period seismic signals: An application to Stromboli Volcano, Italy. *Geophys. Res. Lett.* 33:L04301. doi: 10.1029/2005GL024703

Bean, C. J., Lokmer, I., and O'Brien, G. S. (2008). Influence of near-surface volcanic structure on long-period seismic signals and on moment tensor inversions: Simulated examples from Mount Etna. *J. Geophys. Res.* 113:B08308. doi: 10.1029/2007JB005468

Chouet, B. A. (1996). "New methods and future trends in seismological volcano monitoring," in *Monitoring and Mitigation of Volcano Hazards,* eds R. Scarpa and R. I. Tilling (New York, NY: Springer-Verlag), 23–97.

Chouet, B. A., Dawson, P. B., and Arciniega-Ceballos, A. (2005). Source mechanism of Vulcanian degassing at Popocatepetl Volcano, Mexico, determined from waveform inversions of very long period signal. *J. Geophys. Res.* 110:B07301. doi: 10.1029/2004JB003524

Chouet, B. A., Dawson, P. B., James, M. R., and Lane, S. J. (2010). Seismic source mechanism of degassing bursts at Kilauea Volcano, Hawaii: results from waveform inversion in the 10–50 s band. *J. Geophys. Res.* 115:B09311. doi: 10.1029/2009JB006661

Chouet, B. A., Dawson, P. B., Ohminato, T., Martini, M., Saccorotti, G., Giudicepietro, F., et al. (2003). Source mechanisms of explosions at Stromboli Volcano, Italy, determined from moment-tensor inversion of very-long-period data. *J. Geophys. Res.* 108:2019. doi: 10.1029/2003JB002535

Chouet, B. A., and Matoza, R. S. (2013). A multi-decadal view of seismic methods for detecting precursors of magma movement and eruption. *J. Volcanol. Geotherm. Res.* 252, 108–175. doi: 10.1016/j.jvolgeores.2012.11.013

Dalton, M. P., Waite, G. P., Watson, I. M., and Nadeau, P. A. (2010). Multiparameter quantification of gas release during weak Strombolian eruptions at Pacaya volcano, Guatemala, *Geophys. Res. Lett.* 37:L09303. doi: 10.1029/2010GL042617

Dawson, P. B., Chouet, B. A., and Power, J. (2011). Determining the seismic source mechanism and location for an explosive eruption with limited observational data: Augustine Volcano, Alaska. *Geophys. Res. Lett.* 38:L03302. doi: 10.1029/2010GL045977

Firstov, P. P., and Kravchenko, N. M. (1996). Estimation of the amount of explosive gas released in volcanic eruptions using air waves. *Volcanol. Seismol.* 17, 547–560.

Gerst, A., Hort, M., Aster, R. C., Johnson, J. B., and Kyle, P. R. (2013). The first second of volcanic eruptions from the Erebus volcano lava lake, Antarctica—Energies, pressures, seismology, and infrasound. *J. Geophys. Res. Solid Earth* 118, 3318–3340. doi: 10.1002/jgrb.50234

Goldstein, H., Poole, C. P., and Safko, J. L. (2002). *Classical Mechanics*, 3rd Edn. San Francisco: Addison Wesley. doi: 10.1119/1.1484149

Hudson, J. A., Pearce, R. G., and Rogers, R. M. (1989). Source type plot for inversion of the moment tensor. *J. Geophys. Res*. 94, 765–774.

James, M. R., Lane, S. J., Wilson, L., and Corder, S. B. (2009). Degassing at low magma-viscosity volcanoes: Quantifying the transition between passive bubble-burst and Strombolian eruption, *J. Volcanol. Geotherm. Res.* 180, 81–88. doi: 10.1016/j.jvolgeores.2008.09.002

Johnson, J. B., and Miller, A. J. C. (2014). Application of the monopole source to quantify explosive flux during vulcanian explosions at sakurajima volcano (Japan). *Seismol. Res. Lett.* 85, 1163–1176. doi: 10.1785/0220140058

Kanamori, H., and Given, J. W. (1982). Analysis of long-period seismic waves excited by the May 18, 1980, eruption of mount St. Helens – A Terrestrial Monopole? *J. Geophys. Res.* 87, 5422–5432.

Kitamura, S., and Matías, O. (1995). Tephra stratigraphic approach to the eruptive history of Pacaya volcano, Guatemala. *Sci. Rep. Tohoku Univ. Seventh Ser.* 45, 1–41.

Lanza, F., Kenyon, L. M., and Waite, G. P. (2016). Near-surface velocity structure of Pacaya volcano, Guatemala, derived from small-aperture array analysis of seismic tremor. *Bull. Seism. Soc. Am.* 106, 1438–1445. doi: 10.1785/0120150275

Lanza, F., and Waite, G. P. (2018). A nonlinear approach to assess network performance for moment-tensor studies of long-period signals in volcanic settings, *Geophys. J. Int.* 215, 1352–1367. doi: 10.1093/gji/ggy338

Lighthill, M. J. (1978). *Waves in Fluids*. New York, NY: Cambridge University Press.

Lyons, J. J., and Waite, G. P. (2011). Dynamics of explosive volcanism at Fuego volcano imaged with very long period seismicity. *J. Geophys. Res.* 116:B09303. doi: 10.1029/2011JB008521

Matoza, R. S., Chouet, B. A., Dawson, P. B., Shearer, P. M., Haney, M. M., Waite, G. P., et al. (2015). Source mechanism of small long-period events at Mount St. Helens in July 2005 using template matching, phase-weighted stacking, and full-waveform inversion. *J. Geophys. Res.* 120, 6351–6364. doi: 10.1002/2015jb012279

Ohminato, T., and Chouet, B. A. (1997). A free-surface boundary condition for including 3D topography in the finite-difference method. *Bull. Seism. Soc. Am.* 87, 494–515.

Ohminato, T., Chouet, B. A., Dawson, P. B., and Kedar, S. (1998). Waveform inversion of very long period impulsive signals associated with magmatic injection beneath Kilauea Volcano. *J. Geophys. Res.* 103, 839–823. doi: 10.1029/98JB01122

Ohminato, T., Takeo, M., Kumagai, H., Yamashina, T., Oikawa, J., Koyama, E., et al. (2006). Vulcanian eruptions with dominant single force components observed during the Asama 2004 volcanic activity in Japan. *Earth Planets Space.* 58, 583–593. doi: 10.1186/BF03351955

Richardson, J. P., and Waite, G. P. (2013). Waveform inversion of shallow repetitive long period events at Villarrica Volcano, Chile, *J. Geophys. Res.* 118, 4922–4936. doi: 10.1002/jgrb.50354

Rose, W. I., Palma, J. L., Escobar Wolf, R., and Matias, O. (2013). "A 50 yr eruption of a basaltic composite cone: Pacaya, Guatemala," in *Understanding Open-Vent Volcanism and Related Hazards,* eds W. I. Rose, J. L. Palma, H. D. Granados, and N. Varley (Boulder, CO: Geological Society of America).

Schaefer, L. N., Wang, T., Escobar-Wolf, R., Oommen, T., Lu, Z., Kim, J., et al. (2017). Three-dimensional displacements of a large volcano flank movement during the May 2010 eruptions at Pacaya Volcano, Guatemala. *Geophys. Res. Lett.* 44, 135–142. doi: 10.1002/2016GL071402

Schimmel, M., and Paulssen, H. (1997). Noise reduction and detection of weak, coherent signals through phase-weighted stacks. *Geophys. J. Int.* 130, 497–505. doi: 10.1111/j.1365-246X.1997.tb05664.x

Shearer, P. M. (1994). Global seismic event detection using a matched filter on long-period seismograms. *J. Geophys Res.* 99, 13713–13725. doi: 10.1029/94JB00498

Tape, W., and Tape, C. (2012). A geometric setting for moment tensors, *Geophys. J. Int.* 190, 476–498. doi: 10.1111/j.1365-246X.2012.05491.x

Thurber, C. H., Zeng, X., Thomas, A. M., and Audet, P. (2014). Phase-weighted stacking applied to low-frequency earthquakes. *Bull. Seism. Soc. Am.* 104, 2567–2572. doi: 10.1785/0120140077

Trovato, C., Lokmer, I., De Martin, F., and Aochi, H. (2016). Long period (LP) events on Mt Etna volcano (Italy): the influence of velocity structures on moment tensor inversion. *Geophys. J. Int.* 207, 785–810. doi: 10.1093/gji/ggw285

Waite, G. P., Chouet, B. A., and Dawson, P. B. (2008). Eruption dynamics at Mount St. Helens imaged from broadband seismic waveforms: Interaction of the shallow magmatic and hydrothermal systems. *J. Geophys. Res.* 113:B02305. doi: 10.1029/2007JB005259

Waite, G. P., and Lanza, F. (2016). Nonlinear inversion of tilt-affected very-long-period records 1 of explosive eruptions at Fuego volcano. *J. Geophys. Res.* 121, 7284–7297. doi: 10.1002/2016JB013287

Wnuk, K., and Wauthier, C. (2017). Surface deformation induced by magmatic processes at Pacaya Volcano, Guatemala revealed by InSAR. *J. Volcanol. Geotherm. Res.* 344, 197–211. doi: 10.1016/j.jvolgeores.2017.06.024

Conflict of Interest Statement: The authors declare that the research was conducted in the absence of any commercial or financial relationships that could be construed as a potential conflict of interest.

frontiers
in Earth Science

ORIGINAL RESEARCH
published: 24 January 2019
doi: 10.3389/feart.2018.00238

Isotopic and Petrologic Investigation, and a Thermomechanical Model of Genesis of Large-Volume Rhyolites in Arc Environments: Karymshina Volcanic Complex, Kamchatka, Russia

Ilya N. Bindeman [1]*, ***Vladimir L. Leonov*** [2], ***Dylan P. Colón*** [1], ***Aleksey N. Rogozin*** [2], ***Niccole Shipley*** [1], ***Brian Jicha*** [3], ***Matthew W. Loewen*** [1,4] ***and Taras V. Gerya*** [5]

[1] Department of Earth Sciences, University of Oregon, Eugene, OR, United States, [2] Institute of Volcanology and Seismology, Petropavlovsk-Kamchatsky, Russia, [3] Department of Geoscience, University of Wisconsin, Madison, WI, United States, [4] U.S. Geological Survey, Alaska Volcano Observatory, Anchorage, AK, United States, [5] Department of Earth Sciences, ETH Zurich, Zurich, Switzerland

Edited by:
Katherine Dobson,
Durham University, United Kingdom

Reviewed by:
Marlina A. Elburg,
University of Johannesburg,
South Africa
Michel Grégoire,
Center for the National Scientific
Research (CNRS), France

***Correspondence:**
Ilya N. Bindeman
bindeman@uoregon.edu

Specialty section:
This article was submitted to
Petrology,
a section of the journal
Frontiers in Earth Science

Received: *08 October 2018*
Accepted: *10 December 2018*
Published: *24 January 2019*

Citation:
Bindeman IN, Leonov VL, Colón DP, Rogozin AN, Shipley N, Jicha B, Loewen MW and Gerya TV (2019) Isotopic and Petrologic Investigation, and a Thermomechanical Model of Genesis of Large-Volume Rhyolites in Arc Environments: Karymshina Volcanic Complex, Kamchatka, Russia. Front. Earth Sci. 6:238. doi: 10.3389/feart.2018.00238

The Kamchatka Peninsula of eastern Russia is currently one of the most volcanically active areas on Earth where a combination of >8 cm/yr subduction convergence rate and thick continental crust generates large silicic magma chambers, reflected by abundant large calderas and caldera complexes. This study examines the largest center of silicic 4-0.5 Ma Karymshina Volcanic Complex, which includes the 25 × 15 km Karymshina caldera, the largest in Kamchatka. A series of rhyolitic tuff eruptions at 4 Ma were followed by the main eruption at 1.78 Ma and produced an estimated 800 km^3 of rhyolitic ignimbrites followed by high-silica rhyolitic post-caldera extrusions. The postcaldera domes trace the 1.78 Ma right fracture and form a continuous compositional series with ignimbrites. We here present results of a geologic, petrologic, and isotopic study of the Karymshina eruptive complex, and present new Ar-Ar ages, and isotopic values of rocks for the oldest pre- 1.78 Ma caldera ignimbrites and intrusions, which include a diversity of compositions from basalts to rhyolites. Temporal trends in $\delta^{18}O$, $^{87}Sr/^{86}Sr$, and $^{144}Nd/^{143}Nd$ indicate values comparable to neighboring volcanoes, increase in homogeneity, and temporal increase in mantle-derived Sr and Nd with increasing differentiation over the last 4 million years. Data are consistent with a batholithic scale magma chamber formed by primarily fractional crystallization of mantle derived composition and assimilation of Cretaceous and younger crust, driven by basaltic volcanism and mantle delaminations. All rocks have 35–45% quartz, plagioclase, biotite, and amphibole phenocrysts. Rhyolite-MELTS crystallization models favor shallow (2 kbar) differentiation conditions and varying quantities of assimilated amphibolite partial melt and hydrothermally-altered silicic rock. Thermomechanical modeling with a typical 0.001 km^3/yr eruption rate of hydrous basalt into a 38 km Kamchatkan arc crust produces two magma bodies, one near the Moho and the other engulfing the entire section of upper crust. Rising basalts are trapped in the lower portion of an upper crustal magma body, which exists in a partially molten to solid state. Differentiation products of basalt periodically mix with the resident magma diluting its crustal isotopic signatures.

At the end of the magmatism crust is thickened by 8 km. Thermomechanical modeling show that the most likely way to generate large spikes of rhyolitic magmatism is through delamination of cumulates and mantle lithosphere after many millions of years of crustal thickening. The paper also presents a chemical dataset for Pacific ashes from ODDP 882 and 883 and compares them to Karymshina ignimbrites and two other Pleistocene calderas studied by us in earlier works.

Keywords: high-silica rhyolites, oxygen isotopes (18O), thermomechanical modeling, caldera, Ar-Ar dating, Sr isotopes, Nd isotopes, Kamchatka (Russia)

INTRODUCTION

Voluminous silicic volcanism in island arcs worldwide is a reflection of the production of silicic magmas by mafic magma differentiation and crustal anatexis, and of the crustal redistribution of silicic and mafic materials, which segregates the crust into deep mafic and shallow silicic compositional domains (Vogel et al., 2006; Vogt et al., 2012). Together with arc accretion to continental margins, these processes have contributed to the growth, segregation, and differentiation of continental crust throughout geologic history (Taylor and McLennan, 1995; Rudnick and Gao, 2003). There is always a chicken-and-egg question in continental arcs however, on whether silicic magmas arise via magmatic differentiation, especially in arcs with high convergence rates such as Kamchatka, the Andes, and Japan, or if silicic magmatism occurs because felsic rocks are initially present in preexisting continental crust (Tatsumi, 2005; Winter, 2010). Additionally, continental arcs with older crust are isotopically distinct and this isotopic torque permits the better recognition of the petrogenetic processes that may similarly operate in juvenile oceanic arcs (Hildreth and Moorbath, 1988). Anatexis and remelting of the preexisting silicic crust in continental arcs produce conditions where further segregation of silicic differentiates and partial melts leads to redistribution of silicic components to the upper crust in a positive feedback of crust-building (Bindeman and Simakin, 2014). Isotope geochemistry, petrology, and large-scale thermomechanical modeling serve as tools to address these questions (Tatsumi, 2005; Eichelberger et al., 2006; Winter, 2010; Vogt et al., 2012). Island arcs, and especially continental arcs, that are built on thick crust often display continuous silicic magmatism in one segment of the arc lasting many millions of years, which can be expressed on the surface by overlapping caldera collapses (de Silva and Gosnold, 2007). In other conditions, voluminous silicic magmas appear suddenly without prolonged preconditioning of the crust, and magmatism remains bimodal with basaltic and rhyolitic peaks (Kimura et al., 2015).

The Kamchatka Peninsula in northeast Russia represents the most volcanically active segment of the Pacific Ring of fire, due to in part to fast >8 cm/yr orthogonal subduction with a thick crust in the overriding plate (**Figure 1**, Ponomareva et al., 2007). The eastern margin is constructive with a series of arcs accreting to Kamchatka in the Cenozoic (Konstantinovskaia, 2001; Hourigan et al., 2009) and now forming the basement under the modern volcanic edifices. The last episode of arc-continent collision lasted from 7 to 12 Ma (Lander and Shapiro, 2007; Scholl, 2007). High magma accumulation rates coupled with rapid uplift due to compressional forearc forces leads to the exposure of various basement rocks within the modern arc, providing insights into the arc structure (**Figures 1**, **2**). These include Cretaceous-Eocene metamorphic rocks, 11 Ma granitic bodies exposed on the Pacific shore such as Akhomten Massif, and younger volcanic sequences (Seligman et al., 2014). More volcanic calderas occur in Kamchatka than any other arc worldwide (Bindeman et al., 2010), with examples of both systems with continuous compositional variation in erupted material, as well as of the bimodal end member. An example of the latter is the large Pauzhetka caldera in southernmost Kamchatka, where the crust is the thinnest and consists mostly of greywackes and basalts.

This study mostly focuses on a series of voluminous 4.11–0.50 Ma rhyolites and high-silica rhyolites (HSR) erupted as voluminous ignimbrites and lavas that we collectively refer to as the Karymshina Volcanic Complex (KVC) (**Figures 1**, **2**). The KVC is likely the largest center of silicic volcanism in Kamchatka as is established here. Abundant silicic rocks were first discovered in the area in the course of geologic mapping in the 1960s—1980s and were initially considered to represent several eruptive silicic vents collectively forming a volcano-tectonic depression (Sheimovich and Patoka, 1989; Sheimovich and Khatskin, 1996; Geological Map of the Russian Federation, 2000; Sheimovich and Golovin, 2003). A part of this complex around Tolsty Mys Mountain (1343 m), the highest topographic point in the area (**Figure 2**), was reinterpreted by Leonov and Rogozin (2007) as a resurgent dome inside an uplifted and dissected, hundreds of meters-thick intracaldera tuff, within the large 25 × 15 km Karymshina Caldera. Bindeman et al. (2010) performed Ar-Ar and U-Pb zircon dating and demonstrated that the top and the bottom of the 1,000 m ignimbrite sheet (their **Figure 4**), have identical ages of 1.78 ± 0.02 Ma. Due to the great thickness and lateral extent of this deposit (**Figure 2**), these authors agreed with interpretation of Leonov and Rogozin (2007) that it represents a remnant of densely welded and relatively compositionally unzoned 1.78 Ma intracaldera ignimbrite, brought up by post 1.78 Ma uplift and erosion. The situation is analogous to the 2.8 Ma, two-km thick uplifted and dissected, intracaldera Chegem ignimbrite in the Caucasus and we take instruction from the study of that center by Lipman et al. (1993) in describing and discerning field relations for Karymshina ignimbrite. The search for an identical in age 1.78 Ma extracaldera ignimbrite in past 10 years is still ongoing; this is partly explained by

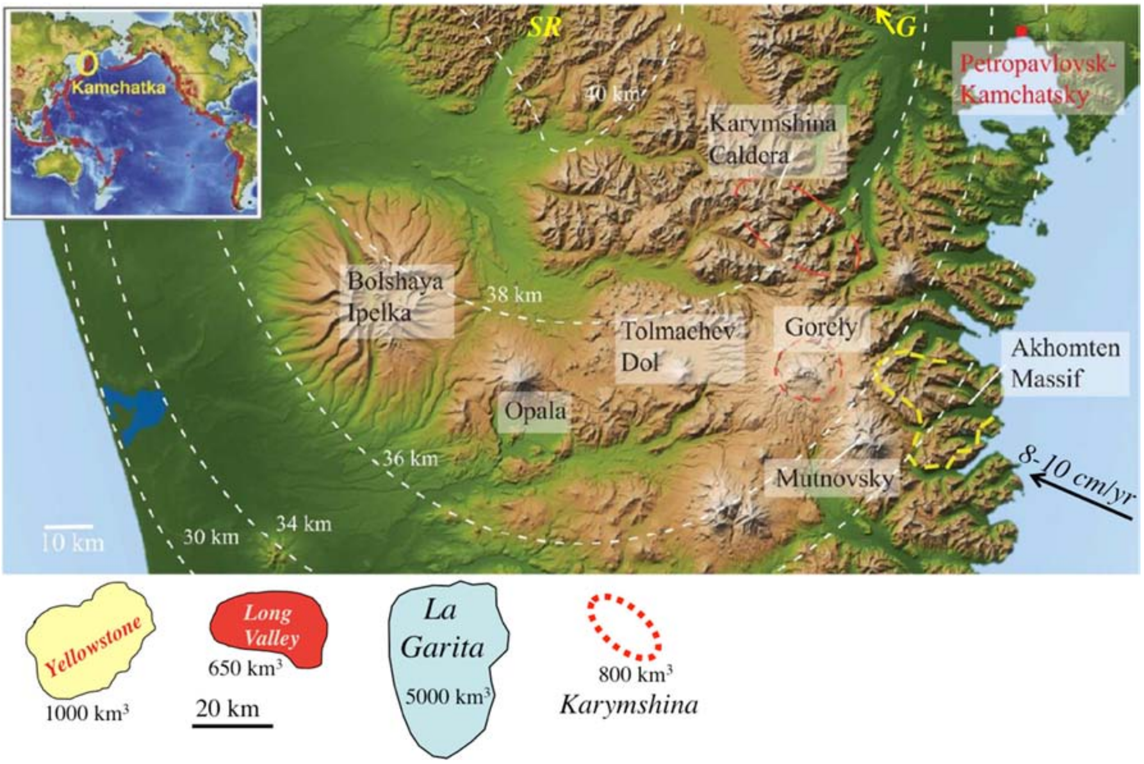

FIGURE 1 | Karymshina Volcanic Complex in Kamchatka. Inset: plate tectonic configuration, and presently active volcanoes of the Eastern Volcanic Front, and extinct volcanic arc in the Sredinny Range. A cross section through south-central Kamchatka shows Karymshina Volcanic Complex and other neighboring volcanoes mentioned in text. Notice uplift and topographic manifestation of Late Pleistocene calderas (e.g., Gorely), ignimbrite sheets around it and glacial coastal fjords and erosional features. Crustal thickness is shown my dashed line from Baboshina et al. (2000). Ganal metamorphic basement (G) with mafic amphibolites of Cretaceous age is to the NW of the letter G, while Sredinny Range with siliceous gneisses extends north of the letter SR. Lower panel shows comparison of caldera outlines mentioned in text and their eruptive volumes.

uplift and erosion, dense vegetation in Kamchatka and difficult logistics. The similarly uplifted and eroded Chegem tuff still preserves scattered outcrops of ∼50 m thick extracaldera Chegem ignimbrite only in the immediate vicinity of caldera (Lipman et al., 1993). Search for an extracaldera 1.78 Ma Karymshina tuff and dating efforts resulted in the discovery of both older and younger, dacitic and rhyolitic tuffs and new extrusions ranging in age from 4.11 to 1.39 Ma (Bindeman et al., 2010, and this study, **Figure 2** and **Table 2**).

Geophysical investigations of the crustal thickness and structure in southern Kamchatka (Baboshina et al., 2000; Geological Map of the Russian Federation, 2000) reveal the presence of reworked continental crust that is 38–40 km thick (**Figure 2**). A wide spectrum of zircon ages going back to 3.4 Ga (Hourigan et al., 2009; Bindeman et al., 2016) indicates metamorphosed mixed siliceous sediment origin. A magnetotelluric profile conducted along the line from Opala volcano to the northwest (line I-I' on **Figure 2**) cross-cuts the Karymshina Caldera just to the north of its center (**Figure 3**). It revealed locally thickened gabbroic lower crust and thinned upper crust, as well as increased thickness of volcanic rocks and volcaniclastic Cenozoic sediments. Although not interpreted by the original authors to reflect the magmatic evolution of KVC, we below interpret this structure as an indication of substitution of the upper crust by a massive series of basaltic sills leading to the "basaltification" of the mid to upper crust via mantle-derived intrusions.

The large-volume rhyolitic eruption at Karymshina at 1.78 Ma represents an unusual and rare event for volcanic arcs, as single caldera-forming eruptions with volumes in excess of 100 km^3 are all but unknown in most volcanic arc segments around the world (de Silva, 2008). Eruptions on this "supervolcanic" scale are instead confined to "flareups" of magmatism which represent events in some continental arcs characterized by extremely rapid production of silicic volcanic rocks and intrusions over a relatively short period of as little as a few Myr (de Silva et al., 2006; Ducea and Barton, 2007; Ducea et al., 2015a,b). These flareups, also referred to as high-volume magmatic events (Ducea et al., 2015a), can be responsible for producing as much as 90% of the granitoid intrusions in a continental arc such as the Sierra Nevada in the western United States (Ducea et al., 2015a). The origin of these flareup events remains controversial, with various authors proposing the underthrusting of fertile upper crust in a compressive tectonic regime to depths suitable for voluminous melting (Ducea and Barton, 2007; DeCelles et al., 2009), a thermal runaway where steady intrusion of basalt produces a

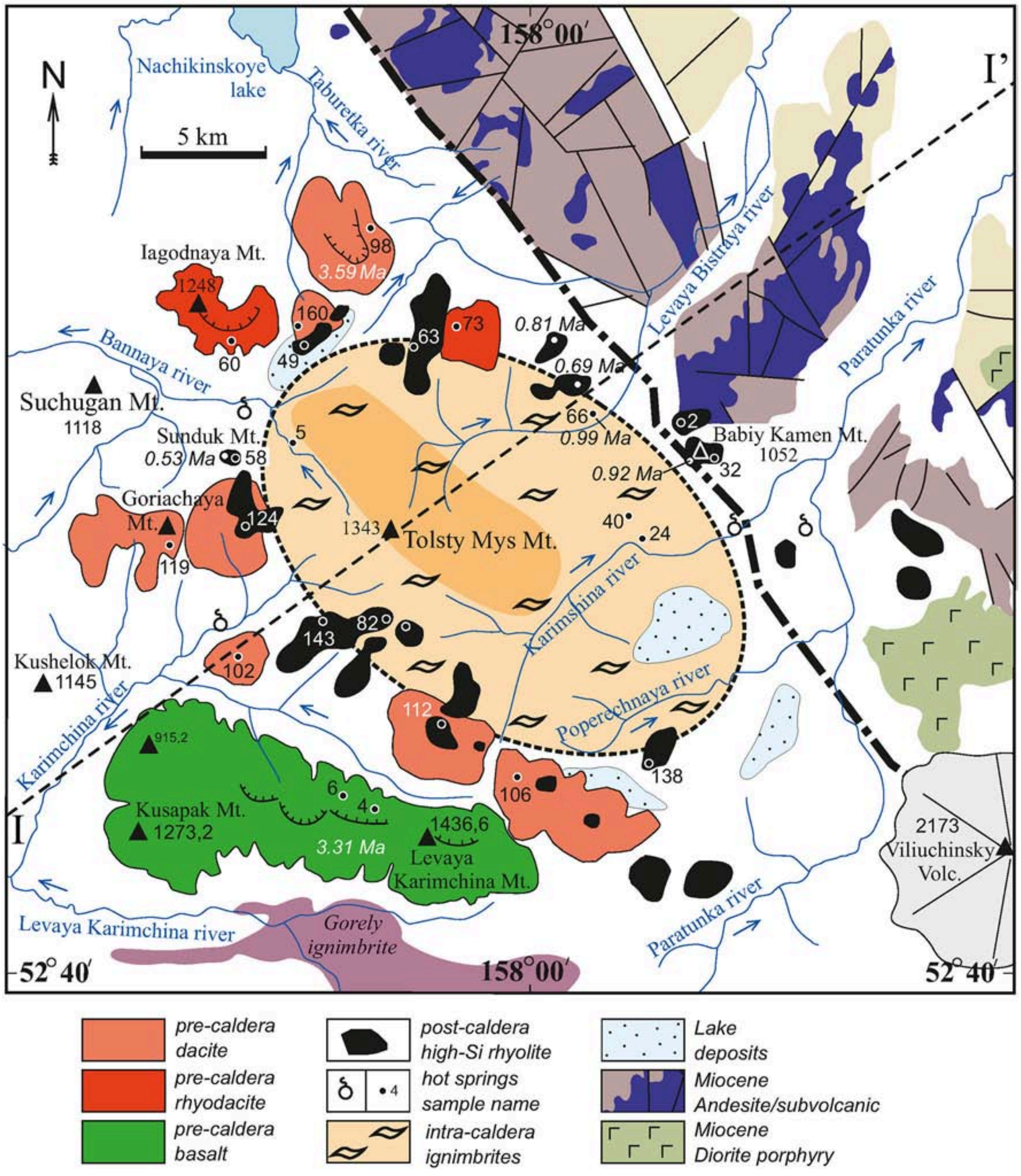

FIGURE 2 | A geologic map of Karymshina Volcanic Complex showing topographic features, inferred 1.78 Ma Karymshina caldera boundary (dashed line), pre- and post-caldera extrusive domes and volcanoes. Numbers represent ages from this study (**Table 2**) and compiled from the literature (**Table 1**). The last two-three digits of sample names from this study (e.g., 119 is 119L-2005) corresponds to the **Table 1**. The area of the caldera contains several ignimbrite sheets, which reach visible thicknesses of 1,000 m on the eastern edge and contain no observable stratigraphic compositional differences (**Table A1**). These ignimbrite sheets wedge out as they approach the edges of the depression near the volcanoes Goryachaya, Yagodnaya, and Sunduk. The volcanic products of those volcanoes and additional large extrusions overlay the ignimbrite sheets along the supposed ring fracture. Miocene porphyries include granodiorites from 11 to 14 Ma Zavoikovsky complex and 11.4 Ma Akhomten granitic complex is to the southeast (**Figure 1**). Dashed line I and I′ represent geophysical profile from Geological Map of the Russian Federation (2000) shown on **Figure 3**.

highly non-linear increase in the amount of crustal melting above a certain threshold (Dufek and Bergantz, 2005; Karakas et al., 2017), or a sudden increase in melting in the mantle wedge due to either rollback of the overriding slab (DeCelles et al., 2009) or the delamination of the dense mafic lowermost crust and mantle lithosphere, leading to sudden decompression

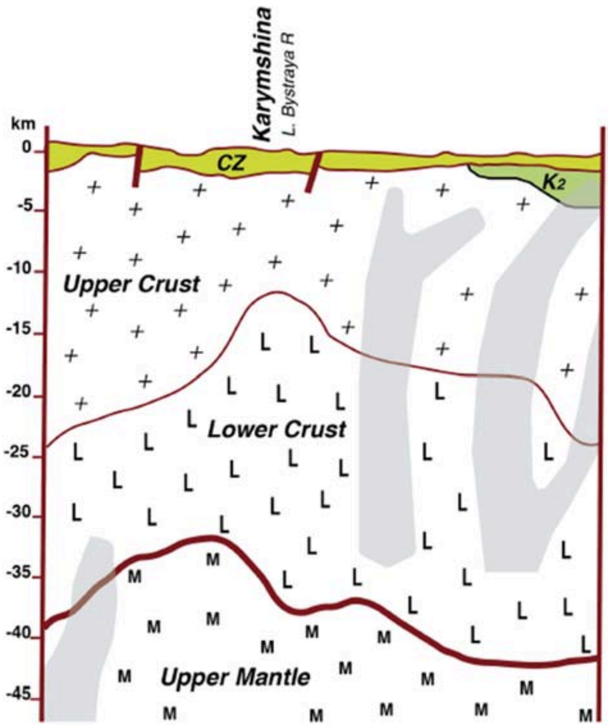

FIGURE 3 | Seismic profile across Karymshina caldera (Geological Map of the Russian Federation, 2000) showing regional 38–40 km thick continental crust and crustal structure. Notice thinned upper crust and locally thickened lower crust under Karymshina that we interpret here as representing basaltic sills that were added to the upper crust causing its partial melting and progressive substitution with more mafic residue and basaltic cumulate in the process of magmatic evolution of Karymshina Volcanic Complex. CZ is Cenozoic volcanic and volcaniclastic cover, K_2 is Upper Cretaceous crust. Vertical gray areas represent faults according to magnetotelluric seismic imaging.

melting of the mantle (de Silva et al., 2006; Lee et al., 2006). DeCelles et al. (2009) argue against this latter model, pointing out that magmas associated with flareups tend to have lower ε_{Nd} values, indicating that crustal melting was disproportionately responsible for producing the silicic intrusions relative to the differentiation of a greater volume of mantle-derived basalts. However, Colón et al. (2018a) pointed out that greater magmatic fluxes from the mantle actually serve to increase the proportion of crustal melt in the resulting rhyolites, as the greater heat allows more crust to melt at a slightly faster rate than it allows for more basalts to be differentiated to rhyolite, a result which we replicate here.

In this study, we summarize data obtained in the past decade and provide geological, mineralogical, whole rock major and trace element characterization of the caldera-forming ignimbrites, and newly described pre- and post-caldera extrusions and ignimbrites, and present results of new geochronology and analysis of O, Sr, Nd, and H isotopes in the eruptive products. We supplement this information with the results of rhyolite-MELTS modeling of crystallization and assimilation, and results from thermomechanical modeling of magma genesis in the unusually voluminous Karymshina system.

METHODS

Mineralogy and Petrography

Thin sections of five samples of the top (36L-2007) and middle-bottom (samples 24L-2006, 40L-2007) of the ignimbrites and postcaldera intrusions (samples 2L-2008, and 58L-2006 in **Table 1**) were analyzed by electron microprobe (**Table A3**, **Figure 4**). An additional three covered thin sections (5G-2005, zh356, and zh423) were used for crystal abundance counting on a petrographic microscope (**Table A1**).

Electron microprobe analyses were performed at Lokey Laboratories at the University of Oregon on a Cameca SX-100 using an accelerating voltage of 15 kV, a 30 nA beam current, and a 10 µm spot beam size. Several plagioclase crystals were analyzed from each sample, as well as some amphiboles, plagioclase crystals within autholithic xenocrysts, and the glass matrix. Three spot analyses were used to classify plagioclase zoning types: normal and reverse concentric, complex, and unzoned. Cores were also analyzed for xenolith-hosted plagioclase. Amphiboles were chosen due to the existence of exsolution rims. Spot analyses of the amphiboles were performed at the core and within the exsolution rims. Glass matrix was analyzed in several locations to check for potential variations. Whole rock major and trace element analyses were performed by XRF using fused Li-Borate discs at Washington State University.

Trace element concentrations were determined by LA-ICP-MS at Oregon State University on matrix glass from ignimbrite samples as well as tephras selected in selected North Pacific IODP drill sites from sediment intervals matching the age of major Kamchatkan ignimbrites. Analytical procedures generally followed Loewen and Kent (2012) using a Photon Machines 193 nm ArF laser coupled to a ThermoScientific X-Series ICP-MS. A 50 µm spot at 7 Hz was used to ablate glass ± epoxy. Blank analyses of epoxy verified that no significant trace element signature was present. Silica from electron microprobe analyses done on the same or similar samples or similar samples was used for an internal standard, and analyses were calibrated with GSE-1G. Results are presented in **Table A2**.

Isotope Geochemistry

Oxygen isotopes were analyzed in plagioclase and quartz using samples weighing ~1.5 mg by CO_2 laser fluorination and the MAT 253 gas source mass spectrometer at the University of Oregon. All analyzed crystals were visually checked under the microscope to ensure they were free of visible inclusions and lacked visible alteration due to weathering. The largest phenocrysts were analyzed individually (**Table 3**) and several crystals were analyzed per sample to check for isotopic variation among the phenocrysts. However, none was found and thus bulk analyses are robust. Two samples of zircon from the top and the bottom of Karymshina ignimbrites 2006L-24 and 2007L-36 were analyzed at the UCLA ion microprobe facility on the Cameca 1270 ion microprobe using a Cs primary beam and polished zircon mounts used previously for U-Pb dating, and the data was presented in Bindeman et al. (2010) and Bindeman and Simakin (2014).

TABLE 1 | Description of samples from Karymshina Volcanic Complex used in this study.

Sample ID	Latitude	Longitude	location/name	Age, Ma	Comment	Minerals, %
PRE-CALDERA EXTRUSIONS						
6L-2010	N 52.725990°	E 157.900490°	Basalt volcano, S edge of caldera			
4L-2010	N 52.721800°	E 157.921780°	Basalt volcano, S edge of caldera	3.312 ± 0.078		
160L-2008	N 52.889056°	E 157.867356°	Small dacite volcano, cut by caldera rim			
102L-2008	N 52.776229°	E 157.839537°	Small dacite volcano, cut by caldera rim			
73L-2011	N 52.888304°	E 157.962367°	Dacite volcano, N rim of caldera			
60L-2004	N 52.883933°	E 157.838324°	Dacite volcano on the rim, NW from it			
98L-2008	N 52.925247°	E 157.911999°	Dacite volcano, rim of caldera	3.586 ± 0.006		
106L-2006	N 52.737887°	E 157.990413°	Dacite volcano, S rim of caldera, ignimbrite are overlying it			
119L-2005	N 52.814119°	E 157.823909°	Dacite volcano, Goryachaya Mt, W of caldera, part of volcano is burried by ignimbrites			
KARYMSHINA IGNIMBRITES						
36L-2007	N 52.835347°	E 158.066208°			*	Pl19%Qz20%Gl46%
37L-2007	N 52.834460°	E 158.066177°	"		*	
38L-2007	N 52.833834°	E 158.065502°	"		*	
39L-2007	N 52.831718°	E 158.064906°	"		*	
40L-2007	N 52.829532°	E 158.065741°	"	1.78 ± 0.02	*	
41L-2007	N 52.827850°	E 158.071454°	"		*	
24L-2006	N 52.818792°	E 158.084820°	"	1.78 ± 0.02	*	Pl25%Qz21%Gl42%
43L-2007	N 52.825947°	E 158.079612°	"		*	
44L-2007	N 52.825029°	E 158.080838°	"		*	
45L-2007	N 52.823854°	E 158.082877°	"		*	
46L-2007	N 52.823223°	E 158.083222°	"		*	
47L-2007	N 52.822530°	E 158.083612°	"		*	
321L-1972	N 52.617045°	E 158.318274°	Zhirovskaya ignimbrite		*	
5G-2005	N 52.846024°	E 157.866544°	Bannaya R Ignimbrite	1.388 ± 0.1	*	Pl46%Qz2%Gl53%
POST-CALDERA EXTRUSIONS						
107L-2005	N 52.886703°	E 157.795909°	Extrusion south of Yagodnaya Mt (older trakhirhyolite complex)			
124L-2005	N 52.818807°	E 157.844167°	Zubia Mt			
143L-2005	N 52.786572°	E 157.882363°	Height 1267.3m, upper R. Karymchina River			
49L-2006	N 52.880648°	E 157.868317°	Height 1047, R bank of Bannaya R			
45L-2004	N 52.843611°	E 157.824156°	Sunduk Mt	*0.53 ± 0.05*	=58L-06	
58L-2006	N 52.842885°	E 157.825792°				Pl23%Qz14Gl54%
63L-2005	N 52.880835°	E 157.929562°	Height 802m, Nachikinsky Creek		=75L-06	
112L-2006	N 52.746464°	E 157.949139°	Heigh 1439m, U Middle Karymchina R			
138L-2006	N 52.733089°	E 158.067444°	Plateau between Ovragia and Poperechnaya			
138L-2006	N 52.733089°	E 158.067444°				

(Continued)

TABLE 1 | Continued

Sample ID	Latitude	Longitude	location/name	Age, Ma	Comment	Minerals, %
80L-2007	N 52.784158°	E 157.921728°	Heigh 1269m, Upper R Karymchina R			
82L-2007	N 52.783616°	E 157.914261°	Height 1250, U R Karymchina R			
2L-2008	N 52.855487°	E 158.090884°	Height 973.8m next to Mt Baby Kamen	*0.5 ± 0.2*		Pl22%Qz17%Gl53%
32L-2007	N 52.840150°	E 158.106371°	Baby Kamen extrusion		0.919 ± 0.084#	*
35L-2007	N 52.840232°	E 158.091856°	Post-Caldera extrusion/dike		*	
66L-2013	N 52.866948	E 158.022530	Intra-caldera ignimbrite	0.988 ± 0.026	*	
PRE CALDERA IGNIMBRITES						
10L-2015	N 52.833937	E 157.208486	Extra-caldera ignimbrite		3.77 ± 0.002	
13L-2015	N 52.745852	E 157.390212	Extra-caldera ignimbrite		3.853 ± 0.022	
89L-2013	N 52.877498	E 157.593793	Extra-caldera ignimbrite		3.622 ± 0.039	
77L-2016_2	N 52.905098	E 157.929458	Q-Bi tuff		3.839 ± 0.029	
139L-2013	N 52.925439	E 157.530176	Extra-caldera ignimbrite		3.634 ± 0.071	
111L-2010	N 52.510582°	E 158.214476°	Karymshina-Zhirovskoy, Falshivaya River 100m under powed station, 4Ma	4.11 ± 0.09#	**	

**Published in Bindeman et al. (2010), **age published in Seligman et al. (2014). Italics - published Ar Ar ages from Sheimovich. # zircon U-Pb age; =sample number is for identical sample.*

Hydrogen isotopes were analyzed in biotite and amphibole using samples weighing ∼1.5 mg on the high temperature conversion/elemental analyzer (TC/EA) coupled with the MAT 253 mass spectrometer at the University of Oregon. Only biotite and amphibole samples from the ignimbrites were microscopically fresh and were analyzed for D/H; lesser and commonly insufficient quantities of these minerals are present in postcaldera intrusions and they are additionally display greater alteration into chlorite. Analyzed 1.5 mg of samples were visually checked for the absence of chloritization or oxidation. Data were normalized relative to new USGS standards 57 and 58 on a SMOW scale (Qi et al., 2017).

Whole rock ^{86}Sr/^{87}Sr and ^{144}Nd/^{143}Nd ratios were analyzed at the New Mexico State University by Dr. Frank Ramos using standard column chemistry and TIMS VG Vector 54 instrument.

^{40}Ar/^{39}Ar analyses were performed at the WiscAr laboratory at the University of Wisconsin-Madison. All ^{40}Ar/^{39}Ar dates are calculated relative to the 28.201 Ma Fish Canyon sanidine standard or the 1.1864 Ma Alder Creek sanidine standard (Jicha et al., 2016) using the decay constants of Min et al. (2000). Complete analytical methods and data are provided in the online supplement.

Magmatic-Thermomechanical Modeling

To further investigate the origins of the huge volumes of magma produced in a relatively short time at Karymshina, we used a slight modification of the 2D model used for the Yellowstone hotspot in Colón et al. (2018a), which is in turn a modification of the original large scale thermomechanical code developed by Gerya and Yuen (2003). The model setup that we use for Kamchatka, where the crust is 30–38 km thick (**Figures 1**, **2**) is identical to what is described in the Colón et al. (2018a) study, with a few key exceptions. We retain the use of a mantle plume to produce melts which fuel volcanism, instead of using a fully realized model of a dehydrating subducting slab, a choice which we justify in light of the fact that we are primarily interested in processes in the top ∼70 km of the crust and upper mantle, rendering the actual source of mantle melting less important, and avoiding for now the complicated task of setting up a realistic subduction geometry. Unlike in the Colón et al. (2018a) model, the lithosphere is fixed relative to the ascending plume, and the plume is much cooler and weaker than in the Yellowstone model, to more accurately reproduce a typical subduction flux for the arc (e.g., Jicha and Jagoutz, 2015). The plume advects from the base of the model at a rate of ∼3,700 km^2/Myr, as in Colón et al. (2018a), but has a much lower potential temperature of 1,475°C (compared to a background value of 1,350°C) to produce the desired amount of mantle melting. We also begin the model with only a 50 km thick lithosphere (compared to 80 km for the Yellowstone study). Further modifications from the code of Colón et al. (2018a) include higher melt fractions for basalts at given temperatures and pressures, to account for the much higher water contents of subduction zone magmas, and minor improvements to the way melt is transported in the crust (these changes described in Colón et al., 2018b).

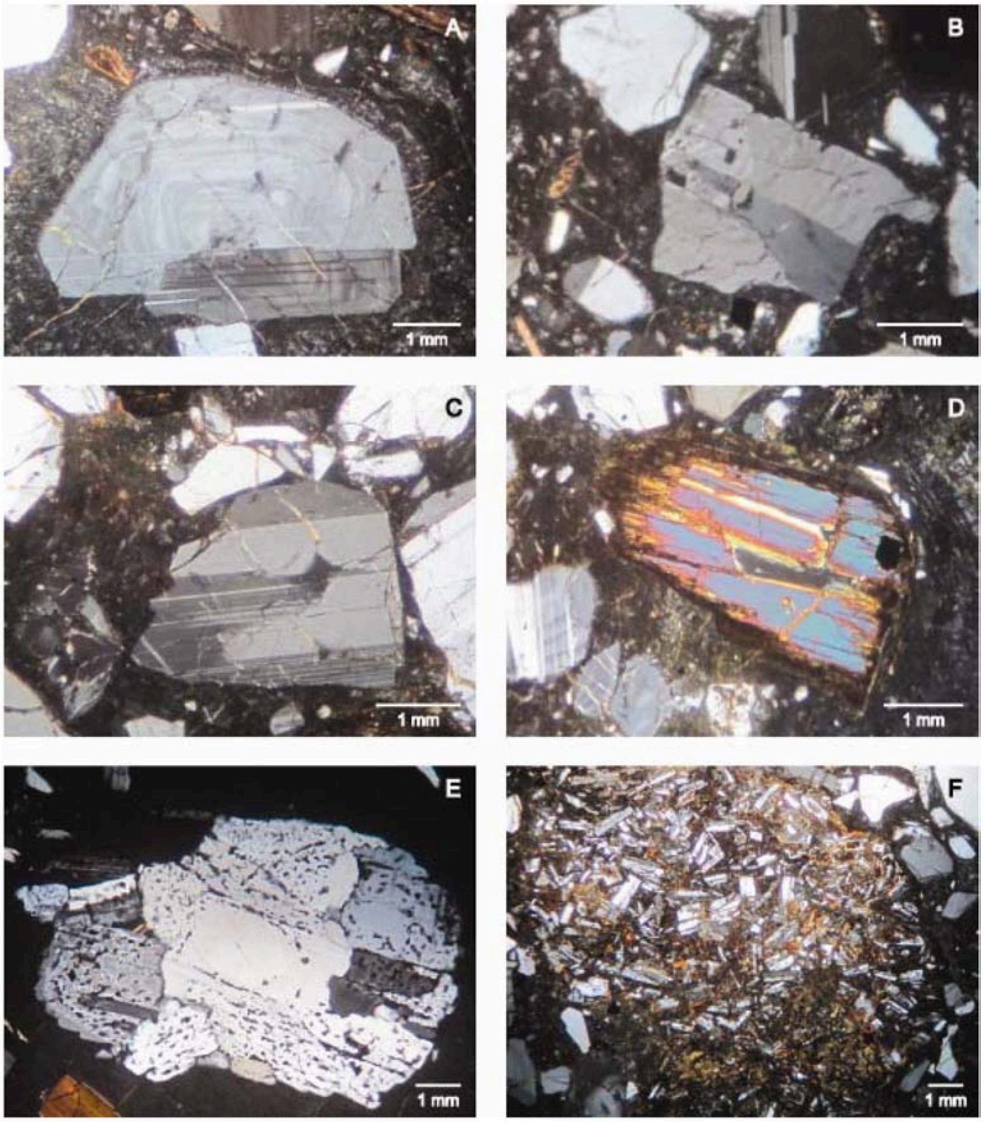

FIGURE 4 | Thin section mineralogy of 1.78 Ma ignimbtite from Karymshina caldera (samples 40L-2007 and 36L-2007). Plagioclase phenocrysts exhibit **(A)** concentric zoning, **(B)** complex zoning, and **(C)** no zoning. Other features present in the Karymshina samples are **(D)** amphibole phenocrysts with reaction rims, **(E)** agglomerations of plagioclase crystals, some with sieve texture, and **(F)** autolithic xenoliths which include small phenocrysts of plagioclase.

RESULTS

Geologic Position and Geochronology of the KVC

The Karymshina Volcanic Complex is located on the active eastern volcanic front of Kamchatka Peninsula, ~50 km southwest of the regional capital city of Petropavlovsk-Kamchatsky (**Figures 1**, **2**). Our new map of the KVC, shown on **Figure 2**, is a result of a decade-long geologic, geochronologic, and geochemical investigation. It demonstrates that the KVC is made of 4.1–0.5 Ma predominantly silicic rocks represented by thick tuff units and pre- and postcaldera extrusions and volcanoes. The area surrounding Karymshina Caldera includes several hot springs (**Figure 2**) suggesting a source of heat from recent magmatic activity younger than synvolcanic 0.5 Ma intrusions at depth. For example, the 300 × 500 m Bannaya River geothermal field in the NW part of ring fracture (**Figure 2**) was mapped in 1976 and is active today with temperatures exceeding 90°C in several places (Kraevoi et al., 1976; Rogozin et al., 2015). Below we describe the geologic position of the KVC based on analysis of regional geology and our new observations.

Subduction Parameters and Basement and Country Rocks

The depth to the subducting plate under KVC is 140 km (Gorbatov et al., 1999, 2001; Baboshina et al., 2000; Nizkous et al., 2007); 110–140 km is a relatively typical configuration for Eastern Volcanic Front volcanoes, including the younger

Gorely caldera directly to the south (Seligman et al., 2014). Seismic data on the crustal structure directly across the KVC (Geological Map of the Russian Federation, 2000, Explanations, **Figure 3**) shows that the KVC has thinner (13–20 km) upper crust and a greater (2 km) thickness of the volcanic layer, an observation that we take below to indicate significant reworking of the whole crustal volume in the course of >4 Myr-long magmatism. Geologic units that immediately surround the caldera include the poorly studied middle Miocene South Bystinskaya volcaniclastic sediments of predominantly andesitic composition with ∼20 Ma K-Ar ages (**Figure 2**, Geological Map of the Russian Federation, 2000) that are uplifted and tectonized. These are coeval with subvolcanic dioritic, dioritic porphyritic, and granodioritic bodies of low-K, calc-alkaline affinity, with ages of 14–11.1 Ma (Zavoikovsky intrusive complex) around Vilyuchik volcano, immediately to the east of Karymshina (**Figure 2**).

Further east, the mid Miocene Akhomten granitic intrusive complex is exposed and ranges from intrusive facies ranging in composition from 60 wt% SiO_2 diorite to leucogranite with 76 wt% SiO_2. The U-Pb zircon age published by Seligman et al. (2014) for one of the units is 11.4 Ma, while previous K-Ar determinations range from 11 to 12.1 Ma in age (Vinogradov, 1995). Rocks of these granodioritic intrusions are petrographically comparable to the Karymshina volcanics and contain biotite and amphibole, with K-feldspar and quartz in the micropegmatoid groundmass. Rocks of Akhomten have also been studied for their whole rock Sr-Nd and O isotopes (Vinogradov et al., 1986; Vinogradov, 1995) and display a diverse range of $^{87}Sr/^{86}Sr$ values (0.7034–0.7036), which are on the high end of younger rocks in the area (Vinogradov et al., 1986). $^{143}Nd/^{144}Nd$ ratios are characteristic of typical mantle (0.51305–0.51325, ε_{Nd} is +3 to +9), while low $\delta^{18}O$ values go down to −3% indicate that this shallow subvolcanic intrusion underwent significant hydrothermal alteration by meteoric waters during emplacement and cooling. Older Cretaceous rocks, also arc derived, are not exposed in the immediate area but are found in greenschist facies volcanics and sediments to the east, around the city of Petropavlovsk (**Figure 1**), and in the uplifted amphibolitic Ganal complex ∼50 km to the north. Gabbro intrusions and detrital zircon in the Ganal amphibolites are 90–55 Ma in age and no older than the late Cretaceous, while metamorphic rims are ∼25 Ma in age (Bindeman et al., 2002) suggesting regional metamorphism was followed by rapid exhumation that brought granulite-grade rocks to the surface. Their Sr isotopes are diverse ($^{86}Sr/^{87}Sr$ from 0.703 to 0.706) and $^{143}Nd/^{144}Nd$ value extend to crustal values of 0.5124 (ε_{Nd} of −4.6; Vinogradov, 1995). These described regional rocks and their isotopic values represent potential source components for magmas in the KVC, used below for discussion of potential mechanisms of magma derivation.

Magmatic Rocks of the Karymshina Volcanic Complex

The thickest and most voluminous unit is represented by the 1.78 Ma rhyolitic intracaldera tuff, filling the area of the 25 × 15 km (**Figure 2,** thin section mineralogy—**Figure 4**). Its central part, Tolsty Mys Mt (1,343 m), is the highest in the area, and the source of several local rivers (**Figures 1**, **2**). Uplift of the Karymshina area as has led to the exposure of intracaldera tuff, obliteration of the topographic caldera expression, and erosion of most extracaldera tuffs except in the west (discovered recently and currently under investigation). Geological mapping in the area (Geological Map of the Russian Federation, 2000) and previous investigation by Sheimovich and Khatskin (1996) failed to identify the collapse caldera. Hundreds of meters of thick intracaldera ignimbrite sections mapped and studied by us across the Karymshina and Bannaya Rivers do not contain obvious mineralogical or compositional breaks (SiO_2 varies by is ∼1 wt% over 1,000 m, **Table A1**), and thus we interpret the section as a single intracaldera cooling unit from a single eruption, though this interpretation is not yet completely certain considering the incomplete nature of the outcrops. Additionally, Bindeman et al. (2010) dated the top and bottom of the 1,000 m thick intracaldera ignimbrite sheet by Ar-Ar and obtained identical ages of 1.78 ± 0.02 Ma. Previously reported U-Pb zircon ages (Bindeman et al., 2010) returned a single population of zircons overlapping within errors with ages 1.87 ± 0.11 Ma ($n = 9$, top ignimbrite) and 1.76 ± 0.09 Ma ($n = 8$, bottom ignimbrite), collectively overlapping within error with the 1.78 ± 0.02 Ma Ar-Ar biotite (eruption) ages for these samples in both cases. The similarity of the zircon crystallization ages to the eruption age indicates that zircon crystallization occurred immediately prior to the eruption, or within a short ∼20 kyr residence time given uncertainties. Cores of nine zircon in selected post-caldera extrusions near Babii Kamen also show no evidence of inheritance (Bindeman et al., 2010).

Using the dimensions of the caldera and the volume of intracaldera ignimbrites (275 km^3) given in Leonov and Rogozin (2007) it can be estimated that the total eruptive volume was about three times this number or close to 800 km^3 if ash and eroded extracaldera deposits are each 275 km^3 based on similar relationships proposed for the western USA calderas (Bacon, 1983). Lithic fragments in ignimbites and post caldera intrusions are represented by autholithic blobs consisting of elongated plagioclase in glass without quartz (**Figure 4F**) and silicified hydrothermally altered materials in quantities not exceeding a few percent. Below and in the **Table A2** we present analyses of the thickest ash layers in the Pacific corresponding to the 1.78 Ma nominal age of the eruption, in an attempt to find a Karymshina deposit there.

Two dozen post-caldera, high-silica rhyolitic extrusions have similar character outcrops and mineralogy but significantly higher silica contents than the ignimbrite. These extrusions form local topographic highs along the proposed caldera ring fractures of the 1.78 Ma caldera (**Figure 2**). Five are dated by us or previous researchers, and they are much younger than the Karymshina ignimbrite, ranging in age from 0.9 to 0.5 Ma. No volcanic rocks younger than ∼0.5 Ma have been dated and extrusive domes are eroded after uplift suggesting that the KVC is extinct, unlike neighboring active volcanoes.

Extracaldera ignimbrite layers that we tried to identify as correlative to the 1.78 Ma Karymshina ignimbrite instead returned ages both younger and older, and compositions that are both more mafic and more silicic (samples 111L-2010, 4.11Ma, 2005G-5, 1.39Ma, **Table 1**). Pre-1.78 Ma dacitic to rhyolitic extrusions and basaltic volcanoes are exposed in the western and southern part of caldera, four of them dated in this study (**Tables 1**, **2**), returning ages of 3.62 and 3.84 Ma. A young dacitic tuff from the Bannaya River area was dated at 1.39 Ma (Bindeman et al., 2010), and is geochemically and isotopically distinct from the 1.78–0.5 Ma eruptive sequence. The quartz-biotite ignimbrites under the Zhirovskoy area near Gorely volcano returned older U-Pb zircon ages of 4.11–4 Ma, and similar tuffs are found in abundance in the western part of Karymshina caldera. These represent the oldest known volcanic units associated with the KVC. The above mentioned 11–14 Ma Akhomten and Zavoikovsky granitic and granodioritic complexes represent the latest dated silicic magmatism in the area before the ∼4.1 Ma onset of the voluminous silicic magmatism in the KVC.

The youngest volcanism in the region consists of the late Pleistocene-Holocene edifices of the surrounding volcanoes Vilyuchik, Gorely, and Mutnovsky, which are comprised by a differentiated series from basalts and basaltic-andesites to silicic domes unrelated to the KVC. The ∼0.5 Ma Zhirovskoy volcano Geological Map of the Russian Federation, 2000 and the voluminous 0.35–0.1 Ma dacitic to rhyodacitic voluminous ignimbrite sheets in the area are associated with caldera volcanism from the morphologically preserved Gorely caldera (**Figure 1**, Seligman et al., 2014) and are also not associated with the KVC, but we consider these products for comparison to the KVC. Given geochemical features, we consider the 1.39 Ma Bannaya River dacitic ignimbrites (2005G-5) exposed within the KVC to likely have originated outside of KVC, and by petrogenetic processes more similar to those at Gorely (Seligman et al., 2014).

Mineralogy and Petrography

Silicic rocks of both pre- and postcaldera rhyolitic lavas and ignimbrites in the KVC contain quartz, biotite, amphibole, plagioclase, and pyroxene, with accessory zircon and apatite (**Figure 4**), while sanidine is mostly absent in all but a few rocks (where it occurs as an interstitial phase), even in the relatively potassium-rich high-silica rhyolites. In contrast, many similar amphibole-biotite intraplate rhyolites with subduction signatures in western North America (e.g., the Fish Canyon and Bishop tuffs) with higher K_2O than the KVC contain sanidine as an abundant phenocryst in rhyolites of comparable SiO_2 content, as do Andean silicic volcanics (**Figure 5**) and many intraplate hotspot-related centers such as Yellowstone. Like Karymshina, neighboring basement granodiorites such as at Akhomten contain K-feldspar mostly in groundmass intergrown with quartz, suggesting that in Kamchatkan arc environments it appears only at near solidus temperatures.

Precaldera intrusions display a range of compositions (**Figure 5**) from basalts to rhyolites, and silicic rocks are also amphibole-bearing. High-K_2O varieties are found among them. The composition of the 1.78 Ma caldera-forming ignimbrites from several locations across the proposed caldera are quite similar, containing up to 40–45% of 0.5–1.5 mm phenocrysts of 16–21 vol% quartz, 19–25 vol% plagioclase, 0–4 vol% amphibole, 5–11 vol% biotite, and 1–3 vol% oxides with 42–48 vol% glass matrix (the rest are bubbles), with accessory zircon and apatite. Electron microprobe analyses are given in **Table A3**, Appendix. The Al-in hornblende barometer of Schmidt (1992) yields a 1.75–1.85 kbar equilibration pressure range for the 1.78 Ma Karymshina ignimbrite.

The ignimbrites examined in thin section and analyzed with the electron-microprobe display visible flow textures within the glass matrix and there appeared to be no alteration, except in the

TABLE 2 | Summary of $^{40}Ar/^{39}Ar$ ages of this study #.

Sample #	Description	Material analyzed	MSWD	$^{40}Ar/^{39}Ar$ age (Ma) ± 2 σ
4L-2010	Basalt volcano, S edge of caldera	Groundmass	1.05	3.31 ± 0.08
98L-2008	Dacite volcano, rim of caldera	Groundmass	1.18	3.59 ± 0.01
2007L-40*	Karymshina Ignimbrite	Biotite	0.51	1.78 ± 0.02
2006L-24*	Karymshina Ignimbrite	Biotite	0.44	1.78 ± 0.02
2005G-5*	Bannaya R Ignimbrite	Plagioclase	1.12	1.39 ± 0.10
10L-2010**	Ignimbrite, west of caldera	Feldspar	0.90	3.77 ± 0.00
66L-2013	Ignimbrite, L Bystraya	Plagioclase	0.97	0.99 ± 0.03
89L-2013**	Ignimbrite, west of caldera	Plagioclase	1.00	3.62 ± 0.04
139L-2013**	Ignimbrite, west of caldera	Plagioclase	1.14	3.63 ± 0.07
77L-2016_2**	Ignimbrite, west of caldera	Feldspar	0.85	3.84 ± 0.03
13L-2015	Ignimbrite, west of caldera	Feldspar	0.67	3.85 ± 0.02
Pau-1	Mt Orlinoye Krylo, pre-Pauzhetka	Groundmass	0.67	3.06 ± 0.12
707-6	Mt Klyuchevskaya, pre-Pauzhetka	Groundmass	0.71	2.88 ± 0.01
69L-2012	Stol Mt basalt	Groundmass	0.42	2.95 ± 0.03

**Ages previously published in Bindeman et al. (2010).*

***Ages calculated relative to 1.1864 Ma Alder Creek sanidine standard (Jicha et al., 2016).*

All other ages are calculated relative to 28.201 Ma Fish Canton standard sanidine standard (Kuiper et al., 2008).

Decay constants used are those of Min et al. (2000).

*#Analytical protocols for each analysis are provided in the **Appendix**, **Table A4** in Supplementary Material.*

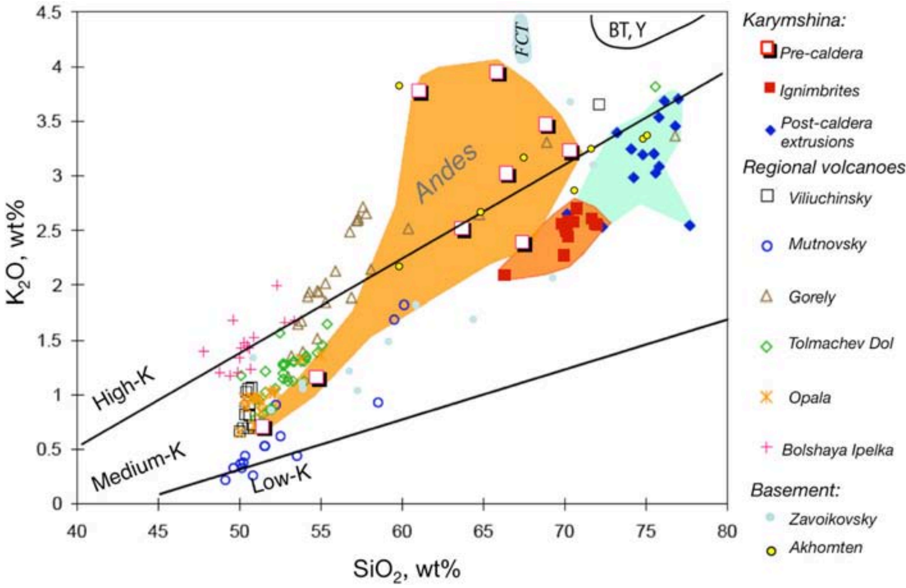

FIGURE 5 | K_2O-SiO_2 graph for Karymshina Volcanic Complex magmas and neighboring volcanoes. Central Andean magma compositional field is from Hildreth and Moorbath (1988). FCT, BT, and Y are ranges in the Fish Canyon tuff, Bishop tuff, and Yellowstone tuffs of western N America respectively, see **Figure 1** for caldera outline comparison.

case of the 1.39 Ma dacitic ignimbrite from the Bannaya River (2005G-5), which contained extensive radial textures indicating post-eruptive alteration of the sample and in which only 2% quartz by volume is present. In the majority of samples, larger phenocrysts of quartz contain hourglass melt inclusions and few phenocrysts of skeletal quartz. The larger phenocrysts also exhibited extensive microfracturing, common in an explosive eruption.

Plagioclase phenocrysts ranged from 19 to 23% by volume in most of the samples but is 46% by volume in sample 2005G-5. Often the larger phenocrysts were made of an aggregate of 3–4 individual crystals (**Figure 4**). Zoning patterns in the larger phenocrysts exhibited a wide range including concentric, normal, reverse, extremely complex (**Figure 4**). Microfracturing in plagioclase phenocrysts was also present, though not as prominently as in the quartz phenocrysts.

The ignimbrites also contain up to 5 vol% amphibole and biotite, almost all of them with reaction rims (**Figure 4D**). The opaque minerals (1–3 vol%) are primarily magnetite and ilmenite, with the presence of trace amounts of oxidation hematite as well. Magnetite-ilmenite thermometry gives a 700–750°C temperature range and an oxygen fugacity 0.25 log units above the NNO buffer. Other similar amphibole-biotite bearing rhyolites of Kamchatka such as the Dikii Greben volcano (Bindeman and Bailey, 1994) yield comparable to slightly more oxidizing f_{O2} buffer conditions (**Table A3**).

Groundmass in the 1.78 Ma Karymshina ignimbrite is variably crystallized and 16 spot analyses by electron microprobe yielded diverse spot to spot compositions, with many spots sensing sanidine crystals. The average of 16 spots in two ignimbrites is given in **Table A3** and has 74 wt% SiO_2 and 5 wt% K_2O.

Small antecrystic inclusions (**Figure 4F**), likely from an earlier episode of crystallization, perhaps from pieces cooled on the walls of the magma chamber contain 47–57 vol% glassy matrix and 43–49 vol% elongated plagioclase crystals. The rest of the inclusions are made of 0–4 vol% quartz, 0–3 vol% biotite, and 0–3 vol% opaque minerals.

The compositionally more evolved, high-silica rhyolitic post-caldera extrusions contain fewer phenocrysts: 22–24 vol% plagioclase, 14–17 vol% of quartz, 4–6 vol% of biotite, and 2–3 vol% of magnetite and ilmenite in a 53–54 vol% glassy and sometimes perlitic matrix. As with the ignimbrites, phenocrysts were often found in intergrown groups rather than individually. Melt inclusions were commonly present in the larger phenocrysts, in several phenocrysts creating a sieve texture. The larger phenocrysts exhibit a range of zoning from concentric to extremely complex. Both normal and reverse extinction patterns were observed. The larger phenocrysts also contained microfractures.

Deep Sea Sediment Record

Large caldera-forming eruptions from Kamchatka typically deposit ash into the north Pacific with dominant prevailing winds. Cao et al. (1995) and Prueher and Rea (2001) identified and stratigraphically dated 450 ash layers from IDDP sites 883 (N51.1983, E167.7688) and 882 (N50.3633, E167.600) ~800 km southeast of Karymshina. We examined 5 of the thickest layers from the 1.6–1.9 Ma interval that could overlap with the 1.78 ± 0.02 Ma Karymshina ignimbrite age given analytical uncertainties and potential offset between stratigraphic and radiometric ages described in Ponomareva et al. (2018). For Hole 883, we studied intervals 7H6 (92–93 cm, 1.621 Ma, 10 cm-thick; 116–117 cm, 1.629 Ma, 8 cm-thick) and 8H-3 (128–129 cm, 1.902 Ma, 10 cm-thick). For Hole 882 we studied intervals 9H-1 (7.5–8.5 cm, 1.637 Ma, 10 cm-thick) and 9H-3 (35–36 cm, 1.728 Ma, 6 cm-thick).

Examined ash samples contained similar biotite-quartz-amphibole mineralogy as Karymshina ignimbrites. Electron microprobe major element and LA-ICP-MS trace element compositions are reported in **Table A2**. We also sampled ash intervals from 0.43 to 0.48 Ma looking for a match for the 0.44 Ma eruption at Pauzhetka (Bindeman et al., 2010) and the 0.35 Ma eruption from Gorely (Seligman et al., 2014), two calderas studied by us previously and available in the same drillholes.

Glass trace element ratios provide the most robust means to evaluate correlations between distal and proximal eruptive deposits—trace elements are more variable and thus provide a more unique compositional fingerprint than major elements, and ratios eliminate the need to use a major element internal standard in LA-ICP-MS analysis. In **Figure 12**, we visually compare our examined offshore ash layers to Karymhina ignimbrite glasses, none of which appear to compositionally overlap with the Karymshina deposit despite their similar ages.

Whole Rock Geochemistry

Table A1 presents new and compiled whole rock and microanalytical chemical analyses of pre- and postcaldera samples, a subset of samples across the 1,000 m-thick 1.78 Ma ignimbrite, and of a series of precaldera and postcaldera domes and ignimbrites. We additionally compiled a dataset for other Kamchatka and Karymshina-area volcanoes (Gorely, Mutnovsky, Opala, Akhomten Massif, and others) for comparison purposes, obtained from individual cited publications and from the GEOROC database. Additional data for the Zavoikovsky and Akhomten 14–11 Ma magmatic complexes was taken from Vinogradov (1995) and Geological Map of the Russian Federation (2000). Trends at the KVC fit the typical differentiation pattern for a metaluminous, medium K_2O magmatic series, spanning a large range from primitive basalts to more evolved rhyolitic magmas (**Figure 5**). New major and trace element data for the KVC shows that there is an overall increase over time in the level of differentiation and a decrease in chemical diversity from pre-caldera to caldera-forming and then to post-caldera extrusions (**Figure 5**, **Figure A1**). The latter represent the most differentiated and homogenous high-silica rhyolitic compositions with 75–77 wt% SiO_2 plotting on the highest end among Kamchatkan magmas, and in the highest known volumetric abundance of such magmas in one center, making it somewhat unique for Kamchatka. High-silica rhyolites have the highest concentrations of K_2O because none of the rocks contain phenocrysts of sanidine, which only occurs as an interstitial mineral in high-silica rhyolitic intrusions, and thus magmas are able to accumulate potassium and other incompatible trace elements in the most silicic differentiates. While high silica rhyolites are abundant in intraplate settings such as those found in the Western USA, they are generally uncommon in arcs (Winter, 2010). The main other occurrence of high silica rhyolites in arcs is the central Andes on top of an especially thick continental crust (**Figure 5**; Hildreth and Moorbath, 1988; de Silva and Gosnold, 2007; Folkes et al., 2011; Grocke et al., 2017).

As Kamchatka (as well as at the Kuriles and Japan) has a strong, many fold increase in K_2O with increasing distance from the trench (or depth to the subducting slab, Volynets, 1994; Duggen et al., 2007; Portnyagin et al., 2007; Kimura and Stern, 2008), the K_2O content of parental basalts or rocks at equal levels of differentiation but of different ages can be used to assess if subduction parameters changed over the duration of magmatism. Volcanic rocks from the KVC spanning 4 Ma plot in the typical mid-K level, between the forearc Mutnovsky and the back-arc Gorely and Tolmachev Dol volcanoes, a similar to other volcanoes of the Eastern Volcanic front. This suggest that the subduction parameters changed insignificantly for the last 4 Ma duration of magmatism. In particular, the 4 Ma quartz-biotite tuffs underneath the KVC largely overlap with the 1.78 Ma and later eruptive units. Additionally, the 14–11 Ma Zavoikovsky and Akhomten complexes and their intrusive equivalents which are proposed to serve as basement rock assimilants for Karymshina have largely overlapping K_2O-SiO_2 relationships.

Rb and Sr concentrations and their ratios put the Karymshina Caldera rocks (**Table A1**) within the typical arc-related I-type granitoids, indicating less differentiation of Rb with respect to Sr (Halliday et al., 1991; Anderson et al., 2000). Sr decreases with time from ∼350 to 150 ppm, while Rb stays consistently around 50–60 ppm, causing Rb/Sr ratios to increase from ∼0.1 to 0.4. The Karymshina caldera rocks appear to be typical of subduction zones under continental crust, coinciding with the Coastal Batholith in Peru and the Kosciousko Batholith (Halliday et al., 1991), consistent with plagioclase fractionation in the absence of sanidine.

Major and trace element profiles through the 1,000 m thick 1.78 Ma intracaldera ignimbrite (samples 2007-L-36 through 47 are listed in stratigraphic position top to bottom; **Table 1** and **Table A1**) show very little elemental variability, with the top ignimbrite tending to be a little more SiO_2 rich at 73 wt% vs. the 72 wt% at the bottom, with MgO, CaO, FeO concentrations, which are correspondingly lower by 0.2 wt%, and trace elements which are lower by 10 relative percent. This homogeneous intracaldera ignimbrite contrasts with the compositionally diverse precaldera lavas and domes. Postcaldera intrusions, despite their diverse ages, all consist of rather homogenous high silica rhyolite with 76–77 wt% silica.

Plotting KVC rocks as a time series with age groups from pre-caldera to caldera-forming to postcaldera (**Figure A1**), we observe a steady increase in SiO_2 that is accompanied by a decrease in compatible elemental concentrations of Y, Sr, Zr, P, Ti, V, Sc, Nd, Ga, Cu, and Zn, suggesting that amphibole, plagioclase, zircon, and apatite saturation and fractional removal can explain the trends for these elements. Besides silica, there is an insignificant and scattered increase in incompatible trace elements, including U, Rb, Ba, and K, as well as in trace elemental ratios such as Rb/Sr, Ba/Sr, K/Sr, and La/Y. Rb and Ba normally concentrate in sanidine with high partition coefficients and form strong trends in many magmas from the western USA such as the Bishop Tuff (Anderson et al., 2000), but these strong correlations are notably absent in Karymshina due to the lack of sanidine as a fractionating phase. Scatter in these elements may also reflect mobilization by hydrothermal solutions. As we observed for major elements, temporal trends in many elements and ratios suggest a decrease in diversity of magmas with increasing youth, becoming more homogeneous as they also become more evolved.

Zirconium concentrations in whole rocks and computed saturation temperatures using the Watson and Harrison (1983) formulation show a slight decrease with time, and are relatively low for all rocks: from 804 ± 20°C for precaldera magmas, to 771 ± 12°C in the 1.78 Ma ignimbrites, to 779 ± 20°C in post caldera intrusions. Given the presence of amphibole and biotite in most magmas and crystal contents in 30–45% range, this agrees with the "cold and wet" magma definition pertinent to continental volcanic arcs (Miller et al., 2003; Loewen and Bindeman, 2016), and matches phase equilibria near-wet solidus conditions described for such systems worldwide, for example in Toba caldera in Indonesia (Chesner, 1998; Budd et al., 2017) or the intracontinental cold and wet Fish Canyon Tuff of the western United States (Bachmann and Bergantz, 2004), which has both oxygen isotopic and zircon saturation temperatures of 750°C.

Hydrogen Isotopes of Amphiboles and Biotites

Hydrogen isotope analyses (**Figure 6**) were only possible to obtain for fresh and cleaned amphibole and biotite crystals (several crystals amounting to ∼2 mg) in the rapidly quenched 1.78 Ma caldera-forming Karymshina ignimbrite as samples from the pre- and postcaldera extrusions were either too altered or lacked amphibole and biotite. As some amphibole crystals were surrounded by alteration rims (**Figure 4D**), we selected only the central parts of crystals for analysis. Biotites, due to their easier chloritization and exchange with recent rain and snow waters are considered as less reliable than amphiboles to record primary magmatic δD values (especially when analyses rely on many tens to hundreds of mg by conventional methods), though we only selected the freshest 1–2 mg. Values of δD ranged from −94 to −127% (SMOW) in biotites and from −105 to −133% in the two amphibole samples (44L-2007 and 47L-2007, respectively; **Figure 6**). The δD values obtained for both the biotites and the amphiboles are lighter than mantle-derived magmas and samples of other volcanic rocks from the Eastern Volcanic Field of Kamchatka studied by Taran et al. (1997), and if taken at face value represent some of the lowest measured δD values in Kamchatka. The H_2O contents in both the Karymshina samples and those from other volcanoes are similar and appropriate for fresh amphiboles and biotites, suggesting that this depletion is not due to chlorite alteration (a mineral with 12 wt% H_2O which easily exchanges with surface water). The large range of δD values, especially in biotites, likely reflects incipient exchange of D and H after intracaldera ignimbrite emplacement into the shallow crust with meteoric waters, and could also be due to post-eruption alteration of the cooling ignimbrite deposits (e.g., Hudak and Bindeman, 2008; Seligman et al., 2018). It is also possible that some of the low δD values are attributable to hydrothermal alteration of the magma source rock prior to genesis and eruption of the 1.78 Ma magma, and reflect lower-δD subglacial meteoric water values as glaciation in the northern hemisphere started at 2–2.6 Ma. Such hydrothermal alteration of the source rock would require assimilation of a shallow crustal source rock and would indicate the presence of a shallow magma chamber, consistent with the 1.8 kbar pressure estimate for the magma obtained with the Al-in hornblende barometer of Schmidt (1992). As hydrogen is a minor element in the crust compared to oxygen, assimilation of a small amounts of low-δD, low-δ^{18}O crust will significantly affect the δD of magma at much smaller assimilant to magma ratios than can change δ^{18}O (Taylor, 1986).

Oxygen Isotopes

Values of δ^{18}O in plagioclase and quartz phenocrysts are presented in **Table 3** and **Figure A2**, and define an overall normal magmatic range. The measured $\delta^{18}O_{Plag}$ and $\delta^{18}O_{Qz}$ values can be used to calculate the δ^{18}O values for the magma using the equations

$$\delta^{18}O_{\mathrm{magma}} = \delta^{18}O_{\mathrm{qz}} - 0.45 \tag{1}$$

$$\delta^{18}O_{\mathrm{magma}} = 0.027(\mathrm{wt\%SiO_2}) - 1.45 + \delta^{18}\mathrm{O}_{\mathrm{plag}} \tag{2}$$

with equation 1 being based on measurements in the Bishop Tuff and the wt% SiO_2 in equation 2 being that for the whole rock (Bindeman et al., 2004).

Pre-caldera basaltic volcanoes have δ^{18}O values of 6.6–6.7% that are ∼1% higher than normal mantle-derived basalts (**Figures 7**, **8**). The overall high-δ^{18}O values in many basalts from Kamchatka are explained by assimilation of high-δ^{18}O, lower crustal amphibolitic sources, such as those exposed in the Ganal Massif (**Figure 1**, Vinogradov, 1995; Bindeman et al., 2004, 2010). The 4.1 Ma quartz-biotite tuffs (e.g., 111L-10) with a δ^{18}O value of 6.75% can be explained by simple fractional crystallization of mantle-derived basalt, while a small precaldera dacite volcano (73L-111) has slightly depleted δ^{18}O values of 5.35%, requiring some low-δ^{18}O rocks in its genesis. This modest heterogeneity in precaldera δ^{18}O values contrasts with overall higher δ^{18}O values and greater homogeneity of the voluminous 1.78 Ma ignimbrite with $\delta^{18}O_{Plag}$ of 5.71–6.53 % and $\delta^{18}O_{Qz}$ of 7.3–7.9%. δ^{18}O homogeneity further increases in the high-silica rhyolitic, post-caldera extrusions with $\delta^{18}O_{Plag}$ of 6.22–6.55% and $\delta^{18}O_{Qz}$ of 7.1–7.55% despite their >1 Myr span in their ages. The mean of pre-caldera, caldera-forming, and post-caldera eruptive products have computed $\delta^{18}O_{Melt}$ values of 6.8 ± 0.6% (1 s.d.), 6.65 ± 0.4% and 6.85 ± 0.1%, respectively, suggesting comparable values averaged from diverse-in-δ^{18}O source rocks (**Table 3**). This overall normal range for silicic rocks in the KVC lacks the major depletions in δ^{18}O explained by the melting and assimilation of hydrothermally altered intracaldera rocks which occur in the neighboring Gorely volcano (Seligman et al., 2014) and in many other Kamchatkan calderas (Bindeman et al., 2004, 2010). The 6.7–6.9% values of the KVC are similar to slightly higher than what would be expected for magmas derived by pure fractional crystallization of a 5.7% MORB source (Bindeman et al., 2004), but slightly lower in δ^{18}O than a differentiation product of the above-mentioned high-δ^{18}O basaltic pre-caldera

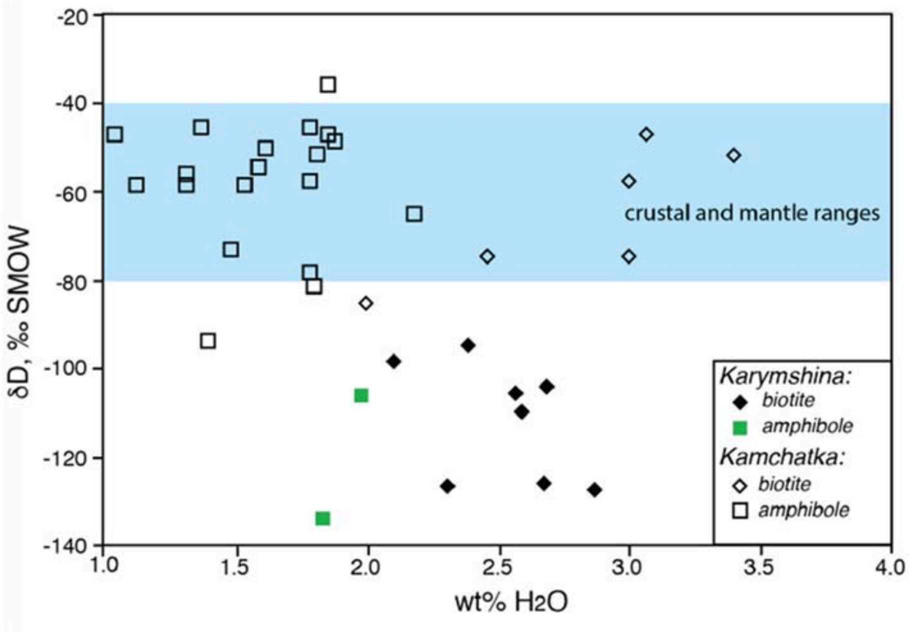

FIGURE 6 | δD and H_2O in Karymshina biotites and amphiboles in comparison to other published data for Kamchatka (Taran et al., 1997; Shipley, 2011). Notice lower δD range for Karymshina magmas but comparable H_2O content suggesting lack of significant chloritization of analyzed minerals. Overall low-δD values (lower than typical crustal and mantle values) would agree with assimilation of hydrothermally-altered rocks, possibly altered by low δD and low $\delta^{18}O$ meteoric waters during Pleistocene glaciation.

volcanoes (4L- and 6L-2010) which have $\delta^{18}O$ values of 6.7%. Pure fractional crystallization of these compositions should yield a ~0.4–0.5% higher silicic differentiation product, with $\delta^{18}O_{melt}$ >7.2%, values rare at KVC. Avoiding these compositions requires the incorporation of some small amount of lower $\delta^{18}O$ hydrothermally altered crustal rock into the higher-$\delta^{18}O$ magma, a process easily justifiable, given the current hydrothermal activity in the area (Bindeman et al., 2004, 2010). A range in $\delta^{18}O$ values from higher-$\delta^{18}O$ amphibolite to lower-$\delta^{18}O$ high silica hydrothermal sinters was used as assimilants in the rhyolite melts models by Shipley (2011) and discussed later in this paper. Further evidence supporting the involvement of rocks hydrothermally altered by low-$\delta^{18}O$ and low-δD meteoric waters in the petrogenesis of the KVC additionally comes from: (i) low-δD values of amphiboles (**Figure 5**) and (ii) heterogeneity of $\delta^{18}O$ values and the presence of low-$\delta^{18}O$ zircon phenocrysts in the 1.78 Ma caldera-forming Karymshina ignimbrite (reported in Bindeman and Simakin, 2014), where zircon shows some modest heterogeneity of $\delta^{18}O$ values from 6.1 ± 0.3% to 4.7 ± 0.3%, with one crystal at 4.2 ± 0.3% (quoted ± are analytical 1 s.d. of ion microprobe analyses based on standards). These authors interpreted zircon diversity as reflecting assembly of diverse-in-$\delta^{18}O$ magma batches in petrogenesis of the Karymshina ignimbrite. Such processes are much more prominent in hot and dry intraplate low-$\delta^{18}O$ rhyolites elsewhere in the world, and are somewhat more muted in cold and wet arc magmas such as the Fish Canyon and Toba Tuffs (Bindeman and Simakin, 2014; Colón et al., 2015, 2018c; Budd et al., 2017).

$^{87}Sr/^{86}Sr$ and $^{143}Nd/^{144}Nd$ Isotope Ratios

$^{87}Sr/^{86}Sr$ ratios in whole rock samples of caldera-forming ignimbrites range from 0.7033 to 0.7035, while ε_{Nd} values range from +6.3 to +13.2 (**Table 3**), indicative of a predominance of depleted mantle-derived material within the magma (**Figures 7**, **8**). The range of values overlaps with isotopic compositions for neighboring Late Pleistocene-Holocene volcanoes and other volcanoes from the Eastern Volcanic Zone of Kamchatka (Hawkesworth et al., 1997; Churikova et al., 2001; Duggen et al., 2007; Seligman et al., 2014; Simon et al., 2014), with the surprising exception of very radiogenic Nd isotopes in three studied post-caldera high-silica rhyolitic intrusions that have ε_{Nd} values of +11 to +13 (**Table 3**, **Figures 7**, **8**), the highest in the region. These ratios suggest that no high-$^{87}Sr/^{86}Sr$ and low-ε_{Nd} reworked Precambrian crust or its associated sediments, such as is found in the Sredinny Range, played a role in magma genesis. Instead, Cretaceous and younger mafic basement crust such as the nearby Ganal amphibolites as well as granites similar to the 11 Ma Akhomten Massif found to the east (**Figure 2**) do serve as possible assimilants with $^{87}Sr/^{86}Sr$ ratios approaching 0.706 (Vinogradov, 1995; Seligman et al., 2014). Thus, the crustal melting required by the $\delta^{18}O$ and δD values which indicate that some crustal component must have been present and undergone hydrothermal alteration and recycling, must consist of predominantly young material.

When plotted as a time series, $^{87}Sr/^{86}Sr(i)$ isotopic ratios corrected for age using measured Rb/Sr ratios decrease, while ε_{Nd} values increase with time (**Figure 8**), demonstrating an increase

TABLE 3 | Isotope analyses of Karymshina Volcanic Complex samples.

Sample ID	SiO_2	K_2O	δ18O	δ18O Qz	δ18O	87Sr/86Sr i	143Nd/144Nd	ε_{Nd}
			Plag	Quartz	Melt*			
PRE-CALDERA EXTRUSIONS								
6L-2010	54.72	1.16	6.7		6.73	0.70335	0.513026	7.6
4L-2010	51.37	0.71	6.62		6.56			
160L-2008	65.79	3.95	5.71		6.04			
102L-2008	63.61	2.52	6.18		6.45			
73L-2011	70.28	3.23	5.35		5.80	0.70343	0.51305	8.0
60L-2004	68.81	3.47	6.4		6.81	0.70350	0.51299	6.9
98L-2008	62.56	3.88	7.48		7.68	0.70353	0.512962	6.3
106L-2006	67.37	2.39	6.49		6.86			
119L-2005	66.38	3.02	6.22		6.56	0.70345	0.513027	7.6
KARYMSHINA IGNIMBRITES								
36L-2007	70.55	2.55	6.53		7.06	0.70331	0.513065	8.3
37L-2007	69.78	2.56						
38L-2007	71.64	2.61						
39L-2007	71.86	2.56						
40L-2007	70.78	2.56	6.33	7.91	7.13	0.70330	0.513048	8.0
41L-2007	70.00	2.53						
24L-2006	70.29	2.58	5.71	7.26; 7.50	6.66			
43L-2007	70.20	2.59						
44L-2007	70.19	2.44						
45L-2007	70.71	2.70						
46L-2007	70.10	2.49						
47L-2007	69.95	2.27		7.75	7.54			
321L-1972	66.01	2.51		7.72	7.42	0.70331	0.513015	7.4
5G-2005	62.91	2.09	5.9; 5.76	4.09(Px)	5.98	0.70332	0.513048	8.0
POST-CALDERA EXTRUSIONS								
107L-2005				7.22	6.77			
124L-2005	74.23	2.98	6.38	7.37	6.93			
143L-2005	76.54	3.96		7.31	6.89	0.703454	0.513326	13.4
49L-2006	70.80	4.30	6.22					
45L-2004	73.01	3.81	6.36	7.08	6.63	0.703312	0.513209	11.1
58L-2006	75.01	4.06						
63L-2005	75.82	3.08	6.39	7.55	7.10			
112L-2006	76.98	3.70	6.34	7.14	6.69			
112L-2006	76.98	3.70	6.49	7.3	6.98			
138L-2006	72.32	2.53	6.51	7.56	7.06			
138L-2006	72.06	4.08						
80L-2007	75.60	3.02	6.33	7.23	6.85			
82L-2007	75.80	3.53	6.56	7.43	7.07			
2L-2008	74.59	4.12	6.36	7.16	6.71	0.703317	0.513199	10.9
32L-2007	77.40	3.20						
35L-2007	73.22	3.39						
66L-2013	72.30	2.74		7.16	6.71			
PRE CALDERA IGNIMBRITES								
10L-2015	71.99	3.55						
13L-2015	70.74	3.22						
89L-2013	72.40	3.23		6.63				
77L-2016	73.00	3.33						
139L-2013	70.18	3.22						
111L-2010	69.07	2.41		6.77	6.32	0.70356	0.51321	11.2

*Sr isotopes are corrected for erution age using Rb and Sr concentrations; underlined is incorrected for age, but likely be 0.7034XX if likely 0.5–1 Ma age is used. *Melt is computed using minerals (see text).*

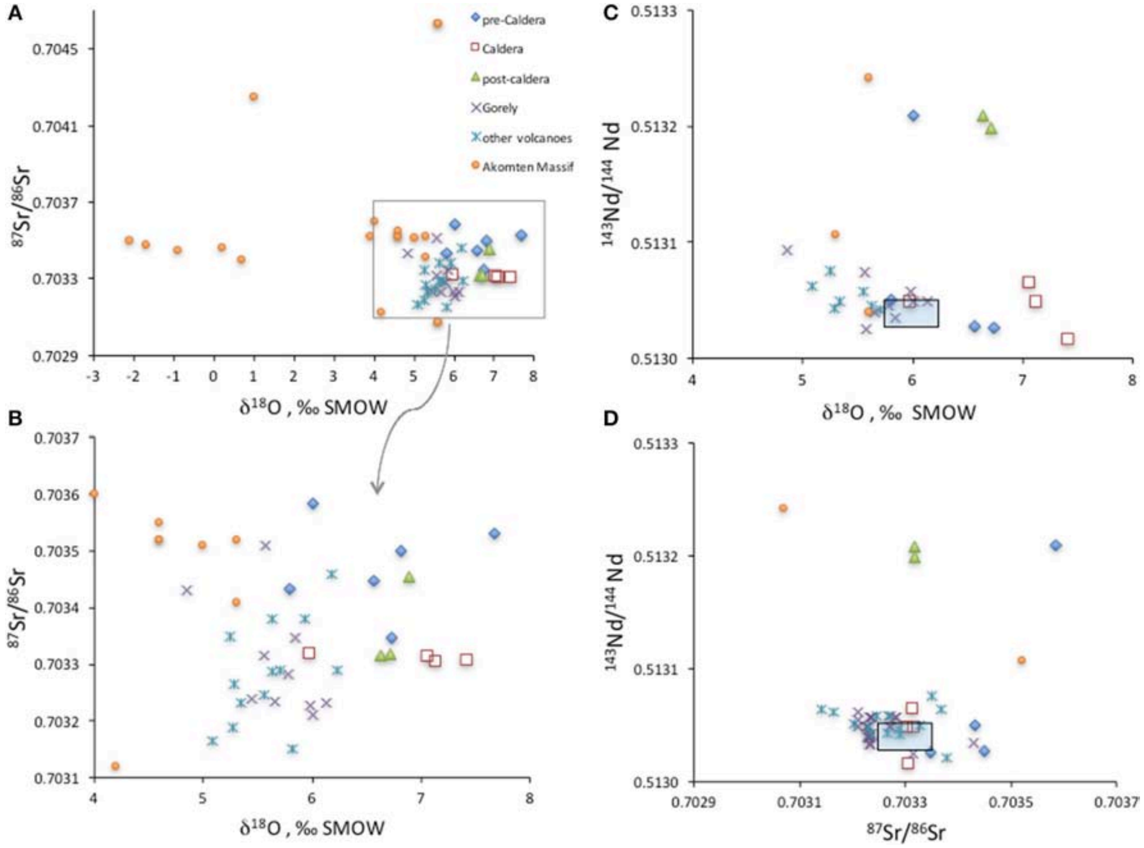

FIGURE 7 | Sr, Nd, and O isotopes in rocks from Karymshina Volcanic Complex in comparison to neighboring volcanoes, and basement rocks (Akhomten granite massif, and Ganal series metamorphics). Small rectangles in **(C,D)** indicate mantle derived basalts and products of their differentiation, and regional Sr and Nd isotopic values from central part of Eastern volcanic front Churikova et al. (2001) and Bindeman et al. (2004). **(A)** Regional pattern, showing low-$\delta^{18}O$ and diverse Sr isotopes in hydrothermally altered crust from Akhomten and overall normal to slightly high-$\delta^{18}O$ values of Karymshina magmas. **(B)** Zoom in on Karymshina and local volcanoes data showing low $\delta^{18}O$ magmas from multi-caldera Gorely volcano (Seligman et al., 2014) and decrease of Sr isotopes from pre to postcaldera stage. **(C)** Nd vs. O, and **(D)** Nd vs. Sr isotopes showing that isotopic ranges of magmas in and around Karymshina are best explained by isotopically diverse crust.

in the proportion of the mantle component with time, despite the increasing degree of differentiation (increase in SiO_2) of the erupted rhyolites (**Figure 5**); this observation serves as the basis for mass and thermal modeling below. Finally, isotopic heterogeneity of Sr and Nd decreases with youth, in line with oxygen isotopic and elemental results above.

Rhyolite-MELTS Modeling

We conducted an extensive set of crystallization and assimilation modeling experiments using the rhyolite-MELTS program of (Gualda et al., 2012; for further results of this modeling campaign, see Shipley, 2011). Several samples of basaltic magmas from nearby volcanoes were compared and we selected a basalt from the Gorely volcano (Seligman et al., 2014) as most closely resembling a primitive magma from which the Karymshina magmas may have been derived. For a crustal assimilant composition, we used an amphibolite partial melt taken from the experiments of Rapp and Watson (1995), which is referred to hereafter as APM. This generic composition was chosen because although there are no partial melting experiments that have been done on rocks found near the Karymshina Caldera, amphibolite is a common metamorphic rock in the Kamchatka Peninsula and in other continental arcs (Wyllie, 1984) is a plausible composition for the lower crust in Kamchatka (Baboshina et al., 2000; Geological Map of the Russian Federation, 2000). A silicified, hydrothermally altered rock, IC50, with SiO_2 contents of 81.34 wt% (referred to hereafter as HAR) was also used as an assimilant as this type of rock may also have been added to the magma, driving the observed minor depletion in $\delta^{18}O$.

Crystallization trials were run with 0 and 2.5 wt% H_2O in the initial basalt and with 0, 25, and 50 wt% APM and 0 and 10 wt% HAR. These trials were conducted at 2 kbar, 8 kbar, and a split starting at 8 kbar and moving to 2 kbar after 50 wt% crystallization. One set of trials using only the initial basalt compositions was conducted with equilibrium crystallization to verify that the compositions seen at the Karymshina caldera could not have been the result of equilibrium crystallization. All other trials were conducted assuming fractional crystallization. In the case of the split pressure trials, the change in pressure

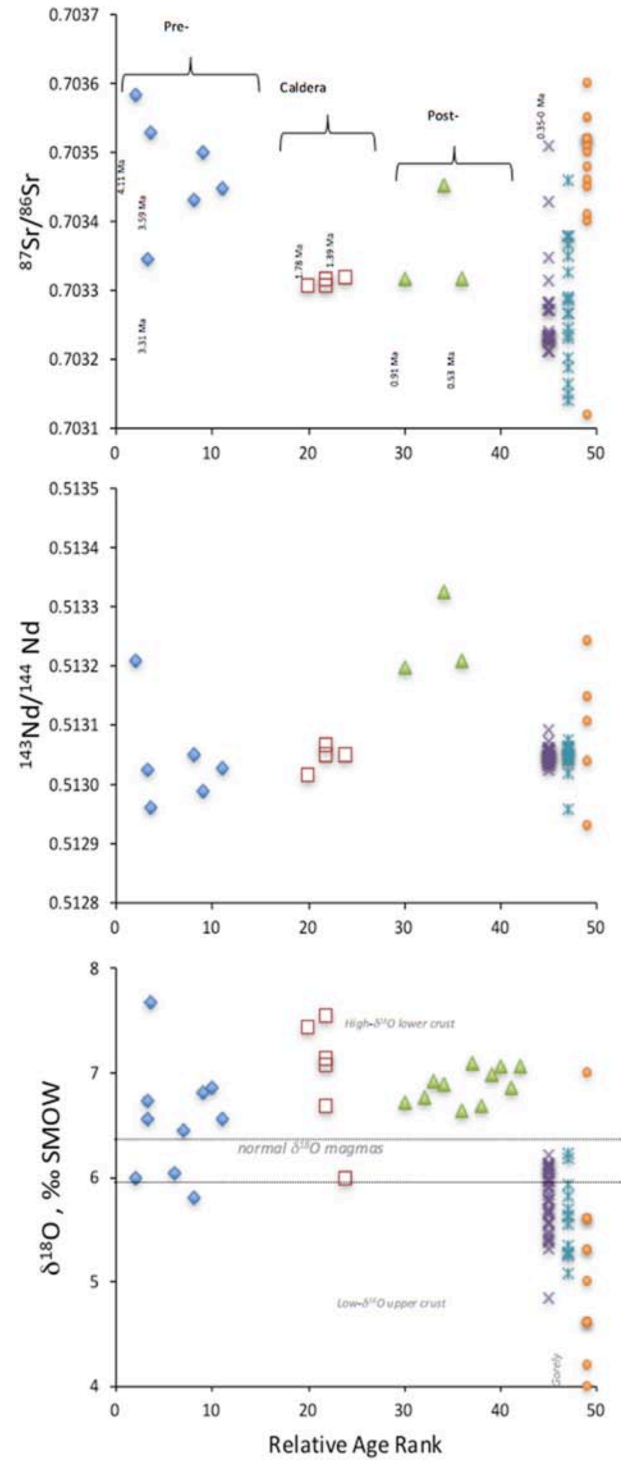

FIGURE 8 | Temporal evolution of the Karymshina Volcanic Complex in comparison to Gorely volcanic center (0–0.35 Ma, Seligman et al., 2014), other volcanoes nearby, and Akhomten granitic massif. Symbols are the same as on **Figure 7**. Units are plotted in relative random order except the ones indicated by arrows with ages from **Table 1** and **Figure 2** based on geochronology of this work and previously reported in Bindeman et al. (2010). Notice overall decrease in Sr and O isotopes, and increase in Nd isotopes from pre to postcaldera intrusions, and an increasing homogenization of isotopes with youth. Sr isotopes are adjusted to their initial values.

was assumed to be instantaneous based on the probable speed of magma ascent from Annen et al. (2006).

As expected, the results for equilibrium crystallization of the basaltic parent magma chosen show that it is impossible to obtain the rhyolitic composition of magma present at the Karymshina caldera. The results of the fractional crystallization trials obtained compositions closer to those observed at Karymshina; these results are shown in **Figure A3** for selected major elements. Most of the fractional crystallization trials resulted in strong enrichments of K_2O. This is most likely due to the initial basalt composition containing more K_2O than was present in the true parent magma of the Karymshina rocks. Fractional crystallization at shallow depths (2 kbar) resulted in the least enrichment of K_2O as well as a greater increase in the SiO_2 content of the remaining magma (**Figure A3**). The trials containing 50 wt% APM and 10 wt% HAR were closest to the actual K_2O and SiO_2 contents of the Karymshina rocks in all trials. Effects of addition of silica-rich HAR to plagioclase saturated magma are shown on **Figure 9**. In the 2 kbar trials, the magma with 2.5 wt% H_2O, 25 wt% APM, and 10 wt% HAR also matched well with the actual values measured in the Karymshina rocks. In the trials with 50 wt% APM, SiO_2 contents equal to those of Karymshina were obtained at all pressure options and approximately when 50 wt% of the magma was crystallized. The trials giving the best approximations of fractional crystallization leading to Karymshina magma compositions also match well with a straight line mixing trend between the initial basaltic magma and the rhyolites, indicating that the Karymshina magmatic series could also be the result of pure magma mixing between some higher-SiO_2 magma and a basaltic magma. If this is the case, the Karymshina magmas would likely be primarily composed of partial melts of amphibolite shallower hydrothermally altered rocks mixed with a small portion (<25 wt%) of basaltic magma.

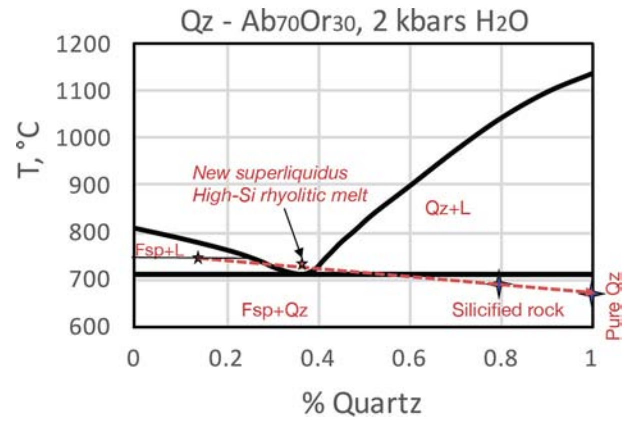

FIGURE 9 | A section through an experimental granite ternary (Tuttle and Bowen, 1958) at 2 kbars of water pressure and to the Ab side of Ab-Or cotectic. An explanation of addition of hydrothermally altered, silica-rich sinters and secondary quartz of diverse δ ^{18}O values (large stars) into crystal-rich plagioclase-bearing rhyolites of Karymshina caldera (small star) to produce high-silica, crystal-poorer and lower temperature post-caldera extrusions. Addition of silicified rocks or silica-rich sinters causes composition-induced melting even if overall temperature of the system is dropping.

The results of the fractional crystallization trials for Al_2O_3, MgO, and CaO were similar to those for the K_2O and SiO_2 contents. The best fits for Al_2O_3 and MgO occurred with 0 and 2.5 wt% H_2O, 50 wt% APM, and 10 wt% HAR in the trial with pressures starting at 8 kbar and ending at 2 kbar. However, the trial at 2 kbar with 2.5 wt% H_2O, 50 wt% APM, and 10 wt% HAR is also a reasonable fit. In terms of CaO, the trials at 2 kbar and 2.5 wt% H_2O with 50 wt% APM and both 0 and 10 wt% HAR as well as the trial with 2.5 wt% H_2O, 25 wt% APM, and 10 wt% HAR are good fits to the Karymshina rocks. Thus, the fractional crystallization trial, which matched most closely the composition of the Karymshina rocks occurred at 2 kbar with 2.5 wt% H_2O, 50 wt% APM, and 10 wt% HAR. It should be noted that the rhyolite-MELTS runs approached but were not able to reproduce the most silicic compositions present at Karymshina. An additional amount of high-silica assimilant like the hydrothermally-altered rock may be required to produce these compositions, or the problem may lie with the formulation of various phase equilibria in the rhyolite-MELTS code.

Modeling using rhyolite-MELTS also requires that the $^{87}Sr/^{86}Sr$ and $^{144}Nd/^{143}Nd$ ratios of this APM be selected within the bounds provided by the Ganal metamorphic Massif (Vinogradov et al., 1991; Bindeman et al., 2004). These values are later diluted by the mantle-like cumulates or the plutonic equivalents of early stages of Karymshina volcanism. Based on the final isotopic values of the magmas, ∼10 wt% crustal material is added, the contribution of the crustal component would make up more than 50 wt% of the magma after more than 75% crystallization of the magma by fractional crystallization processes. This reconciliation of elemental and isotopic parameters predicts that the Sr and Nd values in the added crustal component and in the hydrothermally altered component may be closer to the mantle values, which is typical of Kamchatka.

Thermomechanical Modeling

The I2VIS program (Gerya and Yuen, 2003; Colón et al., 2018a,b) thermomechanical model was allowed to run for approximately 20 Myr of model time at a low mantle input rate averaging ∼200 km^2/Myr, producing significant intrusions of basalt and their cumulates in the crust. These intrusions are ∼60 km in width, similar in magnitude to the Kamchatkan arc, and thicken the crust from an initial value of 35 km (see animation in **Supplementary Material**) to nearly 50 km (**Figure 10**). This thickened crust is also significantly heated until the Moho temperature nears 1,000°C, making the lower crust both weak and dense as it metamorphoses to eclogite in the presence of minor partial melts (**Figure 10a**; the model uses the stability fields of Ito and Kennedy, 1971). Eventually, these conditions produce a Rayleigh-Taylor instability along the boundary between the crust and the mantle (**Figure 10b**). This instability produces a large drip of dense and relatively cool material, which detaches and sinks away from the crust in as little as 0.25 Myr (**Figure 10c**), followed by another instability and drip which forms about 1 Myr later (**Figure 10e**). These drips allow hot mantle to rise into shallower levels than before, producing huge temporary spikes in basaltic melting (**Figure 11a**), which in turn heats the overlying crust extremely rapidly and produces a surge of silicic melt production and volcanism (**Figures 11b,c**). In this delamination event, ∼1,500–2,000 km^3 of felsic rocks in total are erupted. This produces a caldera filled with silicic volcanic rocks (gray in **Figure 10e**), and thins the crust by several kilometers in the region (**Figure 10f**). Melt production quickly recovers to its pre-delamination rate (**Figure 11a**), again thickening the crust and producing another delamination event about 10 Myr after the first, which is accompanied by a similar surge in basalt production and accompanying felsic eruptions. Finally, we note that the delamination and rhyolite production events are characterized by drops in the ε_{Nd} values of the erupted felsic material, caused by spikes in crustal melting caused by the increased basalt intrusion rate.

A movie of delamination events is given as **Movie A1**.

DISCUSSION

High-Silica Rhyolites in Arc Settings and Mode of Their Genesis

True high silica rhyolites (HSR) that are represented by nearly all post-caldera Karymshina extrusions are generally rare in Kamchatka and other arc settings, where when they do occur are mostly found in arcs built on thick continental crust (e.g., Andes, de Silva and Gosnold, 2007; Folkes et al., 2011). HSRs are, by contrast, quite common in intracontinental extension or hotspot environments as can be seen via the GEOROC database. Small volume HSR magmas such as aplites (e.g., Waters and Lange, 2017) can be produced by extreme fractional crystallization of a bigger magma body or a series of such events, especially if they contain very few or no crystals. By contrast, the eruption of large volumes (100s of km^3) of ignimbrites or lavas of HSR magmas requires processing of an even greater volume of low silica rhyolitic crust, and in many cases HSR are associated with large volume (100s to 1,000s of km^3) rhyolitic or dacitic "monotonous intermediate," crystal-rich magmatic centers (Hildreth and Moorbath, 1988; Grocke et al., 2017). HSR extraction from batholithic-scale magma bodies of rhyolitic composition seems like a reasonable proposition (Bachmann and Bergantz, 2004; Watts et al., 2016), and thus HSR genesis requires crust-wide reworking (Lipman, 2007). Previous studies indicate that crust of at least 30 km in thickness is required to produce HSR magmas and the 40 km thickness found at Karymshina is most favorable (Hughes and Mahood, 2008; **Figure 2**). It should also be noted that thicker crust may provide more space for basaltic underplating of one or more differentiating magma bodies, allowing progressively more differentiated silicic partial melts to be sequestered upward through multiple melting-remelting episodes (e.g., Bindeman and Simakin, 2014). Large volumes of silicic magmatism would naturally require a greater proportion of basaltic magmas (Annen and Sparks, 2002; Annen et al., 2006) and we model the initial and final crustal thicknesses below.

Summary of Geologic and Geochronologic Trends in the Karymshina Volcanic Complex

New and compiled geochronology demonstrates the long-lived nature of the Karymshina Volcanic Complex, lasting from ∼4 to 0.5 Ma (**Figure 2**). Eruptions started at ∼4 Ma with quartz

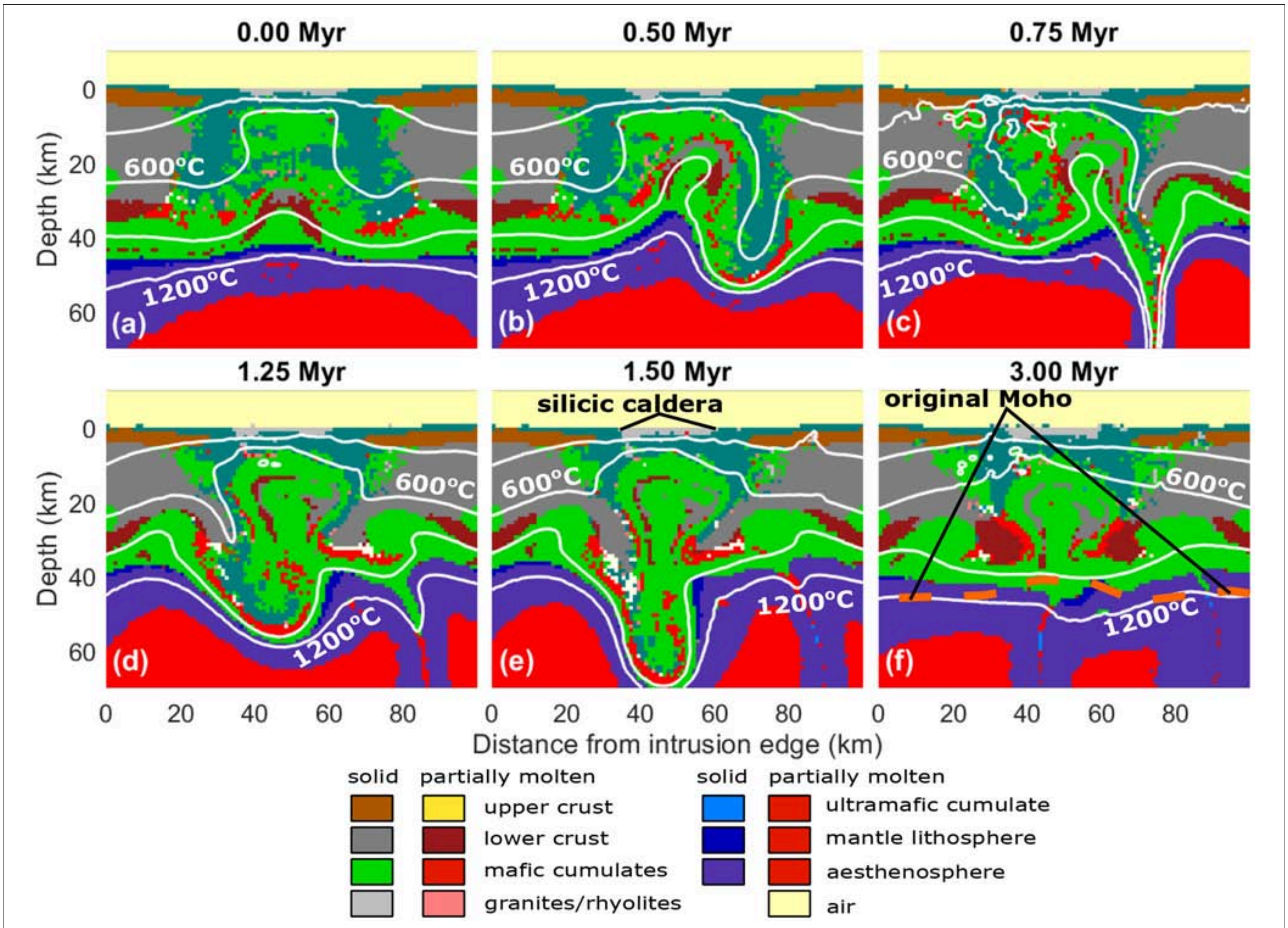

FIGURE 10 | Thermomechanical model of delamination-triggered mantle melting and surface volcanism. White lines are 200°C temperature contours. **(a)** 4 Myr after the initially 35 km-thick crust has been thickened to nearly 50 km by repeated additions of basalt to the crust, basalt addition and heating the crust results in the first signs of Rayleigh-Taylor instabilities in the Moho, **(b,c)** Over the next 1.25 Myr, this develops into a drip which removes the lowermost crust including most of the mafic cumulates, and continental lithosphere, drawing hot mantle up into the resulting space, and causing extensive melting. **(d,e)** From 1.5 to 2.5 Myr after the start of the delamination event, further delamination occurs on the left side of the model, causing another smaller surge of melting. **(f)** Finally, the lower crust cools and begins to solidify after the surge in mantle melting, and a new equilibrium with thinner, ~30 km thick crust begins, starting a new cycle.

bearing biotite tuffs, and continued through 3.62 Ma. The older precaldera group eruptions of 3.4–3.6 Ma formed basaltic, basaltic andesitic and dacitic volcanoes. More geochronology is needed to establish the connection of these precaldera extrusions to the voluminous 1.78 Ma Karymshina ignimbrite, and to understand whether this initially diverse set of volcanic products represents the "waxing and pre-conditioning" the crust with basaltic melts that leads to crustal melting, as is described for the Andes by de Silva and Gosnold (2007) and for western North America by Lipman (2007). A caldera-forming episode at 1.78 Ma produced an estimated 800 km^3 of 71.5–73 wt% SiO$_2$ crystal-rich ignimbrite. After a rather significant time gap, HSR extrusions tracking the approximate caldera ring fractures erupted, with this last stage lasting from 0.9 to 0.5 Ma.

Thus, there appear to be three major eruptive periods, approximately 1 million years apart, a pre-caldera stage from 4 to 3.3 Ma, the caldera-forming eruption(s) at 1.78 Ma, and postcaldera eruptions from 0.9 to 0.5 Ma (**Figures 5**, **8**). As post-caldera extrusions are compositionally continuous (complementary) to the 1.78 Ma ignimbrites, they in theory could be extracted as residual melts from a caldera-wide crystalline mush (Bachmann and Bergantz, 2004) and diluted by hotter melts derived from the hot zone near the Moho with mantle-like Sr and Nd isotopes. However, the large time period between eruptions would indicate the presence of a crystalline mush from which the magma for both eruptions was supplied. This mush would have to be kept constantly heated up by basaltic intrusions to remain semi-molten state within the earth's crust for >1 Ma. The size of Karymshina eruptive center, the caldera dimensions, the duration of volcanism, the crystal-rich nature of eruptive products, and the presence of hydrous phases such as biotite and amphibole allows us to compare it to well-studied ignimbrite succession from the Cenozoic North American ignimbrite flareup (Lipman, 2007), and especially to the Andes (de Silva and Gosnold, 2007; Folkes et al., 2011). Ignimbrite flareups and continuous subsequent volcanism are conventionally interpreted

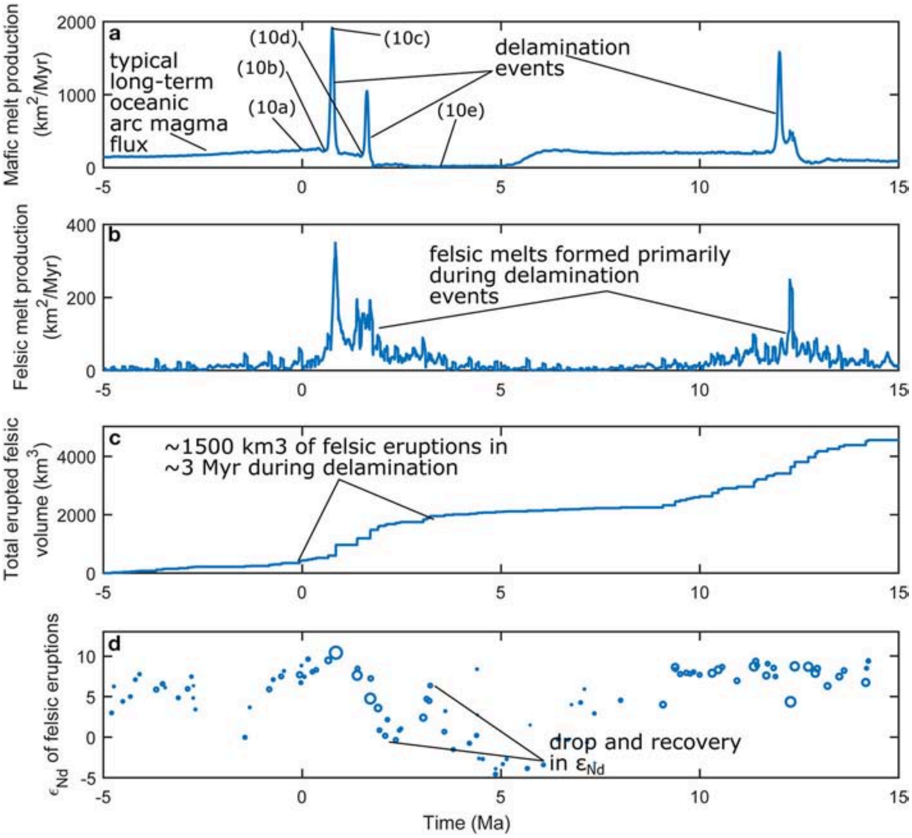

FIGURE 11 | Melt production and volcanism during the delamination event depicted in **Figure 10**. **(a)** The surge in mantle melting lasts <2 Myr, and is punctuated by sharp spikes associated with the actual dripping events. **(b)** The increase in mantle melting is associated with a coeval spike in the production of felsic melts in the crust (including intrusions), and **(c)** in the rate of eruption of rhyolites on the surface (to calculate 3D volumes here we assume a model thickness of 20 km). **(d)** Finally, we note that the surge in rhyolitic volcanism is associated with a noticeable drop in ε_{Hf} used in our models (which linearly correlates with ε_{Nd}) values as a result of a surge of crustal melting. This demonstrates that an increase in mantle melting alone can trigger a drop in ε_{Nd} values, making the underthrusting of fertile crustal material not necessary for all such arc flareup events (Ducea and Barton, 2007; DeCelles et al., 2009).

as resulting from periodic rejuvenation of a batholithic scale mushy magma chamber of rhyolitic composition, from which interstitial high-silica rhyolitic liquids are periodically extracted. The most likely reason for rejuvenation of a nearly frozen yet wet magma system is the continuous supply of basaltic magma, resulting in a variety of segregation processes described in the literature (e.g., Bachmann and Bergantz, 2006; Huber et al., 2011). Given the size of the magma chamber necessary to produce such large volumes of volcanic HSR, comparatively small amounts of basaltic magma likely intruded into the crystalline mush without much mixing with it, avoiding a significant impact on the overall constant composition of the postcaldera intrusions. Based on the hot spring activity near the Karymshina caldera, the last dated eruption at 0.5 Ma, and the overall long cooling timescales of batholith-scale magma bodies (Glazner et al., 2004; Lipman, 2007), it is quite probable that Karymshina is not a fully finished magmatic system despite its uplift and erosion, and that another episode of intracaldera basalt intrusion and rejuvenation would trigger another extrusive dome eruption.

Pacific Sediment Cores and 1.78 Ma Karymshina Eruption

No thick ∼1.78 Ma ash layers in the ODDP 882 and 883 Pacific cores (Cao et al., 1995) compositionally matched the Karymshina ignimbrite despite comparable mineralogy (**Figure 12**). It should be noted that we only analyzed thick 6 to 10 cm ash layers that were within a 0.06–0.12 Ma vicinity of the 1.78 Ma Karymshina age, and did not sample <1 cm ash layers that may also correspond to the 1.78 Ma eruption. We conclude that either the 1.78 Ma Karymshina eruption did not generate a large enough ash cloud to spread to the southwest of the Pacific, which seems surprising given the large estimated size of the caldera and several hundred km^3 inferred volume of the associated eruption (**Figure 2**; Bindeman et al., 2010), or that the winds during the eruption may instead have distributed ash in a different direction. Future efforts should examine cores from the Sea of Okhotsk.

We also compare ash from appropriate stratigraphic intervals to the 0.44 Ma Pauzhetka and 0.3 Ma Gorely caldera eruptions studied simultaneously in the same cores. Three ash layers are partially matched to the Pauzhetka composition, especially in

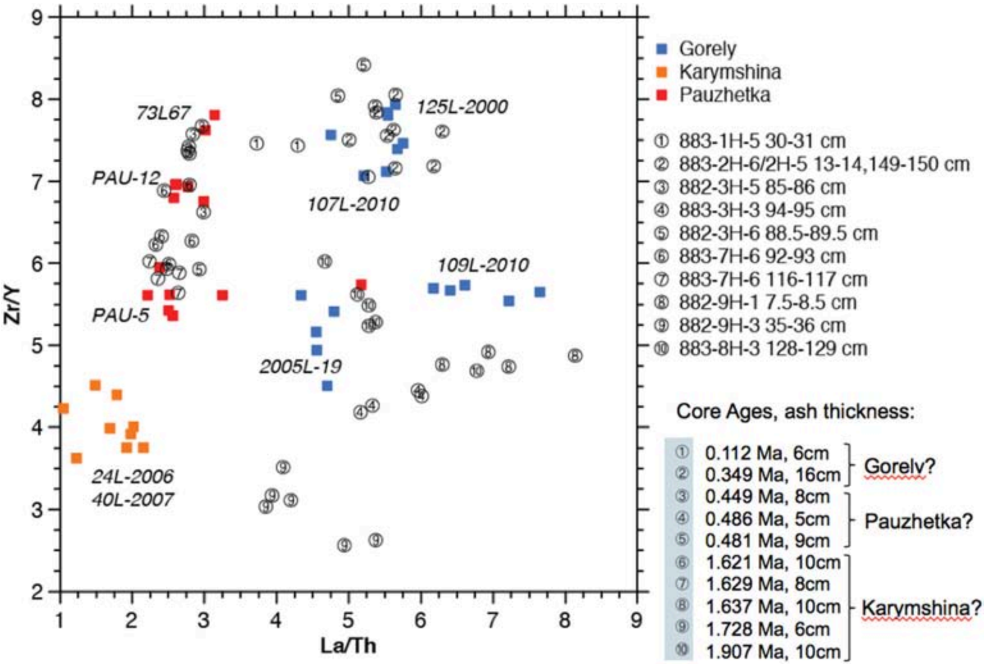

FIGURE 12 | Trace elemental ratio diagram comparing interstitial glass in the 1.78Ma Karymshina ignimbrite and other studied Kamchatkan tephras as compared to the Pacific cores ODDP-882 and 883. Note the match of Pauzhetka and Gorely tephra layers but lack of match for Karymshina. Age and ash thickness data is from Prueher and Rea (2001). See text for discussion and **Table A2** for analyses of analyzed tephras.

Zr/Y and La/Th: 882-3H-5 at 85–86 cm, 883-7H-6 at 92–93 cm, and 883-7H-6 at 116–117 cm. Ponomareva et al. (2018) recently identified Pauzhetka ash in cores from the Pacific and the Sea of Okhotsk via trace elemental match of and calibrated its astrochronologic age to 0.426 Ma.

Isotopic and Trace Elemental Trends

Sr, Nd, and O isotopic trends seen in **Figures 7**, **8** indicate the following.

(1) Erupted magmas have overall mantle-like compositions, suggesting that mafic magma differentiation and the melting of similar young Cenozoic crust can explain the abundant silicic rocks of Karymshina Eruptive Center. (2) Decreasing diversity of these isotopes through time is consistent with the formation of a homogenous batholith-scale magma body prior to the 1.78 Ma eruption. (3) Decreasing $^{87}Sr/^{86}Sr$ and increasing $^{143}Nd/^{144}Nd$ isotopic ratios with youth suggest that the system received continuous inputs from mantle-derived basalt or products of its differentiation (**Figure 8**), thus mantle-derived basalt and products of its differentiation not only contributed heat but participated materially in the petrogenesis of silicic magmas. (4) The youngest group of postcaldera rhyolites, which are true high-silica rhyolites, have the greatest proportion of this mantle component, which seems counter intuitive, given that these magmas are most differentiated. (5) Compatible trace elemental concentrations and their ratios to incompatible elements decrease in diversity and values through time, also consistent with the proposed homogenization of magma reservoir followed by sequestration to more differentiated values. (5) Zr saturation temperatures also decrease with youth. (6) Oxygen isotopes indicate decreasing diversity and requires contributions from high-$\delta^{18}O$ mantle sources and low-$\delta^{18}O$ hydrothermally altered crust. These results are confirmed by zircon $\delta^{18}O$ diversity in the caldera-forming ignimbrite (Bindeman and Simakin, 2014). Finally, (7), potentially supporting evidence for the role of hydrothermal alteration comes from low D/H ratios in amphiboles and biotites (**Figure 6**). However, the final Karymshina magmas are not low-$\delta^{18}O$ in absolute sense, i.e., lower than the mantle-derived differentiate (<6–6.3‰).

Model for Karymshina Silicic Volcanism

The formation of voluminous magmas with rhyolitic (70–74 wt% SiO_2) and especially high-silica rhyolitic (>74 wt% SiO_2) compositions is currently a topic of hot debate in the geologic community (Bachmann and Bergantz, 2004, 2008; Annen et al., 2006; Lipman, 2007; Watts et al., 2011, 2016; Bindeman and Simakin, 2014; Colón et al., 2015). Four end-member processes by which these magmas can form are (1) the fractional crystallization of a basaltic parent, (2) extraction of evolved melt from an evolved crystalline mush, (3) underplating and melting of pre-existing crust or previous cumulates in a "hot zone," and (4) shallow recycling and remelting of erupted and subvolcanic products of already differentiated, commonly hydrothermally altered, composition.

These are not all mutually exclusive and it is likely that the Karymshina magmas were formed by a combination of these mechanisms. The deep crustal hot zone method allows for partial melting of the crust, which would incorporate a crustal component especially as the magma would be buoyant and rise through the crust where it would stall out in a shallow magma chamber (Annen et al., 2006). This deep crustal hot zone would also provide a constant source of magma recharge and heat to the developing magma chamber located at shallower depths. The partial melting of Eocene and younger Kamchatkan crust would also produce a component with high SiO_2 (Rapp and Watson, 1995) and in larger volume, which is necessary according to our MELTS modeling to achieve voluminous rhyolitic compositions. The siliceous crustal partial melt is needed because fractional crystallization alone will not sufficiently raise the SiO_2 content to the levels observed in Karymshina (and similar examples wordwide) rocks, and in sufficient volumes. However, there must also be large amounts (ca 50%) of fractional crystallization to obtain the highest SiO_2 levels observed, which could occur by internal differentiation within a long-lived magma chamber with a crystalline mush (Lipman, 2007; Bachmann and Bergantz, 2008). Finally, in the shallow crust where the crystalline mush (representing the shallow portion of the crystallizing upper crustal batholith) would most likely reside, incorporation of recycled and remelted material would occur, including a small amount of locally silicified, hydrothermally altered crust with very high SiO_2 contents and low $\delta^{18}O$ and δD values (**Figure 6**). This hydrothermally-altered crust must have been incorporated into the magma to allow for the final increase in SiO_2 content to bring the magma to the composition observed. Such a model would also account for the range of values around normal mantle-like $\delta^{18}O$ values in the population of zircon phenocrysts.

Here we propose an additional simple mechanism of obtaining high-silica rhyolite by assimilation and melting of silica-rich hydrothermally altered rocks. Evidence of hydrothermal activity in and around the Karymshina caldera, the presence of inclusions of hydrothermal sinters in the products of Karymshina eruptions, and rhyolite-MELTS experiments that would favor addition of silica-rich compositions to obtain the postcaldera high silica rhyolites makes us to propose a simple model for generating moderate volumes of HSRs using rocks silicified by hydrothermal activity over a period of several million years since initiation of silicic magmatism at 4 Ma. **Figure 9** explains this concept and permits an increase in melt fraction even if there is an addition of nearly isothermal higher silica assimilant. Postcaldera high-silica rhyolitic intrusions have lower Zr saturation temperatures than the 1.78 Ma ignimbrite but contain fewer crystals. Simakin and Bindeman (2012) modeled the situation of excess silica in roof rocks above a magma body and observed no mechanical benefit of eroding low silica vs. a silica oversaturated roof. However, addition of such a high-silica rock permits an increase in melt fractions, which aids in obtaining high silica compositions.

In many recent models of crustal melting and granitic magma differentiation (Annen et al., 2006; Bohrson et al., 2014; Colón et al., 2018b, and many others), the amount of basalt that is required to generate silicic differentiates and provide heat for batholith-scale crustal melting equates to the added thickness of 10–15 km. As crustal thickening producing a cumulate-restite root of this magnitude is not observed in Karymshina seismic images (**Figure 3**) or other similar examples of large volume silicic centers around the world, effective delamination of the lower crust back into the mantle on timescales comparable to the duration of magmatic flare-ups (a few Myr), is required.

Thermomechanical Modeling

Like Yellowstone (Colón et al., 2018a,b), Karymshina is uniquely suited to the type of large-scale thermomechanical modeling we employ here, not only because of the numerous constraints placed on it by this and previous studies, but also because its large size and significant duration make it computationally approachable for models that have relatively long timesteps (5 kyr, in this case), and large regional-scale computation grids with resolutions of 1–2 km, as we use here. We here discuss preliminary results of attempts to model voluminous silicic systems in a subduction setting using the I2VIS code.

We begin with a relatively weak mantle plume as a melt source in the model, with a basalt production rate of approximately 200 km^3/km/Myr of arc (**Figure 11a**), which is in line with the long-term island arc melt production rates calculated by Jicha and Jagoutz (2015). This mantle melting heats and thickens the crust for nearly 20 Myr prior to the time interval which we examine in **Figures 10**, **11**, which marks the appearance of the first Rayleigh-Taylor instabilities at the Moho (**Figure 10a**). At this point, we see two crustal dripping events separated by about 1 Myr occur, the second triggered by the first, which produces a surge of mantle melting leading to the eruption of $\sim$1,500 km^3 of felsic magmas on the surface. These events occur spontaneously after heating and thickening of the crust by the steady intrusion of basalt renders the system unstable. By 3 Myr after the appearance of the initial instability, the system has returned to relative equilibrium (**Figure 10f**), with notably less dense cumulate material (green in **Figure 10**) in the lower crust, and resumes thickening until another delamination event occurs 10 Myrs later. We further note that the thickness of the crust decreases from an intital amount of $\sim$45 km (outlined by the orange dashed line in **Figure 10e** and the original geometry of **Figure 11a**) to a lesser value of about 40 km. The fallen cold material initially disrupts the hot plume in the mantle, producing a lull in basalt production (**Figure 11a**), but the system quickly recovers to a steady-state of mantle melting after a few Myr. Future modeling efforts with a more realistic subduction geometry will help to determine whether such a lull could also be expected to occur in an actual subduction zone rather than the mantle plume-driven model we use here.

The duration of this delamination event in our model is tantalizingly similar to the duration of volcanism at Karymshina, suggesting that such an event may explain the large but apparently temporary felsic melting flare up observed there since 4 Ma. The current crustal thickness at Karymshina of 38 km (**Figure 3**) is up to 5 km less than the surrounding area, suggesting that material below the caldera may have been lost to the mantle. The scale of the silicic volcanics-filled caldera which develops in **Figures 10e,f** (gray material), which is about 20 km wide and 3 km deep, also is quite similar to that seen at Karymshina (**Figures 2**, **3**). Finally, we use Nd isotopes as a proxy in the model for the amount of crustal melting occurring, assuming that they can be compared to any other radiogenic isotope system such as Sr or Hf. For **Figure 11d**, we assume that the entire crust has a ^{143}Nd/^{144}Nd value of 0.51237 ($\varepsilon_{Nd} = -5$) and that the mantle and its melts have a highly depleted ^{143}Nd/^{144}Nd value of 0.5133 ($\varepsilon_{Nd} = +13$). While our model does not directly replicate the values seen in **Figure 7**, we identify a few clear trends. First, we see that the first delamination event (the one shown in **Figure 10**) is associated with a clear excursion toward more unradiogenic (crust-like) values in the initial eruptions, followed by a rapid recovery to more mantle-like values. This trend is less clear in the second delamination event seen in **Figure 11**, but this may be because the crustal material in the model has been more consumed by then and the crust and is no longer available to melt. As for the times between delamination events, such as at 5 Myr, we currently suspect that the model overestimates the crustal melt contribution to erupted rhyolites at very low fluxes, particularly from the lower crust, as these low-percentage melts may be too efficiently extracted, skewing the behavior of the isotopes in **Figure 11d** outside of delamination events. In general, the tendency to recover back to mantle-like values after excursions of crustal melting reflects the "basaltification" of the crust during high-flux volcanic periods discussed above. The initial drop in ε_{Nd} suggests that the crust-like radiogenic isotope signature commonly seen in arc flare-ups (DeCelles et al., 2009) may simply be a result of hotter systems being associated with more rapid rates of intrusion being able to produce more crustal melting. Cooler systems, such as those associated with the post-caldera HSR eruptions at Karymshina, are able to fractionate mantle-derived basalts and the intrusions they produce, but with little excess heat available to melt the crust.

While these modeling results are highly preliminary, they offer a tantalizing glimpse into the potential origins of short-lived large caldera systems like Karymshina in arcs otherwise dominated by more typical stratovolcanoes and shields. Further modeling efforts will need to use more realistic geometries for the crust and mantle, including a fully-realized subducting slab-mantle wedge system, and hopefully 3D modeling to fully capture the inherently non-planar phenomena of delamination and dripping of the lithosphere. Further investigating this problem, and coupling it more closely to the precise geology and geochemistry of arc caldera systems like Karymshina promises to be an exciting field of future research.

CONCLUSIONS

Our observation and modeling suggests that the generation of voluminous rhyolitic and high-silica rhyolitic magmas at the Karymshina Caldera is most likely due to a combination of magma intrusion into a deep crustal hot zone that has led to incremental shallow batholith formation in the upper crust with shallow phenocryst assemblages. This is achieved by incubation by repeated intrusions followed by fractional crystallization in a large magma body. In addition, at shallow depths, a small amount of hydrothermally-altered crustal rock with extremely high SiO_2 content must also have been incorporated into the magma.

Three rhyolitic eruptive periods, at ∼4 Ma, prior to caldera-formation at 1.78 Ma, and the one encompassing the post-caldera extrusions between 0.9 and 0.5 Ma indicate the incremental assembly of a long-lived silicic upper crustal batholith magma body kept in various thermal states throughout its history. The proportion of mantle derived Sr and Nd and crustal derived H is increasing with time advocating progressive "basaltification" of the system in which siliceous differentiates of basaltic magmas dilute the signatures of the original crustal remelts of the initial stages of magmatism.

Geochemically, the 0.9–0.5 Ma post-caldera extrusions appear to be directly evolved from fractional crystallization of the caldera-forming magma; thus in response to continuing basaltic input, this upper crustal rhyolitic body is undergoing internal fractional crystallization to generate homogenous, crystal poorer, high-silica post-caldera rhyolites.

At the typical 0.001 km^3/yr eruption rate, the hydrous basalt intruded into a 38 km typical Kamchatkan arc crust produces two magma bodies, one near the Moho and the other engulfing the entire section of upper crust. Basalt is trapped in the lower portion of the upper crustal magma body, which exists as partially molten to solid state. Differentiation products of basalt periodically mix with the resident magma diluting its crustal isotopic signatures. At the end of the magmatism crust is thickened by 8 km.

Thermomechanical modeling suggests that following a long incubation period of basaltic intrusions, delamination of the lowermost crust and mantle lithosphere due to overthickening can produce brief but extremely intense magmatic flareups which may drive the higher intrusion rates that replace typical arc volcanic behavior with voluminous, caldera-forming eruptions.

Magmatic episodes lasting several million years under the continental arc of Kamchatka in systems comparable to Karymshina lead to crust-wide material redistribution and sequestration of silicic products to the upper crust, likely leading to local batholith formation.

Future Directions

Given the abundant presence of hot springs in the area around the Karymshina magma body, it is important to determine by geophysical methods if magma is still present and is crystallizing beneath the caldera. The compositions of the caldera-forming ignimbrites and the post-caldera extrusions show a high degree of homogeneity, which would also be consistent with extraction of a melt from a large-scale crystallizing mush. Ar-Ar dating of post caldera intrusions should aim at finding the youngest magmatic rock which currently stands at 0.5 Ma. Future research should also concentrate on the search for extracaldera ignimbrites coeval to the 1 km thick 1.78 Ma intracaldera tuff. A lack of topographical expression of the caldera walls presents a problem, but may be due to a combination of erosion by glaciers during the last glacial maximum, tectonic movement along faults, and high rates of erosion during modern times. Further mapping and recognition of collapse features (lag breccia, mega blocks, etc.) is required. Recognition of the 1.78 Ma and older deposits in the sediment cores in the Pacific and the Sea of Okhotsk is required. Finally, our very preliminary thermomechanical models suggest an important role for lithospheric dripping and delamination for driving arc caldera volcanism, which promises to be a fruitful area of future inquiry.

AUTHOR CONTRIBUTIONS

IB conceived the study and executed most of the effort. DC used TG computer program to perform thermomechanical modeling. VL (deceased 2016) and AR contributed fieldwork, samples, and map for the study. NS defended MS thesis under IB on geochemistry of rocks. BJ did Ar-Ar dating. ML determined the chemistry of Pacific ashes and ignimbrite. All authors read the paper and discussed results.

FUNDING

USA NSF grants # EAR 0537872 and EAR 1822977 to IB, and RNF Russian Science Foundation grant #16-17-10035 to VL and AR. Part of work is a based on cited and published thesis by a coauthor NS.

ACKNOWLEDGMENTS

We thank Michel Grègoire (OMP Toulouse), a reviewer and Pavel Izbekov, as well as Katie Dobson for editorial handling. Any use of trade, firm, or product names is for descriptive purposes only and does not imply endorsement by the U.S. Government.

SUPPLEMENTARY MATERIAL

The Supplementary Material for this article can be found online at: https://www.frontiersin.org/articles/10.3389/feart.2018.00238/full#supplementary-material

Table A1 | Chemical analyses of Karymshina Volcanic Center samples used in this study.

Table A2 | Results from North Pacific tephra and Kamchatka volcano glass.

Table A3 | Electron microprobe analyses of mineral phases and glass in ignimbrite and post-caldera extrusions. Done at University of Oregon (John Donovan, analyst).

Table A4 | Details of Ar-Ar dating of studied samples.

Figure A1 | Elemental temporal trends through Karymshina.

Figure A2 | Plag-Qz plots for Karymshina rocks.

Figure A3 | Results of rhyolite MELTS fractional crystallization at 8 and 2 kbars. Pressure with 2.5 wt% of H_2O in the initial. Best match is provided by 75% crystallization at low pressure with addition of 25% of amphibolite partial melt and addition of 10% silica-rich, hydrothermally-altered rocks.

Movie A1 | Delamination events in the course of our modeling.

REFERENCES

Anderson, A. T., Davis, A. M., and Lu, F. (2000). Evolution of Bishop Tuff rhyolitic magma based on melt and magnetite inclusions and zoned phenocrysts. *J. Petrol.* 41, 440–473. doi: 10.1093/petrology/41.3.449

Annen, C., Blundy, J. D., and Sparks, R. S. J. (2006). The Genesis of intermediate and Silicic magmas in deep crustal hot zones. *J. Petrol.* 47, 505–539. doi: 10.1093/petrology/egi084

Annen, C., and Sparks, R. S. J. (2002). Effects of repetitive emplacement of basaltic intrusionson thermal evolution and melt generation in the crust. *Earth Planet. Sci. Lett.* 203, 937–955. doi: 10.1016/S0012-821X(02)00929-9

Baboshina, V. A., Tereshchenkov, A. A., and Kharakhinov, V. V. (2000). *Tectonic Map ofthe Sea of Okhotsk Region*. Institute of the Lithosphere of Marginal Seas, Russian Academy of Sciences, Scale 1:6,500,000, 1 sheet.

Bachmann, O., and Bergantz, G. W. (2004). On the origin of crystal-poor rhyolites: extracted from batholithic crystal mushes. *J. Petrol.* 45, 1565–1582. doi: 10.1093/petrology/egh019

Bachmann, O., and Bergantz, G. W. (2006). Gas percolation in upper-crustal silicic crystal mushes as a mechanism for upward heat advection and rejuvenation of near-solidus magma bodies. *J. Volcanol. Geotherm. Res.* 149 , 85–102 doi: 10.1016/j.jvolgeores.2005.06.002

Bachmann, O., and Bergantz, G. W. (2008). Rhyolites and their source mushes across tectonic settings. *J. Petrol.* 49, 2277–2285. doi: 10.1093/petrology/egn068

Bacon, C. R. (1983). Eruptive history of mount Mazama and Crater Lake caldera Cascade Range USA. *J. Volcanol. Geotherm. Res.* 18, 57–115. doi: 10.1016/0377-0273(83)90004-5

Bindeman, I. N., Anikin, A. P., and Schmitt, A. K. (2016). Archean xenocrysts in modern volcanic rocks from Kamchatka - insight into the basement and paleodrainage. *J. Geol.* 124:684833. doi: 10.1086/684833

Bindeman, I. N., and Bailey, J. C. (1994). A model of reverse differentiation at Dikii Greben' Volcano, Kamchatka: progressive basic magma vesiculation in a silicic magma chamber. *Contrib. Mineral. Petrol.* 117, 263–278.

Bindeman, I. N., Leonov, V. L., Izbekov, P. E., Ponomareva, V. V., Watts, K. E., Shipley, N. K., et al. (2010). Large-volume silicic volcanism in Kamchatka: Ar-Ar and U-Pb ages, isotopic, and geochemical characteristics of major pre-Holocene caldera-forming eruptions. *J. Volcanol. Geotherm. Res.* 189, 57–80. doi: 10.1016/j.jvolgeores.2009.10.009

Bindeman, I. N., Ponomareva, V. V., Bailey, J. C., and Valley, J. W. (2004). Volcanic arc of Kamchatka: a province with high-δ18O magma sources and large-scale 18O/16O depletion of the upper crust. *Geochim. Cosmochim. Acta* 68, 841–865. doi: 10.1016/j.gca.2003.07.009

Bindeman, I. N., and Simakin, A. G. (2014). Rhyolites – hard to produce but easy to recycle and sequester: integrating microgeochemical observations and numerical models. *Geosphere* 10, 930–957. doi: 10.1130/GES00969.1

Bindeman, I. N., Vinogradov, V. I., Valley, J. W., Wooden, J. L., and Natalin, B. A. (2002).Archean protolith, and accretion of crust in Kamchatka: SHRIMP dating of zircons from metamorphic rocks of Sredinny and Ganal Massifs. *J. Geol.* 110, 271–289. doi: 10.1086/339532

Bohrson, W. A., Spera, F. J., Ghiorso, M. S., Brown, G. A., Creamer, J. B., and Mayfield, A. (2014). Thermodynamic model for energy-constrained open-system evolution of crustal magma bodies undergoing simultaneous recharge, assimilation and crystallization: the magma chamber simulator. *J. Petrol.* 55, 1685–1717. doi: 10.1093/petrology/egu036

Budd, D., Troll, V., Deegan, F. M., Jolis, E. M., Smith, V. C., Whitehouse, M. J., et al. (2017). Magma reservoir dynamics at Toba caldera, Indonesia, recorded by oxygen isotope zoning in quartz. *Nature Sci. Rep.* 7:40624. doi: 10.1038/srep40624

Cao, L. Q., Arculus, R. J., and McKelvey, B. C. (1995). "Geochemistry and petrology of volcanic ashes recovered from Sites 881 through 884: a temporal record of Kamchatka and Kurile volcanism," in *Proceedings of the Ocean Drilling Program, Scientiic Results,* vol. 145, eds D. K. Rea, I. A. Basov, D. W. Scholl, and J. F. Allan (College Station, TX: Ocean Drilling Program), 345–381.

Chesner, C. A. (1998). Petrogenesis of the Toba Tuffs, Sumatra, Indonesia. *J. Petrol.* 39, 397–438. doi: 10.1093/petroj/39.3.397

Churikova, T., Dorendorf, F., and Woerner, G. (2001). Sources and fluids in the mantle wedge below Kamchatka, evidence from across-arc geochemical variation. *J. Petrol.* 42, 1567–1593. doi: 10.1093/petrology/42.8.1567

Colón, D. P., Bindeman, I. N., Ellis, B. S., Schmitt, A. K., and Fisher, C. M. (2015). Hydrothermal alteration and batch melting of crust by Columbia River Basalt magmas, fingerprinted by post-CRB rhyolites of the J-P Desert and the Jarbidge Mountains, Idaho and Nevada, USA. *Lithos* 224, 310–323. doi: 10.1016/j.lithos.2015.02.022

Colón, D. P., Bindeman, I. N., and Gerya, T. V. (2018a). Thermomechanical modeling of the formation of a multilevel, crustal-scale magmatic system by the Yellowstone Plume. *Geophys. Res. Lett.* 45, 3873–3879. doi: 10.1029/2018GL077090

Colón, D. P., Bindeman, I. N., and Gerya, T. V. (2018b). Understanding the isotopic and chemical evolution of Yellowstone hot spot magmatism using magmatic-thermomechanical modeling. *J. Volcanol. Geotherm. Res.* doi: 10.1016/j.jvolgeores.2018.12.003. [Epub ahead of print].

Colón, D. P., Bindeman, I. N., Wotzlaw, J.-F., Christiansen, E. H., and Stern, R. A. (2018c). Origins and evolution of rhyolitic magmas in the central Snake River Plain: insights from coupled high-precision geochronology, oxygen isotope, and hafnium isotope analyses of zircon. *Contrib. Mineral. Petrol.* 173:11. doi: 10.1007/s00410-017-1437-y

de Silva, S. (2008). Arc magmatism, calderas, and supervolcanoes. *Geology* 36, 671–672. doi: 10.1130/focus082008.1

de Silva, S. L., and Gosnold, W. D. (2007). Episodic construction of batholiths: Insights from the spatiotemporal development of an ignimbrite flare-up. *J. Volcanol. Geotherm. Res.* 167, 320–335. doi: 10.1016/j.jvolgeores.2007.07.015

de Silva, S. L., Zandt, G., Trumbull, G., Viramonte, J. G., Salas, G., and Jimenez, N. (2006). "Large ignimbrite eruptions and volcano-tectonic depressions in the Cen- tral Andes: a thermomechanical perspective," in *Mechanisms of Activity and Unrest at Large Calderas,* eds C. Troise, et al., (London: Geological Society of London Special Publication), 47–63

DeCelles, P. G., Ducea, M. N., Kapp, P., and Zandt, G. (2009). Cyclicity in Cordilleran orogenic systems. *Nat. Geosci.* 2:251. doi: 10.1038/ngeo469

Ducea, M. N., and Barton, M. D. (2007). Igniting flare-up events in Cordilleran arcs. *Geology* 3, 1047–1050. doi: 10.1130/G23898A.1

Ducea, M. N., Paterson, S. R., and DeCelles, P. G. (2015a). High-volume magmatic events in subduction systems. *Elements* 11, 99–104. doi: 10.2113/gselements.11.2.99

Ducea, M. N., Saleeby, J. B., and Bergantz, G. (2015b). The architecture, chemistry, and evolution of continental magmatic arcs. *Annu. Rev. Earth Planet. Sci.* 43, 299–331. doi: 10.1146/annurev-earth-060614-105049

Dufek, J., and Bergantz, G. W. (2005). Lower crustal magma genesis and preservation: a stochastic framework for the evaluation of basalt–crust interaction. *J. Petrol.* 46, 2167–2195. doi: 10.1093/petrology/egi049

Duggen, S., Portnyagin, M., Baker, J., Ulfbeck, D., Hoernle, K., Garbe-Schönberg, D., et al. (2007). Drastic shift in lava geochemistry in the volcanic-front to rear-arc region of the Southern Kamchatkan subduction zone: evidence for the transition from slab surface dehydration to sediment melting. *Geochim. Cosmochim. Acta* 71, 452–480. doi: 10.1016/j.gca.2006.09.018

Eichelberger, J. C., Izbekov, P. E., and Browne, B. L. (2006). Bulk chemical trends at arc volcanoes are not liquid lines of descent. *Lithos* 87, 135–154. doi: 10.1016/j.lithos.2005.05.006

Folkes, C., de Silva, S., Schmitt, A., and Cas, R. (2011). A reconnaissance of U-Pb zircon ages in the Cerro Galán system, NW Argentina: prolonged magma residence, crystal recycling and crustal assimilation. *J. Volcanol. Geothermal Res.* 206, 136–147. doi: 10.1016/j.jvolgeores.2011.06.001

Geological Map of the Russian Federation (2000). Panel N-57-XXVII (Petropavlovsk-Kamchatky) and Explanatory Notes, scale 1:200000, St Petersburg, VSEGEI Publisher, T.V. Brezhneva and LS Chelnokova (eds), (in Russian)

Gerya, T. V., and Yuen, D. A. (2003). Characteristics-based marker-in-cell method with conservative finite-differences schemes for modeling geological flows with strongly variable transport properties. *Phys. Earth Planet. Inter*. 140, 293–318. doi: 10.1016/j.pepi.2003.09.006

Glazner, A. F., Bartley, J. M., Coleman, D. S., Gray, W., and Taylor, R. Z. (2004). Are plutons assembled over millions of years by amalgamation from small magma chambers? *GSA Today* 14, 4–11. doi: 10.1130/1052-5173(2004)014<0004:APAOMO>2.0.CO;2

Gorbatov, A., Domiguez, J., Suarez, G., Kostoglodov, V., and Gordeev, E. (1999). Tomographic imaging of the P-wave velocity structure beneath the Kamchatka peninsula. *J. Geophys. Res.* 137, 269–279. doi: 10.1046/j.1365-246X.1999.00801.x

Gorbatov, A., Fukao, Y., Widiyantoro, S., and Gordeev, E. (2001). Seismic evidence for a mantle plume oceanward of the Kamchatka-Aleutian trench junction. *Geophys. J. Int.* 146, 282–288. doi: 10.1046/j.0956-540x.2001.01439.x

Grocke, S. B., de Silva, S. L., R., and Iriarte, J. M., Cottrell, L.E. (2017). Catastrophic Caldera-Forming (CCF) monotonous silicic magma reservoirs: geochemical and petrological constraints on heterogeneity, magma dynamics, and eruption dynamics of the 3·49 Ma Tara Supereruption, Guacha II Caldera, SW Bolivia. *J. Petrol.* 58, 227–260. doi: 10.1093/petrology/egx012

Gualda, G. A. R., Ghiorso, M. S., Lemons, R. V., and Carley, T. L. (2012). Rhyolite-MELTS: a modified calibration of MELTS optimized for silica-rich, fluid-bearing magmatic systems. *J. Petrol.* 53, 875–890. doi: 10.1093/petrology/egr080

Halliday, A. N., Davidson, J. P., Hildreth, W., and Holden, P. (1991). Modelling the petrogenesis of high Rb/Sr silicic magmas. *Chem. Geol.* 92, 107–114. doi: 10.1016/0009-2541(91)90051-R

Hawkesworth, C. J., Koloskov, A., Maury, R. C., and Bellon, H. (1997). Trace element and Sr-Nd-Pb isotopic constraints on a three-component model of Kamchatka Arc petrogenesis. *Geochim. Cosmochim. Acta* 61. 577–600. doi: 10.1016/S0016-7037(96)00349-3

Hildreth, W., and Moorbath, S. (1988). Crustal contributions to arc magmatism in the Andes of Central Chile. *Contribut. Mineral. Petrol.* 98, 455–489. doi: 10.1007/BF00372365

Hourigan, J. K., Brandon, M. T., Soloviev, A. V., Kirmasov, A. B., Garver, J. I., Stevenson, J., et al. (2009). Eocene arc-continent collision and crustal consolidation in Kamchatka, Russian Far East. *Am. J. Sci.* 309, 333–396. doi: 10.2475/05.2009.01

Huber, C., Bachmann, O., and Dufek, J. (2011). Thermo-mechanical reactivation of locked crystal mushes: melting-induced internal fracturing and assimilation processes in magmas. *Earth Planet. Sci. Lett.* 304, 443–454. doi: 10.1016/j.epsl.2011.02.022

Hudak, M. R., and Bindeman, I. N. (2008). Conditions of pinnacle formation and glass hydration in cooling ignimbrite sheets from H and O isotope systematics at Crater Lake and the Valley of Ten Thousand Smokes. *Earth Planet. Sci. Lett.* 500, 56–66. doi: 10.1016/j.epsl.2018.07.032

Hughes, G. R., and Mahood, G. A. (2008). Tectonic controls on the nature of large silicic calderas in volcanic arcs. *Geology* 36, 627–630. doi: 10.1130/G24796A.1

Ito, K., and Kennedy, G. C. (1971). An experimental study of the basalt-garnet granulite-eclogite transition. *Struct. Phys. Properties Earth's Crust* 14, 303–314.

Jicha, B. R., and Jagoutz, O. (2015). Magma production rates for intraoceanic arcs. *Elements Vol.* 11, 105–112. doi: 10.2113/gselements.11.2.105

Jicha, B. R., Singer, B. S., and Sobol, P. (2016). Re-evaluation of the ages of ^{40}Ar/^{39}Ar sanidine standards and supereruptions in the western U.S. using a Noblesse multi-collector mass spectrometer. *Chem. Geol.* 431, 54–66. doi: 10.1016/j.chemgeo.2016.03.024

Karakas, O., Degruyter, W., Bachmann, O., and Dufek, J. (2017). Lifetime and size of shallow magma bodies controlled by crustal-scale magmatism. *Nat. Geosci.* 10:446. doi: 10.1038/ngeo2959

Kimura, J.-I., Nagahashi, Y., Satoguchi, Y., and Chang, Q. (2015). Origins of felsic magmas in Japanese subduction zone: Geochemical characterizations of tephra from caldera-forming eruptions <5 Ma: origin of caldera eruptions in Japan. *Geochem. Geophys. Geosyst.* 16, 2147–2174. doi: 10.1002/2015GC005854

Kimura, J.-I., and Stern, R. J. (2008). "Neogene volcanism of the Japan island arc: the K-h relationship revisited," in eds J. E. Spencer and S. R. Titley *Ores and Orogenesis: Circum-Pacific Tectonics, Geologic Evolution, and Ore Deposits* (Tucson, AZ: Arizona Geological Society Digest), 187–202.

Konstantinovskaia, E. A. (2001). Geodynamics of an Early Eocene arc-continent collision reconstructed from the Kamchatka Orogenic Belt, NE Russia. *Tectonophysics* 325, 87–105. doi: 10.1016/S0040-1951(00) 00132-3

Kraevoi, Y., Okhapkin, V. G., and Serezhnikov, A.I. (1976). Results from Hydrogeological and Geothermal Studies in the Bol'she- Bannaya and Karymchina Hydrothermal Systems, Gidrotermal'nye sistemy i termal'nye polya Kamchatki (Hydrothermal Systems and Thermal Fields of Kamchatka), Vladivostok: Far Eastern Scientfic Center, *USSR Academy of Sciences Proceedings*, 179–211.

Kuiper, K. F., Deino, A., Hilgen, F. J., Krijgsman, W., Renne P. R., and Wijbrans, J. R. (2008). Synchronizing rock clocks of Earth history. *Science* 320, 500–504. doi: 10.1126/science.1154339

Lander, A. V., and Shapiro, M. N. (2007). The Origin of the modern Kamchatka zone. Volcanism and Subduction: the Kamchatka Region. *Geophys. Monogr. Ser.* 172, 57–64. doi: 10.1029/172GM05

Lee, C. T. A., Cheng, X., and Horodyskyj, U. (2006). The development and refinement of continental arcs by primary basaltic magmatism, garnet pyroxenite accumulation, basaltic recharge and delamination: insights from the Sierra Nevada, California. *Contrib. Mineral. Petrol.* 151, 222–242. doi: 10.1007/s00410-005-0056-1

Leonov, V. L., and Rogozin, A. N. (2007). Karymshina, a giant supervolcano Caldera in Kamchatka: boundaries, structure, volume of pyroclastics. *Volcanol. Seismol.* 1, 296–309. doi: 10.1134/S0742046307050028

Lipman, P. W. (2007). Incremental assembly and prolonged consolidation of Cordilleran magma chambers. *Geosphere* 3, 42–70. doi: 10.1130/GES00061.1

Lipman, P. W., O. A., Bogatikov, A. A., Tsvetkov, Gazis, C., Gurbanov, A. G., Hon, K., et al. (1993). 2.8-Ma ash-flow caldera at Chegem River in the northern Caucasus Mountains (Russia), contemporaneous granites, and associated ore deposits. *J. Volcanol. Geotherm. Res.* 57, 85–124. doi: 10.1016/0377-0273(93)90033-N

Loewen, M., and Bindeman, I. N. (2016). Oxygen isotope thermometry reveals high magmatic temperatures and petrogenetic differences between hot-dry Yellowstone/ Snake River Plain and Icelandic rhyolites compared to cold-wet systems. *Am. Mineral.* 101, 1222–1227. doi: 10.2138/am-2016-5591

Loewen, M. W., and Kent, A. J. (2012). Sources of elemental fractionation and uncertainty during the analysis of semi-volatile metals in silicate glasses using LA-ICP-MS. *J. Anal. At. Spectrom.* 27, 1502–1508. doi: 10.1039/c2ja30075c

Miller, C. F., McDowell, S. M., and Mapes, R. W. (2003). Hot and cold granites? Implications of zircon saturation temperatures and preservation of inheritance. *Geology* 31, 529–532. doi: 10.1130/0091-7613(2003)031<0529:HACGIO>2.0.CO;2

Min, K., Mundil, R., Renne, P. R., and Ludwig, K. R. (2000). A test for systematic errors in 40Ar/39Ar geochronology through comparison with U/Pb analysis of a 1.1-Ga rhyolite. *Geochim. Cosmochim. Acta* 64, 73–98. doi: 10.1016/S0016-7037(99)00204-5

Nizkous, I., Kissling, E., Sanina, I., Gontovaya, L., and Levina, V. (2007). Correlation of kamchatka lithosphere velocity anomalies with subduction processes. volcanism and subduction: the Kamchatka region. *Geophys. Monogr. Am. Geophys. Union* 172, 97–106. doi: 10.1029/172GM09

Ponomareva, V., Bubenshchikova, N., Portnyagin, M., Zelenin, E., Derkachev, A., Gorbarenko, S., et al. (2018). Large-magnitude Pauzhetka caldera-forming eruption in Kamchatka: astrochronologic age, composition and tephra dispersal. *J. Volcanol. Geotherm. Res.* 336, 1–12. doi: 10.1016/j.jvolgeores.2018.10.006

Ponomareva, V., Melekestsev, I., Braitseva, O., Churikova, T., Pevzner, M., and Sulerzhitsky, L. (2007). Late pleistocene-holocene volcanism on the kamchatka peninsula, northwest pacific region. volcanism and subduction: the Kamchatka Region. *Geophys. Monogr. Am. Geophys. Union* 172, 165–198. doi: 10.1029/172GM15

Portnyagin, M., Hoernle, K., Plechov, P., Mironov, N., and Khubunaya, S. (2007). Constraints on mantle melting and composition and nature of slab components in volcanic arcs from volatiles (H2O, S, Cl, F) and trace elements in melt inclusions from the Kamchatka Arc. *Earth Planet. Sci. Lett.* 255, 53–69. doi: 10.1016/j.epsl.2006.12.005

Prueher, L. M., and Rea, D. K. (2001). Tephrochronology of the Kamchatka±Kurile and Aleutian arcs: evidence for volcanic episodicity. *J. Volcanol. Geotherm. Res.* 106, 67–84. doi: 10.1016/S0377-0273(00)00266-3

Qi, H., Coplen, T. B., Gehre, M., Vennemann, T. W., Brandt, W. A., Geilmann, H., et al. (2017). New biotite and muscovite isotopic reference materials, USGS57 and USGS58, for d2H measurements-a replacement for NBS 30. *Chem. Geol.* 657:89–99. doi: 10.1016/j.chemgeo.2017.07.027

Rapp, R. P., and Watson, E. B. (1995). Dehydration melting of metabasalt at 8-32 kbar: implications for continental growth and crust-mantle recycling. *J. Petrol.* 36, 891–931. doi: 10.1093/petrology/36.4.891

Rogozin, A., Leonov, L., and Sobolevskaya, O. (2015). "Bol'she-bannaya hydrothermal system: new thermometric survey data and the position of the system relative to Karymshina Caldera (South Kamchatka),"in *Proceedings World Geothermal Congress* 2015 Melbourne, Australia, 1–7.

Rudnick, R. L., and Gao, S. (2003). "Composition of the continental crust," in *The Crust. Treatise on Geochemistry,* ed R. L. Rudnick (Oxford: Elsevier-Pergamon), 1–64.

Schmidt, M. (1992). Amphibole composition in tonalite as a function of pressure: an experimental calibration of the Al-in-hornblende barometer. *Contrib. Mineral. Petrol.* 110, 304–310. doi: 10.1007/BF00310745

Scholl, D. (2007). Viewing the tectonic evolution of the kamchatka-aleutian (KAT) connection with an alaska crustal extrusion perspective. volcanism and subduction: the kamchatka region. *Geophys. Monogr. Am. Geophys. Union* 172, 3–35. doi: 10.1029/172GM03

Seligman, A., Bindeman, I. N., Jicha, B., Ellis, B., Leonov, V. L., and Ponomareva, V. V. (2014). Recognizing subtle evidence for silicic magma derivation from petrochemically-similar arc crust: isotopic and chemical evidence for the bimodal volcanic series of Gorely Volcanic Center, Kamchatka. *Russia J. Petrol.* 55, 1561–1594. doi: 10.1093/petrology/egu034

Seligman, A. N., Bindeman, I. N., Van Eaton, A., and Hoblitt, R. (2018). Isotopic insights into the degassing and secondary hydration of volcanic glass from the 1980 eruptions of Mount St. *Helens. Bull. Volcanol.* 80:4. doi: 10.1007/s00445-018-1212-6

Sheimovich, V. S., and Golovin, D. J. (2003). Age of silicic volcanic rocks in the Bolshoy Banny springs. *Volcanol. Seismol.* 1, 21–25

Sheimovich, V. S., and Khatskin, S. V. (1996). Rhyodacitic magmatic formation of southeastern Kamchatka. *Volcanol. Seismol.* 5, 99–105.

Sheimovich, V. S., and Patoka, M. G. (1989). *Geologicheskoe Stroenie Zon Aktivnogo Kainozoiskogo Vulkanizma (The Geological Structure of Zones of Active Cenozoic Volcanism)*. Moscow: Nedra publisher.

Shipley, N. K. (2011). *Isotopic and Petrologic Investigation and Model of Genesis of Large-Volume High-Silica Rhyolites in Arc Environments: Karymshina Caldera, Kamchatka, Russia*. MS Thesis University of Oregon, 76p. Available online at: http://hdl.handle.net/1794/12187

Simakin, A. G., and Bindeman, I. N. (2012). Remelting in caldera and rift environments and the genesis of hot, "recycled" rhyolites. *Earth Planet Sci. Lett*. 337–338, 224–235. doi: 10.1016/j.epsl.2012.04.011

Simon, A., Yogodzinski, G. M., Robertson, K., Smith, E., Selyangin, O., Kiryukhin, A., et al. (2014). Evolution and genesis of volcanic rocks from Mutnovsky Volcano, Kamchatka. *J. Volcanol. Geotherm. Res.* 286, 116–137. doi: 10.1016/j.jvolgeores.2014.09.003

Taran, Y. A., Pokrovsky, B. G., and Volynets, O. N. (1997). Hydrogen isotopes in hornblendes and biotites from Quaternary volcanic rocks of the Kamchatka-Kurile arc. *Geochem. J.* 31, 203–221. doi: 10.2343/geochemj.31.203

Tatsumi, Y. (2005). The subduction factory: how it operates in the evolving earth. *GSA Today* 15:7. doi: 10.1130/1052-5173(2005)015[4:TSFHIO]2.0.CO;2

Taylor, H. P. Jr. (1986). "Igneous rocks:II. Isotopic case studies of circumpacific magmatism," in *Stable Isotopes in High Temperature Geological Processes*, Vol. 16, eds J. W. Valley, H. P. Taylor Jr, and J. R. O'Neil (Washington, DC: Mineralogical Society of America; American Geophysical Union), 273–316.

Taylor, S. R., and McLennan, S. M. (1995). The geochemical evolution of the continental crust. *Rev. Geophys*. 33, 241–265. doi: 10.1029/95RG 00262

Tuttle, O. F., and Bowen, N. L. (1958). *Origin of Granite in the Light of Experimental Studies in the System.* Memoir*:* Geological Society of America, 74

Vinogradov, V. I. (1995). Isotopic evidence of the conversion of oceanic crust to continental crust in the continent-ocean transition zone of Kamchatka. *Geochem. Int.* 32, 70–109.

Vinogradov, V. I., Buyakaite, M. I., Goroshenko, G. L., Lukanin, A. O., and Pokrovsky, B. G. (1991). Isotope and geochronological features of deeply metamor- phosed rocks of Ganal Massif in Kamchatka. *Trans. Russ. Acad. Sci. Earth Sci. Sect*. 318:929–936.

Vinogradov, V. I., V. S., and Grigoriev, and, B. G., Pokrovsky (1986). "Isotopic composition of the oxygen and strontium in the rocks of the Kurile-Kamchatka island arc-key for some genetic constructions(in Russian)," in *Evolution of the System Crust-Mantle*, ed Y. A. Shukolyukov (Moscow: Nauka, Acad.Sci.USSR), 78–102.

Vogel, T., Patino, L. C., Eaton, J. K., Valley, J. W., Rose, W. I., Alvarado, G. E., et al. (2006). Origin of silicic magmas along the Central American volcanic front:

genetic relationship to mafic melts. *J. Volcanol. Geotherm. Res*. 156, 217–228. doi: 10.1016/j.jvolgeores.2006.03.002

Vogt, K., Gerya, T. V., and Castro, A. (2012). Crustal growth at active continental margins: numerical modeling. *Phys. Earth Planet. Interiors* 192–193, 1–20. doi: 10.1016/j.pepi.2011.12.003

Volynets, O. (1994). Geochemical types, petrology, and genesis of Late Cenozoic volcanic rocks from the Kurile-Kamchatka island-arc system. *Int. Geol. Rev.* 36, 373–405. doi: 10.1080/00206819409465467

Waters, L. E., and Lange, R. A. (2017). Why aplites freeze and rhyolites erupt: controls on the accumulation and eruption of high-SiO2 (eutectic) melts. *Geology* 45, 1019–1022. doi: 10.1130/G39373.1

Watson, E. B., and Harrison, T. M. (1983). Zircon saturation revisited: temperature and compositional effects in a variety of crustal magma types. *Earth Planet. Sci. Lett.* 64, 295–304. doi: 10.1016/0012-821X(83)90211-X

Watts, K. E., Bindeman, I. N., and Schmitt, A. K. (2011). Large-volume rhyolite genesis in caldera complexes of the Snake River Plain: Insights from the Kilgore Tuff of the Heise Volcanic Field, Idaho, with comparison to Yellowstone and Bruneau-Jarbidge Rhyolites. *J. Petrol.* 52, 857–890. doi: 10.1093/petrology/egr005

Watts, K. E., John, D. A., Colgan, J. P., Henry, C. D., Bindeman, I. N., and Schmitt, A. K. (2016). Probing the volcanic–plutonic connection and the genesis of crystal-rich rhyolite in a deeply dissected supervolcano in the nevada great basin: source of the late eocene caetano tuff. *J Petrol.* 57, 1599–1644. doi: 10.1093/petrology/egw051

Winter, J. D. (2010). *Principles of Igneous and Metamorphic Petrology 2nd Edn*. London: Pearson Publisher, 720.

Wyllie, P. J. (1984). Constraints imposed by experimental petrology on possible and impossible magma sources and products. *Philos. Trans. R. Soc. Lond. A* 310, 439–456. doi: 10.1098/rsta.1984.0003

Conflict of Interest Statement: The authors declare that the research was conducted in the absence of any commercial or financial relationships that could be construed as a potential conflict of interest.

frontiers in Earth Science

ORIGINAL RESEARCH
published: 19 February 2019
doi: 10.3389/feart.2019.00019

360 Intrusions in a Miniature Volcano: Birth, Growth, and Evolution of an Analog Edifice

Allan Derrien[1]* and *Benoit Taisne*[2,3]

[1] Observatoire Volcanologique du Piton de la Fournaise, Institut de Physique du Globe de Paris, Paris, France, [2] Earth Observatory of Singapore, Nanyang Technological University, Singapore, Singapore, [3] Asian School of the Environment, Nanyang Technological University, Singapore, Singapore

Most volcanoes throughout the world have been monitored with geophysical data (seismology and geodesy) for no more than three decades, a relatively short time compared to their overall life. The consequence is that we lack a long observation of volcanic growth and behavior to get a more complete picture of the interaction between edifice stress state and magma transfer. Here we present the birth and evolution of a 83 x 83 cm analog model, where we reproduce for the first time volcanic growth over 360 successive intrusions (15 mL every half hour, at a rate of 3 mL/min) in an analog elasticity-dominated material (pigskin gelatine). By observing the development of this model volcano, we hope to provide insights to the study of long-term volcanic activity. In particular, we are interested in stress accumulation/release cycles and their role in the triggering of distant eruptions. Our model volcano started as a flat topography and ended 3.82 cm in height at the summit. It displayed cyclic eruptive patterns with alternating phases of eruptive and purely intrusive behavior. Alike to many intraplate volcanoes in nature, main dyke swarms produced in the experiment were disposed in a three-branched radial pattern centered above the injection source ("volcanic rift zones"). They were accompanied by two radial sill networks, at source depth and edifice base. Long-term radial compressive stress building during dyke swarming was likely compensated by radial compressive stress release during sill emplacement. Near-surface stresses, deduced from the main orientation eruptive fissures and "dry" fractures, became more localized as the volcano grew. At the end of the experiment, the shallow stress field was interpreted as generally extensional radial at the summit, extensional tangential on the flanks, and compressive radial in distal areas. This experiment showcases the potential of studying long-term stress permutations in volcanic edifices in the understanding of their morphology and successive activity phases.

Keywords: volcano, growth, edifice, stress state, magma transfer, analog, experiment, intrusions

OPEN ACCESS

Edited by:
Yosuke Aoki,
The University of Tokyo, Japan

Reviewed by:
Matthieu Kervyn,
Vrije University Brussel, Belgium
Alessandro Bonaccorso,
Istituto Nazionale di Geofisica e Vulcanologia (INGV), Italy
Frank Bo Buster Guldstrand,
University of Oslo, Norway

***Correspondence:**
Allan Derrien
derrien@ipgp.fr

Specialty section:
This article was submitted to Volcanology,
a section of the journal Frontiers in Earth Science

Received: *25 October 2018*
Accepted: *31 January 2019*
Published: *19 February 2019*

Citation:
Derrien A and Taisne B (2019) 360 Intrusions in a Miniature Volcano: Birth, Growth, and Evolution of an Analog Edifice. Front. Earth Sci. 7:19. doi: 10.3389/feart.2019.00019

INTRODUCTION

Shield oceanic island volcanoes, such as Kilauea, Piton de la Fournaise or Pico de Fogo, often form far from active tectonics boundaries. Contrary to subduction zone stratovolcanoes, which generally exhibit steep active cones, shield volcanoes are sub-circular, gentle-sloped piles of layered rock. On a such edifices, the eye of an occasional visitor can be confused by the seemingly random distribution of vents, fissure, and craters. A tourist walking on, for instance, Pico de Fogo or Piton de la Fournaise is often surprised to see cones apparently randomly scattered away from the summit. Such a view is far from the iconic idea that one might have from a single vent volcano.

Eruptive cones and fissures are born during eruptive phases, when magma transits from certain depths in the volcano plumbing system to the surface. The upper part of the volcano, where these final transfers happen, is named the *distribution system* (**Figure 1**). It literally distributes the magma supply from shallow storage zones (roughly between 0 and 10 km below the surface; e.g., Michon et al., 2015; Greenfield et al., 2016; Le Corvec and McGovern, 2018) to the surface, both spatially (as evidenced by the wide geographical repartition of eruption markers on most shield volcanoes) and temporally (because it can modulate magma input from continuous supply to discrete eruptions). Depending on the volcano, the source of magma for this final transfer can vary greatly. For instance, it can display a well-developed reservoir with a complex geometry as Kilauea (e.g., Ryan, 1988; Zhai and Shirzaei, 2016), include a single main chamber as Piton de la Fournaise (e.g., Michon et al., 2015, 2016), or have no identified voluminous shallow reservoir as Pico de Fogo (e.g., Mata et al., 2017) (**Figure 1**). In this ultimate phase of the volcanic fluids journey to the surface, magma usually propagates through the intrusion of dykes or sills into the host rock, if no open conduit is available.

Previous studies have shown that the four main parameters (aside from buoyancy) controlling magma propagation in the host rock of the distribution system are (1) structural heterogeneities (such as faulting or layering) (e.g., Gudmundsson, 2002; Kavanagh et al., 2006), (2) local or regional stress field (e.g., Paquet et al., 2007; Sigmundsson et al., 2015), (3) gravitational loading (e.g., Hyndman and Alt, 1987; Dieterich, 1988; Walter and Troll, 2003; Münn et al., 2006; Roman and Jaupart, 2014; Maccaferri et al., 2017), and (4) plumbing system pressure on host rock (e.g., Carracedo, 1994; Gudmundsson, 2012; Tibaldi, 2015). Our study aims to observe how the distribution system (in which magma transits from shallow depths to surface or subsurface) evolves in a "neutral" context, with no extensive/compressive/shear constrain. From this, we aim to get insights on what drives the long-term geometry of distribution systems, in the case of volcanoes that are far from active tectonics boundaries (e.g., intraplate oceanic islands).

It is difficult to answer this question by observing volcanoes in nature. Precious insights can be gained from observing extinct magmatic systems exhumed by erosion, but these are limited when it comes to interpreting dynamic behavior (e.g., Keating et al., 2008; Gudmundsson, 2012; Marsh, 2015). On living, active volcanoes, intervals between intrusive events are at least a few months (e.g., Roult et al., 2012, for the case of Piton de la Fournaise, one of the most active volcanoes on Earth) and volcanoes take a long time to grow, making dynamic observations of active distribution systems short in comparison of their life. In 2018, we have at most 30 years of exploitable geophysical data (earthquakes records, GNSS displacements, InSAR maps, degassing monitoring) for magma transfer imaging at depth at the most well-documented volcanoes of the world. Some of them are 300,000 years old. If volcanoes had a lifespan of one day, we would only have direct access to the last 9 s of their active life, the rest being inferred from geological studies. By creating models that replicate some of nature's volcanoes features, we have a chance to observe, record and analyze a greater amount of successive intrusive events.

Here we present one analog model of the development of a volcanic edifice through the use of gelatine as both host rock and magma. In this experiment, liquid gelatine (simulating magma) was injected at the bottom of a solid gelatine (simulating host rock) tank, at repeated intervals. We analyzed the surface evolution and distribution of eruptive vents, and showed various periods of dyke and sill swarming. This model highlighted the importance of volcanoes distribution system in various phases of their development, and in their long-term morphology.

MATERIALS AND METHODS

Material Choice and Preparation

Crustal analog materials for dyke and sill emplacement and magma transfer inside the crust have been intensively studied in the past two decades, leading to a good knowledge of how to set up a volcano replica in laboratories. Different materials are able to model specific behaviors of volcanic edifices, especially the way they deform, compress or fail under magma injections (e.g., Abdelmalak et al., 2016). Crustal hosts rocks (inside which magma propagates from shallow sources to surface) most often display a complex elasto-plastic behavior at a volcano's scale (Galland et al., 2015). Rheology (rock response to constraints) can be dominated by one end or the other (elastic or plastic), depending on the rock type and scale of observation. Laboratory materials usually enable to model one or the other end (plasticity-dominated media, or on the contrary, elasticity-dominated host rocks) (**Figure 2**).

For instance, at the "weak," or plastic, end of the elasto-plastic scale of crustal analogs, granular materials such as dry or wet sand, flour, diverse metallic powders or a mix of these were used to mimic the properties of large-scale natural objects (tens to hundreds of kilometers wide, where plasticity is the dominant characteristic) and understand better their behavior (e.g., Caldera collapse and dyke propagation, Roche et al., 2001; Kervyn et al., 2009; Delcamp et al., 2012 or magma emplacement in tectonic extension, Bonini et al., 2001; Corti et al., 2001), or model complex dynamics of magma propagation (e.g., Guldstrand et al., 2017). At the "strong" end of the elasto-plastic scale, gels such as water-gelatine mix, agar and acryl gels were used to model smaller scale objects (tens of meters to a few kilometers wide) or well consolidated mediums (e.g., for dyke nucleation and propagation, McLeod and Tait, 1999; Kavanagh et al., 2006; Taisne and Tait, 2009; Taisne et al., 2011; Le Corvec et al., 2013, interactions between two dykes, Ito and Martel, 2002, or the effect of various dyke properties on propagation, Chanceaux and Menand, 2014). Note that this list is non-exhaustive, and that the reader is referred to review articles such as or Galland et al. (2015); Kavanagh et al. (2018) for more encompassing writings about volcano analog modeling.

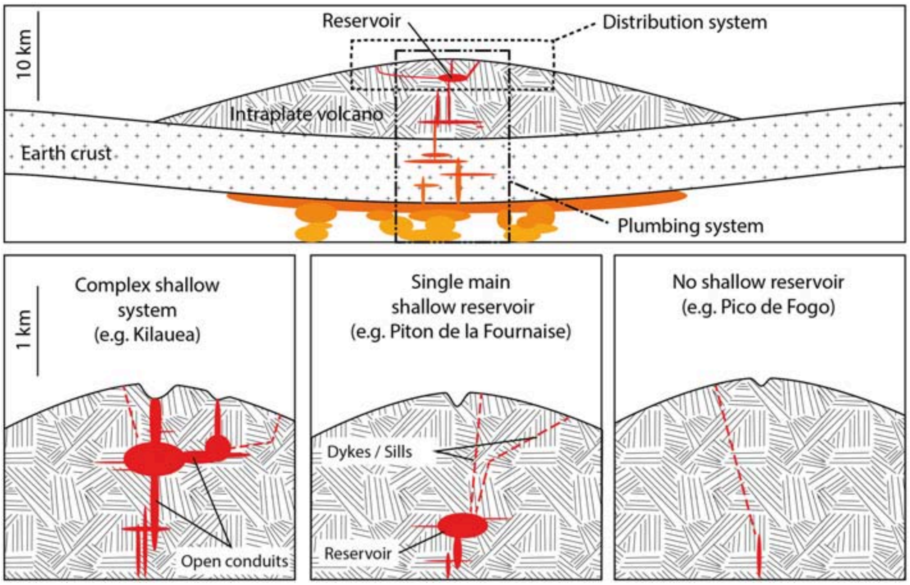

FIGURE 1 | Illustration of typical intraplate shield volcanoes plumbing and distribution systems. The "distribution system" refers to the shallowest part of the host rock, inside which dyke, sills, and open conduits enable the final transfer of magma from shallow reservoirs (or not if not applicable, e.g., Pico de Fogo) to the surface.

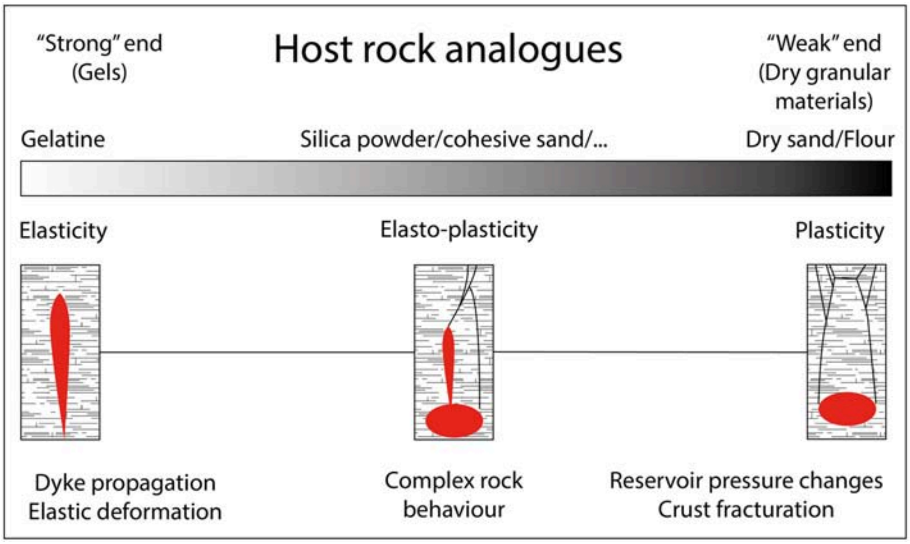

FIGURE 2 | Analog materials used for modeling magma transfer and its interaction with the range of elasto-plastic crustal host rocks.

Compared with other studies, though, ours has one supplementary challenge: we need to use the same material for analog host rock and magma alike. Indeed, since successive injections are made, all dykes, sills, and laccoliths that possibly intrude are becoming part of the host rock for the next injection, so they need to be similar. Previous studies have shown that 2 to 5 wt% pigskin gelatine is a suitable analog for crustal rock intruded by dykes or sills, according to scaling laws (Kavanagh et al., 2013). We thus chose, after some testing, to use pigskin gelatine (food grad, bloom 250, at 4.5 wt% in de-ionized water, with some bleach to prevent bacterial growth). In its liquid state (at temperatures above 29°C), it behaves almost like water with a slightly higher density and viscosity (around 1 g/cm^3 and 0.01 m^2/s at 20°C), making it a good Newtonian fluid for analog magma modeling. Once solidified (at cool temperatures around 5–20°C), it is a transparent, birefringent "strong" gel with a young's modulus of 5–9 kPa (following measurements made on the same gelatine, Pansino and Taisne, 2018 at JGR: Solid Earth), which enables us to visualize intrusions inside the analog host rock and their related relative strain. The only downside is that the mechanical properties of pigskin gelatine change with cooling time (its Young's modulus increases exponentially and reaches a plateau (E_∞) after several hours. E_∞ is a linear function of gelatine concentration while the time to reach 90% of it ($t_{0.9E\infty}$) is controlled by the thickness of gelatine to be cooled and the room temperature (Kavanagh et al., 2013), so that "old" host rock (deposited in the beginning of the experiment) might be stronger than "fresh" one. However, with enough cooling time and sufficiently small injected volumes, this effect can be tempered.

Scaling and Boundary Effects

In this study, we consider typical oceanic islands volcanoes, located on top of hotspots and not affected by intense local tectonics (e.g., Kilauea, Piton de la Fournaise, Fernandina, Fogo). In order to provide a scaled model for the structural development of such volcanoes, we followed the classic similarity procedure described in e.g., Ramberg (1981). The shallow distribution system of these edifices is usually composed of a network of dykes and sills as well as small magma bodies between 0 and 3 km below the summit, while the upper part of the edifice is usually 10–30 km wide (e.g., Hildner et al., 2011; Bagnardi and Amelung, 2012; Michon et al., 2015). Since we had at our disposal a 83 × 83 cm tank (**Figures 3A,B**), the point of analog magma injection should be <8.3 cm below the summit. Thus, at the beginning of the experiment, the injector was placed 3 cm below the surface, leaving a 5.3 cm vertical growth margin). Bear in mind that scaling in this experiment followed similarity alone instead of, for instance, dimensionless ratios as proposed in Galland et al. (2015). The latest approach would have required a bigger number of experiments, which was not possible due to time constraints.

It was also necessary to make sure that the box sides did not significantly affect the model physics, and in particular the stress state of the volume where the magma distribution system was developing (boundary effects). Previous studies have shown that analog edifice gravitational loading and stress adjustments can be affected if the sides of the box are too close to the distribution system (e.g., Corbi et al., 2016). We thus realized preliminary experiments using the same experimental setup. The typical deformation induced by a new intrusion did not reach further than 6 cm away from the dyke (as evidenced by changes on gelatine birefringence colors and surface deformation, see **Supplementary Material**). To prevent boundary effects from the side of the box on dyke propagation, we ended the experiment when the distribution system (composed of dykes and sills) was still a little more than 8 cm away from the box sides (for the farthest 5 intrusions), and even 13 cm for the rest of the intrusions. Corbi et al. (2016) also showed that a box at least twice the diameter of the "central cone" (as defined in their study) was enough to prevent boundary effects that significantly modify gravitational loading. In our case, the box is a 83 × 83 cm square. We stopped the experiment when the central cone was a little <20 cm in diameter. Finally, note that boundary effects from the bottom of the box might (in our experiment) have played a role for deep (around source depth) intrusions.

We wanted to give the miniature volcano a level of activity close to what can be observed at very active intraplate hotspots (e.g., Kilauea, Piton de la Fournaise). The ratio between activated/cooling times of the distribution system in the model (20%) was of the order of what is observed at e.g., Piton de la Fournaise in active phases. This was 11.6% on average over the 1950–2017 period, that includes long rest phases (e.g., Roult et al., 2012), and 20% on average over the 9 eruptions of the 2015–2017 cycles (e.g., Coppola et al., 2017). Following these considerations, we chose to activate injections during 5 min every 30 min (20% activated/cooling time ratio).

Because of this choice of scaling, we are investigating long-term structural growth processes that affect the shallowest part of plumbing systems, roughly from surface to 3 km deep under the summit, on highly-active oceanic islands volcanoes.

Experimental Setup

The experiment took place over the course of 2 weeks in a thermostated (15°C) environment. It was observed by an acquisition system composed of an Arduino (1. on **Figure 3**) controlling DSLR cameras (2.). We grew a miniature volcano in a 83*83*15 cm tank (3.), attached to a gelatine feeding system at its bottom center (4.). This feeding system included a thermostated (35°C) small chamber keeping the gelatine liquid [a heating coil enabled to run warm water inside the chamber without mixing with the analog material (**Figures 3C,D**)]. On top of the chamber we fitted a small elastic balloon (0.5 cm in diameter) that was pierced homogeneously with 20 holes (**Figure 3E**). Temperature (5.) and pressure (6.) in the feeding chamber were planned to be recorded (but due to technical problems only the temperature could be). We used a programmable peristaltic pump (7.) to inject precise volumes of liquid gelatine from a thermostated (35°C) reservoir (8.) into the model. The whole tube enabling the transfer of analog magma from the reservoir to the model was also kept at a constant temperature (35°C) with a warm water circuit (9.), to prevent the freezing of material during repose times. The original host rock analog material (see Material Choice and Preparation) was mixed with de-ionized water for 2 h at 75°C then poured into the tank until 3 cm thick (note that the photograph in **Figure 3A** suggests more than 3 cm, because it comes from an earlier similar experiment with the exact same setup), before observing a 48 h repose time at 15Â○C for solidification.

Experimental Protocol

Once the original host rock analog had solidified (48 h after preparation), we launched the injection cycles. Every 30 min, the injection system (reservoir + pump + chamber) pushed 15 ml of liquid gelatine (at 35°C) inside the tank from the bottom, at a rate of 3 ml/min. Thus, each injection lasted for 5 min, during which analog magma slowly intruded the edifice, and often reached the surface, emplacing a small flow (injection #265 was displayed as an example photograph of the model while the experiment was running, on **Figure 4**). After each injection, the fluid cooled down quickly and solidified, simulating the emplacement of a dyke/sill/external flow and adding volume to the edifice. Gelatine in the reservoir was renewed daily, so that it remained freshly mixed. Four hundred and fifty eight injections (amongst which only the first 360 were selected for the study in the result analysis)

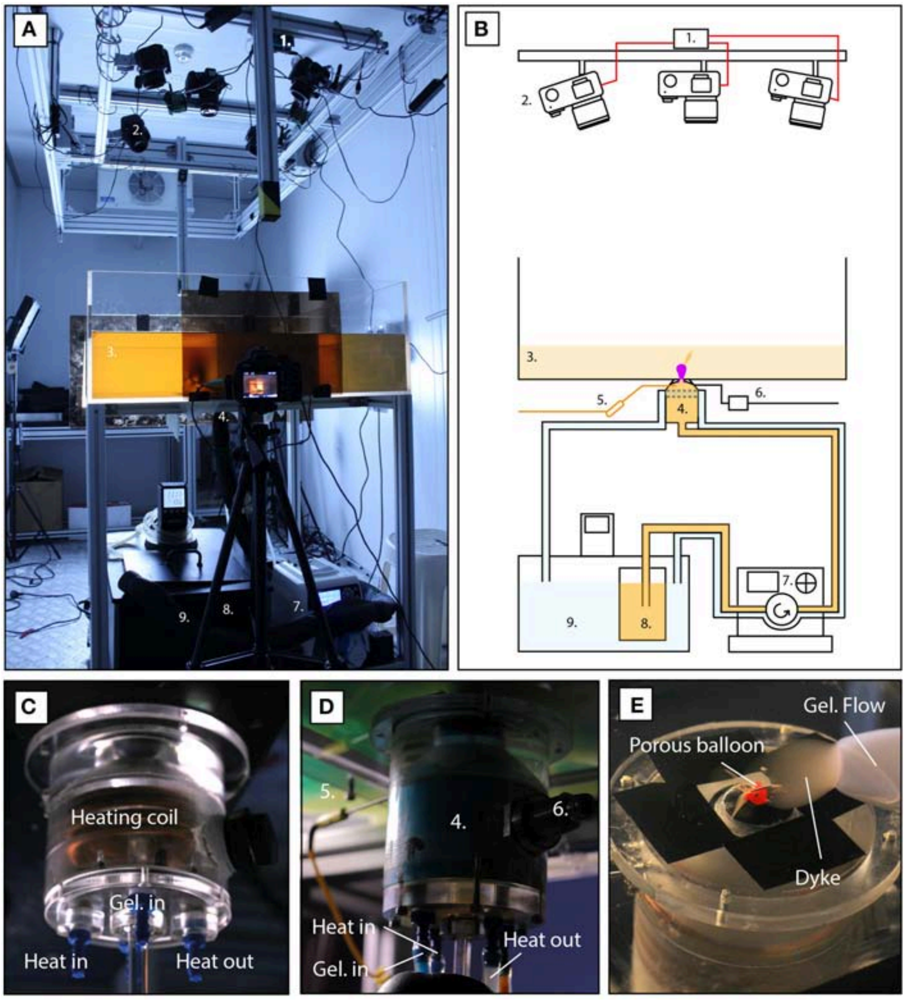

FIGURE 3 | Photographs **(A,C,D,E)** and sketch **(B)** of the experimental setup in the cold room. An Arduino program (1) controls multiple-views cameras (2) to synchronously take regular photographs of the mini-volcano surface. Injections in an initial volume (3) are realized through a porous balloon on top of a heated chamber (4) which pressure and temperature are controlled (5, 6). Injections are controlled by a programmable peristaltic pump (7) that pushes liquid gelatine from the main reservoir (8) into the chamber. To ensure that gelatine stays liquid in the injection system, it is coupled with a hot water circuit (9).

were performed this way over the course of 10 days, without interruption or changes in the room temperature.

The temperatures of the room, of the injection tube, reservoir and chamber were verified by thermocouples. Pressure inside the injection chamber failed to be acquired continuously (technical issues). However, as the injection rate was very low (0.05 ml/s) compared to the chamber volume (0.8 l), variations in the chamber pressure are expected to remain low (around 0.006% per second). The growth of the miniature volcano was monitored by a network of 4 cameras. Three on top of the experiment (for stereo-photogrammetric purposes) and one on the side were synchronized and programmed to take 10 pictures, with an interval of 30 s, starting 1 s before each injection. Stereo-photographs were processed with Agisoft Photoscan Pro (v.1.2.3) (a reliable structure-from-motion software, e.g., Bolognesi et al., 2015; Derrien et al., 2015) to make Digital Elevation Models (DEMs). Occasionally, photographs of particular injections from the side through a polarized sheet (**Supplementary Material**) were taken to visualize dyke propagation and typical strain changes inside the analog crust.

The top-view images (5,184 x 3,456, 0.24 mm/pixel) acquired between each injection were used to create a short timelapse animation of the analog edifice growth (**Supplementary Material**). This set of pictures was used to map the location of eruptive fissures and intrusion tips (accuracy of 0.5 cm). In addition, the top view images could be processed to extract (X,Y) surface deformation using Digital Image Correlation (DIC) (**Supplementary Material**). The DIC code (Version 4) was adapted from a version developed by Dr. Elizabeth Jones© (2013, 2014, 2015) based on previous developments by Christoph Eberl et al. (http://www.mathworks.com/matlabcentral/fileexchange/12413).

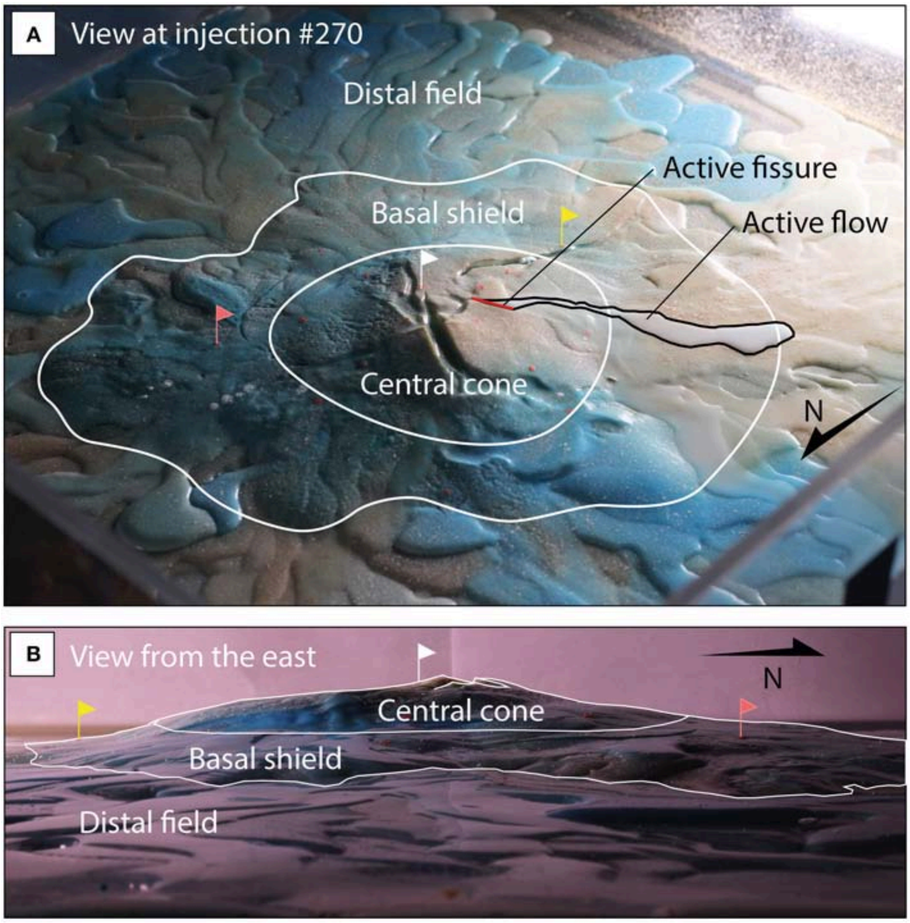

FIGURE 4 | An example of the mini-volcano morphology at injection #323. Note the central cone surrounded by steep slopes, atop a basal shield displaying gentler elevation changes, and finally the distal deposit field where most of the flows are emplaced. The summit, rising 3.64 cm above starting level, is affected by significant type I surface fractures (radially, in perpendicular WNW-ESE and SSW-NNE directions, and tangentially especially south of the summit). **(A)** Oblique photo from the Northwest **(B)** side-view of the central cone from the East.

and using the Matlab image processing toolbox. Note that texture has been added in form of micro-drops of paint sprayed on the model's surface so that displacements could be measured. Bear in mind that the use of DIC in this communication will purposely be limited only to showcase examples of what surface deformation measurements can be achieved. We wish to focus on presenting the long-term growth trends and not enter the detail of each intrusion characteristics.

The multiple-views dataset enabled to produce, for certain time steps, DEMs of the experiment surface using Agisoft's Photoscan (raw photographs and metadata available at NTU repository). Fifteen DEMs were produced at injections #0, #53, #87, #109, #141, #156, #178, #201, #219, #238, #264, #282, #327, #333 and #381 (see examples on **Figures 5A–E**). The surface difference between two successive DEMs was integrated to obtain volume changes. In particular, we differentiated endogenous volume changes (addition of material inside the edifice in dykes and sills) and exogenous volume changes (from external deposits). This was most of the time straightforward, as the two phenomenon did not affect the same areas (see examples on **Figures 5F–I**).

In order to clarify the description and analysis of dyke/sill intrusions and surface fissure opening during the miniature edifice growth, we defined an arbitrary coordinate system based on the orientation of the central top photograph (N/S/E/W corresponding to Up/Down/Right/Left, respectively).

RESULTS

History Summary

During the course of the experiment and throughout the growth of the model, different phases could be observed. **Figure 6A** and **Table 1** summarize the successive intrusion phases described here. The first 141 injections (phase a.) intruded the solid through sub-vertical dykes mainly oriented N-S. Most reached the surface and opened fissures oriented WNW-ESE from which injected material extruded. We differentiated phases a.(1) and a.(2). During phase a.(1) (#0-46) all eruptions originated from the same fissure, while there were slight changes (>2 cm) during

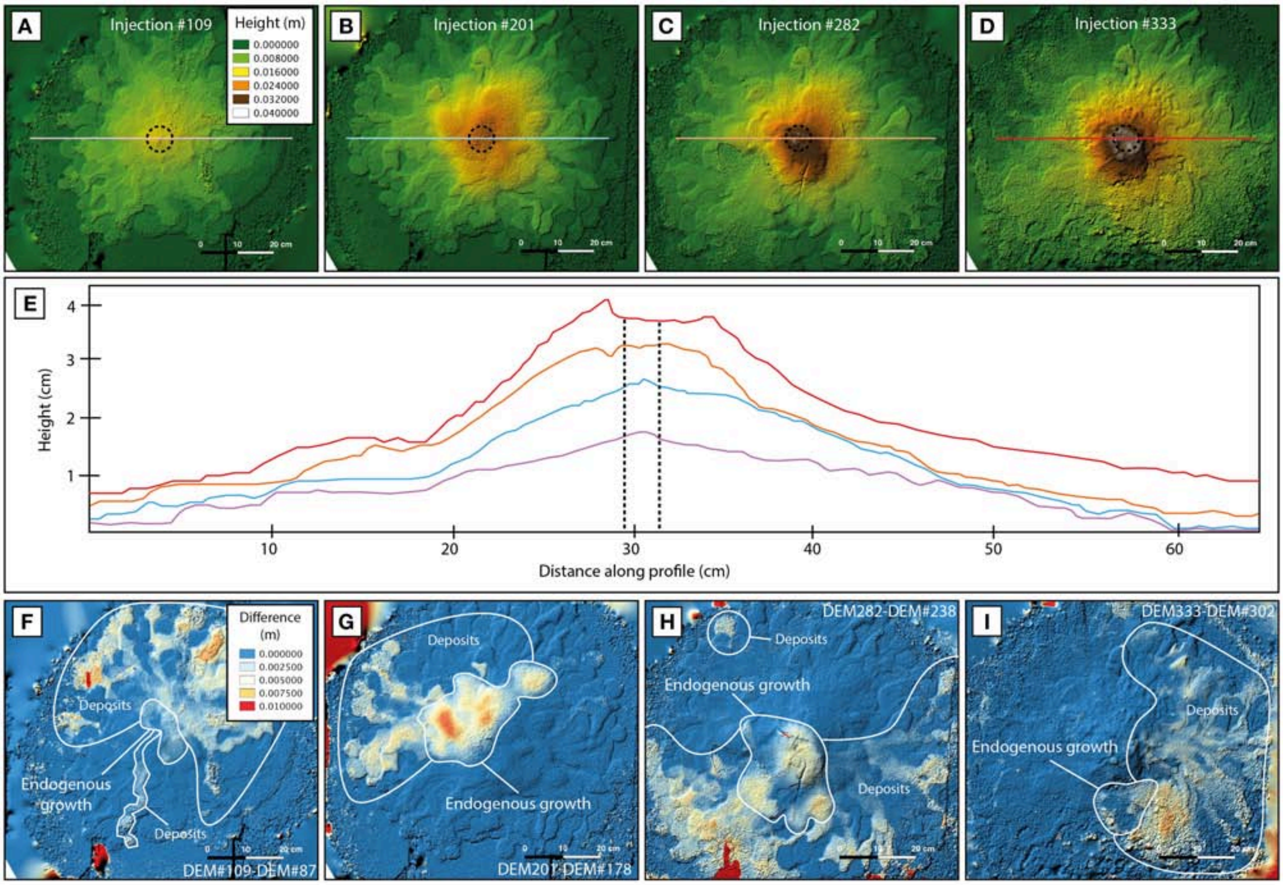

FIGURE 5 | (A–D) DEMs of the experiment, extracted from the multiple-views photograph dataset. **(E)** related cross-sections and detail of the different morphological units present at the end of the experiment (summit, central cone, basal shield, distal field). **(F–I)** Examples of difference of DEMs and segregation of endogenous vs. exogenous growth areas.

phase a.(2) (#47-141). Flows formed a rather flat field of 40–50 cm in diameter.

At injection #142, the intrusive behavior changed radically with a predominance of sub-horizontal sill intrusions, that did not end up with surface fissure opening and extrusion. Sills of this period started intruding to the W from the injection position, gradually and constantly rotating clockwise at each new intrusion. This ended at injection #166 with the opening of distal fissures, (first one at 13.9 cm W of the summit), after a complete rotation around the injection point. Distal eruption sites then migrated clockwise over 17 injections, gradually moving closer to the source (up to 12.6 cm NE of the summit).

After injection #184, dykes started to swarm to the ESE, with extrusions happening close to the summit (5–10 cm). Fissures opened mainly in the N-S direction, indicating a shift of orientation between intrusions at depth (oriented ESE-WNW) and close to the surface [phase f.(1)]. After this period, surface fissures appeared a little closer to the summit [phase f.(2), between #220 and #234], opening radially from the source (ESE-WNW, thus following better the orientation of dykes at depth), while alternating with sill emplacement both close to the source and in distal areas (up to 14 cm to the South). A steeper central cone, 10 to 12 cm in diameter, overlooked a region of lower slopes. Coevally to the emergence of this central structure, the summit surface started to crack in the ESE direction under the extension generated by successive intrusions. The overall edifice (including the farthest external flows) was at that time almost 70 cm in diameter.

Injection #235 marked the start of a new swarming period to the WSW, where fissures started opening radially (WSW-ENE) near the summit and gradually propagated down to the foot of the central cone until injection #298 (phase g.(1), example of injection #265 on **Figure 4**). Between #299 and #310 [period f.(2)], in a first time, 9 sills were emplaced at depth near the source, making the central cone grow internally. Then in a second time, two final distal sills (10–19 cm from the source) intruded to the Northeast, reaching the surface and producing small flows.

Finally, the last swarm emplaced 42 N-S sub-vertical dykes in a swarm oriented N-S, and 8 deep sills near and far from source that mostly did not reach the surface. Dyke intrusions were first followed by opening of eruptive fissures to the east and southeast of the summit, oriented N-S and NE-SW, respectively, close to

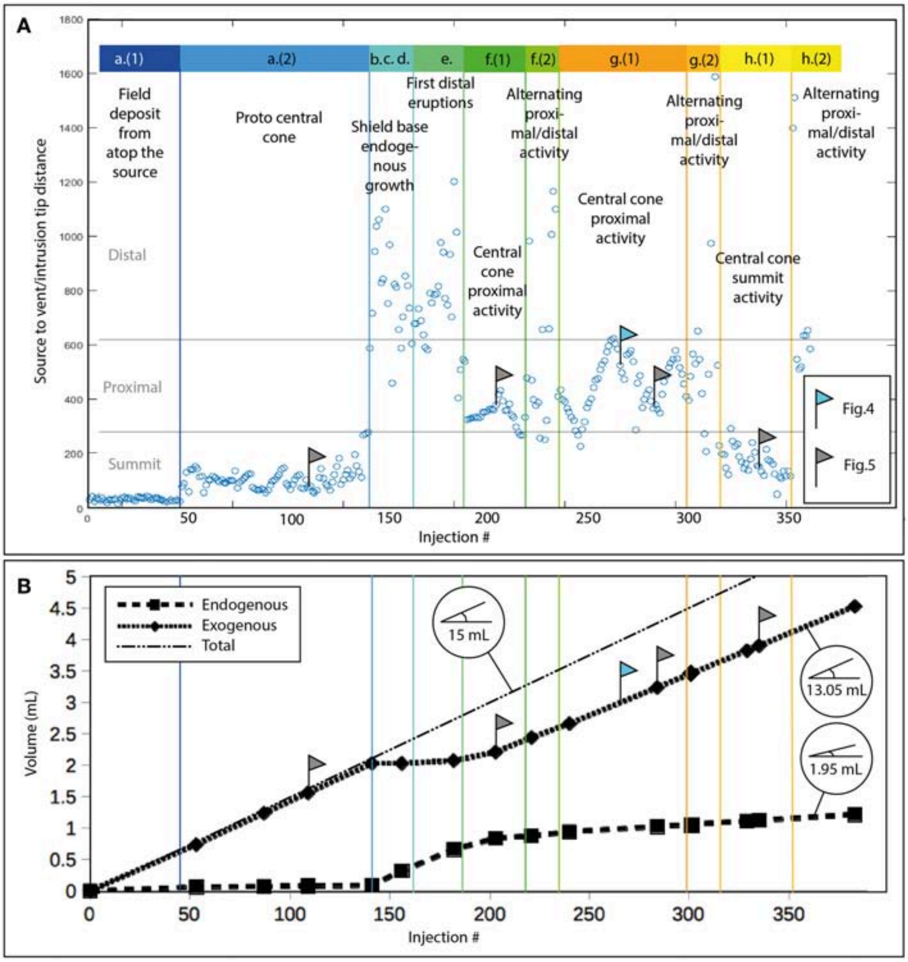

FIGURE 6 | (A) Eruption's radial distance to source throughout the experiment (in pixels on the top image). Several phases can be observed. During phase a (1 and 2, dark blue), magma transited from source to surface through sub-vertical dykes and volcano growth is mostly exogenous. Horizontal compression builds at depth. During phases b–e (light blue), several sill swarms were emplaced, releasing or balancing part of the horizontal compression. During phases f–h, cycles of dyke/horizontal compression and sill/compression release/balancing occurred, resulting in alternating summit/proximal/distal activity. Dyke swarms shifted of around 120° azimuth between each phase. **(B)** Endogenous/exogenous cumulated volume of the model, from the integration of selected areas in the differences of DEMs. Bubbles indicate the average percentage of endogenous growth during phase a, phases b to d and during phase g and h, when a stabilization was observed.

the source [2–5 cm, period h.(1)]. Then finally after two distal sills to the south, 8 fissures oriented NNW-SSE opened at the base of the central cone to the southeast [8–18 cm from the source, period h.(2)].

We made 458 injections in total, but the study period was limited to the first 360 injections. Since it was observed that the model was vulnerable to bacterial growth and chemical changes inside the gelatine. After around 350 injections the miniature volcano started to display surface alteration in very limited areas. Parts of the surface (< 3 mm thick) of the steepest slopes started to melt down and slowly flow downhill in specific locations. This meltdown slowly spread and began to be significant after injection #400, which is why we only used data before injection #360, to keep a safety margin about the reliability of model rheology. Cross-sections in the model after the end of the experiment confirmed that meltdown did not affect the model under 5 mm depth, pointing toward an air-related problem (bacteria growth or chemical reaction).

Morphology

In the tank, we could observe after phase f.(1), and until the end of the experiment, an edifice composed of three distinct parts. A cone-like structure displaying slopes of 20–30%, and 10–18 cm in diameter (growing in size throughout the experiment), rose at the center above the source. This central cone (**Figure 4**) was overlying, and surrounded by, a shield-like base, with slopes of 5–15%, 20–43 cm in diameter (growing in size throughout the experiment). Finally, around the basal shield, we could observe an almost flat field of distal flows, consisting of piled external flows 1–9 mm thick (**Figure 4**). At the end of the experiment, the summit was 3.82 cm high above the initial surface.

TABLE 1 | Successive intrusion phases observed during the course of the experiment, associated with distance to source, swarms and fissures main orientations.

Injection	Type of intrusions	Distance to source (cm)	Swarm orientation at depth	Fissures orientation	Comment
0–46	Dyke swarm	0–2	N-S	WNW-ESE	a.(1)
47–141	Dyke swarm	0–4	N-S	WNW-ESE	a.(2)
142–165	Sills without eruptions	0–13	W->N->E->S	NA	b,c,d.
166–183	Sills with eruptions	12.6–13.9	W->N->NE	Variable	e.
184–219	Dyke swarm	5–10	ESE-WNW	N-S	f.(1)
220–234	Dyke swarm + sills	3–14	ESE-WNW	ESE-WNW	f.(2)
236–298	Dyke swarm	3–8	ENE-WSW	ENE-WSW	g.(1)
299–310	Sills without/with eruptions	2–19	ENE-WSW	Variable	g.(2)
311–349	Dyke swarm + sills	2–5	N-S	N-S/NE-SW	h.(1)
350-360	Dyke swarm + sills	8–18	N-S	NNW-SSE	h.(2)

We integrated DEM differences at regular intervals over the areas of predominant endogenous growth (where volume increase was mostly due to emplacement of sills and, in a lesser amount, dykes: this was easy to distinguish because they mostly did not overlap with areas of external deposits) (**Figures 5F–I**). Thus, we followed the evolution of endogenous vs. exogenous growth (**Figure 6B**). There were three main periods: (1) During phases a.(1,2), the percentage of long-term endogenous growth varied between 4 and 7% of the injected volume. (2) Over phases b,c,d and e. this percentage increased to 92% on average. (3). Finally it tended to stabilize around 13% for the later phases (f,g,h, **Figure 6B**). Overall around 21% of the edifice has been grown from within and 79% from external deposits. Although these deposits made most of the volcanic edifice in the distal regions, the percentage of endogenous growth was greater closer to the summit (**Figures 5F–I**).

Distribution System Geometry

During each injection, the edifice inflated at first, the inflation becoming more and more noticeable as the dyke propagated toward the surface (**Supplementary Material**). Note that some injections did not reach the surface and froze as intrusions. After the opening of an eruptive fissure, the edifice started to deflate as a new flow progressed on the slopes. A remaining deformation was always observed after the end of the injection and freezing of material remaining in the dyke (**Supplementary Material**).

After the end of the experiment, we dissected the model following horizontal planes (at 0, −1, −2 cm). This revealed a surprisingly geometric plumbing system at depths between −3 and 0 cm, displaying 4 main sub-vertical dyke swarms [2xN-S (a. and h.), 1xESE-WNW (f.) and 1xWSW-ENE (g.)] and 4 main sub-horizontal sill swarms [elongated to the NE (b.), SE (c.), SSW (d.) and N (e.)] (**Figure 7**). Amongst the latest, only the N sills were located at shallow depth (between −1 and 0 cm) while the others were emplaced at more than 2 cm depth (**Figure 8**). Shallow sills lead in most cases to distal eruptions, while deep sills lead in most cases to pure intrusions. Surface fissures were often deflected by near-surface effects and not necessarily aligned with their respective feeding dykes at depth **Table 1**. Remarkably, fissures that opened on the sides of the grown central cone were for the majority oriented radially from the source.

The shallow magma distribution system naturally developed in a three-branched radial geometry (**Figures 7**, **8**). In this experiment we could clearly define differentiated periods of activity separated from each other by transition points, where swarming shifted from one dominant orientation to another. For instance, this was well represented at injection #142 by the shift from a series of N-S sub-vertical dykes to a series of sub-horizontal sills. We observed 4 such transition points during the experiment, at #142, #184, #235, and #311, during which the main orientation of dyke/sill swarms shifted significantly. At each transition point the new swarm had either a 120° angle in azimuth with the previous one (in the case of sub-vertical dyke swarms) or a 90° angle in dip (in the case of dyke to sill, or sill to dyke, shift). The sub-vertical part of the distribution system (dykes) was key for the central cone growth (which is predominantly endogenous), while the horizontal part (sills) was mostly responsible for the basal shield construction.

The intrusive behavior could change slightly between the beginning and end of each swarm sequence. Intrusions at the beginning of new swarms tended to leave inside the edifice thicker dykes/sills than intrusions at the end of swarming periods (0.5 to 0.8 mm of surface opening at the beginning vs. 0.1–0.2 mm close to the end). Around the end of sub-vertical dyke swarm sequences, sills could be emplaced [phases f.(2), g.(2), and h.(2)].

DISCUSSION

Processes Behind Swarm Directions and Transitions

In this section we will attempt to interpret our model surface and subsurface evolution, and in particular discuss the reasons behind the observed swarm transitions. We acknowledge that newly formed dykes may damage the host rock, and favor the opening of subsequent dykes in the same direction. However, we observed several transition points where swarming completely changed of direction, thus suggesting an effect overcoming the easiness to intrude damaged host rock.

We already know from previous studies that the stress state of elastic media is a strong influencer of dyke and sill propagation (e.g., Dahm, 2000; Watanabe et al., 2002; Paquet et al., 2007;

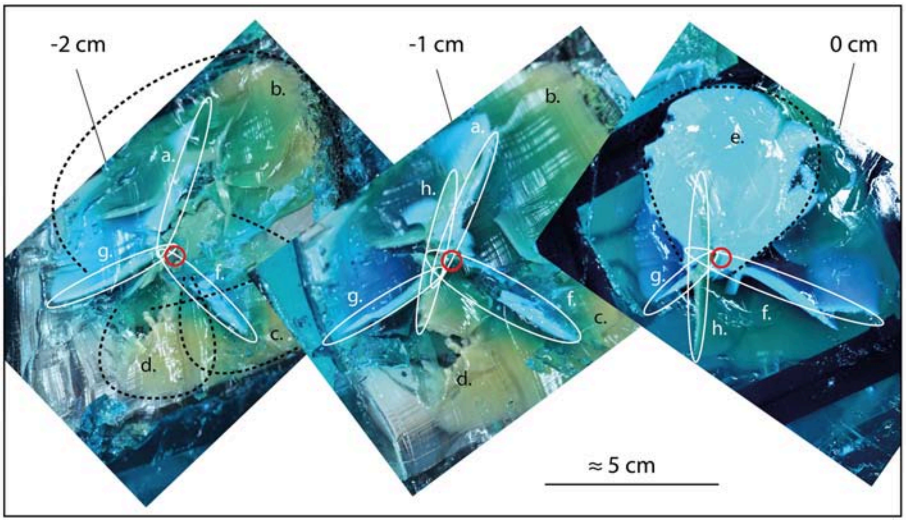

FIGURE 7 | Photographs of dissected model, consisting of horizontal sections at depths of −2, −1, and 0 cm. The various dyke and sill swarms emplaced during phases a–h are drawn on top of the photographs.

Maccaferri et al., 2011; Kavanagh et al., 2013; Le Corvec et al., 2013; Roman and Jaupart, 2014). For instance, reservoir overpressure at Bardarbunga volcano (Iceland), generates a strong radial stress field favoring the propagation of dykes radially around the source, while further away regional stress field takes over and favors parallel dyke swarming (Paquet et al., 2007; Sigmundsson et al., 2015). On the other hand, if the regional stress field is weak, dyke propagation is likely to be influenced by volcano-related stress fields, as reservoir overpressure (for instance during the 2005 Sierra Negra eruption; Jónsson, 2009), cumulative edifice deformation under repeated intrusions, edifice gravitational loading (Hyndman and Alt, 1987; Kervyn et al., 2009; Roman and Jaupart, 2014) or unloading (e.g., Corbi et al., 2015; Maccaferri et al., 2017). In our case, we start with a neutral stress field affected only by an even (vertical) gravitational load. At the beginning of the experiment, there is no significant edifice load so when the reservoir (porous balloon) is pressurized by the peristaltic pump, a 3D radial stress field builds rapidly around it, favoring the propagation of dykes away from the source. Amongst these different directions, dykes preferentially migrate upwards at early stage, because of the even vertical load (**Figure 9A**). However, each new dyke emplacement applies a compressive horizontal stress to the host rock, and each new flow adds to the load of the edifice, modifying the gravity-induced stress field (#1 to #141). Eventually, horizontal compressive stress becomes sufficient to prevent dyke vertical propagation, and injected material starts to migrate horizontally in places where the most important horizontal compression has been applied (e.g., #142 to #183, **Figure 9B**). From there, we can propose the hypothesis that the host rock was significantly compressed horizontally at depth during the first 141 injections (phase a.), because this is where the first sills began to grow during phases (b, c, and d.). Notably, sills were emplaced in a clockwise pattern at depth after phase (a.) highlighting the fact that horizontal/vertical stress ratios were being gradually adjusted all around the core plumbing system between injections #142 and #165. After injection #165, the stress ratio allowed again vertical propagation of analog magma and ended the emplacement of deep sills (**Figure 9C**). Injections #166 to #183 produced shallow sills northwest, north and northeast of the summit (phase e.). This could have meant that there was at this point a shallow compressed zone in the N-S direction favoring the lateral propagation of shallow sills from 2 to 2.5 cm above the source. Indeed, injections #47 to #141 opened fissures oriented mainly WSW-ENE, thus compressing the shallow subsurface in the NNW-SSE direction (**Figure 4**). At injection #184, new sub-vertical swarming to the ESE (f.) started. It is possible that this new behavior was a consequence of the end of stress release to the N of the summit, with stress being still accumulated at shallow depths to the SSE from period (a.). Meanwhile, dyke swarming to the ESE at depth could have increased compression in the SSW direction. It was then consistent to find that the next dyke swarm (g.) was oriented WSW at depth. Finally, swarming returned to the initial N-S principal orientation after injection #310, possibly because remaining accumulated stress has eventually been released or compensated by injections #236 to #310. It seemed like swarms were shifting with a period of between 41 and 74 injections, in our case, with transition points getting closer in time as the volcano grew.

Synthesis on Edifice Stress State, at Depth and Near the Surface

Following the previous section considerations and morphological observations, we can propose the following qualitative model of stress state in the experiment after it entered a stabilized phase (after phase f., **Figure 9D**):

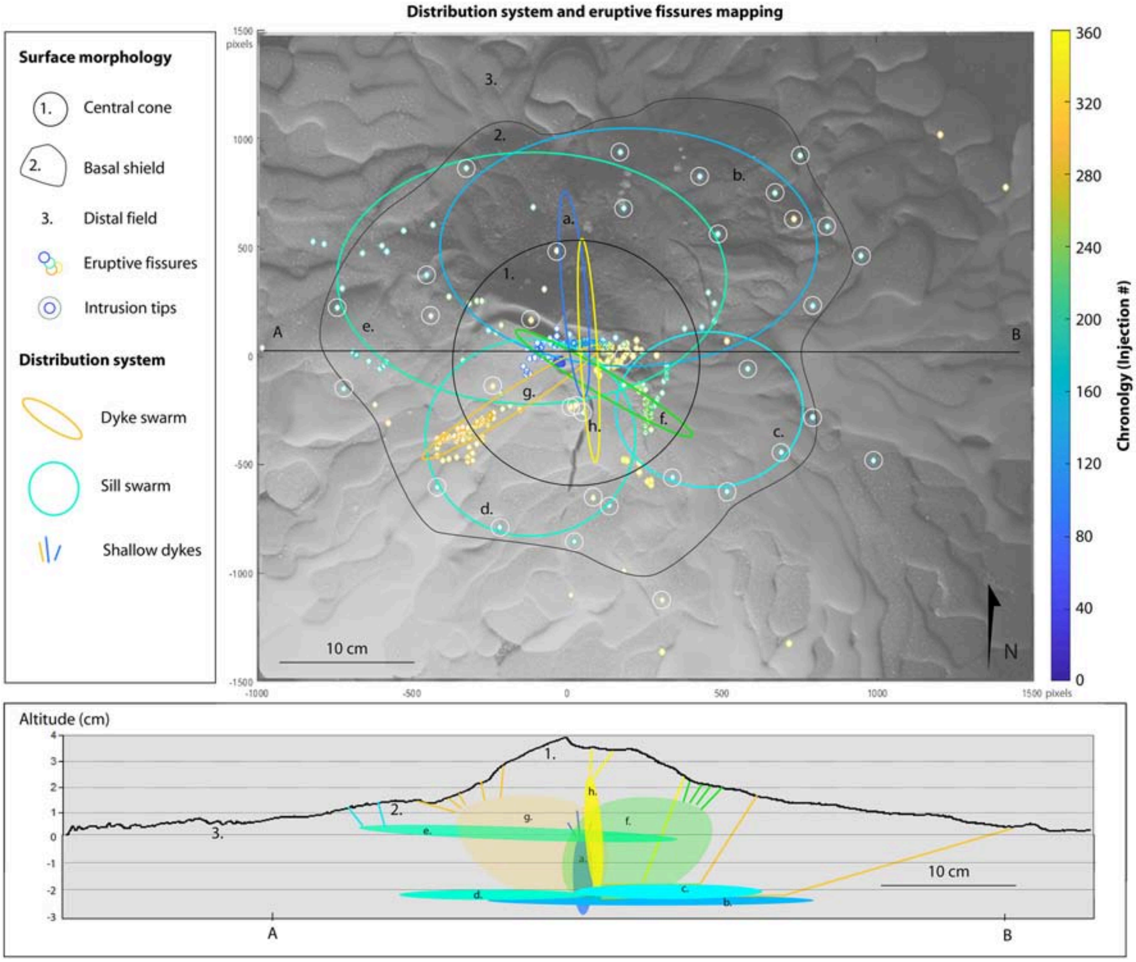

FIGURE 8 | Distribution system geometry (after several cross-sections inside the final edifice, letters a–h representing the main swarms in chronological emplacement order) and extrusion mapping (after semi-automated processing of the top photographs series). Note the triple-branched sub-vertical dyke swarms system below the summit (a, f–h), surrounded by four main sill swarms at depth (b–e). One of them was emplaced closer to the surface (between 0.5 and 1 cm below surface) and lead to numerous distal eruptions.

1- The center of the experiment grew mainly from endogenous deposits above the source. Thus, the surface of the central cone and in particular the summit zone were under significant radial extension. On the summit zone (4–5 cm in diameter), we can infer that σ_3 was oriented radially from the source, near the surface and at shallow depths (0–2 cm below the summit). This stress state could have favored the opening of circular eruptive fissures around the summit during summit eruptions (observed, but rare). It could also have opened a system of type I radial and tangential fractures (non-eruptive) at the surface, in a radial pattern centered above the source. Together these fractures accommodated the extensive radial deformation of the summit. Such tangential/radial eruptive fissures and surface extensional fractures are typical features around caldera rims. Their tangential shape is often attributed to topographic load in the case of calderas at for instance, Fernandina volcano (Galapagos, e.g., Chadwick and Dieterich, 1995).

2- The orientation of eruptive fissures shifted quickly from tangential near the summit "plateau" to mostly radial on the flanks. We interpret this shift as the effect of the stress field induced by topographic load of the central cone (e.g., Chadwick and Dieterich, 1995; Roman and Jaupart, 2014). According to this interpretation, on the flanks and at the base of the central cone σ_3 became tangential at shallow depths (0–1.5 cm below surface), favoring the opening of radial eruptive fissures. In addition, topographic load favored eruptions at the base of the cone rather than in the middle of the flanks (e.g., Kervyn et al., 2009). Type I extensional (non-eruptive) radial fractures could also have accommodated the tangential extension above dyke swarms at depth that did not lead to eruptions (for instance to the south of the central cone). These features could probably have translated into radial grabens in more plasticity-dominated materials, and in real-world volcano morphology. This can be seen as similar to the "volcanic rift zones" observed on several volcanoes around the

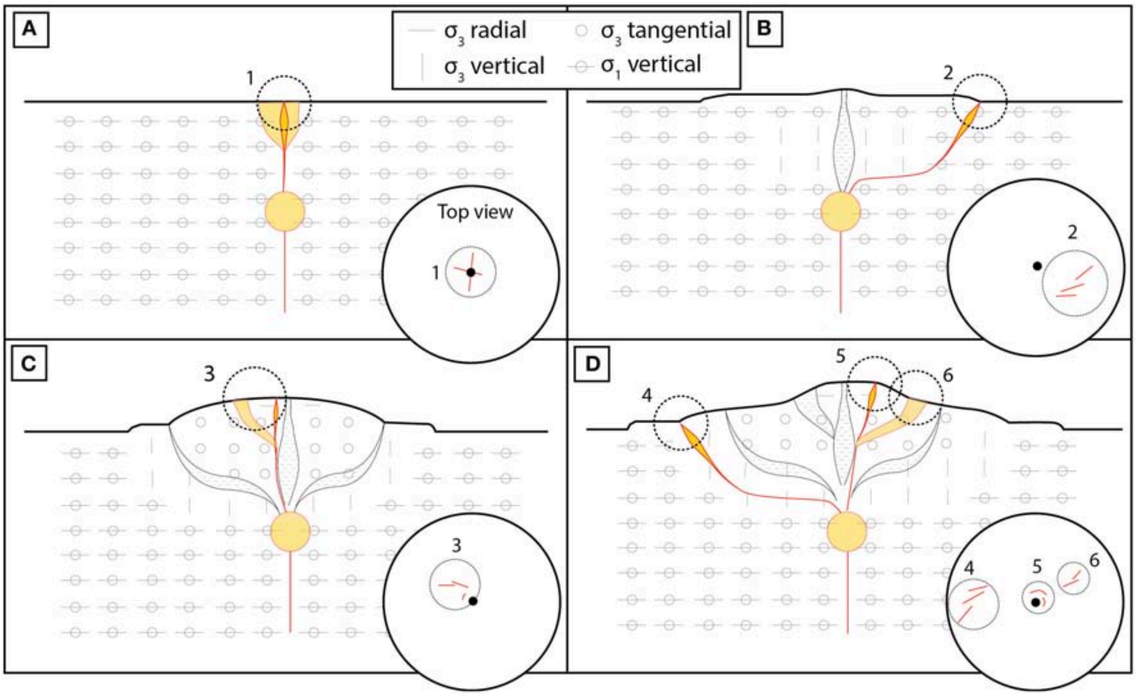

FIGURE 9 | Simplified interpretation of stress state of the miniature volcano, where σ_3 is the direction of least principal stress ("extension") and σ_1 is direction of main principal stress ("compression"). Fractures, eruptive fissures, dykes, and sills are more likely to propagate along planes perpendicular to σ_3. **(A)** Early phases: the edifice load and cumulative intrusive stress do not significantly affect dyke propagation. Most dykes migrate vertically above the source (1). **(B)** Repeated intrusions have created a zone of horizontally compressed medium above source: dyke vertical migration is arrested in this zone and "magma" propagates laterally (sill, 2) until the compression state allows upward migration. The edifice load also favors opening of vents at the foot of the edifice in the near-surface. **(C)** Sill(s) have enabled the release of horizontal compression, allowing dyke vertical migration above source. Topography starts to become significant enough to divert dykes at near-surface depth, resulting in an increase of the proportion of lateral radial fissures (3). **(D)** The volcano enters a steady state phase, where distal (vertical σ_3 at depth, 4) eruptions alternate with summit (radial σ_3 near the surface, 5)/lateral (tangential σ_3 near the surface, 6) eruptions, according to the compression state of the edifice. Lateral intrusions (6) are often diverted to the foot of the central cone by the topographic load. Note that this interpretation of the shallow distribution system is representative of the long-term and edifice-wide general stress trends, but varies locally and at small temporal scales.

world (e.g., Etna, Piton de la Fournaise, Fogo, Marion Island), that are often disposed in a three-branched star pattern, concentrating most of the vents and accommodating most of the edifice extension.

3- At depths <1.5 cm below the surface, we infer that compressive horizontal stresses were dominant (due to successive sub-vertical dykes emplacement). Thus, at this depth σ_3 was sometimes horizontal and sometimes vertical, depending on the ratio of horizontal compression vs. vertical compression. This ratio grew when sub-vertical dykes were emplaced, but diminished when sub-horizontal sills or external flows (topographic load) were emplaced. We can suggest that this is why most sills were emplaced at depths <-1.5 cm, as they accommodated the horizontal compressive stress that was built at depth (**Figure 9D**).

4- Distal zones were globally unaffected by significant stress state changes but could display small radial compression favoring the propagation of radial dykes or sills further away from the source, if the radial migration of the intrusion started deep enough to begin with. Exceptionally, some injections used the deep sill network to propagate radially at depth before starting to propagate upwards, reaching the surface sometimes 18–19 cm away from the source. The more the edifice grew and the more radial compressive stress was accumulated, the farther distal eruptions could happen.

Similarity With Volcanoes in Nature

The vent locations on the model surface tended to cluster in specific locations around the injection point. The density map further showed that vents on the slopes of the model volcano are generally aligned in two radial WSW and ESE directions (**Figure 10A**). Volcanoes in nature also display similar vent alignments, radially from the main reservoir and/or magma rising point. In numerous cases there is two or three "rift zones," radiating from above the principal magma input point. They are often disposed at around 120° angles (Carracedo, 1996). This can for instance be observed on Mauna Kea post-shield edifice (**Figure 10B**), Marion island (**Figure 10C**), Tenerife (**Figure 10D**), Pico de Fogo (**Figure 10E**), and Piton de la Fournaise (**Figure 10F**). This common observation was originally explained by the building of horizontal extensional stresses above a rising plume under the Earth's crust. In an isotropic environment (i.e., not significantly affected by strong regional stress fields), the upward "push" of rising magma will

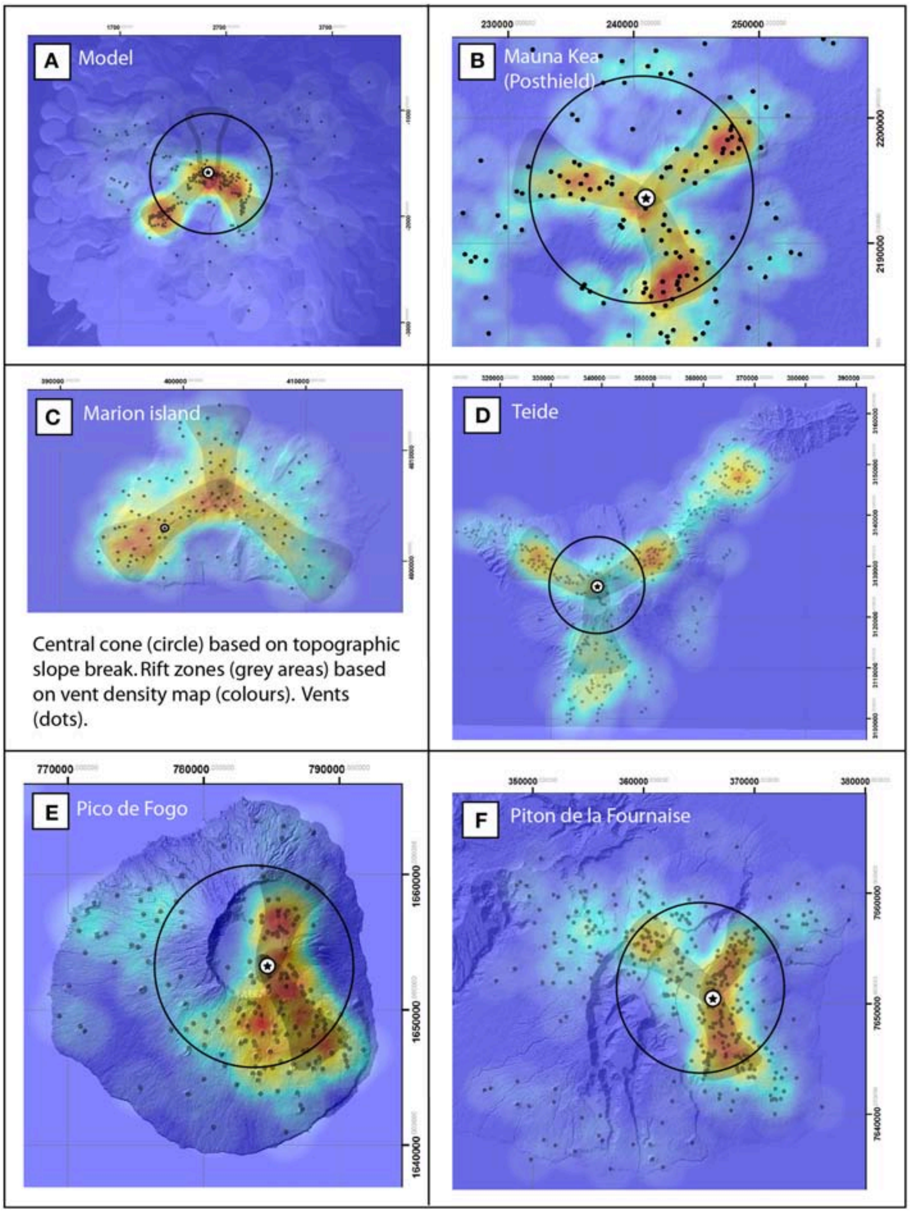

FIGURE 10 | Comparison of model vent density map **(A)** with a selection of intraplate volcanoes, **(B–F)**. Black circles represent the extent of central cones, based on slope break. Rift zone (grayed areas) are based on vent density (warm colors where vent density is higher). Where applicable, straight lines represent the direction of past active center displacement. Vents in the model **(A)** tend to open in two preferential "rift zones" (ESE and WSW). At these intraplate volcanoes, vents statistically gather in three "rift zones" more or less at 120° angle from each other. This is especially true for Mona Kea post-shield edifice **(B)**, Marion island **(C)**, and Teide **(D)**. Pico de Fogo displays a different repartition with a NNE well-defined rift zone and a diffuse SSE one **(E)**. Piton de la Fournaise shows three rift zones (NE, SSE, and WNW) but they are not really well disposed at 120° angle from each other.

create extension of the topping crust. This in turn will favor the opening of both radial and tangential dykes, that tend to swarm in a "least-effort" geometry, i.e., three directions (e.g., Carracedo, 1994). Depending on the volcano, more recent studies suggested that gravitational spreading controls the formation of triple-branched rift systems (i.e., El Hierro in Münn et al., 2006, in which spreading of volcanoes without forceful intrusions is reproduced).

In nature, flank collapses happen regularly (at geological time scales) as shown by significant scarps in their morphology (e.g., Piton de la Fournaise eastern flank, Pico de Fogo, Stromboli, El Teide…) and contribute to redirect shallow magma pathways by releasing accumulated internal stresses and modifying the topographic load (Maccaferri et al., 2017). Finally, regional stress fields can also influence the directional growth of rift zones (for instance in Iceland, e.g., Sigmundsson et al., 2015). These particularities have intentionally not been implemented in our model because the intention was to assess how repeated forceful intrusions alone affect the edifice morphology over time. We focus here on the long-term growth trends resulting from statistically more significant endogenous growth from the rift zones (sub-horizontal growth) and sill swarms (sub-vertical growth).

Although only two "rift zones" could be evidenced by looking at vent density distribution on the model volcano, post-experiment dissection of the edifice revealed a three-branched magma distribution system above the source (**Figure 7**). Such features can also be found on eroded volcanoes in nature, notably at Shiprock paleo-volcano (Delaney and Pollard, 1981). In the model, two of these dyke swarms were related to the ESE and WSW rifts zones defined from the vent density map, respectively (**Figure 10A**). Even though the subsurface clearly revealed that swarms a. and h. extended north and south of the summit on about the same length as the two other zones (i.e.. 4–8 cm), they were related (in majority) to eruptions near the summit [phases (a.(1)), (a.(2)), and (h.(1)), **Figures 6**, **8**]. This explained the lack of surface evidence of this rift zone (i.e., absence of N-S alignment of vents). Since we only grew one volcano in the laboratory, we are unsure if the three-branched star pattern of the model distribution system is a feature that would automatically be present in such experiments. It is possible that it might be the case, considering (1) the high amount of documented natural structures displaying three-branched volcanic rift zones and (2) the crust deformation models confirming that upward migration of magma under the crust is likely to produce such features. However, additional experiments would enable to be more assured on this particular point.

Finally, in the experiment, the long-term dyke/injected volume ratio stabilized at 13% (1.95/15 mL, **Figure 6**). The average of dyke/injected volume on 10 events on Piton de la Fournaise, for instance, is 12.3% (where the injected volume was equal to flow plus dyke volume, and dyke volumes were inferred from multiple ground deformation inversion studies, Fukushima et al., 2005; Peltier, 2007; Staudacher et al., 2009). Note that in both cases (model and Piton de la Fournaise) this percentage varies a lot depending on the source-vent distance, the duration of the eruption (in nature only), the emplacement or not of accompanying sills, the pre-eruptive inflation, etc. However, we found scaling surprisingly close in this case, suggesting that experiments such as the one presented in this communication might be of worth for real-world volcanoes studies.

CONCLUSION

This model was limited by the use of gelatine as a crustal analog: it proved hard, even with precautions learnt from earlier experiences, to maintain its stability and mechanical properties after 400 injections (8 days), and achieve longer observation periods. Additional experiments would also improve the reliability of the observations and conclusions drawn in this contribution, and enable to vary some of the parameters (repose time between injections, edifice size, gelatine temperature) and assess their importance in the geometry of the distribution system.

We could observe the initiation and evolution of the distribution system of volcanoes, without the constrain of a strong regional stress field induced by complex tectonic setting. All injections lead to intrusions inside the elastic host rock, most of which reached the surface and were followed by eruptions (i.e., intraplate oceanic islands volcanoes). After 360 injections the edifice had a flat-topped central cone surrounded by a low-elevation shield and a distal field of external deposits. We could identify several swarming phases lasting between 41 and 74 injections. Each phase emplaced a new swarm oriented at a 90° dip angle, or a 120° strike angle, from the previous one. We interpret this particularity as the release or compensation of stress accumulated by compression from previous phases.

The interaction between edifice growth and magma transfer lead to the building of a three-branched vertical distribution system (dyke swarms concentrated into volcanic rift zones). The consequent horizontal compressive stress field was probably accommodated by a network of sills at source and intermediate depths. A stable growth state achieved in the second half of the experiment suggested that long-term volume of the edifice would be composed at 13% by dykes and sills, which is rather close to what was inferred from ground deformation at e.g., Piton de la Fournaise (12.3%).

Assessing the different characteristics of the subsurface state of a given edifice (layering, mechanical properties, stress state due to activity) through drilling would probably help to build accurate models of successive injections inside active oceanic island volcanoes. Such models, in the future, could provide insights in the probabilities of opening of eruptive fissures in such or such sector of the volcano.

DATA AVAILABILITY

Data (cited as Derrien and Taisne, 2018) is available at: https://researchdata.ntu.edu.sg/dataverse/minivolc_experiment

AUTHOR CONTRIBUTIONS

BT provided the necessary laboratory equipment and contacts. AD and BT carried out the pre-study experimental tests. AD carried out the experiment described in this contribution. AD provided the original text and figures of this contribution, with significant comments and improvements from BT.

FUNDING

This work comprises Earth Observatory of Singapore contribution no. 234 and Institut de Physique du Globe de Paris contribution no. 4014. This research is partly supported by the National Research Foundation Singapore and the Singapore Ministry of Education under the Research Centres of Excellence initiative. This research is partly supported by Ecole Normale Supérieure of Paris (France) specific PhD grant.

ACKNOWLEDGMENTS

We thank the teams from the Earth Observatory of Singapore and the Observatoire Volcanologique du Piton de la Fournaise for their help and counsels throughout the study. In particular, we would like to acknowledge the contribution, as volcano sciences experts, of Aline Peltier and Nicolas Villeneuve during the whole study, the precious help and counsels of Stephen Pansino and Fabio Manta during the volcano model conception, and the comments and advice of Eleonora Rivalta that significantly improved the manuscript quality.

SUPPLEMENTARY MATERIAL

The Supplementary Material for this article can be found online at: https://www.frontiersin.org/articles/10.3389/feart.2019.00019/full#supplementary-material

Supplementary Video 1 | Top-view timelapse of the experiment with one image per injection. The box is 83 × 83 cm.

Supplementary Figure 1 | Example of before/after a typical intrusion, viewed from the side through the transparent gelatine. The model is placed between two polarizing sheet so that stress-related birefringence appears. The difference of images shows the spatial extent of the effect of the new intrusion on the elastic medium.

Supplementary Figure 2 | Examples of (X,Y) surface deformation modulus after intrusions. Displacement values are computed automatically using the DIC code (Version 4) developed by Dr. Elizabeth Jones© (2013, 2014, 2015) based on previous developments by Christoph Eberl et al. (http://www.mathworks.com/matlabcentral/fileexchange/12413) and using the Matlab image processing toolbox.

REFERENCES

Abdelmalak, M. M., Bulois, C., Mourgues, R., Galland, O., Legland, J. B., and Gruber, C. (2016). Description of new dry granular materials of variable cohesion and friction coefficient: implications for laboratory modeling of the brittle crust. *Tectonophysics* 684, 39–51. doi: 10.1016/j.tecto.2016.03.003

Bagnardi, M., and Amelung, F. (2012). Space-geodetic evidence for multiple magma reservoirs and subvolcanic lateral intrusions at Fernandina Volcano, Galápagos Islands. *J. Geophys. Res. Solid Earth* 117. doi: 10.1029/2012JB009465

Bolognesi, M., Furini, A., Russo, V., Pellegrinelli, A., and Russo, P. (2015). Testing the low-cost RPAS potential in 3D cultural heritage reconstruction. *Int. Arch. Photogramm. Remote Sens. Spat. Inf. Sci.* XL-5/W4, 229–235. doi: 10.5194/isprsarchives-XL-5-W4-229-2015

Bonini, M., Sokoutis, D., Mulugeta, G., Boccaletti, M., Corti, G., Innocenti, F., et al. (2001). Dynamics of magma emplacement in centrifuge models of continental extension with implications for flank volcanism. *Tectonics* 20, 1053–1065. doi: 10.1029/2001TC900017

Carracedo, J. C. (1994). The Canary islands: an example of structural control on the growth of large oceanic-island volcanoes. *J. Volcanol. Geotherm. Res.* 60, 225–241. doi: 10.1016/0377-0273(94)90053-1

Carracedo, J. C. (1996). Morphological and structural evolution of the western Canary islands: hotspot-induced three-armed rifts or regional tectonic trends? *J. Volcanol. Geotherm. Res.* 72, 151–162. doi: 10.1016/0377-0273(95)00080-1

Chadwick, W. W. Jr., and Dieterich, J. H. (1995). Mechanical modeling of circumferential and radial dike intrusion on Galapagos volcanoes. *J. Volcanol. Geotherm. Res.* 66, 37–52. doi: 10.1016/0377-0273(94)00060-T

Chanceaux, L., and Menand, T. (2014). Solidification effects on sill formation: an experimental approach. *Earth Planet. Sci. Lett.* 403, 79–88. doi: 10.1016/j.epsl.2014.06.018

Coppola, D., Di Muro, A., Peltier, A., Villeneuve, N., Ferrazzini, V., Favalli, M., et al. (2017). Shallow system rejuvenation and magma discharge trends at Piton de la Fournaise volcano (La Réunion Island). *Earth Planet. Sci. Lett.* 463, 13–24. doi: 10.1016/j.epsl.2017.01.024

Corbi, F., Rivalta, E., Pinel, V., Maccaferri, F., and Acocella, V. (2016). Understanding the link between circumferential dikes and eruptive fissures around calderas based on numerical and analog models. *Geophys. Res. Lett.* 43, 6212–6219. doi: 10.1002/2016GL068721

Corbi, F., Rivalta, E., Pinel, V., Maccaferri, F., Bagnardi, M., and Acocella, V. (2015). How caldera collapse shapes the shallow emplacement and transfer of magma in active volcanoes. *Earth Planet. Sci. Lett.* 431, 287–293. doi: 10.1016/j.epsl.2015.09.028

Corti, G., Bonini, M., Innocenti, F., Manetti, P., and Mulugeta, G. (2001). Centrifuge models simulating magma emplacement during oblique rifting. *J. Geodyn.* 31, 557–576. doi: 10.1016/S0264-3707(01)00032-1

Dahm, T. (2000). Numerical simulations of the propagation path and the arrest of fluid-filled fractures in the Earth. *Geophys. J. Int.* 141, 623–638. doi: 10.1046/j.1365-246x.2000.00102.x

Delaney, P. T., and Pollard, D. D. (1981). *Deformation of Host Rocks and Flow of Magma During Growth of Minette Dikes and Breccia-Bearing Intrusions Near Ship Rock, New Mexico (No. 1202).* Washington, DC:USGPO.

Delcamp, A., de Vries, B. V. W., James, M. R., Gailler, L. S., and Lebas, E. (2012). Relationships between volcano gravitational spreading and magma intrusion. *Bull. Volcanol.* 74, 743–765. doi: 10.1007/s00445-011-0558-9

Derrien, A., and Taisne, B. (2018). *Data repository for: 360 intrusions in a miniature volcano: birth, growth and evolution of an analog edifice.*

Derrien, A., Villeneuve, N., Peltier, A., and Beauducel, F. (2015). Retrieving 65 years of volcano summit deformation from multitemporal structure from motion: the case of Piton de la Fournaise (La Réunion Island). *Geophys. Res. Lett.* 42, 6959–6966. doi: 10.1002/2015GL064820

Dieterich, J. H. (1988). Growth and persistence of Hawaiian volcanic rift zones. *J. Geophys. Res. Solid Earth* 93, 4258–4270. doi: 10.1029/JB093iB05p04258

Fukushima, Y., Cayol, V., and Durand, P. (2005). Finding realistic dike models from interferometric synthetic aperture radar data: the February 2000 eruption at Piton de la Fournaise. *J. Geophys. Res. Solid Earth* 110. doi: 10.1029/2004JB003268

Galland, O., Holohan, E., de Vries, B. V. W., and Burchardt, S. (2015). "Laboratory modelling of volcano plumbing systems: a review," in *Physical Geology of Shallow Magmatic Systems. Advances in Volcanology (An Official Book Series of the International Association of Volcanology and Chemistry of the Earth's Interior)*, eds C. Breitkreuz and S. Rocchi (Cham: Springer), 147–214. doi: 10.1007/11157_2015_9

Greenfield, T., White, R. S., and Roecker, S. (2016). The magmatic plumbing system of the Askja central volcano, Iceland, as imaged by seismic tomography. *J. Geophys. Res. Solid Earth* 121, 7211–7229. doi: 10.1002/2016JB013163

Gudmundsson, A. (2002). Emplacement and arrest of sheets and dykes in central volcanoes. *J. Volcanol. Geotherm. Res.* 116, 279–298. doi: 10.1016/S0377-0273(02)00226-3

Gudmundsson, A. (2012). Magma chambers: formation, local stresses, excess pressures, and compartments. *J. Volcanol. Geotherm. Res.* 237, 19–41. doi: 10.1016/j.jvolgeores.2012.05.015

Guldstrand, F., Burchardt, S., Hallot, E., and Galland, O. (2017). Dynamics of surface deformation induced by dikes and cone sheets in a cohesive Coulomb brittle crust. *J. Geophys. Res. Solid Earth* 122, 8511–8524. doi: 10.1002/2017JB014346

Hildner, E., Klügel, A., and Hauff, F. (2011). Magma storage and ascent during the 1995 eruption of Fogo, Cape Verde Archipelago. *Contrib. Mineral. Petrol.* 162:751. doi: 10.1007/s00410-011-0623-6

Hyndman, D. W., and Alt, D. (1987). Radial dikes, laccoliths, and gelatin models. *J. Geol.* 95, 763–774. doi: 10.1086/629176

Ito, G., and Martel, S. J. (2002). Focusing of magma in the upper mantle through dike interaction. *J. Geophys. Res. Solid Earth* 107, ECV 6-1–ECV 6-17. doi: 10.1029/2001JB000251

Jónsson, S. (2009). Stress interaction between magma accumulation and trapdoor faulting on Sierra Negra volcano, Galápagos. *Tectonophysics* 471, 36–44. doi: 10.1016/j.tecto.2008.08.005

Kavanagh, J. L., Engwell, S. T., and Martin, S. (2018). A review of analogue and numerical modelling in volcanology. *Solid Earth* 9, 531–571.

Kavanagh, J. L., Menand, T., and Daniels, K. A. (2013). Gelatine as a crustal analogue: determining elastic properties for modelling magmatic intrusions. *Tectonophysics* 582, 101–111. doi: 10.1016/j.tecto.2012.09.032

Kavanagh, J. L., Menand, T., and Sparks, R. S. J. (2006). An experimental investigation of sill formation and propagation in layered elastic media. *Earth Planet. Sci. Lett.* 245, 799–813. doi: 10.1016/j.epsl.2006.03.025

Keating, G. N., Valentine, G. A., Krier, D. J., and Perry, F. V. (2008). Shallow plumbing systems for small-volume basaltic volcanoes. *Bull. Volcanol.* 70, 563–582. doi: 10.1007/s00445-007-0154-1

Kervyn, M., Ernst, G. G. J., van Wyk de Vries, B., Mathieu, L., and Jacobs, P. (2009). Volcano load control on dyke propagation and vent distribution: insights from analogue modelling. *J. Geophys. Res. Solid Earth* 114. doi: 10.1029/2008JB005653

Le Corvec, N., and McGovern, P. J. (2018). The effect of ocean loading on the growth of basaltic ocean island volcanoes and their magmatic plumbing system. *Front. Earth Sci.* 6:119. doi: 10.3389/feart.2018.00119

Le Corvec, N., Spörli, K. B., Rowland, J., and Lindsay, J. (2013). Spatial distribution and alignments of volcanic centers: clues to the formation of monogenetic volcanic fields. *Earth Sci. Rev.* 124, 96–114. doi: 10.1016/j.earscirev.2013.05.005

Maccaferri, F., Bonafede, M., and Rivalta, E. (2011). A quantitative study of the mechanisms governing dike propagation, dike arrest and sill formation. *J. Volcanol. Geotherm. Res.* 208, 39–50. doi: 10.1016/j.jvolgeores.2011.09.001

Maccaferri, F., Richter, N., and Walter, T. R. (2017). The effect of giant lateral collapses on magma pathways and the location of volcanism. *Nat. Commun.* 8:1097. doi: 10.1038/s41467-017-01256-2

Marsh, B. D. (2015). "Magma chambers," in *The Encyclopedia of Volcanoes, 2nd Edn.* ed H. Sigurdsson (Elsevier) 185–201.

Mata, J., Martins, S., Mattielli, N., Madeira, J., Faria, B., Ramalho, R. S., et al. (2017). The 2014–15 eruption and the short-term geochemical evolution of the Fogo volcano (Cape Verde): evidence for small-scale mantle heterogeneity. *Lithos* 288, 91–107. doi: 10.1016/j.lithos.2017.07.001

McLeod, P., and Tait, S. (1999). The growth of dykes from magma chambers. *J. Volcanol. Geotherm. Res.* 92, 231–245. doi: 10.1016/S0377-0273(99)00053-0

Michon, L., Ferrazzini, V., and Di Muro, A. (2016). "Magma paths at Piton de la Fournaise volcano," in *Active Volcanoes of the Southwest Indian Ocean,* eds B. Patrick, L. Jean-François, D. M. Andrea, M. Laurent (Berlin; Heidelberg: Springer) 91–106. doi: 10.1007/978-3-642-31395-0_7

Michon, L., Ferrazzini, V., Di Muro, A., Villeneuve, N., and Famin, V. (2015). Rift zones and magma plumbing system of Piton de la Fournaise volcano: How do they differ from Hawaii and Etna? *J. Volcanol. Geotherm. Res.* 303, 112–129. doi: 10.1016/j.jvolgeores.2015.07.031

Münn, S., Walter, T. R., and Klügel, A. (2006). Gravitational spreading controls rift zones and flank instability on El Hierro, Canary Islands. *Geol. Mag.* 143, 257–268. doi: 10.1017/S0016756806002019

Pansino, S., and Taisne, B. (2018). How magmatic storage regions attract and repel propagating dikes. *J. Geophys. Res. Solid Earth.* doi: 10.1029/2018JB016311

Paquet, F., Dauteuil, O., Hallot, E., and Moreau, F. (2007). Tectonics and magma dynamics coupling in a dyke swarm of Iceland. *J. Struct. Geol.* 29, 1477–1493. doi: 10.1016/j.jsg.2007.06.001

Peltier, A. (2007). *Monitoring, Modelling and Evolution of Magma Injection Processes at Piton de La Fournaise Volcano (Reunion island), From a Cross-Analysis of Deformation, Geochemical and Structural Data.* Ph.D. thesis, Université de la Réunion, Réunion France.

Ramberg, H. (1981). *Gravity, Deformation, and the Earth's Crust: in Theory, Experiments, and Geological Application.* Academic press.

Roche, O., De Vries, B. V. W., and Druitt, T. H. (2001). Sub-surface structures and collapse mechanisms of summit pit craters. *J. Volcanol. Geotherm. Res.* 105, 1–18. doi: 10.1016/S0377-0273(00)00248-1

Roman, A., and Jaupart, C. (2014). The impact of a volcanic edifice on intrusive and eruptive activity. *Earth Planet. Sci. Lett.* 408, 1–8. doi: 10.1016/j.epsl.2014.09.016

Roult, G., Peltier, A., Taisne, B., Staudacher, T., Ferrazzini, V., and Di Muro, A. (2012). A new comprehensive classification of the Piton de la Fournaise activity spanning the 1985–2010 period. Search and analysis of short-term precursors from a broad-band seismological station. *J. Volcanol. Geotherm. Res.* 241, 78–104. doi: 10.1016/j.jvolgeores.2012.06.012

Ryan, M. P. (1988). The mechanics and three-dimensional internal structure of active magmatic systems: Kilauea Volcano, Hawaii. *J. Geophys. Res. Solid Earth* 93, 4213–4248. doi: 10.1029/JB093iB05p04213

Sigmundsson, F., Hooper, A., Hreinsdóttir, S., Vogfjörd, K. S., Ófeigsson, B. G., Heimisson, E. R., et al. (2015). Segmented lateral dyke growth in a rifting event at Bárð*arbunga volcanic system, Iceland. *Nature* 517, 191–195. doi: 10.1038/nature14111

Staudacher, T., Ferrazzini, V., Peltier, A., Kowalski, P., Boissier, P., Catherine, P., et al. (2009). The April 2007 eruption and the Dolomieu crater collapse, two major events at Piton de la Fournaise (La Réunion Island, Indian Ocean). *J. Volcanol. Geotherm. Res.* 184, 126–137. doi: 10.1016/j.jvolgeores.2008.11.005

Taisne, B., and Tait, S. (2009). Eruption versus intrusion? Arrest of propagation of constant volume, buoyant, liquid-filled cracks in an elastic, brittle host. *J. Geophys. Res. Solid Earth* 114. doi: 10.1029/2009JB006297

Taisne, B., Tait, S., and Jaupart, C. (2011). Conditions for the arrest of a vertical propagating dyke. *Bull. Volcanol.* 73, 191–204. doi: 10.1007/s00445-010-0440-1

Tibaldi, A. (2015). Structure of volcano plumbing systems: a review of multi-parametric effects. *J. Volcanol. Geotherm. Res.* 298, 85–135. doi: 10.1016/j.jvolgeores.2015.03.023

Walter, T. R., and Troll, V. R. (2003). Experiments on rift zone evolution in unstable volcanic edifices. *J. Volcanol. Geotherm. Res.* 127, 107–120. doi: 10.1016/S0377-0273(03)00181-1

Watanabe, T., Masuyama, T., Nagaoka, K., and Tahara, T. (2002). Analog experiments on magma-filled cracks. *Earth Planets Space* 54, 1247–1261. doi: 10.1186/BF03352453

Zhai, G., and Shirzaei, M. (2016). Spatiotemporal model of Kilauea's summit magmatic system inferred from InSAR time series and geometry-free time-dependent source inversion. *J. Geophys. Res. Solid Earth* 121, 5425–5446. doi: 10.1002/2016JB012953

Conflict of Interest Statement: The authors declare that the research was conducted in the absence of any commercial or financial relationships that could be construed as a potential conflict of interest.

frontiers
in Earth Science

ORIGINAL RESEARCH
published: 12 March 2019
doi: 10.3389/feart.2019.00037

Burial-Related Compaction Modifies Intrusion-Induced Forced Folds: Implications for Reconciling Roof Uplift Mechanisms Using Seismic Reflection Data

Craig Magee[1,2]*, **Murray Hoggett**[3], **Christopher A.-L. Jackson**[1] **and Stephen M. Jones**[3]

[1] Basins Research Group, Department of Earth Science and Engineering, Imperial College London, London, United Kingdom, [2] School of Earth and Environment, University of Leeds, Leeds, United Kingdom, [3] School of Geography, Earth and Environmental Science, University of Birmingham, Birmingham, United Kingdom

Space for shallow-level sills and laccoliths is commonly generated by bending and uplift of overlying rock and sediment. This so-called "roof uplift" produces forced folds, the shape and amplitude of which reflect the geometry of underlying intrusions. The surface expression of forced folds can therefore be inverted to constrain intruding magma body properties, whilst ancient forced folds provide a record of sill and laccolith emplacement. Deciphering how shallow-level intrusion translates into roof uplift is thus critical to enhancing our understanding and forecasting of magma emplacement. To-date, emplacement models and surface deformation inversions are underpinned by the consideration that roof uplift is, to a first-order, an elastic process. However, several studies have suggested inelastic processes can accommodate significant magma volumes, implying first-order roof uplift may be a function of elastic *and* inelastic deformation. In particular, seismic reflection images of forced folds above ancient sills and laccoliths have been used to argue that final fold amplitudes can be substantially less (by up to 85%) than the underlying intrusion thickness. Although these seismic-based observations imply elastic and inelastic deformation accommodated intrusion, these studies do not consider whether burial-related compaction has reduced the original fold amplitude. Here, we use geological (e.g., lithology) and geophysical (e.g., seismic velocity) information from the Resolution-1 borehole offshore eastern New Zealand, which intersects a forced fold and upper ∼50 m of a sill imaged in 2D seismic reflection data, to decompact the folded sequence and recover its original geometry. We show the Resolution Sill is likely ∼117–187 m thick, depending on the interval velocity for the entire intrusion, whereas the forced fold has an apparent maximum amplitude of ∼127 m, corresponding to a sill thickness-fold amplitude discrepancy of up to 47%. Decompaction indicates the original maximum forced fold amplitude likely ranged from ∼131–185 m, suggesting post-emplacement, burial-related compaction of this and other forced folds may be the source of apparent discrepancies between fold amplitude and intrusion thickness. Whilst seismic reflection data can provide fundamental insights into how shallow-level emplacement translates into roof uplift and ground displacement, we

Edited by:
Katherine Dobson,
Durham University, United Kingdom

Reviewed by:
Guillaume Duclaux,
University of Nice Sophia Antipolis,
France
Ikuro Sumita,
Kanazawa University, Japan

***Correspondence:**
Craig Magee
c.magee@leeds.ac.uk

Specialty section:
This article was submitted to
Solid Earth Geophysics,
a section of the journal
Frontiers in Earth Science

Received: 30 October 2018
Accepted: 15 February 2019
Published: 12 March 2019

Citation:
Magee C, Hoggett M, Jackson CA-L and Jones SM (2019) Burial-Related Compaction Modifies Intrusion-Induced Forced Folds: Implications for Reconciling Roof Uplift Mechanisms Using Seismic Reflection Data. Front. Earth Sci. 7:37. doi: 10.3389/feart.2019.00037

show decompaction and backstripping are required to recover the original fold geometry. To assess the relative importance of elastic and inelastic space-making processes during the formation of seismically imaged sills and forced folds, we demonstrate that our method should be applied to remove any post-emplacement, burial-related compaction signature.

Keywords: forced fold, sill, seismic reflection, emplacement, roof uplift, compaction

INTRODUCTION

Generating space to accommodate magma emplacement requires deformation of the host rock. Field- and seismic reflection-based studies of ancient intrusions, supported by various physical, numerical, and analytical modeling approaches, reveal sills and laccoliths emplaced at shallow-levels within the upper crust can be accommodated by elastic bending of the overburden and, potentially, the free surface (so-called "roof uplift"; e.g., Gilbert, 1877; Johnson and Pollard, 1973; Pollard and Johnson, 1973; Koch et al., 1981; Fialko and Simons, 2001; Smallwood and Maresh, 2002; Trude et al., 2003; Hansen and Cartwright, 2006; Bunger and Cruden, 2011; Galland, 2012; Galland and Scheibert, 2013; Jackson et al., 2013; Magee et al., 2013a; van Wyk de Vries et al., 2014; Montanari et al., 2017; Reeves et al., 2018). Geodetic data also suggest that short-timescale ground displacements at active volcanoes, generated by sill or laccolith emplacement, reflect elastic deformation (e.g., Pagli et al., 2012; Castro et al., 2016; Ebmeier et al., 2018). These zones of roof uplift mimic the plan-view geometry of underlying intrusion(s) and can thus be described as a form of "forced fold" (e.g., Hansen and Cartwright, 2006; Magee et al., 2013a); i.e., a fold with a morphology controlled by that of a forcing member below (Stearns, 1978). By assuming purely elastic deformation accommodates magma emplacement at shallow-levels, particularly when the intrusion diameter (D) to emplacement depth (d) ratio is $>>4$, we can expect the original intrusion thickness ($T0_{\max}$) to broadly equal the original amplitude ($F0_{\max}$) of the overlying forced fold (i.e., $F0_{\max}/T0_{\max} = 1$) (Pollard and Johnson, 1973; Fialko and Simons, 2001; Hansen and Cartwright, 2006; Jackson et al., 2013).

Seismic reflection data reveal the current maximum amplitude ($F_{\max}$) of buried forced folds can be up to 85% less than the measured maximum thickness ($T_{\max}$) of underlying, crystallized sills or laccoliths (i.e., $F_{\max}/T_{\max} < 1$; **Figure 1A**) (Hansen and Cartwright, 2006; Jackson et al., 2013; Magee et al., 2013a). Such discrepancies between fold amplitude and intrusion thickness, particularly where $F_{\max}/T_{\max} << 1$, have been suggested to relate to the accommodation of magma by both elastic *and* inelastic deformation (Jackson et al., 2013; Magee et al., 2013a, 2017). Syn-intrusion, fracture-driven porosity reduction, faulting, and fluidization of the host rock around exposed sills confirms that inelastic deformation can partly and, perhaps in some instances, fully accommodate magma emplacement (**Figures 1B,C**) (e.g., Johnson and Pollard, 1973; Morgan et al., 2008; Schofield et al., 2012, 2014; Jackson et al., 2013; Spacapan et al., 2016). It has also been suggested that inelastic ductile strain and vertical compaction of deforming strata can cause fold amplitudes to decay upwards, particularly if D/d is <4 (Hansen and Cartwright, 2006; Jackson et al., 2013). Seismic and field data therefore provide evidence for the accommodation of magma by elastic *and* inelastic deformation, challenging the assumption that emplacement models need only account for elastic processes (e.g., Galland and Scheibert, 2013; Magee et al., 2013a; Holohan et al., 2017; Scheibert et al., 2017; Gerbault et al., 2018).

Seismic reflection data capture the current, and not necessarily the original, geometry of ancient intrusions and forced folds. For example, original fold amplitudes and sill thicknesses, and the ratio between them, may by modified by the: (i) migration of magma away from the seismically resolved intrusion ($T_{\max} < T0_{\max}$) coupled with little or no fold subsidence ($F_{\max} > T_{\max}$) (e.g., Reeves et al., 2018); (ii) deflation of the sill in response to crystallization of and/or volatile release from the magma ($T_{\max} < T0_{\max}$; e.g., Caricchi et al., 2014), which could promote disproportionate fold subsidence ($F_{\max} > T_{\max}$); (iii) erosion of the fold crest ($F_{\max} < T_{\max}$) (Hansen and Cartwright, 2006; Jackson et al., 2013); (iv) interference with neighboring folds (Jackson et al., 2013), which could locally inhibit or enhance folding; and/or (v) burial and compaction of the folded sequence ($F_{\max} < T_{\max}$) (Jackson et al., 2013). No study has yet quantified how post-emplacement, burial-related compaction can modify forced fold geometries and amplitudes. Without incorporating an assessment of how burial-related compaction has affected the seismically resolved forced fold geometry and amplitude, the role of inelastic processes in accommodating magma cannot be determined from seismic reflection data alone.

Here, we examine a saucer-shaped sill, the Resolution Sill, and overlying forced fold imaged in 2D seismic reflection data from the Canterbury Basin, offshore eastern New Zealand and intersected by the Resolution-1 borehole (**Figure 2**). The borehole penetrates the upper ∼50 m of the saucer-shaped sill, which can broadly be categorized as a gabbro. Using velocity information from Resolution-1 we aim to depth convert and decompact the seismic reflection data, allowing us to constrain the original maximum fold amplitude (i.e., $F0_{\max}$) and assess how burial-related compaction impacts fold geometry. We show that burial-related compaction modifies ancient intrusion-induced forced folds within sedimentary basins, reducing discrepancies between fold amplitude and sill thickness. Before using seismic-based examples of ancient intrusion and forced fold pairs to

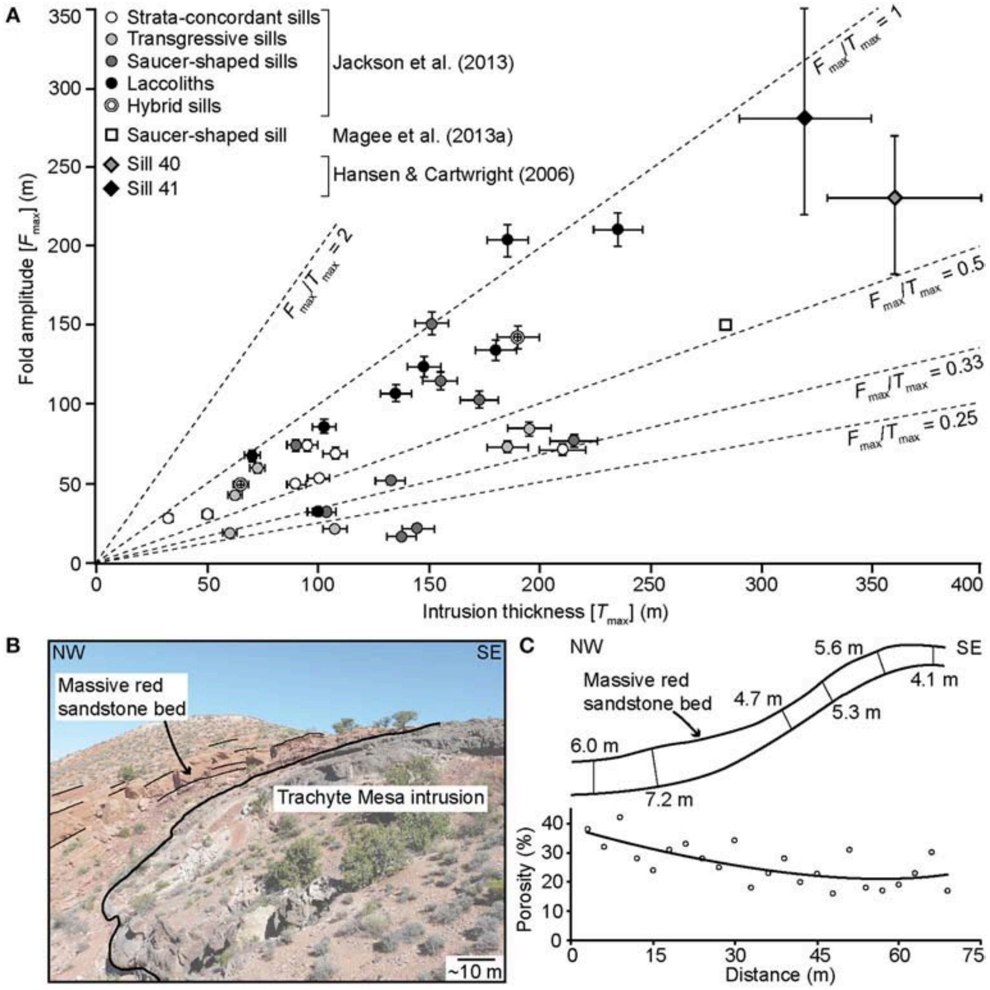

FIGURE 1 | (A) Seismically imaged maximum forced fold amplitudes ($F_{\max}$) plotted against maximum measured thicknesses ($T_{\max}$) of underlying sills or laccoliths from data within the: (i) Bight Basin, offshore southern Australia (Jackson et al., 2013); (ii) Exmouth Sub-basin, offshore north-western Australia (Magee et al., 2013a); and (iii) Rockall Basin, NE Atlantic (Hansen and Cartwright, 2006). See Jackson et al. (2013) and Hansen and Cartwright (2006) for information on error bars. **(B)** Field photograph showing folding of sandstone beds above the Trachyte Mesa intrusion in the Henry Mountains, Utah, USA. **(C)** Sketch showing changes in thickness of a massive red sandstone bed, shown in **(B)**, over the Trachyte Mesa intrusion, which corresponds to a reduction in porosity (after Morgan et al., 2008). The best-fit curve is third order polynomial with an R^2 value of 0.49 (Morgan et al., 2008).

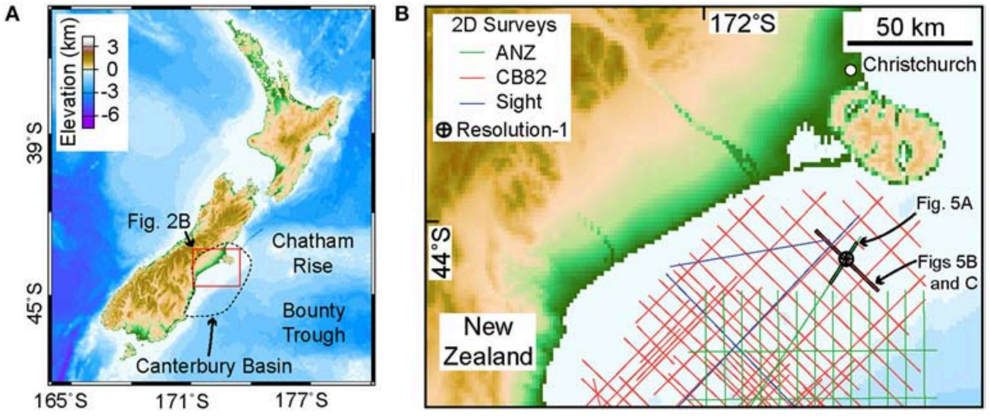

FIGURE 2 | (A) Location of the Canterbury Basin within New Zealand. **(B)** Location of 2D seismic lines and the Resolution-1 borehole used in this study.

postulate emplacement mechanics at active volcanoes, it is essential to first account for burial-related compaction.

GEOLOGICAL SETTING

The Canterbury Basin spans onshore and offshore SE New Zealand and formed during Late Albian-to-Early Campanian rifting between New Zealand, Antarctica, and Australia (**Figure 2**) (Fulthorpe et al., 1996; Lu and Fulthorpe, 2004). The basement typically corresponds to greywacke and argillite meta-sedimentary rocks of the Torlesse Supergroup (Permian-to-Early Cretaceous; **Figure 3**) (Uruski, 2010). In the north of the basin, within the study area, syn-rift sedimentary strata deposited within graben and half-graben are dominated by the paralic coal measures of the Broken River Formation, and marine siltstones and mudstones of the Conway Formation (**Figure 3**) (Carter, 1988; Killops et al., 1997; Schiøler et al., 2011). Onset of post-rift, thermal subsidence in the Maastrichtian led to the deposition of the high-energy marine Charteris Bay Sandstone (Lower Paleocene), which is overlain by tuffs of the View Hill Volcanics, mudstones of the Conway Formation, and calcareous marine mudstones of the Ashley Formation (**Figure 3**) (Carter, 1988; Killops et al., 1997; Schiøler et al., 2011). Micritic limestones attributed to the Amuri Formation were deposited between the Early Oligocene and Early Miocene, although the majority of this time period corresponded to the development of a regional unconformity across much of the Canterbury Basin (**Figure 3**) (Carter, 1988; Killops et al., 1997; Schiøler et al., 2011). Uplift along the Alpine Fault, and an associated increase in the supply of terrigenous silt and sand, resulted in the deposition of the marine Tokama Siltstone, which locally contains tuffs belonging to the Harper Hills Basalt (K-Ar ages of 13.5 ± 0.4–11.0 ± 0.3 Ma), and overlying Kowai Formation (Early Miocene-to-Recent; **Figure 3**) (Sewell and Gibson, 1988; Lu et al., 2005).

Several discrete phases of intra-plate, post-Cretaceous magmatism and volcanism have been recorded in the Canterbury Basin, including the View Hill Volcanics and the Harper Hills Basalt (**Figure 3**) (e.g., Timm et al., 2010; Reeves et al., 2018). It has been suggested that volcanism occurred in response to decompression melting of upwelling heterogeneous asthenospheric mantle following localized removal of gravitationally unstable lithospheric material (Timm et al., 2010).

DATASET

Borehole Data

Resolution-1 is located ~50 km south of Christchurch (**Figure 2**) and was drilled in 1975 for Shell BP Todd Canterbury Services Ltd (Milne et al., 1975). The borehole was drilled in a water depth of 64 m and extends to a total depth of 1,963.05 m, intersecting the Resolution Sill between 1,911.5 and 1,963.05 m (Milne et al., 1975). Data available for the borehole include (Milne et al., 1975): (i) a well-completion report containing petrological descriptions of cuttings and sidewall core, sampled every 5 m between 1,910 and 1,958 m, and continuous core collected between 1,958.2 and 1,963.05 m within the sill; (ii) sonic (ΔT), gamma ray (GR), caliper (CAL), and spontaneous potential (SP) logs (**Figure 4**); (iii) a petrophysical summary log plot; (iv) well-formation tops, ages, and lithological descriptions; and (v) K-Ar ages of 12 ± 2 Ma for the sill. Density logs, neutron porosity logs, thin sections, or photomicrographs are not available to corroborate the petrographic descriptions.

Resolution-1 has sparse time-depth information. To facilitate depth-conversion of the seismic reflection data, we therefore derived a time-depth curve by integrating sonic log data after using a median filter with a window of five samples to remove spikes caused by sample skipping (**Figure 4**). The sonic log data were also used to calculate a compressional wave (V_p) velocity log by taking the reciprocal of the interval transit time log and converting from feet to meters, and to define average interval velocities for different units (**Figure 4**). For example, the average interval velocity within the Resolution Sill intersected by the borehole is 5.2 km s^{-1} (**Figure 4**), with a standard deviation of 0.3 km s^{-1}. Although the average interval velocity of the sill where it is intersected by Resolution-1 can be defined (i.e., 5.2 km s^{-1}), the borehole does not extend through the entire intrusive body; as a result, we model a range of sill velocities (4.5–6.0 km s^{-1}) to estimate possible intrusion thicknesses (Smallwood and Maresh, 2002). Velocity data in the water column and the shallowest sedimentary strata were not recorded, so we assume values of 1.5 km s^{-1} between 0 and 64 m (i.e., seawater) and 1.8 km s^{-1} between 64 and 385 m (i.e., near-seabed sediments) (**Figure 4**).

Petrological Description of the Resolution Sill

The petrological description of the Resolution Sill was provided by Dr. G. A. Challis of the New Zealand Geological Survey (Milne et al., 1975). Based on 5 m-spaced cuttings collected between 1,911.5 and 1,958 m, the Resolution Sill is best described as a medium-to-coarse grained quartz gabbro comprising plagioclase, quartz, titanaugite, and aegerine. Minor amounts of magnetite, ilmenite, and biotite also occur. Some fine-grained, glassy, black rock chips, which contain white spherules, originate from the top contact chilled margin (see below).

At the top of the continuous core collected from the Resolution Sill, which corresponds to a depth of 1,958.2 m, the intrusion is a coarse-grained quartz syenogabbro primarily comprising titanaugite rimmed by aegerine augite, zoned plagioclase (labradorite to oligoclase) rimmed by anorthoclase, and ilmenite; fine-grained, quartz, biotite, apatite, and chlorite also occur (**Table 1**). Below 1,958.3 m, quartz is absent and the Resolution Sill can be broadly classified as a teschenite that consists of plagioclase, titanaugite, analcite, anorthoclase, and occasionally olivine with accessory apatite, ilmenite, magnetite, and zeolites (**Table 1**). Variations in the abundance of olivine and titanaugite between ~1,958 and 1,963 m indicate the Resolution Sill is subtly layered (**Table 1**).

Petrological analyses of cuttings reveal that a 44 m thick (from 1,877.5 to 1,911.5 m) sedimentary succession directly overlying the sill is heavily pyritised and contains abundant zeolites; this is particularly marked in the first 25 m above the sill. These mineral phases may have formed in response to contact metamorphism or hydrothermal alteration and, thereby, potentially define the thermal aureole of the Resolution Sill (**Figure 4**).

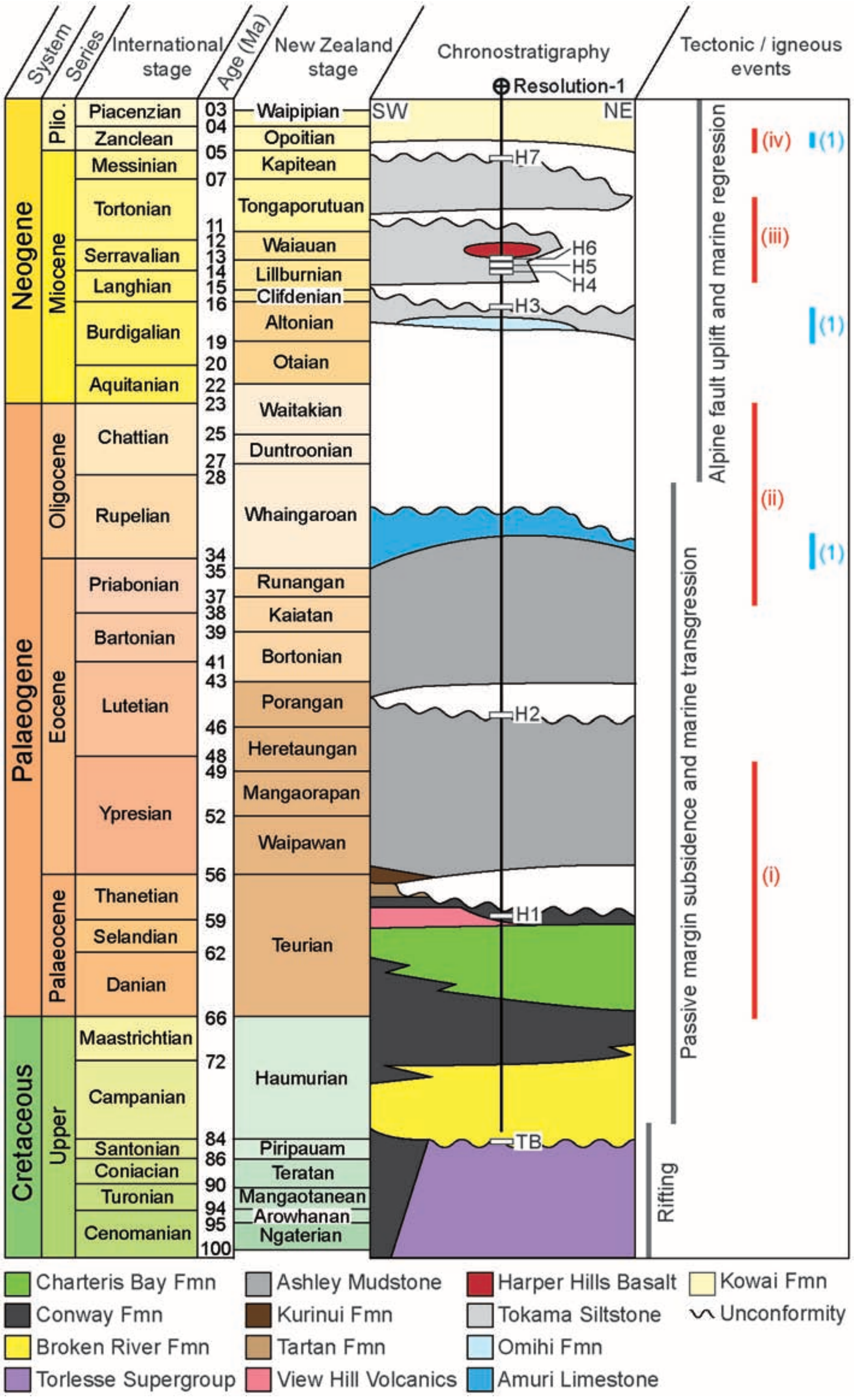

FIGURE 3 | Chronostratigraphic chart for the northern Canterbury Basin around Resolution-1, highlighting different tectonic and igneous events (based on Carter, 1988; Fulthorpe et al., 1996; Killops et al., 1997; Timm et al., 2010; Uruski, 2010; Schiøler et al., 2011; Reeves et al., 2018). Igneous events from Timm et al. (2010) correspond to: (i) Geraldine and Timaru Lavas; (ii) Banks Peninsula; (iii) Cookson Volcanics; (iv) View Hill, Central Canterbury. (1) Offshore sill emplacement events (Reeves et al., 2018). Fmn, formation.

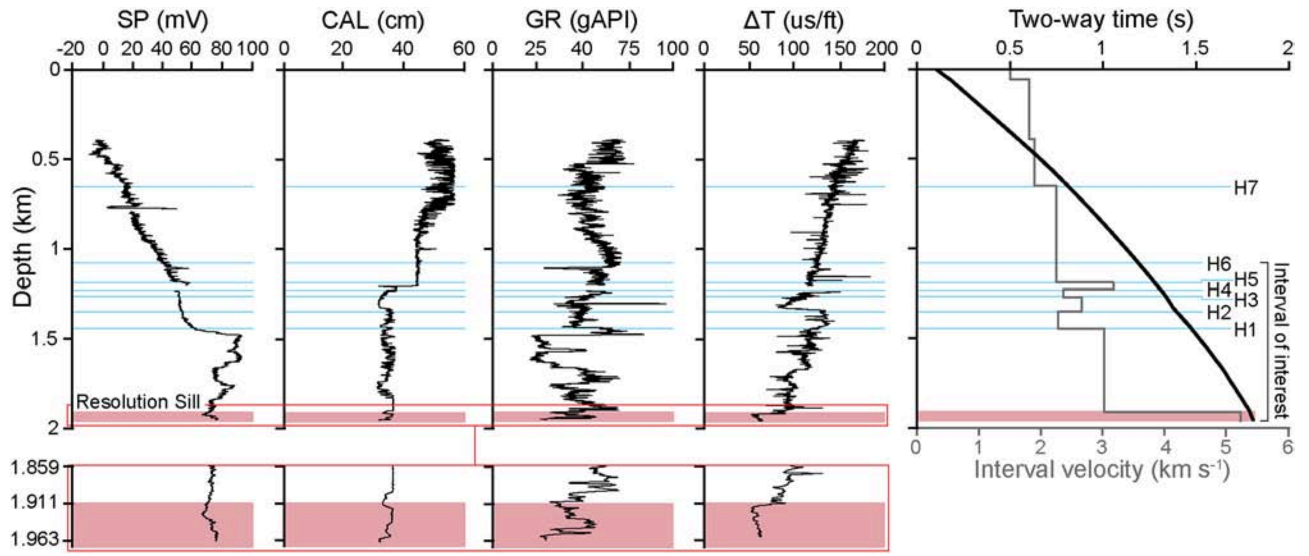

FIGURE 4 | Spontaneous potential (SP), Caliper (CAL), Gamma ray (GR), and Sonic (ΔT) logs from the Resolution-1 borehole plotted against depth. A plot of two-way time and interval velocity changes with depth is also shown. The locations of the mapped horizons and the Resolution Sill are highlighted.

TABLE 1 | Resolution-1 continuous core petrology.

Depth (m)	Rock type	Major phases*	Accessory phases*	Notes
1,958.20	Quartz syenogabbro	Tau, Aeg, Plag, Ano, Ilm	Qtz, Bio, Apa, Chl	Tau is granular and sub-ophitic; Tau rimmed by Aeg; Ano rims Plag
1,958.50	Olivine teschenite	Tau, Ol, Plag, Ana	Horn, Mag, Apa, Chl, Ilm, Ano	Ano occasionally rims Plag; Tau is ophitic and encloses Ol and Plag
1,958.90	Teschenite	Tau, Plag, Ana, Ano	Apa, Ilm, Bio, Ol	Tau forms large ophitic crystals; Ano rims Plag
1,959.20	Olivine teschenite	Tau, Ol, Plag, Ana	Horn, Mag, Apa, Chl, Ilm, Ano	Ano occasionally rims Plag; Tau is ophitic and encloses Ol and Plag
1,959.30	Leucoteschenite	Plag, Ano, Ana	Apa, Ilm, Tau	Ano rims Plag; very little Tau
1,959.45	Teschenite	Tau, Plag, Ana, Ano	Apa, Ilm, Bio, Ol	Tau forms large ophitic crystals; Ano rims Plag
1,959.75	Leucoteschenite	Plag, Ano, Ana	Apa, Ilm, Tau	Ano rims Plag; very little Tau
1,960.30	Teschenite	Tau, Plag, Ana, Ano	Apa, Ilm, Bio, Ol	Tau forms large ophitic crystals; Ano rims Plag
1,960.60	Leucoteschenite	Plag, Ano, Ana	Apa, Ilm, Tau	Ano rims Plag; very little Tau
1,962.30	Teschenite	Tau, Plag, Ana, Ano	Apa, Ilm, Bio, Ol	Tau forms large ophitic crystals; Ano rims Plag
1,962.50	Olivine leucoteschenite	Ol, Plag, Ana	Tau, Horn, Mag, Apa, Chl, Ilm, Ano	Ano occasionally rims Plag
1,962.80	Olivine teschenite	Tau, Ol, Plag, Ana	Horn, Mag, Apa, Chl, Ilm, Ano	Ano occasionally rims Plag; Tau is ophitic and encloses Ol and Plag
1,963.05	Olivine leucoteschenite	Ol, Plag, Ana	Tau, Horn, Mag, Apa, Chl, Ilm, Ano	Ano occasionally rims Plag

**Tau, Titanaugite; Aeg, Aegerine augite; Plag, Plagioclase; Ano, Anorthoclase; Ol, Olivine; Ana, Analcite; Ilm, Ilmenite; Qtz, Quartz; Apa, Apatite; Chl, Chlorite; Horn, Ti-hornblende; Mag, Magnetite; Bio, Biotite.*

Seismic Reflection Data

This study utilizes three, zero-phase, time-migrated, 2D seismic reflection surveys (the ANZ, CB82, and Sight surveys; **Figure 2**). We focus on an area that covers ∼3,000 km^2 and has a total seismic line length of ∼484 km (**Figure 2**). Line spacing for the different vintage seismic data ranges from 3.5 to 16 km (**Figure 2B**). Seismic data are displayed with a zero-phase SEG normal polarity; a downward increase in acoustic impedance correlates to a positive (black/red) reflection, whilst a negative (white/blue) reflection corresponds to a downward decrease in acoustic impedance (**Figure 5**). Interval velocities derived from borehole data were used to convert the seismic reflection data from depth in seconds two-way time (TWT) to depth in meters (**Figures 4**, **5**). We only depth-converted data above Top Basement because the lithology and physical properties (e.g., V_p) of the underlying Torlesse Supergroup are unknown (**Figure 5C**).

Data Resolution

The resolution of a studied interval in seismic reflection data is dependent on the dominant wavelength (λ) of the seismic

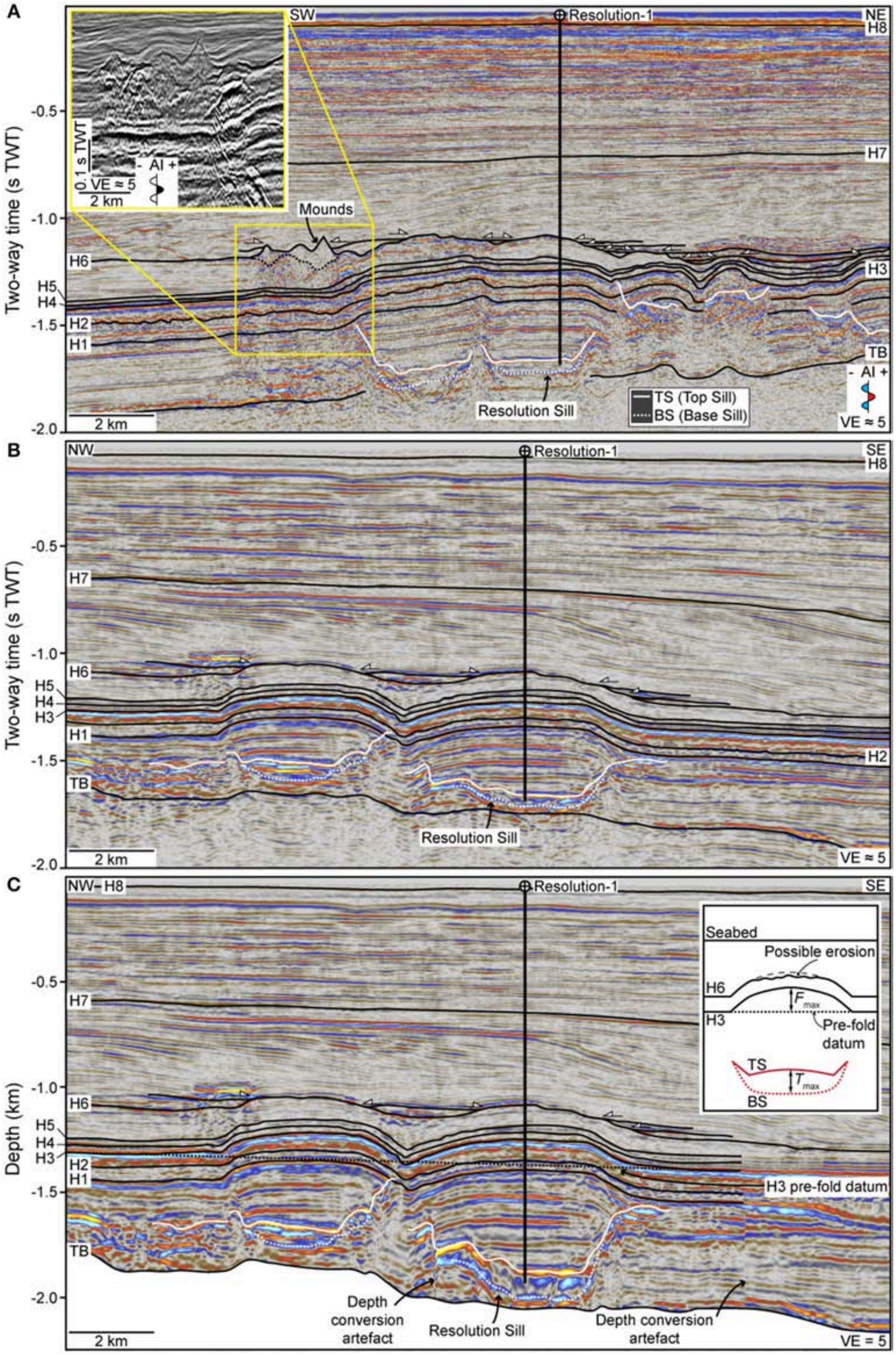

FIGURE 5 | (A,B) Interpreted, time-migrated seismic sections imaging the Resolution Sill and neighboring intrusions. Mapped stratigraphic horizons are marked and white-filled arrows highlight onlap onto H6. Inset in **(A)** shows an uninterpreted, zoomed-in view of the mounded structures. AI, acoustic impedance and VE, vertical exaggeration. See **Figure 2B** for location of the seismic lines. Uninterpreted sections provided in **Supplementary Figure 1**. **(C)** Depth-converted version of the seismic section shown in **(B)**. Inset schematically shows how erosion may modify the top of the fold and how $F_{\max}$ and $T_{\max}$ were measured.

waves, with $\lambda = v/f$, where v is he interval velocity and f is the dominant frequency (Brown, 2011). In order to distinguish reflections emanating from two distinct boundaries (e.g., the top and base of a sill), their vertical distance needs to exceed the limit of separability ($\sim\lambda/4$) for the data (Brown, 2011). If the vertical distance between the boundaries is less than the limit of separability, the two reflections will interfere on their return to the surface and cannot be deconvolved; they will appear as tuned reflection packages, the true thickness of which cannot be determined (Brown, 2011). The limit of visibility ($\sim\lambda/30$) defines the minimum vertical distance between two boundaries required to produce a tuned reflection package that can be distinguished from noise in the seismic reflection data (Brown, 2011). Interval velocities of 2.2–3.2 km s^{-1} for the sedimentary sequence in the section of interest (**Figure 4**), coupled with a seismic dominant frequency that decreases with depth from ~40 to 25 Hz, suggests that the limits of separability and visibility for the data decrease with depth from ~32 to 14 m and ~4 to 2 m, respectively. Assuming the entire Resolution Sill has an interval of velocity of 5.2 km s^{-1}, equal to that of the upper 50 m intersected by Resolution-1, a surrounding dominant frequency of ~25 Hz indicates its limits of separability and visibility are ~52 and ~7 m, respectively. However, if we consider that the average interval velocity of the Resolution Sill is more variable (i.e., 4.5–6.0 km s^{-1}), the maximum limits of separability and visibility may be ~60 and ~6 m, respectively. Reflections from the top and base of the Resolution Sill where it is >60 m thick will therefore be distinguishable in the seismic data, whereas parts of the sill <60 m thick but over >6 m thick will be expressed as tuned reflection packages (see Smallwood and Maresh, 2002; Magee et al., 2015; Eide et al., 2018). Where the Resolution Sill is <7 m thick, it is unlikely to be detectable in the seismic reflection data.

Seismic Interpretation

The study area contains several high-amplitude reflections that are laterally discontinuous and can typically be sub-divided into a strata-concordant inner region surrounded by a transgressive, inward-dipping limb; i.e., they display a saucer-shaped morphology (**Figure 5**). We mapped these reflections and interpret them as sills because: (i) one corresponds to the Resolution Sill intersected by the Resolution-1 borehole (**Figure 5**); and (ii) they are geometrically similar to igneous saucer-shaped sills observed in the field and imaged in other seismic reflection datasets (e.g., Thomson and Hutton, 2004; Planke et al., 2005; Polteau et al., 2008a; Magee et al., 2016a). For all sills we mapped the top contact (TS) and, where seismically resolved, the base sill (BS) (**Figure 5**). In addition to sills, we mapped nine key seismic horizons and tied them to the Resolution-1 borehole (**Figures 3–5**): TB = Top Basement (~84 Ma); H1 = Intra-Conway Formation unconformity, above the View Hill volcanics (Mid-Paleocene, ~58 Ma); H2 = Intra-Ashley Formation unconformity (Mid-Eocene, ~45 Ma); H3 = Top Omihi Formation (Early Oligocene, ~16 Ma); H4 = lowermost Intra-Tokama Formation (Early to Mid-Miocene, ~14 Ma); H5 = Intra-Tokama Formation (Mid-Miocene, ~14 Ma); H6 = Base Harper Hill Basalts (Mid-Miocene, ~13.5 ± 0.4 Ma) and top of the force folds; H7 = Top Tokama unconformity (Miocene to Pliocene, ~6 Ma); and H8 = seabed.

The limited resolution of the seismic reflection data means we cannot ascertain whether erosion has modified the geometry of the fold top (i.e., H6) and reduced its amplitude post-emplacement (e.g., **Figure 5C**). We therefore measure amplitude along the prominent intra-fold horizon H3 (e.g., **Figure 5C**). To determine fold amplitude we measure the vertical distance between the top of H3 and an inferred pre-fold datum constructed by extrapolating the regional trend of H3 from areas where there are no sills or forced folds (**Figure 5C** inset). The maximum vertical distance between H3 and the pre-fold datum is the maximum fold amplitude ($F_{\max}$; **Figure 5C**). Sill thickness is measured as the vertical distance between TS and BS, with the maximum sill thickness defined by $T_{\max}$ (**Figure 5C**).

Decompaction and Backstripping

Whilst several studies suggest cases where $F_{\max}/T_{\max} << 1$ reflects magma accommodated by elastic *and* inelastic deformation processes, they do not quantitatively evaluate the role of burial and compaction in modifying forced fold geometry (Jackson et al., 2013; Magee et al., 2013a, 2017). Loading of sedimentary sequences during burial promotes progressive loss of porosity with depth (i.e., compaction), and causes beds to become thinner and structures (e.g., faults) to flatten. The compaction of strata at any given depth is controlled by its lithology and lithostatic load. Because crystalline intrusive rocks have virtually no porosity and can be considered incompressible, $T_{\max}$ will not change with burial. However, compaction of the overlying sedimentary sequence is expected to reduce $F_{\max}$ and therefore decrease of $F_{\max}/T_{\max}$. The sedimentary sequence adjacent to the sill is overlain by a thicker column of sediment/rock, meaning it will compact more than where it is folded above the sill; this variation in lithostatic load across the fold can promote differential compaction (Hansen and Cartwright, 2006; Schmiedel et al., 2017). Evaluating the role of post-emplacement compaction in modifying forced folds is critical to establishing the relationship between the original maximum fold amplitude ($F0_{\max}$) and intrusion thickness, which can be used to inform interpretation of emplacement mechanics. To extract $F0_{\max}$, we decompact and backstrip the forced fold. Note we do not take into account processes that may alter sill thickness (e.g., contraction during crystallization; Caricchi et al., 2014) and thus assume $T_{\max} = T0_{\max}$.

Forward Modeling

Decompacting and backstripping sedimentary sequences imaged in depth-converted seismic reflection data involves restoring the initial porosity (φ_0) of strata at the top of the sequence from its current porosity (φ), by removing its overburden. This technique normally involves estimating a porosity log from sonic log data using either the Wyllie time-average method or Raymer-Hunt-Gardner empirical relationship (Wyllie et al., 1956; Raymer et al., 1980). However, given the shallow depth of our interval of interest (i.e., 1–2 km) and the limited log data available (e.g., there is no density log), we cannot reliably assess the accuracy of current porosity logs derived from these methods. We therefore apply forward modeling techniques to establish whether plausible decompacted and backstripped scenarios are realistic and how they impact fold geometry. In particular, based on the lithological information from Resolution-1, we model a series of different parameter ranges and combinations to assess potential variations between sill thickness and the original fold amplitude. Because estimates of φ_0 and the compaction length scale (λ), which is the inverse of the compaction coefficient, are not available, we model a range of realistic values (Sclater and Christie, 1980): (i) φ_0 is considered to range from 0.7 to 0.25, consistent with a range of siliciclastic sequences; and (ii) λ ranges from 3.7 to 1.4 km.

Forward modeling involved the standard back-stripping procedure described by Sclater and Christie (1980). The most common function used to model porosity decay with depth is the exponential relationship:

$$\varphi = \varphi_0 e^{-z/\lambda} \tag{1}$$

where z is depth below seafloor. Considering the rock matrix fraction (m) complements porosity (Smallwood, 2009), whereby

$$m = 1 - \varphi \tag{2}$$

we can relate the pre- and post-compactional stratal thicknesses via conservation of mass to give:

$$\int_{z2}^{z1} m\,dz = \int_{z4}^{z3} m\,dz \tag{3}$$

where $z1$ and $z2$ are the initial top and base depths of the sediment package in question (i.e., the present day depth, below the seafloor, of the top forced fold and top sill, respectively), and $z3$ and $z4$ are the original depth below the seafloor of the top and base of the sedimentary package (i.e., the original depth of the forced fold is at the seafloor, hence $z3 = 0$, and $z4$ is the depth of the sill we solve to find). Substituting equations 1 and 2 into equation 3 and integrating gives:

$$z4 - z3 = z2 - z1 + \varphi_0/\lambda(e^{-z1/\lambda} - e^{-z2/\lambda} + e^{-z4/\lambda} - e^{-z3/\lambda}) \tag{4}$$

We solve equation 4 numerically to find the thickness of the original thickness of the folded sedimentary section (i.e., $z4 - z3$) along individual vertical traces; by calculating equation 4 along vertical traces across the width of the sill-fold pair, we recover the original geometry of the forced fold. Because we do not know the correct input values for φ_0 or λ, we calculated multiple iterations of equation 4 using different, realistic combinations of φ_0 (0.7–0.25) and λ (3.7–1.4). This method assumes the folded layer has no elastic thickness, which we consider reasonable because much of the folded section was likely unlithified during deformation. Assuming forced folds have very little, or no, elastic thickness is consistent with forced folds having similar diameters to underlying intrusions (e.g., Hansen and Cartwright, 2006; Jackson et al., 2013).

OBSERVATIONS

Resolution Sill

Resolution Sill Well-Log Response

The Resolution Sill is characterized by an abrupt increase in V_p, from ~3.0 km s^{-1} in the overlying strata to ~5.2 km s^{-1} within the sill (**Figure 4**). Within the sill itself, values of V_p, GR, and SP vary substantially on a meter to decameter-scale (**Figure 4**).

Geometry

The Resolution Sill is observed on two seismic lines, with its top corresponding to a high-amplitude, positive polarity reflection (TS; **Figures 4**, **5**). Where the base of the sill is resolved, it is characterized by a discrete, moderate-to-high amplitude, negative polarity reflection (BS) that appears to coincide with the top of the basement (TB) at a present day depth of ~2 km (**Figure 5**). Although the Resolution Sill can only be mapped on two 2D seismic lines, the constraints these data provide on lateral sill tip locations allow us to interpolate its 3D geometry within a sill outline derived from comparison to exposed and seismically imaged sills (e.g., Chevallier and Woodford, 1999; Planke et al., 2005; Hansen et al., 2008; Polteau et al., 2008b; Magee et al., 2014, 2016a). Overall, the 54 km^2 sill has an elliptical, saucer-shaped morphology with a NW-trending, long axis of ~6.2 km and a NE-trending short axis of ~2.8 km (**Figure 6**). The strata-concordant inner sill is sub-circular, with a diameter (D) of ~2.2 km, passing laterally into gently (8°), inward-dipping, up to ~0.4 km high transgressive limbs to the SE and NW (**Figures 5**, **6**). Toward the south-eastern edge of the Resolution Sill, at its shallowest level, the transgressive limb transitions into a strata-concordant outer rim (**Figures 5**, **6**).

Intrusion thickness appears variable across the strata-concordant inner sill, although there is a first-order decrease away from the center; assuming an interval velocity of 5.2 km s^{-1} for the entire sill, its thickness ranges from ~138 m ($T_{\max}$) to ≤52 m (**Figures 6C**, **7**). Superimposed onto this outward-thinning trend within the inner sill are apparently several abrupt changes in sill thickness (e.g., there is a ~75 m change at A-A′; **Figure 7**). However, because the lower portion of the sill is not intersected by Resolution-1, we do not know if it is characterized by similar velocities. We also do not know whether the interval velocity of the sill varies laterally. We therefore calculate sill thickness using a range of feasible interval velocities (i.e., 4.5–6.0 km s^{-1}). The envelope calculated for this velocity range constrains how thickness may vary along-strike when the sill velocity across (i.e., vertically and laterally) the intrusion is constant (e.g., 4.5 or 5.2 km s^{-1}) or variable (e.g., if the velocity decreases toward its edges) (**Figure 7**). For a range of interval velocities, we show the sill: (i) could be up to ~187 m thick (i.e., $T_{\max}$); (ii) maintains a first-order decrease in thickness from its center outwards; and (iii) thickness still appears to show local, abrupt variations, although the magnitude of these changes may be limited depending on how velocity varies laterally (**Figure 7**). For example, dependent on the sills velocity configuration, the thickness change at A-A′ could be up to ~149 m, or down to ~17 m. The outer portions of the transgressive sill limbs are defined by tuned reflection packages, such that their vertical thickness cannot be measured; where tuning occurs we consider intrusion thickness can range from 60 to 6 m (i.e., the limits of separability and visibility, respectively) (**Figures 5**, **7**).

The Resolution Sill is bordered to the SW, NW, and NE by three additional saucer-shaped sills; we are unable to constrain the 3D geometry of these neighboring sills because they cannot be

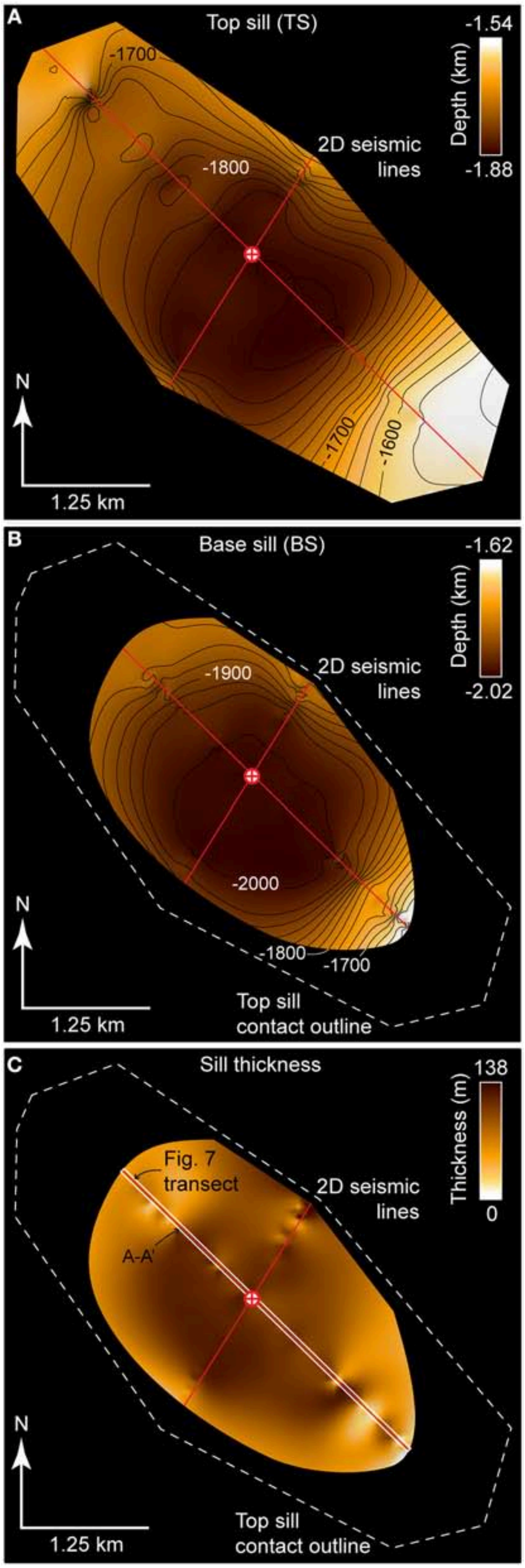

FIGURE 6 | (A,B) Depth-structure maps of top (TS) and base (BS) saucer-shaped sill reflections interpolated from interpretation of the sill on *(Continued)*

FIGURE 6 | the two seismic lines (thin white lines) in **Figure 5**. The selected sill outline is constrained by the seismic reflection data and assumes the sill likely has an elliptical shape, similar to sills observed elsewhere (see Hansen et al., 2008). **(C)** Thickness map of TS–BS, i.e., where both horizons can be seismically resolved, assuming a constant sill interval velocity of 5.02 km s^{-1}.

mapped sufficiently on multiple seismic lines (**Figure 5**). In cross-section, the sills to the SW and NW display similar geometries and emplacement depths to the Resolution Sill, whereas the base of the north-eastern sill broadly coincides with Horizon H1 (**Figure 5**).

Host Rock Structure

Strata directly above the Resolution Sill, up to H6, are folded (**Figures 5**, **8**). The ~58 km^2, elliptical (i.e., ~6.2 km × 3 km) dome is relatively flat-topped, with uplift primarily accommodated by monoclinal bending directly above the transgressive limbs of the Resolution Sill, which cross-cut the lowermost folded strata (**Figures 5**, **8**). The top of the fold corresponds to H6, i.e., the ~12.5 Myr old base of the 9 m thick Harper Hills Basalt, and is onlapped by overlying, sub-horizontal strata of the Tokama Siltstone (**Figures 3**, **5**). Whilst these seismic-stratigraphic onlap relationships indicate H6 represented the syn-intrusion free surface, the limited resolution of the seismic reflection data means we cannot ascertain whether erosion has subtly modified the geometry of the fold crest. The maximum fold amplitude ($F_{\max}$) at H3 is ~127 m, with amplitude gradually and smoothly decreasing toward the fold periphery (**Figure 7**). The vertical distance between H6 and TS is ~0.75 km (**Figure 5C**).

Similar folds are developed above the three sills neighboring the Resolution Sill; the top of these folds all occur at H6 and their boundaries directly overlie lateral sill tips (**Figures 5**, **8**). Although these forced folds merge in places to form compound forced folds (see Magee et al., 2014), depth-conversion of available 2D data suggests our inferred pre-fold datum captures the regional trend of the folded strata (e.g., **Figure 5C**). The supra-sill fold to the SW of the Resolution Sill is associated with several mound-like structures marked by moderate-amplitude, positive polarity (black) reflections that downlap onto Horizon H6 and themselves are onlapped H6–H7 strata (**Figure 5A**). These mounds are up to ~315 ms TWT high (their height in meters cannot be calculated without knowledge of their V_p) and have diameters up to ~3.5 km. The mounds appear to have erosional bases that truncate underlying strata, including H6 (**Figure 5A**). Internal reflections within the mounds are relatively poorly imaged but appear to have a convex-upwards morphology (**Figure 5A**).

Fold Amplitude Compared to Sill Thickness

The maximum sill thickness ($T_{\max}$) is estimated to be ~138 m, but may range from ~117–187 m thick depending on the interval velocity of the entire sill (**Figure 7**). The maximum fold amplitude ($F_{\max}$) measured at H3 is ~127 m (**Figure 7**). $T_{\max}$ may thus be up to 47% greater than $F_{\max}$. Comparing these intrusion and fold measurements suggests $F_{\max}/T_{\max}$ is ~0.92, potentially ranging from ~0.68–1.09. We also note there is a lateral offset of ~400 m between the locations of $F_{\max}$ and $T_{\max}$ (**Figure 7**). Fold amplitude and sill thickness both display a first-order decrease toward their peripheries, although sill thickness does appear to vary abruptly in places where fold amplitude does not (**Figure 7**). It is difficult to determine how fold amplitude relates to the thickness of the transgressive limbs because the latter are only expressed as tuned reflection packages so only their maximum (i.e., the limit of separability, 60 m) and minimum (i.e., the limit of visibility, 6 m) thicknesses can be constrained (**Figures 5**, **7**).

Decompaction and Backstripping Results

Decompaction of the amplitude profile across the top of the fold intersected by Resolution-1 reveals that its shape is maintained but its maximum amplitude increases from ~127 m (i.e., $F_{\max}$) to up to ~131–185 m (i.e., $F0_{\max}$; **Figure 9**). Uncertainties in the decompaction input parameters means the original fold amplitude profile cannot be absolutely determined. Although calculated $F0_{\max}/T_{\max}$ values range from 0.70 to 1.58, the breadth of which is a function of the broader range of possible scenarios compared to $F_{\max}/T_{\max}$, it is clear there is a greater overlap between likely sill thicknesses and amplitude values after decompaction (**Figure 9**). Following decompaction, the vertical distance between H6 and TS (i.e., the emplacement depth) is ~0.8 km.

DISCUSSION

Timing of Sill Emplacement and Forced Folding

The top of the forced fold overlying the Resolution Sill corresponds to Horizon H6, where a thin tuff, which is genetically related to the Harper Hills Basalt, is interbedded with the Tokama Siltstone (**Figure 5**). Onlap of the marine, middle-to-late Miocene Tokama Siltstone onto Horizon H6 suggests it formed the paleo-seabed during sill emplacement and forced folding. Where exposed onshore, the tholeiitic Harper Hills Basalts have K-Ar ages ranging from 13.5 ± 0.4 to 11.5 ± 0.3 Ma (Sewell and Gibson, 1988), which can be used as a proxy for the age of H6. This potential age range for H6 overlaps with the radiometric date obtained for the Resolution Sill (i.e., 12 ± 2 Ma; Milne et al., 1975), suggesting sill emplacement and forced folding occurred ~12 Ma.

Sills and forced folds adjacent to the Resolution Sill display similar seismic-stratigraphic relationships (i.e., H6 marks the fold tops) and, in places, are overlain by mound-like features we interpret as volcanoes based on: (i) their moderate-to-high amplitude, positive polarity top contacts indicative of a downward increase in seismic velocity and density, consistent with a transition from sedimentary to igneous rocks (e.g., Symonds et al., 1998; Planke et al., 2005); (ii) observed truncation underlying strata, similar to eye-shaped hydrothermal vents, suggesting they formed via explosive activity (e.g., Jamtveit et al., 2004; Planke et al., 2005; Hansen, 2006; Magee et al., 2016b); and (iii) they have similar geometries and internal architectures to volcanic vents and volcanoes observed in other sedimentary basins (e.g., Symonds et al., 1998; Jackson, 2012; Magee et al., 2013b). Overall, our seismic-stratigraphic observations, coupled with radiometric dating of the Resolution Sill and the Harper Hills Basalt onshore, indicate a phase of magmatism and volcanic activity across the northern Canterbury Basin during the Mid-Miocene (Sewell and Gibson, 1988; Timm et al., 2010).

Emplacement Mechanics and Burial-Related Compaction

For shallow-level sills and laccoliths accommodated purely by elastic bending of the overburden, we may expect the original fold amplitude, measured at the fold top, and sill thickness to be broadly equal (i.e., $F0_{\max}/T0_{\max} = 1$) (e.g., Pollard and Johnson, 1973; Fialko and Simons, 2001; Hansen and Cartwright, 2006; Jackson et al., 2013). The ratio between the original fold amplitude and sill thickness is partially controlled by the ratio of the inner sill diameter (D) and depth of emplacement (d), with larger sills intruded at shallower depths capable of generating more bending, and thus uplift of the contemporaneous free surface, than a smaller sill at greater depths (e.g., Pollard and Johnson, 1973; Fialko and Simons, 2001; Hansen and Cartwright, 2006; Jackson et al., 2013). In particular, if the D/d ratio is >4, it is considered that the overburden will not resist bending and elastic deformation will therefore fully accommodate magma emplacement (Pollard and Johnson, 1973; Hansen and Cartwright, 2006). Decompaction of our data indicates the Resolution Sill, which has an inner sill diameter (D) of ~2.2 km, was emplaced at a depth (d) of ~0.8 km beneath the contemporaneous surface (i.e., H6) and thus had a D/d ratio of ~2.75. Given a D/d ratio < 4, the model of Pollard and Johnson (1973) suggests that the overburden may have resisted bending and, in addition to elastic deformation, promoted inelastic vertical compaction or ductile strain, thereby suppressing forced fold amplitude (i.e., $F0_{\max} < T0_{\max}$) (see also Hansen and Cartwright, 2006; Jackson et al., 2013).

In contrast to previous studies, we quantitatively assess the impact post-emplacement compaction during burial has on fold geometry (principally amplitude) and, therefore, $F0_{\max}/T_{\max}$ as opposed to $F_{\max}/T_{\max}$ (cf. Hansen and Cartwright, 2006; Jackson et al., 2013; Magee et al., 2013a, 2017). We show that following decompaction and backstripping, the overall fold geometry is maintained but its amplitude increases from 127 m ($F_{\max}$) up to 131–185 m ($F0_{\max}$) (**Figure 9**). These potential $F0_{\max}$ values, coupled with a sill thickness of 117–187 m, means $F0_{\max}/T_{\max}$ ranges from 0.70 to 1.58; this is greater than our measured $F_{\max}/T_{\max}$ range (i.e., 0.68–1.09), which we attribute to the broader range of scenarios we test in calculating $F0_{\max}/T_{\max}$. Considering uncertainties in the various parameters controlling $F0_{\max}/T_{\max}$ measurement (e.g., sill and strata interval velocities, incorrect extrapolation of the pre-fold datum), our calculated $F0_{\max}/T_{\max}$ range of 0.70–1.58 suggests: (i) fold amplitude and sill thickness could be equal; (ii) fold amplitude may be less than sill thickness by up to ~30%, a scenario consistent with a D/d ratio of ~2.75; or (iii) fold amplitude is greater than sill thickness by up to ~37%, which could occur when thin (i.e., with

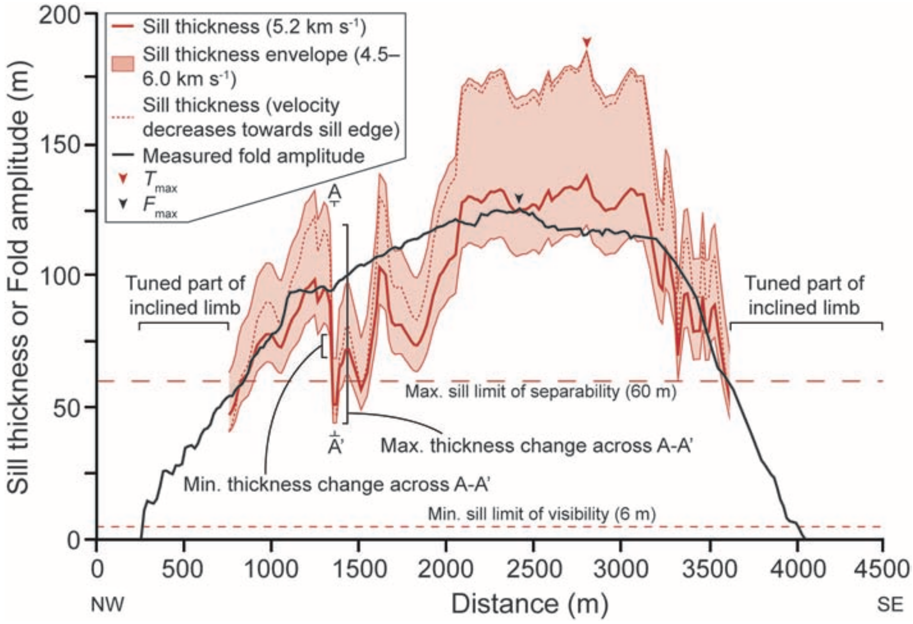

FIGURE 7 | Plot of amplitude across the fold, at H3, measured directly from the seismic reflection data (i.e., **Figure 5C**). We also show a range of sill thicknesses, for different seismic interval velocities, across the intrusion where TS and BS can be distinguished; a sill thickness profile considering a seismic interval velocity of 5.2 km s^{-1} is particularly highlighted because this is the average interval velocity for the upper 50 m of the intrusion where it is intersected by the Resolution-1 borehole. Thicknesses are not shown where the sill corresponds to a tuned reflection package along the inclined limbs, but we do highlight the maximum (max.) limit of separability and minimum (min.) limit of visibility for the sill. Note the lateral offset of $F_{\max}$ and $T_{\max}$.

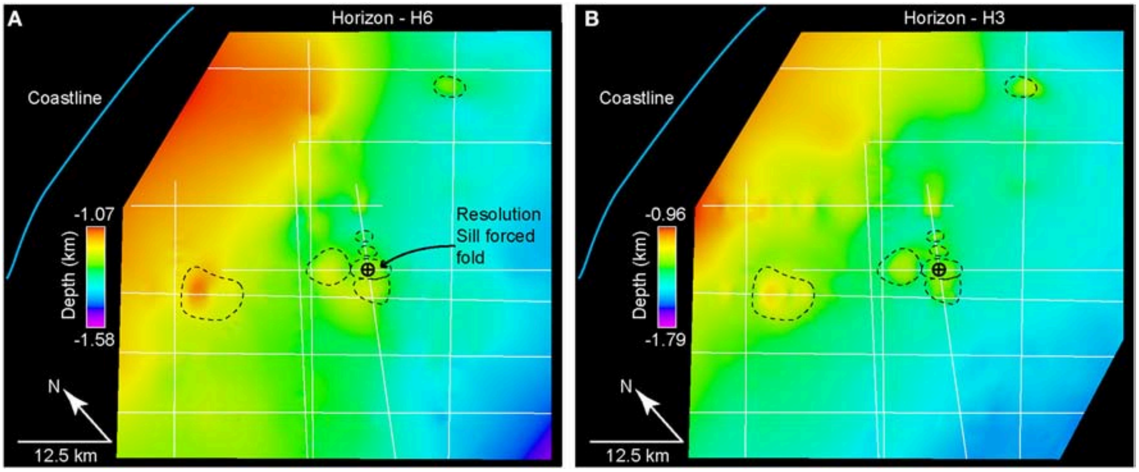

FIGURE 8 | (A,B) Depth-structure maps of horizons H6 and H3, highlighting the location of the Resolution-1 borehole and intrusion-induced forced folds (black dashed lines) in the vicinity. 2D seismic lines (white lines) also shown.

thicknesses below the limit of visibility) sills that contributed to uplift are not seismically resolved (Reeves et al., 2018). Although uncertainties mean we cannot ascertain the true, original sill-fold relationships, there qualitatively appears to be a better fit between the potential ranges of sill thickness and decompacted fold amplitude (**Figure 9**).

In addition to burial-related compaction, it is also worth highlighting that $F_{\max}/T_{\max}$ discrepancies could be attributed to (Hansen and Cartwright, 2006; Jackson et al., 2013; Magee et al., 2013a): (i) reduction of fold amplitude due to erosion of the fold crest; (ii) incorrect depth conversion; (iii) strain interference with adjacent folds during deformation; (iv) out-of-plane deformation; or (v) changes in intrusion geometry. We measure amplitude from an intra-fold horizon (i.e., H3), so discount erosion of the fold crest as a mechanism for reducing $F_{\max}$ and producing $F_{\max}/T_{\max}$ ratios <1 (e.g., 0.81) (**Figure 5C**).

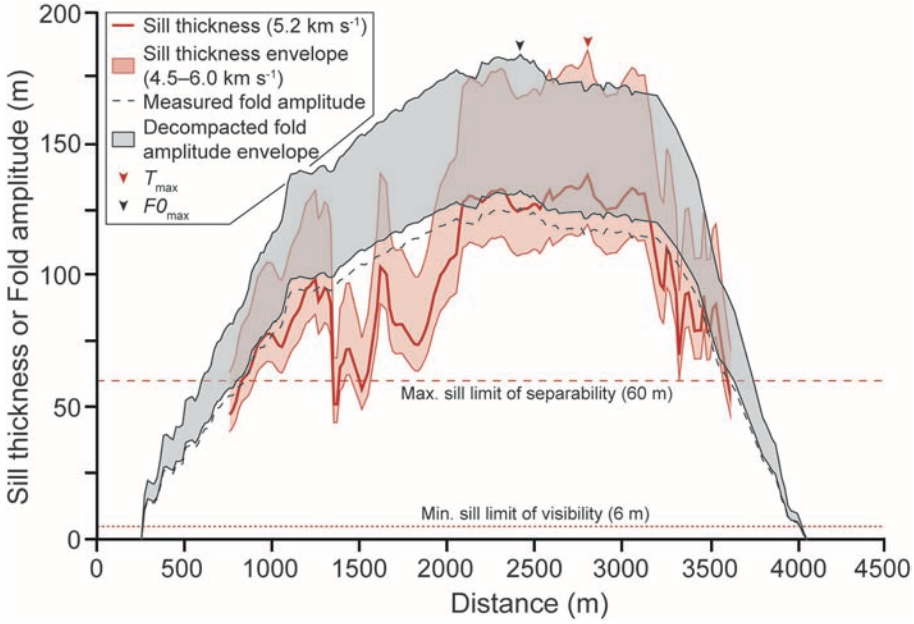

FIGURE 9 | Plot of fold amplitude and sill thickness across the seismic line in **Figure 5C**, highlighting how the measured fold shape and amplitude changes if the seismic data is decompacted and backstripped.

By using velocity data from Resolution-1 and calculating sill thickness for a range of velocity values means we have better control on depth conversion parameters than previous studies, yet our results highlight $F_{\max}/T_{\max}$ discrepancies <1 are still plausible (cf. Hansen and Cartwright, 2006; Jackson et al., 2013; Magee et al., 2013a, 2017). The Resolution Sill and overlying forced fold are adjacent to and abut sill-fold pairs, of the same age, to the NW and SW (**Figures 5**, **8**), implying strain interference between the folds may have enhanced or inhibited fold growth; however, we cannot quantify whether strain interference had a positive of negative impact on $F_{\max}$, particularly without access to 3D seismic reflection data. Abrupt, localized variations in thickness across the sill are not reflected by the overlying fold shape (**Figures 5**, **7**, **9**); this local decoupling between sill and fold shape may suggest vertical displacement induced by sill intrusion is distributed across an area because the overburden has some flexural strength (see Stearns, 1978). The fold profile we measure thus does not capture and may have been modified by localized out-of-plane deformation or changes in intrusion geometry; these observations imply that relatively simple ground deformation patterns may be generated by intrusions with complex geometries. Whether folded strata respond (i.e., deform) to small-scale changes in intrusion thickness is a function of emplacement depth and various host rock properties (e.g., flexural rigidity, bed thickness, co-efficient of friction between layers) (e.g., Stearns, 1978).

Overall, our work implies that explicitly accounting for burial-related compaction likely reduces measured $F_{\max}/T_{\max}$ discrepancies (Magee et al., 2013a; cf. Jackson et al., 2013). We show that emplacement of the Resolution Sill was principally accommodated by elastic bending of the overburden but, without sufficient borehole data to accurately constrain the original fold geometry, cannot confirm whether inelastic deformation also generated space for the intrusion. Further work is required to test the impact of burial-related compaction on the geometry and amplitude of seismically imaged forced folds, and to determine how burial-related compaction signals can be deconvolved from intrusion-related inelastic deformation processes that modify fold geometry.

CONCLUSIONS

Elastic bending and uplift of overlying rock and sediment, and potentially the free surface, can accommodate emplacement of shallow-level, tabular intrusions; this intrusion-induced deformation is a form of "forced folding." Many numerical and analytical models examining sill and laccolith emplacement, as well as inversions of ground displacement data at active volcanoes used to recover information pertaining to subsurface magma movement, typically only incorporate elastic processes and neglect inelastic deformation mechanisms. Whilst the assumption that host rock deformation is purely elastic can be applied to many scenarios, several seismic reflection-based studies have suggested that synchronous elastic *and* inelastic processes can generate space for magma intrusion. This interpretation that elastic and inelastic processes can accommodate magma, which is supported by some outcrop data and analytical modeling, is based on some seismically imaged forced folds having amplitudes much smaller than the thickness of the underlying intrusion; i.e., elastic bending is expected to produce folds with amplitudes broadly equal to the thickness of the underlying intrusion. However, these seismic-based studies do not quantitatively account for post-emplacement, burial-related compaction of forced folds, which may be expected to reduce their amplitude. Through analysis of the Resolution Sill and its overlying forced fold, imaged in seismic reflection data offshore eastern New Zealand and intersected by the Resolution-1 borehole, we present the first robust decompaction and backstripping of an intrusion-induced forced fold to constrain its original geometry. Our results highlight the forced fold had an original amplitude of ∼131–185 m, but burial-related compaction has reduced its amplitude to ∼127 m. The top and base of the Resolution Sill are seismically distinguishable across its center, where it has a maximum thickness of 117–187 m, depending on the interval velocity of the entire sill. Although uncertainties still exist, we show that decompaction reduces and potentially fully accounts for apparent discrepancies between fold amplitudes and sill thicknesses. Our observations also suggest relatively simple fold shapes may be produced by complex intrusion geometries, involving local abrupt changes in thickness. Seismic reflection data provides unprecedented insights into the 3D geometry of natural intrusions and forced folds, but we highlight the need to consider the role of burial-related compaction in modifying fold shapes and amplitudes.

AUTHOR CONTRIBUTIONS

CM designed the study, carried out the seismic interpretation, interpreted the data, and wrote the manuscript. MH conducted decompaction and backstripping analysis, aided data interpretation, and edited the manuscript. CJ and SJ contributed to data interpretation and edited the manuscript.

FUNDING

Open access publication costs to be funded by University of Leeds library.

ACKNOWLEDGMENTS

CM acknowledges funding from an Imperial College Junior Research Fellowship and a NERC Independent Research Fellowship (NE/R014086/1). MH acknowledges funding from NERC studentship NE/1369185. New Zealand Petroleum and Minerals are thanked for providing all data used (i.e., 2D seismic reflection lines, borehole data, and relevant reports), which are freely available through https://www.nzpam.govt.nz/. Schlumberger are thanked for provision of Petrel seismic interpretation software.

SUPPLEMENTARY MATERIAL

The Supplementary Material for this article can be found online at: https://www.frontiersin.org/articles/10.3389/feart.2019.00037/full#supplementary-material

REFERENCES

Brown, A. R. (2011). *Interpretation of Three-Dimensional Seismic Data*. Tulsa, OK: Society of Exploration Geophysicists and American Association of Petroleum Geologists.

Bunger, A. P., and Cruden, A. R. (2011). Modeling the growth of laccoliths and large mafic sills: role of magma body forces. *J. Geophys. Res.* 116:B02203. doi: 10.1029/2010JB007648

Caricchi, L., Biggs, J., Annen, C., and Ebmeier, S. (2014). The influence of cooling, crystallisation and re-melting on the interpretation of geodetic signals in volcanic systems. *Earth Planet. Sci. Lett.* 388, 166–174. doi: 10.1016/j.epsl.2013.12.002

Carter, R. M. (1988). Post-breakup stratigraphy of the kaikoura synthem (Cretaceous-Cenozoic), continental margin, southeastern New Zealand. *N. Z. J. Geol. Geophys.* 31, 405–429. doi: 10.1080/00288306.1988.10422141

Castro, J. M., Cordonnier, B., Schipper, C. I., Tuffen, H., Baumann, T. S., and Feisel, Y. (2016). Rapid laccolith intrusion driven by explosive volcanic eruption. *Nat. Commun.* 7:13585. doi: 10.1038/ncomms13585

Chevallier, L., and Woodford, A. (1999). Morpho-tectonics and mechanism of emplacement of the dolerite rings and sills of the western Karoo, South Africa. *S. Afr. J. Geol.* 102, 43–54.

Ebmeier, S. K., Andrews, B. J., Araya, M. C., Arnold, D. W. D., Biggs, J., Cooper, C., et al. (2018). Synthesis of global satellite observations of magmatic and volcanic deformation: implications for volcano monitoring and the lateral extent of magmatic domains. *J. Appl. Volcanol.* 7:2. doi: 10.1186/s13617-018-0071-3

Eide, C. H., Schofield, N., Lecomte, I., Buckley, S. J., and Howell, J. A. (2018). Seismic interpretation of sill complexes in sedimentary basins: implications for the sub-sill imaging problem. *J. Geol. Soc. Lond.* 175, 193–209. doi: 10.1144/jgs2017-096

Fialko, Y., and Simons, M. (2001). Evidence for on-going inflation of the Socorro magma body, New Mexico, from interferometric synthetic aperture radar imaging. *Geophys. Res. Lett.* 28, 3549–3552. doi: 10.1029/2001GL013318

Fulthorpe, C. S., Carter, R. M., Miller, K. G., and Wilson, J. (1996). Marshall paraconformity: a mid-oligocene record of inception of the Antarctic circumpolar current and coeval glacio-eustatic lowstand? *Mar. Petrol. Geol.* 13, 61–77. doi: 10.1016/0264-8172(95)00033-X

Galland, O. (2012). Experimental modelling of ground deformation associated with shallow magma intrusions. *Earth Planet. Sci. Lett.* 317, 145–156. doi: 10.1016/j.epsl.2011.10.017

Galland, O., and Scheibert, J. (2013). Analytical model of surface uplift above axisymmetric flat-lying magma intrusions: implications for sill emplacement and geodesy. *J. Volcanol. Geotherm. Res.* 253, 114–130. doi: 10.1016/j.jvolgeores.2012.12.006

Gerbault, M., Hassani, R., Novoa Lizama, C., and Souche, A. (2018). Three-dimensional failure patterns around an inflating magmatic chamber. *Geochem. Geophys. Geosyst.* 19, 749–771. doi: 10.1002/2017GC007174

Gilbert, G. K. (1877). *Report on the Geology of the Henry Mountains*. Washington, DC: US Government Printing Office.

Hansen, D. M. (2006). The morphology of intrusion-related vent structures and their implications for constraining the timing of intrusive events along the NE Atlantic margin. *J. Geol. Soc. Lond.* 163, 789–800. doi: 10.1144/0016-76492004-167

Hansen, D. M., and Cartwright, J. (2006). The three-dimensional geometry and growth of forced folds above saucer-shaped igneous sills. *J. Struct. Geol.* 28, 1520–1535. doi: 10.1016/j.jsg.2006.04.004

Hansen, D. M., Redfern, J., Federici, F., Di Biase, D., and Bertozzi, G. (2008). Miocene igneous activity in the Northern Subbasin, offshore Senegal, NW Africa. *Mar. Petrol. Geol.* 25, 1–15. doi: 10.1016/j.marpetgeo.2007.04.007

Holohan, E. P., Sudhaus, H., Walter, T. R., Schöpfer, M. P., and Walsh, J. J. (2017). Effects of host-rock fracturing on elastic-deformation source models of volcano deflation. *Sci. Rep.* 7:10970. doi: 10.1038/s41598-017-10009-6

Jackson, C. A., Schofield, N., and Golenkov, B. (2013). Geometry and controls on the development of igneous sill–related forced folds: a 2-D seismic reflection case study from offshore southern Australia. *Bulletin* 125, 1874–1890. doi: 10.1130/B30833.1

Jackson, C. A. L. (2012). Seismic reflection imaging and controls on the preservation of ancient sill-fed magmatic vents. *J. Geol. Soc. Lond.* 169, 503–506. doi: 10.1144/0016-76492011-147

Jamtveit, B., Svensen, H., Podladchikov, Y. Y., and Planke, S. (2004). Hydrothermal vent complexes associated with sill intrusions in sedimentary basins. *Geol. Soc. Lond. Spec. Publ.* 234, 233–241. doi: 10.1144/GSL.SP.2004.234.01.15

Johnson, A. M., and Pollard, D. D. (1973). Mechanics of growth of some laccolithic intrusions in the Henry mountains, Utah, I: field observations, Gilbert's model, physical properties and flow of the magma. *Tectonophysics* 18, 261–309. doi: 10.1016/0040-1951(73)90050-4

Killops, S. D., Cook, R. A., Sykes, R., and Boudou, J. P. (1997). Petroleum potential and oil-source correlation in the Great South and Canterbury Basins. *N. Z. J. Geol. Geophys.* 40, 405–423. doi: 10.1080/00288306.1997.9514773

Koch, F. G., Johnson, A. M., and Pollard, D. D. (1981). Monoclinal bending of strata over laccolithic intrusions. *Tectonophysics* 74, T21–T31. doi: 10.1016/0040-1951(81)90189-X

Lu, H., and Fulthorpe, C. S. (2004). Controls on sequence stratigraphy of a middle miocene–holocene, current-swept, passive margin: offshore Canterbury Basin, New Zealand. *Geol. Soc. Am. Bull.* 116, 1345–1366. doi: 10.1130/B25225401.1

Lu, H., Fulthorpe, C. S., Mann, P., and Kominz, M. A. (2005). Miocene-recent tectonic and climatic controls on sediment supply and sequence stratigraphy: Canterbury Basin, New Zealand. *Basin Res.* 17, 311–328. doi: 10.1111/j.1365-2117.2005.00266.x

Magee, C., Briggs, F., and Jackson, C. A. (2013a). Lithological controls on igneous intrusion-induced ground deformation. *J. Geol. Soc. Lond.* 170, 853–856. doi: 10.1144/jgs2013-029

Magee, C., Duffy, O. B., Purnell, K., Bell, R. E., Jackson, C. A. L., and Reeve, M. T. (2016b). Fault-controlled fluid flow inferred from hydrothermal vents imaged in 3D seismic reflection data, offshore NW Australia. *Basin Res.* 28, 299–318. doi: 10.1111/bre.12111

Magee, C., Hunt-Stewart, E., and Jackson, C. A. L. (2013b). Volcano growth mechanisms and the role of sub-volcanic intrusions: insights from 2D seismic reflection data. *Earth Planet. Sci. Lett.* 373, 41–53. doi: 10.1016/j.epsl.2013.04.041

Magee, C., Jackson, C. A. L., Hardman, J. P., and Reeve, M. T. (2017). Decoding sill emplacement and forced fold growth in the exmouth sub-basin, offshore northwest Australia: implications for hydrocarbon exploration. *Interpretation* 5, SK11–SK22. doi: 10.1190/INT-2016-0133.1

Magee, C., Jackson, C. A. L., and Schofield, N. (2014). Diachronous sub-volcanic intrusion along deep-water margins: Insights from the Irish Rockall Basin. *Basin Res.* 26, 85–105. doi: 10.1111/bre.12044

Magee, C., Maharaj, S. M., Wrona, T., and Jackson, C. A. L. (2015). Controls on the expression of igneous intrusions in seismic reflection data. *Geosphere* 11, 1024–1041. doi: 10.1130/GES01150.1

Magee, C., Muirhead, J. D., Karvelas, A., Holford, S. P., Jackson, C. A., Bastow, I. D., et al. (2016a). Lateral magma flow in mafic sill complexes. *Geosphere* 12, 809–841. doi: 10.1130/GES01256.1

Milne, A. D., Simpson, C., and Threadgold, P. (1975). *Well Completion Report Resolution-1, for BP, Shell, Todd (Canterbury) Services Limited*. New Zealand Geological Survey. *Unpublished open-file Petroleum Report PR648.*

Montanari, D., Bonini, M., Corti, G., Agostini, A., and Del Ventisette, C. (2017). Forced folding above shallow magma intrusions: Insights on supercritical fluid flow from analogue modelling. *J. Volcanol. Geotherm. Res.* 345, 67–80. doi: 10.1016/j.jvolgeores.2017.07.022

Morgan, S., Stanik, A., Horsman, E., Tikoff, B., de Saint Blanquat, M., and Habert, G. (2008). Emplacement of multiple magma sheets and wall rock deformation: trachyte mesa intrusion, Henry Mountains, Utah. *J. Struct. Geol.* 30, 491–512. doi: 10.1016/j.jsg.2008.01.005

Pagli, C., Wright, T. J., Ebinger, C. J., Yun, S. H., Cann, J. R., Barnie, T., et al. (2012). Shallow axial magma chamber at the slow-spreading Erta Ale Ridge. *Nat. Geosci.* 5:284. doi: 10.1038/ngeo1414

Planke, S., Rasmussen, T., Rey, S. S., and Myklebust, R. (2005), "January. Seismic characteristics and distribution of volcanic intrusions and hydrothermal vent complexes in the Vøring and Møre basins," in *Geological Society, London, Petroleum Geology Conference Series*, Vol. 6 (London: Geological Society of London), 833–844.

Pollard, D. D., and Johnson, A. M. (1973). Mechanics of growth of some laccolithic intrusions in the Henry Mountains, Utah, II: bending and failure of overburden layers and sill formation. *Tectonophysics* 18, 311–354. doi: 10.1016/0040-1951(73)90051-6

Polteau, S., Ferré, E. C., Planke, S., Neumann, E. R., and Chevallier, L. (2008a). How are saucer-shaped sills emplaced? constraints from the Golden Valley Sill, South Africa. *J. Geophys. Res.* 113:B12104. doi: 10.1029/2008JB005620

Polteau, S., Mazzini, A., Galland, O., Planke, S., and Malthe-Sørenssen, A. (2008b). Saucer-shaped intrusions: occurrences, emplacement and implications. *Earth Planet. Sci. Lett.* 266, 195–204. doi: 10.1016/j.epsl.2007.11.015

Raymer, L. L., Hunt, E. R., and Gardner, J. S. (1980). "An improved sonic transit time-to-porosity transform," in *SPWLA 21st Annual Logging Symposium* (Lafayette, LA: Society of Petrophysicists and Well-Log Analysts).

Reeves, J., Magee, C., and Jackson, C. L. (2018). Unravelling intrusion-induced forced fold kinematics and ground deformation using 3D seismic reflection data. *Volcanica* 1, 1–17. doi: 10.30909/vol.01.01.0117

Scheibert, J., Galland, O., and Hafver, A. (2017). Inelastic deformation during sill and laccolith emplacement: insights from an analytic elastoplastic model. *J. Geophys. Res.* 122, 923–945. doi: 10.1002/2016JB013754

Schiøler, P., Raine, J. I., Crundwell, M., Griffin, A., Hollis, C. J., Kulhanek, D. K., et al. (2011). *Revised Biostratigraphy and Well Correlation, Canterbury Basin, New Zealand Ministry of Economic Development. New Zealand*. Unpublished Petroleum Report PR4365.

Schmiedel, T., Kjoberg, S., Planke, S., Magee, C., Galland, O., Schofield, N., et al. (2017). Mechanisms of overburden deformation associated with the emplacement of the Tulipan sill, mid-Norwegian margin. *Interpretation* 5, SK23–SK38. doi: 10.1190/INT-2016-0155.1

Schofield, N., Alsop, I., Warren, J., Underhill, J. R., Lehné, R., Beer, W., et al. (2014). Mobilizing salt: magma-salt interactions. *Geology* 42, 599–602. doi: 10.1130/G35406.1

Schofield, N. J., Brown, D. J., Magee, C., and Stevenson, C. T. (2012). Sill morphology and comparison of brittle and non-brittle emplacement mechanisms. *J. Geol. Soc. Lond.* 169, 127–141. doi: 10.1144/0016-76492011-078

Sclater, J. G., and Christie, P. A. (1980). Continental stretching: an explanation of the post-mid-cretaceous subsidence of the central North Sea basin. *J. Geophys. Res.* 85, 3711–3739. doi: 10.1029/JB085iB07p03711

Sewell, R. J., and Gibson, I. L. (1988). Petrology and geochemistry of tertiary volcanic rocks from inland central and South Canterbury, South Island, New Zealand. *N. Z. J. Geol. Geophys.* 31, 477–492. doi: 10.1080/00288306.1988.10422145

Smallwood, J. R. (2009). Back-stripped 3D seismic data: A new tool applied to testing sill emplacement models. *Petrol. Geosci.* 15, 259–268. doi: 10.1144/1354-079309-844

Smallwood, J. R., and Maresh, J. (2002). The properties, morphology and distribution of igneous sills: modelling, borehole data and 3D seismic from the Faroe-Shetland area. *Geol. Soc. Lond. Spec. Publ.* 197, 271–306. doi: 10.1144/GSL.SP.2002.197.01.11

Spacapan, J. B., Galland, O., Leanza, H. A., and Planke, S. (2016). Igneous sill and finger emplacement mechanism in shale-dominated formations: a field study at Cuesta del Chihuido, Neuquén Basin, Argentina. *J. Geol. Soc. Lond.* 174, 422–433. doi: 10.1144/jgs2016-056

Stearns, D. W. (1978). Faulting and forced folding in the Rocky Mountains foreland. *Laramide folding associated with basement block faulting in the western United States. Geol. Soc. Am. Mem.* 151, 1–37. doi: 10.1130/MEM151-p1

Symonds, P. A., Planke, S., Frey, O., and Skogseid, J. (1998). Volcanic evolution of the western Australian continental margin and its implications for basin development. *Sediment. Basins West. Austr.* 2, 33–54.

Thomson, K., and Hutton, D. (2004). Geometry and growth of sill complexes: insights using 3D seismic from the North Rockall Trough. *Bull. Volcanol.* 66, 364–375. doi: 10.1007/s00445-003-0320-z

Timm, C., Hoernle, K., Werner, R., Hauff, F., van den Bogaard, P., White, J., et al. (2010). Temporal and geochemical evolution of the Cenozoic intraplate volcanism of Zealandia. *Earth Sci. Rev.* 98, 38–64. doi: 10.1016/j.earscirev.2009.10.002

Trude, J., Cartwright, J., Davies, R. J., and Smallwood, J. (2003). New technique for dating igneous sills. *Geology* 31, 813–816. doi: 10.1130/G19559.1

Uruski, C. I. (2010). New Zealand's deepwater frontier. *Mar. Petrol. Geol.* 27, 2005–2026. doi: 10.1016/j.marpetgeo.2010.05.010

van Wyk de Vries, B., Márquez, A., Herrera, R., Bruña, J. G., Llanes, P., and Delcamp, A. (2014). Craters of elevation revisited: forced-folds, bulging and uplift of volcanoes. *Bull. Volcanol.* 76:875. doi: 10.1007/s00445-014-0875-x

Wyllie, M. R. J., Gregory, A. R., and Gardner, L. W. (1956). Elastic wave velocities in heterogeneous and porous media. *Geophysics* 21, 41–70. doi: 10.1190/1.1438217

Conflict of Interest Statement: The authors declare that the research was conducted in the absence of any commercial or financial relationships that could be construed as a potential conflict of interest.

frontiers
in Earth Science

PERSPECTIVE
published: 15 March 2019
doi: 10.3389/feart.2019.00040

Magma Transfer Processes in the NE Japan Arc: Insights From Crustal Ambient Noise Tomography Combined With Volcanic Eruption Records

Georg F. Zellmer[1], Kai-Xun Chen[2], Yuancheng Gung[2], Ban-Yuan Kuo[3] and Takeyoshi Yoshida[4]*

[1] Volcanic Risk Solutions, Massey University, Palmerston North, New Zealand, [2] Department of Geosciences, National Taiwan University, Taipei, Taiwan, [3] Institute of Earth Sciences, Academia Sinica, Taipei, Taiwan, [4] Department of Earth Science, Tohoku University, Sendai, Japan

Edited by:
Mattia Pistone,
Université de Lausanne, Switzerland

Reviewed by:
Pablo Samaniego,
UMR6524 Laboratoire Magmas et Volcans (LMV), France
Sigrún Hreinsdóttir,
GNS Science, New Zealand

***Correspondence:**
Georg F. Zellmer
g.f.zellmer@massey.ac.nz

Specialty section:
This article was submitted to Volcanology, a section of the journal Frontiers in Earth Science

Received: *01 October 2018*
Accepted: *20 February 2019*
Published: *15 March 2019*

Citation:
Zellmer GF, Chen K-X, Gung Y, Kuo B-Y and Yoshida T (2019) Magma Transfer Processes in the NE Japan Arc: Insights From Crustal Ambient Noise Tomography Combined With Volcanic Eruption Records. Front. Earth Sci. 7:40. doi: 10.3389/feart.2019.00040

Subduction zone magmatic budgets and crustal growth processes depend on poorly constrained intrusive:extrusive ratios of arc magmas. Published ambient noise tomography data from northeast Japan reveal upper crustal low-V_S bodies, indicating elevated temperatures of plutonic rocks beneath most sites of active arc-front volcanoes, with the exception of Zao volcano. Strikingly, when small eruptions (VEI 1 to VEI 3) from arc-front volcanoes in the last 2 kyr are considered, Zao has erupted most frequently and has produced a more than three times greater tephra volume than any of the other volcanoes. We propose that the frequent low-volume volcanism at Zao is fed by dikes that traverse the crustal section rapidly, fracturing through brittle lithologies. Beneath the other volcanoes, hotter and more ductile plutonic bodies have developed through repeated intrusive activity, hindering magma transport to the surface. This positive feedback mechanism ultimately results in cataclysmic caldera-forming events. We show that the number of late Cenozoic calderas is higher above the imaged low-V_S crust, consistent with this interpretation. We propose that generation of plutonic bodies is facilitated by volcaniclastic materials buried in a Miocene rift graben, which dampen fracture propagation and promote repeated sill intrusion. In contrast, transcurrent faulting has moved cold Cretaceous basement of the fore-arc range into the arc-front beneath Zao. These brittle rocks instead provide fracture pathways explored by magmas rapidly rising to the surface. The combined data imply that millions of years of crustal growth and tectonic history have a direct control on present-day volcanic eruption style.

Keywords: heat incubation, crustal magma ascent, crustal growth history, volcanic eruption style, Tohoku volcanism, brittle-ductile transition

INTRODUCTION

The relative proportion of intrusive versus extrusive magmatism in volcanic arcs, and the processes that control this ratio, have long been debated (Crisp, 1984; Wallace, 2001; White et al., 2006). Our understanding of magmatic budgets in subduction zones depends on our ability to quantify the time-integrated volumes of emplacement of subvolcanic plutons and the volcanic outputs. At present, estimated intrusive:extrusive proportions range from 10:1 to 2:1 (White et al., 2006), and this relatively large range is indicative of our current ignorance of this aspect of arc magmatism. At global scale, intrusive:extrusive ratios may depend on magma production rates and the volatile content of the primary melts, which are in turn dependent on subduction parameters and the mantle wedge structure (Turner and Langmuir, 2015a,b; Turner et al., 2016), and on crustal thickness and tectonic stresses in the overriding crust. Intrusive:extrusive ratios may thus significantly vary between different subduction zones (Zellmer, 2008; Zellmer et al., 2015).

This study turns to regional scale variations in intrusive versus extrusive magmatism, and the factors that may influence their relative proportion and associated feedbacks to volcanic activity. The NE Japan arc arguably offers one of the most extensive and detailed datasets with regard to Cenozoic geological history, present day crustal structure, and long-term as well as present-day magmatic activity in the world (Yoshida et al., 2014, and references therein). Combined with the most recent ambient-noise tomographic data of the overriding crust (Chen et al., 2018) and volcanic activity data from the Pliocene (Yoshida et al., 1999, 2014; Acocella et al., 2008) to the present day (Global Volcanism Program, 2013), we show that the processes that control intrusive:extrusive proportions are manifold, and that millions of year of crustal history can have a direct influence on present-day volcanic as well as plutonic activity. This study demonstrates that a good geological and geophysical understanding beyond subduction zone magmatism is critical in elucidating this long-standing research topic.

GEOLOGICAL BACKGROUND

Yoshida et al. (2014) has provided a detailed review of the evolution of late Cenozoic magmatism and its link to the crust-mantle structure in the NE Japan Arc. We compiled a simplified structural and geological map (**Figure 1A**) with features relevant to this contribution. The Tohoku region is characterized by a series of Neogene rift basins, which developed simultaneously with the opening of the back-arc basin of the Japan Sea (Sato, 1994; Okamura et al., 1995). Bimodal volcanic activity during the opening of the Japan Sea filled these basins with sediments, including ignimbrites and reworked ignimbrites, many now altered to green tuffs (Yamada and Yoshida, 2011). Miocene to more recent faulting transects these rift basins (**Figure 1A**).

The currently active volcanic arc front is developed on or close to the youngest, easternmost rift system. Magma generation in the mantle wedge is thought to be most productive in so-called "hot fingers" (Tamura et al., 2002), which may be related to small-scale three-dimensional convections within the mantle wedge (Honda and Yoshida, 2005). Most of the young calderas (Yoshida et al., 1999, 2014; Acocella et al., 2008) and all of the Holocene volcanoes have been linked to melt generation in these hot fingers, forming spatially separated clusters of volcanic activity (**Figure 1A**).

There is a significant body of literature on the crustal composition and structure of NE Japan, and many geophysical (including conventional body-wave tomographic) studies have been conducted to elucidate subvolcanic processes and lithologies (e.g., Hasegawa et al., 2000; Nakajima et al., 2001, 2006; Shibazaki et al., 2008; Zhao et al., 2011; Takada and Fukushima, 2013; Chen et al., 2018; Niu et al., 2018). Beneath the modern volcanic arc, the deep crust is likely composed of hornblende pyroxene gabbros and amphibolites, while the mid- to upper crust beneath the volcanic clusters is thought to consist of pluton complexes representing subvolcanic intrusions (Sato et al., 2002; Nishimoto et al., 2005; Nishimoto et al., 2008; Takada and Fukushima, 2013). Likely, ephemeral magma-mush bodies are also present, as indicated by caldera magmatism (Aizawa et al., 2006), but too small to be resolved by current geophysical techniques. Although Chen et al. (2018) interpreted mid- to shallow crustal low velocity zones as magma reservoirs of the Quaternary magmatic system, the magnitude of the observed shear-wave anomalies ($\delta V_S/V_S < 10\%$) is more consistent with high-temperature intrusive rocks than with melt-rich magma chambers.

East of the arc-front, pre-Cenozoic basement rocks are exposed in the Kitakami and Abukuma mountains (**Figure 1A**). The latter consist exclusively of Cretaceous granitic rocks (Tsuchiya and Kanisawa, 1994; Hirahara et al., 2015, and references therein).

METHODS

Yoshida et al. (1999) provides comprehensive age information of all Late Cenozoic calderas of the Tohoku province. Here, we only consider the location of the youngest calderas, formed since the Pliocene (Acocella et al., 2008).

There are two recent tomographic models of the crust beneath the Tohoku region: (i) a conventional body-wave model, with *c.* 10 km depth resolution and *c.* 0.1–0.2° lateral resolution (Niu et al., 2018); and (ii) an ambient noise (surface wave) model (Chen et al., 2018), which employs multiple scales of grid in horizontal dimension with 2–5 km thick layers in the upper to mid-crust, i.e., sampling the upper crust with higher resolution than body-wave tomography. The ambient noise approach has no errors in "earthquake" locations, because each station is treated as an earthquake, and station positions are precisely and accurately known. Uneven distribution of earthquakes that often jeopardizes body wave tomography is also avoided. Furthermore, reduced ray-crossing in the shallow crust due to near-vertical ray paths of body waves approaching the surface is remedied using surface waves. The ambient noise model thus provides improved sensitivity in the mid- to upper crust, but resolving power degrades with depth, a natural limitation of surface waves (cf. Huang et al., 2012). It is important to note that a

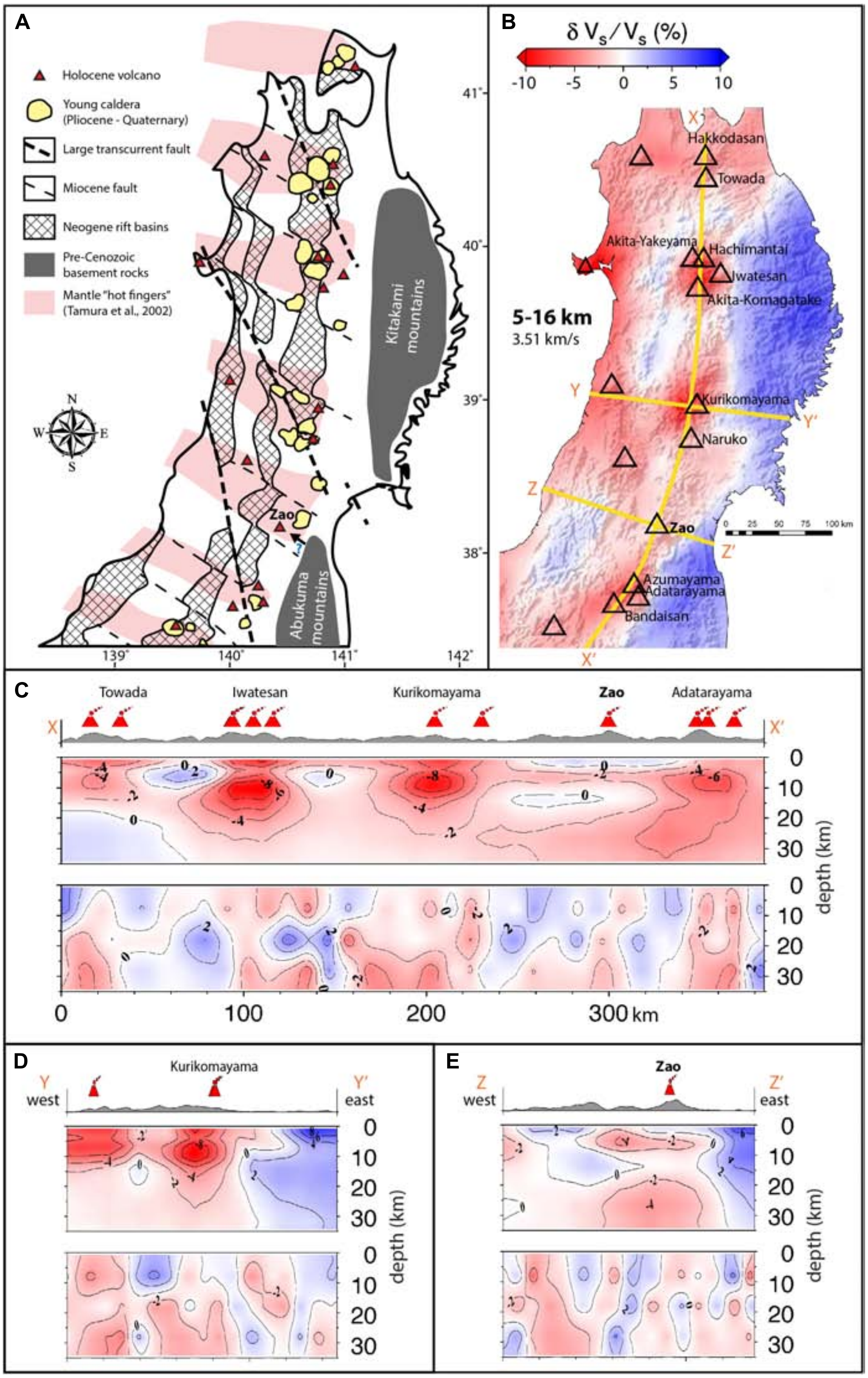

FIGURE 1 | (A) Simplified geological map of the Tohoku region, showing major faults partially offsetting Neogene rift basins (adapted from Yoshida et al., 2014). Mantle low-velocity zones ("hot fingers" of Tamura et al., 2002) are shown, as well as the location of young (Pliocene to Quaternary) calderas (Yoshida et al., 1999; Acocella et al., 2008) and Holocene arc volcanoes (Global Volcanism Program, 2013). At depth, pre-Cenozoic basement rocks of the Abukuma mountains may have displaced (indicated by a small arrow with a blue question mark) into the area of Zao volcano through transcurrent faulting. **(B)** Average $\delta V_S/V_S$ of the recent ambient noise tomography model (Chen et al., 2018) in the Tohoku region, in the depth range of 5–16 km. Note the good correspondence of the greatest arc-front anomalies with the location of young caldera clusters in panel **A**. Yellow lines indicate cross-sections in panels **C–E**. **(C)** Along-arc cross-section of the shear-wave velocity anomaly to a depth of 34 km. Top section shows ambient noise tomography (Chen et al., 2018), as in panel **B**, with highest sensitivity in the mid- to upper crust. Bottom section shows conventional body-wave tomography model (Niu et al., 2018), using local earthquakes, with higher sensitivity in the lower crust. **(D,E)** Across arc profiles through Kurikomayama and Zao volcanoes. Data sources and scales as in panel **C**.

precise, quantitative comparison of spatial resolution between two models requires synthetic modeling with artificial structures for both data sets, which is an unrealistic task. Nevertheless, resolution can be roughly estimated as 20–30 km and 4–5 km in horizontal and vertical directions, respectively, in the upper crust. Brief descriptions of the properties and relative merits of the two recent tomographic models are given in the **Supplementary Material**.

To investigate processes that control magma transfer through the crust, we employed the results of the ambient noise model, generating a tomographic map of S-wave velocity deviations from an average value 3.51 km s^{-1} (±0.11 km s^{-1}, 1SD) at a mid- to upper crustal depth range of 5–16 km (**Figure 1B**). Further, we provide crustal cross-sections of both ambient noise (Chen et al., 2018) and body-wave (Niu et al., 2018) models down to 34 km depth, one along-arc (**Figure 1C**) and two across-arc (**Figures 1D,E**). In these cross-sections, velocity anomalies are referenced to the layer averages of the respective models. We then estimated the subvolcanic intrusive volumes beneath each volcano by integrating the tomographic volume with $\delta V_S/V_S \leq -2\%$ over a depth range of 5–16 km and radii of 4–13 km in 1 km increments. The –2% velocity criterion was chosen, because it is the common feature of mid- to upper crustal ambient noise tomography among the volcanic groups in the Tohoku area (Chen et al., 2018), suggesting that this corresponds to recent igneous material. The radii to be chosen are less well-defined, but reflect the range of distances (8–26 km) between volcanoes in each volcano group. To avoid potential overlap issues of intrusive volumes beneath individual volcanoes, we plot intrusive volume ratios compared to Zao volcano, with uncertainties (1σ) based on the range in chosen radii.

For the record of volcanic eruptions, we have consulted the Global Volcanism Program (2013). We have taken into account all eruptions since AD 0 of the 12 arc-front volcanoes for which subsurface tomographic data was available. The Volcanic Explosivity Index (VEI, Newhall and Self, 1982) of this dataset ranged from 1 to 5. To investigate magma transfer from depth to the surface, this perspective focuses on the small (VEI 1-3) eruptions, because ≥ VEI 4 events typically tap upper crustal reservoirs, rather than representing smaller melt batches ascending from the deep crust (cf. Zellmer and Annen, 2008). Based on Monte Carlo simulations, the average eruptive volumes and uncertainties (1σ) of these small eruptions were estimated as follows: for VEI 1, 0.00055 ± 0.00026 km^3; for VEI 2, 0.0055 ± 0.0026 km^3; and for VEI 3, 0.055 ± 0.026 km^3.

RESULTS

Tomographic Observations

The recent conventional tomography approach (Niu et al., 2018) supports a model for deep crustal hot zones (Annen et al., 2006) above the hot fingers (Tamura et al., 2002), as seen in the lower panels of **Figures 1C–E**. In the mid- to upper crust, however, the resolution and accuracy of the ambient noise tomographic inversion (Chen et al., 2018) is better than that of the conventional tomography, as discussed above. Beneath the arc front, the former reveals slower than average seismic S-wave velocities below the clusters of several Holocene volcanoes and young calderas (**Figure 1B**, and top panels of **Figures 1C,D**). $\delta V_S/V_S$ ratios down to less than –8% are observed. These values are consistent with the existence of hot plutons beneath these clusters (Yoshida et al., 2014). By contrast, the pre-Cenozoic basement rocks east of the arc yield faster than average seismic S-wave velocities (**Figures 1B,D,E**).

Strikingly, however, there is little tomographic evidence for hot plutons beneath Zao volcano (**Figure 1B**, and top panels of **Figures 1C,E**). Zao represents the single Holocene volcano in this area, compared to the clusters of volcanoes in most other areas (**Figure 1A**). In addition, only one young caldera is found within 20 km of Zao, compared to clusters of young calderas in the other volcanically active arc-front areas. Upper crustal S-wave velocity anomalies of down to *c*. –4% are only seen in west of Zao, towards the back-arc (**Figure 1E**).

Volcanological Observations

We have investigated frequency and size of the most recent (since AD 0) volcanic activity in the arc-front volcanoes for which subsurface tomographic data were available. We have restricted this analysis to the last *c*. 2 kyr in order to (i) have a near-complete eruptive record, including the small VEI 1–3 eruptions, and to (ii) be able to link this volcanic activity to the present-day crustal tomographic observations. **Figure 2A** is a compilation of the number of VEI 1 to VEI 5 eruptions recorded in the Global Volcanism Program (2013). It is evident that VEI 1 and VEI 2 eruptions dominate in this region, followed by VEI 3 eruptions. Larger eruptions have been rare during the last 2 kyr. On average, all volcanoes within clusters have erupted 4–5 times over this time period. Strikingly, the eruption frequency at Zao volcano is 7 times higher, with more than 30 small eruptions (VEI 1–3) over the last 2 kyr.

DISCUSSION

We have combined the ambient noise tomographic and the volcanological observations in **Figure 2B**. For each Holocene volcano, we estimated the volume ratios of subvolcanic intrusions in the mid to upper crust compared to Zao (5–16 km depth, 4–13 km radii from vent considered at 1 km intervals, $\delta V_S/V_S \leq -2\%$, see **Supplementary Table S1** in the **Supplementary Material**). For each volcano, we also estimated the total volume generated from small (VEI 1–3) eruptions since AD 0 (see **Supplementary Table S2** in the **Supplementary Material**), to compare the volumes of the most frequent eruptions with the state of the mid- to upper subvolcanic crust. Zao is clearly distinct from the other Holocene arc-front volcanoes on **Figure 2B**, with ≥ 3 times greater estimated eruptive volumes from VEI 1–3 eruptions, at *c*. 2–4 times lower intrusive volume.

If the seismically slow regions of the mid- to upper crust shown in **Figure 1** indeed represent hot intrusive bodies, the combined data suggest that these may mute frequent small eruptions from the overlying volcanic edifices. Intrusive magmatism is likely pronounced in the Tohoku region due to

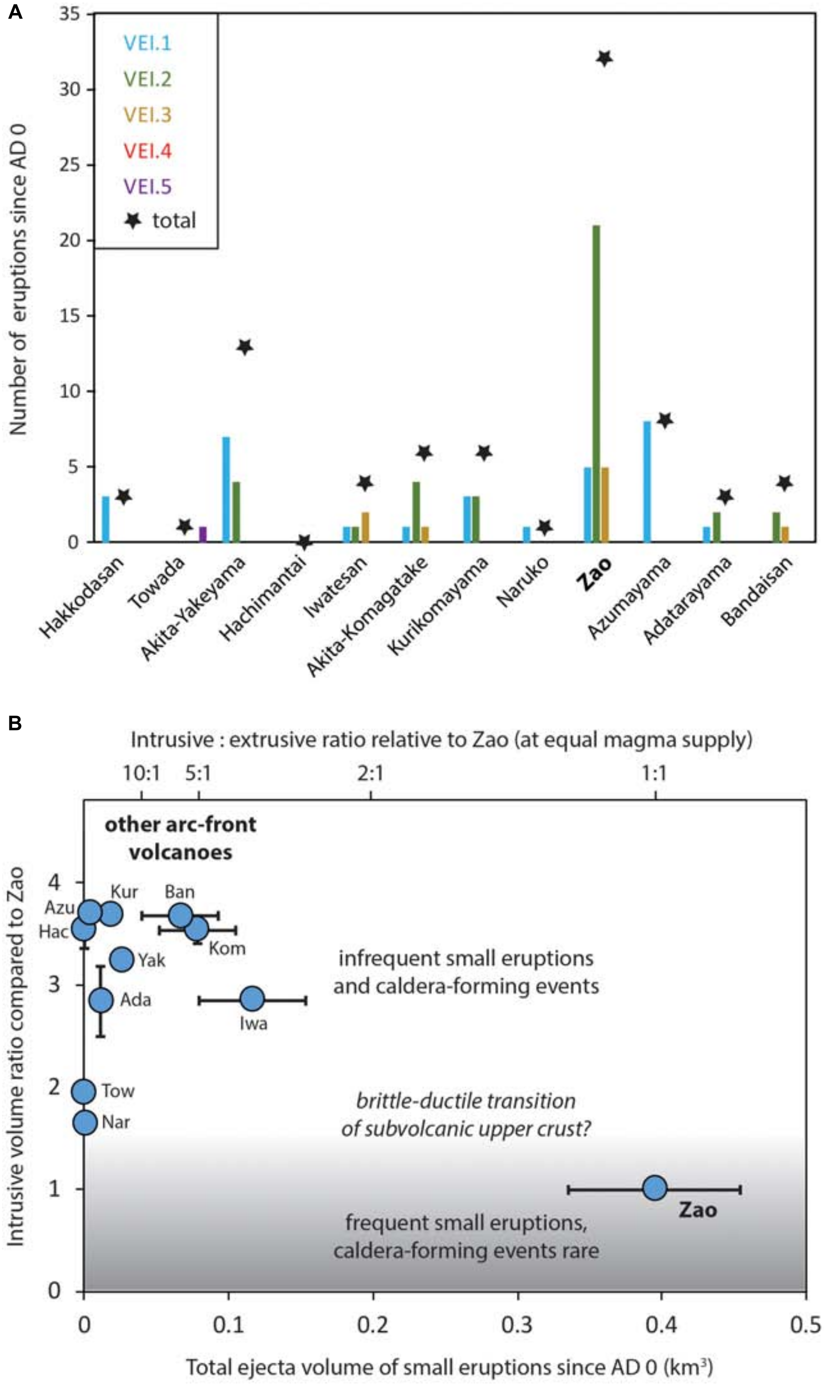

FIGURE 2 | (A) Number of eruptions since AD 0 from each of the arc-front volcanoes listed in **Figure 1**, as recorded by the Global Volcanism Program (2013), split by Volcanic Explosivity Index (VEI), and summed for each center (star). Note the large number of eruptions at Zao, dominated by VEI 2 eruptions. **(B)** Subvolcanic intrusive volume ratios (w.r.t. Zao) versus total ejecta volumes of VEI 1 to VEI 3 eruptions since AD 0. See "Methods" section for details. Uncertainties (1σ) in both parameters are indicated when larger than symbol size. Abbreviations: Towada (Tow), Akita-Yakeyama (Yak), Hachimantai (Hac), Iwatesan (Iwa), Akita-Komagatake (Kom), Kurikomayama (Kur), Naruko (Nar), Azumayama (Azu), Adatarayama (Ada), Bandaisan (Ban). Hakkodasan is excluded, as the ambient noise velocity model has too poor constraints in the northernmost and westernmost regions to confidently estimate intrusive volume, due to sparse ray-path coverage in these areas.

present-day within-arc compressive stresses, which may impede the opening of magmatic conduits when compared to other arcs (Zellmer, 2008; Chaussard and Amelung, 2014). Then, the intrusions may act as an additional barrier for magma ascent to the surface. Hot plutons and potentially some small ephemeral magma-mushes have too low viscosities to allow melt propagation through tensile fractures (Keller et al., 2013; Galetto et al., 2017), leading to trapping of consecutively ascending melt batches. Heat incubation in these systems is the consequence of a positive feedback mechanism, resulting in frequent intrusions but infrequent eruptions, some of which may be large caldera-forming events that drain upper crustal evolved melts from rapidly formed but ephemeral magma-mush bodies (Michaut and Jaupart, 2006). Most volcanoes in Tohoku appear to operate under this regime.

By contrast, the apparent scarcity of recent mid- to upper crustal intrusives beneath Zao volcano may allow a system of frequent, low-volume eruptive events to be established, directly mirroring the frequent transport of low-volume magma batches through the crustal section (e.g., Zellmer and Annen, 2008), originating from the deep crustal hot zone (Annen et al., 2006) that may have been resolved by the conventional tomographic model (Niu et al., 2018, cf. lower panels of **Figures 1C–E**). Here, we envisage brittle, high viscosity mid- to upper crustal lithologies that allow magmatic fractures to propagate to the surface. Intrusions and associated caldera-forming events are less frequent in this case. Eruptive products of Zao volcano might be expected to be more primitive than those of the other arc-front volcanoes. Interestingly, however, neither the petrography nor the geochemistry of eruptives from Zao appear to be fundamentally different from those of other arc-front volcanoes in the Tohoku region (Tatsumi et al., 2008; Takahashi et al., 2013). This may indicate that mafic to intermediate arc magmatic evolution dominantly occurs in the deep crust (Annen et al., 2006), prior to magma ascent.

What lithologies does the brittle crust beneath Zao volcano consist of? We see that left-lateral Miocene faults with significant surface offsets of up to *c.* 25 km exist in southern Tohoku (**Figure 1A**), related to Miocene back-arc opening with large counter-clockwise movements prior to more recent compressional kinematics (Acocella et al., 2008; Yamada and Yoshida, 2011). The total offset of the most recent Neogene rift grabens indicates a net northwestward movement of crustal rocks above the melt generation zone in the mantle beneath Zao. We postulate that cold and brittle mid-to upper crustal Cretaceous granitoids exposed in the Abukuma mountains east of Zao have been displaced to beneath Zao volcano since the Miocene, allowing fracturing of magmas from the deep crust to the surface. Ambient-noise tomographic data (top panels of **Figures 1D,E**) indicate that, at mid-crustal levels, the seismically fast fore-arc region extends further toward the arc front than suggested by the surface outcrops of the Kitakami and Abukuma mountain belts (**Figure 1A**). Further, slightly reduced upper crustal S-wave anomalies in the backarc of Zao (**Figure 1E**) may represent previous arc-front intrusions, which were also displaced westward since the Miocene.

We note that this idea is in contrast to the notion that old within-arc batholiths may act as barriers that deviate vertical melt ascent, which has recently been suggested as a reason for the lateral offset of Mount St. Helens from the main Cascades arc (Bedrosian et al., 2018). We suggest that the tectonic strike-slip movement of the Cretacious granitoids in the eastern Tohoku region resulted in vertical fracture formation, and these fractures are currently exploited by ascending magmas beneath Zao. It is therefore the combination of cold, brittle lithologies and preexisting fractures that would facilitate magma ascent.

Our knowledge of the volcanic and tectonic history of NE Japan also allows us to discuss the potential reasons for an onset of more pronounced intrusive activity in subduction zones in general. As seen in **Figure 1A**, most calderas, which are indicative of intrusions (Aizawa et al., 2006), are situated within the Neogene rift basin filled with volcaniclastic and sedimentary successions (Yoshida et al., 2014). Magma ascent through such strata may be hampered by the existence of subhorizontal rheological and density boundaries that promote lateral magma intrusions and the formation of sills (Taisne and Jaupart, 2009; Menand, 2011; Galetto et al., 2017). In contrast, old and structurally isotropic plutonic basement rocks, as postulated to exist in the upper crust beneath Zao, may not constitute suitable wall-rocks for sill intrusions, which typically require layered, anisotropic hosts lithologies (Rocchi and Breitkreuz, 2018).

This work highlights that the concept of a constant intrusive:extrusive proportion of arc magmatism is fundamentally flawed, at least on a regional level. As we only have a present-day geophysical picture of upper crustal structure, we are unable to quantify intrusion histories. However, our data show that intrusive:extrusive ratios can vary significantly between centers of activity within individual volcanic arcs, and suggest that they may vary significantly through time. If the total magma flux per unit area into the subvolcanic crust is taken as equal for each volcano cluster, intrusive:extrusive ratios relative to Zao will scale with ejecta volumes. Then, **Figure 2B** suggests that intrusive:extrusive ratios at Zao are currently at least 3 times lower than at Iwatesan, and 5 to >20 times lower than at the other Holocene volcanoes in the Tohoku region.

In summary, arc magmatism in the Tohoku area has allowed us to elucidate the long-standing question on the processes that control volcanism versus plutonism in subduction zone environments. Qualitatively, the brittle versus ductile behavior of the subvolcanic crust and variations in the rheology and structural anisotropy of crustal lithologies appear to play a major role in controlling magma transport to the surface. This indicates that typically, millions of years of crustal history and tectonism will exert fundamental controls on the style of subduction zone magmatism, and need to be deciphered before more quantitative progress can be made in assessing the relative proportions of intrusive and extrusive magmatic activity in any volcanically active area.

AUTHOR CONTRIBUTIONS

GZ conceived the idea, combined all data, and wrote the manuscript. K-XC provided tomographic maps and cross sections, calculated subvolcanic intrusive volumes, and compiled the new data from the Global Volcanism Program. YG and B-YK assisted with the interpretation of the ambient noise tomography results. TY contributed to the discussion of crustal geology and magmatic processes in the Tohoku region.

FUNDING

This work was supported by Marsden Standard Grant MAU1704 to GZ, Ministry of Science and Technology, Taiwan (MOST) Grants 107-2116-M-001-MY3 and 106-2116-M-002-001 to B-YK and YG, respectively, and Japan Society for the Promotion of Science (JSPS) KAKENHI Grant 26109003 to TY.

ACKNOWLEDGMENTS

We thank Masao Ban for discussions, and MP for his invitation to contribute to this research topic as well as editorial handling of this perspective.

SUPPLEMENTARY MATERIAL

The Supplementary Material for this article can be found online at: https://www.frontiersin.org/articles/10.3389/feart.2019.00040/full#supplementary-material

REFERENCES

Acocella, V., Yoshida, T., Yamada, R., and Funiciello, F. (2008). Structural control on late miocene to quaternary volcanism in the NE Honshu arc, Japan. *Tectonics* 27:TC5008. doi: 10.1029/2008TC002296

Aizawa, K., Acocella, V., and Yoshida, T. (2006). "How the development of magma chambers affects collapse calderas: insights from an overview," in *Mechanisms of Activity and Unrest at Large Calderas*, Vol. 269, eds C. Troise, G. De Natale, and C. R. J. Kilburn (London: Geological Society, Special Publications), 65–81. doi: 10.1144/GSL.SP.2006.269.01.05

Annen, C., Blundy, J. D., and Sparks, R. S. J. (2006). The genesis of intermediate and silicic magmas in deep crustal hot zones. *J. Petrol.* 47, 505–539. doi: 10.1093/petrology/egi084

Bedrosian, P. A., Peacock, J. R., Bowles-Martinez, E., Schultz, A., and Hill, G. J. (2018). Crustal inheritance and a top-down control on arc magmatism at Mount St Helens. *Nat. Geosci.* 11, 865–870. doi: 10.1038/s41561-018-0217-2

Chaussard, E., and Amelung, F. (2014). Regional controls on magma ascent and storage in volcanic arcs. *Geochem. Geophys. Geosyst.* 15, 1407–1418. doi: 10.1002/2013GC005216

Chen, K.-X., Gung, Y., Kuo, B.-Y., and Huang, T.-Y. (2018). Crustal magmatism and deformation fabrics in northeast Japan revealed by ambient noise tomography. *J. Geophys. Res. Solid Earth* 123, 8891–8906. doi: 10.1029/2017JB015209

Crisp, J. A. (1984). Rates of magma emplacement and volcanic output. *J. Volcanol. Geother. Res.* 20, 177–211. doi: 10.1016/0377-0273(84)90039-8

Galetto, F., Acocella, V., and Caricchi, L. (2017). Caldera resurgence driven by magma viscosity contrasts. *Nat. Commun.* 8:1750. doi: 10.1038/s41467-017-01632-y

Global Volcanism Program (2013). *Volcanoes of the World, v. 4.7.4*, ed. Venzke, E. (Washington, D.C: Smithsonian Institution). Available at: https://doi.org/10.5479/si.GVP.VOTW4-2013 (accessed September 30, 2018).

Hasegawa, A., Yamamoto, A., Umino, N., Miura, S., Horiuchi, S., Zhao, D., et al. (2000). Seismic activity and deformation process of the overriding plate in the northeastern Japan subduction zone. *Tectonophysics* 319, 215–239. doi: 10.1016/S0040-1951(99)00296-6

Hirahara, Y., Senda, R., Takahashi, T., Tsuchiya, N., Kagashima, S., Yoshida, T., et al. (2015). Spatial variation of Sr-Nd-Hf isotopic compositions from Cretaceous to Paleogene granitoids in Northeastern Japan Arc. *Ganseki Kobutsu Kagaku* 44, 91–111. doi: 10.2465/gkk.130830

Honda, H., and Yoshida, T. (2005). Effects of oblique subduction on the 3-D pattern of small-scale convection within the matle wedge. *Geophys. Res. Lett.* 32:L13307. doi: 10.1029/2005GL023106

Huang, T.-Y., Gung, Y., Liang, W.-T., Chiao, L.-Y., and Teng, L. S. (2012). Broad-band rayleigh wave tomography of Taiwan and its implications on gravity anomalies. *Geophys. Res. Lett.* 39:L05305. doi: 10.1029/2011GL050727

Keller, T., May, D. A., and Kaus, B. J. P. (2013). Numerical modelling of magma dynamics coupled to tectonic deformation of lithosphere and crust. *Geophys. J. Int.* 195, 1406–1442. doi: 10.1093/gji/ggt306

Menand, T. (2011). Physical controls and depth of emplacement of igneous bodies: a review. *Tectonophysics* 500, 11–19. doi: 10.1016/j.tecto.2009.10.016

Michaut, C., and Jaupart, C. (2006). Ultra-rapid formation of large volumes of evolved magma. *Earth Planet. Sci. Lett.* 250, 38–52. doi: 10.1016/j.epsl.2006.07.019

Nakajima, J., Hasegawa, A., Horiuchi, S., Yoshimoto, K., Yoshida, T., and Umino, N. (2006). Crustal heterogeneity around the Nagamachi–Rifu fault, northeastern Japan, as inferred from travel-time tomography. *Earth Planets Space* 58, 843–853. doi: 10.1186/BF03351989

Nakajima, J., Matsuzawa, T., Hasegawa, A., and Zhao, D. (2001). Three-dimensional structure of Vp, Vs and Vp/Vs beneath northeastern Japan: implications for arc magmatism and fluids. *J. Geophys. Res.* 106, 21843–21857. doi: 10.1029/2000JB000008

Newhall, C. G., and Self, S. (1982). The volcanic explosivity index (VEI): an estimate of explosive magnitude for historical volcanism. *J. Geophys. Res. Atmos.* 82, 1231–1238. doi: 10.1029/JC087iC02p01231

Nishimoto, S., Ishikawa, M., Arima, M., and Yoshida, T. (2005). Laboratory measurement of P-wave velocity in crustal and upper mantle xenoliths from Ichino-megata, NE Japan: ultrabasic hydrous lower crust beneath the NE Honshu arc. *Tectonophysics* 396, 245–259. doi: 10.1016/j.tecto.2004.12.010

Nishimoto, S., Ishikawa, M., Arima, M., Yoshida, T., and Nakajima, J. (2008). Simultaneous high P–T measurements of ultrasonic compressional and shear wave velocities in Ichino-megata mafic xenoliths: their bearings on seismic velocity perturbations in lower crust of northeast Japan arc. *J. Geophys. Res.* 113:B12212. doi: 10.1029/2008JB005587

Niu, X., Zhao, D., and Li, J. (2018). Precise relocation of low-frequency earthquakes in Northeast Japan: new insight into arc magma and fluids. *Geophys. J. Int.* 212, 1183–1200. doi: 10.1093/gji/ggx445

Okamura, Y., Watanabe, M., Morijiri, R., and Satoh, M. (1995). Rifting and basin inversion in the eastern margin of the Japan Sea. *Island Arc* 4, 166–181. doi: 10.1111/j.1440-1738.1995.tb00141.x

Rocchi, S., and Breitkreuz, C. (2018). "Physical geology of shallow-level magmatic systems - an introduction," in *Physical Geology of Shallow Magmatic Systems. Advances in Volcanology (An Official Book Series of the International Association of Volcanology and Chemistry of the Earth's Interior)*, eds S. Rocchi and C. Breitkreuz (New York, NY: Springer), 1–10. doi: 10.1007/11157_2017_32

Sato, H. (1994). The relationship between Late Cenozoic tectonic events and stress field and basin development in northeast Japan. *J. Geophys. Res.* 99, 22261–22274. doi: 10.1029/94JB00854

Sato, H., Imaizumi, T., and Yoshida, T. (2002). Tectonic evolution and deep to shallow geometry of Nagamachi-Rifu active fault system, NE Japan. *Earth Planets Space* 54, 1039–1043. doi: 10.1186/BF03353298

Shibazaki, B., Garatani, K., Iwasaki, T., Tanaka, A., and Iio, Y. (2008). Faulting processes controlled by the nonuniform thermal structure of the crust and uppermost mantle beneath the northeastern Japanese island arc. *J. Geophys. Res.* 113:B08415. doi: 10.1029/2007JB005361

Taisne, B., and Jaupart, C. (2009). Dike propagation through layered rocks. *J. Geophys. Res.* 114:B09203. doi: 10.1029/2008JB006228

Takada, Y., and Fukushima, Y. (2013). Volcanic subsidence triggered by the 2011 Tohoku earthquake in Japan. *Nat. Geosci.* 6, 637–641. doi: 10.1038/ngeo1857

Takahashi, T., Hirahara, Y., Miyazaki, T., Senda, R., Chang, Q., Kimura, J.-I., et al. (2013). Primary magmas at the volcanic front of the NE Japan arc: coeval eruption of crustal low-K tholeiitic and mantle-derived medium-K calc-alkaline basalts at Azuma volcano. *J. Petrol.* 54, 103–148. doi: 10.1093/petrology/egs065

Tamura, Y., Tatsumi, Y., Zhao, D., Kido, Y., and Shukuno, H. (2002). Hot fingers in the mantle wedge: new insights into magma genesis in subduction zones. *Earth Planet. Sci. Lett.* 197, 105–116. doi: 10.1016/S0012-821X(02)00465-X

Tatsumi, Y., Takahashi, T., Hirahara, Y., Chang, Q., Miyazaki, T., Kimura, J.-I., et al. (2008). New insights into andesite genesis: the role of mantle-derived calc-alcalic and crust-derived tholeiitic melts in magma differentiation beneath Zao volcano, NE Japan. *J. Petrol.* 49, 1971–2008. doi: 10.1093/petrology/egn055

Tsuchiya, N., and Kanisawa, S. (1994). Early Cretaceous Sr-rich silicic magmatism by slab melting in the Kitakami Mountains, northeast Japan. *J. Geophys. Res.* 99, 22205–22220. doi: 10.1029/94JB00458

Turner, S. J., and Langmuir, C. H. (2015a). The global chemical systematics of arc front stratovolcanoes: evaluating the role of crustal processes. *Earth Planet. Sci. Lett.* 422, 182–193. doi: 10.1016/j.epsl.2015.03.056

Turner, S. J., and Langmuir, C. H. (2015b). What processes control the chemical compositions of arc front volcanoes? *Geochem. Geophys. Geosyst.* 16, 1865–1893. doi: 10.1002/2014GC005633

Turner, S. J., Langmuir, C. H., Katz, R. F., Dungan, M. A., and Escrig, S. (2016). Parental arc magma compositions dominantly controlled by mantle-wedge thermal structure. *Nat. Geosci.* 9, 772–776. doi: 10.1038/ngeo2788

Wallace, P. J. (2001). Volcanic SO_2 emissions and the abundance and distribution of exsolved gas in magmas. *J. Volcanol. Geother. Res.* 108, 85–106. doi: 10.1016/S0377-0273(00)00279-1

White, S. M., Crisp, J. A., and Spera, F. J. (2006). Long-term volumetric eruption rates and magma budgets. *Geochem. Geophys. Geosyst.* 7:Q03010. doi: 10.1029/2005GC001002

Yamada, R., and Yoshida, T. (2011). Relationships between Kuroko volcanogenic massive sulfide (VMS) deposits, felsic volcanism, and island arc development in the northeast Honshu arc. *Mineralium Deposita* 46, 431–448. doi: 10.1007/s00126-011-0362-7

Yoshida, T., Aizawa, K., Nagahashi, Y., Sato, H., Ohguchi, T., Kimura, J., et al. (1999). Geological history of late cenozoic island arc volcanism in Northeast Honshu arc and the formation of caldera swarms. *Earth Monthly* 27, 123–129.

Yoshida, T., Kimura, J.-I., Yamada, Y., Acocella, V., Sato, H., Zhao, D., et al. (2014). "Evolution of late Cenozoic magmatism and the crust-mantle structure in the NE Japan Arc," in *Orogenic Andesites and Crustal Growth*, Vol. 385, eds A. Gómez-Tuena, S. M. Straub, and G. F. Zellmer (London: Geological Society, Special Publications), 335–387. doi: 10.1144/SP385.15

Zellmer, G. F. (2008). "Some first order observations on magma transfer from mantle wedge to upper crust at volcanic arcs," in *Dynamics of Crustal Magma Transfer, Storage and Differentiation*, Vol. 304, eds C. Annen and G. F. Zellmer (London: Geological Society, Special Publications), 15–31. doi: 10.1144/SP304.2

Zellmer, G. F., and Annen, C. (2008). "An introduction to magma dynamics," in *Dynamics of Crustal Magma Transfer, Storage and Differentiation*, Vol. 304, eds C. Annen and G. F. Zellmer (London: Geological Society, Special Publications), 1–13. doi: 10.1144/SP304.1

Zellmer, G. F., Edmonds, M., and Straub, S. M. (2015). "Volatiles in subduction zone magmatism," in *The Role of Volatiles in the Genesis, Evolution, and Eruption of arc Magmas*, Vol. 410, eds G. F. Zellmer, M. Edmonds, and S. M. Straub (London: Geological Society, Special Publications), 1–17. doi: 10.1144/SP410.13

Zhao, D., Huang, Z., Umino, N., Hasegawa, A., and Yoshida, T. (2011). Seismic imaging of the Amur–Okhotsk plate boundary zone in the Japan Sea. *Phys. Earth Planet. Inter.* 188, 82–95. doi: 10.1016/j.pepi.2011.06.013

Conflict of Interest Statement: The authors declare that the research was conducted in the absence of any commercial or financial relationships that could be construed as a potential conflict of interest.

frontiers in Earth Science

ORIGINAL RESEARCH
published: 30 April 2019
doi: 10.3389/feart.2019.00090

Bayesian Markov-Chain Monte Carlo Inversion of Low-Temperature Thermochronology Around Two 8 – 10 m Wide Columbia River Flood Basalt Dikes

Leif Karlstrom[1]*, *Kendra E. Murray*[2]† *and Peter W. Reiners*[3]

[1] Department of Earth Sciences, University of Oregon, Eugene, OR, United States, [2] Department of Earth and Environmental Sciences, University of Michigan, Ann Arbor, MI, United States, [3] Department of Geosciences, University of Arizona, Tucson, AZ, United States

Edited by:
Mattia Pistone,
Université de Lausanne, Switzerland

Reviewed by:
Tom Sheldrake,
Université de Genéve, Switzerland
Catherine Annen,
Université Savoie Mont Blanc, France

***Correspondence:**
Leif Karlstrom
leif@uoregon.edu

†Present Address:
Kendra E. Murray,
Department of Geosciences, Idaho State University, Pocatello, ID, United States

Specialty section:
This article was submitted to Volcanology, a section of the journal Frontiers in Earth Science

Received: 30 November 2018
Accepted: 11 April 2019
Published: 30 April 2019

Citation:
Karlstrom L, Murray KE and Reiners PW (2019) Bayesian Markov-Chain Monte Carlo Inversion of Low-Temperature Thermochronology Around Two 8 – 10 m Wide Columbia River Flood Basalt Dikes. Front. Earth Sci. 7:90. doi: 10.3389/feart.2019.00090

Flood basalt volcanism involves large volumes of magma emplaced into the crust and surface environment on geologically short timescales. The mechanics of flood basalt emplacement, including dynamics of the crustal magma transport system and the tempo of individual eruptions, are not well-constrained. Here we study two exhumed dikes from the Columbia River Flood Basalt province in northeast Oregon, USA, using apatite and zircon (U-Th)/He thermochronology to constrain dike emplacement histories. Sample transects perpendicular to the dike margins document transient heating of granitic host rocks. We model heating as due to dike emplacement, considering a thermal model with distinct melt-fraction temperature relationships for basaltic magma and granitic wallrock, and a parameterization of unsteady flow within the dike. We model partial resetting of thermochronometers by considering He diffusion in spherical grains as a response to dike heating. A Bayesian Markov-Chain Monte Carlo framework is used to jointly invert for six parameters related to dike emplacement and grain-scale He diffusion. We find that the two dikes, despite similar dimensions on an outcrop scale, exhibit different spatial patterns of thermochronometer partial resetting away from the dike. These patterns predict distinct emplacement histories. We extend previous modeling of a presumed feeder dike at Maxwell Lake in the Wallowa Mountains of northeastern Oregon, finding posterior probability distribution functions (PDFs) that predict steady heating from sustained magma flow over 1–6 years and elevated farfield host rock temperatures. This suggests regional-scale heating in the vicinity of Maxwell Lake, which might arise from nearby intrusions. The other dike, within the Cornucopia subswarm, is predicted to have a 1–4 year thermally active lifespan with an unsteady heating rate suggestive of low magma flow rate compared to Maxwell Lake, in a cool near-surface thermal environment. In both cases, misfit of near-dike partial resetting of thermochronometers by models suggests either heat transfer via fluid advection in host rocks or pulsed magma flow in the dikes. Our results highlight the diversity of dike emplacement histories within the Columbia River Flood Basalt province and the power of Bayesian inversion methods for quantifying parameter trade-offs and uncertainty in thermal models.

Keywords: Columbia River Flood Basalts, dike mechanics, Bayesian inversion, low temperature thermochronology, large igneous provinces, thermal modeling

1. INTRODUCTION

The emplacement of flood basalt provinces involves a massive flux of magma into the crust from the mantle over 1–10 Myr timescales. Magmas that make it to the surface erupt to produce deposits with volumes of up to $10^3 - 10^4$ km^3 that are the largest known effusive eruptive events. Large volumes of intrusive magmatism accompany surface eruptions, as constrained by exhumed networks of large dikes and sills (e.g., Burgess et al., 2017), geophysical observations (e.g., Davenport et al., 2017), and petrologic mass balance (e.g., White et al., 2006). The extreme nature of these events, which are often associated with mass extinctions of life and oceanic anoxia (Courtillot and Renne, 2003), suggests that individual flood basalt eruptions are also anomalous within the spectrum of volcanic activity.

Eruptive rates estimated based on radioisotopic dating of flow sequences suggests average eruption rates between $\sim 10^{-2}$ and $\sim 10^1$ km^3/yr (e.g., Burgess and Bowring, 2015; Kasbohm and Schoene, 2018). Field observations of lava flows along with paleo-environmental proxies for flow advance (e.g., Thordarson and Self, 1998; Keszthelyi et al., 2006) suggest larger rates of $\sim 10^2 - 10^4$ km^3/yr. Differences in these two estimates are not surprising, given that the geochronology considers an average over many flows and may include eruptive hiatuses. Such differences are an indication that eruptive tempo is highly unsteady over the duration of a typical flood basalt province.

Here we examine the problem of flood basalt eruption longevity and tempo through the lens of an exposed crustal transport network. We focus on two 8–10 m wide dikes exposed within the Chief Joseph Dike Swarm of the Columbia River Flood Basalts (CRFB) in northeastern Oregon, USA (**Figure 1**), integrating new thermochronologic measurements with modeling to constrain the thermal field around dikes produced as magma intruded then cooled and crystallized within the crust. We re-examine the Maxwell Lake dike, where previous modeling of geothermometry from high-temperature phase equilibria in partially melted granitoid host rocks near the dike margin (Petcovic and Grunder, 2003), has generated widely cited constraints on flood basalt eruption longevity. A new thermochronologic transect extends time-temperature constraints at Maxwell Lake to lower temperatures, providing constraints on the thermal history of host rocks as well as the duration of dike emplacement. We compare these results with a dike exposed in the Cornucupia region south of Maxwell Lake that we will refer to as the Lee dike, with similar outcrop scale geometry and a complementary low-temperature thermochronologic transect in granitic host rocks (Reiners, 2005).

To invert thermochronometric data for dike emplacement involves forward modeling of heat transport away from the dike and resetting of thermochronometers, both of which involve substantial uncertainties. We implement a Bayesian Markov-Chain Monte Carlo (MCMC) inversion as an objective information-gathering approach, in which many forward models with parameters stochastically sampled from prior constraints generate a posterior probability distribution function (PDF) representing the extent to which the data constrain unknowns of interest. In our case, these unknowns include dike longevity and time variation in magma flow, background temperature of the crust, thermal conductivity of wall rock, and parameters associated with diffusion of He in apatite and zircon grains.

MCMC inversion predicts that the two dikes have well-resolved but distinct thermal histories. The Maxwell Lake dike shows evidence for steady heating by magma over 1–6 years, within a warmed background environment at temperatures higher than a normal geotherm at paleodepth of ~ 2 km. The Lee dike, slightly thicker than Maxwell Lake, heated host rocks for a similar total duration of 1–4 years but at a highly unsteady rate that implies lower overall magma flux, in a normal geotherm at exposed paleodepth of < 1 km.

In what follows, we first introduce the regional geological context and prior work on the Maxwell Lake and Lee dikes. Sections 3–5 develop the methods for data analysis, forward modeling, and inversion. We then present the MCMC results in section 6, ending in section 7 with a discussion of implications for CRFB eruptive phenomenology and the general merits of the MCMC inversion approach for volcanologic data.

2. FIELD SITES

The CRFB are the youngest Large Igneous Province (LIP) on Earth, encompassing $\sim 210{,}000$ km^3 basalt erupted in eastern Oregon, Washington and western Idaho, USA, in the interval between ~ 17 and 5 Ma. Although total volumes erupted are the smallest of known continental LIPs globally, the degree to which primary structures are well-exposed and a rich history of study (Reidel et al., 2013; Camp et al., 2017) make the CRFB a model for LIP phenomenology.

CRFB dikes are variably exposed throughout the province, although the fraction of these dikes that fed surface flows is unknown. Dikes are particularly well-exposed in northeastern Oregon, where exhumation of the Wallowa mountains (Zak et al., 2015) and granitic bodies to the south provide a cross-sectional view of the shallow CRFB plumbing system. Thousands of dike segments exposed in this region define the Chief Joseph Dike Swarm (Taubeneck, 1970). Dike compositions and ages are similar to lavas from the Imnaha, Grande Ronde, and Wanapum formations, which make up $\sim 84\%$ of the total CRFB volume and may have been erupted in only 300–400 ka (Barry et al., 2013; Ladderud et al., 2015) and perhaps < 100 ka for most of the Grande Ronde (Kasbohm and Schoene, 2018).

We focus on two CJDS segments here, at Maxwell Lake in the Wallowa Mountains and in the Cornucopia region to the south of the Wallowas (**Figure 1**). The Maxwell Lake dike outcrops in tonalite of the ~ 125.6 Ma Craig Mountain pluton of the Wallowa batholith (Zak et al., 2015), at a paleo depth of ~ 2.5 km based on structure contouring the base of Imnaha flows regionally (Petcovic and Grunder, 2003). It strikes N20°E, similar to the average strike of CJDS segments regionally (Taubeneck, 1970). The average dip is near vertical at 75° W, although small amplitude variability on 10s of meter scale along strike is common. Dike width in our study area is ~ 8 m, however width undulations over the ~ 1 km exposed length of the dike

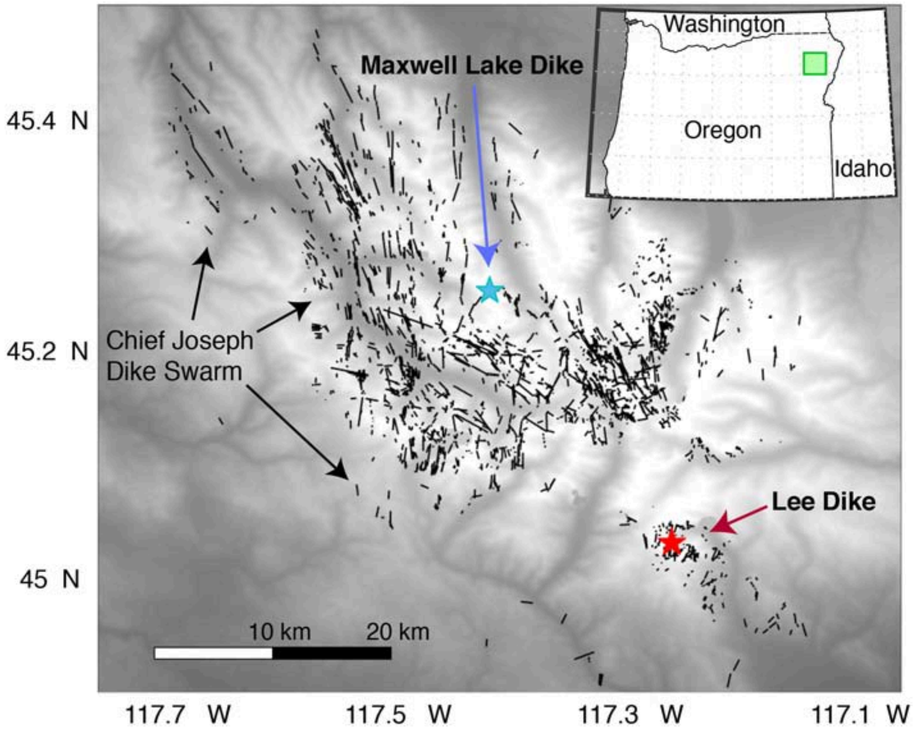

FIGURE 1 | Map showing locations of the Maxwell Lake and Lee dikes, along with distribution of Columbia River Flood Basalt Chief Joseph Dike Swarm segments (green square on inset map).

is suggestive of an intrusive structure that is planar only on larger scales. The dike composition is correlative to the Wapshalla Ridge member of the Grande Ronde basalt (Petcovic and Dufek, 2005), one of the largest flow packages in the CRBG with total volume of 5×10^4 km^3.

Previous work on the Maxwell Lake dike has focused on partial melt observed in wall rocks near the dike margin, which constrains the amount and duration of heat conducted away from the dike during active magma flow and subsequent cooling. Petcovic and Grunder (2003) mapped four zones of distinct mineralogic assemblages containing progressively decreasing partial melt as a function of distance from the dike margin. Although these zones of partial melt vary somewhat in their spatial extent along strike of the dike, on average the zone of partial melt extends 2–4 m from the dike margin. Thermal modeling of this partial melt zone (Petcovic and Grunder, 2003; Petcovic and Dufek, 2005) suggested that active flow of magma occurred for 3–4 years at Maxwell Lake. We collected a 100-m transect of wall rock samples perpendicular to the dike margin exposed at Jackson Lake, ∼ 0.8 km southwest of where (Petcovic and Grunder, 2003) conducted their sampling and mapping.

The Lee dike segment is ∼ 10 m wide and ∼ 1 km long, in the Pine Lakes region of the Cornucopia stock in northeastern Oregon (45.0305°N, 117.250°W), dated to 120–123 Ma from biotite Ar-Ar and Zr U-Pb geochronology (unpublished data from Peter Zeitler and George Gehrels, **Figure 2**). Petcovic (2004) suggested that this dike is Wanapum composition, and described the petrography and textural variations across the exposure of the dike directly adjacent to which we collected a transect of wallrock samples. The strike and dip of the dike in this location is N2°E, 75°W, and the margins are strongly quenched within about 10–20 cm of the wallrock. Principal phases of the dike are plagioclase, clinopyroxene, minor orthopyroxene, and Fe-Ti oxides. Johnson et al. (1997) dated the Cornucopia stock at 116.8 ± 1.2 Ma, though ICP-MS and biotite ^{40}Ar/^{39}Ar dates on the most distal sample we collected were 123 and 122 Ma, respectively. The stock is dominantly two-mica trondhjemite (Taubeneck, 1964), containing plagioclase + quartz + biotite + muscovite + cordierite + Fe-Ti oxides +/− alkali feldspar + trace apatite, zircon titanite, and rare allanite (Johnson et al., 1997). In the vicinity of the Lee dike, wallrock shows some sericitization and possible poikiolitic recrystallization textures within about 5 m of the dike, possible small melt pockets and veinlets in samples 7.3 and 9.5 m away, and chloritization/sericitization around 12–14 m.

2.1. Sample Collection and Analysis

At the Maxwell Lake dike, we collected ∼ 2 kg samples at approximately 2, 5, 11, 20.5, 30, 40, 53.5, 72.5, and 100 m distance from the dike margin. Samples were processed using crushing, sieving, magnetic, and density separation methods at Zirchron, LLC in order to concentrate zircon and apatite crystals. At the University of Michigan HeliUM lab, we selected apatite and zircon grains for (U-Th-Sm)/He and (U-Th)/He analyses, respectively, based on size, clarity, morphology, and the lack of visible inclusions under 120–160x stereo zoom with a Leica M165C microscope. We analyzed three or four apatite and zircon

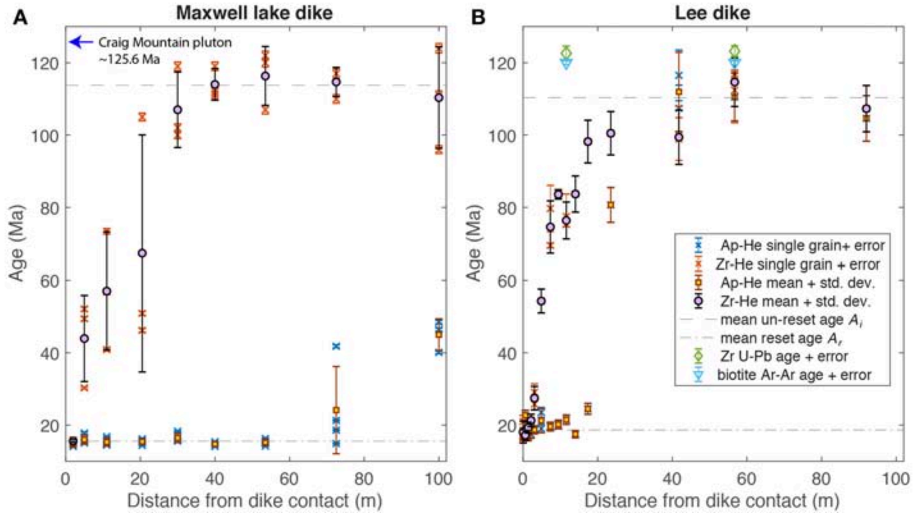

FIGURE 2 | (A,B) Transect of apatite and zircon He thermochronometric ages as a function of distance from Maxwell Lake and Lee dike contacts. Constraints on unrest age of Maxwell Lake comes from Zak et al. (2015), while U-Pb and K-Ar ages constrain host rock ages at Lee dike. Dashed lines are mean of thermochronometric ages used for A_r and A_i in Equation (7).

grains per sample. Grain dimensions were digitally measured under the microscope prior to packing each grain in Nb foil. An Alphachron Helium Instrument was used for He extraction. Using a diode laser, apatite grains were heated to ∼ 900 °C for 3 min and zircon grains were heated to ∼ 1200 °C for 10 min. The extracted He was spiked with 3He, purified using gettering methods, and analyzed on a quadrupole mass spectrometer. A known quantity of ^{4}He was analyzed at regular intervals. We sent degassed grains to the University of Arizona for dissolution and U, Th, and Sm analysis using isotope dilution and solution HR-ICP-MS methods (Guenthner et al., 2016).

Samples from the Lee Dike region were collected in a dike-perpendicular transect at distances ranging from 2 cm to 92 m from the dike margin. Apatite and zircon separates were prepared from 2-kg samples using standard separation procedures similar to those used for the Maxwell Lake samples, and (U-Th)/He measurements were made at Yale University using procedures described in Reiners et al. (2004). Raw (U-Th)/He data for the Maxwell Lake and Lee dikes along with distances from the dike margin are presented in **Supplementary Data**. Slight differences in processing and resultant data arise from the 15 years difference between analysis of Maxwell Lake dike samples (2017) and Lee dike samples (2002).

3. LOW-TEMPERATURE (U-TH)/HE THERMOCHRONOLOGY AND AGE INTERPRETATION

Thermochronometric ages from transects around the Maxwell and Lee dikes are shown in **Figure 2**. Although both dikes are of similar width, the pattern of Zr-He and Ap-He partial resetting perpendicular to the contacts are quite different. Apatite is partially reset out to 100 m from the dike at Maxwell Lake, whereas it reaches unreset background values 40–50 m away from the Lee dike contact. Zircon exhibits a qualitatively similar pattern between dikes, partially reset to smaller distances from the dike contact than apatite.

The low-temperature thermochronologic record of geologically short-duration (days to thousands of years) heating events such as dike emplacement reflects a competition between the rapid rate of the thermal diffusion of heat through rocks and the comparably slow rate of the chemical diffusion of radiogenic daughter products (in the case of (U-Th)/He chronometers, ^{4}He nuclides) in individual apatite and zircon crystals. Both thermal and chemical diffusion depend on large-scale temperature gradients in the domain, although at different scales: thermal diffusion proceeds according to bulk (outcrop-scale) heat capacity and thermal diffusivity, while chemical diffusion is a function of diffusion domain (crystal-scale) size as well as experimentally determined activation energy and diffusivity of the daughter nuclides in the mineral of interest. The patterns of partial resetting around Maxwell Lake and Lee dikes suggest that granitic wallrocks at each location experienced different thermal histories, with a longer or hotter magmatic heat pulse at the Maxwell Lake vs. Lee.

The He content of apatite and zircon crystals is controlled by two processes: the time-dependent radiogenic production of ^{4}He during the alpha-decay of U and Th nuclides and the temperature-dependent diffusive loss of ^{4}He. Assuming a spherical diffusion geometry and uniform distribution of parent nuclides, the He concentration as a function of time t and dimensionless radial position r^* (scaled by radius a of a spherical grain, as in Wolf et al., 1998) is

$$\frac{\partial \mathrm{He}(r^*,t)}{\partial t} = \frac{D(t)}{a^2}\left[\frac{\partial^2 \mathrm{He}(r^*,t)}{\partial r^{*2}} + \frac{2}{r^*}\frac{\partial \mathrm{He}(r^*,t)}{\partial r^*}\right] + P_r(t). \quad (1)$$

$D(t)$ is a chemical diffusivity, which is a function of time-temperature history and activation energy E_a and follows an Arrhenius relationship

$$\frac{D(t)}{a^2} = \frac{D_0}{a^2} \exp\left(-\frac{E_a}{RT(t)}\right), \tag{2}$$

where R is the gas constant, D_0 is He diffusivity at infinite temperature (also called the frequency factor), and $T(t)$ is a thermal history. $P_r(t)$ is the He production rate

$$P_r(t) = 8\lambda_{238}\mathrm{U}(t) + 7\lambda_{235}\mathrm{U}(t) + 6\lambda_{232}\mathrm{Th}(t) + \lambda_{147}\mathrm{Sm}(t), \tag{3}$$

with $\mathrm{U}(t)$, $\mathrm{Th}(t)$, and $\mathrm{Sm}(t)$ the abundance of specific parent nuclides at time t (note that Sm is only measured in apatite) and the λ parameters are decay constants.

The general analytical solution for production-diffusion in a sphere (Equation 1), assuming a constant production rate P_r of He (Wolf et al., 1998), is

$$\frac{\mathrm{He}}{P_r} = \frac{a^2}{D(t)}\left(\frac{1}{15} - \sum_{n=1}^{\infty}\frac{6}{\pi^4 n^4}\exp\left[-\frac{n^2\pi^2 D(t)}{a^2}t\right]\right) + \frac{{}^{*}\mathrm{He}}{P_r}\sum_{n=1}^{\infty}\frac{6}{n^2\pi^2}\exp\left[-\frac{n^2\pi^2 D(t)}{a^2}t\right], \tag{4}$$

defining a helium age He/P_r as a function of time, the parameters that control $D(t)/a^2$ (Equation 2), and an initial He age ${}^{*}\mathrm{He}/P_r$.

Temperature sensitivities of the apatite He and zircon He thermochronometers are commonly described using the closure-temperature concept (Dodson, 1973), because these systems are most commonly used to constrain the rock cooling over millions-of-year timescales that results from rock exhumation (Ehlers and Farley, 2003; Reiners and Brandon, 2006). The closure-temperature concept assumes an initial He age of zero, a monotonic cooling history, and a specific cooling rate (Dodson, 1973). For a 10°C/Myr cooling rate, the closure temperature for typical apatite and zircon crystals is 67 and 183°C, respectively (Farley, 2000; Reiners et al., 2004). Here, we are interested in the resetting of these He thermochronometers over much shorter (yr to kyr) timescales that characterize the emplacement, conduit activity, and thermal relaxation of a magmatic dike.

We calculate the expected fractional loss of He, F_d, that an apatite or zircon crystal would experience given a thermal history predicted for a particular location by the thermal forward model described below. We do not use approximate solutions to diffusive He loss (Watson and Cherniak, 2013), as we can accurately numerically evaluate the exact solution for fractional loss from a spherical diffusion domain with an initially uniform distribution of He (Fechtig and Kalbitzer, 1966; McDougall and Harrison, 1999; Reiners, 2009)

$$F_d = 1 - \frac{6}{\pi^2}\sum_{n=1}^{\infty}\frac{1}{n^2}\exp\left(-n^2\pi^2\sigma_T\right), \tag{5}$$

where σ_T is

$$\sigma_T(T,t) = \frac{D_0}{a^2}\int_0^t \exp\left(\frac{-E_a}{RT(t')}\right)dt'. \tag{6}$$

We evaluate Equation (5) numerically using 1,000 terms. We calculate the approximate observed fractional resetting from the thermochronologic ages measured along each transect (Reiners, 2009; Cassata et al., 2010):

$$F_d \approx 1 - \frac{A - A_r}{A_i - A_r} \tag{7}$$

where A is the observed He age, A_r is the time elapsed since the heating event (emplacement of CRFB dikes), and A_i is the unreset age (crystallization age of the host pluton).

The kinetic parameters, activation energy E_a and frequency factor D_0, vary for different minerals and are derived from diffusion experiments on apatite and zircon standards. For a single mineral system, E_a and D_0 are also known to vary from crystal to crystal, most significantly as a function of self-irradiation dose (Shuster et al., 2006; Flowers et al., 2009; Gautheron et al., 2009; Guenthner et al., 2013). For our fractional resetting calculation, we explore a range of E_a and D_0 values for both apatite and zircon observed in natural crystals of low to moderate self-irradiation dose, as is appropriate for the U-Th compositions and ca. 120 Ma formation age of the crystals dated here.

There is an apparent positive correlation between available E_a and D_0 values (**Figure 3**) for the diffusivity of He in both apatite and zircon. To simplify data inversion, we make use of this relationship to reduce the total number of free parameters in the problem. We find D_0/a^2 as a function of E_a as

$$\log\left(\frac{D_0}{a^2}\right) = p_1 E_a^{p_2}, \tag{8}$$

where (dimensional) p_1 and p_2 define a power regression to the data in **Figure 3**. In the MCMC model we explore a range of apatite $E_{a,Ap}$ of 120–145 kJ/mol with a standard error of 1.414, $p_1 = 2 \times 10^{-11}$ and $p_2 = 5.074$ in Equation (8). For zircon we explore a range $E_{a,Zr}$ of 160–175 kJ/mol with a standard error of 1.288, with $p_1 = 4.5 \times 10^{-4}$ and $p_2 = 2.083$ in Equation (8). Standard errors calculated from the E_a in **Figure 3**. We emphasize that this functional relationship is utilized to simplify grain scale complexity in the face of multi-parameter and multi-physics inversion, rather than to make inferences about the mechanics of He loss in zircon or apatite.

Ideally we would use the emplacement age of the basalt to constrain A_r, and A_i would correspond to the crystallization age of the plutonic host constrained from other methods. However, examination of **Figure 2** suggests that neither the near-dike ages nor the far-field ages correspond precisely to inferred CRFB emplacement times or pluton crystallization ages determined by radiogenic isotopic methods. We do not focus on resolving this apparent discrepancy here, but rather use the consistency in near-dike and far-field thermochonologically determined ages to define apparent reset and unreset ages A_r and A_i (dashed lines in **Figure 2**). These may overestimate the intrusion ages and underestimate the crystallization ages by up to 1–2 Myr. Determining A_r and A_i from the transects allows us to focus on the pattern of partial resetting, which encodes relative differences in dike-induced wall rock heating.

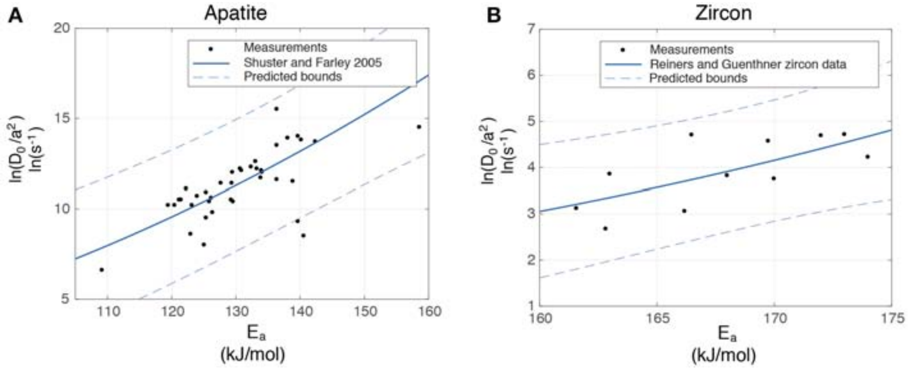

FIGURE 3 | Observed variability in activation energy and frequency factor for the diffusion of He in **(A)** apatite and **(B)** zircon crystals (Reiners et al., 2004; Shuster et al., 2006; Guenthner et al., 2013). In each panel, the black dots are the E_a and D_0/a^2 calculated from diffusion experiments on single crystals or sample aliquot. Solid blue line is power regression fit to this relation, parameter values given in text. Dotted lines are 95% confidence bounds. Apatite data include diffusivity of both ^{4}He (natural) and ^{3}He (doped). Zircon data include the post-high-T results from Reiners et al. (2004) and samples RB140, BR231, M127 from Guenthner et al. (2013).

4. THERMAL MODEL

Emplacement of magmatic dikes induces a transient heating of host rocks such as recorded by the geothermometers described in section 3. Heat transport in host rocks is often assumed to be dominantly conductive, although advection of heated host pore fluid (or magmatic volatiles) also probably contributes. Coupled advection-diffusion of heat may also contribute mechanical impacts. For example, thermal pressurization of host pore fluid has been called upon to explain fracture patterns around some shallow dikes (Delaney, 1982).

The Maxwell Lake dike was previously modeled assuming conductive host rock heating in 1D, with either an analytic parameterization of magma emplacement (Petcovic and Grunder, 2003) or with a numerical 2D advection-diffusion unidirectional flow model of magma transport through a slot (Petcovic and Dufek, 2005). Both methods resulted in similar predictions of dike longevity (3–4 years) that matched near-dike high temperature constraints from petrography. Here we develop a conductive heat transfer model that accounts for distinct non-linear melt-fraction temperature relation in tonalitic host rock and basaltic dike, parameterizes magma flow within the dike, and neglects advective heat transport in wall rocks.

We assume that temperature varies in the dike-perpendicular dimension only. Small deviations from planar dike geometry are often observed and could contribute to complexities in the thermal field, but are excluded here. We model temperature evolution in a multicomponent 1D system consisting of dike material and host rock, following

$$\rho_i c_p \frac{\partial T(x,t)}{\partial t} = \frac{\partial}{\partial x}\left(k \frac{\partial T(x,t)}{\partial x}\right) - \rho_i L \frac{\partial F_i(x,t)}{\partial t}, \tag{9}$$

where the index i is equal to 1 for assumed tonalitic host rock and 2 for basaltic dike material, T is temperature (a function of spatial location x—distinct from r in the chemical model of section 3—and time t), ρ_i is the density of material i, c_p the specific heat capacity, k thermal conductivity, L is the latent heat of fusion, and $F_i(x,t)$ is the melt fraction (**Figure 4**). It is well-known that material thermal properties vary with temperature in the presence of partial melt [non-zero $F_i(x,t)$, Whittington et al., 2009] as well as with composition (Jaupart and Provost, 1985). For reasons discussed in the next section, we do not consider mixture models for thermal parameters or temperature-dependent thermal properties, taking constant c_p and k. We also do not consider differences in density between solid and liquid phases.

Equation (9) is solved on a spatial domain of length R with left end point at the center of a dike with half-width $H/2$. We assume an initially constant temperature domain and sudden dike emplacement, such that initial conditions are piecewise constant

$$T(x,0) = \begin{cases} T_{l,1}, & \text{if } x \le H/2 \\ T_{BG}, & \text{if} x > H/2, \end{cases} \tag{10}$$

where $T_l, 1$ is the dike interior temperature (taken to be the magma liquidus) and T_{BG} is the background temperature of the crust at the paleo depth of the dike. At one end of the domain, a Dirichlet boundary condition $T(x = R, t) = T_{BG}$ for all time mimics a background geotherm. We choose a large domain size (R at least 5 times the farthest sample $\sim$ 100 m from the contact) to minimize boundary influence on transient temperature field near the dike.

At the other end of the domain, we assume that the dike is actively transporting magma for a certain length of time T_f, during which temperature in $x \le H/2$ is specified by a function that parameterizes the effects of monotonically decreasing flow rates within the dike as advection of magma competes with cooling. This function provides the forcing for thermal diffusion within host rocks, given by

$$T_d(x \le H/2, t < \tau_f) = \frac{T_{l,1} - T_{bdy}(t)}{2}\left(1 - \tanh\left[10\frac{(t-\tau_c)}{\tau_w}\right]\right) + T_{bdy}(t), \tag{11}$$

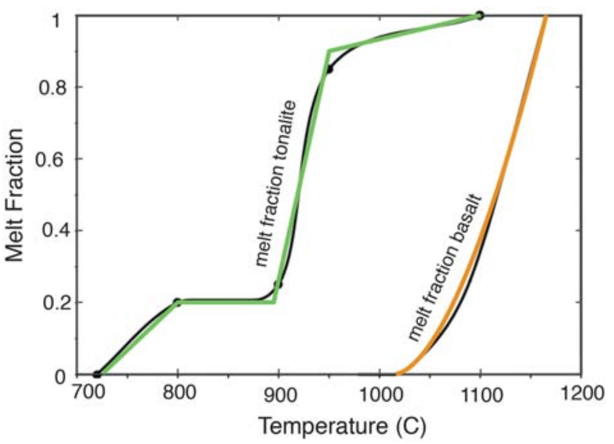

FIGURE 4 | Melt fraction vs. temperature curves for basalt and tonalitic rocks. Black curves are reproduced from Petcovic and Dufek (2005), while colored curves are fits used for thermal modeling in this study.

and imposed only when $T_d \geq T_{bdy}(t)$, with τ_c and τ_w as parameters that control the time variation of temperature within the dike. Parameter τ_c scales the dike's overall longevity; for example, if dike flow is modeled as a step function (as in Petcovic and Grunder, 2003), τ_c is the total duration of flow. Such a model likely oversimplifies many dike emplacement scenarios, because finite magma supply implies pressure gradients that decline over time, which leads to growing thermal boundary layers and decreasing temperature at the dike-host rock contact (Bruce and Huppert, 1989). The parameter τ_w controls how rapidly the dike temperature decreases around τ_c, as a model for such flow steadiness.

Equation 11 states that temperatures within the dike $x \leq H/2$ are set to a spatially uniform but time-varying value. Total longevity of active magma flow modeled by Equation (11) is τ_f, the time at which point the tanh function is within a small threshold δ of unity (we take $\delta = 0.01$). At this time, we assume that the dike has stopped transporting magma and switch to a Neumann boundary condition at the dike center for all subsequent time $\partial T(x = 0, t \geq \tau_f)/\partial x = 0$. Note that Equation (11) needs not provide a boundary condition for all time less than τ_f. Because $T_{l,1} > T_{BG}$, initially dike emplacement drives diffusion of heat away from the dike. However, if at any time prior to τ_f the specified dike temperatures imply $T_d(t) < T_{bdy}(t)$, for example if the dike heats up host rocks then shuts off suddenly, host rocks buffer the dike temperature and (Equation 11) no longer forces dike temperatures (although magma is still assumed to be flowing until time exceeds τ_f).

Figure 5 plots Equation (11), normalized by the contact temperature difference, to illustrate how different flow scenarios translate to boundary heating and how τ_c, τ_w relate to τ_f. Larger values of τ_w result in dike temperatures that more gradually transition from the initial dike temperature (the liquidus $T_{l,1}$) to a time-evolving host rock temperature at the dike boundary $\tau_{bdy}(t)$. Although we are not modeling dike-interior temperatures explicitly, this mimics a monotonic growth of thermal boundary layers as flow rate within the dike goes down (Bruce and Huppert, 1989) to explore a range of emplacement scenarios.

For granitic wall rocks we assume a melt fraction law $F_2(x, t)$ parameterized from Petcovic and Dufek (2005), shown in **Figure 4**. We use a piece-wise linear fit similar to Karlstrom et al. (2010) to capture impacts of variable mineral assemblage on melting regime. For basalt we model the melt fraction temperature relation as

$$F_1(x, t) = \left(\frac{T(x, t) - T_{s,1}}{T_{l,1} - T_{s,1}} \right)^b \tag{12}$$

where $T_{s,1}$ and $T_{l,1}$ are the basalt solidus and liquidus temperatures and b is an exponent that parametrizes the effects of mineral phase assemblage. b close to 1 is appropriate for mafic compositions (e.g., Huber et al., 2009).

To solve Equation (9) we rewrite in terms of an effective heat capacity $c_{eff} = c_p + L\frac{dF_i}{dT}$, for which i is specified by the composition (basalt or granite), in a scaled spatial domain defined by the invertible coordinate transform

$$x = \lambda \tanh \frac{R}{\lambda \xi}. \tag{13}$$

$\xi \in [0, 1]$ is the new spatial coordinate and λ is a stretching factor (Erickson et al., 2017). With these modifications, Equation (9) becomes

$$\rho_i c_{eff} \frac{\partial T(\xi, t)}{\partial t} = \left(\frac{\partial \xi}{\partial x} \right)^2 \frac{\partial}{\partial \xi} \left(k \frac{\partial T(\xi, t)}{\partial \xi} \right) \tag{14}$$

The choice of coordinate transform (Equation 13) is motivated by a need for implementing an efficient numerical solution to Equation (14) that retains high resolution near the dike for accurate prediction of partial melt, described in the next section. When discretized in space, a grid of evaluation points with uniform spacing becomes a staggered grid that concentrates points near the dike where more numerical accuracy is desired. Equation (14) is discretized using 2nd order centered finite differences and an adaptive 4th order Runge Kutta method in time. We have tested this code against a benchmarked numerical solution with equally spaced grid points (Karlstrom et al., 2017).

Typical model output is shown in **Figure 6**. Wall rock time-temperature histories depend on distance from the dike contact, duration and form of the heating event specified by the dike contact boundary condition ($\tau_c = 3$ years, $\tau_w = 0.1$ years in **Figure 6**, with $k = 3$ W/mC), and background temperature enforced by the far-field boundary condition as illustrated by two representative values of T_{BG}. Resetting of thermochronometers is predicted by applying these time-temperature histories to Equations (5) and (7), which result in time dependent partial resetting as plotted in **Figure 7**. This time dependence implies that we must run our thermal models for long enough that near-equilibrium He concentrations are achieved. We find that > 95% of equilibrium thermochrometer partial resetting is achieved in apatite and zircon for the range of parameters considered here if

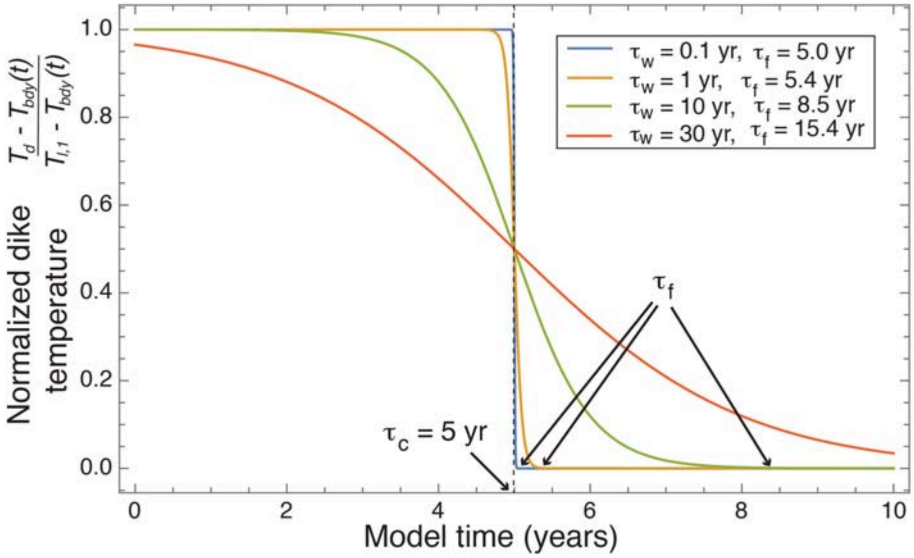

FIGURE 5 | Normalized dike temperature from Equation (11), illustrating trade-offs between the scale for dike active flow τ_C and the scale for flow unsteadiness τ_W. τ_f is the total duration of temperatures elevated over background, and may be similar to τ_C for small τ_W. Equation (11) is enforced in our model for dike contact temperatures $T_d > T_{bdy}(t)$ and times $t < \tau_f$.

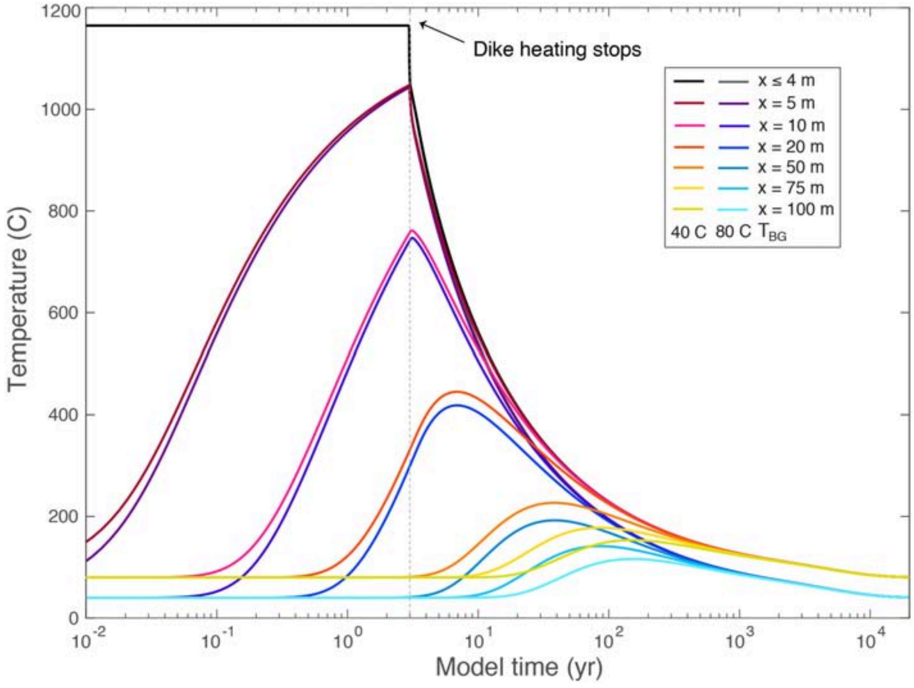

FIGURE 6 | Temperature as a function of distance from dike center x and time for an example $H/2 = 4$ m thick dike emplacement scenario and two background temperatures T_{BG} (red and blue colors). Dike interior temperature evolution is given by the black curve. Forced heating by magma flow is close to a step function in time ($\tau_C = 3$ yr, $\tau_W = 0.1$ yr, giving $\tau_f = 3.04$ yr, $k = 3$ W/mC), and stops at the time indicated by vertical dashed line.

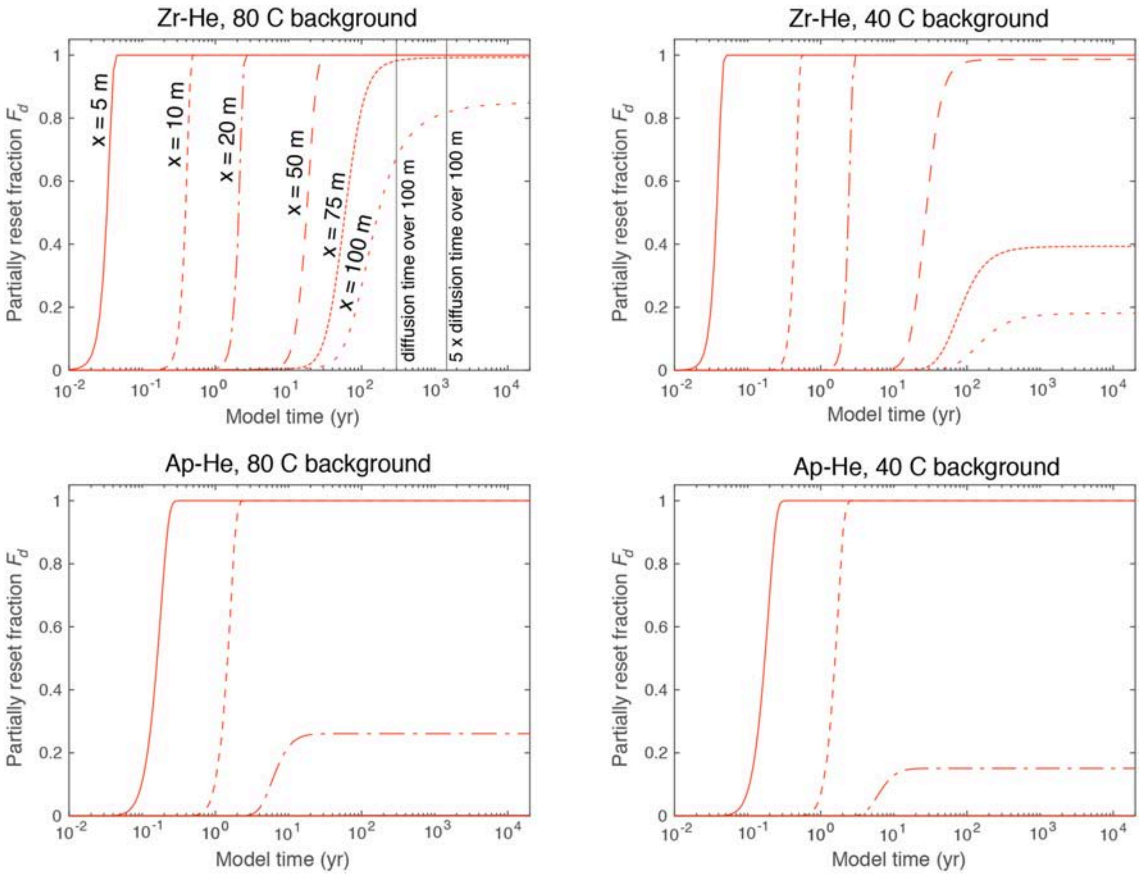

FIGURE 7 | Relationship between partial resetting of apatite and zircon He thermochronometers as a function of heating and hold time (kinetics of thermal vs. chemical diffusion), with the same parameters as **Figure 6** and two background temperatures T_{BG}. Curves on each panel represent listed distances *x* from the dike center, as in **Figure 6**. Vertical lines in upper left panel correspond to multiples of a thermal diffusion time over 100 m ($100^2 \rho c_p/k$).

TABLE 1 | Parameters, uniform prior parameter ranges, and MCMC inversion results.

Parameter	T_{BG} (C)	τ_c (year)	τ_w (year)	k (W/mC)	$E_{a,Zr}$ (kJ/mol)	$E_{a,Ap}$ (kJ/mol)	τ_f (year)	Total residual error (year)
Prior lower bound	25	0.1	0.1	1	160	120		
Prior upper bound	100	15	15	10	170	145		
Maxwell lake dike								
Best	99.6	2.6	0.4	2.4	160.8	143.8	2.7	49.2
Median	82.4	2.3	0.5	4.7	166.6	129.1	2.7	42.7
68% conf. interval	[65.8, 93.7]	[1.3, 4.6]	[0.1 ,3.8]	[2.1 ,8.1]	[162.3, 172.2]	[122.6 ,138.2]	[1.4 ,5.4]	
95% conf. interval	[37.4, 99.0]	[0.9, 9.1]	[0.1 ,12.0]	[1.2 ,9.7]	[160.4, 174.6]	[120.3 ,144.0]	[0.9 ,10.2]	
$\hat{R}$	1.26	1.12	1.06	1.13	5.14	2.67	1.13	
Lee dike								
Best	25.4	0.7	6.4	9.2	160.1	144.6	2.2	7.9
Median	27.7	1.0	6.9	5.5	162.6	142.6	2.6	9.1
68% conf. interval	[25.7 ,31.4]	[0.7, 1.6]	[3.9 ,11.3]	[3.5 ,8.2]	[160.7, 167.2]	[139.6 144.3]	[1.7, 4.1]	
95% conf. interval	[25.1 ,35.8]	[0.6, 2.3]	[2.2 14.4]	[2.0 ,9.7]	[160.1, 172.6]	[136.0 144.9]	[1.1, 5.2]	
$\hat{R}$	1.48	1.24	1.09	1.15	7.25	6.71	1.15	

*τ_f is calculated from Equation (11). The Gelman-Rubin diagnostic $\hat{R}$ is discussed in **Appendix A**.*

simulations are run for at least five thermal conduction timescales over the sampled region (100 m, illustrated by the vertical lines in **Figure 7**).

5. BAYESIAN INVERSE MODELING FRAMEWORK

Epistemic and aleatoric uncertainties limit our ability to accurately invert for the longevity and steadiness of magma flow through CRFB dikes or the pre-intrusion temperature of host rocks. Aleatoric uncertainties in material parameters such as thermal conductivity, activation energy for Helium diffusion in zircon or apatite may trade off with uncertainties in the precise location of samples in relation to the dike. Such uncertainties are minimizable given sufficiently accurate sampling, calibration of fractional resetting models and experimental petrology, and sufficient resources to carry out the needed experiments. However, for the models described in sections 3–4, additional epistemic uncertainties such as the precise 3D geometry of the dike margin, the functional form of the dike temperature through time that parameterizes magma flow, or the presence of advective heat transport (essentially, whether our model describes the relevant physical problem), are convolved with aleatoric uncertainties.

We therefore approach inverse modeling as an information-gathering exercise specific to our hypotheses. We pose a forward model and then systemically vary unknown parameters to assess trade-offs and find a best fit. A generic data vector containing **M** independent datasets $\mathbf{d} = [d_1^T, d_2^T, \ldots, d_M^T]$, may be predicted by a possibly non-linear forward model $G(\mathbf{m})$ with m model parameters such as described in section 4, $d = G(\mathbf{m}) + \epsilon$, where ϵ is a vector of measurement errors. Inversion consists of estimating the m that minimize the residual $\mathbf{r}_k = \mathbf{d}_k - G_k(\mathbf{m})$, accounting for measurement error.

We implement a Bayesian inversion utilizing MCMC sampling of the parameter space. An introduction to Bayesian inversion can be found in Mosegaard and Tarantola (2002), and applications of similar methods to geophysical problems in (e.g., Fukada and Johnson, 2008; Bursik et al., 2012; Anderson and Segall, 2013). We briefly summarize the method here.

Our goal is to derive a multidimensional posterior PDF that represents the inversion solution in accordance with Bayes' Theorem

$$P(\mathbf{m}|\mathbf{d}) \propto P(\mathbf{d}|\mathbf{m})P(\mathbf{m}). \quad (15)$$

Equation (15) states that the posterior PDF $P(\mathbf{m}|\mathbf{d})$, defined as the probability of a model prediction vector m given a data vector **d**, is proportional to the product of an assumed known prior PDF $P(\mathbf{m})$ with a Likelihood function $P(\mathbf{d}|\mathbf{m})$ that measures the misfit of data with model predictions accounting for data uncertainties.

It is worth emphasizing that in the framework of Bayesian statistics, the inverted parameters are given by distributions specified in the posterior PDFs rather than by single best-fitting values. Posterior PDFs reflect both our ability to predict the data with a model and our prior state of knowledge, for which we know some parameters very well and some very poorly. For all parameters in this study we assume a uniform prior distribution with upper and lower bounds. We assume that errors ϵ are uncorrelated, such that their covariance matrix $\Sigma_k = \mathrm{diag}(\sigma_k)$, with σ_k the variance associated with the error ϵ of each dataset. If each dataset is normally distributed, the appropriate likelihood function is then

$$P(\mathbf{d}|\mathbf{m}) = \prod_{k=1}^{M} \left[(2\pi)^{-N_k/2} |\Sigma_k|^{-1/2} \exp\left(-\frac{1}{2} \mathbf{r}_k^T \Sigma_k^{-1} \mathbf{r}_k \right) \right], \quad (16)$$

where $\mathbf{r}_k = \mathbf{d}_k - \mathbf{G}_k(\mathbf{m})$ is the residual vector and $|\Sigma_k|$ is the determinant of the covariance matrix. In our application, the number of datasets M is two for the Maxwell Lake and Lee dikes (Ap-He, Zr-He).

We derive posterior PDFs for model parameters that minimize residuals through MCMC sampling. We implement the Metropolis-Hastings algorithm (Metropolis et al., 1953) where parameters are randomly perturbed many times, and accepted if the posterior probability calculated from Equation (15) is higher than the previous iteration. Multiple Markov Chains are run with randomized initial values, to help ensure that we are exploring the enture parameter space. We follow (Anderson and Segall, 2013; Anderson and Poland, 2016) in using the log of Equation (16) to calculate acceptance of a particular iteration. A random subset of higher probability iterations is also discarded, which helps the minimization procedure escape local minima. Parameters are assumed uniformly distributed between upper and lower prior bounds given in **Table 1**.

5.1. The Challenge of Model Efficiency

For the 1D model and data presented in sections 3 and 4, there are a minimum of 26 parameters that must be constrained at each dike: for both host rock and intruded basalt, we need solidus and liquidus temperatures, melt fraction exponent (if using Equation 12 as a model for compositional dependence of partial melting), mixture density, latent heat of fusion, and two thermal parameters (conductivity and heat capacity). For the fractional resetting calculation to match thermochronometric ages, we further need the activation energies, diffusivities, and mean grain sizes for He diffusion in both apatite and zircon, as well as un-reset ages (crystallization age of pluton) and reset ages (exact timing of dike emplacement). Finally, we have two parameters associated with the dike flow model, mean dike thickness, and the background temperature T_{BG} of the domain.

Our use of solely thermochronologic and structural constraints for models is insufficient to resolve this number of parameters, so we reduce the parameter space dimensionality to focus on particular sensitivities of the inversion. We use experimental values for thermal and Arrhenius parameters in the thermochronologic fractional resetting calculation, then assume known un-reset and reset ages as dictated by the data, approximately the crystallization age and Grande Ronde emplacement age respectively. However, A_r and A_i are determined by the thermochronologic transects described in section 3 in order to focus model inversion on the partial resetting pattern. We assume a uniform dike width approximately equal to field measurements.

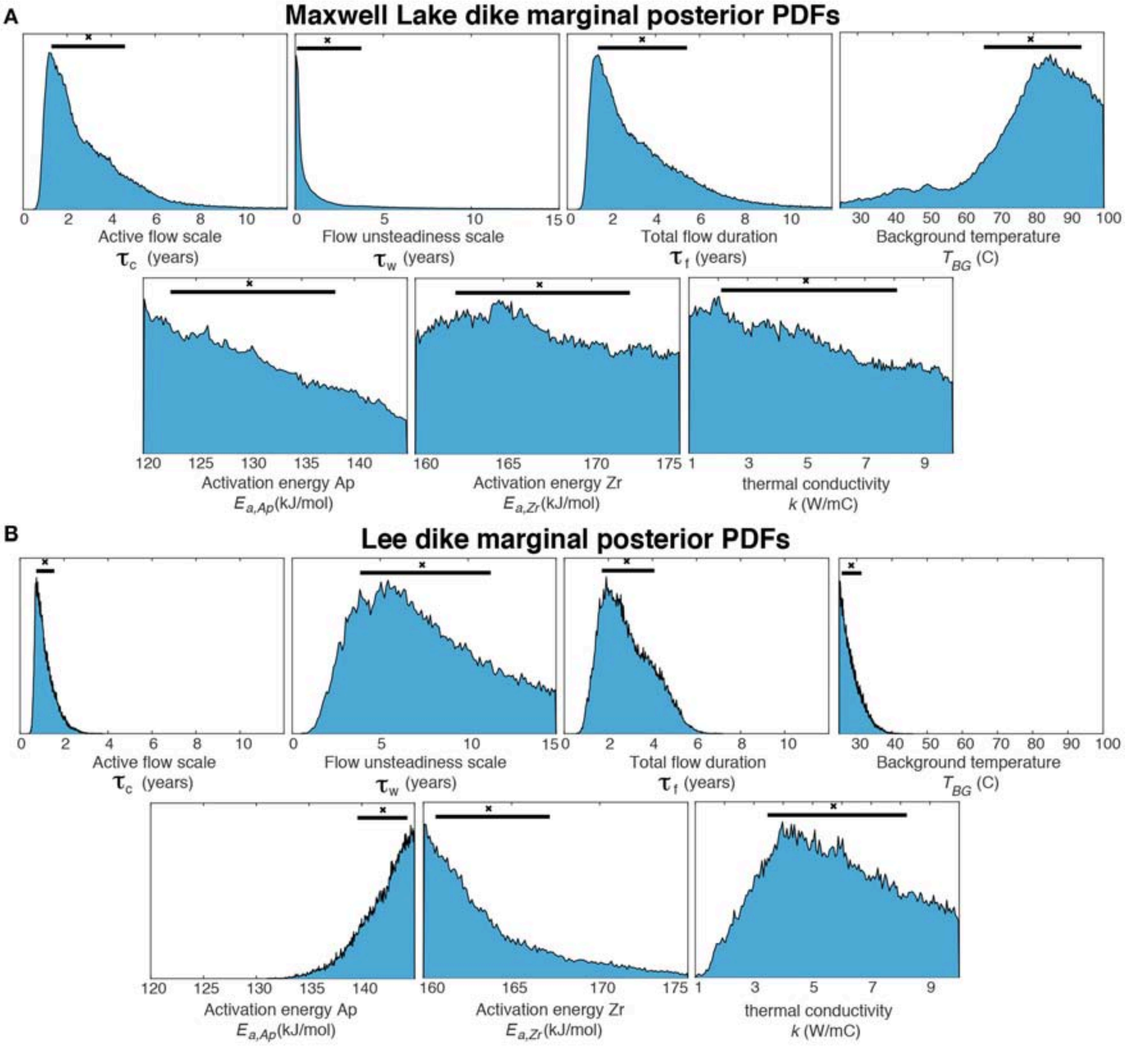

FIGURE 8 | Marginal posterior PDFs for **(A)** Maxwell Lake and **(B)** Lee dike parameters estimated from MCMC inversion (τ_f is derived using Equation 11). Black horizontal bars correspond to 68% confidence intervals associated with expectation values from the posterior PDF, while black symbols are the median of the distribution (**Table 1**).

We can assess much of the inherent trade-offs in thermal models by considering only one unknown thermal parameter—a thermal conductivity k—assuming phase equilibria and melt fraction relations for host rock and dike are known, but that background temperature is unknown. We simplify fractional resetting by parameterizing the ratio D_0/a^2 in terms of activation energy E_a (**Figure 3**), reducing the number of unknown parameters to one each for apatite and zircon. This results in six unknown parameters ($E_{a,Ap}, E_{a,Zr}, T_{bg}, T_w, T_c, k$) at each dike that must be inverted for.

The MCMC method is guaranteed to converge given infinite time (e.g., Mosegaard and Tarantola, 2002), and a sufficiently large number of iterations generates a PDF that closely approximates the true posterior PDF. Unfortunately, there is no way to predict the amount of time required for convergence, and many iterations (perhaps $10^4 - 10^6$, e.g., Anderson and Segall, 2013) may be required to resolve a high dimensional posterior PDF. A certain amount of trial and error is also involved in picking step size for parameter perturbations during an inversion. Thus, MCMC methods require efficient forward models to be practical.

The forward model described in section 4 is only marginally well-suited to this procedure. In each iteration, we must solve a partial differential equation for long enough time that the transient heat pulse from the dike propagates past our farthest-out partially reset samples $\sim$ 100 m from the dike contact. As **Figure 7** demonstrates, the trade-off between heating and holding time inherent to thermochronometers implies that simulations running for less than $\sim$ 5 conductive cooling timescales over the sampled extent $100^2\rho c_p/k$ (as plotted in **Figure 6**) may significantly underpredict partial resetting of apatite. We run each simulation for a total time equal to $5.25 \times 100^2\rho c_p/k$, which ranges from $\sim$ 500-5000 years for the range of thermal parameters considered.

In addition to time stepping, we must use sufficient spatial resolution near to the dike that partial melting of host rocks can be accurately predicted. We find $\sim$ 1 m spatial resolution near the dike to be sufficient. As a final complication, a Dirichlet temperature condition far from the dike is used to enforce a background geotherm in 1D, and we must have a large enough spatial domain that this does not affect the transient heating near to the dike . We find through numerical experimentation that $\sim$ 500 m total domain length is sufficient.

To accomplish the required number of simulations in a reasonable amount of time, we have minimized inversion complexity in two ways. First, we use a parallelized MCMC code package (MCMC Hammer, Anderson and Poland, 2016) to run simultaneous Markov Chains on multiple cores. Second, we simplify our forward model for efficiency. We assume constant material properties, such that our predicted values will average any variation with temperature or melt fraction. We discretize the heat (Equation 14) on a transformed domain (via Equation 13 with $\lambda = R/7$) to reduce the number of spatial points required to achieve both a large domain and high resolution near the dike. We utilize a 4th order adaptive Runge Kutta method for non-uniform time stepping in Matlab. A single forward model required to evaluate Equation (16) takes on the order of 5–10 s with this method.

We run 70–75 Markov chains in parallel with randomized initial guesses until $2 - 4 \times 10^4$ kept MCMC steps per chain are achieved. In total 2.4×10^6 kept samples from all chains are incorporated into a posterior PDFs for Maxwell Lake, with a mean accepted fraction of 0.55 across all chains (meaning that roughly twice as many simulations were performed as kept). For the Lee dike, 3.0×10^6 kept samples are incorporated into a posterior PDF and the MCMC algorithm exhibited a mean accepted fraction of 0.23. Three diagnostics of MCMC convergence are discussed in **Appendix A**. Although non-normality in estimated parameters complicates a robust assessment, we are confident that convergence to the posterior PDF has been achieved at least for the thermal parameters.

6. RESULTS

Marginal posterior PDFs for the Maxwell Lake and Lee dikes are shown in **Figure 8**, along with bivariate covariance plots for each of six parameters (as well as one derived parameter T_f) that were sampled during MCMC inversion in **Figures 9**, **10**. For each dike, these plots provide an assessment of the degree to which each parameter is constrained by the inversion, and how parameters trade off in pair-wise fashion to optimize fitting the data. We can also compare the posterior PDFs of the Maxwell and Lee dikes to each other.

In general, we find that the overall pattern of partial resetting is well-fit by our model. Although total residual errors for the Maxwell Lake dike are lower than for the Lee dike (**Table 1**), this can largely be attributed to relatively greater noise in the Lee dataset. Posterior PDFs are either monotonically sloped or unimodal and peaked, implying reasonably simple and consistent forward model behavior for best fitting parameters. Best fitting parameters and residual error, as well as 68 and 95% confidence intervals that represent ranges of well-fit parameters for each dike, are reported in **Table 1**. Example solutions, using parameters associated with the median best fitting models for each dike, are plotted against thermochronmetric ages in **Figures 11A–C**. Within error we can fit the overall resetting pattern of partial resetting around both Maxwell and Lee dikes well enough to justify the relative simplicity of our thermal model. The largest errors in both cases are near to the dike, for which our best fitting models systematically predict a sharper partial resetting transition in rocks near the dike contact.

Posterior PDFs for each dike exhibit the well-known trade-offs between parameters in a heat conduction model (**Figures 9**, **10**). For example, similar time-temperature histories can be obtained by increasing the longevity of active dike heating or increasing the wall rock thermal conductivity. Similarly, background temperature trades off weakly and inversely with dike longevity. But the distinct pattern of thermochronometer partial resetting at the Maxwell and Lee dike imply resolvable, distinct thermal histories.

The Maxwell dike is best explained by an emplacement scenario in which sustained dike heating (and thus magma flow) occurred over $\tau_f \sim 1.4$–5.4 years, based on the 68% confidence intervals for the posterior PDF (**Table 1**). Small τ_w in the range of $0.1 - 3.8$ years implies that unsteady flow is not likely, so τ_f as derived through Equation (11) is largely a function of the timescale for active flow τ_c. Background temperature is constrained to be between $65.8 - 93.7^{\circ}$C, and is relatively sharply peaked. On the other hand thermal conductivity is predicted to be between 2.1 and 8.1 W/mC, but is not sharply peaked implying poor constraint overall. Activation energies for apatite and zircon are even more poorly constrained. Good fits to thermochronometric ages can be attained for any value of E_{aAp} and $E_{a,Zr}$, and the Gelman-Rubin diagnostic $\hat{R}$—although flawed, as discussed in **Appendix A**—suggests these parameters may have not converged in our inversion. For the Maxwell dike, we consider flow parameters and background temperature to be constrained by Bayesian MCMC inversion.

Further refinements might be made if we assume particular parameter values, due to covariance between some parameters. For example, $E_{a,Ap}$ is seen to be well-correlated to T_{BG}, with higher background temperatures implies higher activation energy parameters. Likewise, a longer lived dike (larger T_f) implies lower background temperature T_{bg} and lower wallrock conductivity. Tonalite rock conductivity of 3 W/mC as assumed by Petcovic and Dufek (2005) implies total flow duration in the range of 2–4 years, in agreement with their predictions based on modeling of high-temperature geothermometry.

For the Lee dike, predicted total heating duration is similar to Maxwell Lake with $\tau_f \sim 1.7$–4.1 years. However, in contrast to Maxwell Lake significant time variation in heating is predicted, with large flow unsteadiness scale $\tau_w \sim 3.9$–11.3 years implying an immediate and extended decrease in boundary temperature over the active duration τ_f. This is illustrated in **Figure 12**, using best fitting τ_c and τ_w for each dike. Thermal conductivity is predicted to be in the range of $k \sim 3.5$–8.2 W/mC, similar

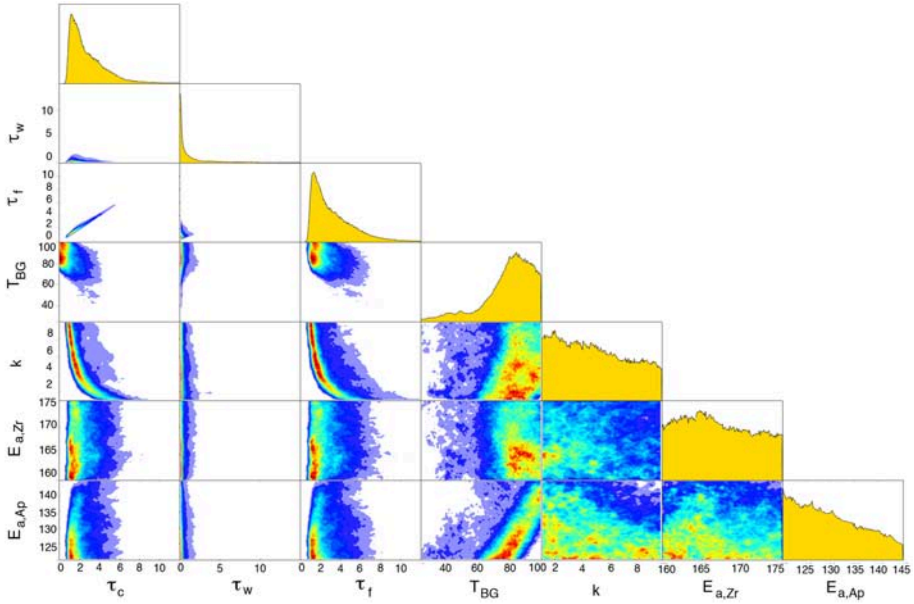

FIGURE 9 | MCMC marginal posterior PDFs as in **Figure 8** and bivariate covariance plots for the Maxwell Lake dike. $T_{BG}, \tau_c, \tau_w, k, E_{a,Ap}, E_{a,Zr}$ are estimated parameters, while total flow duration τ_f is derived using Equation (11). Covariance plots show how parameters trade off with one another within the posterior PDF, warmer colors indicate higher probability.

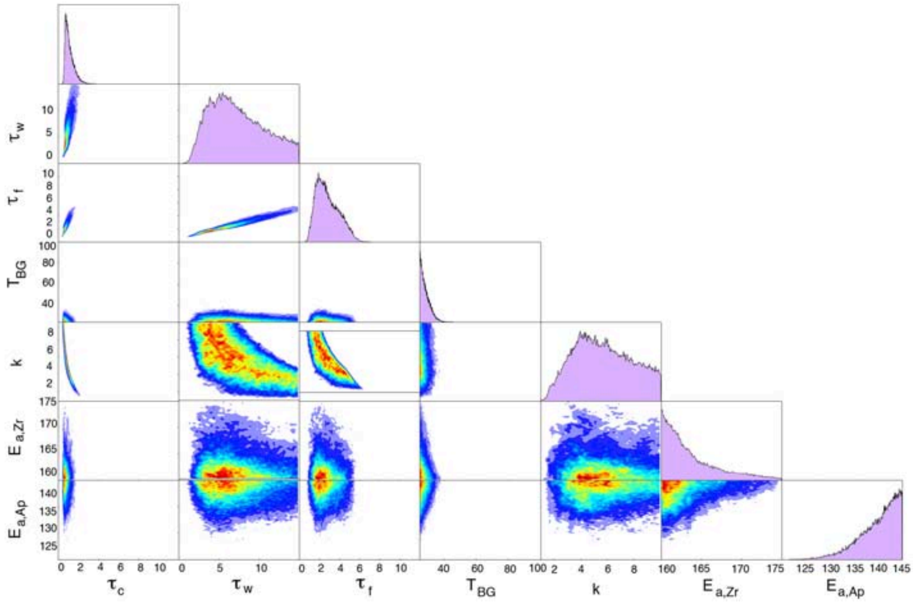

FIGURE 10 | MCMC marginal posterior PDFs as in **Figure 8** and bivariate covariance plots for the Lee dike. Warmer colors in covariance plots indicate higher probability. $T_{BG}, \tau_c, \tau_w, k, E_{a,Ap}, E_{a,Zr}$ are estimated parameters, while total flow duration τ_f is derived using Equation (11).

although somewhat larger in magnitude and more peaked than Maxwell Lake. Background temperature is uniformly small, indistiguishable from near-surface temperatures $T_{BG} \sim 25.7$–31.5 C. The Lee dike inversion appears to place somewhat better constraints on activation energies, predicting $E_{a,Zr} \sim 160.7 - 167.2$ kJ/mol and $E_{a,Ap} \sim 139.6 - 144.3$ kJ/mol. However, MCMC convergence is questionable for these parameters (**Appendix A**), and it is worth noting that the 95% confidence intervals overlap for estimates of the activation energies for the Lee and Maxwell Lake dikes.

Our forward models predict not only the temperature distribution but also the extent and degree of partial melt in the

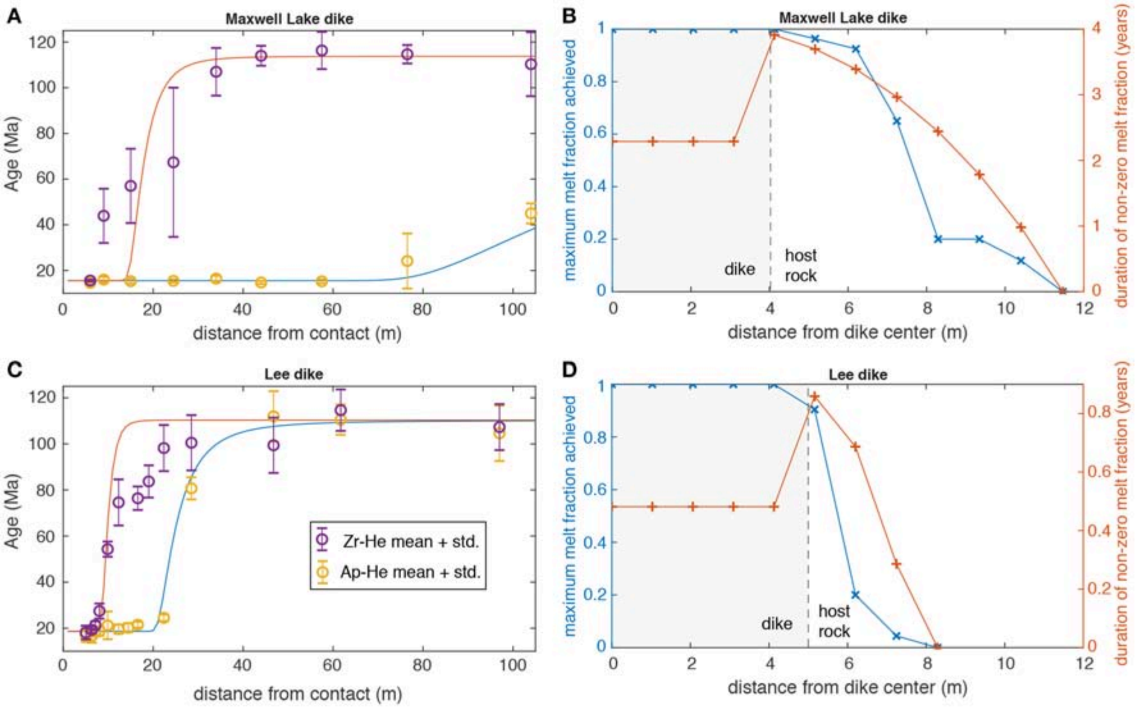

FIGURE 11 | Example fits of Maxwell Lake and Lee dike thermochronology data, plotting curves associated with the median of MCMC-derived PDFs (**Table 1**) for both zircon (red curves) and apatite (blue curves) ages. **(A,C)** show the predicted thermochronometric ages for each dike, using average ages plotted in **Figure 2**. **(B,D)** plot the predicted maximum melt fraction and duration of non-zero melt fraction as a function of distance from the dike center associated with these model runs (dike material is shaded gray, while symbols indicate non-uniformly spaced grid nodes). Duration of partial melt in host rock can exceed the active lifetime of the dikes due to lower solidus of tonalite relative to basalt.

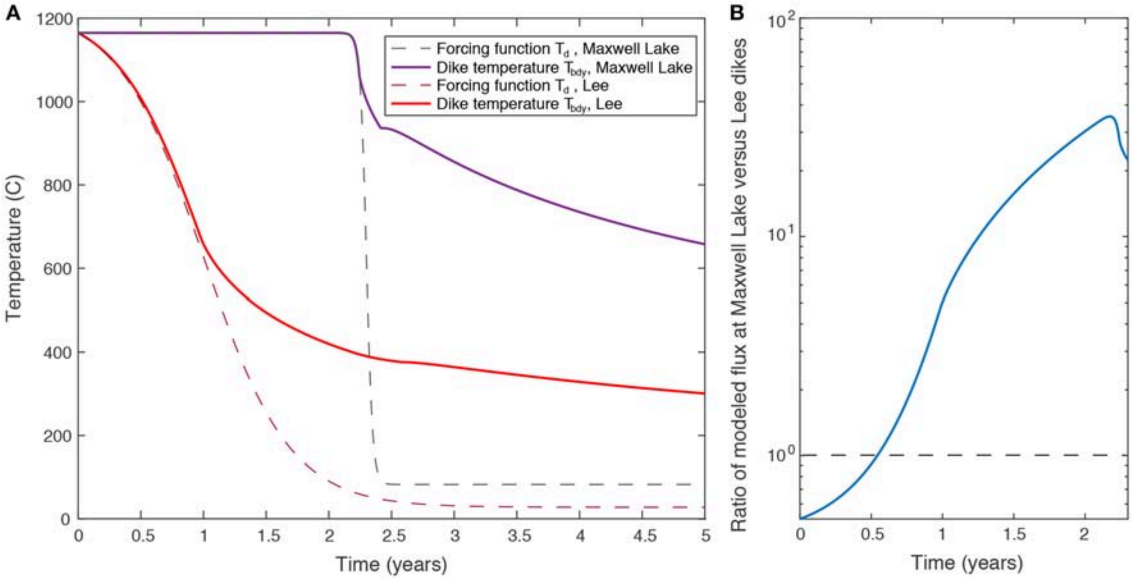

FIGURE 12 | (A) Time variation of predicted Maxwell Lake and Lee dike contact temperatures T_{bdy} taking parameters τ_c, τ_w, k, and T_{BG} from the median of MCMC posterior distributions (**Table 1**). Dashed line is the forcing function T_d from Equation (11). T_{bdy} diverges from T_d in time due to thermal buffering from heated wall rocks. **(B)** Predicted ratio of flux between Maxwell Lake and Lee dikes from Equation (18). Dashed line is equal flux, values greater than unity indicate larger flux from Maxwell Lake dike.

dike and tonalitic host rock (**Figure 4**). **Figures 11B–D** shows the distribution of partial melt predicted at the Lee and Maxwell lake dikes for median fitting models (parameters in **Table 1**), as well as the duration of non-zero melt fraction predicted as a function of distance from the dike center. At Maxwell Lake, partial melt is predicted up to 8 m away from the dike, with significant melt lasting 3–4 years at distances up to 4 m away. At the Lee dike, despite the larger assumed half-width (5 vs. 4 m), the strongly decreasing heating predicted by the thermochronology results in significant melt only in the $\sim$ 1 m nearest to the dike contact, lasting only 0.6–0.8 years. At both dikes, the duration of melt in the dike itself is predicted to be much shorter than in the host rocks, because higher solidus temperature of basalt vs. tonalite results in crystallization of the dike soon after flow stops, while conduction-buffered temperatures in the host rocks remain above the solidus.

At Maxwell Lake, partial melt is readily observed both in handsample and thin section, and was mapped petrographically by Petcovic and Grunder (2003). Although the location of that mapping is $\sim$ 0.8 km along strike of the Maxwell Lake dike from our transet location, melt was observed by those authors out to 4–6 m from the dike margin, in qualitative agreement with our predictions. In contrast, the Lee dike exhibits much more subtle signs of partial melt, although a similarly detailed petrographic analysis has not yet been carried out. Our best fitting thermal models predict a much narrower zone of partial melt around the Lee dike.

7. DISCUSSION

Large Igneous Provinces such as the Columbia River Flood Basalt Group represent an end member of volcanic activity in which large volumes of magma are rapidly emplaced into the Earth's crust and surface environment, with consequences for tectonics, climate, and life. Constraints on the tempo of these events are diverse but always indirect as there are no historical examples of similar magnitude eruptions. This study introduces new constraints on emplacement histories of two 8–10 m wide CRFB dikes from low-temperature thermochronology, using a Bayesian inversion framework that provides estimation of parameters governing heat transport into wall rocks. Previous work by Petcovic and Grunder (2003) and Petcovic and Dufek (2005) focused solely on high temperature, near-dike data at one of our study sites (the Maxwell Lake dike). The low-temperature ($\sim 60-180$ C closure temperature) thermochronology here provides complimentary constraints on magma flow, as well as far-field host rock temperatures at the time of dike emplacement.

There is considerable uncertainty in physical parameters—and to some extent the physical processes themselves—involved in dike emplacement. We utilize a forward model that is relatively simple in the spectrum of magma transport modeling: a parameterization of unsteady but monotonically varying magma advection within a dike that governs 1D heat conduction in host rocks. We also simplify the description of He atomic diffusion in modeling partial resetting of thermochronometric ages, by parameterizing the role of grain size as a function of activation energy in zircon and apatite. Such simplifications permit a Bayesian Markov Chain Monte Carlo inversion approach for exploring a six dimensional parameter space with $\sim 10^6$ forward calculations to resolve posterior PDFs that outline the most likely parameter values.

Conductive heating models fit the apatite and zircon partial resetting patterns in granitic host rocks well, except for regions near to the dike contact. The manner of this misfit (overpredicted ages near to the dike and thus underprediction of heat pulse propagation) is likely evidence for either pulsed non-monotonic flow, or advection of heat by fluids. Petcovic (2004) modeled pulsed heating to explain high temperature thermometry, although did not present a systemic study of such models. Distinguishing between transport-limited vs. diffusion-limit thermal regimes (e.g., Petford and Gallagher, 2001; Karlstrom et al., 2017) or the specific time-variations in magma flow that is allowable by the data is beyond the scope of our study. Such work would also benefit from high temperature near-dike (1–5 m from the margin) constraints in addition to low temperature thermochronology that constrain 10–100 m partial resetting patterns. Here, we focus on the predicted differences in emplacement histories between two otherwise similar dikes, and the physical implications of parameter trade offs. Such uncertainty analysis is a critical aspect of inversion: we can demonstrate that the two dikes have resolvably different emplacement histories but can also identify poorly constrained parameters that will help future model development and data collection efforts.

The Maxwell Lake dike has been geochemically linked to the Wapshilla Ridge member of the Grande Ronde formation (Petcovic and Dufek, 2005), the single most voluminous eruptive unit preserved in the CRFB ($5-10\times10^3$ km^3 erupted in multiple events contained within Wapshilla Ridge). However, macroscale structural characteristics of the Maxwell Lake dike are similar to thousands of other Chief Joseph Dike Swarm segments in the region as illustrated in **Figure 1** (Taubeneck, 1970; Morriss and Karlstrom, 2018). Without petrographic and textural indicators of partial melt in the granitic host rocks that indicate prolonged magma flow and careful geochemical fingerprinting, it would be challenging to identify this segment as a prominant feeder of CRFB flows. Our results show that the Lee dike, located south of the Maxwell Lake dike in a region of high dike segment spatial density and exhibiting similar (slightly larger) width and orientation, has a resolvably different emplacement history recorded by low temperature thermochronetry.

Although the total duration of active heating (and thus magma advection) from the Lee dike is not predicted to be significantly different than the Maxwell Lake dike by our inversion, the time variation of dike-host contact temperature and thus magma flux rate is resolvably different. Our model for unsteady heating at the dike/host rock contact (Equation 11) parameterizes the growth of thermal boundary layers separating flowing magma initially at its liquidus temperature from host rocks with parameters τ_c and τ_w (**Figure 5**). Such decreases could arise from solification or decreases in driving pressure gradient that reduce the effective width of active flow within the dike (Bruce and Huppert, 1990; Petcovic and Dufek, 2005), from along-strike flow localization (Bruce and Huppert, 1989; Wylie et al., 1999), or variations in viscous dissipation (Fialko and Rubin, 1999). Equation (11) also parameterizes unsteady flow as long as pulses are close enough spaced in time that heat transport in wall rocks is diffusion-limited.

We leave explicit consideration of flow mechanics, and thus the assessment of dike-transported flow volumes, for a future study. However, a simple model illustrates some of the expected implications of our results for relative flux between the two dikes. Volumetric flux of unidirectional viscous flow through a slot of length ℓ and halfwidth $H/2$ is

$$Q = -\frac{\ell}{12\mu} H^3 \frac{dP}{dz}, \tag{17}$$

where dP/dz is the non-hydrostatic pressure gradient driving flow and μ is the magma viscosity. Let us assume that the dike-host rock contact temperature $T_{bdy}(t)$ is proportional to effective dike width H and separately to pressure gradient dP/dz, as might occur if growing thermal boundary layers are gradually truncating flow in the dike. If we then assume that all but measured width is equal between dikes, the ratio of flux from Equation (17) between Maxwell Lake and Lee dikes is then related to the different dike widths H_M, H_L cubed. Due to the assumption that boundary temperature is proportional both to vertical pressure gradient and dike thickness, the flux ratio is proportional to boundary temperatures $T_{bdy,M}, T_{bdy,L}$ raised to the fourth power, giving

$$\frac{Q_M}{Q_L} = \left(\frac{H_M}{H_L}\right)^3 \left(\frac{T_{d,M}}{T_{d,L}}\right)^4. \tag{18}$$

Equation (18) is plotted in **Figure 12B** for representative model fit parameters (MCMC median values listed in **Table 1**). We see that, initially, the thicker Lee dike has a higher flux due to the strong dependence on width in Equation (17). However, declining pressure gradients and growth of boundary layers as implied by the predicted dike contact temperature $T_{bdy,L}(t)$ quickly dominate and Maxwell Lake has sustained flow rates more than an order of magnitude larger than Lee for most of its active lifetime. This is consistent with an interpretation that Maxwell Lake was a feeder dike to a significant surface eruption (known to be the case from its chemical composition) whereas the Lee dike might not have generated much if any surface eruptive flux.

MCMC inversion predicts a cooler background temperature (by some 50–70 degrees) for the Lee dike relative to Maxwell. Distinct background temperatures would be expected based on the paleodepth differences between Maxwell and Lee dikes. But partial resetting of apatites out to $>$ 100 m away from the Maxwell dike contact indicate temperatures that are hotter than any reasonable geotherm at $\sim$ 2 km depths. We speculate that CRFB magmatism transiently increased the regional geothermal gradient (e.g., Murray et al., 2018), sufficiently raising the background temperatures to produce the observed apatite He age pattern next to the Maxwell Lake dike without resetting apatite He ages across the Wallowa Mountains region (Crowley and Reiners, 2001). Maxwell Lake lies within a region containing a large spatial density of CRFB dike segments exposed at the surface, with $\sim$ 5 segments per km^2 (Morriss and Karlstrom, 2018). If most segments are Grande Ronde age, recent dating (Kasbohm and Schoene, 2018) implies an eruptive flux of $\sim$ 1 km^3/yr. Crustal magma transport of this magnitude is likely sufficient not only to induce regional heating but also to modulate the bulk rheology of the crustal column participating in magmatism (Karlstrom et al., 2017; Perry-Houts and Karlstrom, 2018).

Marginal posterior PDFs for thermal conductivity of wall rocks are somewhat similar for each dike, in both cases suggesting conductivities larger than typical for intact granitic rocks. We view this result as an indication that our physical model is incomplete. Near-surface advection of hydrothermal fluids are an obvious missing ingredient, as this would result in more efficient heat transport away from the dike contact and a larger apparent thermal conductivity. Such results might also be consistent with the lesser degree of partial melt in the vicinity of Maxwell Lake and Lee dikes than predicted by our model (**Figure 11**), although we expect low permeability of granite would limit the efficiency of fluid movement. We do not attempt to quantify this scenario further here.

Our inversions do not constrain activation energies for the He diffusion model at either Maxwell Lake or Lee dikes, as indicated by the shapes of the PDFs (95% confidence intervals for $E_{a,Zr}, E_{a,Ap}$ overlap for both dikes) and our metrics of inversion convergence (the Gelmin-Rubin diagnostic $\hat{R}$ in **Table 1**). Another thermochronology transect at both dikes to constrain chemical kinetics or petrographic analysis that resolve near-dike temperatures could help better define these parameters. More detailed kinetic models that explicitly invert for grain size and diffusivity along with activation energy may also be required.

8. CONCLUSIONS AND FUTURE DIRECTIONS

Bayesian Markov-Chain Monte Carlo inversion of low temperature thermochronology around two CRFB dikes near the spatial locus of the Chief Joseph Dike Swarm in NE Oregon suggests distinct emplacement histories. By combining physics-based forward models with a probabilistic approach to inversion, we can identify differences in likely patterns of magma flow and in the background temperatures far from the dike contact at the time of emplacement. Although both dikes are of similar spatial dimensions, the Maxwell Lake dike likely transported a larger volume of magma for a longer time than the Lee dike, consistent with near-dike host rock petrography and the correlation of Maxwell Lake dike to Wapshilla Ridge flows. The Lee dike has composition similar to Wanapum lavas but is not yet linked to any particular surface expression. Our inversion suggests that application of thermochronology to other CRFB dikes in granitic host rocks that are common in the Wallowa Mountains region could resolve feeder vs. non-feeder dikes and magma transport mechanics on a LIP scale.

More broadly, this study suggests that Bayesian inversion methods have utility in inverting volcanologic data. We have focused on thermochronology, jointly inverting for partial resetting of two different chronometers by combining models for dike-scale heat conduction with grain-scale models for Helium diffusion in zircon and apatite. Other data, for example from high temperature geothermometry or paleomagnetic partial resetting, could easily be incorporated into this framework and might contribute to a more well-constrained posterior PDF. Model complexity does represent a significant challenge, due to the requirement that many thousands of forward models are needed for the MCMC inversion to converge. More effort is needed to develop reduced-order models for magma transport processes that are faithful parameterizations of computationally intensive multiphysics simulations. The payoff is a more robust predictive understanding of magmatic processes at a level commensurate with data granularity, which is a needed step toward connecting observations of active processes with the geologic record of magmatism.

AUTHOR CONTRIBUTIONS

LK performed MCMC inversions, wrote the forward modeling codes, and the manuscript. KM performed Maxwell Lake dike measurements. PR performed Lee dike measurements. LK and KM devised the study. All authors contributed to manuscript editing.

ACKNOWLEDGMENTS

We thank Matthew Morriss for field assistance during sampling of the Maxwell Lake dike and for discussions surrounding the Chief Joseph Dike Swarm, Heather Petcovic for helpful information about prior work at Maxwell Lake, and Victoria E. Lee for assistance during sampling of the Lee dike. LK acknowledges field work support from the National Science Foundation EAR 1547594. Peter Zeitler and George Gehrels are acknowledged for providing dates on the Cornucopia pluton at the Lee Dike. We thank Kyle Anderson for developing the MCMC Hammer code used for data inversion, Stefan Nicolescu for analytical assistance with the Lee dike samples, and Amanda Maslyn for analytical support at the University of Michigan HeliUM lab. Two reviewers and editor Mattia Pistone provided constructive comments that improved the manuscript.

SUPPLEMENTARY MATERIAL

The Supplementary Material for this article can be found online at: https://www.frontiersin.org/articles/10.3389/feart.2019.00090/full#supplementary-material

Supplementary Data | Table S1 contains thermochronology data for each grain analyzed, sample locations, ages, and errors for Maxwell Lake and Lee dikes.

REFERENCES

Anderson, K., and Segall, P. (2013). Bayesian inversion of data from effusive volcanic eruptions using physics-based models: application to Mount St Helens 2004-2008. *J. Geophys. Res.* 118, 2017–2037. doi: 10.1002/jgrb.50169

Anderson, K. R., and Poland, M. P. (2016). Bayesian estimation of magma supply, storage, and eruption rates using a multiphysical volcano model: Kilauea volcano, 2000-2012. *Earth Planet. Sci. Lett.* 447, 161–171. doi: 10.1016/j.epsl.2016.04.029

Barry, T., Kelley, S., Reidel, S., Camp, V., Self, S., Jarboe, N., et al. (2013). Eruption chronology of the Columbia River Basalt Group. *Geol. Soc. Am. Spec. Pap.* 497, 45–66. doi: 10.1130/2013.2497(02)

Bruce, P. M., and Huppert, H. E. (1989). Thermal control of basaltic fissure eruptions. *Nature* 342, 665–667.

Bruce, P. M., and Huppert, H. E. (1990). "Solidification and melting along dykes by the laminar flow of basaltic magmam" in*Magma Transport and Storage*, ed M. P. Ryan (Chichester, UK: John Wiley and Sons).

Burgess, S. D., and Bowring, S. A. (2015). High-precision geochronology confirms voluminous magmatism before, during, and after Earth's most severe extinction. *Sci. Adv.* 1:e1500470. doi: 10.1126/sciadv.1500470

Burgess, S. D., Muirhead, J. D., and Bowring, S. A. (2017). Initial pulse of Siberian Traps sills as the trigger of the end-Permian mass extinction. *Nat. Commun.* 8:164. doi: 10.1038/s41467-017-00083-9

Bursik, M., Jones, M., Carn, S., Dean, K., Patra, A., Pavolonis, M., et al. (2012). Estimation and propagation of volcanic source parameter uncertainty in an ash transport and dispersal model: application to the Eyjafjlallajokull plume of 14-16 April 2010. *Bull. Volcanol.* 74, 2321–2338. doi: 10.1007/s00445-012-0665-2

Camp, V. E., Reidel, S. P., Ross, M. E., Brown, R. J., and Self, S. (2017). Field-trip guide to the vents, dikes, stratigraphy, and structure of the Columbia River Basalt Group, Eastern Oregon and Southeastern Washington. *Sci. Invest. Rep.* 5022, 1–88. doi: 10.3133/sir20175022N

Cassata, W. S., Shuster, D. L., Renne, P. R., and Weiss, B. P. (2010). Evidence for shock heating and constraints on Martian surface temperatures revealed by ^{40}Ar/^{39}Ar thermochronometry of Martian meteorites. *Geochim. Cosmochim. Acta* 74, 6900–6920. doi: 10.1016/j.gca.2010.08.027

Courtillot, V. E., and Renne, P. R. (2003). On the ages of flood basalt events. *C. R. Geosci.* 335, 113–140. doi: 10.1016/S1631-0713(03)00006-3

Crowley, P. D., and Reiners, P. W. (2001). "Timing of exhumation of the Wallowa Mountains, ne Oregon: a U-Th/He thermochronologic study," in *GSA Annual Meeting Abstracts* (Boston, MA) (108-0).

Davenport, K. K., Hole, J. A., Tikoff, B., Russo, R. M., and Harder, S. H. (2017). A strong contrast in crustal architecture from accreted terranes to craton, constrained by controlled-source seismic data in Idaho and eastern Oregon. *Lithosphere* 9, 325–340. doi: 10.1130/L553.1

Delaney, P. T. (1982). Rapid intrusion of magma into wet rock: Groundwater flow due to pore pressure increases. *J. Geophys. Res.* 87, 7739–7756.

Dodson, M. (1973). Closure temperature in cooling geochronological and petrological systems. *Contrib. Mineral. Petrol.* 40, 259–274.

Ehlers, T., and Farley, K. A. (2003). Apatite (U-Th)/He thermochronometry: methods and applications to problems in tectonic and surface processes. *Earth Planet. Sci. Lett.* 206, 1–14. doi: 10.1016/S0012-821X(02)01069-5

Erickson, B. A., Dunham, E. M., and Khosravifar, A. (2017). A finite difference method for off-fault plasticity throughout the earthquake cycle. *J. Mech. Phys. Solids* 109, 50–77. doi: 10.1016/j.jmps.2017.08.002

Farley, K. A. (2000). Helium diffusion from apatite: general behavior as illustrated by Durango fluorapatite. *J. Geophys. Res.* 105, 2903–2914. doi: 10.1029/1999JB900348

Fechtig, H., and Kalbitzer, S. (1966). The diffusion of Argon in Potassium-bearing solids. in *Potassium Argon Dating*, eds O. A. Schaeffer and J. Zahringer (Berlin: Springer-Verlag), 68–107.

Fialko, Y. A., and Rubin, A. M. (1999). Thermal and mechanical aspects of magma emplacement in giant dike swarms. *J. Geophys. Res.* 104, 23033–23049.

Flowers, R. M., Ketcham, R. A., Shuster, D. L., and Farley, K. A. (2009). Apatite (U–Th)/He thermochronometry using a radiation damage accumulation and annealing model. *Geochim. Cosmochim. Acta* 73, 2347–2365. doi: 10.1016/j.gca.2009.01.015

Fukada, J., and Johnson, K. (2008). A fully Bayesian inversion for spatial distribution of fault slip with objective smoothing. *Bull. Seismol. Soc. Am.* 98, 1128–1146. doi: 10.1785/0120070194

Gautheron, C., Tassan-Got, L., Barbarand, J., and Pagel, M. (2009). Effect of alpha-damage annealing on apatite (U–Th)/He thermochronology. *Chem. Geol.* 266, 157–170. doi: 10.1016/j.chemgeo.2009.06.001

Gelman, A., and Rubin, D. B. (1992). Inference from iterative simulation using multiple sequences. *Stat. Sci.* 7, 457–511.

Guenthner, W. R., Reiners, P. W., and Chowdhury, U. (2016). Isotope dilution analysis of Ca and Zr in apatite and zircon (U-Th)/He chronometry. *Geochem. Geophys. Geosyst.* 17, 1623–1640. doi: 10.1002/2016GC006311

Guenthner, W. R., Reiners, P. W., Ketcham, R. A., Nasdala, L., and Giester, G. (2013). Helium diffusion in natural zircon: radiation damage, anisotropy, and the interpretation of zircon (U-Th)/He thermochronology. *Am. J. Sci.* 313, 145–198. doi: 10.2475/03.2013.01

Huber, C., Bachmann, O., and Manga, M. (2009). Homogenization processes in silicic magma chambers by stirring and mushification (latent heat buffering). *Earth Planet. Sci. Lett.* 283, 38–43. doi: 10.1016/j.epsl.2009.03.029

Jaupart, C., and Provost, A. (1985). Heat focusing, granite genesis and inverted metamorphic gradients in continental collision zones. *Earth Planet. Sci. Lett.* 73, 385–397.

Johnson, K., Barnes, C. G., and Miller, C. A. (1997). Petrology, geochemistrym and genesis of high-Al tonalite and trondhjemites of the Cornucopia stock, Blue Mountains, northeastern Oregon. *J. Petrol.* 38, 1585–1611.

Karlstrom, L., Dufek, J., and Manga, M. (2010). Magma chamber stability in arc and continental crust. *J. Volcanol. Geotherm. Res.* 190, 249–270. doi: 10.1016/j.jvolgeores.2009.10.003

Karlstrom, L., Paterson, S. R., and Jellinek, A. M. (2017). A reverse energy cascade for crustal magma transport. *Nat. Geosci.* 20, 604–608. doi: 10.1038/ngeo2982

Kasbohm, J., and Schoene, B. (2018). Rapid eruption of the Columbia River flood basalt and correlation with the mid-Miocene climate optimum. *Sci. Adv.* 4:eaat8223. doi: 10.1126/sciadv.aat8223

Kass, R. E., Carlin, B. P., Gelman, A., and Neal, R. M. (1998). Markov Chain Monte Carlo in practice: a roundtable discussion. *Am. Stat.* 52, 93–100.

Keszthelyi, L., Self, S., and Thordarson, T. (2006). Flood lavas on Earth, Io and Mars. *J. Geol. Soc. Lond.* 163, 253–264. doi: 10.1144/0016-764904-503

Ladderud, J. A., Wolff, J. A., Rember, W. C., and Brueseke, M. E. (2015). Volcanic ash layers in the Miocene lake Clarkia beds: Geochemistry, regional correlation, and age of the Clarkia flora. *Northw. Sci.* 89, 309–323. doi: 10.3955/046.089.0402

Link, W. A., and Eaton, M. J. (2012). On thinning of chains in MCMC. *Methods Ecol. Evol.* 3, 112–115. doi: 10.1111/j.2041-210X.2011.00131.x

McDougall, I., and Harrison, T. M. (1999). *Geochronology and Thermochronology by the $^{40}Ar/^{39}Ar$ Method*. New York, NY: Oxford University Press.

Metropolis, N., Rosenbluth, W., Rosenbluth, M. N., Teller, A. H., and Teller, E. (1953). Equation of state calculations by fast computing machines. *J. Chem. Phys.* 21, 1087–1092.

Morriss, M. C., and Karlstrom, L. (2018). "The Chief Joseph Dike Swarm of the Columbia River Basalts, and the legacy dataset of William H. Taubeneck," in *American Geophysical Union Fall Meeting Abstracts* (V31H-0216)(Washington, DC).

Mosegaard, K., and Tarantola, A. (2002). "Probabilistic approach to inverse problems," in *International Handbook of Earthquake and Engineering Seismology*, eds P. C. J. William, H. K. Lee, H. Kanamori, and C. Kisslinger (Amsterdam: Academic Press), 237–265.

Murray, K. E., Braun, J., and Reiners, P. W. (2018). Toward robust interpretation of low-temperature thermochronometers in magmatic terranes. *Geochem. Geophys. Geosyst.* 19, 3739–3763. doi: 10.1029/2018GC007595

Perry-Houts, J., and Karlstrom, L. (2018). Anisotropic viscosity and time-evolving lithospheric instabilities due to aligned igneous intrusions. *Geophys. J. Int.* 216, 794–802. doi: 10.1093/gji/ggy466

Petcovic, H. L. (2004). *Feeder Dikes to the Columbia River Flood Basalts: Underpinnings of a Large Igneous Province*. PhD thesis, Oregon State University.

Petcovic, H. L. and Dufek, J. (2005). Modeling magma flow and cooling in dikes: implications for emplacement of Columbia River flood basalts. *J. Geophys. Res.* 110:B10201. doi: 10.1029/2004JB003432

Petcovic, H. L., and Grunder, A. L. (2003). Textural and thermal history of partial melting in tonalitic wallrock at the margin of a basaltic dike, Wallowa Mountains, Oregon. *J. Petrol.* 44, 2287–2312. doi: 10.1093/petrology/egg078

Petford, N., and Gallagher, K. (2001). Partial melting of mafic (amphibolitic) lower crust by periodic influx of basaltic magma. *Earth Planet. Sci. Lett.* 193, 483–499. doi: 10.1016/S0012-821X(01)00481-2

Reidel, S. P., Camp, V. E., Tolan, T. L., and Martin, B. S. (2013). The Columbia River flood basalt province: stratigraphy, areal extent, volume, and physical volcanology. *Geol. Soc. Am. Spec. Pap.* 497, 1–43. doi: 10.1130/2013.2497(1)

Reiners, P. W. (2005). Zircon $(u - th)/he$ thermochronometry. *Rev. Mineral. Geochem.* 58, 151–179. doi: 10.2138/rmg.2005.58.6

Reiners, P. W. (2009). Nonmonotonic thermal histories and contrasting kinetics of multiple thermochronometers. *Geochim. Cosmochim. Acta* 73, 3612–3629. doi: 10.1016/j.gca.2009.03.038

Reiners, P. W., and Brandon, M. T. (2006). Using thermochronology to understand orogenic erosion. *Annu. Rev. Earth Planet. Sci.* 34, 419–466. doi: 10.1146/annurev.earth.34.031405.125202

Reiners, P. W., Spell, T., Nicolescu, S., and Zanetti, K. (2004). Zircon (U-Th)/He thermochronometry: He diffusion and comparisons with 40Ar/39Ar dating. *Geochim. Cosmochim. Acta* 68, 1857–1887. doi: 10.1016/j.gca.2003.10.021

Shuster, D. L., Flowers, R. M., and Farley, K. A. (2006). The influence of natural radiation damage on helium diffusion kinetics in apatite. *Earth Planet. Sci. Lett.* 249, 148–161. doi: 10.1016/j.epsl.2006.07.028

Taubeneck, W. H. (1964). Cornucopia stock, Wallowa Mountains, northeastern Oregon: field relationships. *Geol. Soc. Am. Bull.* 75, 1093–1116.

Taubeneck, W. H. (1970). "Dikes of Columbia River Basalt in northeastern Oregon, western Idaho, and southeastern Washington," in *Proceedings of the second Columbia River Basalt Symposium*, eds E. H. Gilmor and D. Stradling (Cheney, WA: Eastern Washington State College), 73–96.

Thordarson, T., and Self, S. (1998). The Roza Member, Columbia River Basalt Group: a gigantic pahoehoe lava flow field formed by endogeneous processes? *J. Geophys. Res.* 103, 27411–27445.

Watson, E. B., and Cherniak, D. J. (2013). Simple equations for diffusion in response to heating. *Chem. Geol.* 335, 93–104. doi: 10.1016/j.chemgeo.2012.10.054

White, S. M., Crisp, J. A., and Spera, F. J. (2006). Long-term volumetric eruption rates and magma budgets. *Geochem. Geophys. Geosyst.* 7. doi: 10.1029/2005GC001002

Whittington, A. G., Homeister, A. M., and Nabelek, P. I. (2009). Temperature-dependent thermal diffusivity of the Earth's crust and implications for magmatism. *Nature* 458, 319–321. doi: 10.1038/nature07818

Wolf, R. A., Farley, K. A., and Kass, D. M. (1998). Modeling of the temperature sensitivity of the apatite (U-Th)/He thermochronometer. *Chem. Geol.* 148, 105–114.

Wylie, J. J., Helfrich, K. R., Daude, B., Lister, J. R., and Salzig, J. F. (1999). Flow localization in fissure eruptions. *Bull. Volcanol.* 60, 432–440.

Zak, J., Verner, K., Tomek, F., Holub, F. V., Johnson, K., and Schwartz, J. J. (2015). Simultaneous batholith emplacement, terrane/continent collision, and oroclinal bending in the Blue Mountains Province, North American Cordillera. *Tectonics* 34, 1107–1128. doi: 10.1002/2015TC003859

Conflict of Interest Statement: The authors declare that the research was conducted in the absence of any commercial or financial relationships that could be construed as a potential conflict of interest.

APPENDIX A

A.1. Assessment of MCMC Convergence and Parameter Values

Markov Chain Monte Carlo involves the production of a dependent sequence or chain of values which, if run for long enough time, will converge to the underlying posterior distribution (Mosegaard and Tarantola, 2002). Convergence of MCMC chains is impossible to guarantee in practice but several standard tools exist to assess convergence, the degree to which sampling has integrated over the joint posterior PDF (i.e., good parameter "mixing"), and whether the chain involves enough samples to adequetely cover the posterior (Kass et al., 1998).

We perform three tests to assess convergence of our MCMC inversions. As a first test, we computed the posterior distribution with different kept sample populations, experimenting with the number of 'burn in' samples discarded and whether or not to "thin" the distribution (i.e., discard every kth sample, although this is likely unnecessary for sufficiently long chains, Link and Eaton, 2012). We have also experimented with different sampling step sizes (between 80 and 120 steps within uniform priors for each parameter), and logarithmically as well as linearly spaced steps. We run many MCMC chains, and the starting points for each chain are randomized. When the number of samples per chain is larger than $\sim 10^4$, for the tested range of thinning and step size, shapes of the posterior PDFs do not change much. This qualitative test provides some confidence that we are adequately sampling the true posterior.

A second, more quantitative test involves the autocorrelation for each parameter in each chain. **Figure A1** shows the mean autocorrelation for each parameter over 70–75 independent chains, as a function of sample lag. Above lags of $\sim 7 \times 10^3$, the mean autocorrelation for every parameter and both dikes has dropped to near zero and fluctuates about zero as lag increases further. This suggests randomized sampling and is in agreement with the qualitative threshold found in the first test.

As a third test, we compute the Gelman and Rubin (1992) 'Potential Scale Reduction Factor' $\hat{R}$ for each parameter (**Table 1**). The Gelman-Rubin diagnostic is a weighted average of the within-chain variance and between-chain variances. Values below $\hat{R} = 1.2$ are often used as a criteria for convergence. As **Table 1** shows, while most of the parameters do fall within this convergence criterion, there are notable exceptions. Most significantly, the activation energys $E_{a,Zr}$ and $E_{a,Ap}$ are far in excess of 1.2 and the background temperature T_{BG} is close to but not under 1.2 for both dikes.

This could indicate that the MCMC has not converged for these parameters and longer chains are required. However, there are also some reasons to be wary of $\hat{R}$ as a metric for convergence (Kass et al., 1998). The Gelman-Rubin diagnostic $\hat{R}$ assumes the underlying PDF to be normally distributed and over-dispersed starting guesses for chains, which are not possible for all of our parameters on physical grounds: for example, we cannot take background temperatures T_{BG} below 25 C, and above 100 C is implausible in the upper few km of crust. That the predicted posterior PDF for T_{BG} is skewed toward the prior lower limit for the Lee dike, or that the flow unsteadiness parameter τ_w is screwed toward its lower limit for the Maxwell Lake dike, is likely a physical result. We thus have reason to suspect that $\hat{R}$ may not be an accurate metric of convergence for all of our parameters, although do take the large $\hat{R}$ values found for activation energies as another sign that these parameters are not well constrained by our inversions.

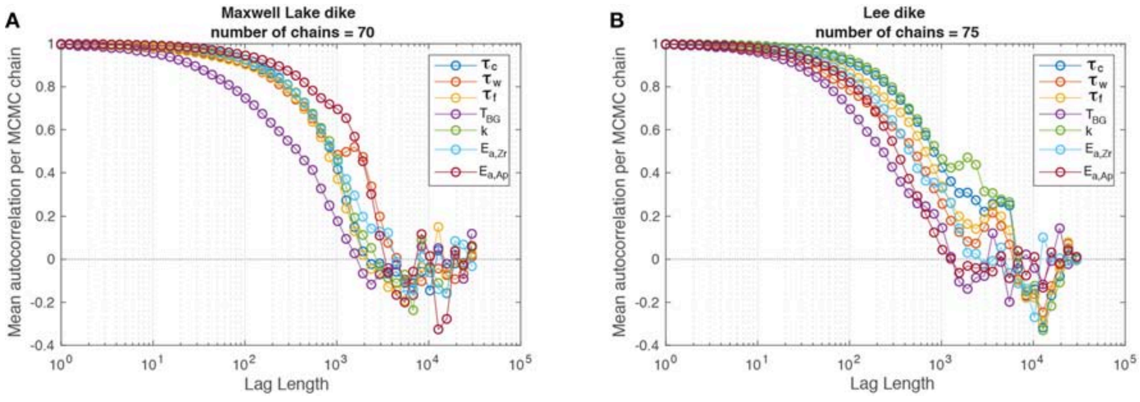

FIGURE A1 | (A) Average autocorrelation of MCMC chains as a function of lag for the Maxwell Lake dike, for each parameter. Autocorrelation is calculated for each of 70 chains with randomized starting points, then averaged at each lag value to produce these curves. **(B)** Same as **(A)** for the Lee dike MCMC simulations, with 75 independent chains considered.

frontiers in Earth Science

ORIGINAL RESEARCH
published: 24 September 2019
doi: 10.3389/feart.2019.00239

Deep Magma Storage Revealed by Multi-Method Elemental Mapping of Clinopyroxene Megacrysts at Stromboli Volcano

Teresa Ubide[1]*, *John Caulfield*[1], *Claire Brandt*[1], *Yannick Bussweiler*[2,3], *Silvio Mollo*[4,5], *Flavio Di Stefano*[4], *Manuela Nazzari*[5] and *Piergiorgio Scarlato*[5]

[1] School of Earth and Environmental Sciences, The University of Queensland, Brisbane, QLD, Australia, [2] TOFWERK AG, Thun, Switzerland, [3] Institut für Mineralogie, Universität Münster, Münster, Germany, [4] Department of Earth Sciences, Sapienza - University of Rome, Rome, Italy, [5] Istituto Nazionale di Geofisica e Vulcanologia, Rome, Italy

Edited by:
Mattia Pistone,
Université de Lausanne, Switzerland

Reviewed by:
Fabio Arzilli,
University of Manchester,
United Kingdom
Chad Deering,
Michigan Technological University,
United States

***Correspondence:**
Teresa Ubide
t.ubide@uq.edu.au

Specialty section:
This article was submitted to
Volcanology,
a section of the journal
Frontiers in Earth Science

Received: 02 March 2019
Accepted: 29 August 2019
Published: 24 September 2019

Citation:
Ubide T, Caulfield J, Brandt C,
Bussweiler Y, Mollo S, Di Stefano F,
Nazzari M and Scarlato P (2019) Deep
Magma Storage Revealed by
Multi-Method Elemental Mapping of
Clinopyroxene Megacrysts at
Stromboli Volcano.
Front. Earth Sci. 7:239.
doi: 10.3389/feart.2019.00239

The magmatic architecture and physicochemical processes inside volcanoes influence the style and timescale of eruptions. A long-standing challenge in volcanology is to establish the rates and depths of magma storage and the events that trigger eruption. Magma feeder systems are remarkably crystal-rich, and the growth stratigraphy of minerals sampled by erupted magmas can reveal a wealth of information on pre-eruptive processes. Here we combine detailed textural and chemical data acquired on large (>5 mm), euhedral augite megacrysts from Roman era activity (Pizzo scoria cone, 2.4–1.8 ka) at Stromboli (Italy) to investigate the plumbing system prior to the onset of current steady-state activity. Our dataset includes novel laser ablation time-of-flight mass spectrometry (LA-ICP-TOFMS) maps, which rapidly visualise multi-element zoning patterns across entire megacryst sections. The clinopyroxene data are complemented with geochemical constraints on mineral and melt inclusions, and adhering glassy tephra. Megacrysts are sector and oscillatory zoned in trace elements, yet their major element compositions are relatively uniform and in equilibrium with shoshonite-buffered melts. Mild sector zoning documents dynamic crystallisation under conditions of low undercooling during magma residence and growth. Clinopyroxene-melt thermobarometric and hygrometric calibrations, integrated with thermodynamically derived equilibrium equations, accurately track the P-T-H_2O path of magmas. The refined models return restricted crystallisation depths that are deeper than those reported previously for historical and current eruptions, but consistent with deep clinopyroxene-dominated crystallisation (≥10 km), resembling other water-rich alkaline mafic systems. Megacryst cores are overgrown by oscillatory zoned mantles recording continuous input of magma that failed to trigger eruption. Crystal rims are characterised by a mild increase in compatible transition metals Cr and Ni, and depletion in incompatible elements, indicative of pre-eruptive mafic replenishment and magma mixing. The volcanic system appears to have been dominated by protracted periods of replenishment, convection, and crystal residence, punctuated by rapid megacryst evacuation and eruption upon arrival of more mafic magma (days-weeks). Since the inception of current steady-state activity, eruption-triggering melts have become appreciably more mafic, suggesting that intrusion of primitive magma may be a key driver of the steady-state regime.

Keywords: clinopyroxene, megacryst, sector zoning, oscillatory zoning, elemental mapping, time-of-flight mass spectrometry (ICP-TOFMS), magma mixing, stromboli

INTRODUCTION

The depths and rates of magma storage, transport, mixing, and eruption are of fundamental importance in igneous petrology, and key in the interpretation of monitoring signs at active volcanoes (e.g., McNutt, 2005; White and McCausland, 2016; Biggs and Pritchard, 2017; Cashman et al., 2017). The pathway of mantle-derived magmas through the crust to eruption can be highly convoluted and includes protracted magma segregation, stagnation, and crystallisation in vertically extended mush columns (Cashman et al., 2017), often conspiring against magmas reaching the Earth's surface. As a result, most magmas do not erupt (Putirka, 2017). Indeed, measurements of degassing at active volcanoes infer volumes of shallow magma that greatly exceed erupted volumes (Shinohara, 2008). Understanding the intensive parameters and timescales of the processes that modulate volcano plumbing systems, and identifying those that tip volcanoes to the point of eruption, are key research directions in modern petrology and volcanology (e.g., Putirka, 2017).

Stromboli volcano (Aeolian archipelago, Italy; **Figure 1**) constitutes an ideal natural laboratory for the detailed investigation of magmatic processes and eruption triggers on geological, to historical, to human timescales (e.g., Francalanci et al., 2013). The stratovolcano is an archetype of steady-state activity, where continuous input of basaltic magma has maintained persistent volcanism for centuries, affording the volcano the unique moniker "Lighthouse of the Mediterranean" (Rosi et al., 2013 and references therein). Frequent mild explosions (every 10–20 min) eject crystal-rich black scoriae sourced from a shallow, highly porphyritic (HP) reservoir. The regular "Strombolian" activity is periodically interrupted by more energetic short-lived blasts, "paroxysms," the latest examples of which occurred on July 3rd and August 28th, 2019. Paroxysms typically erupt HP magma mingled with crystal-poor, volatile-rich, more primitive "golden" pumice fed from a deep, low porphyritic (LP) reservoir. More rarely, the volcano produces lava flows, similar in composition to the regular black scoriae and also sourced from the HP reservoir (e.g., Armienti et al., 2007). An improved understanding of the processes controlling the different eruptive styles is a high priority for civil defence (Burton et al., 2007). Syn-eruptive mixing and mush recycling is recorded by chemical and isotopic heterogeneities at the mineral scale, preserved as complex textures in plagioclase and clinopyroxene (e.g., Landi et al., 2004; Francalanci et al., 2005, 2012; Armienti et al., 2007; Bragagni et al., 2014; Petrone et al., 2018). Olivine-hosted melt inclusions locate the current LP-HP double-tier storage system at ca. 10 and 3 km, respectively (Aiuppa et al., 2010; Métrich et al., 2010), within a vertically extended mush column. Precisely locating distinct reservoirs throughout the history of Stromboli volcanism is crucial given the hazard potential of activating magma pockets with distinct crystallinity and volatile contents. However, independent petrological estimates based on mineral-melt equilibrium have been hampered by a lack of calibrations appropriate for Stromboli magmas.

Products erupted during the last two millennia encompass three successive periods of activity (**Figure 1C**): Epoch 6a (Pizzo, San Bartolo, Bastimento, and Post-Pizzo), 6b and 6c (<1.2 ka Present-day activity; Francalanci et al., 2013). In a recent study on the eruptive products of the Post-Pizzo and the Present-day activity, Petrone et al. (2018) concluded that steady-state activity was already established in the Post-Pizzo period. Using bulk rock and clinopyroxene compositions, together with Fe-Mg diffusion modelling of clinopyroxene zoning, Petrone et al. (2018) suggested a link between the arrival of mafic shoshonite magma and the development of a very well-stirred, dynamic plumbing system characterised by rapid mixing and short-storage timescales. The power of mafic intrusions as drivers of enhanced magmatic activity has also been highlighted through clinopyroxene compositions at Mt. Etna (Ubide and Kamber, 2018), a larger stratovolcano situated on the island of Sicily (**Figure 1**) and characterised by annual volcanic activity. At Stromboli, the question remains as to whether the steady-state activity started in Post-Pizzo times or even earlier. Most importantly, there is a need to better understand the key magmatic processes and plumbing system architectures that bring about changes in eruptive activity through time.

Previous products of Roman era volcanism (2.4–1.8 ka; Pizzo activity; **Figure 1**) crop out near the summit of Stromboli and include pyroclastic deposits that can be compositionally divided into two subgroups: shoshonites (similar to Post-Pizzo and Present-day activity eruptive products) and high-K basalts (common in pre-Pizzo activity but not observed subsequently; Francalanci et al., 2013, 2014). Geochemical investigations on the Pizzo deposits are challenging due to strong alteration by acidic fumarolic gases emitted from the active craters (Francalanci et al., 2014 and references therein). However, detailed stratigraphic and geochemical studies reported that the two compositional subgroups, while coeval, were fed by independent reservoirs located at distinct depths (inferred at ∼3 km for the shoshonites and ∼9–11 km for the high-potassium basalts; Francalanci et al., 2014). The lack of interaction between deep and shallow Pizzo reservoirs contrasts with the current LP-HP configuration, suggesting that the plumbing system may

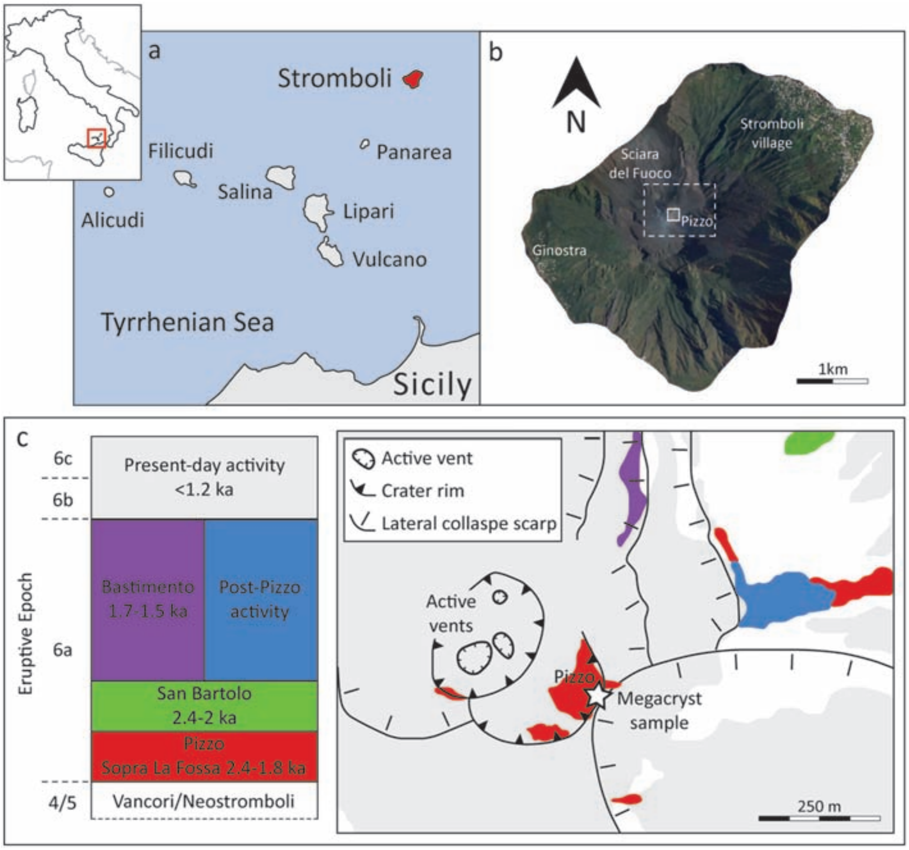

FIGURE 1 | (a) Location of the island of Stromboli in the Aeolian archipelago, Sicily Province, southern Italy. **(b)** Aerial view of Stromboli from Google Earth, outlining summit sample area (Pizzo; solid white square). Dashed white inset denotes location of the geological map in (c). **(c)** Simplified geological map of the Stromboli summit area (modified after Petrone et al., 2018). Legend includes age of eruptive units. The Post-Pizzo activity lacks absolute age constraints but is considered coeval to the Bastimento lavas on the basis of geochemical characteristics (Francalanci et al., 2013). Sampling site is marked with a white star on the map: the clinopyroxene megacrysts were collected from the partially collapsed Pizzo-o-Sopra-la-Fosa (Pizzo) scoria cone, which represents the best viewpoint for observing the Present-day activity at the summit of Stromboli volcano (Francalanci et al., 2014).

have been distinct during Pizzo compared to more recent times. Fresh, perfectly euhedral clinopyroxene (augite) crystals have been long described in these outcrops (Kozu and Washington, 1918) and provide an exciting opportunity to help disentangle protracted magmatic histories and P-T-H_2O constraints for a potential turning-point in the eruptive history of Stromboli.

Clinopyroxene is stable over upper mantle and crustal conditions and has low chemical diffusivity, affording the potential to trace eruption triggering mechanisms and timescales in basaltic to intermediate volcanoes (Putirka, 2017; Petrone et al., 2018; Ubide and Kamber, 2018). The composition of clinopyroxene is highly sensitive to pressure, temperature, and melt water content, and recently optimised calibrations on water-rich, mafic alkaline melts (Perinelli et al., 2016; Mollo et al., 2018) open the possibility of new constraints on the architecture of the plumbing system feeding volcanism at Stromboli. Moreover, a recent reappraisal of sector zoning in clinopyroxene (Ubide et al., 2019) has shown that sector-zoned crystals can provide insight not only into magmatic histories and eruption triggers, but also into magma cooling rates and reservoir dynamics. At Stromboli, sector-zoned clinopyroxene has been reported in the products of historical eruptions (Métrich et al., 2010) but to date, the occurrence, record, and implications of sector zoning have remained largely overlooked.

Here we apply a combination of detailed petrography and *in-situ* major and trace element analysis and mapping of clinopyroxene megacrysts (>5 mm) from the Pizzo activity in Roman times, to explore pre-eruptive processes and plumbing system architecture through protracted growth histories. Megacryst sections were prepared parallel and orthogonal to the *c* crystallographic axis to investigate three-dimensional zoning relationships. We applied a multi-method mapping approach combining electron microprobe, laser ablation quadrupole mass spectrometry (Ubide et al., 2015), and novel laser ablation time-of-flight maps (Burger et al., 2015, 2017) for a detailed investigation of zoning patterns, inclusion populations, and their textural context. Petrological results and P-T-H_2O estimates of clinopyroxene crystallisation bring new insights into deep

FIGURE 2 | Selection of 12 clinopyroxene megacrysts analysed in this study. The crystals are perfectly euhedral augites, oriented with their *c* crystallographic axis in vertical position (following the scale bar). Crystals 2, 7, 11, 23, 27, 31, 34, and 44 are laying on {100}, whereas 1, 13, and 46 are slightly rotated around the *c*-axis showing {110} in the foreground. Samples 11 and 13 are swallow-tail crystals twinned on {100}. Often, crystals have inclusions of olivine on the surface, remnant inclusion indentations (e.g., 31), and/or are coated with glassy matrix (e.g., 34). Sample 49 is a complex glomerocryst.

magma dynamics and the inception of steady-state activity at Stromboli. Our integrated elemental mapping approach highlights methodological advantages, considerations and limitations, providing guidance for the effective investigation of crystal zoning in magmatic systems elsewhere.

THE CLINOPYROXENE MEGACRYSTS

Clinopyroxene megacrysts were collected at the summit of Stromboli volcano in June 2016, from the remnants of the partially collapsed Pizzo-o-Sopra-la-Fosa (Pizzo) scoria cone (**Figure 1**) which currently forms the best viewpoint for observing the Present-day activity (Francalanci et al., 2014). We collected a single bulk sample that comprises pervasively altered, unconsolidated ash- to lapilli-sized scoria from the top of the Roman-age Pizzo sequence (2.4–1.8 ka; Francalanci et al., 2014, see "psf" in their Figure 2). Loose, perfectly euhedral and fresh clinopyroxene megacrysts (>5 mm), often occurring as glomerocrysts, were readily hand-picked from the weathered scoria. Although the origin of the sample cannot be definitively constrained, the extremely friable nature of the matrix material and presence of loose single megacrysts is consistent with the large crystals having weathered out over the last several thousand years. Megacryst preparation and petrographic observations were undertaken at the School of Earth and Environmental Sciences at The University of Queensland.

Fifty-three megacrysts were carefully cleaned (10–45 min ultrasonication cleaning cycles in 3.5N HCl, milli-Q water, and finally ethanol), weighed, measured, and photographed (**Figure 2**). Crystals were named sequentially based on mass (30–550 mg, clinopyroxene 1 is the lightest) and range from 4 to 17 mm in length. The megacrysts have polyhedral habits following the augite crystal model (e.g., Downes, 1974; Leung, 1974; Ubide et al., 2019), characterised by a consistent set of dominant crystal forms {100}, {110}, {010} perpendicular to the *c*-axis, and {−111} along the *c*-axis (**Figure 3**). Twins on {100} yield swallow-tail crystals elongated along the *c*-axis. Less commonly, twins on {101} form cross-shaped crystals (e.g., Welsch et al., 2016). Non-symmetrical crystal intergrowths are also common. A number of crystals have inclusions of olivine/plagioclase on the surface and/or are partially coated with glassy matrix. Olivine, plagioclase, and matrix glass are variably altered, whereas the clinopyroxenes are invariably fresh.

A subset of 12 representative megacrysts (**Figure 2**; **Supplementary Table 1**) were embedded in resin mounts with their {100} plane face down. Where possible, mounts were then cut in half to expose a cross section perpendicular to the *c*-axis (basal section, named "B"). The two halves were remounted in resin, one parallel and one perpendicular to the *c*-axis, and polished. The section parallel to the *c*-axis (named "C") was polished down to the middle of the crystal with the aim of exposing the entire core-to-rim growth pattern. Reflected light microscopy and back-scattered electron (BSE) imaging guided the selection of crystal sections of interest for *in-situ* analysis and mapping. A summary of crystal sections analysed and techniques applied is provided in **Supplementary Table 1**.

ANALYTICAL METHODS

Major Element Analysis and Mapping Using Electron Microprobe

A total of seven sections from five crystals were analysed for major element compositions by electron probe microanalysis (EPMA) at INGV Rome, using a JEOL JXA-8200 instrument equipped with five wavelength dispersive spectrometers. Analyses were performed on carbon-coated resin mounts under high vacuum conditions, using an accelerating voltage of 15 kV, an electron beam current of 7.5 nA, and a beam diameter of 5 µm. Elemental counting times were 10 s on the peak and 5 s on each

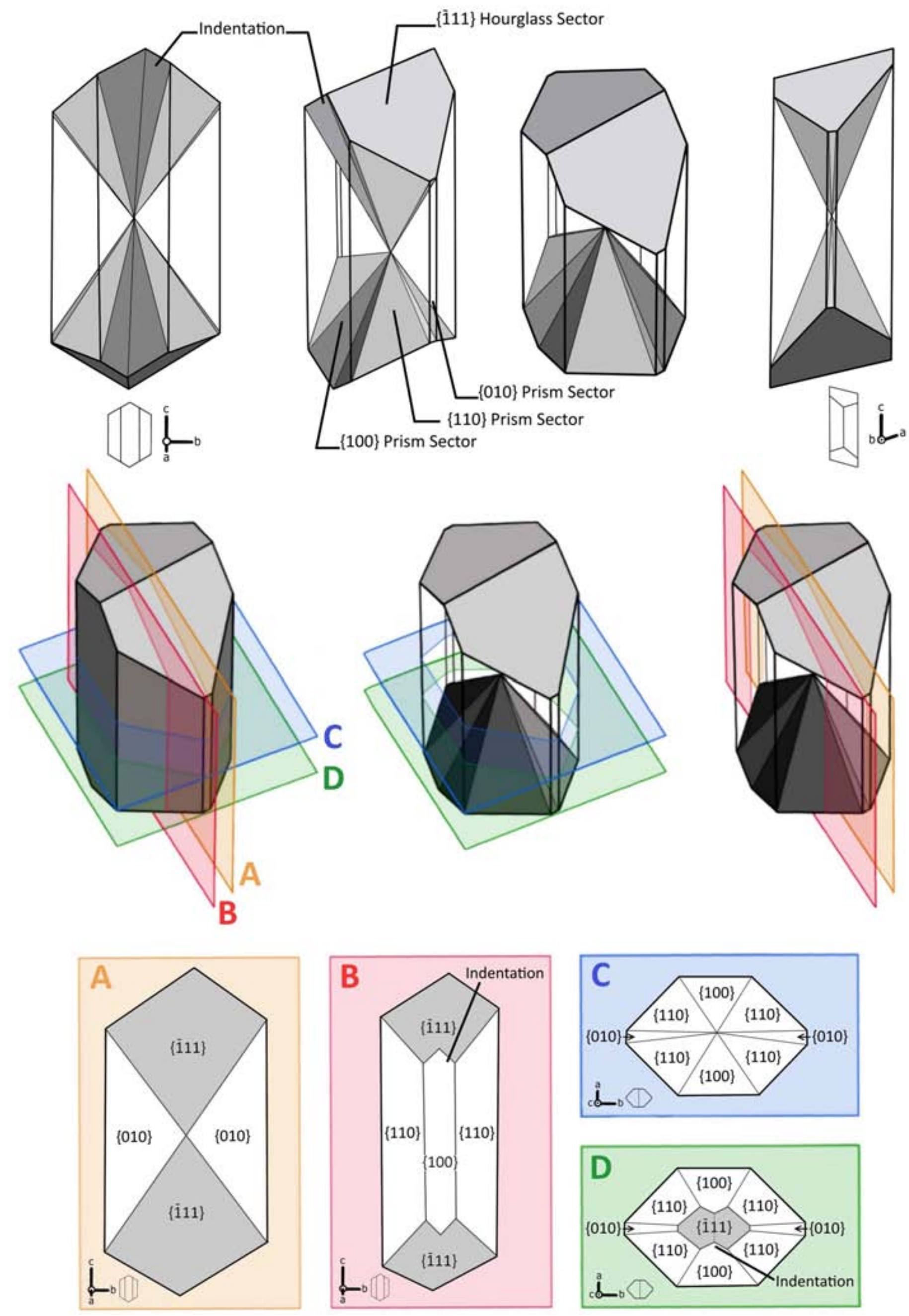

FIGURE 3 | Crystal model based on the habit of sample 31 (**Figure 2**) and following the 12-pyramid morphological model of augite (e.g., Downes, 1974; Leung, 1974; Ubide et al., 2019). The crystal is composed of a total of 12 pyramidal sectors: 8 prism sectors growing perpendicular to the *c*-axis, including the forms {100} x2, {110} x4, and {010} x2, plus 4 hourglass sectors of the form {−111} growing along the *c*-axis. The bottom panel shows theoretical sections along and across the *c*-axis, which expose the prism and hourglass sectors in markedly different locations and shapes. The sections along the *c*-axis are orthogonal to those shown in Ubide et al. (2019): in the present study, elongated sections were prepared along the *c*-*b*-axes, as opposed to the *a*-*c*-axes in Ubide et al. (2019). Note that the angular outline of the hourglass form, generating "valleys" that translate into "indentations" of sector {−111} in two-dimensional crystal sections.

of two background positions. Corrections for inter-elemental effects were made using a ZAF (Z: atomic number; A: absorption; F: fluorescence) procedure. Calibration was performed using a range of standards from Micro-Analysis Consultants (MAC; http://www.macstandards.co.uk): albite (Si-PET, Al-TAP, Na-TAP), forsterite (Mg-TAP), augite (Fe-LIF), apatite (Ca-PET, P-PET), orthoclase (K-PET), rutile (Ti-PET), and rhodonite (Mn-LIF), as well as JEOL Cr metal (Cr-LIF). Rim-to-rim and

TABLE 1 | Instrument parameters used for laser ablation micro-chemical mapping experiments.

		LA-ICP-QMS	**LA-ICP-TOFMS**
Laser system		**ASI Resolution 193 nm**	**Teledyne Analyte G2 193 nm with ARIS**
Laser parameters	Fluence (J/cm 2)	3	3
	Spot size (μm)	20 × 20	20 × 20
	Stage translation speed (μm/s)	20	200 ("10 pixels per second")
	Repetition rate (Hz)	10	10
	Overlap between rasters in maps (μm)	1	0 (no overlap)
	Background between rasters (s)	20	1–2 (between lines), 20 (before and after entire images)
Gas flows	He (ml/min)	350	600
	Ar (ml/min)	850–920	1,500
	N2 (ml/min)	5	0
Mass spectrometer		**Thermo iCAP RQ**	**iCAP RQ icpTOF (TOFWERK AG)**
ICP-MS parameters	Analytes (dwell times in ms)	7Li (15), 23Na (5), 27Al (5), 43Ca (5)*, 45Sc (10), 51V (10), 52Cr (10), 60Ni (10), 90Zr (10), 139La (15), 146Nd (15)	Entire mass spectrum from 23Na to 238U (30 μs per mass spectrum), 29Si*
	Duty cycle	110 ms	"integration time per pixel" ~100 ms.
Limits of detection	LODs** (ppm)	7Li (0.2), 23Na (2), 27Al (0.5), 45Sc (0.05), 51V (0.07), 52Cr (1), 60Ni (0.1), 90Zr (0.006), 139La (0.003), 146Nd (0.006)	23Na (120), 27Al (15), 43Ca (1000), 45Sc (3), 51V (1), 52Cr (7), 60Ni (3), 90Zr (0.6), 139La (0.1), 146Nd (0.01)
Mapping times			
Method comparison	Example dimensions (time)	1,632 × 2,088 μm (180 min)	1,632 × 2,088 μm (18 min)

**internal standard. **limits of detection (LODs) calculated following Longerich et al. (1996).*

rim-to-core profiles were acquired at 5, 10, or 20 μm step spacing along 1,150–6,300 μm transects. Additional spots targeted mineral and melt inclusions across the megacrysts and in the adhering glassy matrix, where present. Results were screened based on stoichiometry and analytical totals, and the final dataset comprises >3,000 analyses (**Supplementary Tables 2–7**). Smithsonian augite (Jarosewich et al., 1980) and MAC augite were used as quality monitor standards; accuracy and precision were better than 1–5% except for elemental abundances below 1 wt.%, for which accuracy was typically better than 1–10% ($n = 20$). For EPMA mapping, we used 2.5 × 2.0 to 3.0 × 2.5 μm pixel size and 60 to 90 ms dwell time per pixel, measuring up to five elements per analysis (one per diffracting crystal). Mapped areas varied in size from 2,560 × 2,048 μm to 3,072 × 2,560 μm, with total analytical run times of 19 h 36 min to 29 h 13 min.

Trace Element Mapping Using LA-ICP-QMS

Eleven crystals were investigated using high-resolution laser ablation inductively coupled plasma quadrupole mass spectrometry (LA-ICP-QMS) trace element mapping, following the rastering technique described in Ubide et al. (2015). Most of the crystals were mapped both perpendicular and parallel to the *c*-axis (B and C sections, respectively). Given the large size of the crystals, we selected mapping strips across different crystal faces to reduce analytical run times. In order to effectively resolve elemental zoning in two dimensions across large crystal faces, strips were typically oriented orthogonal to each other.

Mapping experiments were carried out at The University of Queensland Centre for Geoanalytical Mass Spectrometry, Radiogenic Isotope Facility (UQ RIF-lab). We used an ASI RESOlution 193 nm excimer UV ArF laser ablation system with a dual-volume Laurin Technic ablation cell, coupled to a Thermo iCap RQ quadruple mass spectrometer. The laser system was operated with GeoStar Norris software and the mass spectrometer with Qtegra software. Ablation was performed in ultrapure He (grade 5.0, 99.999% purity) to which the Ar make-up gas and a trace amount of N_2 was added for efficient transport and to aid ionisation. Details of laser parameters, gas flows, and mass spectrometer set-up are given in **Table 1**. The instrument was tuned with scans on NIST SRM 612 glass. Elemental maps were built with Iolite (Paton et al., 2011) v2.5 in quantitative mode, using NIST SRM 612 as calibration standard and calcium concentrations in clinopyroxene obtained previously by electron microprobe (21.4 ± 0.3 wt.% CaO; $n = 2{,}924$) as internal standard. Accuracy and precision were monitored using BHVO-2G, BCR-2G, BIR-1G, and GSD-1G glass reference materials as quality monitor standards (http://georem.mpch-mainz.gwdg.de/). Accuracy was typically better than 1–10% and precision better than 1–5% ($n = 5$ for each glass reference material). Limits of detection (Longerich et al., 1996) were at the sub-ppm level for most analysed elements and ≤2 ppm for Na and Cr (**Table 1**).

Multi-Element Mapping Using LA-ICP-TOFMS

Five sections of crystals 31, 34, and 46 were also mapped using laser ablation inductively coupled plasma "time-of-flight" mass spectrometry (LA-ICP-TOFMS) at TOFWERK AG (Thun, Switzerland). We used an icpTOF time-of-flight mass spectrometer (TOFWERK AG, Thun, Switzerland) coupled to an Analyte G2 193 nm excimer laser ablation system (Teledyne CETAC Technologies, Omaha, USA). The laser system was

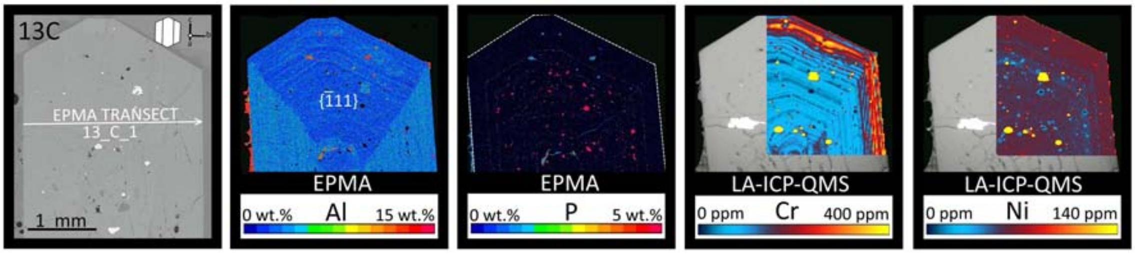

FIGURE 4 | Elongated section of crystal 13, cut along the *c*-axis (section 13C). The section was imaged under reflected light (left panel), and chemically using electron microprobe (Al, P: middle panels) and LA-ICP-QMS (Cr, Ni: right panels). The reflected light image includes a 2D crystal model (top right corner) showing the crystallographic orientation of the section (see also **Figure 3**). Reflected light imaging and micro-chemical mapping provide detailed information on inclusion populations and sector zoning. LA-ICP-QMS maps unveil concentric zonation at the trace element level.

equipped with a HelEx II dual-volume ablation cell and an Aerosol Rapid Introduction System (ARIS) for fast washout of the sample aerosol (Teledyne CETAC Technologies, Omaha, USA). Helium was used as the transport gas, and Ar was added inside the ARIS device prior to introduction of the sample gas into the plasma (see method parameters in **Table 1**). The Analyte G2 laser ablation system was operated with Chromium software (Teledyne CETAC) and the icpTOF mass spectrometer was operated with TOFpilot software (TOFWERK AG). The instrument was tuned with scans on NIST SRM 612 glass. A notch filter was applied to attenuate the Ar peak at 40 m/q.

For analysis of the clinopyroxene samples, "spot-resolved" imaging was performed. This implies that each individual laser shot results in one multi-element pixel in the image (e.g., Burger et al., 2017; Bussweiler et al., 2017). The laser was programmed to raster across the sample area along an array of side-by-side, non-overlapping spots. Based on the signal duration resulting from one laser shot on the sample (measured to be $<$100 ms), a laser repetition rate of 10 Hz was used. The icpTOF records full mass spectra (from ^{23}Na to ^{238}U) at a rate of 33 kHz (e.g., Borovinskaya et al., 2013), so that multiple measurements are obtained across the signal of a single laser shot. Here, for a single laser-pulse signal with a duration of 100 ms, a total of ~3,300 mass spectra were acquired and averaged into one pixel. NIST SRM 612 was measured as calibration standard, in the same way as the clinopyroxene images, including gas blanks, immediately before and after each image. Five lines of ~500 μm length (each lasting 2.5 s) were ablated on the calibration standard during each mapping experiment.

For quantification of the intensity images, the raw data files (HDF5 file format) were processed using an in-house software (Tofware) for TOF baseline subtraction and peak integration (Burger et al., 2017; Hendriks et al., 2017). Images were then quantified against the calibration standard using Iolite software (Paton et al., 2011) with ^{29}Si as the internal standard, assuming a constant content of 23 wt.% Si in clinopyroxene (49.4 ± 0.9 wt.% SiO_2 from microprobe data; $n = 2{,}924$). The typical accuracy and precision of the instrument are reported in Burger et al. (2017). Limits of detection for spot-resolved imaging with LA-ICP-TOFMS as employed here were $<$1 ppm for Zr, La, Nd, $<$10 ppm for Sc, V, Cr, Ni, ~10 ppm for Al, and higher for Na (~120 ppm) and Ca (~1,000 ppm; **Table 1**). Elemental results from LA-ICP-QMS and LA-ICP-TOFMS methods are comparable in terms of zoning patterns and concentration scales (**Figures 4–6**).

Compositional "Interrogation" of Laser Ablation Maps

Following visual examination of LA-ICP-QMS and LA-ICP-TOFMS zoning maps, we used the Monocle add-on for Iolite (Petrus et al., 2017) to further interrogate the quantified elemental maps and to extract average compositions for individual crystal zones (regions of interest, ROIs). This approach provides high precision concentration data by averaging a large number of data points pooled from compositionally homogeneous ROIs (zones), rather than spatially restricted compositions obtained with classic spot analyses, which are also subject to potential downhole-fractionation (Petrus et al., 2017; Bussweiler et al., 2019). Regions of interest were typically defined using Cr zoning.

RESULTS

Identifying Clinopyroxene Complexity

Under reflected light, the megacryst sections appear remarkably uniform (**Figure 4**), the most notable feature being the abundance of concentrically-distributed mineral and melt inclusions in distinct regions of the crystals (see section Exploring Inclusions Across Megacryst Growth). Electron microprobe major element imaging suggests very mild geochemical variations across the clinopyroxenes (**Figure 4**; **Supplementary Figure 1**). Chemical gradients are almost negligible along concentric zones, and sector zoning is only clear in Al. The hourglass form {−111} is relatively Si-Mg-rich and Al-Ti-Fe-poor compared to prism sectors. However, sectoral variations are minor in Ti and Mg, and very subtle in Si and Fe. Major element maps are best suited as indicators of inclusion populations, the most striking example being apatite (highlighted by EPMA P maps; **Figure 4**).

In contrast, LA-ICP-MS trace element maps reveal marked chemical complexity within the megacrysts (**Figures 4–6**).

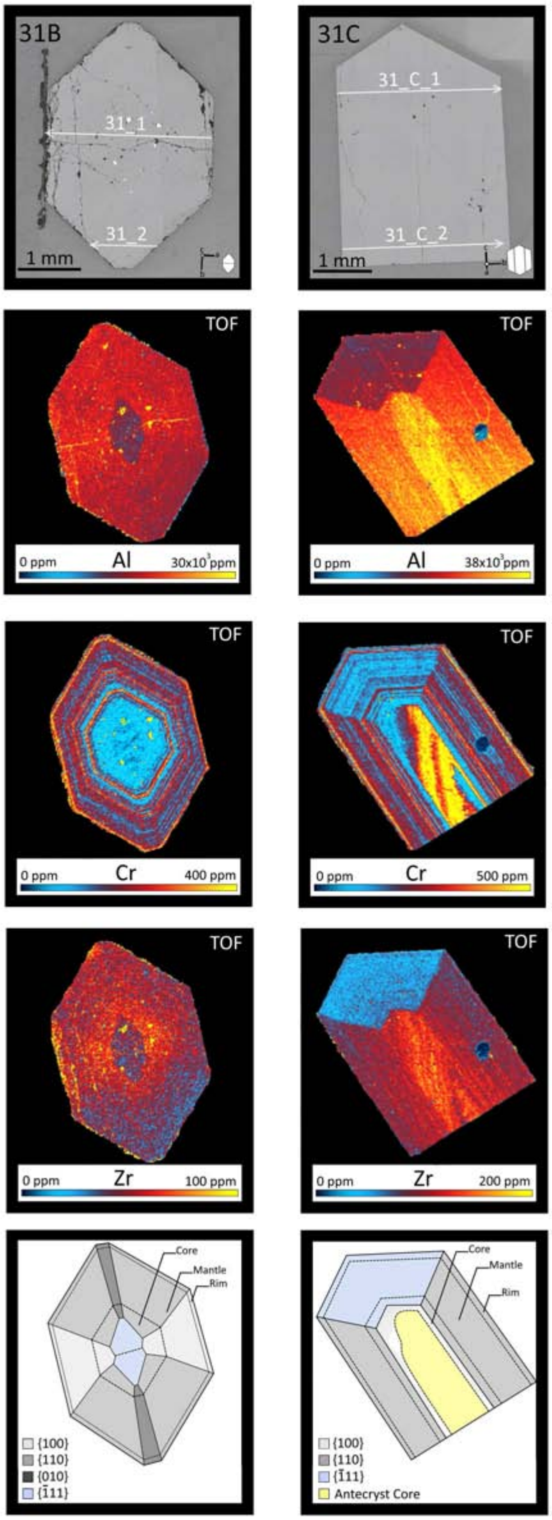

FIGURE 5 | Reflected light scans and LA-ICP-TOFMS maps of crystal 31, cut perpendicular to the *c*-axis (section 31B) and along the *c*-axis (section 31C). This crystal has a perfect polyhedral habit (**Figure 2**) and was used to build the models in **Figure 3**. Chromium shows the largest variations across the crystal, defining a homogeneous, depleted core (∼100 ppm), a finely oscillatory zoned *(Continued)*

FIGURE 5 | mantle (140–200 ppm oscillations) and a Cr-rich rim (∼280 ppm). The elongate cut 31C contains a recycled antecryst with Cr concentrations up to >400 ppm. The antecryst portion is interpreted to finish shortly after the termination of the crystal cut, as it does not appear in the basal cut 31B. Aluminium contrasts reveal the development of the hourglass {−111} form, occurring in the centre of the basal cut and at the end of the elongate cut (see **Figure 3**). Zirconium follows the zonation in Al. The white arrows on reflected light scans (top) mark the location of EPMA traverses in **Supplementary Figure 3**.

Chromium maps show the sharpest variations, revealing µm-scale oscillations that follow euhedral grain boundaries, producing concentric zonation patterns not reflected in major element compositions (e.g., Mg and Fe). The megacrysts can be subdivided into: homogeneous cores (∼90 ppm Cr; $Mg\#_{71-76}$ where Mg# = 100 Mg / (Mg + Fe) with concentrations expressed on a molar basis and Fe = total iron as Fe^{2+}), overgrown by finely oscillatory zoned mantles (70–200 ppm Cr; $Mg\#_{72-78}$), and Cr-rich rims (200–400 ppm Cr; $Mg\#_{72-77}$). Rims show a range of textures from single Cr enrichments (**Figure 5**) to multiple (up to 4) Cr oscillations following euhedral to partially irregular surfaces (**Figures 4**, **6**). Chromium enrichments are mirrored by Ni (80–90 ppm from mantle to rim), along with depletions in mildly incompatible elements, such as La, Nd, and Zr (**Supplementary Figure 2**), suggesting crystallisation from a more mafic melt (Ubide and Kamber, 2018). Some of the crystals contain irregular cores with very high Cr contents (e.g., **Figure 5**; 400–450 ppm Cr), coupled with relative enrichments in Sc, V, and Al, indicative of a recycled (antecryst) origin. Major elements are not significantly different in antecryst cores, with $Mg\#_{73-75}$ variations within the range observed for core, mantle and rim compositions. In addition, cations with high charge including rare earth elements (REE) and high field strength elements (HFSE) show sector zoning following the differential partitioning of Al as a function of crystallographic orientation (**Figures 3**, **4**; **Supplementary Figure 2**; Ubide et al., 2019). Transition metals Cr and Sc show only mild sector zoning, whereas Ni does not partition into sectors (**Figure 4**).

To explore the three-dimensional architecture of zoning patterns, we present LA-ICP-TOFMS maps (TOF maps) of single crystals cut along and perpendicular to the *c*-axis (**Figures 5**, **6**). The TOF-method records a wide range of major and trace element distributions on entire cm-sized sections. The TOF maps corroborate the zonation patterns derived independently using EPMA and LA-ICP-QMS (**Figure 4**) and expand their crystallographic significance, as described below.

Whilst Cr and low charged metals such as Ni and Mn define concentric zonations, Al and highly charged Ti, V, Zr, Hf, and REE (and to a lesser extent Cr and Sc) show clear sector zoning that extends across crystal cores, mantles, and rims (**Figures 3**–**6**). Sector zoning is particularly evident in elongated crystal sections, cut along the *c*-axis (31C and 34C; **Figures 5**, **6**), where the hourglass {−111} form displays sharp indentations following the crystal model depicted in **Figure 3**. Cation depletions in the hourglass {−111} sectors are counterbalanced by enrichments in

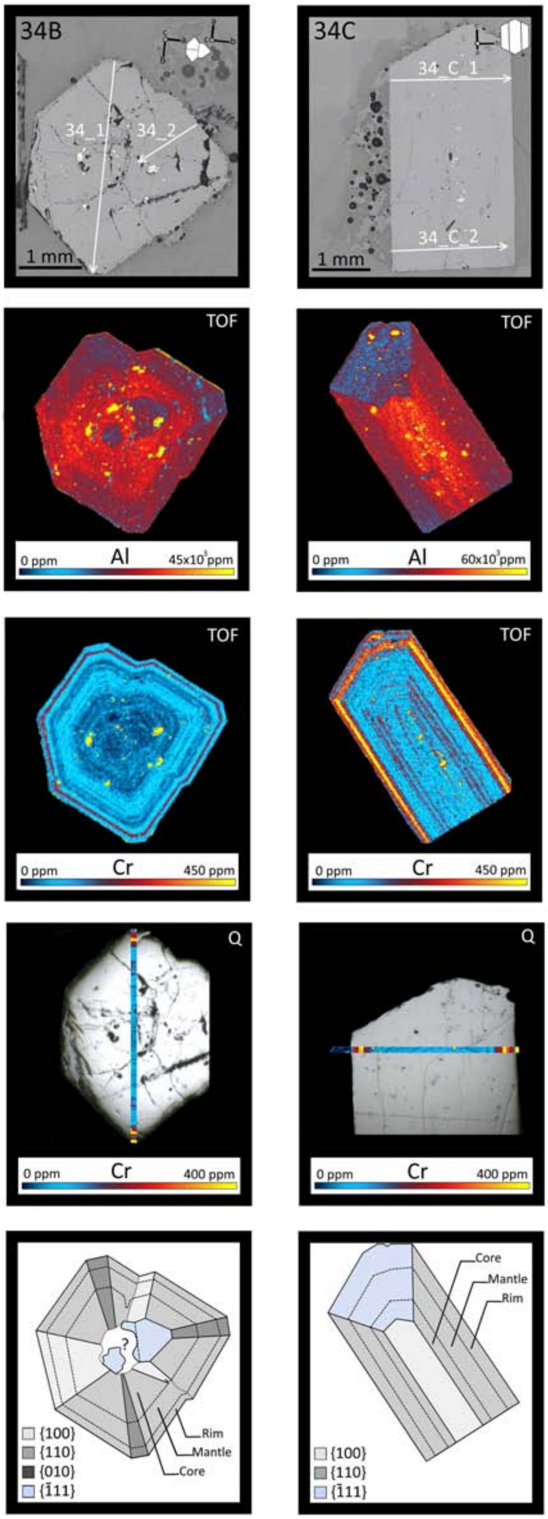

FIGURE 6 | Reflected light scans, LA-ICP-TOFMS and LA-ICP-QMS maps of crystal 34, cut along the *c*-axis (section 34C) and perpendicular to the *c*-axis (section 34B). The basal cut (34B) includes a smaller half-crystal unit oriented parallel to the main crystal but rotated 90-degrees about the *c*-axis. According to Cr zonation, the crystal contains a relatively homogeneous core

(Continued)

FIGURE 6 | (~70 ppm Cr) a finely oscillatory zoned mantle (80–110 ppm Cr) and a Cr-rich rim (~260 ppm). The distribution of Al highlights the occurrence of {−111} sectors in both the elongated and basal cuts. The clinopyroxene is partially coated with glassy matrix (shown in the reflected light images at the top), which includes analysed microlites of plagioclase and Ti-magnetite. Note that the TOF-method provides an unparalleled overview of the internal zonation of the crystal, whilst LA-ICP-QMS maps (Q: overlapping strips) targeted specific crystal regions for high-resolution trace element characterisation.

prism sectors {100}, {110}, and {010}. These latter sectors are compositionally almost identical.

The occurrence of compositional contrasts between hourglass and prism sectors in elongated crystal cuts can be extended to basal cuts (31B and 34B; **Figures 5**, **6**), where hourglass sectors are not immediately apparent and can be easily misinterpreted as "inner" cores (**Figure 3**). Indeed, the Cr-poor cores identified in the basal cuts contain what could initially be interpreted as an Al-poor nucleus or "seed" (**Figures 5**, **6**). However, upon closer examination, the Al-poor nuclei display subtle "valleys" that can be linked to the morphological model of the hourglass form (**Figure 3**). The Al-poor zones are, therefore, not inner cores. Rather, they are basal sections of the hourglass {−111} form, characterised by low Al contents (**Figures 5**, **6**). For a given crystal, the mismatch of zoning patterns between the basal cut and the terminated end of the elongate cut is directly related to the re-mounting and re-polishing of the two crystal halves during sample preparation (see section The Clinopyroxene Megacrysts). In crystal 31, re-polishing of the basal section (31B) led to the loss of the antecryst core and exposure of the hourglass form (**Figure 5**).

The stark zoning patterns revealed by multi-element TOF maps, unresolvable using conventional microscopy, provide crystallographic context to test and quantify compositional variations across the megacrysts (e.g., **Figures 5**, **6**, bottom panels). We use the mapping results to locate and classify individual microprobe analyses into sectors ({−111}, {100}, {110}, {010}) as well as concentric zones (antecryst core, regular core, mantle, rim). Traverses across megacryst 31 (**Figures 2**, **3**, **5**) are presented in **Supplementary Figure 3** and illustrate the minimal extent of major element variations across concentric zones. The traverses highlight the contrast between hourglass and prism sectors (**Supplementary Figure 3**); however, this compositional change would likely remain unnoticed or misinterpreted without the elemental maps for context. Additional transects across the studied crystals (e.g., **Figures 4**, **6**) form a large major element dataset that is graphically summarised in **Figure 7**. As observed in electron microprobe maps (**Figure 4**; **Supplementary Figure 1**), major elements are unzoned relative to core, mantle, and rim regions, and sectoral partitioning is only resolvable for hourglass vs. prism sectors (**Figure 7**; **Supplementary Figure 3**). The hourglass sectors {−111} plot in distinct compositional regions with shifts of up to +3 wt.% SiO_2, +1.5 wt.% MgO, −2 wt.% Al_2O_3, −0.5 wt.% TiO_2 and −1 wt.% FeO^T (total iron as FeO) compared to prism sectors (**Figure 7**). The prism sectors ({100}, {110}, and {010}) are compositionally indistinguishable within analytical uncertainty. All sectors have

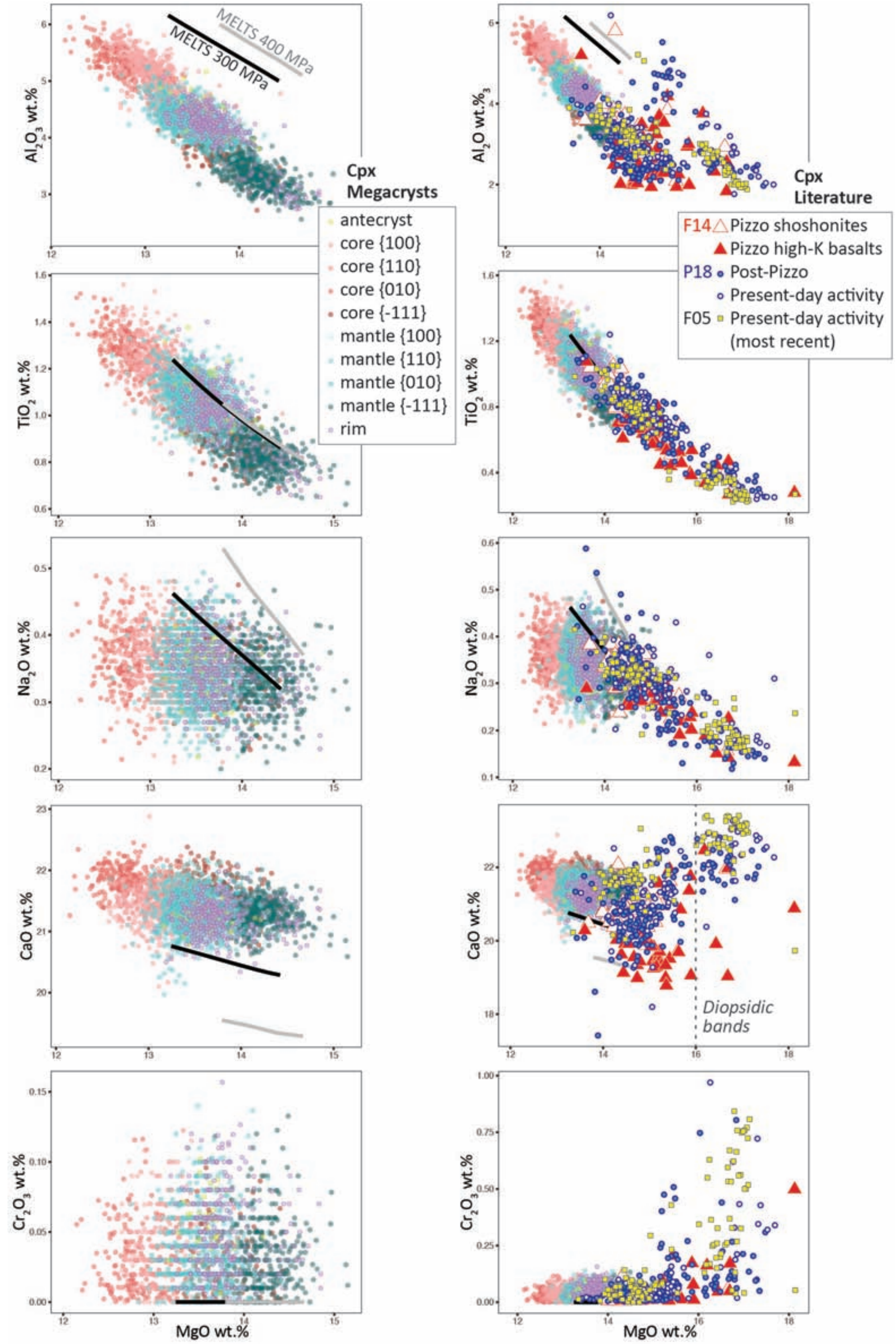

FIGURE 7 | Clinopyroxene compositional variations. **(Left)** Major element compositions across the clinopyroxene megacrysts, obtained by electron microprobe. The data from core, mantle and rim regions are largely coincident, however crystal cores reach highest Al_2O_3-Ti_2O and lowest Si_2O-MgO concentrations. Note the overlap among prism sectors {100}, {110}, and {010}, and the MgO-rich and Al_2O_3-poor composition of hourglass sectors {−111} compared to prism sectors. The black and gray lines represent the evolution of fractionated clinopyroxene modelled with Rhyolite-MELTS (Gualda et al., 2012) from 1,090°C (high MgO) to 1,030°C (low MgO) at isobaric conditions of 300 and 400 MPa, respectively; Rhyolite-MELTS fractionation at 300 MPa reproduces the mineral assemblage and the overall *(Continued)*

FIGURE 7 | compositional characteristics of the megacrysts, and is in agreement with thermobarometric and hygrometric results (**Figure 8**). **(Right)** Comparison of megacryst compositions (same data and symbols as in the left panel) with previous data from Pizzo clinopyroxene (F14: Francalanci et al., 2014; shoshonites and high-K products), as well as Post-Pizzo and Present-day clinopyroxene (P18: Petrone et al., 2018), including recent crystals from 1984 to 1996 eruptions (F05: Francalanci et al., 2005). Note that Pizzo shoshonite clinopyroxenes are similar to mantle and rim compositions in the megacrysts. From the Pizzo high-K subgroup through Post-Pizzo to Present-day activity (for stratigraphic context see **Figure 1**), clinopyroxenes contain diopsidic bands relatively enriched in MgO-CaO-Cr_2O_3.

similar concentrations of CaO and Na_2O. Chromium variations are not resolvable, being below the detection limit of EPMA, even for recycled antecrysts. Compared to clinopyroxene phenocrysts from Mt. Etna (Sicily, Italy; Ubide et al., 2019), sector zoning in Stromboli megacrysts is very weakly developed (**Figure 7**), but the relative partitioning of elements between hourglass and prism sectors is similar. Building on constraints from cooling experiments (Mollo et al., 2010, 2013) and natural samples from alkaline systems (Mollo et al., 2011, 2015; Scarlato et al., 2014; Ubide et al., 2014; Gernon et al., 2016; Ubide and Kamber, 2018), we checked for the occurrence of Al_2O_3-TiO_2 enrichments in the outermost growth layers of the crystals. Increased uptake of these incompatible cations within the crystal structure could be related to kinetically-controlled crystal growth caused by high rates of undercooling during rapid magma ascent and eruption. However, we did not find resolvable Al-Ti-rich outer rims for the studied megacrysts, suggesting that crystallisation occurred at depth and possibly under conditions of near-equilibrium cation partitioning.

Our data are similar to smaller clinopyroxenes (phenocrysts and microcrysts) hosted in the regular shoshonite basalts from the Pizzo sequence at Stromboli (**Figure 7**, right panels; Francalanci et al., 2014). In detail, the smaller crystals mirror the compositions of megacryst mantles ad rims, whereas megacryst cores are slightly more evolved (MgO-poor). In contrast with shoshonite crystals, the high-K clinopyroxenes from Pizzo reach higher MgO values. Compared to clinopyroxene compositions from more recent eruptions (Post-Pizzo and Present-day activity, i.e., Epochs 6a-late and 6c; Francalanci et al., 2005; Petrone et al., 2018), the megacrysts (Pizzo, i.e., Epoch 6a-early) have remarkably low MgO, CaO, and Cr_2O_3 concentrations (**Figure 7**, right panels). Essentially, the megacrysts lack the "diopsidic bands" of clinopyroxenes from recent eruptions, recognised optically as concentric zones of lighter colour under plane polarised light and darker grayscale contrast in BSE images (Francalanci et al., 2004, 2005; Landi et al., 2006; Petrone et al., 2018). The implications of these observations will be discussed later.

Exploring Inclusions Across Megacryst Growth

The megacrysts are speckled with μm-sized inclusions of varied compositions (**Figures 4–6**). In major element maps, melt inclusions have irregular outlines enriched in Al and Na relative to their host. Inclusions of plagioclase, titanomagnetite and olivine are relatively rounded and define "hotspots" of Si-Al, Ti-Fe, and Mg-Mn, respectively. Apatite crystals are readily distinguished as P-Ca enrichments, and show equant to tabular shapes depending on sectioning angle. Trace element maps highlight the compositional contrasts expected for each inclusion type (e.g., Ni-rich inclusions are olivine; REE-rich inclusions are apatite). In addition, some of the megacrysts have patches of glassy groundmass attached to their outer surface (**Figure 4**, see Al map; **Figure 6**, see reflected light images), providing textural and compositional information on the final erupted melt. The groundmass glasses are compositionally similar to melt inclusions in the megacrysts (**Supplementary Figure 4**), whilst the chemistry of groundmass microcrysts (typically plagioclase) agrees with that of mineral inclusions.

Importantly, EPMA analyses indicate that the melt feeding crystal growth was chemically homogeneous, maintaining a shoshonitic composition across the entire growth history of the megacrysts (**Supplementary Table 7**). On average, melt inclusions and groundmass glasses return major element concentrations (52.4 ± 0.5 wt.% SiO_2, 3.5 ± 0.2 wt.% MgO, 4.7 ± 0.3 wt.% K_2O, normalised on a 100 wt.% anhydrous basis; $n = 70$) comparable to those of glasses analysed in the Pizzo-shoshonite series (Francalanci et al., 2014) and the Present-day activity (Petrone et al., 2018; **Supplementary Figure 4**). These studies showed that glass compositions are more evolved than whole rocks, which have similar SiO_2 concentrations but higher MgO (4.5–7.0 wt.%; anhydrous basis) and lower K_2O (1.5–3.0 wt.%; anhydrous basis; Francalanci et al., 2014; Petrone et al., 2018). We note that the Pizzo products are strongly porphyritic, and the shoshonite subgroup typically contains 30–45 vol.% of plagioclase, clinopyroxene and less commonly olivine phenocrysts (Francalanci et al., 2014). Consequently, bulk rock compositions constitute mixtures of crystals and melt that may not be representative of true liquids (crystal-free melts; e.g., Francalanci et al., 2004; Reubi and Blundy, 2007; Cashman and Blundy, 2013; Ubide et al., 2014). The constancy of melt inclusion and groundmass glass compositions during the entire growth of megacryst sections reflects the buffering effect of magma recharge episodes on the erupted magma compositions (e.g., Landi et al., 2004, 2008), as described for the mafic alkaline products at Mt. Etna volcano (Peccerillo, 2005; Armienti et al., 2013).

Most mineral inclusions are homogeneously distributed across the megacrysts and show restricted compositional variations. Plagioclase inclusions and microcrysts show $An_{70\pm5}$ ($n = 62$; **Supplementary Table 4**). Olivine inclusions are less common but are compositionally homogeneous at Fo_{72} ($n = 10$; **Supplementary Table 3**). Titanomagnetite inclusions and one analysed titanomagnetite microcryst are also relatively consistent in composition (9.6 ± 0.6 wt.% TiO_2; $n = 50$; **Supplementary Table 5**) except for Cr_2O_3, which is generally at 0.2–0.3 wt.% concentration levels but increases up to 0.5–0.6 wt.% in inclusions hosted in Cr-rich clinopyroxene rims.

In contrast to other mineral inclusions, apatites are oriented along concentric growth bands and occur within the core and mantle of the megacrysts, but are not found at rims or groundmass (**Figure 4**), nor within recycled antecryst cores. The link between apatite occurrence and concentric zoning in clinopyroxene suggests changes in apatite saturation conditions throughout the megacryst growth history. Apatite compositions are constant across the database (52.8 ± 0.5 wt.% CaO, 43.2 ± 0.5 wt.% P_2O_5; $n = 40$; **Supplementary Table 6**). Halogen concentrations were not determined for this study.

Estimating Clinopyroxene Crystallization Conditions (*P*-*T*-H_2O)

To investigate the temperature, depth, and water content of the melt from which the megacrysts grew, we combined the major element dataset on clinopyroxene with a representative melt composition to apply thermobarometric and hygrometric calibrations. The melts sampled throughout the entire clinopyroxene history are homogeneous and relatively evolved, as documented by EPMA analysis of melt inclusions and groundmass glasses (**Supplementary Figure 4**). We chose a relatively primitive matrix glass composition within the dataset, with 52.4 wt.% SiO_2, 15.2 wt.% Al_2O_3, 3.6 wt.% MgO, and 10.0 wt.% FeO^T (anhydrous basis; see complete composition in **Supplementary Table 7**, analysis 34_A3_glass5).

A plethora of clinopyroxene-melt equilibrium models based on experimental and thermodynamic data attest to the achievement of near-equilibrium conditions between all clinopyroxene compositions and the selected melt (**Supplementary Figure 5**). One of the most widely used tests for equilibrium is the Fe-Mg exchange coefficient $K_D(\text{Fe-Mg})^{\text{cpx}-\text{melt}}$, with an equilibrium range refined at 0.28 ± 0.08 by Putirka (2008). Whilst our data return equilibrium Fe-Mg conditions (**Supplementary Figure 5**), the $K_D(\text{Fe-Mg})^{\text{cpx}-\text{melt}}$ coefficient is known to be dependent on temperature and melt composition (Putirka, 2008; Villaseca et al., 2019), and does not respond to potential kinetic effects during crystal growth (Mollo et al., 2013; Mollo and Hammer, 2017). In fact, the value of 0.28 ± 0.08 represents the weighted arithmetic mean of a much broader equilibrium range of 0.04–0.68 obtained by regressing clinopyroxene-melt compositions from phase equilibrium experiments (Putirka, 2008). Therefore, we applied additional, more robust equilibrium tests that rely on the difference between measured vs. predicted diopside + hedenbergite components ($\Delta DiHd$ of Putirka et al., 1996; Mollo et al., 2013) and clinopyroxene-melt partition coefficients between clinopyroxene and melt (D_{Na} and D_{Ti} of Blundy et al., 1995; Hill et al., 2011, respectively) (cf. details on clinopyroxene-melt equilibrium tests in Mollo et al., 2018; Ubide et al., 2019). The agreement between measured and predicted values for all mineral-melt tests (**Supplementary Figure 5**) supports the reliability of clinopyroxene-melt *P*-*T*-H_2O estimates for the clinopyroxene compositional database presented here.

We adopted the clinopyroxene-melt barometric, thermometric and hygrometric equations recently optimised by Mollo et al. (2018) for alkaline melts: *P*-independent thermometer 33_{MAM} (±28°C uncertainty), *T*-dependent barometer A_{MAM} (±150 MPa uncertainty) and *P*-*T*-dependent hygrometer H_{MAM} (±0.5 wt.% H_2O uncertainty). The new calibrations are based on the equations of Putirka et al. (2003) and Perinelli et al. (2016) for *P*-*T* and H_2O, respectively, and refined for a large dataset of clinopyroxene-melt pairs from alkaline, oxidised and water-rich magmas at Mt. Etna volcano. Stromboli magmas are shoshonitic and highly oxidised (Métrich and Clocchiatti, 1996) and our (relatively evolved) melt returns low clinopyroxene saturation temperatures of 1,080–1,098°C (modelled with the melt-only thermometric equation 34 of Putirka, 2008; ±45°C uncertainty), well within the calibration range indicated by Mollo et al. (2018).

Initial results for crystallisation pressures, temperatures, and melt water contents determined for clinopyroxene megacrysts were 322 (±33) MPa, 1,054 (±7)°C, and 1.8 (±0.2) wt.% H_2O, respectively, where numbers in brackets refer to the standard deviation. The remarkable homogeneity of clinopyroxene major element compositions (**Figures 4–7**) translates into almost constant *P*-*T*-H_2O results across core, mantle and rim regions, as well as across hourglass and prism sectors. Indeed, the standard deviation values on $n = 2{,}924$ estimates are within error of the barometric, thermometric, and hygrometric models, indicating very stable conditions of crystallisation. To determine the most likely *P*-*T*-H_2O conditions, we adjusted the *P*-*T* estimates within the calibration errors of the barometer (±150 MPa) and thermometer (±28°C) to minimise the value of $\Delta DiHd$, thus approaching the ideal equilibrium condition of $\Delta DiHd = 0$ (cf. Mollo and Masotta, 2014). The equilibrium correction provided the most reliable crystallisation conditions for the megacrysts: 1,082 ± 7°C (+28°C addition to T estimates), 316 ± 33 MPa (−6 MPa subtraction from P estimates), and 2.0 ± 0.2 wt.% H_2O (+0.2 wt.% addition to H_2O estimates; **Figure 8**). It is worth noting that water contents are not directly modulated by $\Delta DiHd$, but follow *P*-*T* adjustments. Interestingly, the corrected temperature data approach the saturation temperature of clinopyroxene in the melt (1,080–1,098°C according to equation 34 of Putirka, 2008 as outlined above) and fall within the range of temperatures obtained for compositionally similar clinopyroxenes in Post-Pizzo and Present-day activity products (1,040–1,089°C; low-Mg# zones in Petrone et al., 2018) using clinopyroxene-melt thermometry (Putirka, 2008).

To provide further constraints on the intensive variables controlling the crystallisation conditions of the Stromboli megacrysts, we conducted thermodynamic simulations using Rhyolite-MELTS software v1.2.0 (Gualda et al., 2012). The applicability of this established algorithm to potassic and "exotic" magma compositions typical of many volcanic settings in Italy has been documented by several authors, as in the case of the Campi Flegrei Volcanic Fields (Fowler et al., 2007) and the Sabatini Volcanic District (Del Bello et al., 2014). The fractional crystallisation path of the melt in equilibrium with clinopyroxene megacrysts was modelled at 1,250–1,000°C, 2 wt.% H_2O and fO_2 buffered at nickel–nickel oxide (NNO; Métrich and Clocchiatti, 1996; Di Carlo et al., 2006) and results are presented in **Supplementary Table 8**. At 400 MPa isobaric conditions, the thermodynamic data reproduced the mineral assemblage observed in the megacrysts. Spinel (titanomagnetite) is the liquidus phase (1,250°C), followed by apatite (1,130°C),

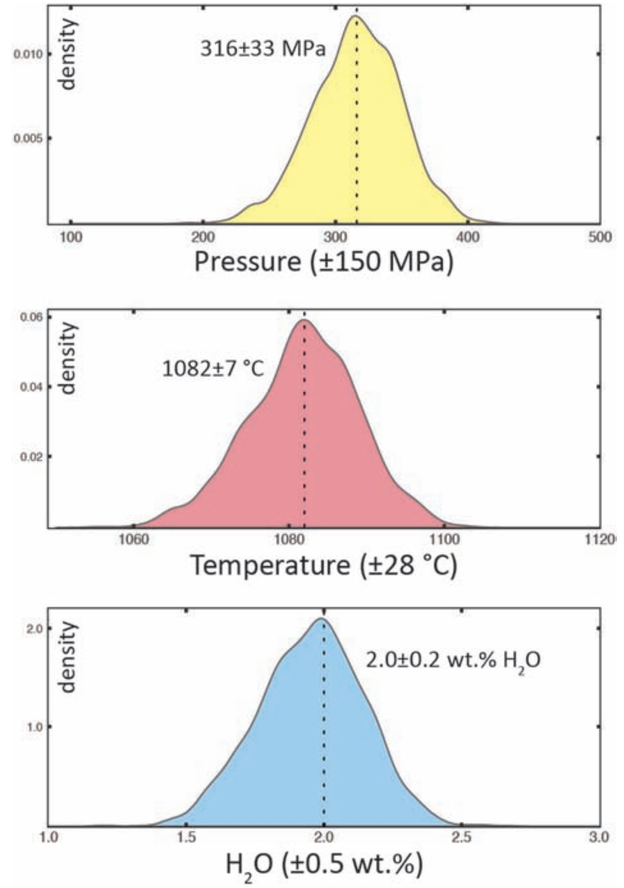

FIGURE 8 | Kernel Density Estimates (KDEs) of magmatic pressure, temperature, and melt water content according to the integrated clinopyroxene-melt calibrations by Mollo et al. (2018), optimised for alkaline basaltic compositions from Mt Etna and further adjusted to minimise deviations from Cpx-melt equilibrium [see details in section Estimating Clinopyroxene Crystallisation Conditions (*P*-*T*-H2O)]. Dashed dotted lines and figures represent mean and standard deviation values for *P*-*T*-H_2O estimates: 316 ± 33 MPa, 1,082 ± 7°C, and 2.0 ± 0.2 wt.% H_2O (*n* = 2,924). The constancy of thermobarometric and hygrometric results (within error of the calibrations: A_{MAM} ± 150 MPa, 33_{MAM} ± 28°C, H_{MAM} ± 0.5 wt.% H_2O) indicate very stable conditions throughout the crystallisation of the megacrysts. Clinopyroxene-melt equilibrium tests are presented in **Supplementary Figure 5**.

olivine (1,110°C), and finally clinopyroxene (1,090°C), which drives the majority of solid fractionation from the liquid (of the total fractionated assemblage, 47.5% mass is clinopyroxene). The composition of clinopyroxene, however, matches our megacryst compositions more accurately at 300 MPa than at 400 MPa (see isobaric fractionation patterns in **Figure 7**). At 300 MPa, model results are in close agreement with the clinopyroxene-melt *P*-*T*-H_2O estimates, and with the inclusion populations. For example, feldspar is not produced at 400 MPa, yet by reducing the pressure to 350 MPa, plagioclase saturates the melt at 1,010°C. Therefore, we conclude that the crystallisation of the megacrysts is best reproduced at 300 MPa pressure. Fluctuations in volatile components may also affect the fractionating assemblage. For example, the melt water content modulates the stability of plagioclase, and thermodynamic simulations at H_2O <2 wt.% expand the stability of feldspar and limit the production of apatite. Fluxing with CO_2 can also dehydrate the melt (Spilliaert et al., 2006) promoting crystallisation of plagioclase (Cashman and Blundy, 2013), and modulating the texture and composition of the crystallising assemblage (Humphreys et al., 2009; Giuffrida et al., 2017). This is particularly relevant at Stromboli, where magmas are enriched in CO_2 relative to typical arc systems (Aiuppa et al., 2010; Allard, 2010).

To the best of our knowledge, *P*-*T*-H_2O estimates from this study are the first set of comprehensive mineral-melt equilibrium constraints on clinopyroxene crystallisation at Stromboli (**Figure 8**). Thermodynamic modelling supports crystallisation of the megacrysts and their inclusions from a relatively evolved shoshonitic melt equilibrating at ∼300 MPa, 1,080°C, 2 wt.% H_2O, and NNO-buffered conditions (**Figure 7**). Our pressure results reflect the relatively high Na_2O and Al_2O_3 concentrations in the clinopyroxene megacrysts (**Figure 7**), consistent with the increasingly compact structure of the mineral at higher pressures (Blundy et al., 1995; Nimis, 1995; see **Supplementary File 1**). Assuming a mean rock density of 2,700 kg/m^3 for the crust at Stromboli (Allard, 2010), clinopyroxene-melt pressure results of 316 ± 33 MPa indicate depths of crystallisation of 11.9 ± 1.2 km, below the major mid-crustal discontinuity beneath the volcano (∼10 km; Morelli et al., 1975). These estimates will be discussed in the context of the plumbing system in section New Insights Into Plumbing System Architecture.

DISCUSSION

Multi-Method Approach to Elemental Mapping

The sharp chemical contrasts revealed within seemingly homogeneous megacrysts (**Figures 4–6**) illustrate the potential of micro-chemical mapping as a new petrological tool with which to better understand the compositional and textural complexities of igneous crystals, as well as other geological materials (e.g., Burger et al., 2015, 2017; Ubide et al., 2015; Gundlach-Graham et al., 2018). The combination of major element maps obtained via electron microprobe, with trace element maps acquired by LA-ICP-QMS, and the significantly extended multi-element mapping capability of LA-ICP-TOFMS, provides a powerful means to interrogate magmatic histories recorded in clinopyroxene megacrysts (**Figures 4–6**). Here we discuss the main benefits and drawbacks of the mapping approaches, and highlight key textural and compositional information extracted using each method.

Most notably, the outstanding record of zoning patterns visualised with the TOF maps provides fundamental navigation for subsequent analyses and crystal-scale interpretations. The icpTOF instrument mapped the mass spectrum from ^{23}Na to ^{238}U on entire, mm-sized crystal sections in as little as 1 h (**Table 1**). Together with our crystallographically controlled sectioning approach, LA-ICP-TOFMS maps provide invaluable rapid insights not only into the general core-to-rim major and trace element zonation, but also into the complex sectioning effects of hourglass and prism sectors (**Figures 3**, **5**, **6**).

LA-ICP-QMS mapping generated trace element images of increased-resolution and -sensitivity that revealed fine textural details and subtle compositional variations (e.g., **Figure 4**). Compared to the TOF approach, conventional LA-ICP-QMS mapping is limited by the number of analytes and requires longer analytical run times (**Table 1**). Relative to the 1 laser spot = 1 pixel approach used with the icpTOF (Burger et al., 2015; Bussweiler et al., 2017), the LA-ICP-QMS spot-overlapping technique improves spatial resolution at a given spot size and, therefore, the LA-ICP-QMS maps were preferred to undertake precise thickness measurements on Cr maps for timescale estimates (section Crystal Storage and Mobilisation Timescales). We note that the benefit of spot-resolved imaging is that each pixel is exactly in the right location and that the rastering approach involves the risk of signal smearing and/or spectral skew. However, Ubide et al. (2015) showed that for modern analytical systems with fast washout times, and limited total dwell cycles (dictated by the repetition rate), the spatial resolution of the rastering approach is better than the spot size. The improved sensitivity of the LA-ICP-QMS technique employed here is exemplified in maps showing mild compositional contrasts such as Ni (**Figure 4**), which remained undetected with the TOF method.

The spatial resolution of laser-based approaches is primarily controlled by the spot size, which was set at 20 μm for all the analyses in this study (**Table 1**). Importantly, vertical sample "destruction" in mapping experiments is negligible compared to traditional spot analysis, and has been quantified at <1 μm depth relative to the original sample surface in clinopyroxene LA-ICP-QMS maps (Ubide et al., 2015). Hence, samples can be mapped multiple times and then re-polished for traditional petrography or electron beam techniques.

Electron microprobe maps on large areas of the megacrysts (**Figure 4**, **Supplementary Figure 1**) provided general sectoral variations as well as valuable information on the occurrence and distribution of inclusion populations. Whilst more time consuming and less sensitive for trace elements than laser mass spectrometry methods, electron-based imaging techniques are commonly available to petrologists and mineralogists and provide a powerful approach for resolving micro-chemical complexities in major and minor elements.

Dynamic Crystallisation of Clinopyroxene Megacrysts

The megacrysts are markedly euhedral and their chemical complexity is only revealed via micro-chemical imaging. Interestingly, compositional zoning patterns vary according to element group. A large proportion of major elements appear relatively homogeneous to mildly sector zoned, whereas minor and trace elements show decoupled distributions in oscillatory zones and/or sectors. Within the overall homogeneity, Al, Ti, (Fe), and highly charged trace cations including V, REE, and HFSE are enriched in prism sectors relative to hourglass sectors. This distribution agrees with that observed in sector zoned clinopyroxenes at Mt. Etna (Downes, 1974; Duncan and Preston, 1980; Ubide et al., 2019) and other volcanic systems world-wide (Hollister and Gancarz, 1971; Ferguson, 1973; Leung, 1974). In a recent study on major and trace element zoning of sector zoned clinopyroxene, Ubide et al. (2019) demonstrated that sector zoning is strongly dependent on the charge/size of a given cation and its ability to charge-balance the clinopyroxene structure after incorporation of Al^{3+} in tetrahedral substitution for Si^{4+}. The authors showed that sector zoning can develop under conditions of low undercooling, and proposed that the extent of sectoral partitioning might be related to the degree of undercooling. Interestingly, sectoral partitioning is significantly stronger in Etnean phenocrysts than in Stromboli megacrysts. The differential partitioning of hourglass and prism sectors in Etna phenocrysts is typically twice as large compared to Stromboli megacrysts, and the compositions of prims sectors {100}, {110}, and {010} are distinct from each other at Etna but indistinguishable at Stromboli (compare Figure 6 in Ubide et al., 2019 with **Figure 7**, this study). In this regard, the comparatively mild sector zoning of the studied megacrysts from Stromboli could be linked to very low degrees of undercooling and crystallisation conditions very close to thermodynamic equilibrium. In fact, all the sectors in the megacrysts are in equilibrium with shoshonite melt (**Supplementary Figure 5**). Furthermore, very low undercooling conditions are consistent with the formation of large megacrysts under growth-dominated crystallisation, whereas higher undercooling conditions would favour smaller phenocrysts through nucleation-dominated crystallisation (Kirkpatrick, 1977; Landi et al., 2019). The origin of the mild undercooling conditions has important implications for the interpretation of crystallisation dynamics. One possible explanation could be megacryst crystallisation during very slow magma ascent. However, given the protracted magma storage suggested by the large size of the megacrysts, we consider crystallisation at the margin of a reservoir, which could undergo convection (e.g., Welsch et al., 2009), as a more plausible hypothesis. Such a scenario would impose low, relatively constant undercooling conditions that agree with the mild sector zoning ubiquitous across megacryst cores, mantles, and rims.

The homogeneous major element data recovered for crystal and melt portions across the clinopyroxene megacrysts indicate that crystallisation was supplied by continuous input of uniform shoshonitic melts, as suggested by crystal size distribution analysis of the products of historical eruptions at Stromboli (e.g., Armienti et al., 2007). The megacrysts may therefore offer a record of incremental magma body growth (Cashman and Blundy, 2013), where successive inputs of magma of buffered bulk composition replenished and interacted with prior melts and crystals. Mineral inclusions are abundant across the megacrysts (**Figures 4–6**) suggesting that new magma inputs promoted heterogeneous nucleation of clinopyroxene and other phases on pre-existing clinopyroxene crystals (Kirkpatrick, 1977). To investigate subtle modulations in the history of melt compositions involved in clinopyroxene growth, we hereafter deconstruct the Cr record across the megacrysts. As a slow diffusing and highly compatible cation in the clinopyroxene structure (D'Orazio et al., 1998; Costa and Morgan, 2011), chromium defines fine concentric variations with only minor sector partitioning (Ubide et al., 2019).

Some of the megacrysts contain Cr-rich antecryst cores (e.g., **Figure 5**) that lack sector zoning and could have formed under very slow crystallisation conditions before being partially dissolved and incorporated into new shoshonitic melt. Because antecryst cores lack internal features, however, we cannot rule out the possibility of diffusive resetting during protracted storage at magmatic temperatures (e.g., Costa and Morgan, 2011). Whilst similar to other clinopyroxene compositions in major elements, the Cr-rich antecryst cores lack apatite inclusions, suggesting crystallisation from a relatively mafic and volatile-poor shoshonitic melt. Resorbed cores with distinct chemical signatures have also been described in the Pizzo high-K subgroup (Francalanci et al., 2014), as well as in the Post-Pizzo to Present-day sequence (Petrone et al., 2018), and during the most recent activity of Stromboli (Francalanci et al., 2005, 2012; Bragagni et al., 2014). In all these previous studies, the antecryst cores have been interpreted as older cumulates derived from the crystal mush zone, recycled or "cannibalized" (Cashman and Blundy, 2013) by volatile-rich, hot, mafic magmas.

Megacryst cores and mantles differ in the nature of their concentric zonations. The mantles show fine Cr oscillations that could be linked to changes in intensive or extensive parameters through time. However, the euhedral textures of concentric zones, together with the compositional consistency of mineral and melt inclusions, indicate that such changes were relatively minor. A plausible explanation is continued replenishment of the megacryst-crystallising reservoir with shoshonite-buffered magmas, followed by minor magma fractionation, reduction of Cr levels and further replenishment. Additionally, convection of the megacrysts within a chemically heterogenous reservoir could result in crystallisation from slightly different melts through time. It is interesting that the megacryst cores do not show such inner oscillations, however they are also sector zoned. If sector zoning relates to cooling rate (Welsch et al., 2009, 2016; Garrison et al., 2018; Ubide et al., 2019), then the thermal path of cores and mantles should be the same. Therefore, the cores and mantles could have crystallised at the margin of a reservoir and: (a) the reservoir was relatively stable during the crystallisation of the cores and was repeatedly replenished during the crystallisation of the mantles; or (b) the megacryst convected within an initially homogeneous reservoir that became compositionally zoned with time. Recharge events are common drivers of convective dynamics in magmatic reservoirs (Bergantz et al., 2015; Landi et al., 2019; and references therein) and a recent investigation on the textural and compositional records of K-feldspar megacrysts from Southern Tuscany (Italy) by Landi et al. (2019) suggested that repeated influx of hot magma can, in fact, favour the growth of large megacrysts.

The primary distinguishing feature of megacryst rims is their Cr-rich composition (**Figures 4–6**). This applies not only to clinopyroxene rims, but also to rim-hosted titanomagnetite inclusions, which are more Cr-rich than core- and mantle-hosted titanomagnetites. Such variations, coupled with milder enrichments in Ni and depletions in incompatible elements, suggest crystallisation from a more mafic melt (Streck, 2008; Ubide and Kamber, 2018). Given the lack of apatite inclusions at megacryst rims (e.g., **Figure 4**) and adhering groundmass, the recharge magma was possibly less volatile-rich than the resident magma. Chromium-rich rims occur in all the studied crystals, implying ubiquitous mixing shortly before eruption (e.g., Kent et al., 2010). Mafic recharge and mixing may therefore represent the eruption-triggering mechanism (Ubide and Kamber, 2018). Numerical modelling has shown that stirring and swirling of crystals upon recharge can generate a variety of zonation patterns (Bergantz et al., 2015). Such reservoir dynamics involving interaction between crystals and melts could well explain the spectrum of rim textures recorded in the megacrysts, including multiple oscillations and discontinuous dissolution between Cr-poor and subsequent Cr-rich layers (e.g., **Figure 4**). Still, the major element compositions of the clinopyroxene rims and rim-hosted mineral and melt inclusions are consistent with those of core, mantle and groundmass regions, suggesting mixing between compositionally similar shoshonitic melts. In a study of clinopyroxene megacrysts from the infamous 1669 eruption at Mt. Etna, Magee et al. (in press) have suggested that the pressure oversaturation of the system leading to the onset of eruption could have been triggered by a large-volume mafic injection, and not necessarily by a major compositional change in the intruding magma. Similarly, the recharge that tipped the Stromboli megacrysts to erupt was likely "cryptic," only compositionally distinct at the trace element level (e.g., Magee et al., in press).

Crystal Storage and Mobilisation Timescales

The relative sizes of growth zones in the megacrysts (e.g., thin rims) suggest rapid melt mobilisation upon recharge and mixing, in contrast to the longer timescales of crystal residence implied by large megacryst cores and mantles. Chromium zonations are very sharp in spite of the lack of major element variation, which precludes application of Fe-Mg diffusion chronometry (e.g., Costa and Morgan, 2011; Petrone et al., 2018). Experimental data on crystallisation kinetics of Stromboli and Etna basalts show that at low degrees of undercooling, crystal growth rates can be considered constant (Vona and Romano, 2013). Therefore, the thickness of crystal zones can be used to approximate the time of crystallisation in deep magmatic environments, provided that crystal growth rates are well-constrained and the growth of a given mineral zone can be considered continuous (Ubide and Kamber, 2018). The megacrysts studied here have polyhedral shapes and major element compositions that indicate crystallisation in deep-seated reservoirs, under constant P-T-H_2O conditions from core to rim (**Figure 8**). Melt inclusions trapped throughout megacryst growth have similar compositions to groundmass glasses, including incompatible and slow diffusing elements such as P and Al (**Supplementary Table 7**). This observation implies that the melt inclusions are not the trapped remnants of a liquid boundary layer surrounding rapidly growing clinopyroxenes, which would be enriched in incompatible elements relative to the bulk melt composition (Baker, 2008). Thus, we assume that the megacrysts formed at depth under conditions of low undercooling, supported by presence of only weak sector zoning.

Studies on clinopyroxene growth kinetics in alkaline basaltic melts from Mt. Etna, conducted both in experiments (Orlando et al., 2008; Mollo et al., 2013) and through crystal size distribution analyses of natural products (Armienti et al., 2013), have constrained clinopyroxene growth rates on the order of 10^{-8} cm/s at low degrees of undercooling ($\Delta T <$ 10–20°C). Because the rims record the final crystallisation stage and potentially the eruption trigger, we assume that they grew continuously and immediately prior to eruption (Ubide and Kamber, 2018). We, therefore, apply the 10^{-8} cm/s growth rate to the thicknesses measured across crystal rims to estimate the timescales of magma mixing and mush mobilisation upon magma intrusion. Results can be discussed as recharge-to-eruption timescales under the assumption that magma ascent is rapid to instantaneous. Indeed, olivine growth during the Present-day paroxysms at Stromboli suggests magma ascent from 350 MPa within a few hours to a few tens of hours (Bertagnini et al., 2003). To minimise the effect of differential growth in different crystallographic orientations, we limit our timescales to measurements across the prism sectors {100}, {010}, and {110}, and disregard measurements across the faster growing hourglass sectors {-111} as they yield longer timescales than the prism group. Results for 58 rim thicknesses across prism sectors on 11 megacrysts and 20 crystal sections converge at 200 ± 99 µm, returning timescales of mixing and evacuation following recharge of 22 ± 10 days. This estimate is of the same order of magnitude as maximum mixing, stirring and triggering timescales of 10 days obtained from thickness measurements on clinopyroxenes from younger Stromboli products (Post-Pizzo to Present-day activity; Petrone et al., 2018). In the Present-day shallow plumbing system, plagioclase crystal size distributions in natural scoriae combined with growth rates from decompression experiments indicate minimum mixing-to-equilibration timescales of hours to days (Agostini et al., 2013).

The recharge-to-eruption timescales, whilst dependent on the veracity of growth rate estimates, are in good agreement with results of numerical simulations of magma recharge in basaltic mush systems, which show that mixing processes that precondition magmas for eruption can operate on timescales of days-weeks (Schleicher et al., 2016). These authors quantified that the volume of magma mobilised by the intruding melt depends on the mass flux of the intrusion, further supporting the notion that compositionally similar but volumetrically significant magma recharge has the potential to trigger eruption.

Growth prior to the final recharge event was likely discontinuous, and we lack constraints on potential hiatuses in crystallisation during storage, violating the premise of continuous growth required for timescale calculations. We also note that repeated replenishment of the crystallising reservoir with hot magma could have led to dissolution episodes (see also Landi et al., 2004, 2008; Armienti et al., 2007). The fine oscillatory zoning of megacryst mantles may reflect repeated mafic injections; however, dissolution features are uncommon between growth layers (e.g., **Figures 4–6**), except around antecrysts. In any case, it is reasonable to assume that crystallisation of the core-mantle portions of the megacrysts took place over protracted periods of magma storage. Indeed, previous studies obtained decadal-centennial timescales of magma residence, based on: (1) Fe-Mg diffusion modelling of clinopyroxene zoning profiles from the Post-Pizzo and Present-day activity (typically 1–50 years after crystallisation of diopsidic bands, and up to 150 years at the initial phase of the Post-Pizzo sequence; Petrone et al., 2018); (2) Sr isotope data on clinopyroxenes from the twentieth century activity (19 years; Francalanci et al., 1999); and (3) time series analysis of U-series disequilibria of 1996–2007 products (<55 years in the deep LP reservoir and 2–10 years in the shallow HP reservoir; Bragagni et al., 2014).

New Insights Into Plumbing System Architecture

The plumbing system feeding Stromboli volcanism has been extensively studied from volcanological, petrological and geochemical perspectives (cf. reviews by Francalanci et al., 2013; Cashman and Edmonds, 2019 and references therein). The feeder system is depicted as a vertically extended mush column that, at present, has an open-conduit configuration feeding the unique, constant eruptive activity at the summit craters (e.g., Métrich et al., 2010). Steady-state Strombolian explosions produce black scoriae deposits with high phenocryst (HP) contents (up to ca. 50 vol.% of crystals; Armienti et al., 2007) and low volatile contents (<1.5 wt.% H_2O; Aiuppa et al., 2010; Métrich et al., 2010). Periodically, the persistent Strombolian activity is punctuated by more energetic explosive eruptions (paroxysms) that eject light-coloured ("golden") pumices with low phenocryst (LP) contents (<5–10 vol.% of crystals; Armienti et al., 2007) and high volatile contents (2.5–3.5 wt.% H_2O and 0.15–0.2 CO_2; Aiuppa et al., 2010; Métrich et al., 2010), mingled with the regular HP scoriae. More sporadically (every 4 years since 1888; Aiuppa et al., 2010), effusive episodes produce lava flows with HP petrological characteristics (Armienti et al., 2007). At present, the LP magmas have more mafic compositions than HP magmas and are interpreted to tap deeper, undegassed magmas that travel quickly to the surface (Bertagnini et al., 2003; Métrich et al., 2010). According to olivine-hosted melt inclusions (Aiuppa et al., 2010; Métrich et al., 2010), HP and LP magmas are fed by magma bodies located at 50–100 MPa (2–4 km depth below the summit vents) and 190–260 MPa (7–10 km depth below the summit vents), respectively. The shallow magma ponding zone at 2–4 km is supported by geodetic data (Bonaccorso et al., 2008) and plagioclase compositions (Landi et al., 2004; Francalanci et al., 2005). This depth range coincides with the depth of the interface between volcanic rocks and the basement (2.4–3.5 km; Di Roberto et al., 2008), and connects with the upper feeder dyke-conduit (Burton et al., 2007). Meanwhile, the location of the LP reservoir is consistent with a major mid-crustal discontinuity at 10 km (Morelli et al., 1975) and with precursory seismic signals and geochemical anomalies in crater plume emissions prior to recent paroxysmal activity (Pino et al., 2011).

Over time, different magma reservoirs have been tapped due to edifice collapse, however, two common levels of magma storage (similar to the current HP-LP double-tier architecture described above) have persisted throughout the entire known history of the volcano, located at ∼3 and ∼9–11 km depth (Francalanci et al., 2013, 2014 and references therein). In Pizzo times, the deep and shallow reservoirs were independent, and fed contemporaneous high-K and shoshonite products, respectively (Francalanci et al., 2014). While the Pizzo-shoshonite magma chamber was periodically recharged and still persists (HP reservoir), Francalanci et al. (2014) stressed that there is no evidence of a clear high-potassium signature in the products erupted after the Pizzo period. All erupted magmas postdating Pizzo activity are invariably shoshonitic basalts (Petrone et al., 2018), and only a minor high-K component has been identified in the LP magmas (Francalanci et al., 2013, 2014). The proto-LP-HP configuration and connectivity was established as early as the Post-Pizzo era (Petrone et al., 2018) and syn-eruptive mixing has persisted until today (Francalanci et al., 2013).

We find that the megacrysts studied here are compositionally akin to the Pizzo shoshonite subsystem (**Figure 7**), yet they return significantly deep conditions of crystallisation (∼300 MPa; **Figure 8**) relative to the Present-day HP reservoir (**Figure 9**). In detail, the majority of megacryst domains are compositionally indistinguishable from smaller pyroxenes hosted in Pizzo shoshonites (**Figure 7**, right panels). Similarly, the megacryst-hosted melt inclusions have a compositional affinity with the glass compositions in the shoshonite subgroup (Francalanci et al., 2014; **Supplementary Figure 4**). Hence, the megacrysts are inferred to have crystallised from Pizzo shoshonite melt, but at relatively high pressure, below the depth of the 10 km mid-crustal discontinuity beneath Stromboli (Morelli et al., 1975; **Figure 9**). The megacrysts grew from relatively evolved magma at temperatures of ∼1,080°C, water contents of ∼2 wt.% H2O, and NNO-buffered conditions [see section Estimating Clinopyroxene Crystallisation Conditions (*P*-*T*-H2O)]. Tests for equilibrium between clinopyroxene and melt compositions confirm the reliability of our estimates (**Supplementary Figure 5**), which were obtained with recently optimised clinopyroxene-melt *P*-*T*-H_2O calibrations (Mollo et al., 2018), further adjusted to approach ideal equilibrium conditions (**Figure 8**), and corroborated by thermodynamic simulations using Rhyolite-MELTS (Gualda et al., 2012; **Figure 7**). The implications of our estimates may therefore be discussed in the context of the plumbing system feeding volcanism at Stromboli.

Our pressure estimates at ∼300 MPa agree with the deepest roots of the plumbing system at Stromboli probed by melt inclusions (Aiuppa et al., 2010). It is important to stress that the pressures (depths) deduced from olivine-hosted melt inclusions only record the conditions of olivine crystallisation. In contrast, clinopyroxene-hosted melt inclusions have not provided reliable pressure constraints at Stromboli (Métrich et al., 2010). These authors noted that magma batches feeding olivine growth at current HP-LP reservoirs necessarily rise from deeper levels, and our data suggest clinopyroxene megacrysts crystallised at ≥10 km in Pizzo times. Clinopyroxene is known to crystallise from basaltic magmas across a wide range of pressures (e.g., Putirka, 2017) and can dominate the deep plumbing system of alkaline and hydrous volcanoes, for example Mt. Etna (Armienti et al., 2013; Mollo et al., 2015; Ubide and Kamber, 2018). At Stromboli, ponded partial melts have been resolved down to the base of the 17-km thick continental crust, where a low *Vp* and *Vs* volume has been seismically detected (Barberi et al., 2007).

Plagioclase stability expands under water-poor conditions and becomes dominant upon degassing of water-rich magmas at shallow depth (e.g., Francalanci et al., 2004; Landi et al., 2004, 2008; Giacomoni et al., 2014). At Stromboli, the transition from closed- to open-system degassing (and LP to HP magma in the current plumbing system) occurs at shallow depths of 2–4 km below summit vents (Aiuppa et al., 2010), with plagioclase becoming ubiquitous when the H_2O concentration of the melt reaches ≤1 wt.% (Landi et al., 2004). Hence, we propose that the vertical configuration of the plumbing system at Stromboli in Pizzo times could have been stratified into mid-crustal clinopyroxene-rich mushes transitioning to olivine crystallisation and finally plagioclase dominance in shallow degassing reservoirs (**Figure 9**), similar to other H_2O-rich basaltic systems such as Mt. Etna (Armienti et al., 2013; Mollo et al., 2015; Ubide and Kamber, 2018; Magee et al., in press). The implications of deep clinopyroxene crystallisation must be considered when calculating magma ascent rates (e.g., Petrone et al., 2018) and in volcano monitoring efforts (including seismic crises; e.g., Pino et al., 2011). Compared to the megacrysts, recent clinopyroxenes have relatively lower Na_2O and Al_2O_3 contents (**Figure 7**, right panels) and thus may have crystallised under shallower conditions (e.g., Nimis, 1995). Therefore, further barometric evidence from clinopyroxenes across the eruptive history of Stromboli is needed to test if the stratified plumbing system configuration inferred for the Pizzo megacrysts also controlled other Pizzo products and later eruptive periods, up until Present-day activity.

Two Millennia of Magmatic Invasion Leading to Steady-State Activity

Stromboli affords an opportunity to explore the evolution of an active volcano on short, geological to historical, and even human timescales. The bulk rock compositions of the products erupted in the last 13 ka (from the onset of Epoch 5-Neostromboli through to Epoch 6-Recent Stromboli, including Pizzo to the Present-day activity; **Figure 1**) show a progressive decrease in SiO_2, incompatible elements (e.g., Rb, Zr) and $^{87}Sr/^{86}Sr$ with time, coupled with an increase in MgO and $^{143}Nd/^{144}Nd$ (Francalanci et al., 2013 and references therein). This magmatic evolution indicates a progressive change to more primitive melts with distinct source characteristics. On shorter timescales, whole rock and clinopyroxene compositional variations from Post-Pizzo and Present-day products are consistent with the time progression of the Stromboli system toward more mafic compositions (Petrone et al., 2018). On even shorter (decadal)

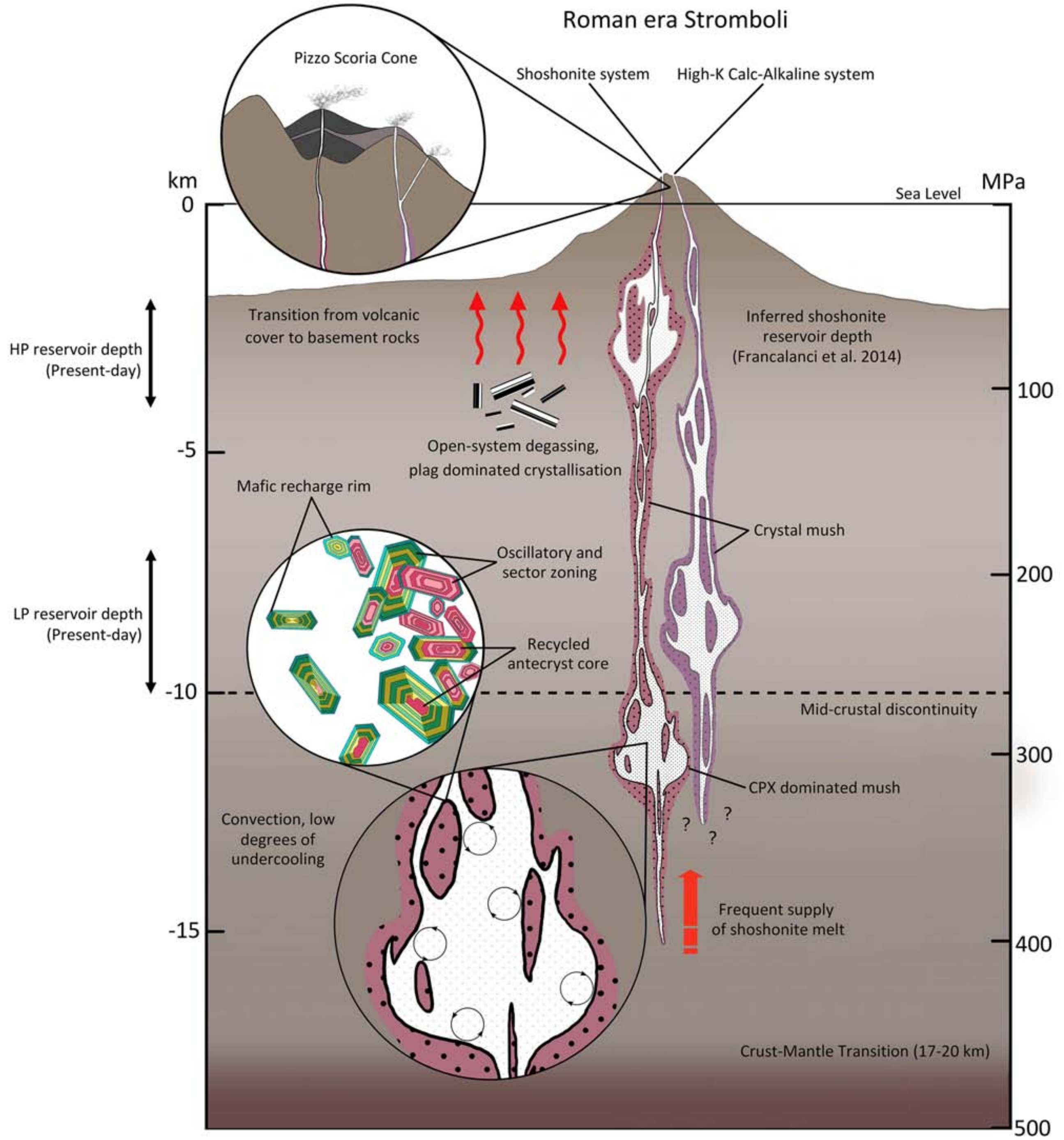

FIGURE 9 | Working model for the extended plumbing system at Stromboli volcano during Pizzo (Roman) times. Clinopyroxene megacrysts crystallised below the 10 km mid-crustal discontinuity (Morelli et al., 1975), deeper than the reservoir depths inferred for Pizzo, Post-Pizzo, and Present-day activity based on olivine-hosted melt inclusions (Aiuppa et al., 2010; Métrich et al., 2010; Francalanci et al., 2013; double-headed arrows mark the depth ranges of current HP-LP reservoirs). The megacrysts grew from incremental replenishments and convection of shoshonite magma under conditions of low undercooling, generating mild concentric and oscillatory zonations which sometimes overgrow inherited cores. As suggested by Francalanci et al. (2014), the Roman-age feeding systems of the shoshonite subgroup (studied through clinopyroxene megacrysts here) and the high-K calc-alkaline subgroup were independent. The magnifying glass at the top highlights eruptive relationships between the two magmas. The lack of Mg-rich (diopsidic) bands in the studied megacrysts, typical of Post-Pizzo and Present-day clinopyroxenes (Petrone et al., 2018), suggests that the inception of the steady-state activity may be related to the invasion of the plumbing system with mafic magma in the last two millennia, after eruption of the megacrysts. The crust-mantle transition under Stromboli has been inferred at 17 km (Panza et al., 2007; Métrich et al., 2010) to 20 km (Laiolo and Cigolini, 2006), and the interface between volcanic rocks and the basement lies at about 2.4–3.5 km depth (Di Roberto et al., 2008); both transitions are denoted by transitional grading in the figure.

timescales, Sr isotope systematics in bulk rocks decreased significantly from the 1980s until 2000 (Francalanci et al., 2004). Within that period, micro-drilled portions of clinopyroxene and plagioclase crystals indicated a rapid decrease of $^{87}Sr/^{86}Sr$ in crystal mantles followed a mild increase at the rims, implying replenishment with mafic magma followed by mixing prior to eruption (Francalanci et al., 2005). Here, we use the clinopyroxene compositional variations to track changes in magma composition back to the Roman era (Pizzo, 2.4–1.8 ka).

The Pizzo megacrysts lack a key feature of clinopyroxenes from more recent eruptions. Clinopyroxene crystals from Post-Pizzo and Present-day activity show "diopsidic bands" identified as darker grayscale contrast zones in BSE images (lighter coloured under plane polarised light), with up to Mg#$_{\sim 90}$ (Francalanci et al., 2004, 2005; Landi et al., 2006; Armienti et al., 2007; Petrone et al., 2018; **Figure 7**, right panels) that record the intrusion of hot and significantly more mafic magma into the system (Petrone et al., 2018). The diopsidic composition is typically found as thin, euhedral mantle (intermediate) zones, but can also occur as resorbed cores or at crystal rims (Francalanci et al., 2004, 2005; Landi et al., 2006; Armienti et al., 2007; Petrone et al., 2018). In contrast, the megacrysts studied here have remarkably homogeneous major element compositions with Mg#$_{71-78}$. A compilation of clinopyroxene compositions from Pizzo (shoshonite and high-K subgroups; Francalanci et al., 2014), Post-Pizzo and Present-day activity (Francalanci et al., 2005; Petrone et al., 2018) shows a distinct Mg#-rich group (not present in Pizzo megacrysts) that becomes more prevalent through time (**Figure 7**). During the Pizzo era, shoshonite-hosted crystals show similar compositions to the megacrysts studied here, whereas high-K basalt-hosted clinopyroxenes show an incipient increase in Mg#. The diopsidic compositions become more frequent through Post-Pizzo and Present-day activity products (Petrone et al., 2018). Even though all compositions generate a common evolutionary path in SiO_2, TiO_2, and Na_2O vs. MgO bivariate plots, the low-Mg# augitic compositions and high-Mg# diopsidic compositions are separated by steps in Al_2O_3, CaO, and Cr_2O_3 vs. MgO (**Figure 7**, right panels) that suggest a change in the crystallisation environment (see also Francalanci et al., 2004). Interestingly, Mg-rich zones are relatively enriched in CaO (**Figure 7**), a feature mirrored in bulk rock compositions (Bertagnini et al., 2003). Hence, according to the compiled database, the mafic magma invading Stromboli in historical times may have first appeared as high-K magma in Pizzo times, when the megacryst environment remained uninvaded. The data suggest a genetic link between the Pizzo high-K magmas and the invading magma, which is intriguing because the intruding magma reported from Post-Pizzo times is shoshonitic in composition (Francalanci et al., 2013; Petrone et al., 2018). However, Francalanci et al. (2014) noted that while the high-K component has not directly erupted after Pizzo times, it has been present for a long period in the Stromboli plumbing system and could be undergoing dormant recharge. Tentatively, the clinopyroxene data may point to the role of a minor (diluted) high-K component in the Present-day shoshonite magmas, as suggested by Francalanci et al. (2013). In line with the idea of enhanced mixing in the feeder system through time, Francalanci et al. (2004) reported that clinopyroxenes from eruptions spanning the twentieth century are remarkably uniform in major and minor elements.

It is pertinent to observe that the inception of steady-state activity at Stromboli (at least since Post-Pizzo times; Petrone et al., 2018) is in agreement with the invasion of the plumbing system with distinctly mafic magma, as recorded by clinopyroxene crystals (Petrone et al., 2018; **Figure 7**). Bulk rock Sr isotope ratios become progressively less radiogenic from Pizzo shoshonite products up until Present-day activity, and bulk rock major elements record a mafic trend since Post-Pizzo times (Petrone et al., 2018), shortly after the eruption of the megacrysts. Timescales of magma mixing and crystal mobilisation upon recharge obtained in this study (22 ± 10 days, Pizzo) are within error of those of Petrone et al. (2018; up to 10 days, Post-Pizzo—Present-day). Although it may appear that the triggering timescales have shortened somewhat from Pizzo to Post-Pizzo and Present-day activity, further data are required to establish if the invading mafic magma has brought about increased eruption-triggering efficiency. Similarly, Petrone et al. (2018) highlighted that crystal residence timescales have decreased from the initial phase of the Post-Pizzo activity onwards. In agreement with the hypothesis of progressive invasion, Petrone et al. (2018) found that the top of the Post-Pizzo sequence contains abundant clinopyroxenes with multiple diopsidic bands, suggesting the occurrence of more frequent replenishment events than at the inception of Post-Pizzo activity, as well as a potential link between injections of new recharging magma and eruption frequency, as suggested for the persistent Present-day activity (Taddeucci et al., 2013).

In their Sr-isotope study of recent eruptions, Francalanci et al. (2005) linked the $^{87}Sr/^{86}Sr$ decrease in scoria and lavas from ∼1980 to greater volumes of recharge magma in the volcano plumbing system and increased intensity of Strombolian activity prior to the 1985 lava eruption. Here, the compilation of clinopyroxene major element data suggests that the inception of the steady-state activity might be directly related to the invasion of the plumbing system with mafic magma on historical timescales (from the Roman era until today). A similar relationship between magma invasion and enhanced eruptive activity was observed on decadal timescales for the recent enhanced volcanism at Mt. Etna (Cannata et al., 2018; Ubide and Kamber, 2018). The latter study showed that Cr zonations in clinopyroxene can hold detailed records of magma pathways through volcanic systems, and our compiled Stromboli dataset shows that diopsidic bands are clearly enriched in Cr_2O_3 (**Figure 7**). Further inspection of the textural and chemical budgets of clinopyroxenes in recent Stromboli products holds promise to help build an updated view of the feeder system, track its evolution through time and explore relationships with changes in eruptive style, all of which are important for volcano monitoring efforts.

CONCLUSIONS

A detailed understanding of clinopyroxene records opens a new perspective into the study of dynamic crystallisation and the space-time evolution of magmatic plumbing systems. We have investigated the textural and compositional complexities of Roman era (2.4–1.8 ka; Pizzo) megacrysts from Stromboli volcano using a crystallographically controlled approach, providing petrological constraints that can be further tested on clinopyroxenes from more recent (and older) eruptions, as well as on smaller Pizzo phenocrysts. We conclude that:

- High-resolution major and trace element mapping constitutes an exciting petrological tool for the study of magmatic records from a combined textural-compositional perspective. In particular, laser ablation time-of-flight (LA-ICP-TOFMS) mapping provides very rapid visualisation of the chemical complexity of large sample materials, for a wide range of major and trace elements.
- Sector-zoned crystals provide unparalleled insight into the study of crystallisation dynamics; low charge cations (Cr, Ni; oscillatory zoned) carry information on melt history whereas Al and high charge cations (e.g., HFSE; sector zoned) carry information on cooling history (cf. Ubide et al., 2019). The Pizzo megacrysts show very mild oscillatory and sector zoning, most clearly discernible at the trace element level. Megacryst growth is interpreted in the context of incremental recharge by pulses of shoshonite melt and associated convection, generating a protracted crystallisation environment with low degrees of undercooling.
- Barometric, thermometric and hygrometric models indicate crystallisation under relatively constant P-T-H_2O conditions, at depths below the 10 km mid-crustal discontinuity beneath Stromboli. We suggest a stratified plumbing system architecture where clinopyroxene crystallisation dominates at depth and olivine-plagioclase crystallise at shallower depths from increasingly degassed melts. Deep storage and crystallisation have not previously been identified at Stromboli, and future work will investigate if the stratified configuration is a long-standing feature of Stromboli magmas.
- Megacryst rims are not significantly distinct in terms of major elements, but have enrichments in Cr that suggest the arrival of a slightly more mafic magma prior to eruption. The thicknesses of Cr-rich rims provide an approximation of the timescales of crystal mobilisation following growth over protracted (decadal-centennial) periods. If correct, the assumed growth rates imply that the clinopyroxene megacrysts erupted very quickly (days-weeks) after magma injection and mixing.
- The Pizzo megacrysts show very constant augitic major element compositions, whereas clinopyroxenes in coeval high-K products and younger eruptive products show abundant diopsidic growth bands inferred to reflect mafic invasion of the Stromboli plumbing system on historical timescales. Mafic invasion may have driven the inception of the world-famous steady-state activity at the volcano.

DATA AVAILABILITY

Datasets for this study are included in the manuscript and the **Supplementary Files**. Data are also available on request from the corresponding author (TU).

AUTHOR CONTRIBUTIONS

TU and JC collected the samples and designed the research and CB prepared the megacrysts sections. TU and MN analysed the samples with electron microprobe, and TU, SM, and FD led subsequent data treatment and barometric, thermometric, and hygrometric modelling. Mapping experiment design and data reduction were undertaken by YB (LA-ICP-TOFMS) and JC, CB, and TU (LA-ICP-QMS). CB carried out the timescale calculations. All authors were actively involved in the discussion and interpretation of the data and participated in the preparation of the manuscript.

FUNDING

This work was supported by The University of Queensland (ECR grant UQECR1717581 and MRFF grant RM2016000555 to TU), the Australian Geoscience Council and the Australian Academy of Science (34th IGC Travel Grant to TU). We thank the HP-HT laboratory of Experimental Geophysics and Volcanology (INGV Rome) and EPOS TCS MSL for access to electron microprobe analysis. We thank TOFWERK for access to LA-ICP-TOFMS instrumentation and analytical time, and support with data handling and processing. At the University of Münster, YB gratefully acknowledges support through a Marie Skłodowska-Curie Fellowship (Project ID 746518).

ACKNOWLEDGMENTS

We thank Daniele Andronico, Chiara M. Petrone, Ruadhán Magee, Matteo Masotta, and Alessio Pontesilli for insightful discussions on Stromboli volcanism and clinopyroxene zoning. We thank Dale Harpley for help photographing the megacrysts. We thank the reviewers and editors for insightful comments which helped improve the original version of the paper.

SUPPLEMENTARY MATERIAL

The Supplementary Material for this article can be found online at: https://www.frontiersin.org/articles/10.3389/feart.2019.00239/full#supplementary-material

Supplementary Figure 1 | Major element maps of megacryst section 13C, obtained with electron microprobe.

Supplementary Figure 2 | Minor and trace element maps of megacryst section 13C, obtained with LA-ICP-QMS.

Supplementary Figure 3 | Electron microprobe traverses of clinopyroxene megacryst 31, obtained by electron microprobe (locations in **Figure 5**). The compositions of core, mantle, and rim regions are largely coincident, although crystal cores reach slightly lower Si-Mg and higher Al-Ti concentrations than mantles and rims. The antecryst core is slightly enriched in Al-Ti compared to the host clinopyroxene. In terms of sectoral variations, compositions across prism sectors {100}, {110}, and {010} are virtually homogeneous. Hourglass sectors {−111} are Mg-rich and Al-poor compared to prism sectors.

Supplementary Figure 4 | Chemical classification of melts sampled by Stromboli clinopyroxene megacrysts, including clinopyroxene-hosted melt inclusions (white circles) and glass contained in the adhering groundmass (dark circles); the matrix glass composition used for clinopyroxene-melt thermobarometry and hygrometry

(**Figure 8**) is denoted by the large square symbol. The compositional fields for all Stromboli whole rocks and Eruptive Epoch 6 whole rocks are provided for comparison (Francalanci et al., 2013). The compositional fields for glass data from Pizzo and Present-day activity products are also provided (Francalanci et al., 2014; Petrone et al., 2018). Data are plotted on an anhydrous basis. In spite of the potential inter-laboratory bias, glass compositions sampled by the clinopyroxene megacrysts are compositionally similar to Pizzo shoshonite glasses and Present-day glasses, and distinct from Pizzo high-K calc-alkaline glasses.

Supplementary Figure 5 | Clinopyroxene-melt equilibrium tests (K_D(Fe-Mg)$^{cpx-melt} = 0.28 \pm 0.08$, Putirka, 2008; $\Delta DiHd$, Putirka et al., 1996; Mollo et al., 2013; D_{Na}, Blundy et al., 1995; D_{Ti}, Hill et al., 2011; Mollo et al., 2018) indicate that all clinopyroxene compositions are in chemical equilibrium with the glass hosted in the megacrysts and adhering glassy matrix, which are all consistently shoshonitic in composition. To approach the Fe^{2+} content in the melt (to test K_D(Fe-Mg)$^{cpx-melt}$), we computed our melt composition in Rhyolite-MELTS (Gualda et al., 2012) under the NNO oxygen fugacity buffer (Métrich and Clocchiatti, 1996; Di Carlo et al., 2006) and constant *P-T* conditions of 320 MPa and 1,080°C (**Figure 8**).

Supplementary Table 1 | Stromboli clinopyroxene megacrysts analysed in this study, collected from scoria at the top of the Pizzo sequence (Eruptive Epoch 6a; Francalanci et al., 2013, 2014), at 38°47′33″N 15°12′49″E.

Supplementary Table 2 | Major element data (wt.% oxides) obtained by electron microprobe on clinopyroxene megacrysts.

Supplementary Table 3 | Major element data (wt.% oxides) obtained by electron microprobe on clinopyroxene megacryst-hosted olivine inclusions.

Supplementary Table 4 | Major element data (wt.% oxides) obtained by electron microprobe on clinopyroxene megacryst-hosted plagioclase inclusions, and plagioclase microcryts in adhering glassy tephra.

Supplementary Table 5 | Major element data (wt.% oxides) obtained by electron microprobe on clinopyroxene megacryst-hosted titanomagnetite inclusions, and titanomagnetite microcryts in adhering glassy tephra.

Supplementary Table 6 | Major element data (wt.% oxides) obtained by electron microprobe on clinopyroxene megacryst-hosted apatite inclusions.

Supplementary Table 7 | Major element data (wt.% oxides) obtained by electron microprobe on clinopyroxene megacryst-hosted melt inclusions and adhering glass.

Supplementary Table 8 | Summary of results from Rhyolite-MELTS isobaric fractionation models at 300 and 400 MPa, from 1,250 to 1,030°C. For a given fractionation (cooling) step, melt data are listed first, followed by data on fractionated clinopyroxene (where present).

Supplementary File 1 | Ubide et al. (2019) *Frontiers in Earth Science*.

REFERENCES

Agostini, C., Fortunati, A., Arzilli, F., Landi, P., and Carroll, M. R. (2013). Kinetics evolution as a probe to magmatism at Stromboli (Aeolina Archipelago, Italy). *Geochim. Cosmochim. Acta* 110, 135–151. doi: 10.1016/j.gca.2013.02.027

Aiuppa, A., Bertagnini, A., Métrich, N., Moretti, R., Di Muro, A., Liuzzo, et al. (2010). A model of degassing for Stromboli volcano. *Earth Planet. Sci. Lett.* 295, 195–204.

Allard, P. (2010). A CO_2-rich gas trigger of explosive paroxysms at Stromboli basaltic volcano, Italy. *J. Volcanol. Geotherm. Res.* 189, 363–374. doi: 10.1016/j.jvolgeores.2009.11.018

Armienti, P., Francalanci, L., and Landi, P. (2007). Textural effects of steady state behaviour of the Stromboli feeding system. *J. Volcanol. Geotherm. Res.* 160, 86–98. doi: 10.1016/j.jvolgeores.2006.05.004

Armienti, P., Perinelli, C., and Putirka, K. D. (2013). A new model to estimate deep-level magma ascent rates, with applications to Mt. Etna (Sicily, Italy). *J. Petrol.* 54, 795–813. doi: 10.1093/petrology/egs085

Baker, D. R. (2008). The fidelity of melt inclusions as records of melt composition. *Contrib. Mineral. Petrol.* 156, 377–395. doi: 10.1007/s00410-008-0291-3

Barberi, G., Zhang, H., Scarfì, L., Cocina, O., Castellano, M., Chiarabba, C., et al. (2007). Crustal evidence of a low velocity Vp and Vs volume beneath Stromboli, Italy. *Geophys. Res. Abstracts* 9:02621.

Bergantz, G. W., Schleicher, J. M., and Burgisser, A. (2015). Open-system dynamics and mixing in magma mushes. *Nat. Geosci.* 8, 793–796. doi: 10.1038/ngeo2534

Bertagnini, A., Métrich, N., Landi, P., and Rosi, M. (2003). Stromboli volcano (Aeolian Archipelago, Italy): an open window on the deep-feeding system of a steady state basaltic volcano. *J. Geophys. Res.* 108:2336. doi: 10.1029/2002JB002146

Biggs, J., and Pritchard, M. E. (2017). Global volcano monitoring: what does it mean when volcanoes deform? *Elements* 13, 17–22. doi: 10.2113/gselements.13.1.17

Blundy, J. D., Falloon, T. J., Wood, B. J., and Dalton, J. A. (1995). Sodium partitioning between clinopyroxene and silicate melts. *J. Geophys. Res. Solid Earth* 100, 15501–15515. doi: 10.1029/95JB00954

Bonaccorso, A., Gambino, S., Guglielmino, F., Mattia, M., Puglisi, G., and Boschi, E. (2008). Stromboli 2007 eruption: deflation modeling to infer shallow-intermediate plumbing system. *Geophys. Res. Lett.* 35:L06311. doi: 10.1029/2007GL032921

Borovinskaya, O., Hattendorf, B., Tanner, M., Gschwind, S., and Günther, D. (2013). A prototype of a new inductively coupled plasma time-of-flight mass spectrometer providing temporally resolved, multi-element detection of short signals generated by single particles and droplets. *J. Anal. Atomic Spectrom.* 28, 226–233. doi: 10.1039/C2JA30227F

Bragagni, A., Avanzinelli, R., Freymuth, H., and Francalanci, L. (2014). Recycling of crystal mush-derived melts and short magma residence times revealed by U-series disequilibria at Stromboli volcano. *Earth Planet. Sci. Lett.* 404, 206–219. doi: 10.1016/j.epsl.2014.07.028

Burger, M., Gundlach-Graham, A., Allner, S., Schwarz, G., Wang, H. A., Gyr, L., et al. (2015). High-speed, high-resolution, multielemental LA-ICP-TOFMS imaging: part II. Critical evaluation of quantitative three-dimensional imaging of major, minor, and trace elements in geological samples. *Anal. Chem.* 87, 8259–8267. doi: 10.1021/acs.analchem.5b01977

Burger, M., Schwarz, G., Gundlach-Graham, A., Käser, D., Hattendorf, B., and Günther, D. (2017). Capabilities of laser ablation inductively coupled plasma time-of-flight mass spectrometry. *J. Anal. Atomic Spectrom.* 32, 1946–1959. doi: 10.1039/C7JA00236J

Burton, M., Allard, P., Muré, F., and La Spina, A. (2007). Magmatic gas composition reveals the source of slug-driven Strombolian explosive activity. *Science* 137, 227–230. doi: 10.1126/science.1141900

Bussweiler, Y., Borovinskaya, O., and Tanner, M. (2017). Laser ablation and inductively coupled plasma–time-of-flight mass spectrometry—A powerful combination for high-speed multielemental imaging on the micrometer scale. *Spectroscopy* 32, 14–20.

Bussweiler, Y., Giuliani, A., Greig, A., Kjarsgaard, B. A., Petts, D., Jackson, S. E., et al. (2019). Trace element analysis of high-Mg olivine by LA-ICP-MS–Characterization of natural olivine standards for matrix-matched calibration and application to mantle peridotites. *Chem. Geol.* 52, 136–137. doi: 10.1016/j.chemgeo.2019.06.019

Cannata, A., Di Grazia, G., Giuffrida, M., Gresta, S., Palano, M., Sciotto, M., et al. (2018). Space-time evolution of magma storage and transfer at Mt. Etna volcano (Italy): The 2015–2016 Reawakening of Voragine Crater. *Geochem. Geophys. Geosyst.* 19, 471–495. doi: 10.1002/2017GC007296

Cashman, K., and Blundy, J. (2013). Petrological cannibalism: the chemical and textural consequences of incremental magma body growth. *Contrib. Mineral. Petrol.* 166, 703–729. doi: 10.1007/s00410-013-0895-0

Cashman, K. V., and Edmonds, M. (2019). Mafic glass compositions: a record of magma storage conditions, mixing and ascent. *Phil. Trans. R. Soc. A* 377:20180004. doi: 10.1098/rsta.2018.0004

Cashman, K. V., Sparks, R. S. J., and Blundy, J. D. (2017). Vertically extensive and unstable magmatic systems: a unified view of igneous processes. *Science* 355:eaag3055. doi: 10.1126/science.aag3055

Costa, F., and Morgan, D. (2011). "Time Constraints from Chemical Equilibration in magmatic crystals," in: *Timescales of Magmatic Processes: From Core to Atmosphere,* eds. A. Dosseto, S. P. Turner, and J. A. Van Orman (Hoboken, NJ: Blackwell Publishing Ltd.), 125–159. doi: 10.1002/9781444328509.ch7

Del Bello, E., Mollo, S., Scarlato, P., von Quadt, A., Forni, F., and Bachmann, O. (2014). New petrological constraints on the last eruptive phase of the Sabatini

Volcanic District (central Italy): Clues from mineralogy, geochemistry, and Sr–Nd isotopes. *Lithos* 205, 28–38. doi: 10.1016/j.lithos.2014.06.015

Di Carlo, I., Pichavant, M., Rotolo, S. G., and Scaillet, B. (2006). Experimental crystallization of a high-K arc basalt: the golden pumice, Stromboli volcano (Italy). *J. Petrol.* 47, 1317–1343. doi: 10.1093/petrology/egl011

Di Roberto, A., Bertagnini, A., Pompilio, M., Gamberi, F., Marani, M. P., and Rosi, M. (2008). Newly discovered submarine flank eruption at Stromboli volcano (Aeolian Islands, Italy). *Geophys. Res. Lett.* 35:L16310. doi: 10.1029/2008GL034824

D'Orazio, M., Armienti, P., and Cerretini, S. (1998). Phenocryst/matrix trace-element partition coefficients for hawaiite-trachyte lavas from the Ellittico volcanic sequence (Mt. Etna, Sicily, Italy). *Mineral. Petrol.* 64, 65–68. doi: 10.1007/BF01226564

Downes, M. J. (1974). Sector and oscillatory zoning in calcic augites from M. Etna, Sicily. *Contrib. Mineral. Petrol.* 47, 187–196. doi: 10.1007/BF00371538

Duncan, A. M., and Preston, R. M. F. (1980). Chemical variation of clinopyroxene phenocrysts from the trachybasaltic lavas of Mount Etna, Sicily. *Min. Mag.* 43, 765–770. doi: 10.1180/minmag.1980.043.330.10

Ferguson, A. K. (1973). On hour-glass sector zoning in clinopyroxene. *Min. Mag.* 39, 321–325. doi: 10.1180/minmag.1973.039.303.08

Fowler, S. J., Spera, F., Bohrson, W., Belkin, H. E., and De Vivo, B. (2007). Phase equilibria constraints on the chemical and physical evolution of the Campanian Ignimbrite. *J. Petrol.* 48, 459–493. doi: 10.1093/petrology/egl068

Francalanci, L., Avanzinelli, R., Nardini, I., Tiepolo, M., Davidson, J. P., and Vannucci, R. (2012). Crystal recycling in the steady-state system of the active Stromboli volcano: a 2.5-ka story inferred from *in situ* Sr-isotope and trace element data. *Contrib. Mineral. Petrol.* 163, 109–131. doi: 10.1007/s00410-011-0661-0

Francalanci, L., Braschi, E., Di Salvo, S., Lucchi, F., and Petrone, C. (2014). When magmas do not interact: paired Roman-age activity revealed by tephra studies at Stromboli volcano. *Bull. Volcanol.* 76, 1–17. doi: 10.1007/s00445-014-0884-9

Francalanci, L., Davies, G. R., Lustenhouwer, W., Tommasini, S., Mason, P. R. D., and Conticelli, S. (2005). Intra-grain Sr isotope evidence for crystal recycling and multiple magma reservoirs in the recent activity of stromboli Volcano, Southern Italy. *J. Petrol.* 46, 1997–2021. doi: 10.1093/petrology/egi045

Francalanci, L., Lucchi, F., Keller, J., De Astis, G., and Tranne, R. (2013). Eruptive, volcano-tectonic and magmatic history of the Stromboli volcano (north-eastern Aeolian archipelago. *Geol. Soc. Lond. Memoirs* 37, 397–471. doi: 10.1144/M37.13

Francalanci, L., Tommasini, S., and Conticelli, S. (2004). The volcanic activity of Stromboli in the 1906–1998 AD period: mineralogical, geochemical and isotope data relevant to the understanding of the plumbing system. *J. Volcanol. Geotherm. Res.* 131, 179–211. doi: 10.1016/S0377-0273(03)00362-7

Francalanci, L., Tommasini, S., Conticelli, S., and Davies, G. R. (1999). Sr isotope evidence for short magma residence time for the 20th century activity at Stromboli volcano, Italy. *Earth Planet. Sci. Lett.* 167, 61–69. doi: 10.1016/S0012-821X(99)00013-8

Garrison, J. M., Sims, K. W. W., Yogodzinski, G. M., Escobar, R. D., Scott, S., Mothes, P., et al. (2018). Shallow-level differentiation of phonolitic lavas from Sumaco Volcano, Ecuador. *Contrib. Mineral. Petrol.* 173:6. doi: 10.1007/s00410-017-1431-4

Gernon, T. M., Upton, B. G. J., Ugra, R., Yücel, C., Taylor, R. N., and Elliott, H. (2016). Complex subvolcanic magma plumbing system of an alkali basaltic maar-diatreme volcano (Elie Ness, Fife, Scotland). *Lithos* 264, 70–85. doi: 10.1016/j.lithos.2016.08.001

Giacomoni, P. P., Ferlito, C., Coltorti, M., Bonadiman, C., and Lanzafame, G. (2014). Plagioclase as archive of magma ascent dynamics on "open conduit" volcanoes: the 2001–2006 eruptive period at Mt. Etna. *Earth Sci. Rev.* 138, 371–393. doi: 10.1016/j.earscirev.2014.06.009

Giuffrida, M., Holtz, F., Vetere, F., and Viccaro, M. (2017). Effects of CO_2 flushing on crystal textures and compositions: experimental evidence from recent K-trachybasalts erupted at Mt. Etna. *Contrib. Mineral. Petrol.* 172:90. doi: 10.1007/s00410-017-1408-3

Gualda, G. A. R., Ghiorso, M. S., Lemons, R. V., and Carley, T. L. (2012). Rhyolite-MELTS: a modified calibration of MELTS optimized for silica-rich, fluid-bearing magmatic systems. *J. Petrol.* 53, 875–890. doi: 10.1093/petrology/egr080

Gundlach-Graham, A., Garofalo, P. S., Schwarz, G., Redi, D., and Günther, D. (2018). High-resolution, quantitative element imaging of an upper crust, low-angle cataclasite (Zuccale Fault, Northern Apennines) by laser ablation ICP time-of-flight mass spectrometry. *Geostand. Geoanal. Res.* 42, 559–574. doi: 10.1111/ggr.12233

Hendriks, L., Gundlach-Graham, A., Hattendorf, B., and Günther, D. (2017). Characterization of a new ICP-TOFMS instrument with continuous and discrete introduction of solutions. *J. Anal. Atomic Spectrom.* 32, 548–561. doi: 10.1039/C6JA00400H

Hill, E., Blundy, J. D., and Wood, B. J. (2011). Clinopyroxene-melt trace element partitioning and the development of a predictive model for HFSE and Sc. *Contrib. Mineral. Petrol.* 161, 423–438. doi: 10.1007/s00410-010-0540-0

Hollister, L. S., and Gancarz, A. J. (1971). Compositional sector-zoning in clinopyroxene from the Narce area, Italy. *Am. Mineral.* 56, 959–979.

Humphreys, M. C. S., Edmonds, M., Christopher, T., and Hards, V. (2009). Chlorine variations in the magma of Soufrière Hills Volcano, Montserrat: Insights from Cl in hornblende and melt inclusions. *Geochim. Cosmochim. Acta* 73, 5693–5708. doi: 10.1016/j.gca.2009.06.014

Jarosewich, E., Nelen, J. A., and Norberg, J. A (1980). Reference samples for electron microprobe analysis. *Geostand. Newslett.* 4, 43–47. doi: 10.1111/j.1751-908X.1980.tb00273.x

Kent, A. J. R., Darr, C., Koleszar, A. M., Salisbury, M. J., and Cooper, K. M. (2010). Preferential eruption of andesitic magmas through recharge filtering. *Nat. Geosci.* 3, 631–636. doi: 10.1038/ngeo924

Kirkpatrick, R. J. (1977). Nucleation and growth of plagioclase, Makaopuhi and Alae lava lakes, Kilauea Volcano, Hawaii. *Geol. Soc. Am. Bull.* 88, 78–84. doi: 10.1130/0016-7606(1977)88<78:NAGOPM>2.0.CO;2

Kozu, S., and Washington, H. S. (1918). Augite from Stromboli. *Am. J. Sci.* 4–45, 463–469. doi: 10.2475/ajs.s4-45.270.463

Laiolo, M., and Cigolini, C. (2006). Mafic and ultramafic xenoliths in San Bartolo lava field: new insights on the ascent and storage of Stromboli magmas. *Bull. Volcanol.* 68, 653–670. doi: 10.1007/s00445-005-0040-7

Landi, P., Francalanci, L., Pompilio, M., Rosi, M., Corsaro, A., Petrone, C. M., et al. (2006). The December 2002–July 2003 effusive event at Stromboli volcano, Italy: insights into the shallow plumbing system by petrochemical studies. *J. Volcanol. Geotherm. Res.* 155, 263–284. doi: 10.1016/j.jvolgeores.2006.03.032

Landi, P., La Felice, S., Petrelli, M., Vezzoli, L. M., and Principe, C. (2019). Deciphering textural and chemical zoning of K-feldspar megacrysts from Mt. Amiata Volcano (Southern Tuscany, Italy): insights into the petrogenesis and abnormal crystal growth. *Lithos* 324–325, 569–583. doi: 10.1016/j.lithos.2018.11.032

Landi, P., Metrich, N., Bertagnini, A., and Rosi, M. (2004). Dynamics of magma mixing and degassing in plagioclase at Stromboli (Aeolian Archipelago, Italy). *Contrib. Mineral. Petrol.* 147, 213–227. doi: 10.1007/s00410-004-0555-5

Landi, P., Métrich, N., Bertagnini, A., and Rosi, M. (2008). Recycling and "re-hydration" of degassed magma inducing transient dissolution/crystallization events at Stromboli (Italy). *J. Volcanol. Geotherm. Res.* 174, 325–336. doi: 10.1016/j.jvolgeores.2008.02.013

Leung, I. S. (1974). Sector-Zoned titanaugites: morphology, crystal chemistry and growth. *Am. Mineral.* 59, 127–138.

Longerich, H. P., Jackson, S. E., and Günther, D. (1996). Laser ablation inductively coupled plasma mass spectrometric transient signal data acquisition and analyte concentration calculation. *J. Anal. Atomic Spectrom.* 11, 899–904. doi: 10.1039/JA9961100899

Magee, R., Ubide, T., and Kahl, M. (in press). The lead-up to Mount Etna's most destructive historic eruption (1669). Cryptic recharge recorded in clinopyroxene. *J. Petrol.*

McNutt, S. R. (2005). Volcanic seismology. *Annu. Rev. Earth. Planet. Sci.* 33, 461–491. doi: 10.1146/annurev.earth.33.092203.122459

Métrich, N., Bertagnini, A., and Di Muro, A. (2010). Conditions of magma storage, degassing and ascent at stromboli: new insights into the volcano plumbing system with inferences on the eruptive dynamics. *J. Petrol.* 51, 603–626. doi: 10.1093/petrology/egp083

Métrich, N., and Clocchiatti, R. (1996). Sufur abundance and its speciation in oxidized alkaline melts. *Geochim. Cosmochim. Acta* 60, 4151–4160. doi: 10.1016/S0016-7037(96)00229-3

Mollo, S., Blundy, J., Scarlato, P., De Cristaofaro, S. P., Tecchiato, V., Di Stefano, F., et al. (2018). An integrated P-T-H_2O-lattice strain model to quantify the role of clinopyroxene fractionation on REE+Y and HFSE patterns of mafic alkaline magmas: application to eruptions at Mt. Etna. *Earth Sci. Rev.* 185, 32–56. doi: 10.1016/j.earscirev.2018.05.014

Mollo, S., Blundy, J. D., Iezzi, G., Scarlato, P., and Langone, A. (2013). The partitioning of trace elements between clinopyroxene and trachybasaltic melt during rapid cooling and crystal growth. *Contrib. Mineral. Petrol.* 166, 1633–1654. doi: 10.1007/s00410-013-0946-6

Mollo, S., Del Gaudio, P., Ventura, G., Iezzi, G., and Scarlato, P. (2010). Dependence of clinopyroxene composition on cooling rate in basaltic magmas: implications for thermobarometry. *Lithos* 118, 302–312. doi: 10.1016/j.lithos.2010.05.006

Mollo, S., Giacomoni, P. P., Andronico, D., and Scarlato, P. (2015). Clinopyroxene and titanomagnetite cation redistributions at Mt. Etna volcano (Sicily, Italy): footprints of the final solidification history of lava fountains and lava flows. *Chem. Geol.* 406, 45–54. doi: 10.1016/j.chemgeo.2015.04.017

Mollo, S., and Hammer, J. (2017). Dynamic crystallization in magmas. *EMU Notes Mineral.* 16, 373–418. doi: 10.1180/EMU-notes.16.12

Mollo, S., Lanzafame, G., Masotta, M., Iezzi, G., Ferlito, C., and Scarlato, P. (2011). Cooling history of a dike as revealed by mineral chemistry: a case study from Mt. Etna volcano. *Chem. Geol.* 283, 261–273. doi: 10.1016/j.chemgeo.2011.06.016

Mollo, S., and Masotta, M. (2014). Optimizing pre-eruptive temperature estimates in thermally and chemically zoned magma chambers. *Chem. Geol.* 368, 97–103. doi: 10.1016/j.chemgeo.2014.01.007

Morelli, C., Giese, P., Cassinis, R., Colombi, B., Guerra, I., Luongo, G., et al. (1975). Crustal structure of southern Italy. A seismic refraction profile between Puglia-Calabria-Sicily, *Boll. Geofis. Teor. Appl.* 17, 183–210.

Nimis, P. (1995). A clinopyroxene geobarometer for basaltic systems based on crystals-structure modeling. *Contrib. Mineral. Petrol.* 121, 115–125. doi: 10.1007/s004100050093

Orlando, A., D'Orazio, M., Armienti, P., and Borrini, D. (2008). Experimental determination of plagioclase and clinopyroxene crystal growth rates in an anhydrous trachybasalt from Mt. Etna (Italy). *Eur. J. Mineral.* 20, 653–664. doi: 10.1127/0935-1221/2008/0020-1841

Panza, G. F., Peccerillo, A., Aoudia, A., and Farina, B. (2007). Geophysical and petrological modelling of the structure and composition of the crust and upper mantle in complex geodynamic settings: the Tyrrhenian sea and surroundings. *Earth Sci. Rev.* 80, 1–46. doi: 10.1016/j.earscirev.2006.08.004

Paton, C., Hellstrom, J., Paul, B., Woodhead, J., and Hergt, J. (2011). Iolite: freeware for the visualisation and processing of mass spectrometric data. *J. Anal. Atomic Spectrom.* 26, 2508–2518. doi: 10.1039/c1ja10172b

Peccerillo, A. (2005). *Plio-Quaternary Volcanism in Italy*. Berlin: Springer-Verlag.

Perinelli, C., Mollo, S., Gaeta, M., Pia de Cristofaro, S., Palladino, D. M., Armienti, P., et al. (2016). An improved clinopyroxene-based hygrometer for Etnean magmas and implications for eruption triggering mechanisms. *Am. Mineral.* 101, 2774–2777. doi: 10.2138/am-2016-5916

Petrone, C. M., Braschi, E., Francalanci, L., Casalini, M., and Tommasini, S. (2018). Rapid mixing and short storage timescales in the magma dynamics of a steady-state volcano. *Earth Planet. Sci. Lett.* 492, 206–221. doi: 10.1016/j.epsl.2018.03.055

Petrus, J. A., Chew, D. M., Leybourne, M. I., and Kamber, B. S. (2017). A new approach to laser-ablation inductively-coupled-plasma mass spectrometry (LA-ICP-MS) using the flexible map interrogation tool 'Monocle'. *Chem. Geol.* 463, 76–93. doi: 10.1016/j.chemgeo.2017.04.027

Pino, N. A., Moretti, R., Allard, P., and Boschi, E. (2011). Seismic precursors of a basaltic paroxysmal explosion track deep gas accumulation and slug upraise. *J. Geophys. Res.* 116:B02312. doi: 10.1029/2009JB000826

Putirka, K. D. (2008). Thermometers and barometers for volcanic systems. *Rev. Mineral. Geochem.* 69, 61–120. doi: 10.2138/rmg.2008.69.3

Putirka, K. D. (2017). Down the crater: where magmas are stored and why they erupt. *Elements* 13, 11–16. doi: 10.2113/gselements.13.1.11

Putirka, K. D., Johnson, M., Kinzler, R. J., Longhi, J., and Walker, D. (1996). Thermobarometry of mafic igneous rocks based on clinopyroxene-liquid equilibria, 0–30 kbar. *Contrib. Mineral. Petrol.* 123, 92–108. doi: 10.1007/s004100050145

Putirka, K. D., Mikaelian, H., Ryerson, F., and Shaw, H. F. (2003). New clinopyroxene-liquid thermobarometers for mafic, evolved, and volatile-bearing lava compositions, with applications to lavas from Tibet and the Snake River Plain, Idaho. *Am. Mineral.* 88, 1542–1554. doi: 10.2138/am-2003-1017

Reubi, O., and Blundy, J. (2007). A dearth of intermediate melts at subduction zone volcanoes and the petrogenesis of arc andesites. *Nature* 461, 1269–1273. doi: 10.1038/nature08510

Rosi, M., Pistolesi, M., Bertagnini, A., Landi, P., Pompilio, M., and Di Roberto, A. (2013). Stromboli volcano, Aeolian Islands (Italy): present eruptive activity and hazards. *Geol. Soc. Lond. Mem.* 37, 473–490. doi: 10.1144/M37.14

Scarlato, P., Mollo, S., Blundy, J., Iezzi, G., and Tiepolo, M. (2014). The role of natural solidification paths on REE partitioning between clinopyroxene and melt. *Bull. Volcanol.* 76:810. doi: 10.1007/s00445-014-0810-1

Schleicher, J. M., Bergantz, J. W., Breidenthal, R. E., and Burgisser, A. (2016). Time scales of crystal mixing in magma mushes. *Geophys. Res. Lett.* 43. doi: 10.1002/2015GL067372

Shinohara, H. (2008). Excess degassing from volcanoes and its role on eruptive and intrusive activity. *Rev. Geophys.* 46, 1–31. doi: 10.1029/2007RG000244

Spilliaert, N., Allard, P., Métrich, N., and Sobolev, A. V. (2006). Melt inclusion record of the conditions of ascent, degassing, and extrusion of volatile-rich alkali basalt during the powerful 2002 flank eruption of Mount Etna (Italy). *J. Geophys. Res.* 111:B04203. doi: 10.1029/2005JB003934

Streck, M. J. (2008). Mineral textures and zoning as evidence for open system processes. *Rev. Mineral. Geochem.* 69, 595–622. doi: 10.2138/rmg.2008.69.15

Taddeucci, J., Palladino, D. M., Sottili, G., Bernini, D., Andronico, D., and Cristaldi, A. (2013). Linked frequency and intensity of persistentvolcanic activity at Stromboli (Italy). *Geophys. Res. Lett.* 40, 1–5. doi: 10.1002/grl.50652

Ubide, T., Galé, C., Larrea, P., Arranz, E., and Lago, M. (2014). Antecrysts and their effect on rock compositions: the Cretaceous lamprophyre suite in the Catalonian Coastal Ranges (NE Spain). *Lithos* 206–207, 214–233. doi: 10.1016/j.lithos.2014.07.029

Ubide, T., and Kamber, B. (2018). Volcanic crystals as time capsules of eruption history. *Nat. Commun.* 9, 326–326. doi: 10.1038/s41467-017-02274-w

Ubide, T., McKenna, C. A., Chew, D. M., and Kamber, B. S. (2015). High-resolution LA-ICP-MS trace element mapping of igneous minerals: in search of magma histories. *Chem. Geol.* 409, 157–168. doi: 10.1016/j.chemgeo.2015.05.020

Ubide, T., Mollo, S., Zhao, J. X., Nazzari, M., and Scarlato, P. (2019). Sector-zoned clinopyroxene as a recorder of magma history, eruption triggers, and ascent rates. *Geochim. Cosmochim. Acta* 251, 265–283. doi: 10.1016/j.gca.2019.02.021

Villaseca, C., Dorado, O., and Orejana, D. (2019). Mineral chemistry of megacrysts and associated clinopyroxenite enclaves in the Calatrava volcanic field: crystallization processes in mantle magma chambers. *J. Iber. Geol.* 45, 401–426. doi: 10.1007/s41513-019-00101-3

Vona, A., and Romano, C. (2013). The effects of undercooling and deformation rates on the crystallization kinetics of Stromboli and Etna basalts. *Contrib. Mineral. Petrol.* 166, 491–509. doi: 10.1007/s00410-013-0887-0

Welsch, B., Faure, F., Bachèlery, P., and Famin, V. (2009). Microcrysts record transient convection at Piton de la Fournaise Volcano (La Réunion Hotspot). *J. Petrol.* 50, 2287–2305. doi: 10.1093/petrology/egp076

Welsch, B., Hammer, J., Baronnet, A., Jacob, S., Hellebrand, E., and Sinton, J. (2016). Clinopyroxene in postshield Haleakala ankaramite: 2. Texture, compositional zoning and supersaturation in the magma. *Contrib. Mineral. Petrol.* 171:6. doi: 10.1007/s00410-015-1213-9

White, R., and McCausland, W. (2016). Volcano-tectonic earthquakes: A new tool for estimating intrusive volumes and forecasting eruptions. *J. Volcanol. Geotherm. Res.* 309, 139–155. doi: 10.1016/j.jvolgeores.2015.10.020

Conflict of Interest Statement: YB was employed by company TOFWERK AG at the onset of this project.

The remaining authors declare that the research was conducted in the absence of any commercial or financial relationships that could be construed as a potential conflict of interest.

frontiers in Earth Science

ORIGINAL RESEARCH
published: 16 February 2018
doi: 10.3389/feart.2018.00010

Evidence for Cyclical Fractional Crystallization, Recharge, and Assimilation in Basalts of the Kimama Drill Core, Central Snake River Plain, Idaho: 5.5-Million-Years of Petrogenesis in a Mid-crustal Sill Complex

Katherine E. Potter[1]*, *John W. Shervais*[1], *Eric H. Christiansen*[2] and *Scott K. Vetter*[3]

[1] Department of Geology, Utah State University, Logan, UT, United States, [2] Department of Geological Sciences, Brigham Young University, Provo, UT, United States, [3] Department of Geology, Centenary College of Louisiana, Shreveport, LA, United States

OPEN ACCESS

Edited by:
Olivier Bachmann,
ETH Zurich, Switzerland

Reviewed by:
Matthew Brueseke,
Kansas State University, United States
Erik Klemetti,
Denison University, United States

***Correspondence:**
Katherine E. Potter
katie.potter@usu.edu

Specialty section:
This article was submitted to Volcanology, a section of the journal Frontiers in Earth Science

Received: *30 September 2017*
Accepted: *29 January 2018*
Published: *16 February 2018*

Citation:
Potter KE, Shervais JW, Christiansen EH and Vetter SK (2018) Evidence for Cyclical Fractional Crystallization, Recharge, and Assimilation in Basalts of the Kimama Drill Core, Central Snake River Plain, Idaho: 5.5-Million-Years of Petrogenesis in a Mid-crustal Sill Complex. Front. Earth Sci. 6:10. doi: 10.3389/feart.2018.00010

Basalts erupted in the Snake River Plain of central Idaho and sampled in the Kimama drill core link eruptive processes to the construction of mafic intrusions over 5.5 Ma. Cyclic variations in basalt composition reveal temporal chemical heterogeneity related to fractional crystallization and the assimilation of previously-intruded mafic sills. A range of compositional types are identified within 1,912 m of continuous drill core: Snake River olivine tholeiite (SROT), low K SROT, high Fe-Ti, and evolved and high K-Fe lavas similar to those erupted at Craters of the Moon National Monument. Detailed lithologic and geophysical logs document 432 flow units comprising 183 distinct lava flows and 78 flow groups. Each lava flow represents a single eruptive episode, while flow groups document chemically and temporally related flows that formed over extended periods of time. Temporal chemical variation demonstrates the importance of source heterogeneity and magma processing in basalt petrogenesis. Low-K SROT and high Fe-Ti basalts are genetically related to SROT as, respectively, hydrothermally-altered and fractionated daughters. Cyclic variations in the chemical composition of Kimama flow groups are apparent as 21 upward fractionation cycles, six recharge cycles, eight recharge-fractionation cycles, and five fractionation-recharge cycles. We propose that most Kimama basalt flows represent typical fractionation and recharge patterns, consistent with the repeated influx of primitive SROT parental magmas and extensive fractional crystallization coupled with varying degrees of assimilation of gabbroic to ferrodioritic sills at shallow to intermediate depths over short durations. Trace element models show that parental SROT basalts were generated by 5–10% partial melting of enriched mantle at shallow depths above the garnet-spinel lherzolite transition. The distinctive evolved and high K-Fe lavas are rare. Found at four depths, 319, 1045, 1,078, and 1,189 m, evolved and high K-Fe flows are compositionally unrelated to SROT magmas and represent highly fractionated basalt, probably accompanied by crustal assimilation. These evolved lavas may be sourced from the Craters of the Moon/Great Rift system to the northeast. The Kimama drill core is the longest record of geochemical variation in the central Snake River Plain and reinforces the concept of magma processing in a layered complex.

Keywords: snake river plain, mid-crustal sill complex, olivine tholeiite, craters of the moon, kimama drill core, yellowstone-snake river plain hotspot

INTRODUCTION

The relationship between volcanic rocks erupted on Earth's surface and their putative plutonic roots is a long-standing geologic problem (e.g., Bachmann et al., 2007; Annen et al., 2015; Cashman et al., 2017). The petrologic and chemical evolution of volcanic provinces and the formation of continental crustal plutonic complexes are typically studied in isolation from one another, yet each of these topics has implications for the other related to magmatic flux, intrusion geometries, fractionation mechanisms, and the effects of partial melting and assimilation (Annen et al., 2015). Previous efforts to understand linkages between pluton construction and eruptive processes have focused largely on silicic systems: the assembly of granitic batholiths and rhyolite ignimbrite eruptions (e.g., Lipman, 1984; Metcalf, 2004; Annen et al., 2006). Although large mafic layered intrusions have been studied extensively (e.g., Irvine, 1970) and the effect of basalt intrusions on crustal heat flux has been modeled (Annen and Sparks, 2002), there are few studies that infer mafic plutonic evolution from basalt compositions in long-lived mafic volcanic provinces (e.g., Shervais et al., 2006). In this paper we use the petrologic and geochemical evolution of basalt recovered in drill core to infer crustal magmatic processes over 5.5 Ma of mafic volcanism in continental crust.

The Snake River Plain (SRP) of central Idaho is a manifestation of Yellowstone-Snake River Plain (YSRP) hotspot volcanism and contains intriguing evidence for mantle hotspot impingement on continental crust (Pierce and Morgan, 1992; Hanan et al., 2008; Shervais and Hanan, 2008; Smith et al., 2009; Jean et al., 2014). The region contains a record of continuous bimodal volcanism extending over 17 Ma (Shervais and Hanan, 2008; Coble and Mahood, 2012; Henry et al., 2017) to the present, and documents the migration of time-transgressive rhyolitic volcanism from the Bruneau-Jarbidge volcanic center (circa 12 Ma) to its present location beneath the Yellowstone Plateau (Pierce and Morgan, 1992; Anders et al., 2009). Interaction between the mantle hotspot and overlying continental lithosphere has resulted in large rhyolite caldera-forming eruptions, followed by eruption of smaller basaltic shield volcanoes (Bonnichsen et al., 2008; Christiansen and McCurry, 2008; McCurry and Rodgers, 2009). Post-caldera basaltic flows form a veneer over the rhyolite ash flows and lavas and mask the complete volcanic record. Understanding the origin and evolution of the post-caldera basalts is a challenge because the lack of later uplift and erosion means that younger lava flows conceal older basalts. High-recovery continental scientific drilling is an effective method to address questions of geochemical and volcanic evolution through time, especially in relatively young volcanic provinces that lack exposure.

Project Hotspot drilled three deep boreholes in the Snake River Plain in order to provide a more complete understanding of the volcanic history of the SRP (Shervais et al., 2011, 2012, 2013). The 1,912 m deep Kimama borehole, located in the Axial Volcanic Zone of the Snake River Plain (**Figure 1**), recovered over 1,900 m of continuous core, including 1,803 m of basalt and 110 m of intercalated sediment (including sidetrack core; Potter, 2014). We present here a detailed petrologic and geochemical investigation of basalts from the Kimama core to determine the nature and extent of chemical changes through time at a fixed location, where physical and chemical characteristics of the crust and mantle lithosphere are relatively set. These data document long-term (5.5 Ma) petrogenetic processes common to intracontinental basalts associated with mantle hotspots and large igneous provinces.

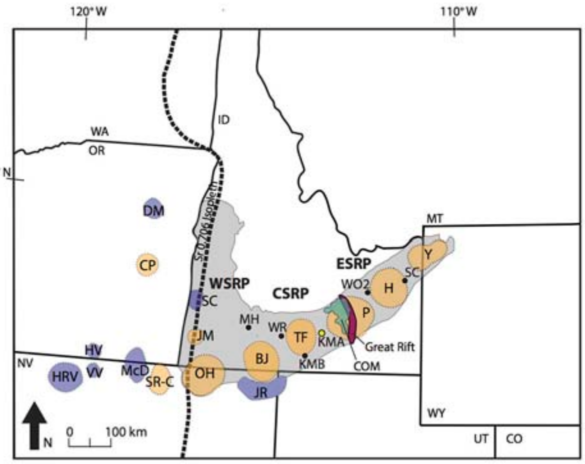

FIGURE 1 | Map of the Snake River Plain showing location of the Kimama drill site (KMA, yellow circle) in relation to inferred locations of Yellowstone-Snake River Plain silicic volcanic centers, the Sr 0.706 isopleth, Craters of the Moon (COM), a Pleistocene-Holocene locus of evolved magmatism, and the Great Rift, a source of Quaternary olivine tholeiite eruptions on the eastern SRP. Regionally significant drill core locations are shown in the central and eastern Snake River Plain: Mountain Home (MH, 1.3 km depth), Wendell-RASA (WR, 0.3 km depth), Kimberly (KMB, 2 km depth), INL-WO2 (WO2, 1.5 km depth) and Sugar City (SC, 0.7 km depth). Miocene volcanic centers in eastern Oregon, northern Nevada, and Idaho are also shown: High Rock volcanics (HRV), Hawk Valley (HV), Virgin Valley (VV), Castle Peak (CP), Dooley Mtn (DM), McDermitt (McD), Santa Rosa-Calico (SR-C), Silver City (SC), Juniper Mtn (JM), Owhyhee Humbolt (OH), Bruneau-Jarbidge (BJ), Jarbidge Rhyolite (JR) Twin Falls (TF), Picabo (P), Heise (H), and Yellowstone (Y). Figure modified from Shervais and Hanan (2008); location of Great Rift and Craters of the Moon from Hughes et al. (2002a).

Other deep boreholes on the SRP include the Sugar City borehole (0.7 km; Embree et al., 1978; Jean et al., in revision), the Idaho National Laboratory (INL) hole WO-2 (1.52 km; Shervais et al., 2006), and the Wendell-RASA borehole (0.3 km; Jean et al., 2013) (**Figure 1**). Geochemical and isotope analyses conducted by previous workers indicate that significant fractionation occurred at lower or mid-crustal depths in layered mafic magma reservoirs, and that interaction with continental lithosphere is the primary external influence on SRP basalt chemistry. The most important mechanism of magma differentiation is thought to be fractional crystallization accompanied by assimilation of genetically-related, previously-intruded mafic sills in mid-crustal magma chambers (Shervais et al., 2006; Jean et al., 2013). The range of primary magma compositions suggests the involvement of multiple, small magma batches (Leeman, 1982; Vetter and Shervais, 1992; Geist et al., 2002; Hughes et al., 2002a,b; Shervais et al., 2006; Jean et al., 2013). Shifts in the composition of primary magma sources through time and space have been documented by Vetter and Shervais (1992), Shervais et al. (2006), and Shervais and Vetter (2009). As the longest and most complete record of basalt volcanism and magma differentiation in the SRP, the Kimama drill core ties mafic volcanism to a transcrustal network of sills and sill complexes where magmas are processed and cycled to the surface.

Geological Background

Regional Setting

The central SRP is loosely defined as the portion of the SRP between the Owyhee Plateau, a highland in southwest Idaho, and the Great Rift, a north-northwest-trending fissure system that extends ~50 km southward from Craters of the Moon lava flow field to the Wapi shield volcano (Kuntz et al., 1982, 1992). Major rhyolitic volcanic fields of the central SRP include the 11-6 Ma Twin Falls eruptive center (Knott et al., 2016), and the 10.4-6.6 Ma Picabo eruptive center, for which the boundaries are poorly defined (**Figure 1**) (Bonnichsen et al., 2008; Drew et al., 2013). These rhyolitic centers are buried by younger basaltic lava flows. Beyond the SRP, to the north and south of the Kimama drill site, is the Miocene to recent Basin and Range Province.

During the late Pliocene through Pleistocene, the SRP was the locus of densely-spaced mafic volcanic centers along the axis of the YSRP hotspot track that erupted thick packages of basalt flows and formed the *Axial Volcanic High* (Hackett et al., 2004; Shervais et al., 2005). Mafic volcanism on the SRP began within 1-2 Ma of the cessation of YSRP silicic volcanism, and is primarily expressed by the eruption of monogenetic olivine tholeiite basalts (Hughes et al., 2002a). Although time-progressive basalt eruptions are evident at the inception of post-rhyolitic volcanism, Pliocene-Holocene basalt lavas on the SRP are distributed throughout the volcanic province and do not follow the progression of silicic volcanism to the NE (Hughes et al., 1999; Bonnichsen and Godchaux, 2002). Most SRP basalt volcanism is manifested as monogenetic, single-pulse lava fields, erupted as low volume (3–5 km^3) flows from shields during short-duration (tens to hundreds of years) eruptions (Kuntz et al., 1992).

The unique style of SRP volcanism has been recognized as a product of small, mid-crustal magma chambers feeding eruptions from coalesced low-relief shield volcanoes, over relatively short durations. Volcanism is described as "plains-style" by Greeley (1982). "Plains-style" volcanism is similar to modern flow processes on the island of Hawaii and transitional between quiescent Hawaiian-style and the large volume flood-style volcanism typified by the Columbia River Basalt Group (Greeley, 1982). Vent constructs for SRP volcanoes are typically low due to the efficient transport of low-viscosity lava away from the vent in lava tubes. Eruptive centers often blend in with the surrounding topography because relatively little lava accumulates near the vent (Self et al., 1998). Between periods of volcanism, lava flows in low areas were mantled by loess and by lacustrine and fluvial sediments.

Snake River Plain Basalt Stratigraphy

The high effusion rate of basalts on the SRP favors emplacement via inflated pahoehoe flows, whereby lava travels through the molten core of the flow and breaks out of the flow front as flow lobes (Walker, 1991; Chitwood, 1994; Hon et al., 1994; Self et al., 1998). The transport of pahoehoe basalt lava over large distances is facilitated via lava tubes, tube complexes, or surface channelization by inflation processes (Self et al., 1998; Hughes et al., 1999). On the Snake River Plain, lava flows may extend as much as 50–60 km from the vent of origin (Shervais et al., 2005). Self et al. (1998) recognized that the inflation mechanism of pahoehoe produces lava flows that display similar geometries at variable spatial scales. In order of increasing scale, basalt lavas are emplaced as flow lobes (flow units), flows, and flow groups (Walker, 1991; Chitwood, 1994; Self et al., 1998).

Over the duration of a "plains-style" eruption, sheet flows and flow units from a single magma reservoir interlayer to form a complex aggregate of flows termed flow group (Hughes et al., 2002a,b; Welhan et al., 2002). Lava flow groups have thicknesses of <1–106 m (flow groups 12 and 73, respectively). They are the two-dimensional equivalents of compound lava flow fields, such as the Wapi and Hell's Half Acre lava fields on the SRP, which have areal dimensions of kilometers to tens of kilometers. Each flow group or lava flow field comprises all of the volcanic activity from a monogenetic volcanic center over time scales of tens to hundreds of years (Greeley, 1982; Kuntz et al., 1992; Welhan et al., 2002; Champion, pers. commun. 2014). In core, flow groups are distinguished from one another by lithostratigraphic relationships, paleomagnetic polarity reversals or inclination changes, sediment interbeds, and by significant geochemical variation.

Monogenetic eruptive centers on the SRP are most likely fed by individual magma sources, as demonstrated by chemical variation between and within flow groups (Hughes et al., 2002b). However, in order to produce separate magma batches for every monogenetic center on the SRP, a stratified source region in which melts were produced over a range of depths and degrees of melting would be required (Hughes et al., 1997).

METHODS

We selected 265 whole rock samples from the Kimama core for analysis, representing 74 of 78 identified basalt flow groups. Samples were preferentially selected from the massive interiors of lava flows to avoid oxidation and alteration. Major elements were analyzed by fused bead X-ray fluorescence spectrometry (XRF), and trace elements were analyzed by inductively coupled plasma mass spectrometry (ICP-MS).

One-inch diameter mini cores were extracted from the whole round cores and a portion of each plug was broken in two to three fragments using a rock hammer. Samples were crushed using a Gyral Grinder shatterbox with a tungsten carbide vessel, and then ground again with an agate mortar and pestle. Samples for major element analysis were ignited at 800°C for 24 h, after which 1 g of ignited sample was mixed with 5 g of a Claisse Li-borate flux and 6 drops of LiI (added as a releasing agent). Sample mixes were melted in Pt-Au metal crucibles at 1200°C in a muffle furnace, then poured into a heated Pt-Au metal disk mold and quenched into glass. Major element (SiO_2, TiO_2, Al_2O_3, MnO, Fe_2O_3, MgO, CaO, Na_2O, K_2O, P_2O_5 Cr_2O_3) were analyzed with a Philips 2400 X-Ray fluorescence (XRF) spectrometer at Utah State University or with a Rigaku ZSX Primus II XRF spectrometer at Brigham Young University.

The standard deviation for replicated values for USGS standard BCR-1 for XRF analyses conducted at Brigham Young University are SiO_2: 0.06%, TiO_2: 0.004%, Al_2O_3: 0.05%, Fe_2O_3: 0.06%, MnO: 0%, MgO: 0.02%, CaO: 0.01%, Na_2O: 0.01%, K_2O: 0.01%, and P_2O_5: 0%. The standard deviation for replicated values for USGS standard BHVO-1 for XRF analyses conducted at Utah State University are SiO_2: 0.12%, TiO_2: 0.03%, Al_2O_3: 0.09%, Fe_2O_3: 0.04%, MnO: 0%, MgO: 0.12%, CaO: 0.08%, Na_2O: 0.01%, K_2O: 0.01%, and P_2O_5: 0.01%. Samples were ignited to convert all Fe to Fe^{3+} for analyses. Loss on ignition (LOI) was performed for 184 samples to identify potential alteration. All tables and figures depict major element values normalized to 100% on a volatile free basis with Fe_{total} reported as Fe_2O_3. Fe_{total} as FeO* is also reported for convenience in Table 1 in Supplementary Material.

Trace-element concentrations were measured at Centenary College (Shreveport, LA) using a PerkinElmer 600 inductively coupled plasma-mass spectrometer (ICP-MS). Approximately 60 mg of each sample was dissolved in 2 mL HF and 3 mL HNO_3 for 3 h, with watch glasses preventing evaporation. Watch glasses were then removed and samples dried, after which another 3 mL of HNO_3 was added to the samples. The sample solution was left at 50°C overnight, and then dried at 90°C. A further addition of 3 mL of HNO_3 to the sample preceded immediate drying. Finally, the sample was brought into solution with 2–3 mL of 50% HNO_3, and brought to a total volume of 50 mL with 5% HNO_3. This procedure is modified from Jenner et al. (1990) and Neal (2001). Five milliliters of 10 ppb In, Rh, and Ru were added to the sample solution as internal standards to calibrate measured concentrations. Plasma lab software was used to map out sampling order and record measurements over the duration of the experiment. Major and trace element analyses made at Utah State University (XRF), Brigham Young University (XRF), and Centenary College (ICP-MS) are distinguished by symbols in Table 1 in Supplementary Material. To compare Kimama major and trace element analyses with compositions from regional SRP basalt lavas, we used published values from Kuntz et al. (1992) and Hughes et al. (2002b).

RESULTS

Flow Groups and Flows in the Kimama Core

The Kimama area includes late Neogene to Quaternary basalts that were erupted from low-relief shield volcanoes, most of which are normal magnetic polarity lavas erupted during the (>781 ka) C1n Brunhes Normal Polarity Chron (Shervais et al., 2005). 21 paleomagnetic Chrons and subchrons were identified in the Kimama core (Potter, 2014). Basaltic lava flows overlie rhyolite in the Twin Falls and Picabo volcanic centers (Shervais et al., 2005, 2011, 2012, 2013; Knott et al., 2016). Rhyolite was not encountered in the Kimama drill core (Potter et al., 2011; Potter, 2014).

Potter (2014) identified 432 basalt flow units comprising 183 lava flows. In core, flows and flow groups are distinguished by lithostratigraphic relationships, paleomagnetic polarity reversals or inclination changes, sediment interbeds, and by significant geochemical variation. The lithostratigraphy, paleomagnetic characteristics, the paleomagnetic and Ar-Ar age model, and the accumulation rate of the Kimama drill core basalts are discussed in Potter (2014).

Using this stratigraphic framework, paleo-secular variations in magnetic stratigraphy, and geochemical indicators (e.g., FeO* = total iron as ferrous, TiO_2, K_2O, La/Lu), we recognize 78 distinct flow groups in the Kimama core, ranging from 0.274 to 105.6 m thick. (**Figure 2**, Table 2 in Supplementary Material). Flow groups 41 and 42, identified by paleomagnetic indicators, were too thin and rubbly to sample. Flow groups 57 and 75, identified by distinct stratigraphic and paleomagnetic indicators, were not sampled due to alteration. Based upon paleomagnetic and Ar-Ar data, as well as stratigraphic relationships, we document that this sequence represents ∼5.5 million years of volcanism (from 6 Ma to 475 ka) (Potter, 2014).

Major Elements

The whole-rock major-and trace-element compositions of Kimama core samples (Table 1 in Supplementary Material), and variation diagrams (**Figures 3**, **4**) reveal similarity to SROT lavas from the central and eastern SRP. Geochemistry displayed in stratigraphic context (**Figure 5**) demonstrates more variation. Kimama basalts have major-element compositional ranges of 43.2–50.4 wt. % SiO_2, 9.80–17.6 wt. % FeO*, 1.22–4.65 wt. % TiO_2, 5.00–11.0 wt. % MgO, 8.84–14.0 wt. % CaO, 11.5–15.8 wt. % Al_2O_3, 1.75–2.75 wt. % Na_2O, and 0.12–0.92 wt. % K_2O, 0.17–1.65 wt. % P_2O_5. In general, most Kimama SROT basalts document smooth increases of TiO_2, FeO*, P_2O_5, and K_2O and decreases of Al_2O_3, CaO, and Ni decreasing MgO (**Figure 3**).

Loss on ignition (LOI) is largely negative above 1055 m depth, with an average of −0.56 (range 0.34 to −2.24) wt% as a result of weight gain as FeO is oxidized to Fe_2O_3 during heating. Below

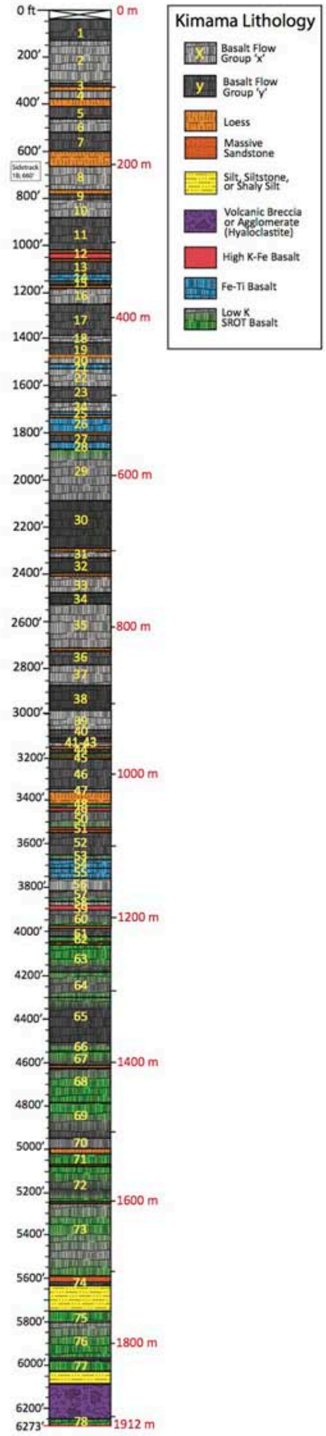

FIGURE 2 | Lithologic log showing stratigraphic locations of Kimama flow groups, numbered 1 through 78 from 13 m (43 ft) through 1,912 m (6,273 ft) depth. SROT basalt is represented by alternating gray and light gray layers. Low K SROT, high Fe-Ti, high K-Fe, and evolved flow groups are represented by green, blue, and red layers (respectively). A green gradient on gray layers demonstrates the location of low K alteration within SROT flow groups. Sediment interbeds of loess (orange) in the upper section of the drill core, and sandstone and siltstone (orange and yellow) are present in the lower depths of the drill core. Hyaloclastite (purple) is present at the base of the drill core.

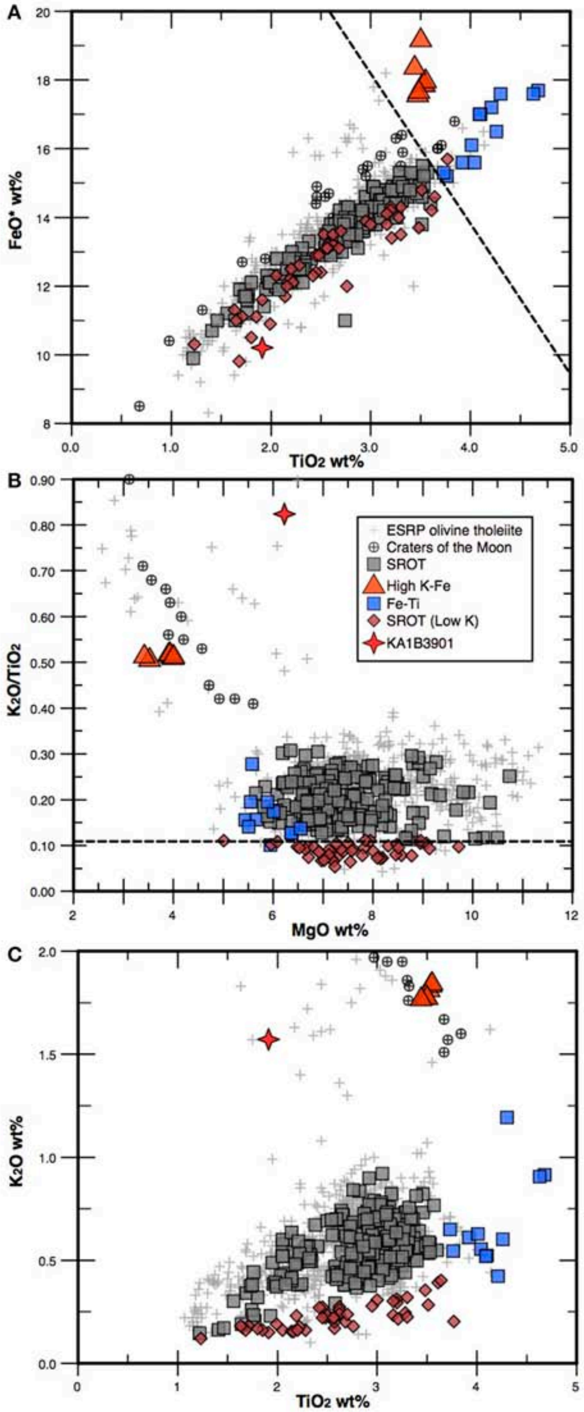

FIGURE 3 | Selected major and trace element variation diagrams showing Kimama compositional groups: group 1 (SROT samples; gray squares), group 2 (high Fe-Ti samples; blue squares), group 3 (high K-Fe samples; red triangles), evolved sample KA1B3901 (red star) and group 4, low K SROT samples (maroon diamonds). Dashed black lines in **(A,B)** indicate compositional thresholds for high Fe-Ti and low K SROT basalts: 0.11 wt% K_2O/TiO_2 for low K SROT lavas, and 3.6 wt% TiO_2 and 15 wt% FeO* for high Fe-Ti lavas. In **(C)**, high K-Fe lavas have FeO > 17.5 wt% and K_2O > 0.65 wt%. The evolved lava (sample KA1B3901) has 1.91 wt% TiO_2, and 1.57 wt% K_2O.

1,055 m depth, loss on ignition values are largely positive, with an average of 1.43 (range 9.41 to −0.83) wt%. The highest LOI (8.5–9.4 wt%) are found below 1,700 m depth, indicating extensive alteration by hydrothermal fluids.

These data reveal that the Kimama basalts define three geochemically-distinct groups: (1) Snake River Olivine Tholeiite (SROT), which includes most of the basalts from surface outcrops on the SRP, (2) tholeiitic basalts rich in iron and titanium ("Fe-Ti basalts"), and (3) a suite of rare high K_2O-FeO*-rich basalts similar to mafic lavas from the Craters of the Moon. In addition, there is a fourth group of low-K basalts that includes members of Group 1 basalts and is characterized by low K_2O (typically <0.25 wt%) and K_2O/TiO2 ratios of ≤0.11 wt% (**Figure 2**).

Group 1 SROT dominate the sample set, with >90% of all analyzed samples from throughout the length of the drill core. They are similar in composition to ocean island basalts, and characterized by phenocrysts or glomerocrysts of olivine and plagioclase. Group 2 Fe-Ti basalts are characterized by high TiO_2 (3.6–4.5 wt%) and FeO* (15–18 wt%). They occur at five depth ranges: 343–359, 459–465, 522–548, 561–566, and 1,117–1,151 m depth. The Fe-Ti basalts fall on extensions of the SROT trends on element variation diagrams, and are inferred to be related to SROT by low-pressure fractionation. The Group 3 high K-Fe lavas are characterized by K_2O >0.65 wt% and 17.5–18.5 wt% FeO*, with distinctively high K_2O/TiO_2 ratios >0.5, and low MgO contents. They are found at only two depth ranges: near 318 m (flow group 12), 1,048 m (Flow group 49), and 1,077 m (flow group 51) (**Figures 2**, **5**, Table 2 in Supplementary Material).

Group 4 includes 36 samples; all but one of these occur below 1,043 m depth. The low-K basalts appear to be normal SROT basalts that have lost K_2O in response to hydrothermal alteration. This is supported by the correlation of low-K basalts with high K_2O/TiO_2 ratios and high LOI (**Figure 6**, Table 1 in Supplementary Material). Alteration within the Kimama drill core is manifest as vesicle fillings at around 700 m depth, forming amygdules filled with calcite and quartz. By 950 m depth, amygdules filled with smectites and/or zeolites become common. Below 1,300 m, alteration becomes more pervasive, with iddingsitization of olivine phenocrysts and the alteration of interstitial glass to clay minerals (Sant, 2013).

Finally, there is one sample that cannot be easily fit into any of these groups, although it seems most comfortable in the high-K-Fe group: KA1B3901 (flow group 59). This sample is characterized by relatively high SiO_2 (53 wt%), high K_2O (1.57 wt%), and moderate MgO (6.21 wt%) (Table 1 in Supplementary Material).

Trace Elements

Trace element variations in the Kimama basalts generally mimic trends observed in correlative major elements. Thus, Zr, Nb, Y, and the REE correlate positively with FeO*, TiO_2 and P_2O_5, and Ba and Rb correlate with K_2O, whereas compatible elements such as Ni and Cr correlate positively with MgO.

Kimama basalts are modestly enriched in the light rare earth elements (LREE) relative to the heavy rare earth elements (HREE), with chondrite-normalized La/Lu = 3–8 and smooth patterns that lack Eu anomalies (or have very modest negative anomalies); they are generally similar to those observed in surface basalts of the eastern and central SRP (**Figure 7A**). This includes all SROT, Fe-Ti, and low-K SROT. Evolved high K-Fe basalts (Group 3) have similar slopes on chondrite-normalized plots but have higher concentrations, similar to or slightly higher than evolved basalts and trachybasalts from Craters of the Moon (**Figure 7A**).

Multi-element (spider) diagrams document further similarities to published data for surface basalts and evolved Craters of the Moon-type lavas. Notable features include strong enrichments in Ba (similar to other basalts in the western USA), and depletions in Th, Sr and Y relative to primitive mantle values (**Figure 7B**).

DISCUSSION

Chemical Suites and Stratigraphic Trends

Despite the overall chemical similarity in SRP Neogene basalts, flow groups in the Kimama drill core exhibit several compositional trends (**Figure 2**). Whole rock MgO, FeO*, TiO_2, P_2O_5, and K_2O (all wt%), plotted against stratigraphic depth isolate three basalt compositional types (**Figure 4**). Oxides such as Al_2O_3 and Na_2O vary without discernible trends, perhaps owing to the crystallization and flotation of plagioclase within the magma, however CaO (not shown) also varies systematically, but Al_2O_3 and Na_2O (also not shown) have no discernable trends.

SROT and high K-Fe flow groups are thought to represent unrelated magma batches, whereas the Fe-Ti flow groups probably represent evolved SROT magmas. In the following paragraphs, we discuss whether Fe-Ti, high K-Fe, and SROT basalts are compositionally related by similar petrogenetic processes, and the significance of low-K basalts below 1200 m depth. We also discuss the significance of the anomalously evolved sample KA1B3901 in flow group 59.

Out of 74 sampled flow groups, a total of 42 flow groups are classified as SROT based upon compositional ranges of 5.00–11.0 wt% MgO, 11.0–15.8 wt% FeO*, 0.21–0.92 wt% K_2O, and 1.76–3.63 wt% TiO_2. Flow groups 1–11, 13, 15–20, 22–24, 27, 30–40, 43, 44, 46, 47, 52, 58, 61, 64, and 70 display SROT chemical trends. SROT flows are found through the entire Kimama drill core, with the highest number of flows in the 16–1,200 m depth range. Seven flow groups are identified as high Fe-Ti lava flows based upon elevated concentrations of FeO* (13.8–17.6 wt%), and TiO_2 (2.67–4.65 wt%). High Fe-Ti flows are preferentially located in the upper 754 m of the drill core in flow groups 14, 21, 25, 26, 28, 54, and 55; two high Fe-Ti flow groups are present stratigraphically deeper at 1,119 and 1,138 m (flow groups 54 and 55, respectively). We identify 21 low-K lava flow groups (29, 45, 48, 50, 53, 57, 60, 62, 63, 65–69, 71–73, and 75–78) dominated by low K_2O/TiO_2 (≤0.11). Low-K SROT flows are concentrated from 1,200 to 1,912 m depth (**Figure 2**, Table 2 in Supplementary Material) and are discussed in the following section.

SROT flows below ∼1,200 m depth are dominantly primitive, with low concentrations of FeO*, TiO_2, P_2O_5, and K_2O, and relatively high MgO, CaO, Cr, and Ni. The latter are less susceptible to alteration than K and are indicators of recharge

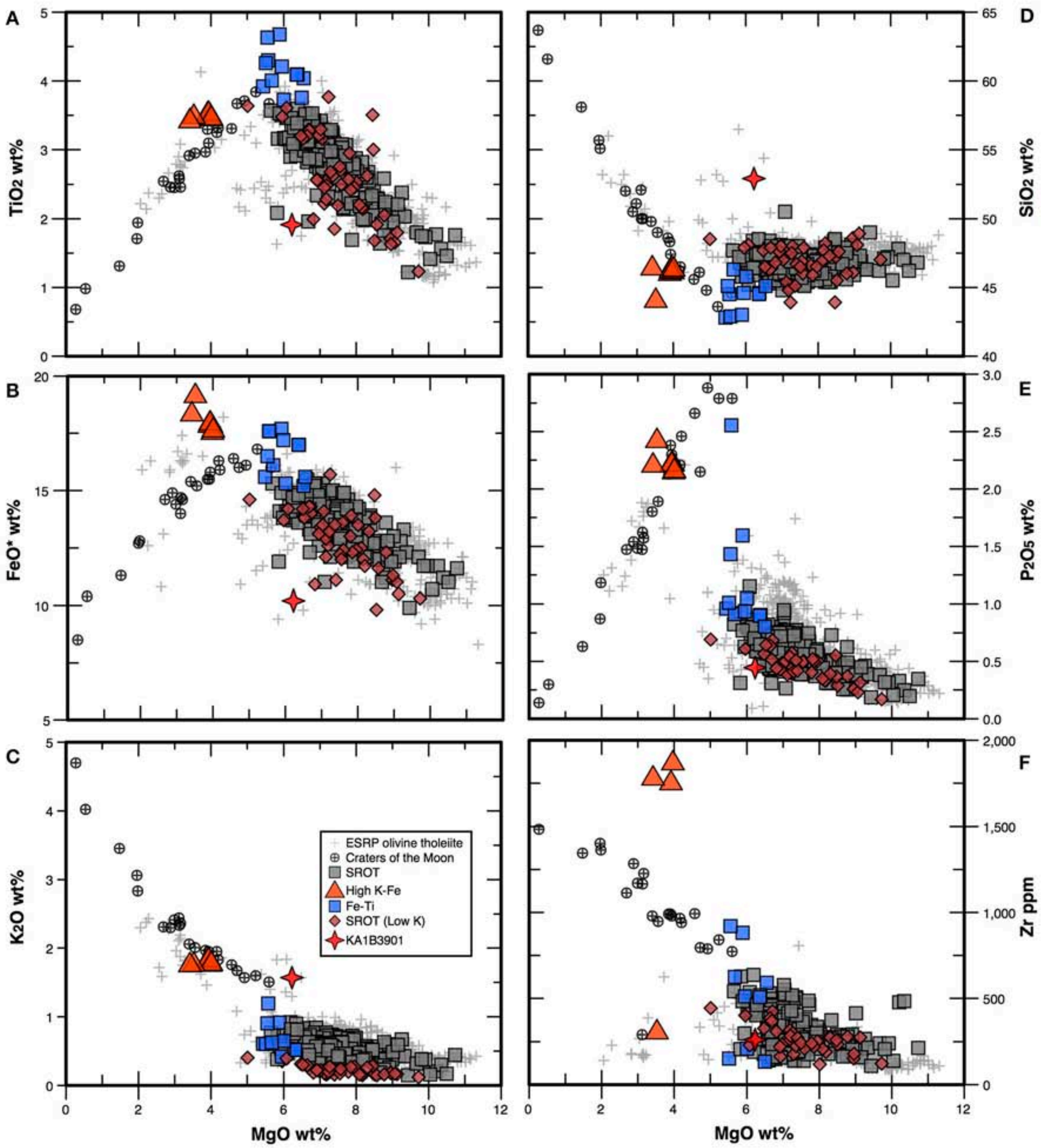

FIGURE 4 | Selected major and trace element variation diagrams with compositions for basalts from the Kimama drill core (colored symbols denote compositional type) compared to compositions of eastern Snake River Plain (ESRP) olivine tholeiites (crosses; Hughes et al., 2002b) and Craters of the Moon evolved lavas (circles; Kuntz et al., 1982). All diagrams show variation with respect to MgO wt%: **(A)**, TiO_2 wt%; **(B)**, FeO* wt%; **(C)**, K_2O wt%; **(D)**, SiO_2 wt%; **(E)**, P_2O_5 wt%, and **(F)**, Zr ppm.

processes. Many of these SROT flows are also low-K basalts, with abnormally low K_2O due to hydrothermal alteration. Nonetheless, the low-K SROT flows below 1,200 m depth are also low in FeO*, TiO_2, and P_2O_5, with high MgO, CaO, Cr, and Ni. Above 1,200 m depth, most SROT flows display cyclic variations in composition that are correlated with fractional crystallization and magma recharge, as discussed below.

SROT flows also exhibit a generalized increase of incompatible elements up section (e.g., K_2O and P_2O_5) that may reflect fractionation enrichment and/or the assimilation of previously emplaced ferrodioritic melts. Flow groups deeper in the drill core exhibit more primitive major and trace element concentrations (e.g., **Figure 5**). This trend may result from the addition of more enriched primitive magmas or progressively higher amounts of assimilation, as discussed below. Concentrations of REE and other incompatible elements also vary with depth, and substantiate recharge and fractionation cycles observed in the major element data (**Figure 7**).

Three flow groups were classified as high K-Fe lavas based upon anomalously high values of FeO* (≥17.8 wt%), K_2O (1.77

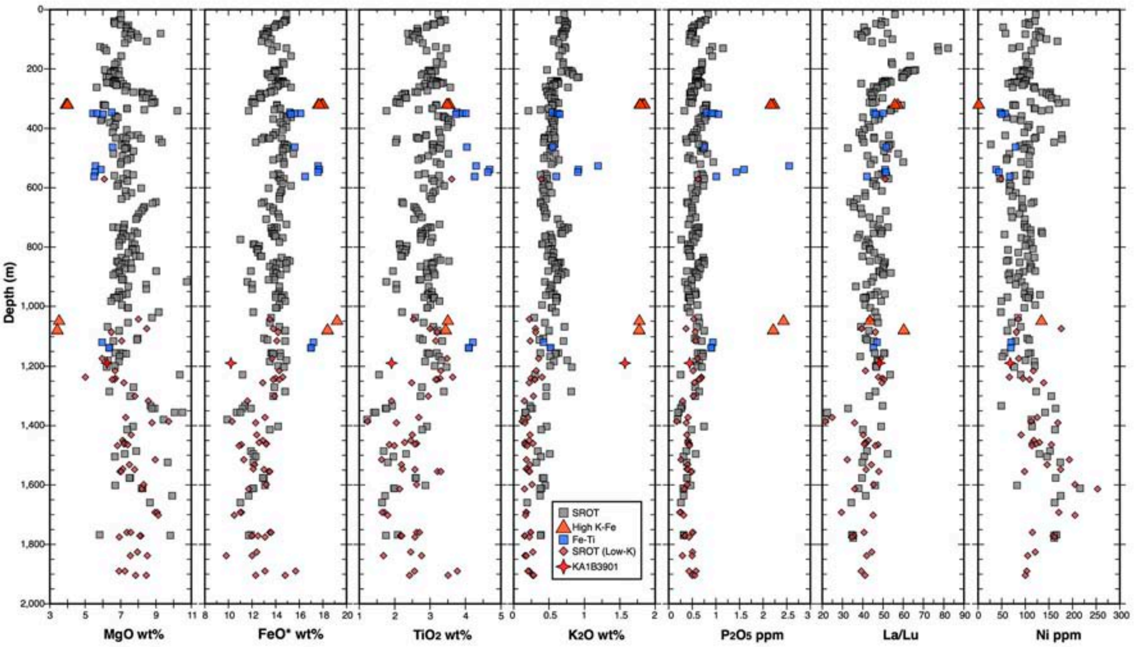

FIGURE 5 | Generalized stratigraphic column and selected chemical compositions of the Kimama drill core as a function of depth below the surface (in meters). We identify 78 flow groups and four compositional groups. Depths of SROT flows (gray squares) low K SROT flows (maroon diamonds), high Fe-Ti flows (blue squares), high K-Fe flows (red triangles), and the evolved sample (red diamond) are presented. Refer to Tables 1 and 2 in Supplementary Material for flow group compositional and stratigraphic details. Progressive up section fractional crystallization within flow groups are evident in upward-trending concentrations of FeO*, K_2O, TiO_2, and La/Lu. Recharge is evident as upward trending concentrations of MgO, P_2O_5, and Ni within flow groups.

to 1.84 wt%), and TiO_2 (3.43–3.54 wt%), coupled with low MgO (3.40–3.94 wt%). Flow groups 12, 49, and 51 have compositions that are similar to those erupted within Craters of the Moon during the latest Pleistocene and Holocene. High K-Fe lavas are located at 318, 1,045, and 1,077 m depths, respectively (Table 2 in Supplementary Material). Sample KA1B3901 (flow group 59) has low FeO* (10.2 wt%) and TiO_2 (1.91 wt%) relative to the high K-Fe lavas, but nevertheless displays a similar evolved geochemical signature, including high SiO_2 (52.9 wt%), high Na_2O (2.70 wt%), and high K_2O (1.57 wt%). The members of the high K-Fe and evolved suites are the most chemically distinct flows in the Kimama drill core.

The REE patterns of SROT, low-K SROT, and Fe-Ti suites are broadly similar, implying a genetic connection. High K-Fe flow groups are 10x more enriched in both LREE and HREE concentrations than other Kimama chemical groups and fall within the Craters of the Moon compositional array (**Figure 7**).

Hydrothermal Alteration with Depth

Normal SRP lavas contain little to no water and are characterized by negative loss on ignition values, which reflects the conversion of FeO to Fe_2O_3 during ignition; this effect is especially noticeable because all SRP tholeiites have relatively high FeO/Fe_2O_3. Positive ignition loss reflects bound water in excess of that needed to offset the oxidation of ferrous iron. Since these basalts are basically anhydrous when fresh, this bound water represents hydrothermal alteration of groundmass glass to smectite, as documented by Sant (2013). Temperature logs from the Kimama bore hole record a geothermal gradient of 72–75 from about 980–1,440 m depth, with an average heat flow of 132 mW/m^2 (Lachmar et al., 2017). Plots of LOI vs. depth show that hydrothermally altered basalt is dominant below 1050 m depth, although the effects are variable and do not correlate in a simple fashion; only the deepest flows (>1,700 m) have consistent low K_2O and high LOI (**Figure 6**).

The effect of hydrothermal alteration on major element concentrations is seen most clearly in the K_2O/TiO_2 ratios: ratios > 0.11 follow normal igneous trends consistent with other SROT basalts (e.g., Hughes et al., 2002b). Samples with K_2O/TiO_2 ratios ≤ 0.11 plot below other SROT analyses. During normal differentiation of SROT basalts, K_2O and TiO_2 behave incompatibly. Since TiO_2 is generally immobile in hydrothermal fluids, the low K_2O/TiO_2 ratios must represent leaching of K_2O from the samples during the conversion of groundmass glass and mesostasis to smectite. On a plot of TiO_2 vs. K_2O, the low-K group clearly lies below the main field of SROT basalts, consistent with this interpretation (**Figure 3C**). All samples with K_2O/TiO_2 ratios ≤ 0.11 have positive LOI values, but not all samples with positive LOI have low K_2O/TiO_2 ratios.

A plot of K_2O/TiO_2 ratio vs. depth shows that the low-K samples all lie below 1,050 m depth, although many samples from >1,050 m depth plot on a trend consistent with the SROT at less than 1,050 m depth, suggesting that these samples still retain their primary signatures.

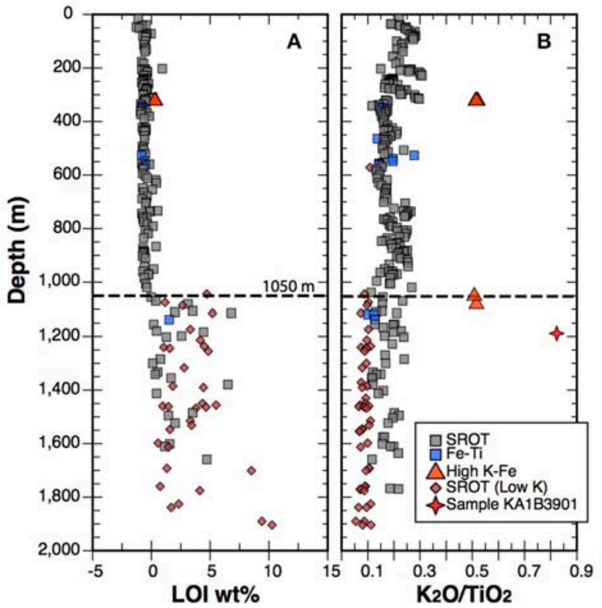

FIGURE 6 | Loss on Ignition (LOI in wt%) and K_2O/TiO_2 plotted against stratigraphic depth. **(A)**: LOI shows greatest variability below ∼1,050 m (3,444 ft) depth, with the highest LOI measurement (10.26 wt%) recorded at 1,905 m (6,247 ft) depth. Above ∼1,050 m depth, measurements fall into a tight range between 0.34 and −1.27 wt% LOI. **(B)**: The lowest K_2O/TiO_2 ratios (∼0.12) are dominantly present in low K SROT samples below ∼1,050 m depth, possibly indicating increased hydrothermal alteration and the removal of K_2O from SROT basalts. Fractional crystallization trends are visible as progressive, up section decreases in K_2O/TiO_2 in SROT samples between ∼300 and 0 m depth.

Fractionation/Enrichment and Recharge Cycles

The progressive enrichment of incompatible elements in stratigraphically upsection flow groups is commonly interpreted to represent ongoing eruptions from a fractionating magma chamber. Likewise, progressive depletion in incompatible elements, and concomitant enrichment of compatible elements upsection in a flow group, is interpreted to represent magma chamber recharge with primitive or parental melt compositions (Shervais et al., 2006). Upward fractionation cycles are indicated by a decrease in MgO (Cr, and Ni) and increases in FeO*, TiO_2, P_2O_5, and K_2O as a result of fractionation of Mg-rich olivine, Ca-Al-rich plagioclase, and Cr-spinel. Recharge cycles are indicated by increasing MgO and Ni, and decreases in FeO*, TiO_2, K_2O, and P_2O_5 (**Figure 5**).

Stratigraphically defined flow groups based on lithology, paleosecular magnetic variations, and sediment intercalations, as defined by Potter (2014), appear to correspond to magma fractionation or recharge cycles (**Figure 5**). However, flow groups 7, 9, 18, 20, 23, 48, 53, 54, 57, 58, 66, 68, 70, 75, and 78 show relatively constant compositions with depth, suggesting the emptying of a magma reservoir over relatively short time spans, with little or no coeval fractional crystallization. This is consistent with relatively high eruption rates that could empty a magma reservoir quickly.

Upward fractionation cycles are recognized in 21 flow groups in the Kimama drill core: flow groups 2, 5, 8, 10, 11, 13, 17, 19, 29, 33-37, 47, 58, 63, 64, 67, 72, and 73. Seven flow groups show brief intervals of upward fractionation superimposed on recharge trends (flow groups 8, 22, 23, 29, 65, 69, and 77). These short upward fractionation "steps" probably represent periods of quiescence during which neither eruptions nor magma recharge occur.

Other flow groups document progressive recharge of their magma chambers coeval with ongoing eruptions, such that lavas become progressively more primitive upsection, trending to low-K, high MgO compositions. This can be observed in six flow groups: 4, 16, 26, 27, 30, and 39. Flow groups 14, 38, 50, 52, and 60 also display brief intervals of recharge superimposed on the dominant fractionation trends.

The three high K-Fe flow groups and the evolved flow group (groups 12, 49, 51, and 59) are compositionally constant, but too thin to represent prolonged time intervals. Although all four sit atop underlying upward fractionation cycles, the large offset from REE patterns between SROT and high K-Fe or evolved flow groups suggests either a distinct parent magma or the assimilation of a crustal source, likely compositionally similar to Graveyard Point Intrusion gabbros or ferrodiorites (White, 2007). Therefore, connecting high K-Fe and evolved flows to underlying flow groups is problematic.

The occurrence of upward fractionation cycles and recharge cycles is consistent with the proposals of Shervais et al. (2006) and Brueseke et al. (2016) that magmas are processed through mid-crustal intrusions, in which individual sills form complex layers as the cumulate extract of crystal-melt fractionation. These layered mafic intrusions act as reactive filters which process the magma before it erupts. Individual sills may represent a single pulse of primitive magma which differentiates as it feeds a single monogenetic volcano on the surface.

Fractionation-Assimilation

Major processes that may control the evolution of continental basalts include fractional crystallization with no significant assimilation, fractional crystallization accompanied by assimilation of older crustal materials, and fractional crystallization accompanied by assimilation of previously intruded mafic magmas (ACMI-*assimilation of consanguineous mafic intrusions*; Shervais et al., 2006). These processes can be distinguished using plots of lithophile element ratios vs. a fractionation indicator such as Mg# (Shervais et al., 2006). In **Figure 8** we plot Mg# (which decreases with fractional crystallization) against ratios of La/Lu and K_2O/P_2O_5. The ratio of La/Lu varies little during fractional crystallization of olivine and plagioclase, but will increase progressively in response to fractional crystallization-assimilation of either older continental crust or older mafic intrusions. In contrast, K_2O/P_2O_5 ratios will increase strongly with assimilation of older crustal materials, but decrease in response to assimilation of mafic intrusions. In Kimama SROT lavas, La/Lu ratios increase progressively as Mg# decreases, whereas K_2O/P_2O_5 ratios decrease progressively,

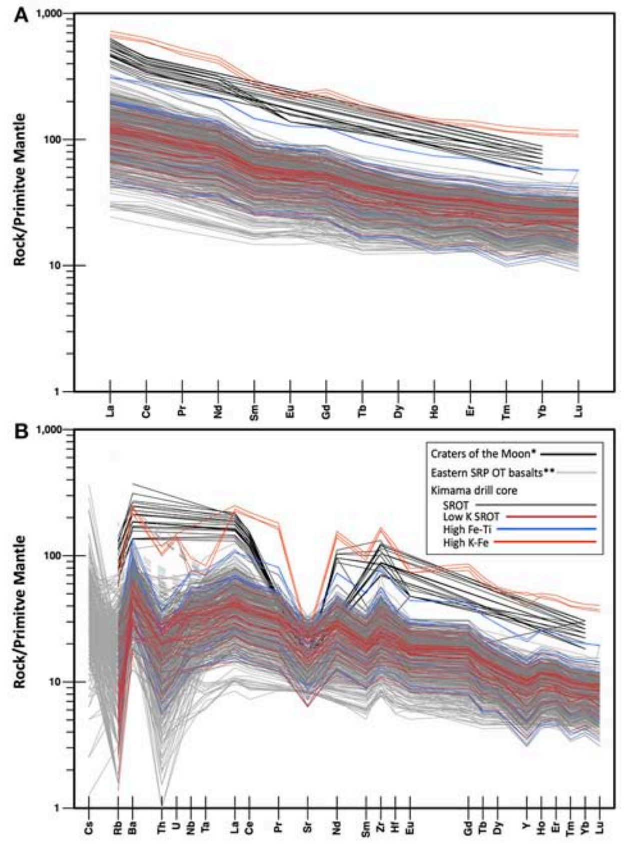

FIGURE 7 | (A) Rare earth-element (REE) plot of Kimama core basalts (blue lines), normalized to primitive mantle (McDonough and Sun, 1995) and **(B)** multi-element patterns for Snake River Plain (SRP) olivine tholeiites and Craters of the Moon evolved lavas are plotted for comparison (Kuntz et al., 1982; Hughes et al., 2002b). Trace elements are arranged in order of decreasing compatibility from right to left.

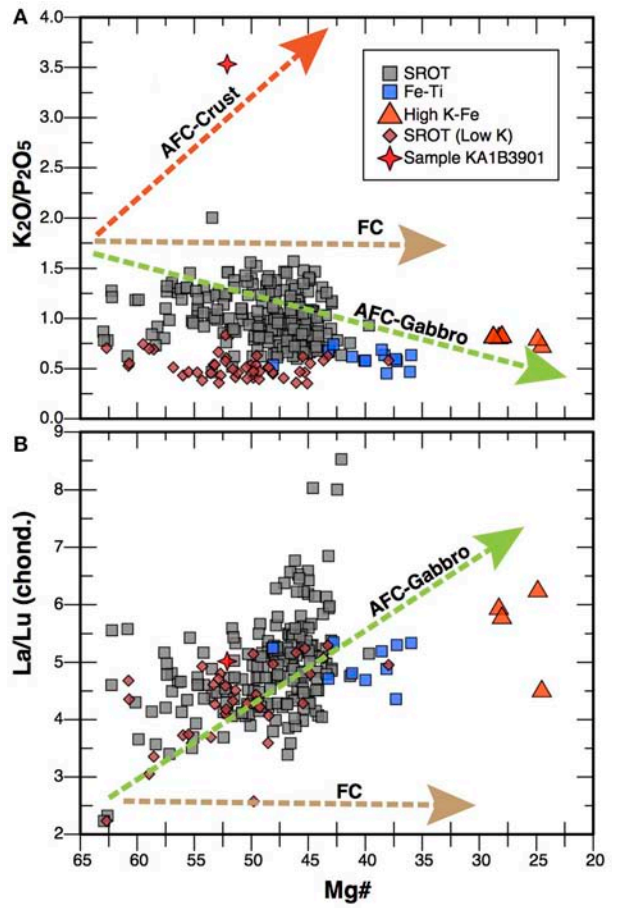

FIGURE 8 | Ratio plots of K_2O/P_2O_5 and La/Lu (chondrite normalized; McDonough and Sun, 1995) vs. Mg# (100*Mg/[Mg + Fe]). **(A)** Decreasing K_2O/P_2O_5 with decreasing Mg# is consistent with the assimilation of gabbroic host rock. **(B)** An increase in La/Lu with decreasing Mg# suggests the assimilation of a gabbroic component during fractional crystallization. Brown arrows show the expected fractional crystallization (FC) pathways, red arrows show the expected pathways of assimilation-fractional crystallization of continental crust, and green arrows show the expected pathways for assimilation and fractional crystallization of gabbro (AFC-gabbro).

showing that AFC involving older mafic intrusive rocks was the dominant process (**Figure 8**). The high K-Fe flow group displays the same trends of increasing La/Lu and decreasing K_2O/P_2O_5 ratios with decreasing MgO, showing that this group also must form by large degrees of fractional crystallization and assimilation of a gabbroic intrusion. In contrast, sample KA1B3901 (flow group 57) displays an increase in K_2O/P_2O_5 ratio with decreasing MgO, and may be a result of fractional crystallization with assimilation of continental crust (**Figure 8A**). The variation in La/Lu at high mg# in SROT implies a range of parental magma compositions formed either by different degrees of partial melting or by small variations in source composition.

Origin of Highly Evolved Flow Groups

High K-Fe lavas do not appear to be simply related to the parental basalts (**Figures 3–5**, **7**). Variation diagrams of trace elements (Zr/Y-Nb/Y), and MgO variations demonstrate a lack of congruity, and elevated concentrations of REE and other incompatible elements suggest either a different magma source or a unique magmatic differentiation scenario. These lavas were generated in a similar fashion as Craters of the Moon lavas, via extreme fractional crystallization accompanied by assimilation (e.g., Whitaker et al., 2006, 2008; Putirka et al., 2009). However, the decrease in K_2O/P_2O_5 ratios (**Figure 8**) implies that older felsic crust was not involved forming in these flows (or Craters of the Moon), and that extreme fractional crystallization perhaps accompanied by assimilation of slightly older mafic sills was the dominant process.

Although flow group 59 (sample KA1B3901) has a similar major and trace element composition to Craters of the Moon evolved basalts, high K-Fe flows in the Kimama drill core have distinctly higher FeO, Zr, Sr, Sc, La, and lower Al_2O_3, at the same MgO compositions when compared with more "traditional" Craters of the Moon evolved lavas and may represent a different fractionation or assimilation process (Hughes et al., 2002b; Putirka et al., 2009).

The evolved and high K-Fe flow groups in the Kimama drill core may represent the distal portions of early Craters of the Moon lava flows that reached the Kimama site. The fact that these flows are thin is consistent with this idea. High K-Fe lavas range from 0.27 m (flow group 12) to 3.75 m (flow group 49) thick, and the evolved flow group (59) is 6.49 m thick. These thicknesses are well below the average flow group thickness of 23.6 m. However, the Kimama drill site is about 20 km from the exposed terminus of the exposed Craters of the Moon lava flows (Kuntz et al., 2007). This is less than half the maximum observed flow lengths in the SRP (50–60 km; Shervais et al., 2005), so long, thin flows may have reached the Kimama site. On the other hand, age projections from Potter (2014), suggest that high K-Fe flow groups 12, 49, and 51 (317.7–318.9, 1,045.0–1,048.8, and 1,077.1–1,078.5 m depths, and the evolved flow group 59 (1,185.0–1,191.5 m depth) erupted at ∼1.0, ∼3.3, ∼3.4, and ∼3.7 Ma (respectively), well beyond the 480 ka maximum recorded age of Craters of the Moon basalts (Putirka et al., 2009). Thus, either Craters of the Moon-type lavas erupted from other sources farther to the west, or magmatism at Craters of the Moon is much older than documented by surface flows, and the Kimama drill core samples the distal portions of early lava flows.

Melt Source Modeling

Chemical variations in parental basalts may be attributed either to differing degrees of partial melting, different depths of melting, or to different source compositions (e.g., Hughes et al., 2002b; Putirka et al., 2009; Shervais and Vetter, 2009). We have constructed a series of melt models to test these options, using three representative source compositions (primitive mantle, depleted MORB-source mantle, and enriched E-MORB source mantle. Each source region is modeled for a range of melt fractions (from 1 to 20%) using non-modal batch melting in two different depth regimes: shallow spinel-facies melting (<3 GPa or ∼100 km depth) and deeper garnet-facies melting (>3 GPa or ∼100 km depth). We compare the model results to five representative high-MgO (>9.28 wt%) basalts from the Kimama drill core on primitive mantle-normalized multi-element plots (**Figure 9**).

Partial melting of an N-MORB composition source in the spinel lherzolite facies results in depleted LREE concentrations (relative to HREE) in model melts. At extremely low melt fractions (less than 2%), HREE concentrations in the model melts are too high and LREE/HREE ratios too low to match observed primitive basalt compositions (**Figure 9A**). High field strength elements (HFSE) and K_2O also show suppressed values in the model melts. Within the garnet lherzolite facies, partial melting of an N-MORB composition source results in model melts that are depleted in LREE relative to HREE. An exception to this observation occurs at extremely low melt fractions (<2%), in which case HREE, K_2O, and HFSE concentrations in the model melts are too low to fit the data (**Figure 9B**).

When primitive mantle source compositions are melted in the spinel lherzolite facies (**Figure 9C**), the model melts generated are too low in LREE and LREE/HREE ratios. Partial melting of a primitive mantle composition in the garnet lherzolite facies produces model melts with LREE concentrations that are too low at large melt fractions and HREE concentrations that are too high at low melt fractions. At all but the lowest melt fractions, the model melts have HFSE concentrations that are too low to match SRP tholeiites (**Figure 9D**).

The best fit to the trace element patterns of the primitive Kimama basalts was for model melts generated from the partial melting of an E-MORB source in the spinel lherzolite facies (**Figure 9E**). Coherence is observed for all elements in the 7–15% melting range with the exception of Sr, which is consistently high in all of the model melts. Using the same source composition in a garnet lherzolite mode resulted in fits for the LREE within the ∼10–20% melting range, but poor fits for the HREE (**Figure 9F**).

The depth of melting inferred from the trace element models (see also Jean et al., 2013, in revision) is also consistent with estimates using phase equilibria and silica geobarometry for Kimama basalts which give melt segregation depths between 80 and 110 km and within the spinel lherzolite facies (Bradshaw, 2012). These relatively low pressures imply that melting must occur within the sublithospheric conduit that has been imaged seismically (Schutt and Dueker, 2008; Stachnik et al., 2008; Obrebski et al., 2010) beneath the eastern Snake River Plain as inferred by Hanan et al. (2008).

Implications for Magma Evolution in Continental Volcanic Settings

Although SRP olivine tholeiites (SROT) are relatively homogenous, chemical variation between separate magmatic events (flow groups) is evident. Previous workers have demonstrated that chemical variation between SRP basalt flows is a result of fractional crystallization, crustal contamination, and partial melting occurring within the mid-crustal sill at pressures of ∼0.6 GPa and temperatures of 1,205 ± 27°C (Kuntz et al., 1992; Shervais et al., 2006; Christiansen and McCurry, 2008; McCurry and Rodgers, 2009; Miller and Hughes, 2009; Putirka et al., 2009). For Kimama drill core basalts specifically, Bradshaw (2012) estimated pre-eruptive crystallization occurred at 0.2–0.5 GPa (7–17 km) and between 1,155 and 1,255°C. Putirka et al. (2009) argue for a three-stage process to explain the entire range of SRP lava compositions. For typical SRP olivine tholeiites (SROT), mantle-derived picrites ascend to the middle crust at depths of 20–10 km, where they undergo partial crystallization of olivine ± clinopyroxene. Storage of olivine tholeiite magmas in the middle crust (20–10 km) causes magma compositions to evolve to moderate MgO wt% (10%), at which point positive buoyancy is reached and migration through the middle crust occurs. The lack of clinopyroxene phenocrysts in SRP basalts requires that SRP magmas continued to evolve in shallow subvolcanic reservoirs prior to eruption, forming the low-pressure phenocryst assemblage olivine-plagioclase.

More evolved magmas, such as those associated with Craters of the Moon, require additional processing at depths of 15–0 km, where differentiation and resulting volatile content increases (1–2 wt% H_2O) causing the final eruption and ascent of magma

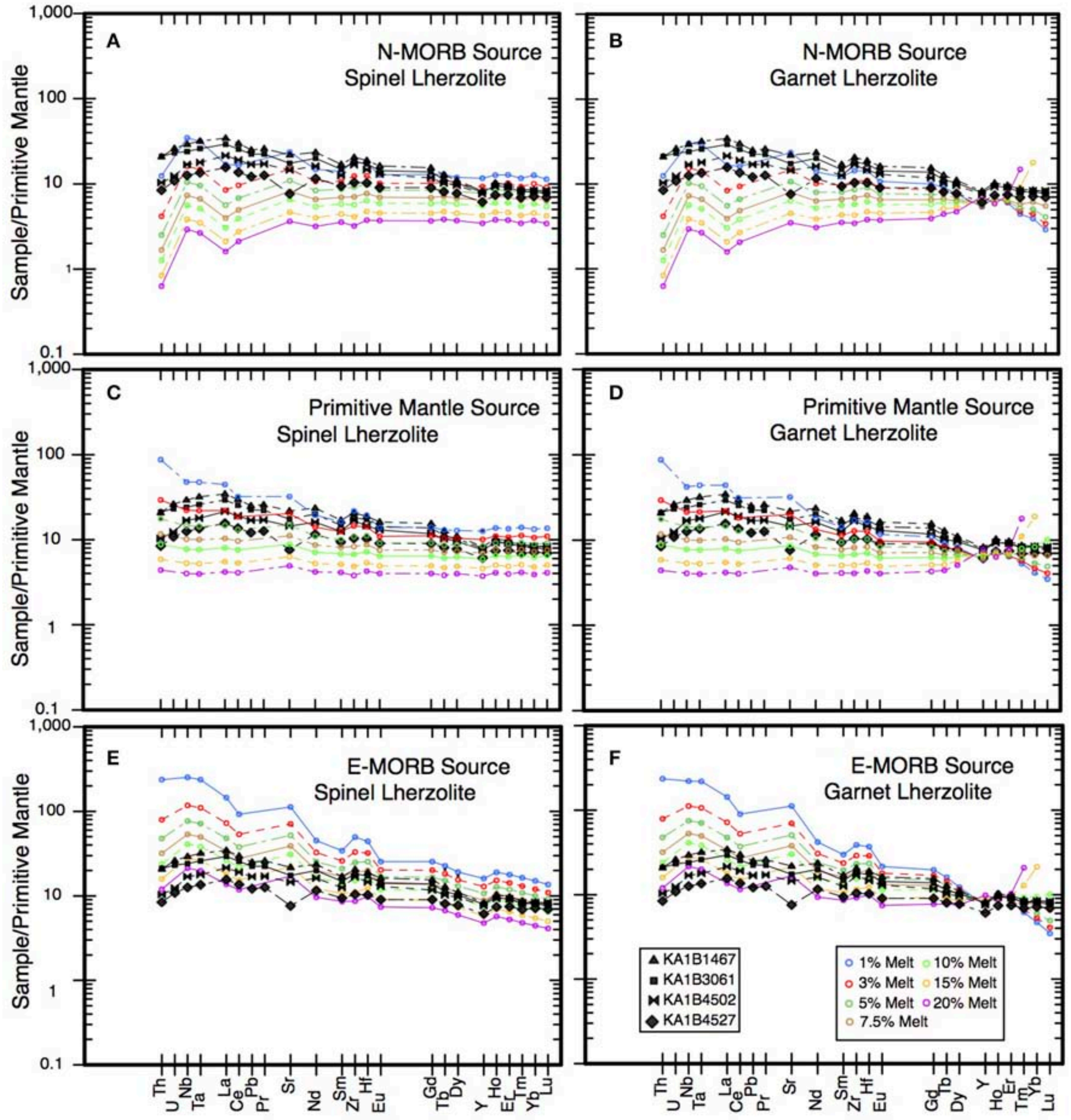

FIGURE 9 | Multi-element patterns normalized to primitive mantle (McDonough and Sun, 1995) for Kimama core basalts. Partial melts from three source compositions are plotted for varying mineralogy (spinel lherzolite and garnet lherzolite) and percentages of melting. **(A,B)** Enriched mid ocean ridge basalt (E-MORB), **(C,D)** normal mid ocean ridge basalt (N-MORB), and **(E,F)** primitive mantle (PM) source compositions of spinel lherzolite and garnet lherzolite are used. We compare compositions of four primitive basalt samples, proxies for parent magmas, to determine the composition and melting conditions of the source for the Kimama drill core magmas. Trace elements are arranged in order of decreasing compatibility from right to left.

through the middle and upper crust (e.g., Annen et al., 2006; Putirka et al., 2009).

The data presented here also document the cyclic nature of magma intrusion, fractional crystallization, and magma recharge, consistent with magma evolution in a series of stacked layered intrusions in the lower to middle crust, which has also been documented in other deep drill cores from the SRP (e.g., Shervais et al., 2006; Jean et al., 2013). These data support the SRP magma petrogenetic model of Shervais et al. (2006), in which magmas are shown to evolve through complex pathways of fractional crystallization, assimilation, and mixing at multiple crustal levels before eruption. A particular aspect of this model also supported here is the process referred to as *"assimilation of consanguineous mafic intrusions"* (ACMI; Shervais et al., 2006). This refers to the process in which the assimilant is not pre-existing continental crust (e.g., Shirley, 2013), but rather slightly older intrusions of genetically-related mafic magmas that form the layered mafic sill complex in the middle crust. This process is documented by the fractionation-related increase in LREE/HREE ratios accompanied by decreases in lithophile/high-field strength element ratios such as K_2O/P_2O_5 (**Figure 8A**).

Assimilation of consanguineaous mafic intrusions is facilitated by two processes. First, newly intruded magma is less dense than previously intruded sills that are now mostly crystallized. This means that new magma will tend to pond above older intrusions, and subsequent intrusions will continue to stack above older ones. Second, the newly intruded magmas will interact with more evolved portions of the older sills, which are typically located in the upper part of the crystallized sill. Overall, the evolved diorites of an older sill will have lower melting points than the sill, thereby facilitating assimilation.

In some cases, if the older sill is not completely crystallized, the freshly recharged magma will preferentially inject into the evolved residual magma (mush) of the older sill, mixing with the evolved residual magma (mush) to form a hybrid magma. This may result in wholesale replacement of the older magma mush, or may proceed gradually, resulting in progressively more primitive magma over time. Our data present evidence for both scenarios: in some cases, fractionation cycles succeed one another with no observed gradual recharge; in others, gradual recharge of the magma chamber takes place, as documented by the recharge cycles. These processes are observed in other deep core suites from the central and eastern SRP (Shervais et al., 2006; Jean et al., 2013).

The occurrence of recharge cycles in particular suggests that magma evolution in the middle crust takes place in relatively large (possibly km-scale?) layered intrusions, not 100-m scale sills (Shervais et al., 2006), and that layered mafic intrusions such as the Muskox (Irvine, 1970) may provide more robust analogies for this evolution than smaller sills like the Graveyard Point Intrusion (White, 2007). The continuous increase in concentrations of incompatible elements upsection in the drill core (e.g., La, **Figure 5**) is more compatible with longer-lived large scale intrusions than with many small, ephemeral intrusions, which are unlikely to result in continuous enrichment of the magma system. These sill-shaped layered intrusions are stacked in the upper middle crust by density contrasts with the underlying lower crust and overlying upper crust (Annen et al., 2015). Each subsequent intrusion will tend to pond above previous intrusions, which are denser than the newly intruded magma, or may tend to localize within the zone of residual melt of a previously intruded sill.

One consequence of this recharge-mixing-assimilation model is that successive magma bodies become progressively more enriched in incompatible elements over time. This is reflected in the progressive increase in K_2O, P_2O_5, and La/Lu upsection (**Figure 5**). This process is depicted schematically in **Figure 10**, which shows how mixing of newly recharged magma with residual melt (or assimilated fractional melt) from prior intrusions leads to enrichment of the mixed melt. Over time, successive mixtures become progressively enriched even though the recharge magma remains the same. Similar enrichments may also occur due to in situ crystallization in a large magma chamber (e.g., Langmuir, 1989).

The physical manifestation of our stacked sill model is depicted in **Figure 11**. Mantle-derived mafic magmas move upwards through the lower crust (not shown) and form large sill-like intrusions in the upper middle crust. The larger sill-like plutons (which form during episodes of high magma flux) evolve by crystal fractionation to form layered mafic intrusions (e.g., Irvine, 1970) that are periodically refreshed by new magma. Magma escaping from these layered plutons may erupt directly to the surface, or may be processed through small subvolcanic magma bodies at shallow depths (2–4 km) that are typically associated with a single volcano. As each pluton freezes, new sill-like intrusions pond above the older plutons to form a stacked sill complex. This process leads to *assimilation of consanguineous mafic intrusions*, as later intrusions cannibalize older ones and evolve by AFC processes that generally do not include pre-existing crustal rocks (e.g., Shervais et al., 2006).

We suggest that the physical and chemical connections that we observe in the Kimama drill core are common to intra-continental basalts and their crustal plutons, and may characterize mafic magma systems in continental crust, especially when magma flux is relatively high.

CONCLUSIONS

Geochemical data, along with previously-determined drill core stratigraphy and paleomagnetic data (Potter, 2014), show that basalts from the Kimama drill core on the axial high of the Snake River Plain vary between two main compositional arrays throughout 5.5 Ma of continuous eruption. Snake River olivine tholeiites (SROT) and their high Fe-Ti differentiates make up >99% of sampled flows. The remaining flows (<1%) comprise minor volumes of evolved high K-Fe lavas that share a compositional affinity to evolved flows erupted at Craters of the Moon.

The Kimama borehole samples lava flows presumably erupted from multiple shields in the region, but the similarity of mantle melting conditions, transport paths, or depths of evolution has resulted in lavas with generally similar compositions. The compositional variance within SROT and high Fe-Ti lavas observed in the Kimama drill core must reflect differing processes of petrogenesis from magmas of the same source. Low K flows below 1,050 m depth are correlated to increasing LOI, and we invoke secondary alteration of SROT lavas to explain these composition variants. Upward fractionation, or upsection increases in incompatible elements, K_2O and FeO* suggest fractional crystallization cycles as observed in layered mafic intrusions. Chemical reversals, or upsection increases in compatible elements and MgO concentrations, suggest episodes of progressive recharge of the system by more primitive melt.

We interpret the multiple chemical cycles evident in stratigraphic comparisons of Kimama drill core geochemistry to represent the fractionation of individual magma batches and the progressive recharge of crustal magma reservoirs, with each cycle representing eruptions from a nearby vent or vent system.

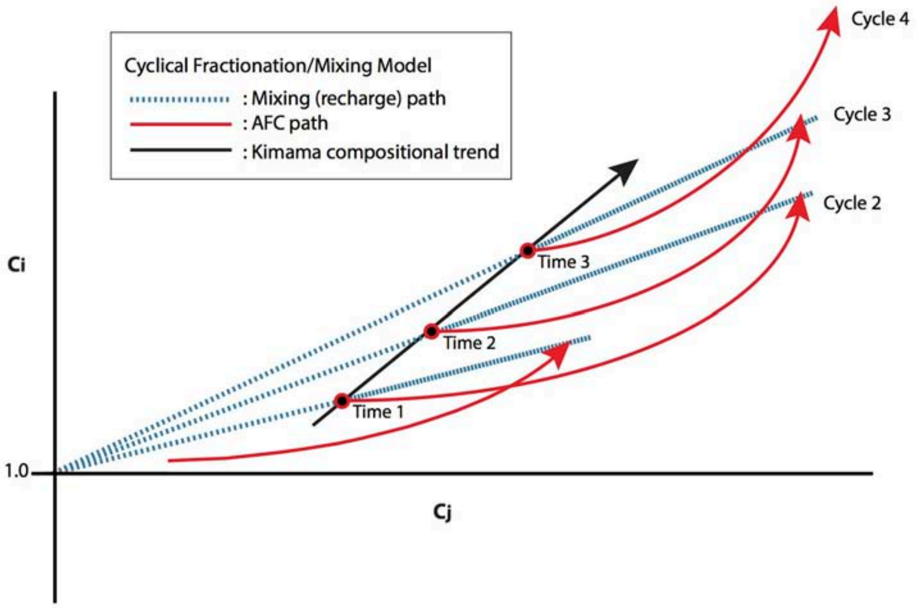

FIGURE 10 | In large mafic igneous provinces with high magma flux such as the SRP, pre-existing mafic magma intrusions are assimilated by genetically-related newer magma intrusions in a process we call *"assimilation of consanguineous mafic intrusions"* process (ACMI; Shervais et al., 2006). This conceptual diagram shows the time-progressive effects of ACMI. Ci and Cj are the concentrations of two different incompatible trace elements for which the bulk distribution coefficient (D) of C_i is less than that of C_j (e.g., $D_{ci} < D_{cj} < 1$). The curved red arrows demonstrate assimilation and fractional crystallization (AFC) pathways that lead to progressively more evolved compositions and where the assimilant is solid intrusive rock of the same magma system. The blue dashed lines indicate recharge by more primitive magma. The mixed magma then experiences another cycle of evolution beginning with AFC. The compositional trend (black line) of Kimama basalts shows the "stair-step" effect of multiple cycles of AFC and recharge leading to more evolved compositions and echoing patterns visible in **Figures 5**, **6B**.

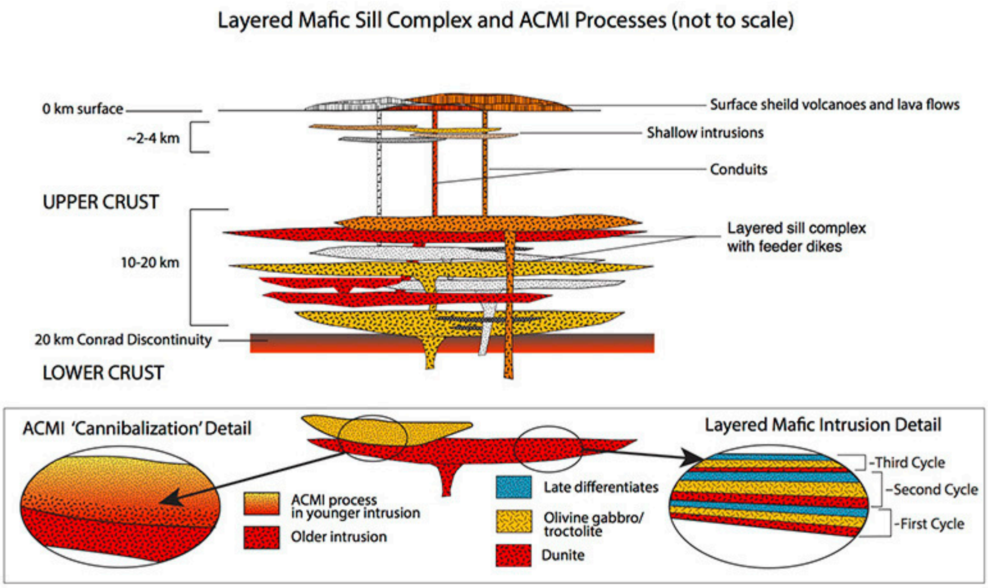

FIGURE 11 | Conceptual diagram of a layered mafic sill complex illustrating the process of *"assimilation of consanguineous mafic intrusions"* (ACMI). In this model, mantle-derived mafic magmas move upwards through the lower crust and form large sill-like plutons within the middle crust (10–20 km depth) during periods of high magma flux. The large sill-like plutons evolve through fractional crystallization and are periodically refreshed by newer magmas, eventually forming a layered mafic intrusion comprising cumulates of dunite, olivine gabbro, troctolite, and late-stage differentiates including ferrogabbro and ferrodiorite (e.g., Irvine, 1970). New sill-like intrusions pond above cooled sill-like intrusions to form a stacked sill complex. Within the stacked sill complex, new sills cannibalize older sills and undergo ACMI processes without the influence of pre-existing continental crust. Magmas may be transported to the surface through dikes, or they may be stalled and processed in small, subvolcanic intrusions at shallow depths (2–4 km).

Fractional crystallization is accompanied by assimilation, as shown by increases in La/Lu ratios with decreasing MgO, but the concomitant decrease in K_2O/P_2O_5 ratios shows that the assimilant is not pre-existing continental crust, but older mafic intrusions related to the continuing SROT volcanism. This is consistent with our FC-AFC models that use the Graveyard Point Intrusion diorite (White, 2007) as an analog for the mid-crustal sill complex. These fractionation and reversal trends provide evidence of a dynamic magma processing system over relatively short to long periods of time.

Our data show the importance of "*assimilation of consanguineous mafic intrusions*" (Shervais et al., 2006). In this model, large-volume mafic igneous provinces evolve by AFC processes in which the assimilant is dominantly older intrusions related to the same magma suite, not pre-existing continental crust. We suggest that model may be generally applicable to all mafic igneous provinces with high magma flux. This likely require large, km-scale layered intrusions in the middle to lower crust in order to produce the gradual replenishment trends seen throughout the drill core (**Figure 11**).

The stratigraphically thin (<1.5 m) high K-Fe lavas found in the Kimama drill core are compositionally unrelated to SROT. We propose that high K-Fe flows erupted from Craters of the Moon and flowed southwest into the Kimama area, and that evolved magmas have been generated and episodically erupted from the Craters of the Moon region since at least 3.4 Ma.

Finally, we note that continental scientific drilling of volcanic provinces with $>99\%$ drill core recovery is a highly effective way to study both the overall chemical evolution of these provinces and their evolution through time (e.g., Shervais et al., 2014). It is particularly effective for understanding magma evolution in the crust and for inferring magma chamber processes in relatively young volcanic provinces.

AUTHOR CONTRIBUTIONS

JS provided guidance during the preparation of the manuscript, specifically discussions of assimilation processes in the mafic mid-crustal sill complex of the Snake River Plain (central Idaho). JS oversaw the progress and completion on the dissertation that inspired this manuscript as my primary academic advisor at Utah State University (USU). JS also provided lab facilities and materials at USU where the majority of major element analyses on the Kimama drill core samples were conducted. EC provided guidance in the interpretation of major and trace element geochemical trends in Snake River Plain basalts, including identifying the relationship between some major element oxide percentages and loss on ignition (LOI) values. EC also oversaw the preparation and analysis of several Kimama drill core samples via X-ray fluorescence at Brigham Young University. SV provided lab facilities at Centenary College for the preparation of samples and the analysis of trace element concentrations via inductively coupled plasma mass spectrometry (ICPMS). KP logged and sampled the Kimama drill core while a Ph.D student at Utah State University. While a graduate student, KP prepared samples and conducted geochemical analyses, obtaining the data to identify compositional trends and make the larger-scale magma petrogenesis interpretations upon which this manuscript is based. The manuscript is based, in part, on KP Utah State University dissertation research (Potter, 2014), but later geochemical analyses were conducted by KP during her post-doc at Utah State University. The majority of the manuscript was written by KP with minor additions contributed by JS.

ACKNOWLEDGMENTS

This work was supported by DOE awards DE-EE0002848 DE-EE0006733, by the International Continental Drilling Program (ICDP), and by a consortium of universities, and is based upon the doctoral dissertation of Potter (2014). This dissertation is available online through the Utah State University library. We thank Jared Bryan and the BYU geochemistry lab for assistance, and for the helpful suggestions of reviewers. Discussions with Marlon Jean, Duane Champion, and the Hotspot Science Team (http://www.usu.edu/geo/shervais/Shervais-USU-Geology/Hotspot_Science_Team.html) were especially helpful, but any errors are our own.

SUPPLEMENTARY MATERIAL

The Supplementary Material for this article can be found online at: https://www.frontiersin.org/articles/10.3389/feart.2018.00010/full#supplementary-material

REFERENCES

Anders, M. H., Saltzman, J., and Hemming, S. R. (2009). Neogene tephra correlations in eastern Idaho and Wyoming for Yellowstone hotspot-related volcanism and tectonic activity. *Geol. Soc. Am. Bull.* 121, 837–856. doi: 10.1130/B26300.1

Annen, C., and Sparks, R. S. J. (2002). Effects of repetitive emplacement of basaltic intrusions on thermal evolution and melt generation in the crust. *Earth Planet. Sci. Lett.* 203, 937–955. doi: 10.1016/S0012-821X(02)00929-9

Annen, C., Blundy, J. D., and Sparks, R. S. J. (2006). The genesis of intermediate and silicic magmas in deep crustal hot zones. *J. Petrol.* 47/3, 505–539. doi: 10.1093/petrology/egi084

Annen, C., Blundy, J. D., Leuthold, J., and Sparks, R. S. J. (2015). Construction and evolution of igneous bodies. towards an integrated perspective of crustal magmatism. *Lithos* 230, 206–221. doi: 10.1016/j.lithos.2015.05.008

Bachmann, O., Miller, C. F., and Silva, S. (2007). The volcanic–plutonic connection as a stage for understanding crustal magmatism. *J. Volcanol. Geotherm. Res.* 167, 1–23. doi: 10.1016/j.jvolgeores.2007.08.002

Bonnichsen, B., and Godchaux, M. M. (2002). "Late Miocene, Pliocene, and Pleistocene geology of southwestern Idaho with emphasis on basalts in the Bruneau-Jarbidge, Twin Falls, and western Snake River Plain regions," in *Tectonic and Magmatic Evolution of the Snake River Plain Volcanic Province*, Vol. 30, Idaho Geological Survey Bulletin (Idaho Geological Survey Press), 233–312.

Bonnichsen, B., Leeman, W. P., Honjo, N., McIntosh, W. C., and Godchaux, M. M. (2008). Miocene silicic volcanism in southwestern Idaho: geochronology, geochemistry, and evolution of the central Snake River Plain. *Bull. Volcanol.* 70, 315–342. doi: 10.1007/s00445-007-0141-6

Bradshaw, R. W. (2012). *Mineral Chemistry of Basalts Recovered from Hotspot Snake River Scientific Drilling Project, Idaho: Source and Crystallization Characteristics*. Master's thesis, Brigham Young University, Provo.

Brueseke, M. E., Hobbs, J. M., Bulen, C. L., Mertzman, S. A., Puckett, R. E., Walker, J. D., et al. (2016). Cambrian intermediate-mafic magmatism along the laurentian margin: evidence for flood basalt volcanism from well cuttings in the southern Oklahoma Aulacogen (U.S.A.). *Lithos* 260, 164–177. doi: 10.1016/j.lithos.2016.05.016

Cashman, K. V., Sparks, R. S., and Blundy, J. D. (2017). Vertically extensive and unstable magmatic systems: a unified view of igneous processes. *Science* 355:eaag3055. doi: 10.1126/science.aag3055

Chitwood, L. A. (1994). Inflated basaltic lava: examples of processes and landforms from central and southeast Oregon. *Or. Geol.* 56, 11–21.

Christiansen, E. H., and McCurry, M. (2008). Contrasting origins of cenozoic silicic volcanic rocks from the western cordillera of the United States. *Bull. Volcanol.* 70, 251–267. doi: 10.1007/s00445-007-0138-1

Coble, M. A., and Mahood, M. A. (2012). Initial impingement of the Yellowstone plume located by widespread silicic volcanism contemporaneous with Columbia River flood basalts. *Geology* 40, 655–665. doi: 10.1130/G32692.1

Drew, D. L., Bindeman, I. N., Watts, K. E., Schmitt, A. K., Fu, B., and McCurry, M. (2013). Crustal-scale recycling in caldera complexes and rift zones along the Yellowstone hotspot track: O and Hf isotopic evidence in diverse zircons from voluminous rhyolites of the Picabo volcanic field, Idaho. *Earth Planet. Sci. Lett.* 381, 63–77. doi: 10.1016/j.epsl.2013.08.007

Embree, G. F., Lovell, M. D., and Doherty, D. J. (1978). *Drilling Data from Sugar City Exploration Well, Madison County, Idaho*. U.S. Geological Survey Open File Report 78-1095.

Geist, D. J., Sims, E. N., Hughes, S. S., and McCurry, M. (2002). Open-system evolution of a single episode of Snake River Plain magmatism, in Link, P. K., and Mink, L. L., eds., Geology, hydrogeology, and environmental remediation, Idaho National Engineering and Environmental Laboratory, eastern Snake River Plain, Idaho. *Geol. Soc. Am.* 353, 193–204. doi: 10.1130/SPE353

Greeley, R. (1982). The Snake River Plain, Idaho: representative of a new category of volcanism. *J. Geophys. Res.* 87, 2705–2712. doi: 10.1029/JB087iB04p02705

Hackett, W. R., Smith, R. P., and Khericha, S. (2004). Volcanic hazards of the Idaho National Engineering and Environmental Laboratory, southeast Idaho, in B. Bonnichsen, C.M. White, and M. McCurry, eds., Tectonic and magmatic evolution of the Snake River Plain Volcanic Province. *Idaho Geol. Survey Bull.* 30, 461–482.

Hanan, B. B., Shervais, J., and Vetter, S. (2008). Yellowstone plume-continental lithosphere interaction beneath the Snake River Plain. *Geology* 36, 51–54. doi: 10.1130/G23935A.1

Henry, C. D., Castor, S. B., Starkel, W. A., Ellis, B. S., Wolff, J. A., Laravie, J. A., et al. (2017). Geology and evolution of the McDermitt caldera, northern Nevada and southeastern Oregon, western USA. *Geosphere* 13, 1066–1112. doi: 10.1130/GES01454.1

Hon, K., Kauahikaua, J., Denlinger, R., and Mackay, K. (1994). Emplacement and inflation of pahoehoe sheet flows: observations and measurements of active lava flows on Kilauea Volcano, Hawaii. *Geol. Soc. Am. Bull.* 106, 351–370. doi: 10.1130/0016-7606(1994)106<0351:EAIOPS>2.3.CO;2

Hughes, S. S., McCurry, M., and Geist, D. J. (2002b). Geochemical correlations and implications for the magmatic evolution of basalt flow groups at the Idaho National Engineering and Environmental Laboratory, in Link, P.K., and Mink, L.L., eds., geology, hydrogeology, and environmental remediation: Idaho National Engineering and Environmental Laboratory, eastern Snake River Plain, Idaho. *Geol. Soc. Am. Special Pap.* 353, 151–173. doi: 10.1130/0-8137-2353-1.151

Hughes, S. S., Wetmore, P. H., and Casper, J. L. (2002a). "Evolution of Quaternary tholeiitic basalt eruptive centers on the eastern Snake River Plain, Idaho," in *Tectonic and Magmatic Evolution of the Snake River Plain Volcanic Province*, Vol. 30, Idaho Geological Survey Bulletin, eds B. Bonnichsen, C. M. White, and M. McCurry (Idaho Geological Survey Press), 363–385.

Hughes, S. S., Smith, R. P., Hackett, W. R., and Anderson, S. R. (1999). "Mafic volcanism and environmental geology of the eastern Snake River Plain, Idaho," in *Guidebook to the Geology of Eastern Idaho* (Pocatello, ID: Idaho Museum of Natural History), 143–168.

Hughes, S., Wetmore, P., and Casper, J. (1997). Geochemical interpretation of basalt stratigraphy and Quaternary mafic volcanism, eastern Snake River Plain, Idaho. *Geol. Soc. Am. Abstracts Prog.* 29, A-298.

Irvine, T. N. (1970). "Crystallization sequences in the Muskox intrusion and other layered intrusions," in *Symposium on the Bushveld Igneous Complex and Other Layered Intrusions*, Vol. 1 (Pretoria: Geological Society of South Africa Special Publication), 441–476.

Jean, M. M., Hanan, B. B., and Shervais, J. W. (2014). Yellowstone Hotspot – continental lithosphere interaction. *Earth Planet. Sci. Lett.* 389, 119–131. doi: 10.1016/j.epsl.2013.12.012

Jean, M. M., Shervais, J. W., Champion, D. E., and Vetter, S. K. (2013). Geochemical and paleomagnetic variations in basalts from the Wendell Regional Aquifer Systems Analysis (RASA) drill core: evidence for magma recharge and assimilation–fractional crystallization from the central Snake River Plain, Idaho. *Geosphere* 9, 1319–1335. doi: 10.1130/GES00914.1

Jenner, G. A., Longerich, H. P., Jackson, S. E., and Fryer, B. J. (1990). ICP–MS—A powerful tool for high- precision trace-element analysis in Earth science: evidence from analysis of selected U.S.G.S. reference samples. *Chem. Geol.* 83, 133–148. doi: 10.1016/0009-2541(90)90145-W

Knott, T. R., Reichow, M. K., Branney, M. J., Finn, D. R., Coe, R. S., Storey, M., et al. (2016). Rheomorphic ignimbrites of the Rogerson Formation, central Snake River plain, USA: record of mid-Miocene rhyolitic explosive eruptions and associated crustal subsidence along the Yellowstone hotspot track. *Bull. Volcanol.* 78:23. doi: 10.1007/s00445-016-1003-x

Kuntz, M., Champion, D., Spiker, E., Lefebvre, R., Covington, H., and McBroome, L. (1982). The Great Rift and the evolution of the Craters of the Moon lava field, Idaho, in Bill Bonnichsen and R.M. Breckenridge, eds., Cenozoic Geology of Idaho. Idaho *Bureau Mines Geol. Bull.* 26, 423–438.

Kuntz, M., Covington, H., and Schorr, L. (1992). An overview of basaltic volcanism of the eastern Snake River Plain, Idaho, in P.K. Link, M.A. Kuntz, and L.P. Platt, eds., regional geology of eastern Idaho and western Wyoming. *Geol. Soc. Am. Memoir* 179, 227–267. doi: 10.1130/MEM179-p227

Kuntz, M. A., Skipp, B., Champion, D. E., Gans, P. B., Van Sistine, D. P., and Snyders, S. R. (2007). *Geologic Map of the Craters of the Moon 30' x 60' quadrangle, Idaho.* U.S. Geological Survey Scientific Investigations Map 2969, 64-p. pamphlet, 1 plate, scale 1:100,000 (Washington, DC).

Lachmar, T. E., Freeman, T. G., Sant, C. J., Walker, J. R., and Blackwell, D. D. (2017). Effect of an 860-m thick, cold, freshwater aquifer on geothermal potential along the axis of the eastern Snake River Plain, Idaho. *Geotherm. Energy* 5:16. doi: 10.1186/s40517-017-0086-8

Langmuir, C. (1989). Geochemical consequences of *In situ* crystallization. *Nature* 340, 199–205. doi: 10.1038/340199a0

Leeman, W. P. (1982). Olivine tholeiitic basalts of the Snake River Plain, Idaho, in Bill Bonnichsen and R.M. Breckenridge, eds., Cenozoic Geology of Idaho. Idaho. *Bureau Mines Geol. Bull.* 26, 181–191.

Lipman, P. W. (1984). The roots of ash-flow calderas in western North America: windows into the tops of granitic batholiths. *J. Geophys. Res.* 89, 8801–8841. doi: 10.1029/JB089iB10p08801

McCurry, M., and Rodgers, D. W. (2009). Mass transfer along the Yellowstone hotspot track I: petrologic constraints on the volume of mantle-derived magma. *J. Volcanol. Geotherm. Res.* 188, 86–98. doi: 10.1016/j.jvolgeores.2009.04.001

McDonough, W. F., and Sun, S. S. (1995). The composition of the Earth. *Chem. Geol.* 120, 223–253. doi: 10.1016/0009-2541(94)00140-4

Metcalf, R. V. (2004). Volcanic–plutonic links, plutons as magma chambers and crust–mantle interaction: A lithospheric scale view of magma systems. *Earth Environ. Sci. Trans. R. Soc. Edinb.* 95, 357–374. doi: 10.1017/S0263593300001127

Miller, M., and Hughes, S. (2009). Mixing primitive and evolved olivine tholeiite magmas in the eastern Snake River Plain, Idaho. *J. Volcanol. Geotherm. Res.* 188, 153–161. doi: 10.1016/j.jvolgeores.2009.06.004

Neal, C. R. (2001). The interior of the Moon: The presence of garnet in the primitive, deep lunar mantle. *J. Geophys. Res.* 106, 27865–27885. doi: 10.1029/2000JE001386

Obrebski, M., Allen, M. R., Xue, M., and Hung, S.-H. (2010). Slab-plume interaction beneath the Pacific Northwest. *Geophys. Res. Lett.* 37:L14305. doi: 10.1029/2010GL043489

Pierce, K. L., and Morgan, L. A. (1992). "The track of the Yellowstone hotspot: volcanism, faulting, and uplift," in *Regional Geology of Eastern Idaho and Western Wyoming*, Vol. 179, eds P. K. Link, M. A. Kuntz, and L. B. Platt (Boulder, CO: Geological Society of America Memoir), 1–54. doi: 10.1130/MEM179-p1

Potter, K. E. (2014). *The Kimama Core: A 6.4 Ma Record of Volcanism, Sedimentation, and Magma Petrogenesis on the Axial Volcanic High, Snake River Plain*. I. D. Dissertation. Utah State University, Logan.

Potter, K. E., Bradshaw, R., Sant, C. J., King, J., Shervais, J. W., and Christiansen, E. J. (2011). Project hotspot: insight into the subsurface stratigraphy and geothermal potential of the Snake River Plain. *Geotherm. Resourc. Council Transac.* 35, 967–971.

Putirka, K. D., Kuntz, M. A., Unruh, D. M., and Vaid, N. (2009). Magma evolution and ascent at the Craters of the Moon and neighboring volcanic fields, Southern Idaho, USA: implications for the evolution of polygenetic and monogenetic volcanic fields. *J. Petrol.* 50, 1639–1665. doi: 10.1093/petrology/egp045

Sant, C. (2013). *Geothermal Alteration of Basaltic Core from the Snake River* Plain, Idaho. Master's thesis. Utah State University, Logan.

Schutt and Dueker (2008). Crust and upper mantle velocity structure of the Yellowstone hotspot and surroundings. *J. Geophys. Res*. 113:B03320. doi: 10.1029/2007JB005109

Self, S., Keszthelyi, L., and Thordarson, T. (1998). The importance of pahoehoe. *Annu. Rev. Earth Planet. Sci.* 26, 81–110. doi: 10.1146/annurev.earth.26.1.81

Shervais, J. W., and Hanan, B. B. (2008). Lithospheric topography, tilted plumes, and the track of the Snake River–Yellowstone hotspot. *Tectonics* 27:5 doi: 10.1029/2007TC002181

Shervais, J. W., and Vetter, S. K. (2009). High-K alkali basalts of the western Snake River Plain (Idaho): abrupt transition from tholeiitic to mildly alkaline plume-derived basalts. *J. Volcanol. Geotherm. Res.* 188, 141–152. doi: 10.1016/j.jvolgeores.2009.01.023

Shervais, J. W., Arndt, N., and Goodenough, K. M. (2014). Drilling the solid earth: global geodynamic cycles and earth evolution. *Int. J. Earth Sci*. 95, 85–92. doi: 10.1007/s00531-014-1073-y

Shervais, J. W., Evans, J. P., Christiansen, E. H., Schmitt, D. R., Kessler, J. A., Potter, K. E., et al. (2011). Project hotspot: the Snake River scientific drilling project. *Geotherm. Resourc. Council Transac.* 35, 995–1003.

Shervais, J. W., Kauffman, J. D., Gillerman, V. S., Othberg, K. L., Vetter, S. K., Hobson, V. R., et al. (2005). Basaltic volcanism of the central and western Snake River Plain: a guide to field relations between Twin Falls and Mountain Home, Idaho. *Field Guides* 6, 27–52. doi: 10.1130/2005.fld006(02)

Shervais, J. W., Nielson, D. L., Evans, J. P., Christensen, E. J., Morgan, L., Shanks, W. C., et al. (2012). Hotspot: the Snake River geothermal drilling project – initial report. *Geotherm. Resourc. Council Transac.* 36, 767–772.

Shervais, J. W., Schmidt, D. R., Nielson, D., Evans, J. P., Christiansen, E. H., Morgan, L., et al. (2013). First results from HOTSPOT: the Snake River Plain scientific drilling project, Idaho, U.S.A. *Sci. Drilling* 15, 36–45. doi: 10.5194/sd-15-36-2013

Shervais, J. W., Vetter, S. K., and Hanan, B. B. (2006). Layered mafic sill complex beneath the eastern Snake River Plain: evidence from cyclic geochemical variations in basalt. *Geology* 34, 365– 368. doi: 10.1130/G22226.1

Shirley, E. K. (2013). *A Precambrian history of cratonic North American crust beneath the Snake River Plain*, Idaho. Master's thesis. Boise State University, Boise, ID.

Smith, R. B., Jordan, M., Steinberger, B., Puskas, C., Farrell, J., Waite, G. P., et al. (2009). Geodynamics of the Yellowstone hotspot and mantle plume: seismic and GPS imaging, kinematics, and mantle flow. *J. Volcanol. Geotherm. Res*. 188, 26–56 doi: 10.1016/j.jvolgeores.2009.08.020

Stachnik, J. C., Dueker, K., Schutt, D. L., and Yuan, H. (2008). Imaging Yellowstone plume– lithosphere interactions from inversion of ballistic and diffusive Rayleigh wave dispersion and crustal thickness data. *Geochem. Geophys. Geosyst*. 9:Q06004. doi: 10.1029/2008GC001992

Vetter, S. K., and Shervais, J. W. (1992). Continental basalts of the Boise River Group near Smith Prairie, Idaho. *J. Geophys. Res. B Solid Earth Planets* 97, 9043–9061. doi: 10.1029/92JB00209

Walker, G. P. L. (1991). Structure, and origin by injection under surface crust, of tumuli, "lava rises," "lava-rise pits," and "lava inflation clefts" in Hawaii. *Bull. Volcanol*. 53, 546–558. doi: 10.1007/BF00298155

Welhan, J.A., Johannesen, C. M., Reeves, K. S., Clemo, T. M., Glover, J. A., and Bosworth, K.W. (2002). Morphology of inflated pahoehoe lavas and spatial architecture of their porous and permeable zones, eastern Snake River Plain, Idaho. *Geol. Soc. Am. Special Pap.* 353, 135–150. doi: 10.1130/0-8137-2353-1.135

Whitaker, M. L., Nekvasil, H., Lindsley, D. H., and Difrancesco, N. J. (2006). The role of pressure in producing compositional diversity in intraplate basaltic magmas. *J. Petrol.* 48, 365–393. doi: 10.1093/petrology/egl063

Whitaker, M. L., Nekvasil, H., Lindsley, D. H., and McCurry, M. (2008). Can crystallization of olivine tholeiite give rise to potassic rhyolites? —an experimental investigation. *Bull. Volcanol.* 70, 417–434. doi: 10.1007/s00445-007-0146-1

White, C. M. (2007). The Graveyard Point Intrusion: an example of extreme differentiation of Snake River Plain basalt in a shallow crustal pluton. *J. Petrol.* 48, 303–325. doi: 10.1093/petrology/egl062

Conflict of Interest Statement: The authors declare that the research was conducted in the absence of any commercial or financial relationships that could be construed as a potential conflict of interest.

ORIGINAL RESEARCH
published: 04 April 2018
doi: 10.3389/feart.2018.00029

Magmatic Densities Control Erupted Volumes in Icelandic Volcanic Systems

Margaret Hartley[1,2]* *and John Maclennan*[2]

[1] School of Earth and Environmental Sciences, University of Manchester, Manchester, United Kingdom, [2] Department of Earth Sciences, University of Cambridge, Cambridge, United Kingdom

Magmatic density and viscosity exert fundamental controls on the eruptibility of magmas. In this study, we investigate the extent to which magmatic physical properties control the eruptibility of magmas from Iceland's Northern Volcanic Zone (NVZ). By studying subaerial flows of known age and volume, we are able to directly relate erupted volumes to magmatic physical properties, a task that has been near-impossible when dealing with submarine samples dredged from mid-ocean ridges. We find a strong correlation between magmatic density and observed erupted volumes on the NVZ. Over 85% of the total volume of erupted material lies close to a density and viscosity minimum that corresponds to the composition of basalts at the arrival of plagioclase on the liquidus. These magmas are buoyant with respect to the Icelandic upper crust. However, a number of small-volume eruptions with densities greater than typical Icelandic upper crust are also found in Iceland's neovolcanic zones. We use a simple numerical model to demonstrate that the eruption of magmas with higher densities and viscosities is facilitated by the generation of overpressure in magma chambers in the lower crust and uppermost mantle. This conclusion is in agreement with petrological constraints on the depths of crystallization under Iceland.

Keywords: magma, basalt, Iceland, density, viscosity, volcanism, volumes

Edited by:
Olivier Bachmann,
ETH Zürich, Switzerland

Reviewed by:
MIchael Robert Carroll,
University of Camerino, Italy
Olivier Namur,
KU Leuven, Belgium

***Correspondence:**
Margaret Hartley
margaret.hartley@manchester.ac.uk

Specialty section:
This article was submitted to Volcanology, a section of the journal Frontiers in Earth Science

Received: *07 November 2017*
Accepted: *16 March 2018*
Published: *04 April 2018*

Citation:
Hartley M and Maclennan J (2018) Magmatic Densities Control Erupted Volumes in Icelandic Volcanic Systems. Front. Earth Sci. 6:29. doi: 10.3389/feart.2018.00029

1. INTRODUCTION

It has long been understood that the range of lava compositions sampled at mid-ocean ridges is strongly linked to the buoyancy of magma in the oceanic crust (Huppert and Sparks, 1980; Sparks et al., 1980) and the viscosity of the magma (Walker, 1971). Primary melts generated at depth are expected to rise through the crust until $\rho_m - \rho_c \approx 0$, that is, the point at which the magma density ρ_m and crustal density ρ_c are equal. The ponding of magmas at their level of neutral buoyancy in the crust (Ryan, 1993) is considered to be an important factor in the prolonged existence of shallow magma chambers (Ryan, 1987).

Neutral buoyancy concepts can also be applied within magma chambers. Huppert and Sparks (1980) and Sparks et al. (1980) considered a fluid-dynamical approach to explore the conditions under which magma stored in stratified chambers may be erupted at the surface. As melt crystallizes within the chamber, the density of the residual liquid evolves until a density minimum is reached. Typical suites of mid-ocean ridge basalts (MORB) reach this density minimum at ~7–10 wt.% MgO (Sparks and Huppert, 1984); the buoyant residual liquids may then ascend to their level of neutral buoyancy, resulting in an eruption if the liquid remains buoyant all the way to the surface.

Further crystallization of the residual liquid causes the density to increase once more, reducing the buoyancy and hence the eruptibility of the melt. Stolper and Walker (1980) defined a "window of eruptibility" for potential eruptive magmas, whereby the crust acts as an effective filter to high-density magmas. The range of compositions that can pass through this window depends firstly on the crustal density, and secondly on the position of the density minimum, which will itself vary depending on the initial composition and liquid line of descent of the parental melt. For mid-ocean ridge tholeiites erupting through typical oceanic crust, the window of eruptibility is found at melt MgO contents between 7 and 10 wt.%, or magnesium numbers (Mg#, molar Mg/(Mg+Fe^{2+}) around 0.55–0.70. This fluid-dynamical approach predicts that basalts with MgO contents >10 wt.% are very unlikely to erupt (Huppert and Sparks, 1980). However, dense olivine-phyric magmas with whole-rock MgO contents >15 wt.% and Mg#>0.8 have been erupted on Iceland's neovolcanic zones. The eruption of these dense magmas cannot be simply explained by neutral buoyancy alone.

In this study, we explore the relationship between physical properties and erupted volumes for magmas from Iceland's Northern Volcanic Zone (NVZ). We then use a simple numerical model to explore how variations in magma chamber depth, country rock density and fracture strength, can facilitate the eruption of dense magmas to the surface.

2. MAGMATISM IN ICELAND

Iceland is situated where a mantle plume underlies the Mid-Atlantic Ridge. High mantle potential temperatures beneath Iceland (e.g., McKenzie and O'Nions, 1991; Langmuir et al., 1992; Matthews et al., 2016) cause a greater degree of melting than under normal mid-ocean ridges, producing anomalously thick crust that is exposed above sea level. Iceland is thus the only part of the global spreading system where lava compositions can be routinely tied to eruptions of known age and volume. Iceland's active neovolcanic zones provide an excellent opportunity to better understand the role of the crust as a density filter for magma. Previous studies of the density filter have focused on MORB, using statistical analysis of many hundreds of samples to determine the eruption probability for different magma compositions and densities. However, this approach is limited because it has rarely been possible to associate samples dredged from submerged spreading centers with individual eruptions of known age and volume. The geological controls available on Iceland allow us to study not only the range of erupted magma compositions but also the volumetric distribution of lavas with different compositions and different physical properties.

Neutral buoyancy and fluid-dynamical models assume that magma ascent will always be limited by neutral buoyancy. Eruption at the surface must therefore be facilitated by crystallization in one or more crustal magma chambers until the melt is sufficiently buoyant to be erupted at the surface, which is likely to occur when the magma is at or near the density minimum (Sparks et al., 1980). These models are appropriate for some volcanic settings in Iceland, notably central volcanoes such as Krafla where seismic surveys indicate the presence of a shallow magma chamber at ~3 km depth (Brandsdóttir et al., 1997). However, evidence from ophiolite sections (Kelemen et al., 1997; Korenaga and Kelemen, 1997) and from clinopyroxene crystallization pressures in basaltic lavas across Iceland (e.g., Maclennan et al., 2001) indicate that polybaric fractional crystallization occurs in sill-like bodies at a range of crustal depths, including near-Moho depths of 25–30 km (0.8–1.1 GPa; Maclennan et al., 2003; Maclennan, 2008; Winpenny and Maclennan, 2011; Neave and Putirka, 2017). The presence of modally layered gabbroic sills intruding dunite in the Moho transition zone of the Semail ophiolite suggests that magmas can be stored at, and undergo crystallization at, depths far greater than their level of magmatic neutral buoyancy (Kelemen et al., 1997) before the residual liquids ascend and erupt. Similarly, the presence of chrome-diopside in many of Iceland's lava shields suggests that these magmas did not undergo significant low-pressure fractionation, but were fed directly by primitive melts sourced from the base of the crust (Sigurdsson and Sparks, 1978). The lava shields include large-volume eruptions of more evolved basalts (e.g., Stóravíti, ~30 km^3; Skjaldbreiður, ~11 km^3) and smaller volumes of dense picrite containing up to 20% olivine macrocrysts (e.g., Háleyjabunga, 0.013 km^3).

3. MAGMA DENSITY AND VISCOSITY

A dataset comprising 108 whole-rock samples from the Theistareykir and Krafla volcanic systems of Iceland's Northern Volcanic Zone was used to investigate the links between magmatic physical properties and the volumetric distribution of lava as a function of its composition. The samples correspond to postglacial eruptions of known volume and major element chemistry, and for each sample the modal proportion of macrocrysts has been visually estimated (Nicholson, 1990; Nicholson et al., 1991; Slater, 1996; Slater et al., 1998). For selected samples, we verified the modal proportions of olivine, plagioclase and rare clinopyroxene macrocrysts by point counting of thin sections. Macrocryst compositions in these sections were then determined using a Cameca SX100 electron microprobe at the University of Cambridge, using a beam diameter of 2 μm, current of 10 nA and accelerating voltage of 15 kV for all analyses. Whole-rock, point counting and mineral compositional data are provided as an electronic **Datasheet 1**.

The major element compositions of the NVZ samples are shown in **Figure 1A**. The change in trend at ~9.5 wt.% MgO reflects a change in fractionating mineral assemblage. Maclennan et al. (2001) used principal component analysis to demonstrate that the compositions of Theistareykir samples with 9.5–14.0 wt.% MgO can be explained by the addition or removal of a wehrlitic assemblage of 43% olivine, 47% clinopyroxene and 10% plagioclase, while the Theistareykir and Krafla samples with 6–9.5 wt.% MgO are best modeled

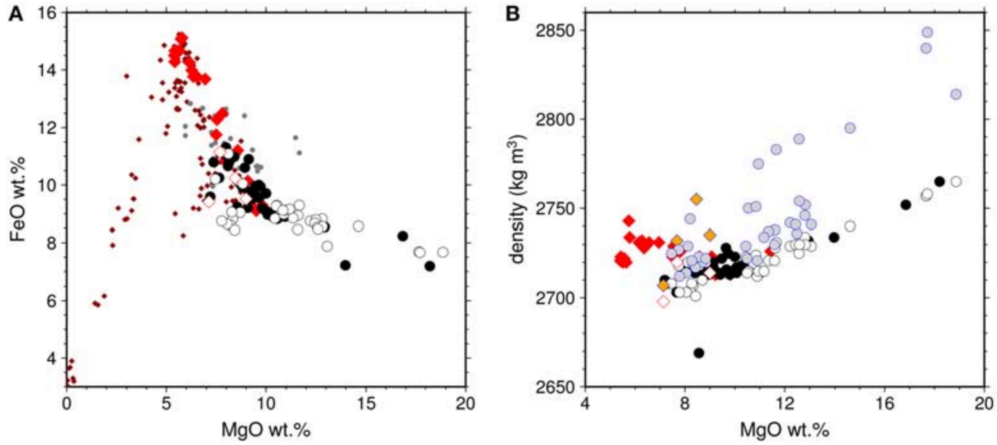

FIGURE 1 | (A) Whole-rock major element compositions of postglacial lava samples from the Theistareykir (black circles) and Krafla (red diamonds) volcanic systems. Large filled symbols show samples that are aphyric, or for which the modal macrocryst content is not recorded. Large open symbols show samples with ≥1 vol.% macrocrysts. Small filled symbols show whole-rock compositions of Theistareykir and Krafla lavas of glacial or unknown age. **(B)** Relationship between whole-rock composition and density for postglacial NVZ samples, calculated assuming that the whole-rock composition represents a crystal-free magmatic liquid. Pale filled symbols with blue outlines show magmatic densities for macrocryst-bearing samples, recalculated from the liquid and mineral densities and volume fractions according to Equation (2).

by crystallization of a gabbroic assemblage with a modal mineralogy of ∼10% olivine, ∼40% clinopyroxene and ∼50% plagioclase.

The density of a melt consisting of N components with mole fractions x_j (j = 1,2,3...N) is typically calculated:

$$\rho = \frac{\sum_{j=1}^{N} x_j M_j}{\sum_{j=1}^{N} x_j V_j} \tag{1}$$

where M is the molar mass and V the partial molar volume. This equation is often used to calculate the density of a magma from its whole-rock major element oxide composition, which is appropriate if the whole-rock composition represents a melt, i.e., a magmatic liquid. However, whole-rock analyses of phyric lavas provide the bulk average composition of the carrier melt and crystal components. Thus, the density calculated assuming that the whole-rock composition represents a magmatic liquid is not necessarily identical to the density of the magma, i.e., liquid plus crystals. For example, a melt carrying olivine macrocrysts will be denser than a liquid with the same bulk composition. Similarly, the liquid component of a magma might be buoyant with respect to the crust, but the same liquid carrying a cargo of olivine or clinopyroxene macrocrysts will have a higher bulk density and will not be able to ascend unless the macrocrysts settle from the liquid (Stolper and Walker, 1980). The density of a crystal-rich magma is best calculated as follows:

$$\rho_m = F_{ol}\rho_{ol} + F_{pl}\rho_{pl} + (1 - F_{ol} - F_{pl})\rho_l \tag{2}$$

where F is a volume fraction, ρ is a density, and the subscripts ol, pl, l, and m refer to olivine, plagioclase, liquid, and magma (i.e., liquid plus macrocrysts) respectively. Other macrocryst phases such as clinopyroxene may also be included in this calculation; however, clinopyroxene macrocrysts are very rare in the NVZ samples and so are not considered here.

We first calculated the density and viscosity of the NVZ samples assuming that the whole-rock composition represented a melt. We used Petrolog3 (Danyushevsky and Plechov, 2011) to calculate the liquidus temperature of the putative melt composition. The melt density at the liquidus temperature was then calculated from the molar volumes and mass fractions of the major element oxide components (**Figure 1B**). Partial molar volumes and thermal expansion coefficients were taken from Lange (1997), Lange and Carmichael (1990), Bottinga and Weill (1970), and Bottinga et al. (1982). Viscosities for the putative melt compositions were calculated at their liquidus temperatures using the model of Giordano et al. (2008).

To obtain a more realistic estimate of carrier liquid compositions in the NVZ, each whole-rock composition was corrected for the presence of macrocrysts. Point-counting data were used to obtain modal abundances for each macrocryst phase; where point-counting data were not available, we used published visual estimates of modal macrocryst abundance. Electron microprobe data were used to obtain representative compositions of each macrocryst phase in each sample. In individual samples, olivine and plagioclase macrocryst compositions tend to cluster around well-defined peaks with standard deviations of no more than 2.5 mol.% forsterite for olivine, and no more than 4 mol.% anorthite for plagioclase. Similar composition distributions have been obtained for olivine-phyric lavas across Iceland (Thomson and Maclennan, 2013). For each sample, the most probable macrocryst composition was used to calculate the mean macrocryst density, modeling forsterite-fayalite and albite-anorthite as ideal solid solutions with linear relationships between the densities of their endmembers (Fei, 1995). The mean macrocryst compositions were then subtracted from the whole-rock composition according to their modal abundances, and the remaining oxides renormalized to 100 wt.% to provide an estimate of the carrier liquid composition at the time of eruption. Densities and viscosities of these carrier liquids were calculated at their liquidus temperatures following the same method as for the whole-rock composition. Finally, the magmatic density (i.e., liquid plus crystals) was calculated from the liquid and mineral densities and volume fractions, according to Equation (2) (**Figure 1B**).

Of the 108 samples considered in this study, 63 were sparsely phyric to aphyric. Forty-five samples were recorded as containing >1% macrocrysts. Of these, 16 contained <5% macrocrysts and, for these samples, the difference between the density calculated from the whole-rock composition and the magmatic density (i.e., liquid plus crystals) is negligible (6 kg m^{-3} mean). The remaining samples contain up to 28.5% macrocrysts. These include olivine-phyric samples from Borgarhraun and the Theistareykir picrites, and plagioclase-phyric samples from Stóravíti. For the six samples containing ≥10 vol.% olivine macrocrysts, magmatic densities are on average 67 kg m^{-3} higher than the densities calculated under the assumption that their whole-rock compositions represent erupted liquids. For the ten samples containing ≥5 vol.% plagioclase macrocrysts and ≤2 vol.% of any other mineral phase, magmatic densities are on average 14 kg m^{-3} higher than the equivalent liquid density. The effect of uncertainty in the macrocryst modal proportions, either from point counting or visual estimation, on the calculated magmatic density is dependent on the density of the macrocryst phase of interest. An uncertainty of ±1% in the plagioclase modal abundance affects the calculated magmatic density by no more than ±1 kg m^{-3}, while ±1% olivine affects the magmatic density by ±6 kg m^{-3}.

Magmatic viscosities were calculated at the liquidus temperature of the carrier liquid from the melt viscosity and the macrocryst content, according to the Einstein-Roscoe equation:

$$\mu = \mu_0(1 - \Phi/\Phi_m)^{-n} \tag{3}$$

where μ_0 is the viscosity of the liquid and Φ is the crystal fraction. Φ_m and n are adjustable parameters that vary with the size, shape and distribution of particles in the melt; for magmatic processes these can be modeled using Marsh's constants $\Phi_m = 0.6$ and $n = 2.5$ (Lejeune and Richet, 1995). We also tested the more sophisticated viscosity model of Costa (2005), which reduces to the Einstein-Roscoe equation at low crystal fractions. The two models yielded near-identical calculated magma viscosities for the NVZ samples, which is unsurprising given their low macrocryst contents.

At atmospheric pressure, calculated magmatic densities are at a minimum for samples with 0.635<Mg#<0.670. The density minimum roughly corresponds to the predicted arrival of plagioclase on the liquidus and the observed shift from dominantly olivine-phyric to plagioclase-phyric samples. The position of the density minimum is little affected by the choice of pressure at which the melt liquidus temperature is calculated: melt densities at the liquidus temperature of a given sample decrease by ∼5–10 kg m^{-3} on increasing pressure from 0.001 to 0.9 GPa, and this effect is almost uniform for all of the samples considered. In order to highlight the control on physical properties from melt composition and macrocryst content, the results presented hereafter refer to densities calculated at atmospheric pressure.

4. CRYSTALLIZATION, ACCUMULATION, AND VESICULATION

The compositional array of magmas reflects the control of magmatic evolution by both fractional crystallization and melt mixing. The minimum available density and viscosity of magma is controlled by the fractionation and mixing paths of those magmas. The variation of density and viscosity as a function of melt fraction crystallized was calculated using Petrolog3. Calculations were run at a range of crustal pressures (0.001–0.9 GPa) and putative primary melt compositions. The choice of crystallization pressure affects the order in which olivine, plagioclase and clinopyroxene appear on the liquidus, but the position of the density minimum varies by only ∼5–6 kg m^{-3}. The density minimum is predicted to be lowest for isobaric crystallization at 0.9 GPa and highest for isobaric crystallization at 0.001 GPa, with polybaric crystallization models predicting density minima lying between the two isobaric cases. In all crystallization models we calculate a cusp in the predicted evolution of density and viscosity during fractional crystallization (**Figure 2A**). This cusp relates to the arrival of plagioclase on the basalt liquidus.

Subglacial basalts from the NVZ contain nominally undegassed H_2O contents of 0.1–0.5 wt.% (Nichols et al., 2002). The effect of adding up to 1 wt.% H_2O on melt liquid lines of descent was calculated in Petrolog3 using the mineral-melt equilibria of Danyushevsky (2001), and assuming that H_2O does not degas. Density and viscosity were calculated as a function of melt fraction crystallized, with water included as a phase in the density calculation using data from Ochs and Lange (1999). Increasing the H_2O content of the melt decreases its viscosity, and decreases the temperature at which olivine and plagioclase appear on the liquidus. The net result of these competing effects is that there is little change in the position of the viscosity minimum, where plagioclase joins the crystallizing assemblage (**Figure 2A**). Increasing the melt H_2O content decreases the melt density at all points along the crystallization pathway, but the position of the density minimum itself is minimally affected: for the NVZ picrite shown in **Figure 2A** the density minimum lies at 2,703 kg m^{-3} for an anhydrous melt, and 2,699 kg m^{-3} for a crystallization model with an initial 1 wt.% H_2O.

Volatile outgassing and vesiculation are expected to significantly lower the magmatic density and viscosity. Crystal-hosted melt inclusions from Borgarhraun indicate that nominally undegassed primitive magmas from the NVZ may contain up to 0.2 wt.% H_2O, 1,300 ppm CO_2 and 1,000 ppm S (Hauri et al., 2018). A basaltic melt with these volatile concentrations is predicted to become vapor-saturated at ∼220

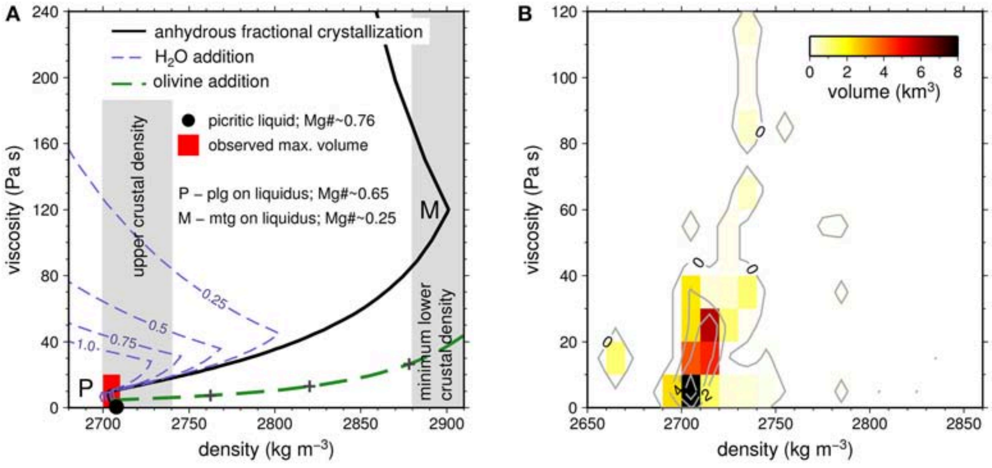

FIGURE 2 | (A) Fractional crystallization of a NVZ picrite with a whole-rock composition in equilibrium with Fo_{90} olivine. The crystallization model shown was calculated in Petrolog3 using a pressure of 0.4 GPa. The black solid line shows the density and viscosity evolution of the melt (i.e., residual liquid) assuming that it undergoes perfect fractional crystallization. The arrivals of plagioclase (P) and magnetite (M) on the liquidus are associated with shifts in the density evolution of the melt. Thin blue dashed lines show crystallization models for the same starting composition but under hydrous conditions, with the starting wt.% H_2O labeled on each line. The thick green dashed line shows the effect of adding olivine crystals to the starting composition on the magmatic (i.e., liquid plus crystals) density and viscosity; crosses show intervals of 10% olivine addition. **(B)** Relationship between magmatic density, viscosity, and erupted volume for postglacial lavas from Iceland's NVZ. The cumulative lava volume in each box is colored according to the scale at the top and contoured in 2 km^3 intervals.

MPa (Newman and Lowenstern, 2002). Much of the CO_2 is expected to exsolve at pressures >50 MPa, and may be lost through open-system degassing if magma is stored in the shallow crust prior to eruption. After vapor saturation is reached H_2O exsolves continuously, but significant H_2O loss is not expected to occur until pressures around 10 MPa, while S may remain dissolved in the melt until pressures around 5 MPa. The pressure at which vigorous exsolution and bubble growth occurs is dependent on both the initial volatile content and the decompression rate, but is expected to occur once the melt has ascended to pressures <3 MPa (e.g., Gerlach, 1986). While the mean vesicularity in the NVZ samples considered in this study is 5% (range 0–25%), vesiculation is expected to occur primarily during magma ascent through the uppermost crust, and thus has minimal effect on magma buoyancy in the mid- to lower crust. Given that the volatile contents and decompression rates of the NVZ magmas in this study are poorly constrained, we hereafter assume volatile-free conditions.

5. ERUPTIVE VOLUME CONTROL BY PHYSICAL PROPERTIES

The physical properties of magmas exert a strong control on the erupted volumes. By dividing the number of samples from a given eruption by the total volume of that eruption, we calculate a representative erupted volume for each NVZ sample. Hence, we obtain the volume of magma erupted at a given density and/or viscosity.

Despite the large range in predicted magma densities (2,670–2,840 kg m^{-3}) and viscosities (5–180 Pa s) for postglacial lavas from the NVZ, the largest eruptions cluster close to the density and viscosity minima associated with the arrival of plagioclase on the basalt liquidus (**Figure 2**). Over 50% of the total erupted volume lies at densities <2,710 kg m^{-3}, and over 85% below <2,720 kg m^{-3}. Similarly, over 80% of the total erupted volume lies at viscosities <30 Pa s. The lowest density cluster on **Figure 2B** represents a single macrocryst-free sample from the postglacial lava shield Stóravíti (30 km^3). Of the 27 samples from Stóravíti considered in this study, all but one have densities below 2,720 kg m^3 and lie within the density well on **Figure 2B**. Stóravíti dominates the postglacial volumetric output of the Theistareykir volcanic system, but its exceptionally large volume cannot be simply explained by enhanced melt production and eruption rates during early postglacial times following deglaciation (Jull and McKenzie, 1996; Maclennan et al., 2002), since these are common to all the early postglacial eruptions in this study. Instead, we argue that it is the physical properties of the Stóravíti magma that result in the large volume of this eruption in comparison with other early postglacial eruptions such as the Theistareykir picrites.

Only 0.75% of the erupted volume from the NVZ has predicted density >2,750 kg m^{-3}. This includes the Theistareykir picrites, and olivine-rich samples from Borgarhraun. Just over 5% of the total erupted volume has predicted viscosity >50 Pa s. Most of this volume corresponds to aphyric samples with the lowest MgO contents (MgO <7 wt.%) in the NVZ dataset; these higher viscosities therefore correspond to the samples with the lowest calculated liquidus temperatures rather than a population of magmas that have erupted after magnetite saturation and SiO_2 enrichment. The remaining high-viscosity samples (1% of the total erupted volume) have relatively low liquidus temperatures, and carry 6–16 vol.% macrocrysts. The volume maximum sits close to the minimum density and viscosity of magma available in the NVZ, while no samples in our dataset have both high density and high viscosity. This demonstrates the fundamental control of density and viscosity on volumetric output.

While upper crustal density plays an important role in controlling eruptive volumes, dense magmas (>2,800 kg m^{-3}) are able to rise above their levels of neutral buoyancy in the crust. The eruption of such magmas is driven by the development of sufficient overpressure in near-Moho to mid-crustal magma chambers. One way to generate this overpressure is as buoyant melts encounter local permeability barriers such as unfractured or more rigid (including colder and thus stronger) country rock. The rapid crystallization of basaltic melt lenses also creates zones of reduced porosity and permeability such that ascending melts are trapped beneath these zones. Kelemen and Aharonov (1998) develop this model based on field evidence from the Moho transition zone of the Semail ophiolite, where gabbroic sills, relics of basaltic melt lenses, formed in denser harzburgitic country rock. Continuous melt influx to the region beneath a permability barrier leads to increasing overpressure, eventually generating a melt-filled fracture which may reach the surface and result in eruption. Alternatively, ascending magma may be halted by either encountering another permeability barrier, rheological contrast and/or rigidity contrast (e.g., Kavanagh et al., 2006; Menand, 2011), or by reaching its level of neutral buoyancy in the crust.

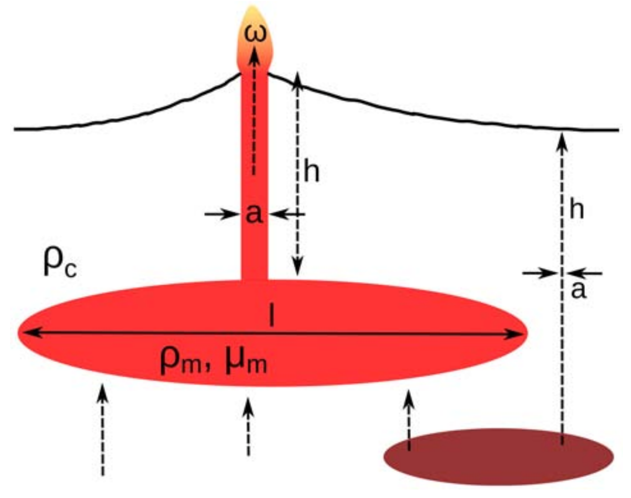

FIGURE 3 | Schematic illustration of a crustal magma reservoir at depth *h*, with an open fracture allowing magma to ascend with velocity ω from the top of the reservoir. Modified after Kelemen and Aharonov (1998). The fracture of width *a* forms when the overpressure in the magma chamber exceeds the fracture stress of the crust. The magma reservoir may be fed directly by mantle melts or from deeper, sill-like melt lenses. Under certain conditions, high-density olivine-phyric magmas are enabled to erupt from deep magma chambers directly to the surface. See text for details.

TABLE 1 | Parameters used in eruption modeling.

Variable	Description	Dimensions
a	Width of open fracture (dyke)	m
h	Magma chamber depth	km
G	Shear modulus of country rock	Pa
ω	Melt velocity	m s^{-1}
ρ	Density	kg m^{-3}
μ	Viscosity	Pa s
$\Delta\rho g$	Buoyancy term	
P_f	Overpressure required for fracture	Pa

6. LINKING ERUPTED VOLUMES TO PHYSICAL PROPERTIES

6.1. Constant Overpressure in a Magma Chamber

The observed relationship between density, viscosity and erupted volume can be explored using simple models of the development of overpressure in melt lenses, which relate magma viscosity, density and input flux to ascent rate, volumetric output rate and eruption frequency (Kelemen and Aharonov, 1998). Melt influx to melt lenses at depth h may cause a fracture of width a to form when the overpressure exceeds the fracture stress of the country rock (**Figure 3**; see **Table 1** for the notation used in the modeling). It is assumed that such fractures open instantaneously. Once open, the surrounding country rock is assumed to behave elastically with respect to the fracture. Melt flow through the fracture is assumed to be laminar and constant with height, and thus can be described by an average melt velocity. Assuming constant overpressure and ignoring horizontal extensional stresses, the dyke width and melt flow speed are given by:

$$a = \frac{hP_f}{G}, \qquad \omega \approx \frac{a^2}{12\mu h}(P_f + \Delta\rho g h) \tag{4}$$

The predicted flux, the product $a\omega$, was calculated using the above equations for a range of magma densities and viscosities, setting P_f = 1 MPa, G = 10 GPa and h = 10 km (**Figure 4**). The magma chamber depth is set to lie within the Icelandic mid-crust. The values of P_f and G are not well known. Kelemen and Aharonov (1998) selected a value of G = 10 GPa after Turcotte and Schubert (2014), although Auriac et al. (2013) suggest that G for the Icelandic lower crust may lie closer to 75 GPa. P_f, the overpressure required for fracture, is poorly constrained. Kelemen and Aharonov (1998) selected a value of 10 MPa, but we initally found a good match between our observations and model predictions at P_f = 1 MPa.

This generalized model cannot encapsulate all the details of individual eruptions (for example, the assumption of constant a is unlikely to be correct) but illustrates possible mechanisms for the control exerted by physical properties. Given its simplicity, it provides a surprisingly good fit to the observed relationship between physical properties and erupted volumes. There is some trade-off between P_f, G, and h as we attempt to fit the NVZ observations: for example, higher values of G will require higher values of P_f. Model predictions match the NVZ observations with a wide range of values for G and h: there is little difference in the

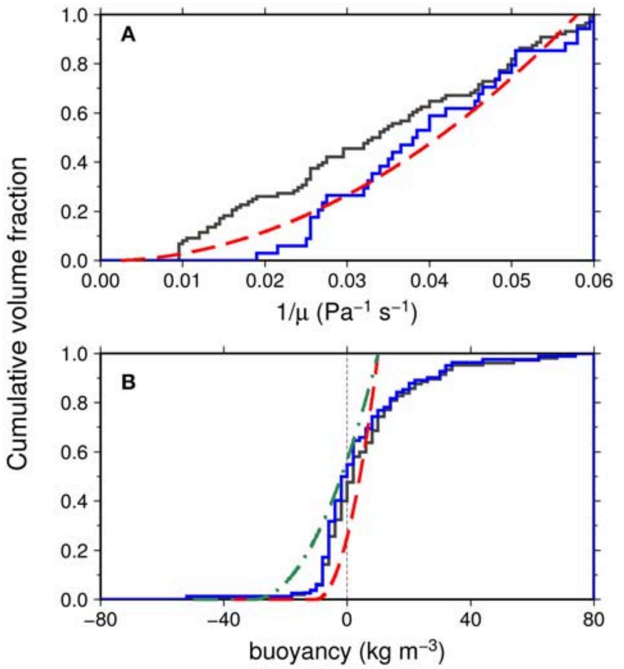

FIGURE 4 | Comparison of sill model predictions and observed relationship between erupted volume and magmatic density and viscosity. **(A)** Cumulative histogram of the relationship between inverse viscosity and fraction of total erupted volume. The black continuous line shows all observations from the NVZ. The blue line shows NVZ samples with density under 2,720 kg m^{-3}. The predicted relationship between magma viscosity and maximum melt flux rate is shown as a dashed red curve. This curve was calculated only for magma with the viscosity range in samples with densities under 2,720 kg m^{-3}. The density of the model magma was held constant at 2,710 kg m^{-3} for these calculations. **(B)** Cumulative histogram showing the relationship between erupted volume fraction and sample density, relative to a reference density of 2,710 kg m^{-3}. The black continuous line shows all observations from the NVZ; the blue line shows samples with viscosity under 50 Pa s. The model results shown as a dashed red curve were calculated for the density range found in melts with viscosity under 50 Pa s. The viscosity of the model magma was held constant at 50 Pa s for these calculations. For both plots, the red curves are calculated using the following reference values: G = 10 GPa; h = 10 km; P_f = 1 MPa. The green dashed curve in **(B)** shows the effect of changing the reference values to G = 75 GPa and P_f = 3 MPa.

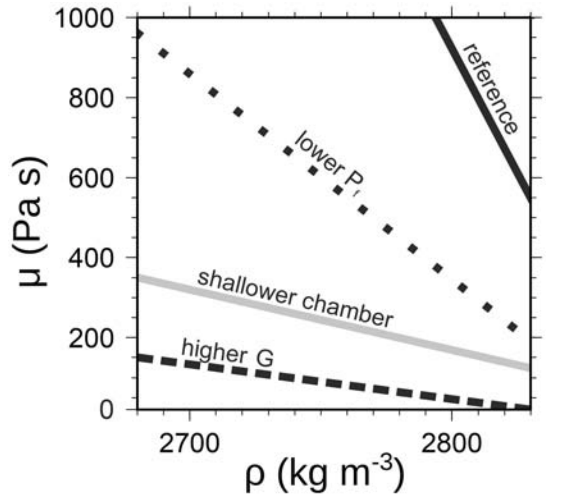

FIGURE 5 | Results of constant volumetric influx rate models. Lines show boundary between density-viscosity corresponding to no predicted eruption (top right) and predicted eruption (bottom left). The solid black line shows an arbitrary reference set of conditions, with magma chamber depth at h = 20 km, P_f = 5 MPa, and G = 25 GPa. Note that eruption is expected for a wide range of magma densities and viscosities from this chamber. The other lines show the effect of varying the parameters individually, all in a sense which reduces the range of melt densities and viscosities that can be erupted. Dotted black line: effect of reducing P_f to 4 MPa, with all other parameters set at the reference values. Solid gray line: effect of setting h = 10 km with all other parameters set at the reference values. Dashed black line: effect of increasing G to 50 GPa, with all other parameters set at the reference values.

model predictions for $10 < G < 100$ GPa. The model predictions are most sensitive to variations in P_f. We obtain a reasonable fit to the observations for P_f values up to 3. For $P_f > 3$ the model predicts that dense magmas will be buoyant, but the model curves no longer fit the observations. We emphasize that, while the details of our model predictions are unlikely to be correct, our model nonetheless facilitates a simple physical exploration of the plausibility of the suggested relationship between erupted volumes and magmatic physical properties.

The influence of viscosity on the erupted volumes can be isolated when the magma density is held fixed in the models, or the observations filtered to lie within a narrow density range. Both model predictions are predominantly concave-up on **Figure 4A**, indicating that greater erupted volumes are found at lower viscosity. The role of buoyancy is clear from inspection of the results of calculations performed with fixed magma viscosity and varying density (**Figure 4B**). These model predictions indicate that as a result of the magmatic overpressure ~15% of the erupted melt may have a density greater than that of the country rock. Assuming a reasonable country rock density of 2,710 kg m^{-3} (e.g., Staples et al., 1997), this proportion is roughly in agreement with the observations. The model results predict that magmas with density >10–15 kg m^{-3} greater than that of the country rock are not erupted. However, 5–10% of the observed erupted volume is composed of magma with densities of 2,730 kg m^{-3} or greater, and some picrites have densities of >2,800 kg m^{-3}, well in excess of expected Icelandic upper crustal densities. The eruption of such magma is not predicted by the simple sill models and may indicate that magma chambers feed eruptions from a variety of physical surroundings, as explored below.

6.2. Constant Volumetric Influx Rate to Magma Chamber

In order to account for the eruption of dense magmas through low-density upper crust, the physical conditions of the magma chambers supplying Icelandic eruptions must vary. More complex models were used to investigate the role of varying magma chamber depth, country rock density and fracture strength. This fuller realization of the models was explored by solving the differential equations for inflation of a magma chamber, fracture of its walls, release of magmatic overpressure and solidification of the dyke. Rather than maintaining constant magmatic overpressure, this scheme involves constant volumetric influx rate to the magma chamber and allows significant overpressure fluctuations to occur. The governing equations, posed by Kelemen and Aharonov (1998), were solved with a 4th order Runge-Kutta scheme paying particular attention to numerical accuracy at the time of fracture development, when predicted magma fluxes vary rapidly. The output magmatic flux was compared with an input at constant rate to the chamber.

Increasing h (i.e., deeper magma chamber), decreasing P_f, and/or increasing G encourage eruption at high densities and viscosities (**Figure 5**). Therefore, increased chamber depth may allow picrites to erupt at the surface, past their level of neutral buoyancy. Similarly, if the density of the country rock is increased, then eruption of denser magma is permitted. Magma chambers for picrites are therefore likely to be in the lower crust or uppermost mantle, where country rock densities of $\geq$2,950 kg m^{-3} are expected (Staples et al., 1997). This inference is in agreement with petrological constraints on the depth of magma chambers, which indicate that crystallization of picrites and high-Mg# basalts under Theistareykir occurs at depths of 15–30 km (Maclennan et al., 2001, 2003; Winpenny and Maclennan, 2011).

7. CONCLUSIONS

The physical properties of magmas exert key controls on the erupted volumes from Iceland's active neovolcanic zones. The largest volume of erupted material sits at a well-defined density and viscosity minimum coincident with the arrival of plagioclase on the basalt liquidus. These basalts are buoyant with respect to the Icelandic upper crust. Almost 70% of the erupted volume in the NVZ comprises basalts that sit close to this minimum.

The density filter is, however, leaky. Several small-volume eruptions with densities greater than the Icelandic upper crust are found in the NVZ. These eruptions include primitive basalts and olivine-phyric picrites, which may contain up to ~25% olivine macrocrysts. The eruption of these dense magmas is facilitated by the generation of overpressure in magma chambers in the lower crust or uppermost mantle. This conclusion is consistent with petrological constraints on the depth of crystallization of high-Mg# melts under Iceland.

AUTHOR CONTRIBUTIONS

Initial concept by JM. MH conducted the point-counting and electron microprobe analyses; calculated magmatic densities, viscosities and crystallization models; and wrote the manuscript. JM provided samples and wrote the numerical code solving the Kelemen and Aharonov (1998) governing equations. Both authors contributed to data interpretation.

FUNDING

We acknowledge support from the Department of Earth Sciences, University of Cambridge, and funding through NERC grants NE/N018575/1 and NE/P002331/1.

ACKNOWLEDGMENTS

We thank Thierry Menand and Oli Shorttle for their comments on earlier versions of this work, and two reviewers for their thoughtful comments which improved and clarified the manuscript. We thank Olivier Bachmann for editorial handling.

SUPPLEMENTARY MATERIAL

The Supplementary Material for this article can be found online at: https://www.frontiersin.org/articles/10.3389/feart.2018.00029/full#supplementary-material

Datasheet 1 | (1) Eruption volumes, whole-rock compositions, macrocryst abundances, and calculated densities for samples from Iceland's Northern Volcanic Zone. **(2)** Mineral point-counting data for NVZ postglacial basalt samples. **(2)** Mineral compositional data for NVZ postglacial basalts.

REFERENCES

Auriac, A., Spaans, K. H., Sigmundsson, F., Hooper, A., Schmidt, P., and Lund, B. (2013). Iceland rising: solid Earth response to ice retreat inferred from satellite radar interferometry and visocelastic modeling. *J. Geophys. Res. Solid Earth* 118, 1331–1344. doi: 10.1002/jgrb.50082

Bottinga, Y., Weill, D., and Richet, P. (1982). Density calculations for silicate liquids. I. Revised method for aluminosilicate compositions. *Geochim. Cosmochim. Acta* 46, 909–919. doi: 10.1016/0016-7037(82)90047-3

Bottinga, Y., and Weill, D. F. (1970). Densities of liquid silicate systems calculated from partial molar volumes of oxide components. *Amer. J. Sci.* 269, 169–182. doi: 10.2475/ajs.269.2.169

Brandsdóttir, B., Menke, W., Einarsson, P., White, R. S., and Staples, R. K. (1997). Faroe-Iceland ridge experiment. 2. Crustal structure of the Krafla central volcano. *J. Geophys. Res. Solid Earth* 102, 7867–7886. doi: 10.1029/96JB03799

Costa, A. (2005). Viscosity of high crystal content melts: dependence on solid fraction. *Geophys. Res. Lett.* 32:L22308. doi: 10.1029/2005GL024303

Danyushevsky, L. V. (2001). The effect of small amounts of H_2O on crystallisation of mid-ocean ridge and backarc basin magmas. *J. Volcanol. Geother. Res.* 110, 265–280. doi: 10.1016/S0377-0273(01)00213-X

Danyushevsky, L. V., and Plechov, P. (2011). Petrolog3: integrated software for modeling crystallization processes. *Geochem. Geophys. Geosyst.* 12, 1–32. doi: 10.1029/2011GC003516

Fei, Y. (1995). "Thermal expansion," in *Mineral Physics and Crystallography: A Handbook of Physical Constants*, vol. 2, ed T. J. Ahrens (Washington, DC: AGU), 29–44.

Gerlach, T. M. (1986). Exsolution of H_2O, CO_2, and S during eruptive episodes at Kilauea Volcano, Hawaii. *J. Geophys. Res.* 91, 12177–12185. doi: 10.1029/JB091iB12p12177

Giordano, D., Russell, J. K., and Dingwell, D. B. (2008). Viscosity of magmatic liquids: a model. *Earth Planet. Sci. Lett.* 271, 123–134. doi: 10.1016/j.epsl.2008.03.038

Hauri, E. H., Maclennan, J., McKenzie, D., Gronvold, K., Oskarsson, N., and Shimizu, N. (2018). CO_2 content beneath northern Iceland and the variability of mantle carbon. *Geology* 46, 55–58. doi: 10.1130/G39413.1

Huppert, H. E., and Sparks, R. S. J. (1980). Restrictions on the compositions of mid-ocean ridge basalts - A fluid dynamical investigation. *Nature* 286, 46–48. doi: 10.1038/286046a0

Jull, M., and McKenzie, D. (1996). The effect of deglaciation on mantle melting beneath Iceland. *J. Geophys. Res. Solid Earth* 101, 21815–21828. doi: 10.1029/96JB01308

Kavanagh, J. L., Menand, T., and Sparks, R. S. J. (2006). An experimental investigation of sill formation and propagation in layered elastic media. *Earth Planet. Sci. Lett.* 245, 799–813. doi: 10.1016/j.epsl.2006.03.025

Kelemen, P. B., and Aharonov, E. (1998). "Periodic formation of magma fractures and generation of layered gabbros in the lower crust beneath oceanic spreading ridges," in *Geophysical Monograph*, vol. 106, eds W. R. Buck, P. T. Delaney, J. A. Karson, and Y. Lagabrielle (Washington, DC: AGU), 267–289.

Kelemen, P. B., Koga, K., and Shimizu, N. (1997). Geochemistry of gabbro sills in the crust-mantle transition zone of the Oman ophiolite: implications for the origin of the oceanic lower crust. *Earth Planet. Sci. Lett.* 146, 475–488. doi: 10.1016/S0012-821X(96)00235-X

Korenaga, J., and Kelemen, P. B. (1997). Origin of gabbro sills in the Moho transition zone of the Oman ophiolite: implications for magma transport in the oceanic lower crust. *J. Geophys. Res.* 102, 27729–27749. doi: 10.1029/97JB02604

Lange, R. A. (1997). A revised model for the density and thermal expansivity of K_2O-Na_2O-CaO-MgO-Al_2O_3-SiO_2 liquids from 700 to 1900 K: extension to crustal magmatic temperatures. *Contrib. Mineral. Petrol.* 130, 1–11. doi: 10.1007/s004100050345

Lange, R. L., and Carmichael, I. S. E. (1990). Thermodynamic properties of silicate liquids with emphasis on density, thermal-expansion and compressibility. *Rev. Mineral. Geochem.* 24, 25–64.

Langmuir, C. H., Klein, E. M., and Plank, T. (1992). "Petrological constraints on melt formation and migration beneath mid-ocean ridges," in *Geophysical Monograph*, vol. 71, eds J. Phipps Morgan, D. Blackman, and J. M. Sinton (American Geophysical Union), 183–280.

Lejeune, A. M., and Richet, P. (1995). Rheology of crystal-bearing silicate melts - an experimental study at high viscosities. *J. Geophys. Res. Solid Earth* 100, 4215–4229. doi: 10.1029/94JB02985

Maclennan, J. (2008). Concurrent mixing and cooling of melts under Iceland. *J. Petrol.* 49, 1931–1953. doi: 10.1093/petrology/egn052

Maclennan, J., Jull, M., McKenzie, D., Slater, L., and Grönvold, K. (2002). The link between volcanism and deglaciation in Iceland. *Geochem. Geophys. Geosyst.* 3:1062. doi: 10.1029/2001GC000282

Maclennan, J., McKenzie, D., Grönvold, K., Shimizu, N., Eiler, J. M., and Kitchen, N. (2003). Melt mixing and crystallization under Theistareykir, northeast Iceland. *Geochem. Geophys. Geosyst.* 4:8624. doi: 10.1029/2003GC000558

Maclennan, J., McKenzie, D., Grönvold, K., and Slater, L. (2001). Crustal accretion under northern Iceland. *Earth Planet. Sci. Lett.* 191, 295–310. doi: 10.1016/S0012-821X(01)00420-4

Matthews, S., Shorttle, O., and Maclennan, J. (2016). The temperature of the Icelandic mantle from olivine-spinel aluminum exchange thermometry. *Geochem. Geophys. Geosyst.* 17, 4725–4752. doi: 10.1002/2016GC006497

McKenzie, D., and O'Nions, R. K. (1991). Partial melt distributions from inversion of rare-earth element concentrations. *J. Petrol.* 32, 1021–1091. doi: 10.1093/petrology/32.5.1021

Menand, T. (2011). Physical controls and depth of emplacement of igneous bodies: a review. *Tectonophysics* 500, 11–19. doi: 10.1016/j.tecto.2009.10.016

Neave, D. A., and Putirka, K. D. (2017). A new clinopyroxene-liquid barometer, and implications for magma storage pressures under Icelandic rift zones. *Amer. Mineral.* 102, 777–794. doi: 10.2138/am-2017-5968

Newman, S., and Lowenstern, J. B. (2002). VolatileCalc: a silicate melt-H_2O-CO_2 solution model written in Visual Basic for excel. *Comput. Geosci.* 28, 597–604. doi: 10.1016/S0098-3004(01)00081-4

Nichols, A. R. L., Carroll, M. R., and Hóskuldsson, A. (2002). Is the Iceland hot spot also wet? Evidence from the water contents of undegassed submarine and subglacial pillow basalts. *Earth Planet. Sci. Lett.* 202, 77–87. doi: 10.1016/S0012-821X(02)00758-6

Nicholson, H. (1990). *The Magmatic Evolution of Krafla, NE Iceland*. Ph.D. thesis, University of Edinburgh.

Nicholson, H., Condomines, M., Fitton, J. G., Fallick, A. E., Grönvold, K., and Rogers, G. (1991). Geochemical and isotopic evidence for crustal assimilation beneath Krafla, Iceland. *J. Petrol.* 32, 1005–1020. doi: 10.1093/petrology/32.5.1005

Ochs, F. A., and Lange, R. A. (1999). The density of hydrous magmatic liquids. *Science* 283, 1314–1317. doi: 10.1126/science.283.5406.1314

Ryan, M. P. (1987). "Neutral buoyancy and the mechanical evolution of magmatic systems," in *Magmatic Processes: Physicochemical Principles*, ed B. O. Mysen (Geochemical Society Special Publication 1), 259–287.

Ryan, M. P. (1993). Neutral buoyancy and the structure of mid-ocean ridge magma reservoirs. *J. Geophys. Res. Solid Earth* 98, 22321–22338. doi: 10.1029/93JB02394

Sigurdsson, H., and Sparks, R. S. J. (1978). Lateral magma flow within rifted Icelandic crust. *Nature* 274, 126–130. doi: 10.1038/274126a0

Slater, L. (1996). *Melt Generation Beneath Iceland*. Ph.D. thesis, University of Cambridge.

Slater, L., Jull, M., McKenzie, D., and Grönvold, K. (1998). Deglaciation effects on mantle melting under Iceland: results from the Northern Volcanic Zone. *Earth Planet. Sci. Lett.* 164, 151–164. doi: 10.1016/S0012-821X(98)00200-3

Sparks, R. S. J., and Huppert, H. E. (1984). Density changes during the fractional crystallization of basaltic magmas - Fluid dynamic implications. *Contrib. Mineral. Petrol.* 85, 300–309. doi: 10.1007/BF00378108

Sparks, R. S. J., Meyer, P., and Sigurdsson, H. (1980). Density variation amongst mid-ocean ridge basalts - Implications for magma mixing and the scarcity of primitive lavas. *Earth Planet. Sci. Lett.* 46, 419–430. doi: 10.1016/0012-821X(80)90055-2

Staples, R. K., White, R. S., Brandsdóttir, B., Menke, W., Maguire, P. K. H., and McBride, J. H. (1997). Faroe-Iceland Ridge Experiment. 1. Crustal structure of northeastern Iceland. *J. Geophys. Res. Solid Earth* 102, 7849–7866. doi: 10.1029/96JB03911

Stolper, E., and Walker, D. (1980). Melt density and the average composition of basalt. *Contrib. Mineral. Petrol.* 74, 7–12. doi: 10.1007/BF00375484

Thomson, A., and Maclennan, J. (2013). The distribution of olivine compositions in Icelandic basalts and picrites. *J. Petrol.* 54, 745–768. doi: 10.1093/petrology/egs083

Turcotte, D., and Schubert, G. (2014). *Geodynamics*, *3rd Edn*. Cambridge University Press.

Walker, G. P. L. (1971). Viscosity control of the composition of ocean floor volcanics. *Philos. Trans. R. Soc. Ser. A* 268, 727–729. doi: 10.1098/rsta.1971.0023

Winpenny, B., and Maclennan, J. (2011). A partial record of mixing of mantle melts preserved in icelandic phenocrysts. *J. Petrol.* 52, 1791–1812. doi: 10.1093/petrology/egr031

Conflict of Interest Statement: The authors declare that the research was conducted in the absence of any commercial or financial relationships that could be construed as a potential conflict of interest.

frontiers
in Earth Science

ORIGINAL RESEARCH
published: 24 July 2018
doi: 10.3389/feart.2018.00095

A NanoSIMS Investigation on Timescales Recorded in Volcanic Quartz From the Silicic Chon Aike Province (Patagonia)

Susanne Seitz [1]*, ***Benita Putlitz*** [1]*, ***Lukas Baumgartner*** [1], ***Anders Meibom*** [1,2], ***Stéphane Escrig*** [2] ***and Anne-Sophie Bouvier*** [1]

[1] Institute of Earth Sciences, University of Lausanne, Lausanne, Switzerland, [2] Laboratory for Biological Geochemistry, Federal School of Technology Lausanne, Lausanne, Switzerland

Textural and chemical differences in coeval rhyolitic effusive and explosive eruptions are commonly observed, and numerical models predict different timescales for the eruption of crystal-rich mushes versus crystal-poor magmas. We compare quartz zonation and diffusion timescales of crystal-rich rhyolitic ignimbrites and crystal-poor rhyolitic lava flows from the Jurassic Chon Aike Province exposed in Patagonia (Argentina). The timescales are assessed by using diffusion modeling based on nanoscale secondary ion mass spectrometry (NanoSIMS) analysis of titanium (Ti) concentration profiles in quartz crystals oriented by image analysis using micro-tomography. Quantitative Ti-data were acquired by SIMS to estimate crystallization temperatures. The textural and geochemical analysis revealed clear differences between crystal-poor rhyolitic lava flows and crystal-rich rhyolitic ignimbrites. Quartz crystals from rhyolitic lava flows display simple oscillatory cathodoluminescence (CL) zoning interpreted to be magmatic and diffusion chronometry suggest a short timescale for quartz crystallization from 5.6 ± 2.2 to 41.6 ± 9.8 years. Resorption textures are rare, and hence crystals in rhyolitic lava flows recorded a simple, rapid extraction, transport and eruption history for these crystal-poor melts. Rhyolitic ignimbrites, in contrast, reveal complex zoning patterns, reflecting several episodes of partial resorption and growth throughout their crystallization history. The complex quartz zoning textures together with longer diffusion times (<350 years), rather suggest a storage in a mush with fluctuating pressure and temperature conditions leading to intermittent resorption. Yet, a final quartz overgrowth rim occurred over a much shorter timescale in the order of years (<3 years). This implies, that crystal-rich mushes can be re-mobilized very fast, as fast as crystal-poor magmas. The use of in-situ methods with a high spatial resolution, like NanoSIMS, is critical to resolve very short magmatic timescales.

Keywords: NanoSIMS, diffusion chronometry, magma storage, Chon Aike Province, quartz zoning textures

Edited by:
Olivier Bachmann,
ETH Zürich, Switzerland

Reviewed by:
Teresa Ubide,
The University of Queensland, Australia
Chad Deering,
Michigan Technological University, United States

Correspondence:
Susanne Seitz
susanne.seitz@unil.ch
Benita Putlitz
benita.putlitz@unil.ch

Specialty section:
This article was submitted to Volcanology, a section of the journal Frontiers in Earth Science

Received: *08 December 2017*
Accepted: *22 June 2018*
Published: *24 July 2018*

Citation:
Seitz S, Putlitz B, Baumgartner L, Meibom A, Escrig S and Bouvier A-S (2018) A NanoSIMS Investigation on Timescales Recorded in Volcanic Quartz From the Silicic Chon Aike Province (Patagonia). Front. Earth Sci. 6:95. doi: 10.3389/feart.2018.00095

INTRODUCTION

The understanding of silicic volcanic systems is constantly evolving. Nevertheless, many important questions as to the nature of crustal magma storage, including magma chamber geometry and dynamics, the “trigger” of large eruptions and the time of magma accumulation before eruption are still under discussion. To explain the commonly observed textural and chemical differences in coeval rhyolitic effusive and explosive eruptions, many studies propose a crystal mush extraction model (Bachmann and Bergantz, 2004, 2008; Hildreth, 2004; Allan et al., 2013; Cooper and Wilson, 2014). This model postulates that crystal-rich intermediate to silicic rocks represent reactivated crystal mushes and crystal-poor silicic magmas represent the extracted interstitial melt. Numerical models predict different timescales on which crystal-rich mushes and crystal-poor magmas can be erupted (Huber et al., 2012), e.g., 100–1,000 years for crystal-rich mushes and a few years for crystal-poor magmas. These short times cannot be resolved with conventional, absolute dating techniques at present, despite the remarkable advances made in the last decade (Michel et al., 2008; Leuthold et al., 2012; Barboni and Schoene, 2014; Wotzlaw et al., 2014). Diffusion chronometry, on the other hand, has provided new insights into these very short timescales of volcanic processes. Compositional profiles across zoned crystals can be acquired and transformed into time estimates using known diffusion rates and estimates for magmatic temperatures. It is essential, however, to measure an element or isotope concentration profile with a spatial resolution that is significantly better than the characteristic diffusion length scale of the element in question (Saunders et al., 2014; Till et al., 2015; Seitz et al., 2016; Bradshaw and Kent, 2017). So far, the majority of studies used either grayscale profiles, which were acquired from backscattered secondary electron (BSE) and cathodoluminescence (CL) images, or element profiles measured by electron microprobe (EPMA). A non-exhaustive review of diffusion chronometry to explore the timescale of magma chamber rejuvenation prior to large-scale eruptions is given here (**Table 1**). See also the review by Cashman and Giordano (2014). The intriguing results of these recent studies are the short timescale they report with the implication that large volumes of silicic melt may accumulate over a short period of time, in centuries or less, and that late stage crystallization immediately prior to eruption may occur at even shorter timescale of decades, years or months (Turner and Costa, 2007). Examples come from the Bishop Tuff (USA), where the last magma recharge event supposedly occurred < 100–150 years before eruption (Ti diffusion in quartz; Wark et al., 2007; Chamberlain et al., 2014). Similar timescales (<100 years; Ti, Sr, Mg diffusion in plagioclase) were found for the "Minoan" caldera-forming eruption of Santorini volcano (Greece) by Druitt et al. (2012). Studies from the Taupo Volcanic Zone (New Zealand) report slightly shorter timescales of 10–85 years (Ti diffusion in quartz, Saunders et al., 2010; Matthews et al., 2012) for the magma recharge event before eruption. Finally, with the application of high-spatial-resolution analysis by NanoSIMS, Till et al. (2015) suggested ∼10 months (Sr, Ba, Mg diffusion in sanidine) for the rejuvenation of the rhyolitic lava of the Yellowstone caldera (USA). We presented NanoSIMS data for quartz crystals from rhyolites from Patagonia (Argentina), which indicated similar short time scales of the order of a few years (Seitz et al., 2016). Even shorter times of only 1–14 weeks (Mg-Fe diffusion in orthopyroxene) were found for the final recharge event of 1912 Novarupta-Katmai (Alaska) rhyolite eruption (Singer et al., 2016). Note, that the advances in new analytical techniques with a sub-micrometer spatial resolution, e.g., NanoSIMS, TOF-SIMS, and FEG-EPMA are crucial to these studies (e.g., Hellebrand et al., 2005; Charlier et al., 2012; Lloyd et al., 2014; Saunders et al., 2014; Ferry et al., 2015; Till et al., 2015; Seitz et al., 2016).

Quartz is an important constituent in silicic systems. It resists alteration and it is often the best or only viable candidate for diffusion chronometry. Since the calibration of the Ti-in-quartz thermometer (Wark and Watson, 2006; see also Thomas et al., 2010; Huang and Audétat, 2012) and the experimental determination of the relevant diffusion parameters (Cherniak et al., 2007) quartz is thus increasingly used in diffusion studies. CL intensity in quartz has been shown to display a positive correlation with Ti-concentration (Wark and Spear, 2005). CL provides a practical method of observing Ti-zoning in quartz (Spear and Wark, 2009), and is now routinely used for textural analyses. Quartz often records a detailed growth history with small-scale zoning patterns, which can be linked to changes in temperature, pressure or chemistry of the magmatic system in response to processes such as magma recharge, mixing, assimilation or decompression (Streck, 2008). Nevertheless, other elements like aluminum for example, can also produce variation in CL intensity (Götze et al., 2001), making it imperative to prove that Ti is the sole element responsible for the CL pattern observed.

In this paper, we address the differences in estimated diffusion times and formation conditions between crystal-rich rhyolitic ignimbrites and crystal-poor rhyolitic lava flows. The studied silicic volcanic rocks belong to the Jurassic Chon Aike Province (Patagonia). The province, is one of the few silicic large igneous provinces, but so far, relatively little is known about magma storage conditions, magma extraction, and related timescales. This study provides novel results from well-characterized magmatic quartzes to highlight the difference between rhyolitic lava flows and rhyolitic ignimbrites based on systematic analyses of zoning textures as determined by CL. To determine diffusion timescales, we take advantage of the ultra-high spatial resolution of the NanoSIMS to obtain semi-quantitative Ti concentration profiles across quartz both from rhyolitic ignimbrites and rhyolitic lava flows. SIMS analyses complement the Ti-in-quartz analyses. We use those high-resolution Ti profiles in combination with petrographic arguments, rhyolite-MELTS modeling, and diffusion modeling to decode the archive stored in quartz.

GEOLOGICAL SETTING

Chon Aike Province

The Chon Aike Province (**Figure 1**) is one of the world's largest silicic provinces (Pankhurst et al., 1998, 2000; Bryan et al., 2002) covering large parts of Patagonia and the Antarctic Peninsula. The volume is estimated at 235,000 km^3 (Pankhurst et al., 1998). Volcanism occurred over about 40 Ma and partly coincides with the Karoo-Ferrar mafic magmatism. It is concentrated in three main volcanic episodes: the first episode (V1) occurred between 188 and 178 Ma, the second episode (V2) between 172 and 162 Ma and the third episode (V3) between 157

TABLE 1 | Summary of magmatic timescales in silicic volcanic systems using diffusion chronometry.

Study	Volcanic system	Mineral (element)	Method	Time scale [years]	Interpretation
Wark et al., 2007	BT	Quartz (Ti)	CL, diffusion chronometry	<100	Final recharge
Chamberlain et al., 2014	BT	Quartz (Ti)	FEG-CL, diffusion chronometry	<150	Final recharge
		Orthopyroxene (Fe-Mg)	BSE, diffusion chronometry		
		Sanidine (Sr, Ba)	BSE, EMPA, diffusion chronometry		
Till et al., 2015	BT	Sanidine (Sr, Ba, Mg)	NanoSIMS, diffusion chronometry	∼10 month	Final recharge
Gualda et al., 2012	BT	Quartz (Ti)	CL, synchrotron x-ray microfluorescence maps, diffusion chronometry	500–3,000	Mush evolution
		Quartz	Faceting of melt inclusions		
		Quartz	Crystal size distribution		
		Quartz	Heat flow modeling		
Pamukcu et al., 2015	BT	Quartz	Faceting of melt inclusions	<600	Mush evolution
Saunders et al., 2010	TVZ	Quartz (Ti)	CL, diffusion chronometry	<300	Final recharge
Matthews et al., 2012	TVZ	Quartz (Ti)	CL, diffusion chronometry	10–85	Final recharge
Matthews et al., 2012	TVZ	Quartz (Ti)	Synchrotron x-ray microfluorescence maps, diffusion chronometry	10–60	Final recharge
		Quartz (Ti)		10^3–10^4	Mush evolution
Pamukcu et al., 2015	TVZ (Okurmamaku)	Quartz	Faceting of melt inclusions	<50	Mush evolution
	TVZ (Oruanui)	Quartz	Faceting of melt inclusions	<300	Mush evolution
Singer et al., 2016	NK	orthopyroxene (Fe-Mg)	FEG-EMPA, diffusion chronometry	1–14 weeks	Final recharge

BT, Bishop Tuff; TVZ, Taupo Volcnic Zone; NK, Novarupta Katamai (Alaska).

and 153 Ma (Pankhurst et al., 2000). Volcanism in Patagonia and Antarctic Peninsula developed in an overall extensional regime along the proto-Pacific margin of Gondwana during the initial stage of the continental break-up. The province has a bimodal composition, but is dominated by rhyolitic ignimbrites, which vary in their degree of welding from high-grade rheomorphic ignimbrites to volumetrically dominant non-welded lithic-rich ignimbrites. Intermediate compositions are rare (Pankhurst et al., 2000). Locally calderas could be identified as eruption centers (e.g., Aragón et al., 1996). The ignimbrites are intercalated with volumetrically less important rhyolitic lava flows and domes, fallout deposits, debris flow deposits and epiclastic deposits (e.g., Riley et al., 2010). In Patagonia, the province can be divided into two regions—eastern Patagonia and the Andean Cordillera. In eastern Patagonia, the ignimbrites are flat-lying and non-deformed. They overlie Precambrian to early Jurassic crystalline basement rocks and Lower Jurassic rift-related sediments. The narrow outcrops in the Andean Cordillera are locally deformed and tilted.

Study Area

Here we present data from the El Quemado Complex which was deposited during the V3 episode (Pankhurst et al., 2000; Fildani and Hessler, 2005). Outcrops of this formation cover a large area along the Patagonian Andes (**Figure 1**), from Lago Argentino in the south to Lago Pueyerredón in the North. The El Quemado Complex mainly consists of rhyolitic and dacitic ignimbrites, as well as air-fall tuffs intercalated with andesitic to rhyolitic lava flows, which overlie in some areas a basal breccia or conglomerate horizon (Llanos et al., 2003). The samples are from a small area (**Figure 1**) located around the Fitz Roy Plutonic Complex (Ramírez de Arellano et al., 2012), at the border between Chile and Argentina in Southern Patagonia.

We sampled km-size rhyolitic lava domes and flows (further referred to as flows). The several kilometer-long domes are build up from meters to tens of meter thick flows, locally intercalated with tuffs and breccia flows. The rhyolitic ignimbrites sampled (further referred to as ignimbrites) form meter to tens of meter thick units, which can be followed for several kilometers. No detailed maps exist at this point to fully estimate the instantaneous volumes erupted. Flows are folded together with the Cretaceous Rio Mayer Formation (**Figure 2A**). They preserved magmatic textures like flow banding and vesicles (**Figure 2B**). Samples come from three different localities (within a very restricted area). For sample localities see Supplementary Material. **Figure 2A** shows the Loma de las Pizarras ridge with two of the samples sites. Ignimbrites in the study area discordantly overly the Paleozoic clastic sequence of the Bahía de la Lancha Formation (**Figure 2D**). Ignimbrites can contain

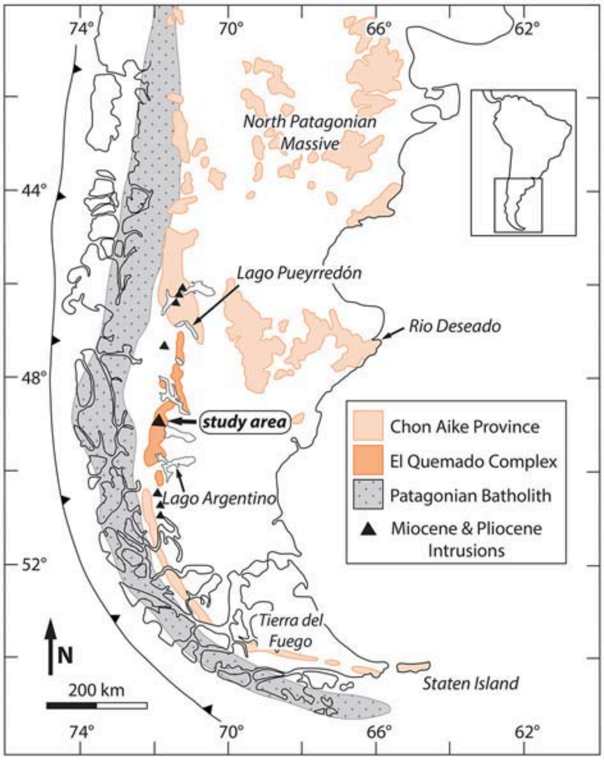

FIGURE 1 | Map showing the main outcrop areas of the Jurassic Chon Ake Province and the El Quemado Complex in Patagonia. Also shown the Patagonian Batholith (after Pankhurst et al., 1998; Hervé et al., 2007; modified from Seitz et al., 2016). The study area is in the vicinity of the Fitz Roy Plutonic Complex, as indicated.

volcanic bombs and they often show lithic fragments and fiamme (**Figure 2E**). The investigated samples come from a single locality (Cerro Polo) as shown in **Figure 2D**.

Flows and ignimbrites are very similar with regard to their chemistry; they have a peraluminous character and a high silica content (75–82 wt% $\mathrm{SiO_2}$). They are distinct, however, in their crystal cargo. Flows are crystal-poor (4–10%) and ignimbrites are crystal-rich (25–40%; **Figures 2C,F**). The flows (**Figures 2A–C**) contain between 4 and 6% quartz and between 1 and 4% feldspar crystals in a very fine-grained matrix of quartz and feldspar interpreted to have been glass. Accessory minerals are biotite, zircon and secondary ilmenite. Some subhedral quartz crystals show embayments and contain recrystallized melt inclusions. Most quartz crystals show magmatic zoning, like oscillatory zoning, in CL images. Ignimbrites (**Figures 2D–F**) are crystal-rich and contain between 15 and 25% quartz and between 10 and 15% feldspar crystals in a very fine-grained matrix of quartz and feldspar. As accessory minerals biotite, zircon and secondary ilmenite occur. Quartz shows a greater variety in zoning patterns with oscillatory, normal and reverse zoning and internal dissolution textures. In total, we studied 261 quartz crystals from 16 samples of ignimbrites and flows by CL, SIMS, and NanoSIMS.

ANALYTICAL METHODS

Sample Preparation Using X-ray Microtomography

All quartz samples for NanoSIMS analysis were cut perpendicular to the c-axis, as verified by X-ray micro-tomography at the Institute of Earth Sciences (University of Lausanne, Switzerland). See Skora et al. (2006) for additional details on the procedure. Before imaging, ∼1.5 cm wide and ∼3 cm long rock cores were marked with small saw cuts every millimeter. The rock cores were scanned for about 14–15 h with a SkyScan1173® instrument at the following conditions: 70 kV/140 nA or 80 kV/100 nA with a step size of 0.23° for a 360° rotation and a frame averaging of 40. For volume rendering and image analysis the SkyScan® software package was used. Finally, quartz crystals were chosen based on their shape and a 1 mm thick section of the rock core was cut a few tens of μm above the chosen crystal. The quartz crystals were then carefully extracted from the rock.

Several extracted quartz crystals were mounted together with a quartz standard grain (Audétat et al., 2014) for Ti analysis by SIMS in a 25 mm diameter epoxy mounts. The epoxy mounts were polished in several steps using a diamond paste with decreasing grain sizes, from 15 μm and to 0.5 μm until quartz cross-sections—corresponding to the central tomographic images—were exposed.

The CamScan MV2300 (Institute of Earth Sciences, University of Lausanne, Switzerland) was used in the panchromatic mode at an acceleration voltage of 20 kV to collected CL images of the crystal zoning. CL images have a resolution of 1,024 × 928 pixels.

Ti Concentration Measurements by SIMS

The Ti concentration was measured with the ion microprobe IMS 1280HR at the SwissSIMS laboratory (University of Lausanne, Switzerland). The sample surface, which was previously coated with a 40 nm thick layer of gold, was bombarded with an $\mathrm{O^-}$ primary beam of 2 nA accelerated at 13 kV. The extracted secondary ions were accelerated at 10 kV into the mass spectrometer. Using the axial electron multiplier (EM) $^{30}\mathrm{Si}^{+}$ and $^{48}\mathrm{Ti}^{+}$ were analyzed on mono-collection mode, with the field aperture was set to 4,000 μm and the energy slit to 50 μm. To assure no interference from other masses with $^{30}\mathrm{Si}^{+}$ and $^{48}\mathrm{Ti}^{+}$ the entrance slit was closed to 61 μm and the exit slit to 405 μm.

Before each analysis, the sample surface was cleaned by a presputtering of 90 s using a raster beam of 40 μm. Just after the pre-sputtering and before each analysis, an automatic calibration on $^{30}\mathrm{Si}$ and centering of field aperture were made. Each analysis consists of 15 cycles of the peak-stepping sequence $^{30}\mathrm{Si}^{+}$ (2 s) and $^{48}\mathrm{Ti}^{+}$(10 s). The Ti count rate on the quartz standard (Audétat et al., 2014) was around 5.1 × 103 counts/s. The background on the EM was less than 2 counts/h. The relative standard deviation for the runs typically varied between 2SD = 5% and 2SD = 10% on the quartz standard, which has a reported Ti concentration of 57 ± 4 ppm (Audétat et al., 2014).

High-Resolution Ti Analyses by NanoSIMS

High-resolution Ti profiles across the quartz crystals were obtained with the NanoSIMS 50L ion microprobe at the Center

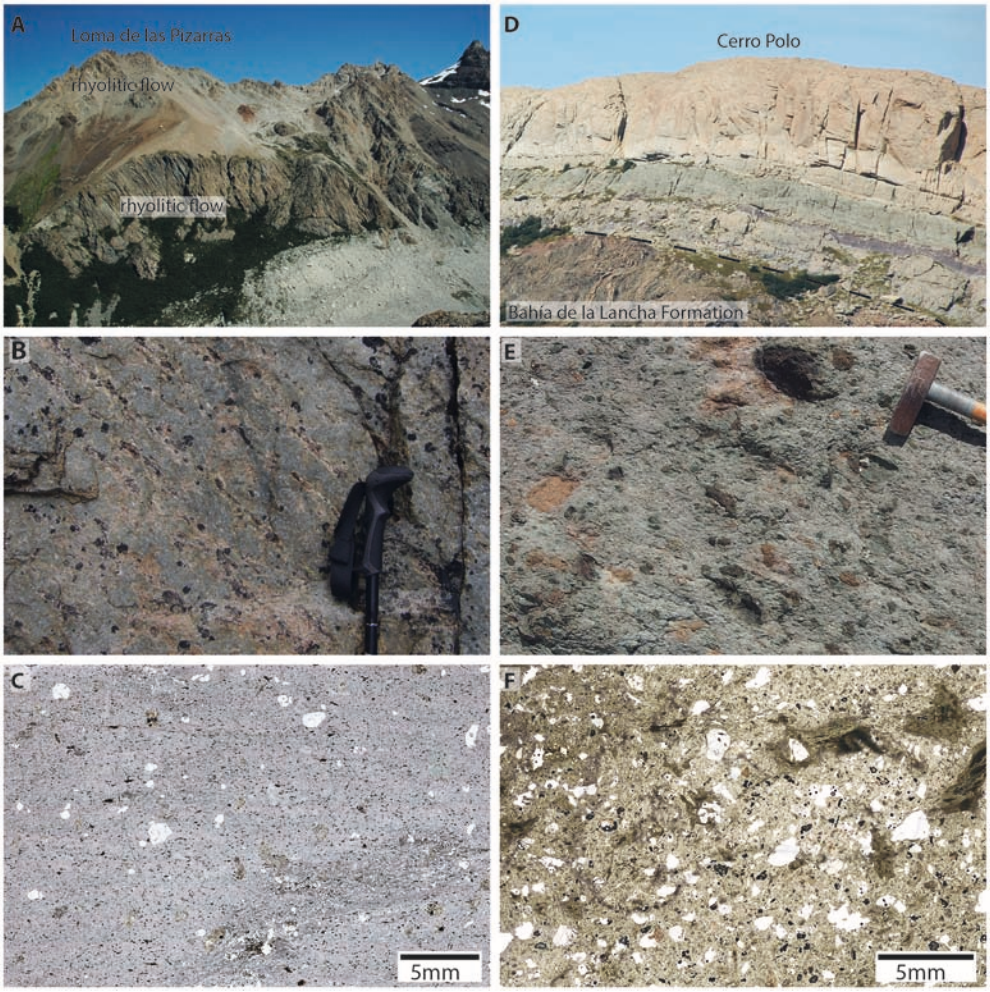

FIGURE 2 | (A) View of the Loma de las Pizarras ridge showing the typical appearance of rhyolitic lava flows of the El Quemado Complex and the folded Cretaceous pelitic series. Sample rhyPN73 was taken from the outcrop building the top of the ridge, samples rhyB7 and rhyE5 come from the half-moon like outcrop forming the lower part of the ridge. **(B)** Rhyolitic lava flows typically preserved flow banding and vesicles. **(C)** Thin section image of a typical crystal-poor rhyolitic flow. **(D)** View of the Cerro Polo ridge with the multiple deposits of the Jurassic rhyolitic ignimbrites of the El Quemado Complex discordant overlying a Palaeozoic clastic sequence. Note trees for scale. The samples ignA5 and ignA6 were taken from the upper ignimbrite deposit. **(E)** Fiamme structures as often shown by the rhyolitic ignimbrites. **(F)** Thin section image of a typical crystal-rich rhyolitic ignimbrite.

of Advanced Surface Analysis (CASA, Lausanne, Switzerland), by bombarding Au-coated (15 nm-thick layer) samples with a focused O^- primary beam. Simultaneous collection of $^{30}Si^+$ and $^{48}Ti^+$ secondary ions with electron multipliers at a mass resolution of about 6,000, assured that any potential interference was eliminated. To remove the effect of local variation in the ionization and extraction processes, the data are reported as $^{48}Ti/^{29}Si$ ratio.

A two-step approach was used to quantify the relative change in titanium concentrations. First, a series of point analyses (**Figure 7A**) were obtained to identify the zones of interest, then high resolution line scans were made. The primary ion beam (beam current: 25 pA, beam size: 650 nm, 120 s pre-sputtering, 200 s data acquisition) was held stationary while the stage moved in 3 μm steps.

Second, high-resolution line scans (**Figures 7b–v**) were collected scanning continuously across the transitions identified by the point analysis data. Therefore, 30 × 30 to 60 × 60 μm images of the area of interest were first acquired (with a 256 × 256 pixel resolution) which helped to choose the precise location and orientation of the line scans using the NanoSIMS software. During 3 cycles (dwell time: 2 sec/pixel) a pre-sputtering was performed. The data were acquired (beam current: 23 pA, beam size: 650 nm, dwell time: 2 s/pixel) over 20 cycles and are reported as cumulated counts. The first 2.5 μm of each side of the scan were excluded to remove possible edge effects.

To identify any inclusions simultaneous measurements of ^{23}Na and ^{27}Al were performed. Spikes higher than 25% of the average variation in the $^{23}Na^+$ and $^{27}Al^+$ profile are considered as inclusions and the corresponding parts in the cumulated $^{48}Ti^+$

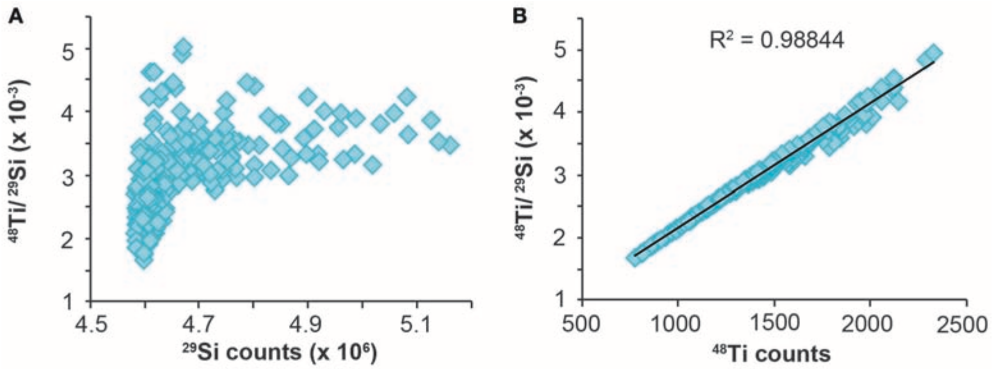

FIGURE 3 | Plot of the ^{48}Ti/^{29}Si ratio vs. ^{29}Si counts **(A)** and vs. ^{48}Ti counts **(B)** of sample rhyPN73. There is no correlation between the ^{48}Ti/^{29}Si ratio and ^{29}Si counts **(A)**, but there is an excellent correlation between the ^{48}Ti/^{29}Si ratio and ^{48}Ti counts **(B)**. This demonstrates that the ^{48}Ti/^{29}Si ratio depends only on variations Ti concentration.

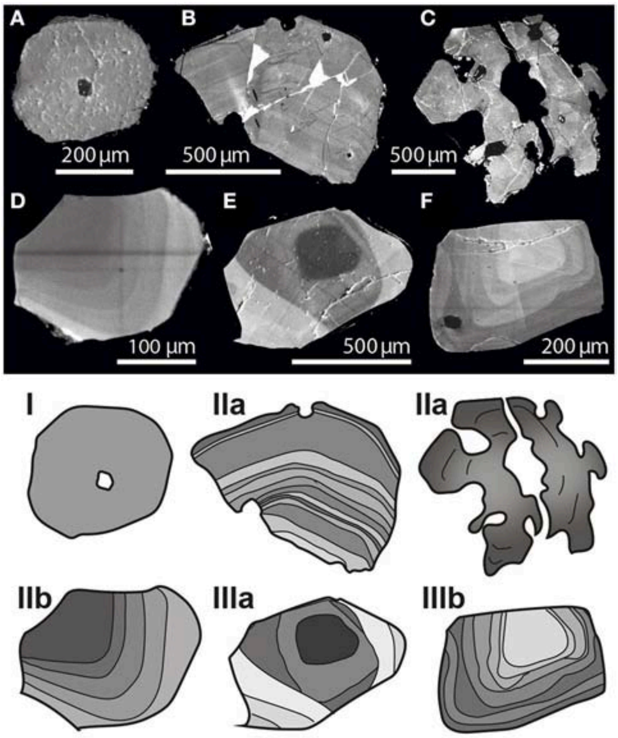

FIGURE 4 | Representative quartz crystals from ignimbrites and flows on the top and the corresponding classification at the bottom. Quartz of type I show no visible zonation **(A)**. Type II typically has embayment features **(B–D)** and recrystallized melt inclusions. It lacks internal dissolution textures and is either normally zoned (type IIa) or reversely zoned (type IIb). The crystals of type III show a clear zonation with internal dissolution textures **(E + F)**, the rim might be zoned as well **(E)**. Type III can be normally zoned (type IIIa) or reversely zoned (type IIIb).

profile are removed. Furthermore, we looked at each of the 20 cycles of the ^{48}Ti^{+} profile to identify artifacts. Spikes higher than 25% of the average variation, which are not observed in all cycles are removed from the cumulated ^{48}Ti^{+} profile. The absolute variations in the ^{48}Ti/^{29}Si ratio is entirely driven by variation in the ^{48}Ti^{+} count rate (**Figure 3**).

Modeling Parameters

An understanding of the geometry of the diffusion profiles is crucial. All profiles were measured perpendicular to the growth zoning and only cuts oriented perpendicular to the C-axis (and the zoning) were used. The following assumptions entered the diffusion calculations and fitting of the profiles: (1) each chemical zone is homogeneous at the beginning, with (2) a vertical interface between two zones, and (3) diffusion occurred only perpendicular to the interfaces. Diffusion coefficients were calculated by the Arrhenius relationship. We used the diffusion coefficient $D_0 = 7.01 \times 10^{-8}$ m^2/s, and the activation energy $E_a = 273 \pm 12$ kJ/mol based on the diffusion experiments of Ti in quartz by Cherniak et al. (2007).

Profiles were normalized to the maximum value of each profile, before fitting error functions to the measured profiles using a weighted Marquardt fitting routine (Press et al., 1992). The uncertainty of the fits was estimated using residual χ^2 of each profile and the uncertainty for each point estimated from the variation in the flat concentration parts adjacent to each profile. Uncertainties do not include those linked to the experimentally determined diffusion coefficient for Ti in quartz (Cherniak et al., 2007).

RESULTS

Quartz Classification

Quartz crystals often record a complex growth history, which are linked to changes in temperature, pressure, magma chemistry, or growth velocity (see for example Wark et al., 2007; L'Heureux, 2013; Pamukcu et al., 2016). Those changes, in turn, are linked to different processes in a volcanic system, such as magma recharge, magma mixing or assimilation (Streck, 2008). Cathodoluminescence is an efficient way to visualize the history recorded in the magmatic zoning. We studied a total of 261 quartz crystals from 9 ignimbrites ($n_{quartz} = 150$) and 7 flows ($n_{quartz} = 111$). Based on the observed CL zoning pattern, we defined three classes (**Figure 4**).

Type I: These quartz crystals have no visible zonation (**Figure 4A**).

Type II: Quartz crystals are zoned but lack any indication of internal dissolution textures. Nevertheless, they commonly have embayment features (**Figure 4C**) emanating from the crystal surface, filled with recrystallized fined grained matrix interpreted to have been glass. Depending on the cut orientation, these embayments can be perceived as crystallized melt inclusions. They can either have light cores, with one or several darker rims (referred to as normally zoned, type IIa, **Figures 4B,C**), or they show reverse zonation (type IIb, **Figure 4D**), where a dark core is surrounded by several lighter rims.

Type III: Quartz crystals show clear internal dissolution textures, indicated by more or less complex intersecting zoning patterns. They are either normally (type IIIa, **Figure 4E**) or reversely (type IIIb, **Figure 4F**) zoned.

Quartz crystals from ignimbrites and flows show similar patterns, but the abundance of different quartz classes (**Figure 5**), especially the type III-zonation are significantly different.

Type IIa or normally zoned quartz crystals are the largest group in flows making up 62% of the population; type IIb represents only 4%. Embayment features of the crystal surface have been recognized in 40% of the quartz. Note that, just 5% of the quartz crystals in the flows belong to type III, i.e., are characterized by internal dissolution textures. Within the type III group we can further distinguish between: (a) crystals with embayment-like internal dissolution contacts, they contribute with 60% to this population, and (b) crystals with round cores; they make up 40% of the type III group.

Normally zoned (type IIa) crystals are dominant in ignimbrites as well; in addition, reversely zoned quartz crystals (type IIb) are important, making up 18% of the population. Embayment features at the crystal surfaces are less abundant in ignimbrites; they have been noted for 25% of all quartz crystals. Type III crystals are a notable quantity (15%) of the ignimbrite quartz population, a difference to flows (see above). Within the type III groups we recognize again (a) embayment-like internal dissolution contacts in 26% of the crystals and (b) round cores in 74% of the crystals. Note, that respective percentage (embayment vs. round) is distinct to flows.

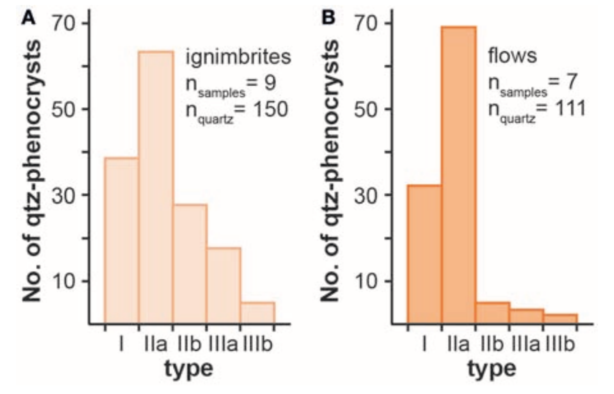

FIGURE 5 | (A) Histogram of classification of quartz crystals from ignimbrites (9 samples, $n_{quartz} = 150$). **(B)** Histogram of classification of quartz crystals from flows (7 samples, $n_{quartz} = 111$). Note that type IIb, IIIa, and IIIb are almost not present in the flow samples.

Estimation of the Quartz Crystallization Temperature

Diffusion time estimates depend critically on the temperature-time history experienced by the crystal. Unfortunately, estimating temperatures for quartz growth is difficult for the rhyolitic flows, since no Ti-phases are present, making a direct application of Ti in quartz thermometry impossible without introducing arbitrary estimates on Ti activity (e.g., Wark and Watson, 2006). Below, we discuss alternative attempts to obtain temperatures. These include estimates using zircon saturation temperatures and temperatures estimated combining Ti-in-quartz thermometry and rhyolite-MELTS calculation (Gualda et al., 2012; Ghiorso and Gualda, 2015). Calculations are even more difficult for the ignimbrites, where we argue that most quartz crystals are ante- or even xenocrysts, making the melt composition elusive. A summary of all temperature estimates is given in **Table 2**. One should keep in mind that to calculate maximum diffusion times a minimum temperature for quartz crystallization should be used.

Zircon Saturation Temperature

We calculated the zircon saturation temperature using the zirconium (Zr) content of 29 whole rock analyses (Seitz, 2016) of ignimbrites and flows with the calibration of Watson and Harrison (1983). All samples have low Zr content between 60 ppm and 155 ppm. The Zr content for the samples discussed here are given in **Table 3**. The calculated temperatures vary between 710°C and 830°C. Zircons are small ($<125\,\mu$m) and only two zircons from a flow preserved an inherited core. As argued by Miller et al. (2003), this indicates that the melt was Zr undersaturated during its formation, implying that the zircon saturation temperature represents a minimum estimate for melt generation. Hence quartz crystallization temperatures could be significantly higher. These temperatures are considered to be minimum values.

Ti-in-Quartz Thermometry Combined With Thermodynamic Estimates Based on the Whole Rock Ti-composition of Rhyolitic Flows

The Ti-activity is less than one in the flows, since no rutile is present. We attempted to estimate the Ti-activity in the melt using the measured Ti-content in flows and compare this to the rutile solubility values of Hayden and Watson (2007). We assumed an ideal mixing to calculate Ti activity (a_{Ti}). The Ti-concentrations are a good approximation for the Ti-content of the melt, because only minor amounts of quartz crystals (4–6%) are present. Ti concentrations of whole rocks range from 298 to 810 ppm, while those of quartz vary from 9 to 176 ppm (see **Table 3**). A simultaneous solution for the equilibration

TABLE 2 | Summary of temperature estimates based on zircon saturation, TitaniQ, 4vol%-quartz-temperature (4QT) and rhyolite-MELTS.

Sample	Temperature [°C]					Pressure [GPa]			aTi	H_2O [%]		
	Zircon saturation	TitaniQ	4QT		Rhyolite-MELTS	4QT		Rhyolite-MELTS				
	a	b+c	d+e	d+f	d	d+e	d+f	d	b+c	d+e	d+f	d
rhyL5	755	825	820–1235	1070		0.4–0.6	0.05		0.16	0–7.5	0	
rhyPN73	775	775	850–1220	1080		0.3–0.5	0.05		0.50	0–6	0	
rhyB7		800	840–1235	1110		0.4–0.5	0.1		0.29	0–7.5	0	
rhyE5		945							0.08			
ignA5	710	755			700–900 /720–880 /760–960			0.6/0.4 /0.1	0.52			1–7.5 /1–6 /1–3
ignA6	790											
ignA9		940							0.15			
ignA10		1000*							0.10*			
ignSLB3		900							0.15			

For details, see explanation in the text.

*[a]Watson and Harrison (1983), [b]Hayden and Watson (2007), [c]Wark and Watson (2006), [d]Gualda et al. (2012), Ghiorso and Gualda (2015), [e]Thomas et al. (2010), [f]Huang and Audétat (2012), *A solution was only found for grain 10.*

TABLE 3 | Ti and Zr concentration for whole rock (XRF) and Ti concentration of quartz crystals (SIMS) from flows (rhy) and ignimbrites (ign) of the El Quemado Complex.

	Ti (ppm)		Zr (ppm)
Sample	Whole rock	Quartz	Whole rock
rhyL5	298	29.1–33.8	78
rhyPN73[a]	538	34.8–61.9	94
rhyB7	417	9.4–44.0	
rhyE5	721	18.8–45.4	
ignA5	453	38.8–72.0	74
ignA6	520	22.1–43.3	100
ignA10**	810	77.9–175.9	
		51.1–65.8	
ignSLB3[a]	570+	26.2–115.1	

[a]Sample from Nescher (2013) or Leresche (2013).
+Estimation.
***Two quartz crystals.*

temperature was sought for the rutile activity, calculated with Ti-in-quartz thermometry (further referred to as TitaniQ) and the calculated rutile activity in the melt. This yields temperatures between 775°C and 945°C for the calibration of Wark and Watson (2006). The calculated activities of Ti in the melt varies between 0.08 and 0.50 for the flows (see **Table 2**). Neither the calibration of Wark and Watson (2006) for TitanQ, nor the rutile solubility of Hayden and Watson (2007) contain a pressure dependence. To investigate the sensitivity to pressure changes, we attempted to couple TitaniQ of Thomas et al. (2010) and Huang and Audétat (2012) with activities calculated from melts, using different pressures and water contents for the melts.

Ti-in-quartz thermometry can be combined with rhyolite-MELTS calculation (Gualda et al., 2012; Ghiorso and Gualda, 2015) to obtain temperature estimates. Whole rock geochemistry is given in the Supplementary Material. The results are given in **Table 2**. We again used the Ti-concentrations of the whole rock for the flows. Calculated Ti-activities will depend on pressure, water content and temperature. Hence the system is under-determined. Assuming the majority of the quartz crystals to be phenocrysts in the rhyolite flows, we can also use the modal abundance of quartz phenocrysts to further constrain these variables. In a first step the temperature was calculated corresponding to a crystallization of 4 vol% quartz (further referred to as 4QT) with rhyolite-MELTS as well as the Ti-activity (a_{Ti}). The obtained a_{Ti} was used for TitaniQ to calculate temperatures for the different calibrations (Thomas et al., 2010; Huang and Audétat, 2012). The solution for the equilibration temperature was sought by minimizing the difference between the temperature based on 4QT and TitaniQ (**Figure 6**).

Using the calibration for TitaniQ by Thomas et al. (2010) solutions were found between 1220°C and 850°C, 0.3 GPa and 0.5 GPa and a water content between 0 and 6% for sample rhyPN73 (**Table 2**) and between 1235°C and 820°C, 0.4–0.6 GPa and 0–7.5% H_2O for sample rhyL5 (**Figure 6**). For sample rhyB7 temperatures were found between 840°C and 1235°C, with pressures of 0.4–0.6 GPa and 0–7.5% H_2O. The calibration of Huang and Audétat (2012) yielded a narrow pressure range from 0.05 GPa to 0.1 GPa, and only for a water free melt yielding temperatures of 1080°C for sample rhyPN73, 1070°C for sample rhyL5 and 1110°C for sample rhyB7 (**Table 2**). Sample rhyE5 did not yield reliable results, as it shows late secondary alteration, notably replacement of the matrix by carbonate minerals. The minimum temperature of 820°C obtained from these calculations is about 50°C higher than the minimum temperature obtained for the zircon saturation. The two pressure sensitive calibrations yield a crystallization for quartz in two significantly different environments: either relatively deep (10–20 km) and hydrous at highly variable temperatures (between

820°C and 1235°C) depending on water content or very shallow (1.5–4 km) and dry in a narrow temperature range of 1070–1110°C. See below for an in-depth discussion of the consequences of these estimates.

Temperature Estimates for Rhyolitic Ignimbrites

A temperature estimate for the ignimbrites is more difficult as quartz crystals recorded multiple changes in the volcanic system and have likely seen different magmas during the evolution of the system. Quartz crystals commonly show internal dissolution textures; hence no information is recorded between the dissolution event and the overgrowth of a new quartz rim. As in all ignimbrite samples quartz crystals with various zonation textures are observed, it is clear that quartz crystals recorded complex magmatic histories, involving a changing magma system. In fact, the crystal charge in the ignimbrites precludes using whole rock composition to repeat the above calculations, and none of the ignimbrites has glass shards preserved, which could be used to estimate the composition of a remobilizing magma. Therefore, a temperature estimate based on TitaniQ and melt a_{Ti} is not a reliable approximation for the ignimbrites.

In light of this point, we estimate the minimum temperature based on rheological arguments. At a crystallinity of 50% it is unlikely that the magma would be erupted (Bachmann and Bergantz, 2008). We calculated the temperature that correspond to a 50% crystallinity threshold using rhyolite-MELTS. This estimate depends on the pressure and the water content of the melt. We obtained a temperature of about 700°C at 0.6 GPa for a water saturated melt (7.5% water). For a low water content in the melt (1% water) the temperature would rise to 900°C. At a slightly lower pressure of 0.4 GPa we obtain temperatures between 720°C (6% water) and 880°C (1% water), while at 0.1 GPa temperatures vary between 760°C (3% water) and 960°C (1% water). It is clear that if the quartz crystals were stored in a partially, or even completely solidified magma chamber as proposed by many authors (see e.g., Bachmann and Bergantz, 2008), temperature of storage could have been significantly lower, and hence residence times significantly longer. Nevertheless, we believe that these numbers give us a good estimate of temperature immediately prior to, and during, eruption. We believe that the storage of the mush occurred at shallow levels in accordance with most prevailing models (Bachmann and Bergantz, 2008), so that we will use a minimum temperature of 760°C for mush remobilization.

Diffusion Times

We measured profiles (**Figure 7**) over each major growth zone by NanoSIMS. The profiles cover representative quartz crystals of each classification type from flows and ignimbrites. The intensity in the CL images, in general, correlates well with the Ti variation in the NanoSIMS profiles, with the brighter zones having higher Ti concentration. Yet, slopes and concentration values are not always identical. A discussion of this topic can be found in Seitz et al. (2016). Indeed CL images have been found to reflect Al-differences in quartz (Götze et al., 2001) in some cases. Therefore, it is essential to establish the diffusing element through chemical analysis. Using the NanoSIMS allowed us to identify the diffusing element and to use the actual chemical data for diffusion modeling. Our NanoSIMS measurements determined Ti as the only diffusing element (**Figure 3**). Other trace elements, such as Na and Al, did not show any zonation.

We used the measured Ti profiles to calculate diffusion times at the minimum temperature of 820°C based on 4QT for the crystals from rhyolite flows, and we used 760°C for the ignimbrite samples, which corresponds to the 50% crystal limit of magma at 0.1 GPa. Since temperature estimates are uncertain for the ignimbrites, we also calculated the diffusion times at 820°C, to allow for a rapid comparison of the data between ignimbrites and flows (**Table 4**). The shape of the pre-diffusion profile influences

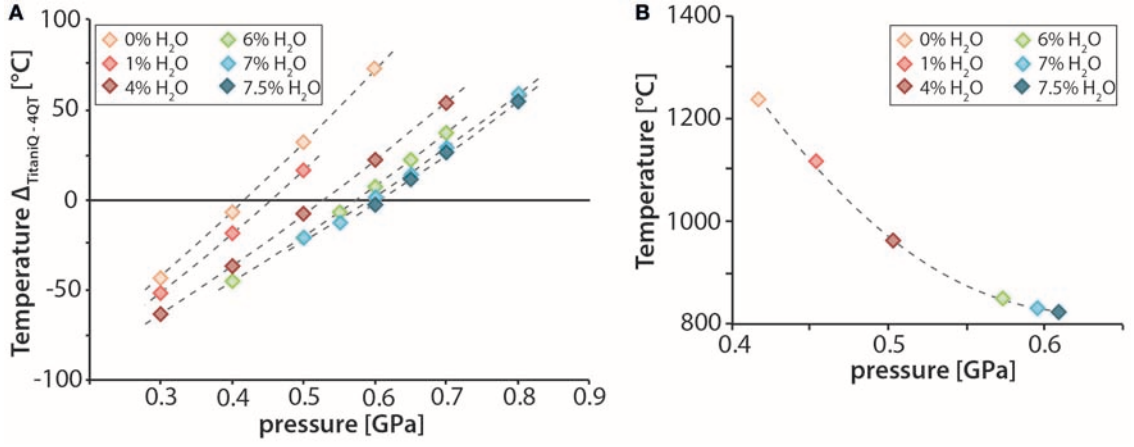

FIGURE 6 | (A) Example for sample rhyL5 showing the differences between the temperature based on Ti-inquartz thermometry (calibration of Thomas et al., 2010) and rhyolite-MELTS (corresponding to crystallization of 4 vol% quartz) for different pressures and water contents in the rhyolitic melt. Ti-in-quartz thermometry and rhyolite-MELTS yield the same temperatures between 0.4 GPa and 0.6 GPa. **(B)** Corresponding equilibrium temperature for different pressures and water contents. For details, see explanations in the text.

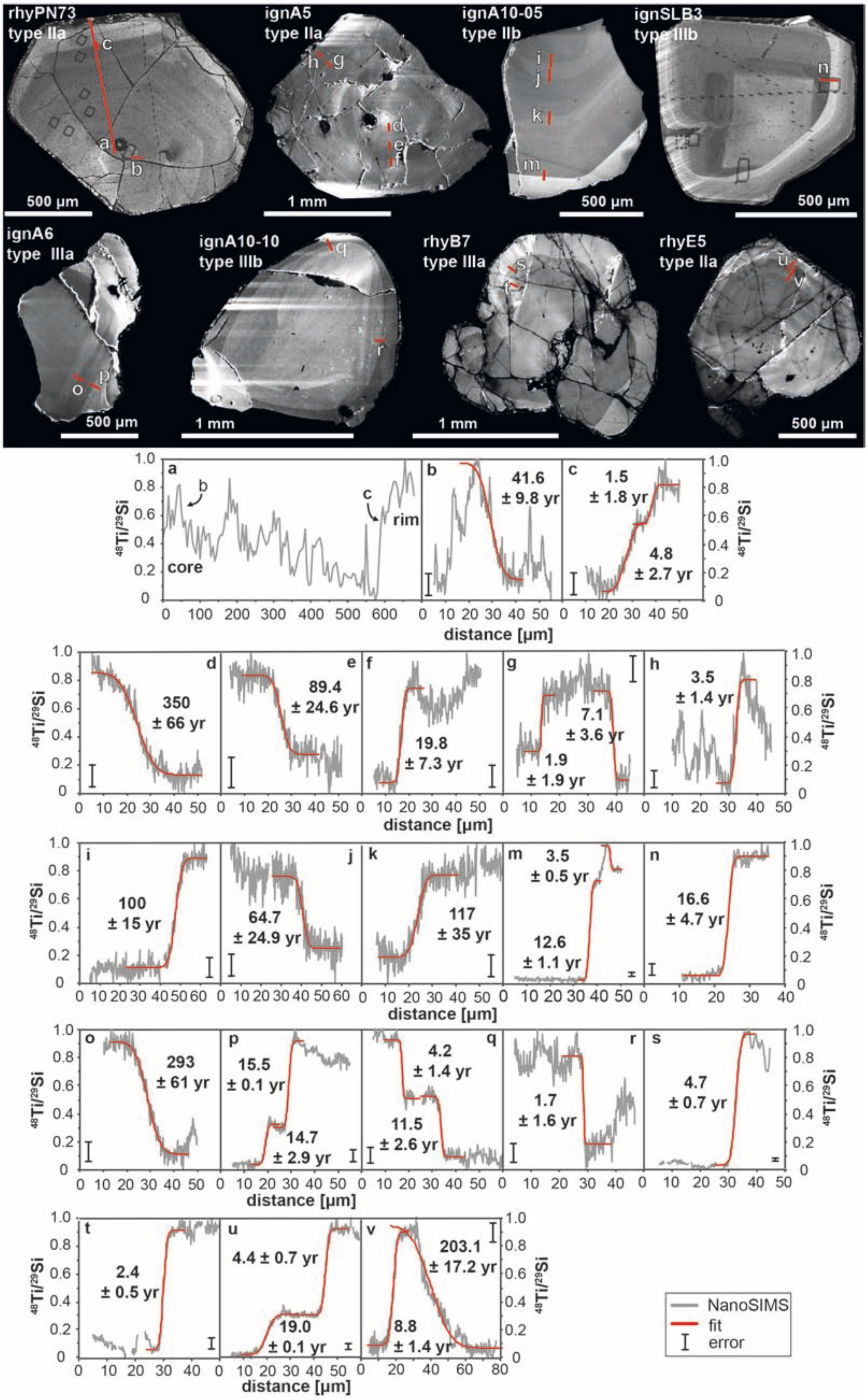

FIGURE 7 | Continued.

FIGURE 7 | CL images of quartz from flows (rhy) and ignimbrites (ign) with the location of the measured NanoSIMS profiles (upper). The corresponding NanoSIMS line scans are shown in the lower **(b–v)**. The orientation of the profiles is from core (left) to rim (right). The data are reported as normalized ^{48}Ti/^{29}Si ratio (gray line). For comparison (see explanation in text), a point profile is shown in **(a)** with the location of the corresponding line scans **(b,c)**. Only line scans were used for diffusion modeling. The fitted diffusion profiles are represented with the red line. The calculated diffusion times are marked in all profiles. Error bars represent the errors of the fit and do not include uncertainties of the diffusion coefficient and activation energy. Sample rhyPN73 and ignSLB3 show also spots of SIMS analysis.

the time estimates. We assume a step-function for the initial profile, since this results in maximum diffusion times, despite the fact that pressure, temperature, or growth velocity changes will most likely result in smooth profiles for Ti-concentrations (e.g., Fowler et al., 2002; L'Heureux, 2013; Seitz et al., 2016; see section Discussion below).

In the following paragraphs, we separately present the results for flows and ignimbrites. A summary of the diffusion times is given in **Figure 8** and **Table 4**.

Rhyolite Flows

Only quartz crystals of type IIa were analyzed by NanoSIMS. The quartz from sample rhyPN73 (**Figure 7**) shows an undisturbed magmatic zoning. A lighter core is surrounded by several darker and lighter zones. The outermost zone is formed by a lighter rim. From core to rim (**Figures 7a–c**, **Table 4**) diffusion times are 41.6 ± 9.8, 4.8 ± 2.7, and 1.5 ± 1.8 yr. Seitz et al. (2016) obtained diffusion times of 5.6 ± 2.2, 4.7 ± 2.0, and 4.1 ± 2.2 yr (shorter diffusion times toward the rim) for sample rhyL5, which is in the same order of magnitude as the rim of sample rhyPN73. CL images from two slightly deformed flow samples reveal that they still preserve their magmatic zonation. The calculated diffusion times from core to rim for sample rhyB7 (**Figures 7s,t**, **Table 4**) are 2.4 ± 0.5 and 4.7 ± 0.7 yr. Diffusion calculation for sample rhyE5 (**Figures 7u,v**, **Table 4**) yields 8.8 ± 1.4, 203 ± 17.2, 19.0 ± 0.1, and 4.4 ± 0.7 yr (from core to rim).

Rhyolitic Ignimbrites

Quartz crystals from class IIa to IIIb were analyzed. Sample ignA5 (type IIa) shows undisturbed normal growth zoning with several lighter and darker zones. The outermost rim is formed by a light zone. We measured several profiles (**Figures 7d–h**) over each major growth zone. Calculation of diffusion times (at 760°C) yield from core to rim 350 ± 67, 89.4 ± 24.6, 19.8 ± 7.3, 1.9 ± 1.9, 7.1 ± 3.6, and 20.7 ± 7.4 yr (**Table 4**). Quartz crystal ignA10-05 and ignA10-10 are from the same sample. IgnA10-05 shows a type IIb quartz with reverse magmatic zonation, here a dark core surrounded by several lighter zones. Over each major zone, we measured a Ti profile (**Figures 7i–m**) and calculated the diffusion time at 760°C. From core to rim they result in 100 ± 15, 64.7 ± 24.9, 117 ± 35, 12.6 ± 1.1, and 3.5 ± 0.5 yr (**Table 4**). The type IIIb crystal (ignA10-10) preserved reverse magmatic zoning with resorption features. A complexly zoned light core is surrounded by a darker overgrowth rim. We measured several profiles (**Figures 7q,r**) over the core-rim interface. The measured profiles were used to calculated diffusion times, those are 4.2 ± 1.4, 11.5 ± 2.6, and 1.7 ± 1.6 yr (**Table 4**). The crystals from samples ignSLB3 and ignA6 belong to type IIIa. They show a more complex zoning with dissolution textures where a darker core is surrounded by

TABLE 4 | Summary of calculated diffusion times at 820°C for flows (rhy) and at 760°C for ignimbrites (ign).

Sample	Zonation	Diffusion time [years]	Location	Initial profile
rhyL5^{a}	IIa			
Figure 2B^{a}		5.6 ± 2.2	Core	sf
Figure 2C^{a}		4.7 ± 2.0	Mantle	sf
Figure 2D^{a}		4.1 ± 2.2	Rim	sf
rhyPN73	IIa			
Profile b		41.6 ± 9.8	Core	sf
Profile c		4.8 ± 2.7	Rim	sf
Profile c		1.5 ± 1.8	Rim	sf
rhyB7	IIIa			
Profile t		4.7 ± 0.7	Rim	cg
Profile s		2.4 ± 0.5	Mantle	cg
rhyE5	IIa			
Profile v		4.4 ± 0.7	Rim	?
Profile v		19.0 ± 0.1	Rim	?
Profile u		203 ± 17	Mantle	deg
Profile u		8.8 ± 1.4	Mantle	deg
ignA5	IIa			
Profile d		350 ± 66 (62.3 ± 12.9)	Core	sf
Profile e		89.4 ± 24.4 (15.6 ± 4.4)	Mantle	sf
Profile f		19.8 ± 7.3 (3.4 ± 1.49	Mantle	sf
Profile g		1.9 ± 1.9 (0.32 ± 0.55)*	Mantle	sf
Profile g		7.1 ± 3.6 (1.2 ± 0.8)	Mantle	deg
Profile h		20.7 ± 7.4 (3.5 ± 1.4)	Rim	deg
ignA6	IIIa			
Profile o		293 ± 61 (51.2 ± 10.7)	Mantle	sf
Profile p		15.5 ± 0.1 (2.64 ± 0.65)	Rim	sf
Profile p		14.7 ± 2.9 (2.58 ± 0.58)	Rim	sf
ignA10-05	IIb			
Profile i		100 ± 15 (17.5 ± 2.6)	Core	sf
Profile j		64.7 ±24.9 (11.4 ± 4.5)	Mantle	sf
Profile k		117 ± 35 (20.4 ± 6.2)	Mantle	deg
Profile m		12.6 ± 1.1 (1.0 ± 0.1)	Rim	sf
Profile m		3.5 ± 0.5 (0.59 ± 0.13)	Rim	sf
ignA10-10	IIIb			
Profile q		4.2 ± 1.4 (0.68 ± 0.32)	Core	cg
Profile q		11.5 ± 2.6 (2.0 ± 0.5)	Rim	cg
Profile r		1.7 ± 1.6 (0.31 ± 0.49)*	Rim	cg
ignSLB3	IIa			
Profile n		16.6 ± 4.7 (2.9 ± 0.9)	Rim	Sf

Corresponding NanoSIMS profiles are shown in ***Figure 7****. sf, step function; deg, disequilibrium growth, cg, cutting geometry.*

Diffusion times in brackets are calculated at 820°C.

**Below minimum time of 2.9 years at 760°C (0.52 years at 820°C); ^{a}Data from Seitz et al. (2016).*

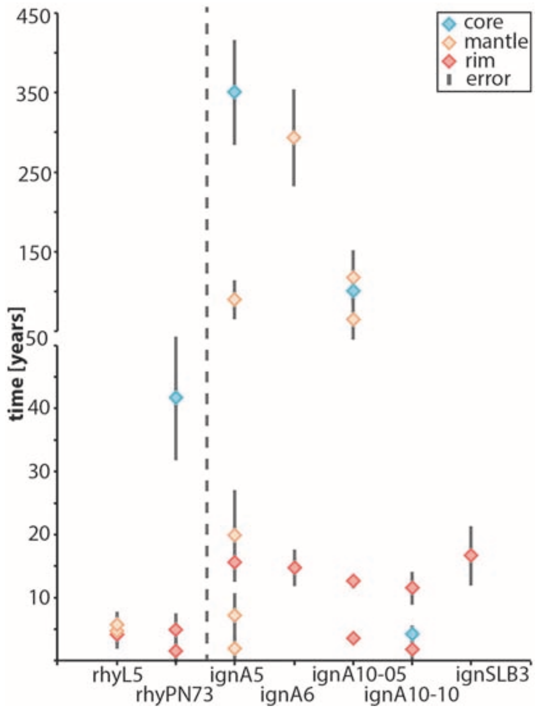

FIGURE 8 | Summary of the calculated diffusion times for the flows (rhyL5 from Seitz et al., 2016) at 820°C and ignimbrites at 760°C. The diffusion time for the overgrowth rim of the ignimbrite samples are in good agreement with the quartz rims from the flows. Note the general trend of shorter diffusion times toward the rim. The deformed flow samples are not shown, as the measured profiles, do not represent clear diffusion profiles.

a lighter overgrowth rim. The profile over the rim of sample ignSLB3 (**Figure 7n**, **Table 4**) gives a diffusion time of 16.6 ± 4.7 yr. For sample ignA6 the core (**Figure 7o**) yields 293 ± 61 yr, the rim (**Figure 7p**, **Table 4**) yields a diffusion time of 15.5 ± 0.1 and 14.7 ± 7.4 yr. For comparison, if the temperature of 820°C is used for diffusion modeling of the ignimbrites, the core profiles in **Figures 7d,i** yield diffusion times as short as 62.3 ± 12.9 and 17.5 ± 2.6 yr.

DISCUSSION

The above textural results show that quartz crystals from ignimbrites have a prolonged and complex history. They often document multiple phases of growth and resorption. Quartz crystals from flows typically have a simpler, and likely shorter history. Most crystals show continuous growth, followed by a single, final stage of resorption. Ignimbrite quartz shows residence and crystallization times which are tens to hundreds of years, depending on the temperature used. Quartz crystallized in less than 5–40 years in flows. In light of the observed differences, we would like to further discuss potential uncertainties and their selective effect on the results from ignimbrites and flows.

A Critical Discussion of Diffusion Chronometry: Importance of Temperature Estimates, Geometry of Zoning Patterns and Spatial Resolution of the Analytical Technique

An important source of uncertainty in diffusion chronology is the temperature-time evolution experienced by the crystal. Temperature has an exponential effect on the diffusion times modeled via Equation (1). A temperature change of ±50°C would change the calculated diffusion time by about one order of magnitude (Spear, 2014). We therefor sought the most realistic estimation for the minimum temperature of quartz crystallization to obtain maximum diffusion times. The 4QT temperature estimation describe most accurately the quartz crystallization temperature as it accounts for textural observations (4% quartz crystals in flows). Additionally, it investigates the pressure sensitivity and the effect of the water content of the melt on the temperature. For this reason, we applied the latter temperature for the diffusion modeling. While we used conservative estimates for the temperature, it is clear that the absolute values of the residence and crystallization times might have a large uncertainty. Below we discuss additional factors that influence the obtained crystallization and residence times. We focus on the effects these have on the flows as compared to the ignimbrites.

Slow cooling of flows and ignimbrites after eruption could result in prolonged cooling times and broaden the diffusion profiles. The relatively small thickness of the flows resulted in fast cooling, which, together with the exponentially decreasing diffusion coefficient with temperature, will minimize the effect of cooling on the calculated diffusion times. The minimum temperature used (820°C) should be therefore a good approximation. The ignimbrites virtually cool instantaneously upon eruptions. Hence, the differences in timescales between flows and ignimbrites would be increasing, since quartz crystallization times of flows would be overestimated, while those of the ignimbrites would not change.

The rhyolite-MELTS modeling suggests that dissolution of quartz is either due to temperature increase, pressure decrease or decrease of the water activity (a_{H2O}) in the melt. Typically those changes are thought to be caused by injection of new magma (e.g., Wark et al., 2007). Events of dissolution occurred in quite a few crystals in the ignimbrites. Looking at the differences in zoning textures in ignimbrites and flows, it is clear that many quartz crystals are antecrysts or xenocrysts. Hence estimating temperature of formation and storage of grains before incorporation into the magma which leads to the eruption is challenging. As such, diffusion times calculated for these grains are highly uncertain.

The 3D-geometry associated with the Ti-profile critically influences the slope due to intersection geometry (see e.g., Shea et al., 2015; Krimer and Costa, 2017). The use of micro-tomography permits cutting through the morphological center of quartz crystals to reduce the danger of oblique cuts through the Ti-zonation, which would artificially increase the diffusion times obtained. Finding the morphological center is quite feasible for crystals which show undisturbed magmatic growth zoning parallel to the crystal faces. Resorbed crystals, with dissolution and resorption textures, make it more difficult to interpret the initial geometry, hence the probability for oblique cuts is higher. We measured the depth of each NanoSIMS profile with a Bruker Contour GT 3D optical microscope (**Figure 9**). The acquisition depth varies between 10 and 100 nm. Thus, the ratio between profile depth and beam size (∼650 nm) is small. Hence, in all but the most oblique cuts this should not influence the profile slopes in a significant way. Finally, cutting the crystals perpendicular to the c-axis permitted to reduce uncertainties due to diffusion directions in quartz.

Naturally, the spatial resolution of the analytical method is essential for a robust interpretation of diffusion data (e.g., Saunders et al., 2014; Ferry et al., 2015; Till et al., 2015; Seitz et al., 2016); namely to resolve magmatic processes at an annual timescale, a spatial resolution in the sub-micrometer scale is required. We measured Ti-in quartz transect with a spatial resolution of ∼650 nm. This returns a minimum resolvable time interval of 0.52 yr at 820°C and 2.9 yr at 760°C (using the data from Cherniak et al., 2007).

The initial shape of a diffusion profile is essential for diffusion chronometry. Usually a step profile is taken to present the initial condition prior to diffusion (Costa et al., 2008; Zhang, 2010), since this results in a maximum diffusion time. This assumption might be suitable in cases where an instantaneous change of the melt composition occurs. Nevertheless, intrusion of a new magma, even close by, will result in dissolution, and subsequent cooling should result in a continuous profile. Similarly, a rapid pressure decrease at constant composition (due to an eruption) would likely result in dissolution, and a subsequent pressure increase in precipitation; this would also produce a continuous profile. Till et al. (2015) showed for example, that even for the formation of a new overgrowth rim, the assumption of a step profile might be the wrong choice. Oscillatory zoning of feldspar or zircon e.g., is proposed to be the result of disequilibrium growth as a result of variations in the growth rate and the self-regulation of the boundary layer (Allègre et al., 1981; Fowler et al., 2002; L'Heureux, 2013), and similar mechanisms were implied for quartz growth (e.g., Pamukcu et al., 2015, 2016; Seitz et al., 2016). This mechanism would cause exponential changes in elemental concentration, where the initial slope of the diffusion profile depends on the ratio between the growth rates and element diffusion rate in the melt. A growth-rate-dependent incorporation of trace elements in minerals crystallizing from a melt has been proposed (e.g., Ginibre et al., 2002; Shea et al., 2015) and experimentally observed by Huang and Audétat (2012) for quartz in a fluid. It is, thus, likely that initial profiles were smooth functions of distance, not step functions. Since the initial profiles were most likely flatter at the start of diffusion, times are overestimated. In some cases, it is possible to show that indeed no step function was present. **Table 4** provides a summary of this discussion listing all investigated samples.

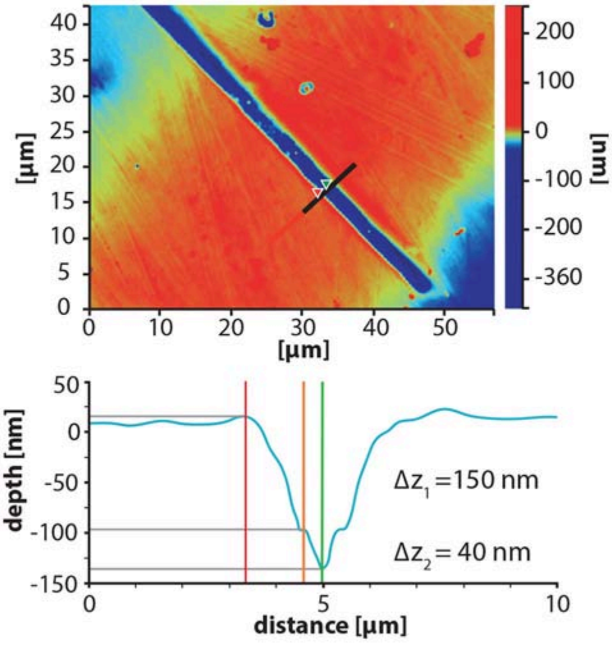

FIGURE 9 | Typical depth profile of a NanoSIMS profile obtained with Bruker Contour GT 3D optical microscope. $\Delta = z_1$ is the total depth (pre-sputtering and acquisition), $\Delta = z_2$ is the depth of the acquisition.

The quartz crystal from the ignimbrite sample ignA5 (**Figure 7**) shows undisturbed growth zoning. The fit for the profiles **Figures 7d–f** continuously resolve shorter diffusion times from core toward the rim (350 ± 66, 89.4 ± 24.6, and 19.8 ± 7.3 yr). The three outer profiles (**Figures 7g–h**), in contrast, show an inverse correlation. The calculated diffusion times are getting longer toward the rim with 1.9 ± 1.9 yr (this is below the resolvable minimum time of 2.9 yr at 760°C), 7.1 ± 3.6 and 20.7 ± 7.4 yr). Obviously, internal zones experienced diffusion before the outer zones were crystallized, along with the whole history experienced by the outer zones. We believe that the larger times obtained in the outer zones are due to concentration profiles which were no step functions, but most likely exponential, due to disequilibrium growth. The shortest calculated diffusion time is shorter than the resolvable minimum time due to spatial resolution of the NanoSIMS spots. Consequently, the rim grew less than 2.9 yr before eruption. Similar observation can be made by looking at sample ignA10-05. The diffusion time obtained for profile in **Figure 7k** is also overestimated (117 ± 35 yr). The diffusion times of 64.7 ± 24.9 and 12.6 ± 1.1 yr, as suggested by the profiles in **Figures 7j,m** represent the maximum growth and residence times.

The quartz crystal from sample ignA10-10 shows a complexly zoned light core with a darker rim. Dissolution texture can be observed at the core-rim interface. The diffusion times calculated for two traverses across the rim (**Figures 7q,r**) are not the same. They vary between 11.5 ± 2.6 and 1.7 ± 1.6 yr, which is below the resolvable minimum time (see above). In addition, for profile **Figure 7q** the diffusion time calculated for the innermost profile results in shorter times (4.2 ± 1.4 yr) than the outermost profile (11.5 ± 2.6 yr). This discrepancy could be either explained by an effect of the cutting geometry in relation to the core-rim interface or by the invalid assumption of a step profile as initial condition or a combination of both. It follows, that the rim grew in less than 4.2 yr before eruption.

Two samples, rhyB7 and rhyE5, are from slightly deformed flows. Nevertheless, they preserved the magmatic zonation. The crystal from sample rhyB7 belongs to class IIIa. We measured a profile over the interface of the two overgrowth rims (**Figures 7s,t**). The calculated diffusion times are increasing toward the rim, yielding 2.4 ± 0.5 and 4.7 ± 0.7 yr, respectively. As mentioned before, this could be either explained by an effect of the cutting geometry in relation to the core-rim interface or by exponential initial profiles or a combination of both. For sample rhyE5 we measured two profiles across the outer zones (**Figures 7u,v**). From the inner to the outer most profile the calculated diffusion times are 8.8 ± 1.4, 203 ± 17, 19.0 ± 0.1, and 4.4 ± 0.7 yr. The profile in **Figure 7v** is highly asymmetric and it is unlikely that the initial profile of the right part (yielding the longest diffusion times of 203.1 ± 17.2 yr) was a step function. The shape of the profile rather argues for disequilibrium growth.

Linking Quartz Zoning Patterns, P-T Constraints and Timescales

There are clear differences of quartz zoning observed between the flows and the ignimbrites of the El Quemado Complex in the study area. The flows are crystal poor; the majority of quartz crystals show uninterrupted rhythmic zoning, as well as a late stage dissolution along the rims. This indicates a "single stage crystallization" terminated by a single dissolution event. Crystallization and dissolution occurred rapidly, as indicated by the small diffusion times obtained. There is no indication of changing host magma around the crystal during growth. Given that the crystals erupted in a crystal poor magma, the simplest explanation is to attribute the dissolution features observed to decompression during eruption (see below). Hence the majority of the crystals document a simple, 1-stage cooling, followed by eruption.

On the other hand, ignimbrites are crystal-rich and contain quartz crystals that commonly display rhythmic zoning interrupted by dissolution, followed by additional rhythmic quartz precipitation. Dissolution textures in the interior part of the crystal lead to roundish cores, rarely to lobate textures. Hence dissolution was homogenous in ignimbrites, rather than lobate, as in flows, suggesting close to equilibrium dissolution. In addition, dissolution textures on the quartz surface are rare in ignimbrites. Residence and growth times for quartz crystals are difficult to estimate exactly, because of the uncertainty of the determination of quartz crystallization temperatures. Nevertheless, if times are calculated at the most likely temperature of remobilization of the crystals, e.g., 760°C, times obtained are significantly longer. Even if times are calculated at the same temperature as for the flows (820°C) the times obtained cluster toward the upper end of the times measured. We interpret the complex history to record repeated cooling and heating during a prolonged growth.

Depth and Geometry and of the Magmatic Reservoirs

It was possible to constrain pressure and temperature of quartz crystallization for the flows to either a pressure of 0.3–0.6 GPa or less than 0.1 GPa (**Table 2**), depending on the pressure calibration used for the Ti-content in quartz. The lowest pressures we obtained for quartz crystallization in flows range between 0.05 and 0.1 GPa for a water free melt, using rhyolite-MELTS and the calibration for TitaniQ of Huang and Audétat (2012). Temperatures are between 1070° and 1110°C (see **Table 2**). This crystallization environment is depicted as Model 1 in **Figure 10**.

The idea of a shallow magma reservoir is compatible with many models and studies, which suggest the presence of a crystal-poor melt in the upper crust—either as pocket or more often as "melt cap" connected to an underlying mush (see review in Bachmann and Huber, 2016). The high temperature estimates we obtained (ca. 1100°C) require a virtually water free magma. In this model, the diffusion times reported in **Table 4** for the flows have to be reduced by 2 orders of magnitude, requiring rapid crystallization of quartz, and the dissolution of the crystals would be due to heating just prior to eruption. However, vesicles are abundant in these rocks, suggesting that they contained a significant amount of water, released upon solidification.

In Model 2 (**Figure 10**) the higher pressures of 0.3–0.6 GPa (**Table 4**) using the pressure dependence proposed by Thomas et al. in 2010 requires crystallization of quartz in a deep-seated environment. As the magmas of the El Quemado Complex were generated in an extensional regime during the break-up of Gondwana (Pankhurst et al., 2000), the estimated depth of 10–20 km would correspond to depth of the lower crust. For example, the crustal thickness of the Afar depression, East African Rift system, is varying between 16 and 26 km with a normal thickness of the crust in this region outside the rift zone of about 35–45 km (e.g., Hammond et al., 2011). Quartz crystals would have to crystalize during a cooling initiated a few years prior to eruption, and final quartz dissolution would be the result of decompression during ascent for eruption.

A decision based on phase petrology criteria between the two models presented above will only be possible once improved thermodynamic data for the Ti-in quartz and activity models for Ti in melts becomes available. In addition, additional studies are required to better understand the reasons for oscillatory quartz growth, to be able to estimate potential disequilibrium during growth (L'Heureux, 2013; Pamukcu et al., 2016).

A reliable estimate of pressure-temperature conditions for the formation of quartz in ignimbrites could not be obtained since the complex growth/dissolution/regrowth history suggests that they are to a great extent antecrysts. The protracted, complicated growth history is most likely due to their residence in a mush environment. The lack of a pressure estimate makes it impossible to place the mush at a specific depth in the crust. Hence, we suggest to follow earlier proposals, and place the storage of the mush in the upper crust (e.g., Bachmann and Bergantz, 2008; Bachmann and Huber, 2016).

Figure 10 summarizes in a schematic model the results obtained. Model 1 depicts a single magma chamber with a crystal-rich mush at its base and the crystal-free cape. The majority of investigated quartz crystals in the rhyolites will be phenocrysts; they are unzoned or show simple zoning pattern (type I and type II), and dissolution is evident only at crystal surfaces due to heating before eruption. The few crystals with complex zoning would have been introduced into the flow from the mush below. Since both ignimbrites and flows originate from the magma chamber, it would be surprizing that only quartzes from flows experienced abundant quartz resorption during or immediately prior to eruption, while quartz crystals in ignimbrites escaped this dissolution. Alternatively, the dissolution could be due to decompression, in which case it would be even less comprehensible, that this was only experienced by the crystals in the flow.

It is simpler to explain the significant differences in textures using a multi-stage model as shown in model 2. The main difference is that we use the pressures obtained using the Thomas et al. (2010) Ti in quartz pressures dependence. These pressures are 0.3–0.6 GPa, (**Table 2**). Flows, show simple quartz textures suggesting a magma evolution dominated by one major quartz growth event before eruption (**Figure 11**). The ascent rate must have been rather fast without important cooling during magma ascent, as we observe late stage decompression driven quartz dissolution resulting in embayments of the rims. Such embayement texture is hence interpreted to be due to rapid decompression, as has also been argued by e.g., Girard et al. (2001) and Loewen et al. (2017). While most (95%) of the quartz

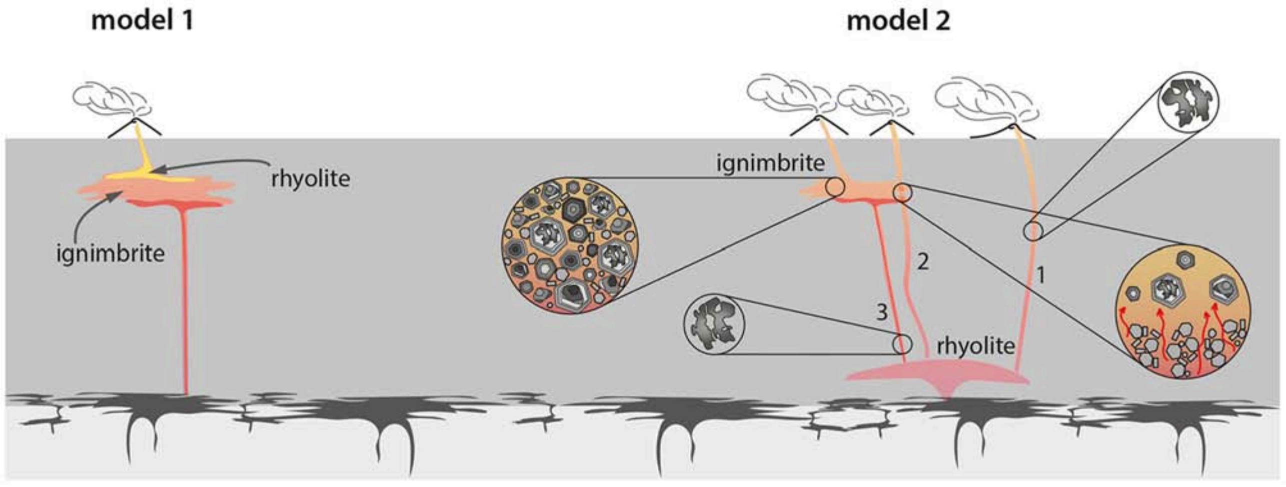

FIGURE 10 | Proposed models for the generation of rhyolitic ignimbrites and flows. For a detailed description of the different models see discussion. Flows and ignimbrites are extracted from a single magma chamber in the upper crust (model 1) at pressures below 0.1 GPa. Flows and ignimbrites are extracted from two different magma chambers (model 2) at various depth. Flows crystallized in a magma chamber in the lower crust at pressures of 0.4–0.7 GPa. They can be either directly extracted (path 1) or interact with an upper magma chamber (path 2) where they picked up a notable amount of antecrysts. Rapid ascent resulted in embayments of the rim. Ignimbrites were extracted from a magma chamber, which experienced several rejuvenation events, resulting in roundish quartz dissolution textures. Recharge from a lower magma chamber (path 3) carried also quartz crystals with embayments textures. Sketch not to scale.

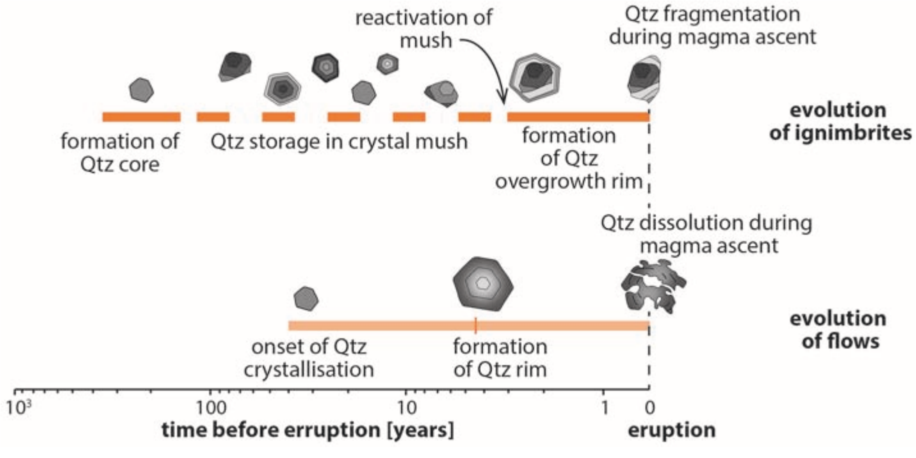

FIGURE 11 | Timescales of the evolution of the rhyolitic ignimbrites and rhyolitic flows of the El Quemado Complex.

crystals can be explained by this simple magma evolution (path 1 in model 2, **Figure 10**), there is a small amount of quartz crystals (5%) with internal dissolution textures, similar to those observed in ignimbrites (type III in **Figures 4**, **5**), which must be considered antecrysts. Those crystals could have been picked up by the magmas passing the crystal mush in the upper crust, shortly before eruption. The amount of crystals studied, and especially the amount of rhyolite samples studied does not allow us to conclude if all magmas passed by the mush (path 2, model 2) or if some magmas arrived at the surface without interacting with the mush (path 1, model 2). The presence of these type III quartz antecrysts opens up the possibility that these crystal poor rhyolites might even represent the part of the magma which triggered ignimbrite eruption. At this point it is not possible to be more affirmative, since detailed maps and stratigraphic sections are lacking for the study area.

The crystal-rich ignimbrites contain quartz crystals with a great variability of zoning textures and many reveal internal dissolution textures in CL images. Dissolution and new phenocryst rim growth are commonly interpreted to reflect changes in temperature, pressure, or a_{H2O} in response to heating, decompression, and/or addition of volatiles to the system (Bachmann et al., 2002; Wark et al., 2007; Cashman and Blundy, 2013). This is often thought to be linked to an intrusion of a new hot magma, which might be the marker of processes leading to the final eruption (Chamberlain et al., 2014) or the "trigger" itself (Wark et al., 2007). In both cases this indicates the rejuvenation of the crystal mush. We argue that a process of rejuvenation is recorded by over 70% of type III quartz crystals, as indicated by their roundish internal dissolution surfaces.

Timescales

Quartz crystals from rhyolitic lava flows display simple oscillatory CL zoning and diffusion chronometry suggest short timescale for quartz crystallization between 5.6 and 41.6 years. Since these were calculated using a minimum temperature, they are maximum crystallization times for these crystals. The timescales are indeed short and require growth for the zoned crystals only years before eruption. Nevertheless, there is a significant amount of quartz crystals (ca. 40%) which are not zoned. They could be crystals which grew homogeneously, in which case they contain no discernable information for diffusion chronology, or they were homogenized. In this case, they represent crystals which spend very long time at high temperatures in the magma, and they are the early crystallized crystals at depth during initial cooling.

Modeling of diffusion times is hampered in the ignimbrites by the challenging temperature estimations. It is difficult to account for temperature fluctuation expected in a crystal mush (for a discussion see Cooper and Kent, 2014). In fact, if crystals cooled significantly below 700°C, which would result in temporary solidification, this time interval would be barely recorded in the diffusion interval. The rejuvenation events, in contrast, would be preferentially recorded due to accelerated diffusion. However, it is reasonable to assume the formation of overgrowth rims occurred at temperatures above 700°C. Comparing diffusion times for the crystal-rich ignimbrite yields two disparate timescales: core values are significantly longer than the time allowed for the rim. This might indicate that crystals were stuck in a mush for hundreds to thousands of years, and then eruption occurred relatively fast. Actual times calculated depend on the temperatures used (see **Table 4**). At 760°C, storage could have been up to 350 years. Taking the 820°C minimum temperature of the rhyolite flows to represent an estimate for the mush reactivation temperature, the final quartz rims in ignimbrites would have to have grown not more than 2.9 yrs before eruption (**Figure 11**).

Interesting is the similarity in timescales for the final quartz growth event from ignimbrites and flows, as it implies reactivation of crystal-rich magma occurs at the same short timescales as the mobilization of crystal-poor magmas. However, numerical models predict different timescales for the reactivation of crystal-rich vs. crystal-poor magmas. Huber et al. (2012), for example, proposed 100–1,000 years for crystal-rich mushes and a few years for crystal-poor magmas. Yet, in conceptual models (e.g., Parmigiani et al., 2016) discussing the conditions that allow crystal-rich magmas to be evacuated, the predicted timescales for reactivation vary widely: from months to tens of years (Burgisser and Bergantz, 2012) to thousands of years (Huber et al., 2012), also depending on the mechanism of reactivation proposed and the size of the magma reservoir. Our data would support rapid reactivation but are not conclusive due to limited temperature estimates.

This study took advantage of the high resolution capacity of the NanoSIMS, and the quartz data from the EL Quemado Complex provide compelling evidence for sharp internal boundaries, providing a robust estimation of time scales. The here presented diffusion times corroborate evidence in support of short magmatic times scales (**Table 4**) in accordance with recent works from well investigated silicic systems (**Table 1**). For example, month to a few thousands of years were found for the Bishop Tuff, USA (Wark et al., 2007; Gualda et al., 2012; Chamberlain et al., 2014; Pamukcu et al., 2015; Till et al., 2015). Tens to ten-thousands of years for the Taupo Volcanic Zone, New Zealand (Saunders et al., 2010; Matthews et al., 2012; Pamukcu et al., 2015).

Our study highlights the potential of NanoSIMS techniques. A series of recent works review the applications, potential and limitations of using diffusion profiles to constrain times scales (Costa et al., 2008; Saunders et al., 2014; Shea et al., 2015; Bradshaw and Kent, 2017; Kohn and Penniston-Dorland, 2017; Krimer and Costa, 2017). These studies conclude that the analytical spatial resolution is the most important factor controlling the accuracy of short time scales obtained from diffusion modeling (Bradshaw and Kent, 2017). In addition, NanoSIMS permits analyses of a large range of trace elements (e.g., Till et al., 2015; Seitz et al., 2016; Manzini et al., 2017) and provides thus the potential number of elements that can be used for diffusion modeling (across and within minerals or samples). Importantly, it allows verification of the diffusing element(s). Testing the analytical capacities (and their limits) of in-situ techniques such as NanoSIMS will result in a better understanding of the often complex chemical patterns observed and offer new insights into the geological significance of short-duration events. Finally, this study attest to the robustness of quartz as magmatic tracer. Quartz - in absence of recrystallization—can be used to decipher magmatic time scales even in old volcanic formations—the El Quemado Complex is of Jurassic age—where most of the crystal cargo, such as feldspar or hornblende, might be altered and thus cannot be used for diffusion modeling.

CONCLUSION

Our results from the El Quemado Complex highlight the difference between crystal-poor rhyolitic lava flows and crystal-rich rhyolitic ignimbrites. The El Quemado rhyolitic flows provide good evidence for the rapid extraction from a deep reservoir, transport, and eruption predicted for a crystal-poor melt. Rhyolitic ignimbrites, have a more complex, and likely protracted history as would be expected for a crystal-rich magma or mush. We propose that the small- to medium-sized eruptions were generated by ascending isolated magma batches from low-crustal magma chambers, at pressures between 0.3 GPa and 0.6 GPa. The flows erupted shortly (5–40 years) after initial onset of quartz crystallization (**Figure 11**), though some early crystals might have been homogenized (group I crystals) indicating an early crystallization. Decompression-driven quartz dissolution occurred during magma ascent, resulting in the observed embayments on the rims of the crystals. During magma ascent, flows extracted minor amounts of quartz crystals with internal dissolution textures from an upper magma chamber. The ignimbrites were most likely extracted from a shallow magma chamber. Quartz zoning textures suggest that this magma chamber experienced several recharge and rejuvenation events. The whole evolution of the ignimbrite took at least 350 years, though prolonged storage in sub-solidus conditions can of course not be excluded. The formation of the quartz overgrowth rim, observed in ignimbrite samples, occurred at temperatures similar to the crystallization temperature of the flows. Accordingly, the last stage of the evolution of the ignimbrite took place within a few years (<3 years), similar to the timescales observed for the flow. This implies that crystal-rich ignimbrites can be mobilized for eruption as fast as crystal poor flows.

AUTHOR CONTRIBUTIONS

All authors were actively involved in this project, and participated in writing and editing of the presented manuscript. SS, as first author, obtained a Ph.D. at the University of Lausanne in 2016 and this manuscript is part of her thesis work on oxygen isotope data and magmatic timescales from the Chon Aike Province in Patagonia (Argentina). She has carried the major workload in sample preparation (starting from field work), analyses (CL, tomography, NanoSIMS, SIMS) and writing of the manuscript. BP was the Ph.D. director and principal PI of the project and is responsible for the design (and finances) of the project and gave support in divers analytical aspects (e.g., tomography). Diffusion modeling benefited especially from the expertise of LB (Co-PI of the project). As director of the SwissSIMS he also granted access to the laboratory. BP and LB were also very much involved in the discussion and manuscript editing. AM, as director of the NanoSIMS introduced us to the NanoSIMS and generously granted accesses to his laboratory. SE as his lab manager signed responsible for the technical aspects during the analytical sessions. A-SB, the SIMS-lab manager, carried out the Ti-concentration measurements at the SwissSIMS.

ACKNOWLEDGMENTS

We thank the authorities of the Parque Nacional de los Glaciares (Argentina) for the permission to sample and the rangers in El Chaltén for their support. A special thank you goes to A. Kosmal (El Chaltén) for his hospitality, logistic support and geological insights. We also like to thank our field assistants N. Buchs and E. May for their help. We thank P. Vonlanthen for the introduction to the cathodoluminescence laboratory. We thank L. Caricchi and O. Müntener for discussions. We greatly acknowledge the constructive suggestions by T. Ubide and C. Deering, which have led to a significant improvement of the manuscript. We acknowledge funding by the Swiss National Science Foundation to BP and LB (200020_172513, 200021_153094) and KIP 6 funding for the Center for Advanced Surface Analysis (to LB and AM).

SUPPLEMENTARY MATERIAL

The Supplementary Material for this article can be found online at: https://www.frontiersin.org/articles/10.3389/feart.2018.00095/full#supplementary-material

REFERENCES

Allan, A. S. R., Morgan, D. J., Wilson, C. J. N., and Millet, M.-A. (2013). From mush to eruption in centuries: assembly of the super-sized Oruanui magma body. *Contrib. Mineral. Petrol.* 166, 143–164. doi: 10.1007/s00410-013-0869-2

Allègre, C. J., Provost, A., and Jaupart, C. (1981). Oscillatory zoning: a pathological case of crystal growth. *Nature* 294, 223–228. doi: 10.1038/294223a0

Aragón, E., Rodriguez, A. M. I., and Benialgo, A. (1996). A calderas field at the Marifil Formation, new volcanogenic interpretation, Norpatagonian Massif, Argentina. *J. S. Ame. Earth Sci.* 9, 321–328. doi: 10.1016/S0895-9811(96)00017-X

Audétat, A., Garbe-Schönberg, D., Kronz, A., Pettke, T., Rusk, B., Donovan, J. J., et al. (2014). Characterisation of a natural quartz crystal as a reference material for microanalytical determination of Ti, Al, Li, Fe, Mn, Ga and Ge. *Geostand. Geoanal. Res.* 39, 171–184. doi: 10.1111/j.1751-908X.2014.00309.x

Bachmann, O., and Bergantz, G. W. (2004). On the Origin of crystal-poor rhyolites: extracted from batholithic crystal mushes. *J. Petrol.* 45, 1565–1582. doi: 10.1093/petrology/egh019

Bachmann, O., and Bergantz, G. W. (2008). Rhyolites and their Source Mushes across Tectonic Settings. *J. Petrol.* 49, 2277–2285. doi: 10.1093/petrology/egn068

Bachmann, O., Dungan, M. A., and Lipman, P. W. (2002). The Fish Canyon magma body, san juan volcanic field, colorado: rejuvenation and eruption of an upper-crustal batholith. *J. Petrol.* 43, 1469–1503. doi: 10.1093/petrology/43.8.1469

Bachmann, O., and Huber, C. (2016). Silicic magma reservoirs in the Earth's crust. *Am. Mineral.* 101, 2377–2404. doi: 10.2138/am-2016-5675

Barboni, M., and Schoene, B. (2014). Short eruption window revealed by absolute crystal growth rates in a granitic magma. *Nat. Geosci.* 7, 524–528. doi: 10.1038/ngeo2185

Bradshaw, R. W., and Kent, A. J. R. (2017). The analytical limits of modeling short diffusion timescales. *Chem. Geol.* 466, 667–677. doi: 10.1016/j.chemgeo.2017.07.018

Bryan, S. E., Riley, T. R., Jerram, D. A., Stephens, C. J., and Leat, P. T. (2002). "Silicic volcanism: an undervalued component of large igneous provinces and volcanic rifted margins," in *Volcanic Rifted Margins,* eds M. A. Menzies, S. L. Klemperer, C. J. Ebinger, and J. Baker (Boulder, CO: Geological Society of America), 99–120.

Burgisser, A., and Bergantz, G. W. (2012). A rapid mechanism to remobilize and homogenize highly crystalline magma bodies. *Nature* 471, 212–215. doi: 10.1038/nature09799

Cashman, K. V., and Blundy, J. D. (2013). Petrological cannibalism: the chemical and textural consequences of incremental magma body growth. *Contrib. Mineral. Petrol.* 166, 703–729. doi: 10.1007/s00410-013-0895-0

Cashman, K. V., and Giordano, G. (2014). Calderas and magma reservoirs. *J. Volcanol. Geothermal. Res.* 288, 28–45. doi: 10.1016/j.jvolgeores.2014.09.007

Chamberlain, K. J., Morgan, D. J., and Wilson, C. J. N. (2014). Timescales of mixing and mobilisation in the bishop tuff magma body: perspectives from diffusion chronometry. *Contrib. Mineral. Petrol.* 168:1034. doi: 10.1007/s00410-014-1034-2

Charlier, B. L. A., Morgan, D. J., Wilson, C. J. N., Wooden, J. L., Allan, A. S. R., and Baker, J. A. (2012). Lithium concentration gradients in feldspar and quartz record the final minutes of magma ascent in an explosive supereruption. *Earth Planet. Sci. Lett.* 319–320, 218–227. doi: 10.1016/j.epsl.2011.12.016

Cherniak, D. J., Watson, E. B., and Wark, D. A. (2007). Ti diffusion in quartz. *Chem. Geol.* 236, 65–74. doi: 10.1016/j.chemgeo.2006.09.001

Cooper, G. F., and Wilson, C. J. N. (2014). Development, mobilisation and eruption of a large crystal-rich rhyolite: the ongatiti ignimbrite, New Zealand. *Lithos* 198–199, 38–57. doi: 10.1016/j.lithos.2014.03.014

Cooper, K. M., and Kent, A. J. R. (2014). Rapid remobilization of magmatic crystals kept in cold storage. *Nature* 506, 480–483. doi: 10.1038/nature12991

Costa, F., Dohmen, R., and Chakraborty, S. (2008). Time scales of magmatic processes from modeling the zoning patterns of crystals. *Rev.Mineral. Geochem.* 69, 545–594. doi: 10.2138/rmg.2008.69.14

Druitt, T. H., Costa, F., Deloule, E., Dungan, M. A., and Scaillet, B. (2012). Decadal to monthly timescales of magma transfer and reservoir growth at a caldera volcano. *Nature* 482, 77–80. doi: 10.1038/nature10706

Ferry, J. M., Stubbs, J. E., Xu, H., Guan, Y., and Eiler, J. M. (2015). Ankerite grains with dolomite cores: a diffusion chronometer for low- to medium-grade regionally metamorphosed clastic sediments. *Ame. Mineral.* 100, 2443–2457. doi: 10.2138/am-2015-5209

Fildani, A., and Hessler, A. M. (2005). Stratigraphic record across a retroarc basin inversion: rocas verdes–magallanes basin, patagonian andes, chile. *Geol. Soc. Am. Bull.* 117:1596. doi: 10.1130/B25708.1

Fowler, A. D., Prokoph, A., Stern, R. A., and Dupuis, C. (2002). Organization of oscillatory zoning in zircon: analysis, scaling, geochemistry, and model of a zircon from Kipawa, Quebec, Canada. *Geochim. Cosmochim. Acta* 66, 311–328. doi: 10.1016/S0016-7037(01)00774-8

Ghiorso, M. S., and Gualda, G. A. R. (2015). An H_2O–CO_2 mixed fluid saturation model compatible with rhyolite-MELTS. *Contrib. Mineral. Petrol.* 169, 1–30. doi: 10.1007/s00410-015-1141-8

Ginibre, C., Wörner, G., and Kronz, A. (2002). Minor- and trace-element zoning in plagioclase: implications for magma chamber processes at Parinacota volcano, northern Chile. *Contrib. Mineral. Petrol.* 143, 300–315. doi: 10.1007/s00410-002-0351-z

Girard, J.-P., Munz, I. A., Johansen, H., Hill, S., and Canham, A. (2001). Conditions and timing of quartz cementation in Brent reservoirs, Hild Field, North Sea: constraints from fluid inclusions and SIMS oxygen isotope microanalysis. *Chem. Geol.* 176, 73–92. doi: 10.1016/S0009-2541(00)00350-8

Götze, J., Plötze, M., and Habermann, D. (2001). Origin, spectral characteristics and practical applications of the cathodoluminescence (CL) of quartz – a review. *Mineral. Petrol.* 71, 225–250. doi: 10.1007/s007100170040

Gualda, G. A. R., Ghiorso, M. S., Lemons, R. V., and Carley, T. L. (2012). Rhyolite-MELTS: a modified calibration of MELTS optimized for Silica-rich, Fluid-bearing magmatic systems. *J. Petrol.* 53, 875–890. doi: 10.1093/petrology/egr080

Hammond, J. O. S., Kendall, J.-M., Stuart, G. W., Keir, D., Ebinger, C., Ayele, A., et al. (2011). The nature of the crust beneath the Afar triple junction: evidence from receiver functions. *Geochem. Geophys. Geosyst.* 12:Q12004. doi: 10.1029/2011GC003738

Hayden, L. A., and Watson, E. B. (2007). Rutile saturation in hydrous siliceous melts and its bearing on Ti-thermometry of quartz and zircon. *Earth Planet. Sci. Lett.* 258, 561–568. doi: 10.1016/j.epsl.2007.04.020

Hellebrand, E., Snow, J. E., Mostefaoui, S., and Hoppe, P. (2005). Trace element distribution between orthopyroxene and clinopyroxene in peridotites from the Gakkel Ridge: a SIMS and NanoSIMS study. *Contrib. Mineral. Petrol.* 150, 486–504. doi: 10.1007/s00410-005-0036-5

Hervé, F., Calderón, M., Massonne, H. J., and Theye, T. (2007). Metamorphic P-T conditions of Late Jurassic rhyolites in the Magallanes fold and thrust belt, Patagonian Andes, Chile. *J. Iberian Geol.* 33, 5–16. doi: 10.1016/j.lithos.2007.01.007

Hildreth, W. (2004). Volcanological perspectives on long valley, mammoth mountain, and mono craters: several contiguous but discrete systems. *J. Volcanol. Geothermal Res.* 136, 169–198. doi: 10.1016/j.jvolgeores.2004.05.019

Huang, R., and Audétat, A. (2012). The titanium-in-quartz (TitaniQ) thermobarometer: a critical examination and re-calibration. *Geochim. Cosmochim. Acta* 84, 75–89. doi: 10.1016/j.gca.2012.01.009

Huber, C., Bachmann, O., and Dufek, J. (2012). Crystal-poor versus crystal-rich ignimbrites: a competition between stirring and reactivation. *Geology* 40, 115–118. doi: 10.1130/G32425.1

Kohn, M. J., and Penniston-Dorland, S. C. (2017). Diffusion: obstacles and opportunities in petrochronology. *Rev. Mineral. Geochem.* 83, 103–152. doi: 10.1515/9783110561890-005

Krimer, D., and Costa, F. (2017). Evaluation of the effects of 3D diffusion, crystal geometry, and initial conditions on retrieved time-scales from Fe-Mg zoning in natural oriented orthopyroxene crystals. *Geochim. Cosmochim. Acta* 196, 271–288. doi: 10.1016/j.gca.2016.09.037

Leresche, S. (2013). Etude Structurale, Géochimique, Géochronologique et Pétrographique d'une Partie Des Roches Encaissantes à l'Est de l'Intrusion du Mt. Fitz Roy (Patagonie, Argentine). Lausanne: University of Lausanne.

Leuthold, J., Müntener, O., Baumgartner, L. P., Putlitz, B., and Chiaradia, M. (2012). A detailed geochemical study of a shallow arc-related laccolith; the torres del paine mafic complex (Patagonia). *J. Petrol.* 54, 273–303.. doi: 10.1093/petrology/egs069

L'Heureux, I. (2013). Self-organized rhythmic patterns in geochemical systems. *Philosophical Transactions R. Soc. A Mathematical, Phys. Eng. Sci.* 371:20120356 doi: 10.1098/rsta.2012.0356

Llanos, M. P. I., Lanza, R., Riccardi, A. C., Geuna, S., Laurenzi, M. A., and Ruffini, R. (2003). Palaeomagnetic study of the El quemado complex and marifil formation, patagonian jurassic igneous province, argentina. *Geophys. J. International.* 154, 599–617. doi: 10.1046/j.1365-246X.2003.01923.x

Lloyd, A. S., Ruprecht, P., Hauri, E. H., Rose, W., Gonnermann, H. M., and Plank, T. (2014). NanoSIMS results from olivine-hosted melt embayments: magma ascent rate during explosive basaltic eruptions. *J. Volcanol. Geothermal Res.* 283, 1–18. doi: 10.1016/j.jvolgeores.2014.06.002

Loewen, M. W., Bindeman, I. N., and Melnik, O. E. (2017). Eruption mechanisms and short duration of large rhyolitic lava flows of yellowstone. *Earth Planet. Sci. Lett.* 458, 80–91. doi: 10.1016/j.epsl.2016.10.034

Manzini, M., Bouvier, A.-S., Baumgartner, L. P., Müntener, O., Rose-Koga, E. F., Schiano, P., et al. (2017). Weekly to monthly time scale of melt inclusion entrapment prior to eruption recorded by phosphorus distribution in olivine from mid-ocean ridges. *Geology* 45, 1059–1062. doi: 10.1130/G39463.1

Matthews, N. E., Pyle, D. M., Smith, V. C., Wilson, C. J. N., Huber, C., and van Hinsberg, V. (2012). Quartz zoning and the pre-eruptive evolution of the ∼340-ka Whakamaru magma systems, New Zealand. *Contrib. Mineral. Petrol.* 163, 87–107. doi: 10.1007/s00410-011-0660-1

Michel, J., Baumgartner, L. P., Putlitz, B., Schaltegger, U., and Ovtcharova, M. (2008). Incremental growth of the patagonian torres del paine laccolith over 90 k.y. *Geology* 36, 459–462. doi: 10.1130/G24546A.1

Miller, C. F., McDowell, S. M., and Mapes, R. W. (2003). Hot and cold granites? Implications of zircon saturation temperatures and preservation of inheritance. *Geology* 31, 529–532. doi: 10.1130/0091-7613(2003)031<0529:HACGIO>2.0.CO;2

Nescher, P. (2013). *Petrography, Structural Geology, Geochemistry and Metamorphism of the Rocks in the Eastern Fitz Roy Foothills in Patagonia, Argentina*. Lausanne: University of Lausanne.

Pamukcu, A. S., Ghiorso, M. S., and Gualda, G. A. R. (2016). High-Ti, bright-CL rims in volcanic quartz: a result of very rapid growth. *Contrib. Mineral. Petrol.* 171, 1–9. doi: 10.1007/s00410-016-1317-x

Pamukcu, A. S., Gualda, G. A. R., Bégué, F., and Gravley, D. M. (2015). Melt inclusion shapes: timekeepers of short-lived giant magma bodies. *Geology* 43, 947–950. doi: 10.1130/G37021.1

Pankhurst, R. J., Leat, P. T., Sruoga, P., Rapela, C. W., Márquez, M., Storey, B. C., et al. (1998). The chon aike province of patagonia and related rocks in West Antarctica: a silicic large igneous province. *J. Volcanol. Geothermal. Res.* 81, 113–136. doi: 10.1016/S0377-0273(97)00070-X

Pankhurst, R. J., Riley, T. R., Fanning, C. M., and Kelley, S. P. (2000). Episodic silicic volcanism in patagonia and the antarctic peninsula: chronology of magmatism associated with the break-up of Gondwana. *J. Petrol.* 41, 605–625. doi: 10.1093/petrology/41.5.605

Parmigiani, A., Faroughi, S., Huber, C., Bachmann, O., and Su, Y. (2016). Bubble accumulation and its role in the evolution of magma reservoirs in the upper crust. *Nature* 532, 492–495. doi: 10.1038/nature17401

Press, W. H., Teukolsky, S. A., Vetterling, W. T., and Flannery, B. P. (1992). "Numerical recipes," in *The Art of Scientific Computing, 2nd Edn* (New York, NY: Cambridge University Press), 1–1018.

Ramírez de Arellano, C., Putlitz, B., Müntener, O., and Ovtcharova, M. (2012). High precision U/Pb zircon dating of the Chaltén Plutonic Complex (Cerro Fitz Roy, Patagonia) and its relationship to arc migration in the southernmost Andes. *Tectonics* 31:TC400. doi: 10.1029/2011TC003048

Riley, T. R., Flowerdew, M. J., Hunter, M. A., and Whitehouse, M. J. (2010). Middle jurassic rhyolite volcanism of eastern Graham Land, Antarctic Peninsula: age correlations and stratigraphic relationships. *Geol. Mag.* 147, 581–595. doi: 10.1017/S0016756809990720

Saunders, K. E., Buse, B., Kilburn, M. R., Kearns, S., and Blundy, J. D. (2014). Nanoscale characterisation of crystal zoning. *Chem. Geol.* 364, 20–32. doi: 10.1016/j.chemgeo.2013.11.019

Saunders, K. E., Morgan, D. J., Baker, J. A., and Wysoczanski, R. J. (2010). The Magmatic evolution of the whakamaru supereruption, New Zealand, constrained by a microanalytical study of plagioclase and quartz. *J. Petrol.* 51, 2465–2488. doi: 10.1093/petrology/egq064

Seitz, S. (2016). *Oxygen Isotope Data and Constraints on Magmatic Timescales From the Chon Aike Province (Patagonia, Argentina)*. dissertation, Université de Lausanne, Lausanne.

Seitz, S., Putlitz, B., Baumgartner, L. P., Escrig, S., Meibom, A., and Bouvier, A.-S. (2016). Short magmatic residence times of quartz phenocrysts in Patagonian rhyolites associated with Gondwana breakup. *Geology* 44, 67–70. doi: 10.1130/G37232.1

Shea, T., Lynn, K. J., and Garcia, M. O. (2015). Cracking the olivine zoning code: distinguishing between crystal growth and diffusion. *Geology* 43, 935–938. doi: 10.1130/G37082.1

Singer, B. S., Costa, F., Herrin, J. S., Hildreth, W., and Fierstein, J. (2016). The timing of compositionally-zoned magma reservoirs and mafic "priming" weeks before the 1912 novarupta-katmai rhyolite eruption. *Earth Planet. Sci. Lett.* 451, 125–137. doi: 10.1016/j.epsl.2016.07.015

Skora, S., Baumgartner, L. P., Mahlen, N. J., Johnson, C. M., Pilet, S., and Hellebrand, E. (2006). Diffusion-limited REE uptake by eclogite garnets and its consequences for Lu–Hf and Sm–Nd geochronology. *Contrib. Mineral. Petrol.* 152, 703–720. doi: 10.1007/s00410-006-0128-x

Spear, F. S. (2014). The duration of near-peak metamorphism from diffusion modelling of garnet zoning. *J. Metamorph. Geol.* 32, 903–914. doi: 10.1111/jmg.12099

Spear, F. S., and Wark, D. A. (2009). Cathodoluminescence imaging and titanium thermometry in metamorphic quartz. *J. Metamorph. Geol.* 27, 187–205. doi: 10.1111/j.1525-1314.2009.00813.x

Streck, M. J. (2008). Mineral textures and zoning as evidence for open system processes. *Rev. Mineral. Geochem.* 69, 595–622. doi: 10.2138/rmg.2008.69.15

Thomas, J. B., Bruce Watson, E., Spear, F. S., Shemella, P. T., Nayak, S. K., and Lanzirotti, A. (2010). TitaniQ under pressure: the effect of pressure and temperature on the solubility of Ti in quartz. *Contrib. Mineral. Petrol.* 160, 743–759. doi: 10.1007/s00410-010-0505-3

Till, C. B., Vazquez, J. A., and Boyce, J. W. (2015). Months between rejuvenation and volcanic eruption at Yellowstone caldera, Wyoming. *Geology* 43, 695–698. doi: 10.1130/G36862.1

Turner, S. P., and Costa, F. (2007). Measuring timescales of magmatic evolution. *Elements* 3, 267–272. doi: 10.2113/gselements.3.4.267

Wark, D. A., Hildreth, W., Spear, F. S., Cherniak, D. J., and Watson, E. B. (2007). Pre-eruption recharge of the Bishop magma system. *Geology* 35:235. doi: 10.1130/G23316A.1

Wark, D. A., and Spear, F. S. (2005). Ti in quartz: Cathodoluminescence and thermometry. *Geochim. Cosmochim. Acta Suppl.* 69:592.

Wark, D. A., and Watson, E. B. (2006). TitaniQ: a titanium-in-quartz geothermometer. *Contrib. Mineral. Petrol.* 152, 743–754. doi: 10.1007/s00410-006-0132-1

Watson, E. B., and Harrison, T. M. (1983). Zircon saturation revisited: temperature and composition effects in a variety of crustal magma types. *Earth Planet. Sci. Lett.* 64, 295–304. doi: 10.1016/0012-821X(83)90211-X

Wotzlaw, J.-F., Bindeman, I. N., Watts, K. E., Schmitt, A. K., Caricchi, L., and Schaltegger, U. (2014). Linking rapid magma reservoir assembly and eruption trigger mechanisms at evolved Yellowstone-type supervolcanoes. *Geology* 42, 807–810. doi: 10.1130/G35979.1

Zhang, Y. (2010). Diffusion in minerals and melts: theoretical background. *Rev. Mineral. Geochem.* 72, 5–59. doi: 10.2138/rmg.2010.72.2

Conflict of Interest Statement: The authors declare that the research was conducted in the absence of any commercial or financial relationships that could be construed as a potential conflict of interest.

frontiers in Earth Science

ORIGINAL RESEARCH
published: 20 August 2018
doi: 10.3389/feart.2018.00117

Unraveling the Physics of the Yellowstone Magmatic System Using Geodynamic Simulations

Georg S. Reuber[1]*, *Boris J. P. Kaus*[1,2,3], *Anton A. Popov*[1] and *Tobias S. Baumann*[1]

[1] Institute of Geosciences, Johannes Gutenberg University, Mainz, Germany, [2] Center for Computational Sciences Mainz, Johannes Gutenberg University, Mainz, Germany, [3] Volcanoes, Atmospheres and Magmatic Open Systems Research Center, Johannes Gutenberg University, Mainz, Germany

The Yellowstone magmatic system is one of the largest magmatic systems on Earth, and thus an ideal location to study magmatic processes. Whereas previous seismic tomography results could only image a shallow magma reservoir, a recent study using more seismometers showed that a second and massive partially molten mush reservoir exists above the Moho (Huang et al., 2015). To understand the measurable surface response of this system to visco-elasto-plastic deformation, it is thus important to take the whole system from the mantle plume up to the shallow magma reservoirs into account. Here, we employ lithospheric-scale 3D visco-elasto-plastic geodynamic models to test the influence of parameters such as the connectivity of the reservoirs and rheology of the lithosphere on the dynamics of the system. A gravity inversion is used to constrain the effective density of the magma reservoirs, and an adjoint modeling approach reveals the key model parameters affecting the surface velocity. Model results show that a combination of connected reservoirs with plastic rheology can explain the recorded slow vertical surface uplift rates of around 1.2 cm/year, as representing a long term background signal. A geodynamic inversion to fit the model to observed GPS surface velocities reveals that the magnitude of surface uplift varies strongly with the viscosity difference between the reservoirs and the crust. Even though stress directions have not been used as inversion parameters, modeled stress orientations are consistent with observations. However, phases of larger uplift velocities can also result from magma reservoir inflation which is a short term effect. We consider two approaches: (1) overpressure in the magma reservoir in the asthenosphere and (2) inflation of the uppermost reservoir prescribed by an internal kinematic boundary condition. We demonstrate that the asthenosphere inflation has a smaller effect on the surface velocities in comparison with the uppermost reservoir inflation. We show that the pure buoyant uplift of magma bodies in combination with magma reservoir inflation can explain (varying) observed uplift rates at the example of the Yellowstone volcanic system.

Keywords: yellowstone, 3D modeling, inversion, adjoint, magmatic systems, geodynamics

Edited by:
Mattia Pistone,
Université de Lausanne, Switzerland

Reviewed by:
Catherine Annen,
University of Bristol, United Kingdom
Oleg E. Melnik,
Lomonosov Moscow State University, Russia
Jamie Farrell,
University of Utah, United States

Correspondence:
Georg S. Reuber
reuber@uni-mainz.de

Specialty section:
This article was submitted to Volcanology, a section of the journal Frontiers in Earth Science

Received: *06 February 2018*
Accepted: *30 July 2018*
Published: *20 August 2018*

Citation:
Reuber GS, Kaus BJP, Popov AA and Baumann TS (2018) Unraveling the Physics of the Yellowstone Magmatic System Using Geodynamic Simulations. Front. Earth Sci. 6:117. doi: 10.3389/feart.2018.00117

1. INTRODUCTION

Understanding magmatic systems has been a long-standing research topic within the solid-Earth geosciences. To understand the underlying processes better, several volcanic areas on the Earth have been geophysically monitored, geologically mapped and interpreted. At the same time numerical or analog models have been developed to unravel the mechanical driving forces. As a result, a paradigm shift has happened over the last decade, and we now know that magmatic systems are lithospheric-scale systems composed by many smaller pulses of melt (Cashman et al., 2017). Yet, our understanding of the physics of such systems remains somewhat limited.

Classically, models have been used to link surface deformation data to the depth, size and overpressure of a magma reservoir. If the rocks are elastic and the magma reservoir is spherical and embedded in an infinite halfspace, an analytical solution exists (Mogi, 1958). This approach has been widely applied, for example, to show that surface uplift above the Hekla volcano (Iceland) is consistent with a reservoir at 8 km depth (Lanari et al., 1998), to constrain the depth of the magma source beneath Etna (Kjartansson and Gronvold, 1983), or to reproduce cyclicity in ground deformation at Montserrat as a result of pressurization of a dike-conduit system (Hautmann et al., 2009). The Mogi approach has been extended to account for topographic effects and crustal heterogeneities in both 2D (e.g., Trasatti et al., 2003) and 3D (e.g., Manconi et al., 2010). Furthermore, the analytical solution has been extended to include viscous effects, for example by Del Negro et al. (2009), who compare the temperature-dependent visco-elastic to the elastic solution and show that the required overpressures to fit observed uplift at Etna is about a third lower in the visco-elastic case, which is more consistent with the lithospheric stress state. Such overpressures may nevertheless exceed the yield strength of crustal host rocks, in which case the material deforms plastically rather than (visco-)elastic. An evaluation of such elasto-plastic effects shows that these produce higher uplift rates for the same overpressure (Currenti et al., 2010; Gerbault et al., 2012). Davis et al. (1974) argue that at Hawaii this will likely result in fracturing of the host rock around the magma reservoir and result in a net of pathways, which is inconsistent with spherical source of overpressure. Battaglia and Segall (2004) also point out the limitations of the assumption that magmatic bodies are spherical, and show that whereas uplift rates can often be reproduced with a spherical models, the resulting depth of the source is incorrect.

Many of these previous studies focus on upper-crustal magma reservoirs and consider a single pulse of magma. Yet, as magmatic systems are likely formed by many pulses, it is important to take those into account, as done by Degruyter and Huber (2014) who investigated the effect of pulses on the style and frequency of eruptions and provide scaling laws for mechanical locking of the magma reservoir due to thermal cooling. The work by Annen (2011) and Annen and Sparks (2002) demonstrates that subsequent magmatic pulses help keep the system hot and partially molten, which may significantly change the mechanics of magma transport once a critical amount of heating has occurred (Karlstrom et al., 2017).

Seismic tomography studies of magmatic systems give important insights into the 3D structure at depth. Yet, interpreting these results in terms of melt content with depth is not straightforward as the seismic wavelengths themselves are several kilometers in size and the distribution of seismometers is often sub-optimal. Some attempts have been made to perform a joint inversion in which thermal models and melting parameterizations are combined with tomographic inversions. Results for Montserrat show that melt fractions obtained in this manner are substantially larger than those directly inferred from interpreting seismic data (Paulatto et al., 2012). Yet, whereas this gives important new insights in the geometry of the system, it does not tell much about the physics of magmatic systems, which is the focus of our work.

We use the Yellowstone magmatic system (Wyoming, US) as a case study, as it is one of the best studied volcanic systems on Earth that has a significant hazard potential having ejected around 1000 km^3 during the last eruption (∼640 ka). A comprehensive summary on the evolution and petrology of the Yellowstone magmatic system is given by Christiansen (2001). Geophysically, Yellowstone is a well-studied area. **Figure 1** summarizes the available observational data constraints that include gravity anomaly, GPS uplift velocities for a period of high activity from 2003 to 2008 (Vasco et al., 2007), and the orientation of the minimum principal stress (Waite and Smith, 2004). Furthermore, Smith and Braile (1994) and Smith et al. (2009) give an overview over the seismic tomography, earthquakes, surface uplift and stress orientations within and at the system. Even though the exact geometry of the Yellowstone magmatic system remains under discussion, recent publications,

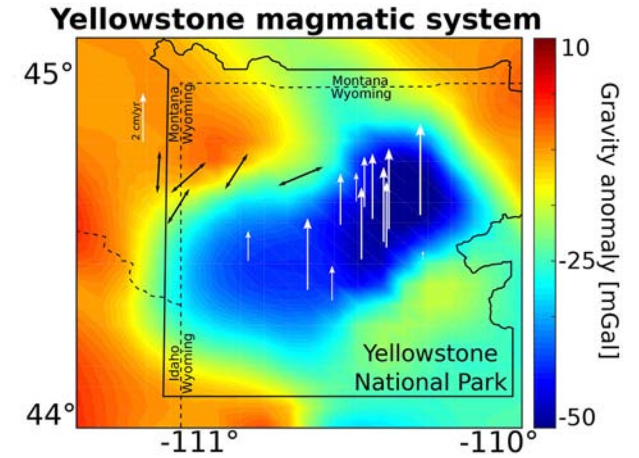

FIGURE 1 | Overview of some geophysical data for Yellowstone used in this work. The area corresponds to the computational domain presented in this work. Colors indicate the bouguer gravity anomaly in the area referenced to the anomaly close to the boundary of the area. Data is taken from the online archive of the Pan American Center for Earth and Environmental Sciences (PACES) and DeNosaquo et al. (2009). White vertical arrows indicate the GPS velocities during a period of high activity from 2003 to 2008 (Vasco et al., 2007). Black arrows represent the orientation of the minimum principal stress (σ_3) (taken from Waite and Smith (2004) and references therein).

(e.g., Huang et al., 2015 based on seismic tomography), suggest that the system extends over lithospheric scales ranging from a deep mantle plume over a magma reservoir within the lower crust at a depth of 40 km (~46,000 km^3) to a shallow magma reservoir (~10,000 km^3) in the upper crust at a depth of 15 km. A 2D numerical study of the Yellowstone magmatic system has been published very recently (Colón et al., 2018). They investigated the effect of rheological changes in the magma reservoir during the emplacement of the magma bodies. A thermal mantle plume emplaced in the asthenosphere results after several Ma in strong magmatic reworking of the crust. Due to rheological contrasts at the crust-mantle (Moho) transition and the lower-upper crustal (Conrad) transition, magmas may stall at such locations and experience chemical differentiation (e.g., fractional differentiation from basalt to rhyolite). As a conclusion the authors highlight the importance of taking the large scale dynamics (lithosphere scale) and complex rheologies of crust and mantle into account while studying magmatic systems. However, with the current computing capacity it is unfeasible to systematically study the full evolution of such systems in 3D. Our aims are to fit the present day geophysical observations by instantaneous numerical models and to understand the processes that influence these observables. In particular we want to investigate the effect of a visco-elasto-plastic rheology on the surface observables in combination with the effect of inflation of the magmatic chambers. We retrieve the present day geometry by interpreting the tomographic results and converting the velocity anomalies into a 3D geometry of the magma reservoirs. We then perform instantaneous 3D mechanical models of the system, taking the visco-elasto-plastic rheology of rocks into account and compare model predictions with present day data. An instantaneous numerical model is usually described as the solution of the numerical model after one time step, as such the model is essentially not time dependent. Since we include elasticity in the models we refer to the term instantaneous as the solution of the numerical model after reaching elastic relaxation (see Supplementary Material in **Appendix 2**).

Recently, it was shown that geodynamic inversion frameworks can serve as a powerful tool to link geophysical observations with thermo-mechanically consistent deformation models to infer rheological properties of the crust and lithosphere (Baumann et al., 2014; Baumann and Kaus, 2015). Here, we apply a gradient-based adjoint inversion technique combined with data assimilation (Ratnaswamy et al., 2015) to constrain the dynamics of the Yellowstone magmatic system, and discuss whether full 3D models are required for such systems, or 2D models are sufficient. In the following sections we describe the underlying numerical method (Kaus et al., 2016), the adjoint inversion framework, and provide some background on the thermodynamical modeling that is incorporated in this study. We present two different approaches to simulate the effect of inflation of a crustal magma reservoir, while simultaneously taking the buoyancy effect of the lithospheric-scale magmatic system into account. We systematically test the effect of rheological complexities on surface uplift and incorporate the most successful of these models in an inversion approach to constrain the material parameters from data.

2. METHODS

2.1. Physics and Numerics

In this work we solve for the conservation of momentum and mass in a compressible formulation. For a domain Ω with a boundary $\partial\Omega$ the underlying coupled equation system is given by:

$$\frac{\partial \tau_{ij}}{\partial x_j} - \frac{\partial P}{\partial x_i} + \rho g_i = 0, \tag{1}$$

$$\frac{1}{K}\frac{DP}{Dt} + \frac{\partial v_i}{\partial x_i} = 0. \tag{2}$$

Here $x_i (i = 1, 2, 3)$ denotes Cartesian coordinates, v_i is the velocity vector, P is the pressure, τ_{ij} is the Cauchy deviator stress tensor, ρ is the density, g_i is the gravity acceleration vector, K is the elastic bulk modulus, and D/Dt stands for the material time derivative. Here and below we imply the Einstein summation convention. Due to a moderate time span of the models considered in this work ($\sim 10^4$ years), we ignore the effect of temperature advection and diffusion, and therefore omit the solution of the energy balance equation. On a free-slip boundary with a normal vector pointing in i-th direction we enforce the following condition:

$$v_i = \overline{v}, \quad \frac{\partial v_j}{\partial x_i} = 0, \quad j \neq i, \tag{3}$$

where $\overline{v}$ is the normal velocity component. On a no-slip boundary we apply $v_i = 0$.

The deviatoric stress tensor is defined by a set of visco-elasto-plastic constitutive equations of the form:

$$\dot{\varepsilon}_{ij} = \dot{\varepsilon}_{ij}^{el} + \dot{\varepsilon}_{ij}^{vs} + \dot{\varepsilon}_{ij}^{pl} = \frac{\overset{\diamond}{\tau}_{ij}}{2G} + \frac{\tau_{ij}}{2\eta} + \dot{\gamma}\frac{\partial Q}{\partial \tau_{ij}}, \tag{4}$$

$$\dot{\varepsilon}_{ij} = \frac{1}{2}\left(\frac{\partial v_i}{\partial x_j} + \frac{\partial v_j}{\partial x_i}\right) - \frac{1}{3}\frac{\partial v_k}{\partial x_k}\delta_{ij}, \tag{5}$$

$$\overset{\diamond}{\tau}_{ij} = \frac{\partial \tau_{ij}}{\partial t} + \tau_{ik}\omega_{kj} - \omega_{ik}\tau_{kj}, \tag{6}$$

$$\omega_{ij} = \frac{1}{2}\left(\frac{\partial v_i}{\partial x_j} - \frac{\partial v_j}{\partial x_i}\right), \tag{7}$$

where $\dot{\varepsilon}_{ij}$ is the total deviatoric strain rate tensor, δ_{ij} is the Kronecker delta, the superscripts el, vs, and pl correspond to elastic, viscous, and plastic strain rate components, respectively, G is the elastic shear modulus, $\overset{\diamond}{\tau}_{ij}$ is the Jaumann objective stress rate, ω_{ij} is the spin tensor, η is the creep viscosity, $\dot{\gamma}$ is the magnitude of plastic strain rate (plastic multiplier), and Q is the plastic potential function. The effective viscosity is defined as a function of temperature, and strain-rate according to the dislocation creep mechanism (e.g., Kameyama et al., 1999):

$$\eta = \frac{1}{2}\left(B_n\right)^{-\frac{1}{n}}\left(\dot{\varepsilon}_{II}\right)^{\frac{1}{n}-1}\exp\left(\frac{E_n}{nRT}\right). \tag{8}$$

In the above expression, $\dot{\varepsilon}_{II} = \left(\frac{1}{2}\dot{\varepsilon}_{ij}\dot{\varepsilon}_{ij}\right)^{1/2}$ denotes the effective strain rate measure (square root of the second invariant), n is the stress exponent of the dislocation creep, and B_n, E_n, are the creep constant, and activation energy, respectively, R is the gas constant and T is temperature.

The magnitude of plastic multiplier is determined by enforcing the Drucker-Prager failure criterion (Drucker and Prager, 1952), given by:

$$F = \tau_{II} - \sin(\phi)\, P - \cos(\phi)\, C \leq 0, \tag{9}$$

where $\tau_{II} = \left(\frac{1}{2}\tau_{ij}\tau_{ij}\right)^{1/2}$ is the effective deviatoric stress, ϕ is the friction angle, and C is the cohesion. To prevent the non-symmetry in the Jacobian matrix required by the adjoint method (see section 2.2) we use the lithostatic, instead of the fully dynamic pressure in the equation (9) in the simulations presented here. In this work we do not consider the effect of strain softening on the friction and cohesion parameters, since we solve instantaneous models. Softening would require time integration of the plastic strain. We adopt the dilatation-free non-associative Prandtl-Reuss flow rule, defined by the following plastic potential function:

$$Q = \tau_{II} \tag{10}$$

The dependence of the density field on the pressure and temperature is assumed to be given by a phase diagram (see section 2.3). The computation is performed externally using the consistent thermodynamic modeling with Perple_X. The feedback between density and influencing parameters is updated every nonlinear iteration.

We discretize and solve a coupled set of conservation and constitutive equations using 3D thermo-mechanical code LaMEM (Kaus et al., 2016), which is based on a staggered finite differences approximation (e.g., Harlow and Welsh, 1965; Gerya and Yuen, 2007; Tackley, 2008). The material properties are advected using a marker-and-cell method (Harlow and Welsh, 1965). To guarantee the computational stability for a large time step we employ a stabilized free surface boundary condition using the sticky-air approach (Kaus et al., 2010; Duretz et al., 2011). Nonlinearities are handled by a preconditioned Jacobian-Free Newton-Krylov (JFNK) method with line-search as implemented in the PETSc SNES nonlinear solver framework (Balay et al., 2016). The gravity anomaly computation adopted in LaMEM is based on a rectangular prism approximation (e.g., Plouff, 1976; Turcotte and Schubert, 2014). Further information regarding the computational efficiency of LaMEM, and the computational infrastructure used to compute the models is given in Supplementary Material in **Appendix 1**.

2.2. Adjoint Equations

The adjoint method for solving inverse problems is a powerful tool (e.g., Ismail-Zadeh et al., 2003). It is essentially based on a gradient-based inversion approach such as BFGS (Broyden-Fletcher-Goldfarb-Shanno) Quasi-Newton method (e.g., Ratnaswamy et al. (2015)). The gradients of the cost function with respect to model parameters are computed using an efficient (adjoint) procedure. The adjoint operator allows for the computation of all material gradients at once with the cost of only one linear solve. The adjoint gradients computation can be summarized as follows:

$$\psi = \left(\boldsymbol{J}^T\right)^{-1} \left(\frac{\partial F}{\partial \boldsymbol{x}}\right)^T, \tag{11}$$

$$\frac{dF}{d\boldsymbol{p}} = -\psi^T \frac{\partial \boldsymbol{r}}{\partial \boldsymbol{p}}, \tag{12}$$

where $\boldsymbol{p}$ is the model parameter vector, e.g., densities, viscosities, etc., $\boldsymbol{J} = \partial \boldsymbol{r}/\partial \boldsymbol{x}$ is the Jacobian matrix of the forward problem, namely the derivative of the residual ($\boldsymbol{r}$) with respect the solution vector ($\boldsymbol{x}$), F is the objective (cost) function, quantifying the misfit between the observations and simulation results. The partial derivatives $\partial \boldsymbol{r}/\partial \boldsymbol{p}$ might be difficult to compute analytically. In these cases they can be approximated by finite differences. Numerical codes that solve the nonlinear equations by a Newton-Raphson method usually have the Jacobian matrix readily available. The adjoint gradient computation procedure can be rendered efficient since it only involves a single linear solve irrespective of the number of gradients.

The adjoint gradients can be used not only to solve the inverse problem but also to quantify the influence of model parameters on the model solution, i.e., to construct a scaling law (Reuber et al., in press). The essence of the adjoint scaling law can be briefly summarized as follows. We start with redefining the cost function (F) to be an arbitrary solution parameter of the forward model, e.g., (non-dimensional) velocity, instead of the misfit between the model and observation. Next, we assume that the actual scaling law for the solution parameter (F) can be approximated by the following multiplicative from:

$$F \approx A_F\, p_1^{b_1}\, p_2^{b_2} \ldots p_n^{b_n}, \tag{13}$$

where A_F is the dimensionally-consistent prefactor. We can now conveniently compute the scaling exponents (b_i) of the approximate scaling law using the following expressions:

$$b_i = \frac{dF}{dp_i}\,\frac{p_i}{F}. \tag{14}$$

Here we use adjoint gradient procedure (Equations 11, 12) to estimate the derivatives of the solution parameter (F) with respect to models parameters ($\boldsymbol{p}$).

2.3. Thermodynamic Modeling

To create a thermodynamically consistent model of the Yellowstone magmatic system, we use the thermodynamic modeling tool Perple_X (Connolly, 2009), version 6.7.4. Perple_X is freely available software which ensures the reproducibility of the results shown in this work. Furthermore, Perple_X has already proven its applicability to the field of thermomechanical modeling in multiple publications (e.g., Baumann et al., 2010; Angiboust et al., 2012; Koptev et al., 2016, in press). By Gibbs free energy minimization Perple_X computes material properties including phase changes. Here, we use it to compute rock densities as functions of pressure and temperature. The calculations were performed using the database of Holland and

TABLE 1 | Major element composition (in weight percent oxide) for all rock types used in this work.

Oxide	Rhyolite[b]	Upper crust[a]	Basalt[b]	Lower crust[a]
SiO_2	72.29	66.62	49.51	53.40
TiO_2	0.16	0.64	2.28	0.82
Al_2O_3	13.40	15.40	15.96	16.90
FeO	0.00	5.04	9.00	8.57
MnO	0.04	0.10	0.18	0.10
MgO	0.20	2.48	6.27	7.24
CaO	0.85	3.59	9.79	9.59
Na_2O	2.77	3.27	2.69	2.65
K_2O	5.40	2.80	0.57	0.61
H_2O	1.82	3.00	1.00	1.50

[a] *Rudnick and Gao (2003)*
[b] *Christiansen (2001)*

Powell (1998). As an approximation for the crust surrounding the Yellowstone magmatic reservoirs we take the average crust compositions from Rudnick and Gao (2003), described in **Table 1**.

To generate an initial guess for the effective densities of the magma reservoirs we used the method described in Bottinga and Weill (1970) for the whole rock data analysis described by Christiansen (2001). The used rock composition is shown in **Table 1**. In the gravity inversion, we vary the density between the completely molten and solid end-members to find a fit to the gravity signal.

3. MODEL SETUP AND DATA INTEGRATION

The seismic study of Huang et al. (2015) represents the most recent seismic tomography model of the Yellowstone magmatic system, including a mantle plume and two distinct magma reservoirs in the lower and upper crust, respectively. We make use of their interpretation of the velocity anomalies and construct a 3D geometry of the magma reservoirs by digitizing the horizontal and vertical cross sections from Huang et al. (2015). The geometry on the horizontal and vertical sections was subsequently turned into a 3D model using the freely available software package geomIO (Baumann and Bauville, 2016). The computational domain includes the entire Yellowstone National Park and the eastern part of Idaho, which is roughly 110 km in East-West and 120 km in North-South direction, respectively (see **Figure 2**). The depth of the domain is restricted to 90 km, combined with an internal free surface at 0 km, overlain by a 10 km thick free-air layer (Crameri et al., 2012). The numerical resolution is 128 × 128 × 256 nodes in x, y and z direction. All boundaries are treated as free slip. The first two kilometers of the domain consist of a sediment layer. This layer represents a weak (potentially fractured due to hydrothermal activity, e.g., Morgan, 2007) cap. It is followed by 12 km of upper crust including the shallow magma reservoir. The lower crust includes the lower magma reservoir and extends 36 km in the vertical direction. The bottom of the domain is defined by the mantle lithosphere until a depth of 70 km and followed by asthenosphere. A connection of the mantle plume to the lower boundary simulates the connection to the deeper mantle. Additionally, connection channels are added to the model setup between the plume and the reservoirs, which can be activated to simulate weak connective areas, comparable to diking areas. Inflation of the magma reservoirs from the deeper mantle can be simulated by applying an overpressure at the lower bottom in the region of this connection. Alternatively, simultaneous deflation and inflation of the reservoirs in the lower and upper crust, respectively, can be simulated by activating a kinematic internal boundary condition inside the connection between the reservoirs.

The temperature structure consists of three linear geotherms. In the sediment and the upper crust the geotherm is 15 K/km, followed by 3 K/km in the lower crust and lithosphere and 0.5 K/km for the rest of the domain. The surface temperature is assumed to be 0°C. We make the assumption that the surrounding material behaves like an "average" crust. As such the geotherm represents more the crust far away from the Yellowstone system. With this assumption the effect of the temperature in our models is of second order importance compared to the input of the thermodynamic model and the effective (constant) viscosity of the magma reservoirs, that already represents a composite hotter zone of partially molten rock. The effect of the temperature on the reservoirs is simulated by increasing the composite viscosity of the partially molten zones, representing a lower melt fraction. Our aim is to study the direct effect of the density and the viscosity on the dynamics of the system. One could in a future study of course directly invert for a temperature structure that would (nonlinear) influence the density, viscosity and even the size of the magma reservoir to fit the geophysical data. However, it is not straightforward to couple these parameters in a consistent way.

The initial setup is shown in **Figure 2**, while the employed material properties of all phases/rocktypes are summarized in **Table 2**.

4. INVERSE MODELING APPROACH

For the inversions, we assume that the overall large-scale geometry of the Yellowstone magmatic system does not change, particularly with respect to the shape of the reservoirs and the structure of the layers. Since the buoyancy force is a major driving force controlling surface uplift, we will first constrain the density structure of the model by fitting the gravity anomaly (**Figure 1**). We change the effective densities of the two reservoirs, while keeping the densities of the surrounding crusts fixed (and computed from phase diagrams). The melt content of the mush reservoirs influences the effective density of the reservoirs. In this work we will not investigate the exact amount of melt in the magma reservoirs but rather invert directly for the effective density difference between the reservoir and surrounding rocks, as this is the key parameter that controls gravity anomalies. If the density difference between the crystal-free magma (i.e., melt

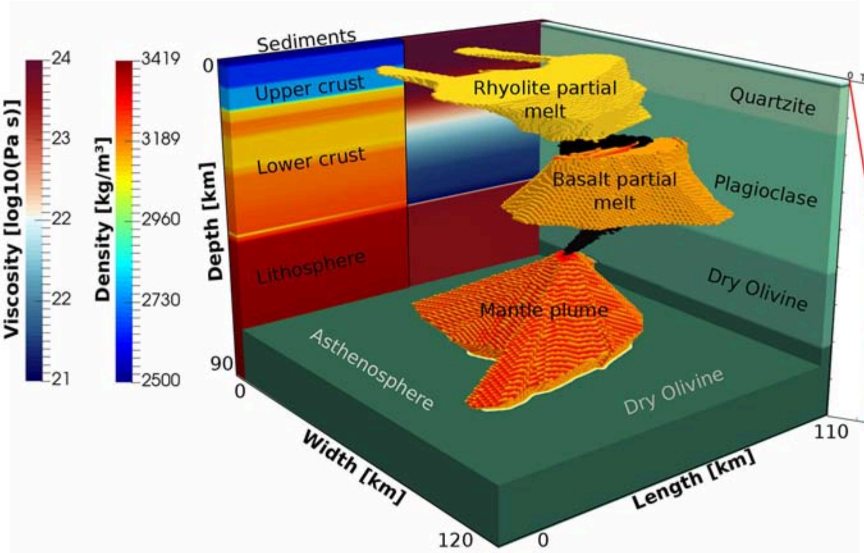

FIGURE 2 | Model setup of the computational domain representing the lithospheric scale Yellowstone magmatic system. The positions and shapes of the phases are inspired by the seismic tomography data shown in Huang et al. (2015). Chambers and mantle plume are connected, while these connections can be active or made inactive (by giving it the same material properties as the host rock). Colors at the back of the domain show the density (left side) and viscosities (right side) at this location, while temperature along a 1D profile through the middle of the domain is shown at the right.

TABLE 2 | Material properties used in this work.

Phase	Density [kg/m^3]	Viscosity [Pa s]	Shear modulus (G) [GPa]
Free-Air	1	10^{19}	none
Sediment	2,500	Wet Quartzite	50
Upper crust	phase diagram	Quartzite	50
Lower crust	phase diagram	Plagioclase (An75)	50
Lithosphere	3,400	Dry Olivine	50
Asthenosphere	3,400	Dry Olivine	50
Upper reservoir	2,519	$10^{19}/10^{21}$	50
Lower reservoir	2,660	$10^{19}/10^{21}$	50
Mantle plume	3,060	10^{19}	50

All phases with constant density have a thermal expansion coefficient, α of 3×10^{-5} K^{-1}. All phases except the free-air phase are defined by a constant thermal conductivity (k) of 3 W/(mK) and a heat capacity (cp) of 1000 J/(kgK). All phases except the free-air phase are defined by a constant cohesion (C) of 1 MPa and a friction angle of 30°. All phases except the free-air phase have a poison ratio of 0.3. The magma reservoir viscosities are constant. The rheological flow laws for the viscosities are taken from Ranalli (1995): Wet Quartzite $A_n = 3.2\times10^{-4}$ MPa^{-n}/s, $n = 2.3$, $E_n = 154$ kJ/(MPa mol), $V_n = 0$ m^3/mol; Quartzite $A_n = 6.7\times10^{-6}$ MPa^{-n}/s, $n = 2.4$, $E_n = 156$ kJ/(MPa mol), $V_n = 0$ m^3/mol; Plagioclase (An75) $A_n = 3.3\times10^{-4}$ MPa^{-n}/s, $n = 3.2$, $E_n = 238$ kJ/(MPa mol), $V_n = 0$ m^3/mol; Dry Olivine $A_n = 2.5\times10^{-4}$ MPa^{-n}/s, $n = 3.5$, $E_n = 532$ kJ/(MPa mol), $V_n = 17\times10^{-6}$ m^3/mol. Other parameters are taken from Turcotte and Schubert (2014).

phase) and the solid rock end-member is known, we can retrieve melt content from it (e.g., Bottinga and Weill, 1970). In doing this, we make the implicit assumption that the melt content within each of the reservoirs in our model setup is constant in space and time. In nature, it is quite possible that the melt content within the reservoirs varies as well, and our approach should thus be considered to only catch the first order effects on both the gravity field and the dynamics of the system. Gravity anomalies are well-known to be non-unique with respect to the relative density and geometry of the anomaly. Baumann et al. (2014) showed that using a joint geodynamic inversion of surface velocities and gravity data reduces the ambiguities of the inverse problem, that is why we additionally perform an inversion for the surface velocities through changing the viscosities of the layers. For the gravity inversion, we compute the misfit between the data and the simulation at each parameter combination. Our reference gravity field is based on the density profile at a vertical boundary of the domain, excluding magma reservoirs and the mantle plume. The only free parameters in this setup are the effective densities of the two reservoirs, which makes it a computationally efficient problem, permitting a grid search inversion.

To obtain a good starting guess for the velocity inversion, we first compute the sensitivities of the surface velocities to the changes in material parameters, and identify those that have largest influence on the results. This is accomplished by computing and comparing the adjoint scaling exponents for each material parameter as described in section (2.2). We found that there are 8 parameters that are crucial, and we therefore restricted our inversion to these ones.

The actual inversion for the surface velocities combines the adjoint gradients with gradient descent inversion framework that includes a line search algorithm. The gradient-based inversions (in contrast to e.g., grid search) are characterized by an inability to map all parameter combinations, but instead follow the gradient toward the next (local) best fit. The advantage is that it makes the inversions computationally more efficient, but the disadvantage is that it is not guaranteed to converge to the global minimum.

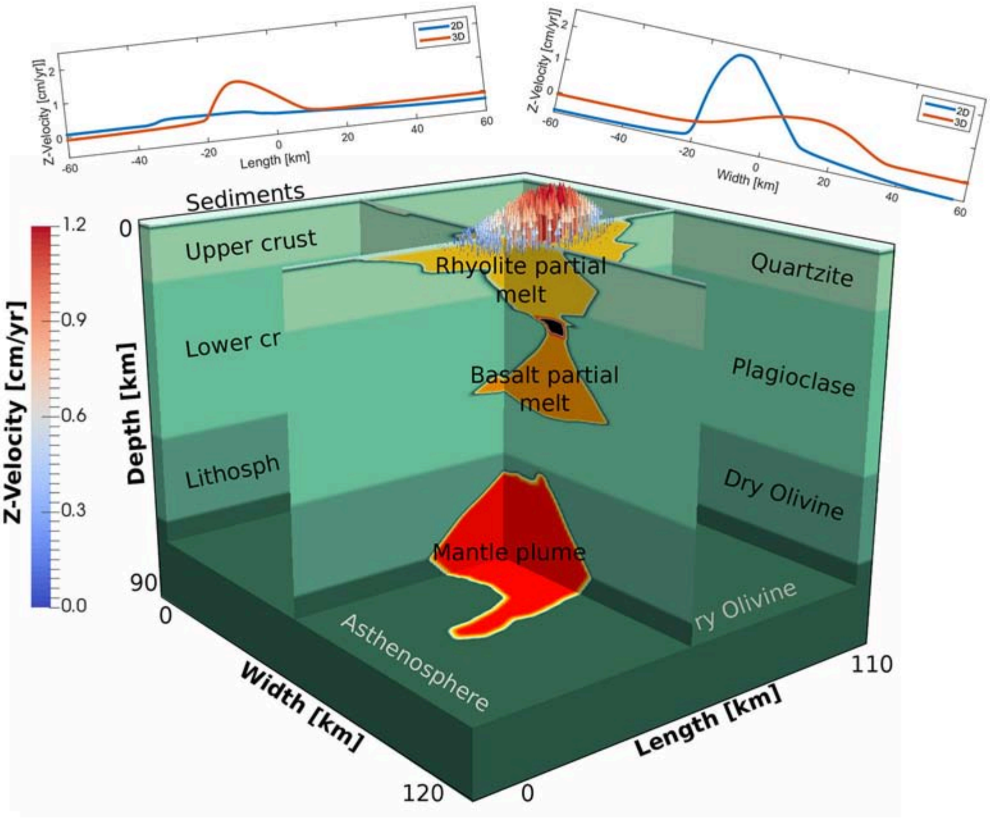

FIGURE 3 | Result of the comparison between 2D and 3D models. Two cross sections are shown with their respective surface velocity in 2D or 3D. The velocity profile is very distinct, suggesting that 3D effects are important to take into account.

5. RESULTS

5.1. 2D vs. 3D

Since 3D simulations are computationally more expensive than 2D ones, it is advantageous to know whether a substantial part of the inversions can be done in 2D. To address this, we take two cross-sections from our reference visco-elasto-plastic 3D model, with connected reservoirs, along profiles shown in **Figure 3**, and perform simulations with identical parameters as the corresponding 3D simulation. As the comparison of vertical surface velocities shows, there is a significant difference between 2D and 3D results. This suggests that it is important to take 3D effects into account, particularly if model predictions are to be directly compared with data. The reason for the discrepancy is 2-fold. On one hand, 2D simulations effectively treat magma reservoirs as infinitely long cylinders, which will overestimate the available buoyancy in the system. On the other hand, three-dimensional connections between the magma reservoirs, as are present in our 3D setup, may not be sampled in a 2D model depending on where the cross-section was taken. If these connections are not taken into account, there is no pathway for flow between the reservoirs and the surface signal may be significantly underestimated. This effect is present in the left cross-section in **Figure 3**, which has the result that the 2D simulation sees the two magma reservoirs as being unconnected whereas they are actually connected in 3D. This explains why the 2D velocities are significantly smaller in this setup, whereas they are larger in the rightmost cross-section where the connection between the reservoirs is sampled in the 2D models. We therefore only employ 3D models in the remainder of this work.

5.2. Gravity Anomaly Inversion

Before performing actual geodynamic simulations, we first derive a density structure of the magma reservoirs of the Yellowstone magmatic system, as gravity anomaly computations are much faster than geodynamic simulations. We implement the gravity computation as described in Turcotte and Schubert (2014). As comparison we use the compiled Bouguer anomaly data of DeNosaquo et al. (2009) (online archive of the Pan American Center for Earth and Environmental Sciences (PACES), shown in **Figure 1**), who performed a 2D inversion for the density structure. By varying the effective density of the two magma reservoirs, we invert for the 3D density structure. We vary the effective densities from 2340 kg/m^3 to 2690 kg/m^3 for the upper and from 2590 kg/m^3 to 2730 kg/m^3 for the lower reservoir, consistent with the effective density values resulting from the parametrization of Bottinga and Weill (1970) for the major elements found by Christiansen (2001), also shown in **Table 1**. Four end member cases are considered:

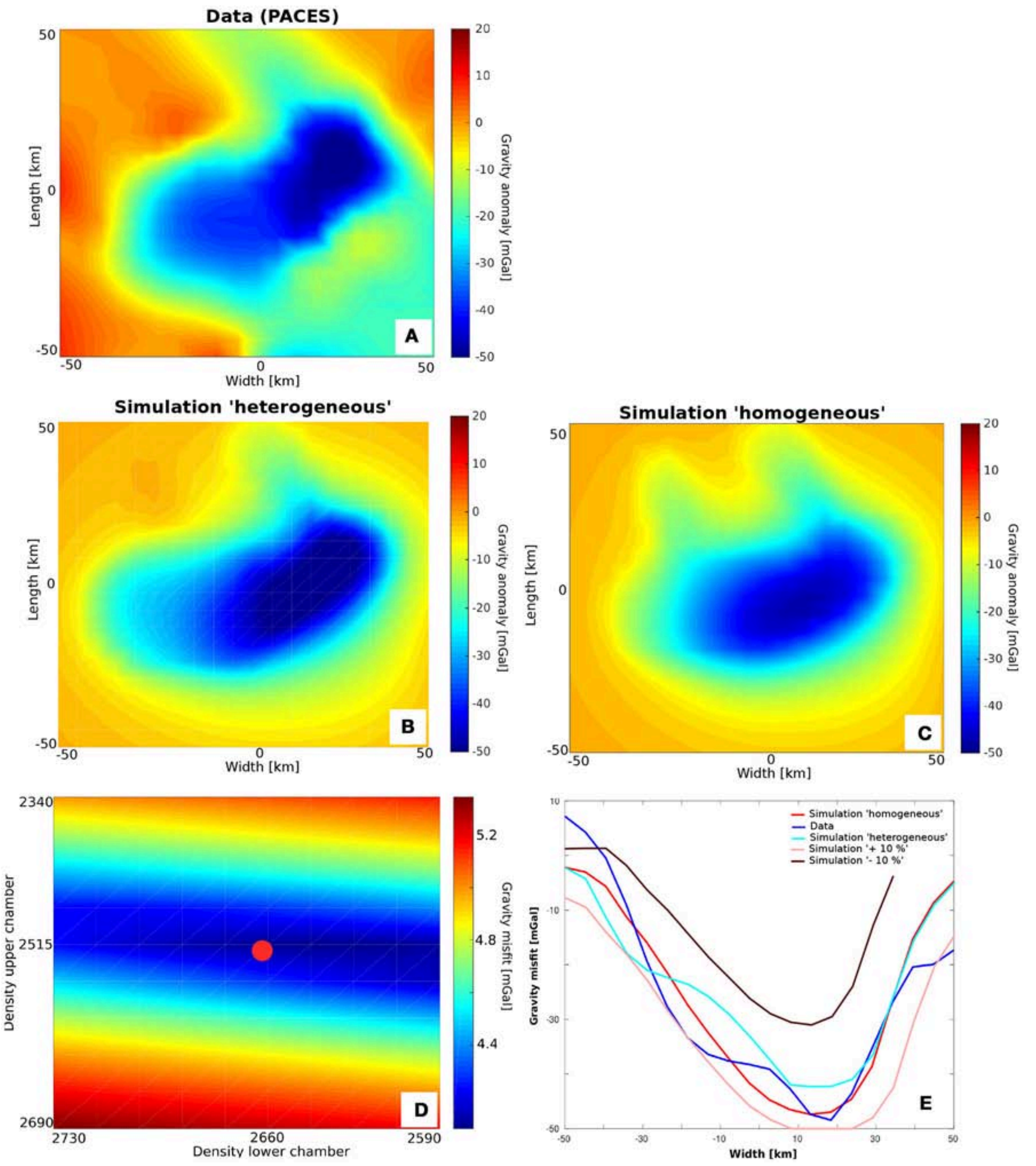

FIGURE 4 | Result of the gravity inversion. **(A)** Observed gravity anomaly data from PACES. **(B)** Best manual fit assuming heterogeneous magma reservoir densities. **(C)** Best fit model by grid search inversion, keeping the density of the reservoirs homogeneous. **(D)** Misfit function in the grid search inversion. The color represents the least square misfit between the simulation and data, with blue colors indicating a good fit to the data. **(E)** Gravity anomaly comparison between simulation result and data at a representative 1D line across the surface (along length = 0 km).

1. Grid search inversion: In this case, the gravity anomaly is fitted by varying the effective densities of the reservoirs as a whole, as shown in **Figure 4A** (data), **Figure 4C** (simulation result), **Figure 4D** (mapped misfit function), and **Figure 4E** (representative 2D cross section). Results show that we obtain an overall good fit to the data, with deviations of around 5-10 mGal (see **Figure 4E**). There is a trade-off between the two densities (**Figure 4D**). As expected, the gravity anomaly is more sensitive to the density of the shallower magma reservoir. The final result has a density of 2496 kg/m^3 in the upper reservoir, and a density of 2,684 kg/m^3 for the lower reservoir.
2. Heterogeneous magma reservoirs: We present a hand-made fit based on the result of the grid search inversion to the

gravity anomaly in which we include smaller areas within the reservoirs that are allowed to have higher or lower densities. As starting point, the best fit from approach (1) was used. The result is shown in **Figures 4B,E**. In particular, a denser heterogeneity (slightly denser than the surrounding crust) within the north east part of the reservoir removed the anomalous perturbation in the gravity signal. Furthermore, the center of the magma reservoir was divided in a slightly denser part in the west and a less dense part in the east. As a result the misfit is reduced in some areas, and increases in others. Doing a better fit would potentially be possible if we allow for a full, laterally varying, density structure. Given the above-described non-uniqueness of the gravity problem it is however unclear whether this will give significant new insights in the dynamics of the system, while increasing the model parameters significantly.

3. Slightly larger reservoirs: Since the geometry is inspired by the seismic tomography data, which includes a regularization as part of the inversion, there is still significant room for interpretation regarding the reservoir size (which we constrained using the shape of the seismic velocity contour lines). To investigate this effect, we performed simulations with 10% larger reservoirs, which significantly overdetermines the gravity signal, shown in **Figure 4E**.
4. Slightly smaller reservoirs: Similarly, a reduction of the volume of the reservoirs by 10 %, while using the same density difference between reservoir and host rock, significantly underestimates the gravity signal, as shown in **Figure 4E**.

Based on these results, we use the best-fit density structure of the grid search inversion in the remainder of this work. This assumes a density difference between upper reservoir and surrounding upper crust of around 100 kg/m^3, independent of how this density difference is achieved. The density difference between the lower reservoir and lower crust has an approximately 3 times smaller effect on the gravity signal, as can be seen precisely in **Figures 4D**, **9C**.

5.3. Forward Modeling

In the next step, we perform 3D visco-elasto-plastic compressible geodynamic simulations. Since we are mainly interested in the present-day deformation of the lithosphere, we need to run the simulations for a few time steps until stresses have elastically build-up and do not change significantly with time after which we evaluate the simulation (see Supplementary Material in **Appendix 2** for additional details).

In our simulations, the long term surface uplift is driven by the buoyancy force, caused by the density difference between reservoirs and crust or plume and mantle, respectively, and is inverse proportional to the effective viscosity of the layers. In addition, magma pulses may further inflate a magma reservoir and induce a surface signal. We model this by either activating an overpressure lower boundary condition, or by a kinematic internal boundary condition, as explained later. Both conditions are activated only after a steady-state stress state has been achieved in the models, which is why these simulations take both the long-term geodynamic effects and the shorter-lived magmatic pulse into account. In the following, we discuss the impact of several end member simulations.

5.3.1. No Connections, Visco-Elastic

During phases of tectonic quietness, the magma reservoirs act as buoyant bodies emplaced in a elastically loaded crust. We tested this by performing a model with unconnected reservoirs and a visco-elastic crust without taking plasticity (generation of faults or weak zones in the crust) into account. Maximum surface velocities are on the order of 0.2 cm/year, shown in **Figure 5A**. Furthermore, significant deviatoric stress occur between the reservoirs of up to 120 MPa, which suggests that it is likely that brittle failure would actually occur in these places and connect the reservoirs.

5.3.2. Connections, Visco-Elastic

In a next test, we therefore inserted a connection between the reservoirs in the models (as shown in **Figure 5B**). This increased the maximum surface uplift velocities of up to 0.8 cm/year, which is consistent with the lower bound of the observed uplift velocities in Yellowstone, recorded during phases of low activity (e.g., Chang et al., 2007, 2010; Vasco et al., 2007).

5.3.3. Connections, Visco-Elasto-Plastic

The crust above large scale volcanic systems is faulted in many places (e.g., Reid, 2004). For rocks, a first order representation of the stress at which they yield is given by Byerlee's law which can be numerically mimicked by a Drucker-Prager frictional plasticity law (Drucker and Prager, 1952). Numerical simulations that implement this will limit the stresses to remain below or at the yield stress. To understand the effect of this on the large-scale dynamics of the system we performed a simulation in which plasticity was activated (with a friction angle of 30°, and a cohesion of 1 MPa). The results show that plastic yielding is predominantly active above the magma reservoirs. As it effectively weakens the crust, it results in higher surface velocities of up to 1.2 cm/year (**Figure 5C**). To give a better feeling of the overall velocity field within the system we created a movie consisting of passively advected markers. The movie is given in the online supplement and is described in Supplementary Material in **Appendix 4**.

5.3.4. Connections, Visco-Elasto-Plastic, Sill-Type Body

The presently most common view of magmatic systems is that they are not composed of homogenized, partially molten bodies, but rather of sill complexes Cashman et al. (2017). As such the assumption that we made before, of having magmatic bodies with a constant density and viscosity, may be an oversimplified representation of volcanic systems such as the Toba caldera as proposed by Jaxybulatov et al. (2014). To test the effect of a sill-like, rather than a homogeneous, magma body we cut the two upper magma reservoirs by layers of the representative crust. This leads to sill like structures of partially molten layers with a height of about 4 km that alternate with colder crustal layers that are roughly 2 km high. A simulation with unconnected sill bodies and without a connection to the mantle plume results in

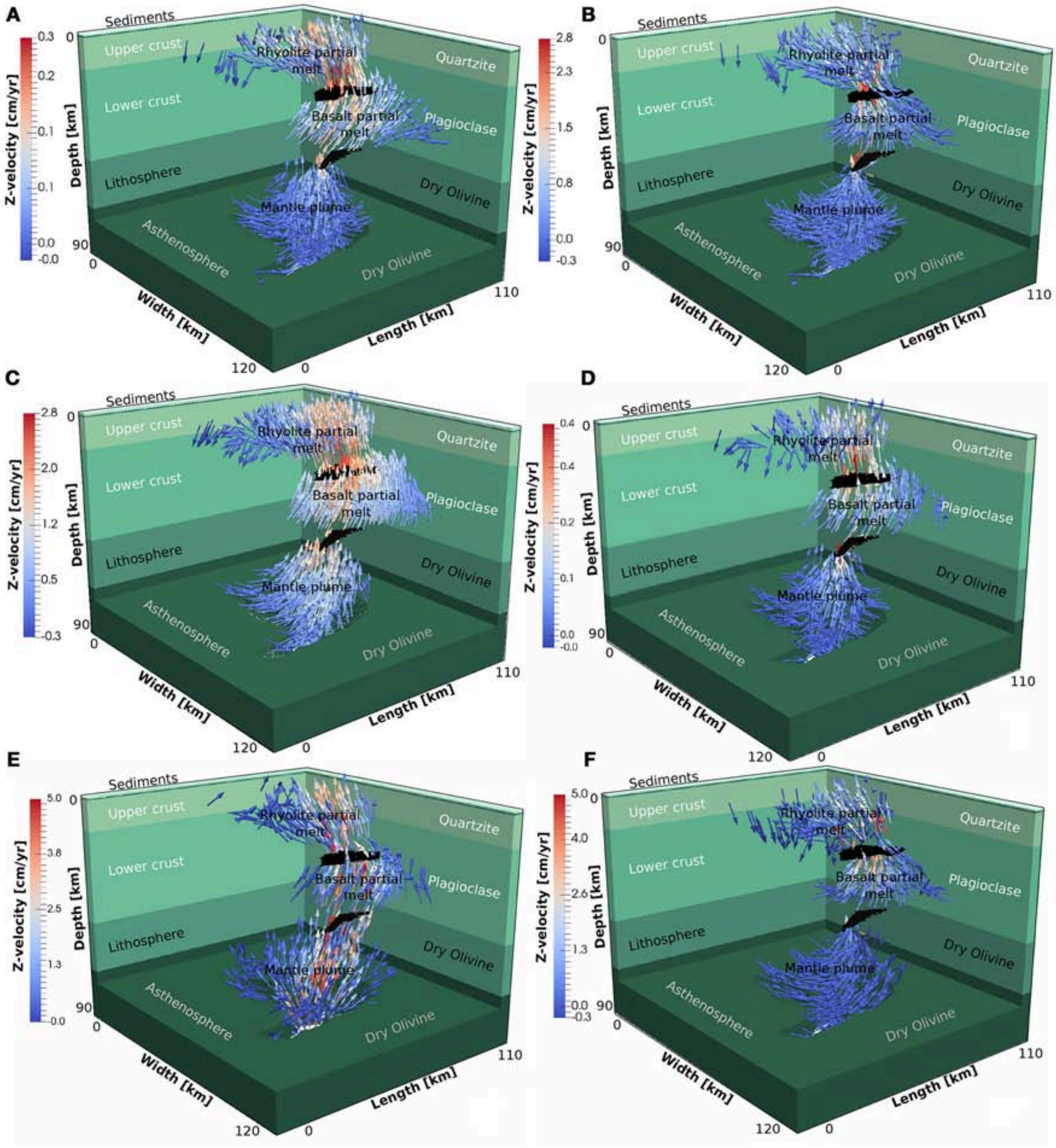

FIGURE 5 | Summary of the velocity structure of different end member simulations. **(A)** No connection between the reservoirs and no plasticity. Maximum vertical velocities at the surface are 0.2 cm/year. Black parts show the connection between the reservoirs which is set to the surrounding crustal viscosities in case they are inactive. **(B)** Connections between the reservoirs and no plasticity. Maximum vertical velocities at the surface are 0.8 cm/year. **(C)** Connections between the reservoirs and plasticity. Maximum vertical velocities at the surface are 1.2 cm/year. **(D)** Connections between the reservoirs, plasticity and a higher viscosity of the reservoirs of 10^{21} Pa s, implying a lower melt content. The maximum vertical velocity at the surface is 0.2 cm/year. **(E)** Case with slightly larger connections between the reservoirs, plasticity and a basal boundary overpressure of 50 MPa. Maximum vertical velocity at the surface is 2.4 cm/year. **(F)** Case with a prescribed kinematic boundary condition between the reservoirs to simulate influx from the middle to the upper reservoir of around 8 cm/year. Maximum vertical velocity at the surface is 2 cm/year. The downwards center of the reservoir is moving upwards which must result in a (low magnitude) downwards movement of material elsewhere.

a maximum surface velocity of 0.3 cm/year, comparable to the unconnected case discussed in section 5.3.1. Connecting the sill bodies internally and adding a connection to the mantle plume increased the surface velocity to 1 cm/year. The endmember with connections is shown in Supplementary Material in **Appendix 5**.

5.3.5. Connections, Visco-Elasto-Plastic, Less Melt

So far, our models considered the partially molten viscous reservoirs to have a uniform and low viscosity of 10^{19} Pa s, which implies that the melt content is sufficiently large to weaken the effective viscosity of the reservoirs to this amount (from an effective solid rock viscosity of $10^{23} - 10^{24}$ Pa s). Yet, seismic tomography results suggests that the melt fraction in the upper reservoir may be no more than 10% and even less in the deeper reservoir (Huang et al., 2015). Whereas it is unclear how robust these findings are, given the km-scale wavelength of seismic waves and the dampening used in seismic tomography inversions, it is at least feasible that the effective viscosity is larger than we assumed. We therefore performed an additional simulation in which the viscosity of the magma reservoirs was increased by two orders of magnitudes. Results show that this reduces the maximum surface velocities by a factor 6, from 1.2 to 0.2 cm/year (**Figures 5D**, **9D**). This suggests that the viscosity of the reservoirs does play an important role for the surface velocities, and that this is not solely affected by the rheology of the host rocks.

5.3.6. Connections, Visco-Elasto-Plastic, Mantle Influx

In volcanology, uplift rates of volcanoes are often interpreted by comparing them with predictions of analytical or numerical models that consider a (spherical) magma reservoir that is emplaced at a given depth and has a certain amount of overpressure applied at its boundary. Physically, this approach mimics the inflation of a magma reservoir after the addition of a new batch of magma, and if this magma reservoir is embedded in a compressible elastic host rock, it will deform both the host rocks and the free surface (e.g., Battaglia and Segall, 2004; Gerbault et al., 2012). In numerical codes, this is typically done by treating the magma reservoir itself as a boundary condition, which can be benchmarked vs. the elastic Mogi solution (Mogi, 1958) or a visco-elastic variation of it (Del Negro et al., 2009). Whereas this approach is certainly applicable to address deformation within the shallow crust beneath a volcano, there are a number of problems of employing it to the whole lithosphere. The first issue is related to where the magma pulse comes from. In Yellowstone, magma in the upper reservoir may either come from the mantle plume (an influx condition in our setup), or from extraction of melt from the lower reservoir, which would result in both inflation in the upper crust and deflation in the lower crust. We consider both scenarios.

The first scenario assumes that additional magma in the upper crust comes from a new pulse of magma in the asthenosphere. The usual way of implementing this in numerical models, by setting an internal pressure boundary condition, has the disadvantage of eliminating the background lithospheric uplift rate, caused by the density difference between the magma reservoir and the host rocks. This thus implies that such models only consider the effect of overpressure on deformation. An alternative approach, which we follow here, is to apply an overpressure condition at the lower boundary of the model, which propagates through the system and causes an inflation of the upper reservoir, as long as it is connected to the lower boundary through weak zones. This has the advantage that it mimics more closely what happens in nature and allows for more complex partially molten regions, while at the same time taking the buoyancy effect of the reservoirs into account. To test whether this approach works, we benchmarked our implementation with the Del Negro viscoelastic benchmark (Supplementary Material in **Appendix 3**).

To test the effect of mantle magma influx on the Yellowstone model configuration, we applied an additional constant overpressure of 50 MPa at the intersection between the mantle plume and the lower boundary. Results show that this significantly increases the velocities within the mantle plume, while only resulting in slightly larger surface velocities (**Figure 5E**). The effectiveness with which the overpressure influences the surface velocity scales with the size of the weak connection zones between the reservoirs. Small connections result in a significant increases of the velocity field within the mantle plume, of which only a small amount is transferred to the surface. Increasing the size of the connections increases the surface uplift velocity, which can go up to 2.4 cm/year for large connection zones (see **Figure 9E**).

An additional advantage of our implementation is that it allows recomputing the effect of the overpressure in terms of an influx or an inflation volume. One can compute the influx volume by multiplying the boundary velocity, resulting from applying the overpressure, by the timespan of the inflation, or the timespan of high surface uplift velocities and retrieve the amount of added volume of magma to the system. The area of applied overpressure in all simulations is 50 km^2. If one assumes an overpressure of 50 MPa, resulting in an average z-velocity of 23.4 cm/year at the boundary (approximately 3 cm/year within the plume), and timespan of high activity described by Chang et al. (2010) from 2003 to 2008 the magma inflation volume is 0.06 km^3 at the mantle plume level after only 5 years.

5.3.7. Connections, Visco-Elasto-Plastic, Influx Reservoirs

The second scenario to add magma into the upper crustal reservoir, is by taking it from partial melting or fractional crystallization of the lower crustal magma reservoir. This implies that inflation in the upper magma reservoir is accompanied by deflation in the lower reservoir, which can be implemented numerically by introducing a connecting zone ('dike') between the two reservoirs in which a Poiseuille-flow (quadratic) velocity field is prescribed as an internal boundary condition. By varying the magnitude of the velocity we can control both the mass flux and the pressure gradient between the reservoirs. If only a connecting dike zone is present, the self consistent (buoyant) velocity in the channel has an average value of 4.3 cm/year, which is equal to moving a volume of 0.006 km^3 between the reservoirs within 5 years. If we increase this velocity to an average of 8 cm/year, the surface velocities increase from 1.2 to 2 cm/year and the inflation volume to 0.012 km^3 (**Figure 5F**). The volume of the applied velocity is 50 km^3 and the cross sectional area is 30 km^2. This thus has the largest impact on the surface velocities of all the scenarios we considered (see **Figure 9F** for a summary).

5.4. Stress Directions

Our models also compute stress orientations, which can be compared against available observations. In Yellowstone, Waite and Smith (2004) assembled the local stress orientation of the minimum principal stress σ_3 for selected locations by

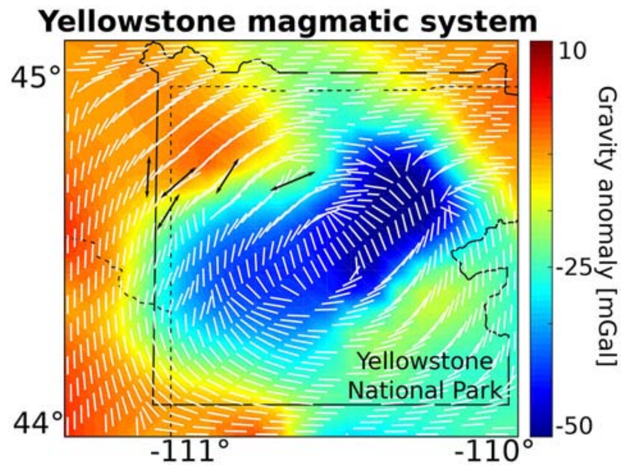

FIGURE 6 | Orientation of the minimum principal stress. Black arrows represent the orientation of the minimum principal stress taken from Waite and Smith (2004) and references therein. White arrows show the result of the simulation with no connection between the reservoirs, while grey arrows show the result of the simulation with connected reservoirs and a mantle plume (**Figure 5C**). The stress orientation is computed at the surface. Results reproduce the rotation of the stress field from West-East to North-South. Furthermore, the connected vs. the unconnected case do not show significant differences.

using earthquake focal mechanisms (white arrows in **Figure 1**). Comparing modeled with observed principal stress directions reveals that there is a good agreement, particularly with respect to the stress orientation that changes from West-East to North-South (**Figure 6**). Furthermore, both the connected and unconnected geometries have almost the same patterns, suggesting that both scenarios correlate well with the data.

5.5. Parameter Sensitivity

So far, we focused on how the connectivity between the reservoirs, the type of rheology and the inflation affect the surface velocity. However, in addition, material parameters such as the powerlaw exponent or the density will affect the dynamics of the system. We therefore perform a parameter sensitivity analysis, shown in **Figure 7**, to determine the model parameters that play a key role in controlling the surface velocity. We compute these sensitivities for the representative simulation with visco-elasto-plastic rheology and connected reservoirs. Results are obtained for the cases in which we take the activation energy, the power law exponent and the density of the reservoirs into account, which amounts to 16 parameters in total. Of these, the viscosity parameters of the lower crust, as well as the density of the upper crust, are the most important parameters as can be seen in **Figure 7**. The size of the spheres in the figure visualize the normalized relative importance of the parameters. To enable direct comparison, each parameter type, e.g., activation energies, is normalized over the maximum parameter value within the type.

5.6. Adjoint Inversion

In the next step we solve an inverse problem based on our "best-scenario" model from previous section to obtain an improved fit between the simulations and observed GPS velocities. We allow the inversion to vary the activation energy and the power law exponent of the upper and lower crust, the asthenosphere and lithosphere. **Figure 8A** shows the viscosity field, which was used as initial guess. The final viscosity field has a significantly weakened crust as a result of an increased power law exponent of the upper crust from 2.4 to 3 and from 3.2 to 4.6 for the lower crust (**Figure 8B**). The inverse problem is solved by a steepest descent method and typically demonstrates a quick convergence, facilitated by a robust line-search algorithm (**Figure 8E**).

A comparison between the modeled and observed velocity field between September 2007 and September 2008 (interpolated from data from Chang et al., 2010), shows that the pattern and magnitude are similar (**Figures 8C,D**). This suggests that it is possible to fit the long-term or background surface velocities above magmatic systems by changing the viscosity structure of the crust. Lowering the viscosity allows for larger displacements in a shorter amount of time, that are triggered by the density difference, resulting in higher velocities. Smaller-scale differences that can be observed toward the boundaries, may occur because we consider the rheology of the crust to be homogeneous outside the magma reservoirs, whereas in nature weakening of the nearby surrounding crust may result from phases of inflation, heating, or deflation. In general, changing the viscosity structure only influences the long term surface velocities and stresses, and does not represent a short term signal like the inflation models discussed in section 5.3.6.

6. DISCUSSION

Our results imply that buoyancy driven uplift for large magma reservoirs at large magmatic systems such as Yellowstone is active on a long term scale (thousands of years) with small rates. The rate itself strongly depends on the connectivity between the reservoirs or sills within the magmatic system. If the magma bodies are only connected sporadically, the background uplift signal will be even smaller since the buoyancy effect from deeper reservoirs becomes negligible. The strength of this effect is further limited by the viscosity of the surrounding material and by the viscosity of the magma bodies. Thus, a larger amount of partial melt would decrease the viscosity of the magma bodies and would result in higher uplift rates. In order to show the difference between the long-term and more short-term processes we conclude that the effect of magma injection on the surface uplift can be much higher than the long term buoyancy signal. Even small amounts of injected magma at the level of the mantle plume can be recorded at the surface. However, effects such as volatile degassing were not taken into account in this study which may result in changes in the dynamics of a magmatic system on a very short time scale (Vargas et al., 2017). Other effects, that could potentially play an important role, and should ultimately be considered in these type of models, are: (i) deformation of a two- or three-phase mush, (ii) volume changes resulting

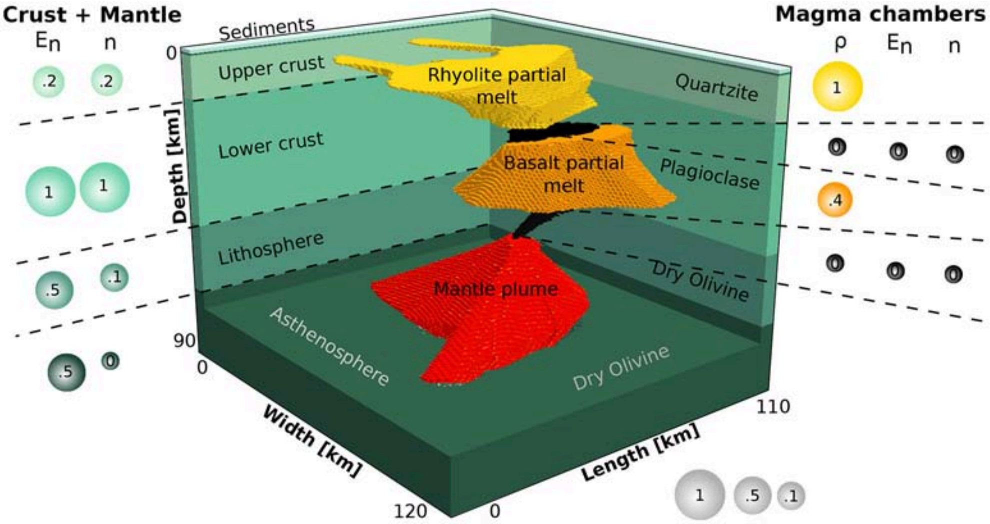

FIGURE 7 | Result of the adjoint parameter sensitivity study. The size of the sphere represents the relative importance of the parameter in affecting the surface velocity above the uppermost magma reservoir. Every physical parameter is normalized by its value for each rock phase (e.g., the activation energies of all phases are normalized with respect to each other). The viscosity of the lower crust, lithosphere and the lower crustal magma reservoir together with the densities of the magma reservoirs are the key model parameters.

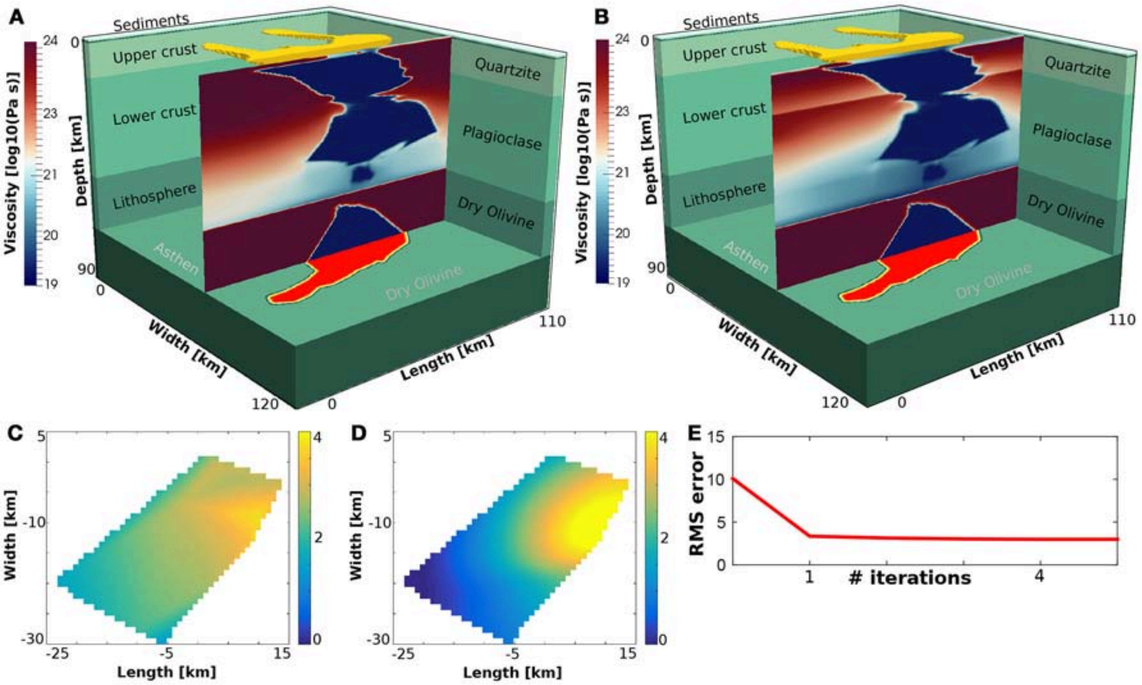

FIGURE 8 | Summary of the adjoint inversions for material parameters. **(A)** Initial viscosity field of the visco-elasto-plastic connected case was (**Figure 5C**) used as starting guess for the inversion. **(B)** Final viscosity field after converged iterations, showing a significantly weakened crust by increasing the powerlaw exponents of the crust. **(C)** Map view of interpolated surface uplift from Chang et al. (2010) during the period of September 2007–September 2008, which is used as data for our inversions. **(D)** Map view of the vertical surface velocity field after converged iterations. Both the patterns and magnitude are similar, even though the numerical model has lower velocities toward the boundaries of the map, perhaps caused by crustal heterogeneities that were not taken into account in the models. **(E)** Cost function as root mean square of vertical surface velocity vs. number of iterations. Due to a good initial guess and robust line search acceleration, convergence is achieved quickly.

from crystallization and melting (Fournier, 1989), (iii) the effect of volatiles in the viscous formulation of the partially molten rocks. In addition, we can potentially increase the robustness of the inversions by taking more data into account, such as seismic activity as an estimation for the proximity to failure within the crust, or by directly inverting for stress orientations as well. Furthermore, instead of inverting for the direct parameters viscosity and density one could invert for a parameter that couples the effective material parameters in magmatic systems, such as temperature or melt fraction.

Seismic observations may not be sufficient to precisely constrain the volume of a reservoir, furthermore the possible interpretations on the dynamics of the reservoir are still debated. For such problems it is helpful to include results from numerical simulations as presented in this work. Taking the seismic observations as initial guess for the shape and sizes of the reservoirs and then inverting for the material parameters based on the misfit between the mechanical result and the measured surface velocities (GPS or InSAR) can shed additional light on the dynamics of the reservoir and can help constraining effective parameters of viscosity and density more precisely. From these effective quantities one could, by taking area specific thermodynamic data into, recompute melt fractions. Furthermore, geodynamic simulations can easily test different volumes (within the uncertainty of the seismic observations) and quantify the difference in the effective parameters, and provide uncertainties on these parameters. One example presented, shows that a reduction of the reservoir volume by 10% reduces the gravity signal by about 30 %. As such a density that is 10% higher should fit the gravity signal sufficiently well. This can further be explained by a different volume of melt fraction, a lower solid rock density (possibly due to a high temperature) or possibly a sill like body which cannot be resolved by seismic imaging techniques due to wavelengths of several kilometers in size. If one, as mentioned above, couples the reservoir parameters, such as density and viscosity, to one key parameter such as temperature, one should be able to uniquely retrieve a volume of the reservoir that is consistent with observations at the surface. The uniqueness of this parameter combination can be supported y including additional data into the inversion, such as stresses orientations at depth.

This method can be applied in the future to any well monitored volcanic system such as the Phlegrean Fields (caldera system) or Etna (no caldera system) where it can help constraining which of the mechanical processes—viscous, elastic or plastic—are active and have a key influence the surface observations. It can further help to estimate the long term background stress state around the magmatic system, which can potentially be incorporated as boundary conditions into smaller scale numerical models focussing on part of the system. With our approach we can easily incorporate complex 3D structures and retrieve more complex surface responses than previous approaches (like the traditionally applied Mogi source). In case 4D seismic observations are available, there is the possibility to invert for the different stages of the seismic observations, and determine how the volumes and effective parameters at each stage of the seismic observation changed with time. It would be interesting to apply this approach to other, geophysically well-studied, magmatic systems.

7. SUMMARY AND CONCLUSIONS

In this work, we present 3D visco-elasto-plastic numerical modeling of the lithospheric scale Yellowstone magmatic system. The geometry of our models is inspired by the recent seismic study of the area described in Huang et al. (2015). Additionally, the effective densities of the magma host rocks and the crust are obtained by thermodynamically consistent modeling using Perple_X (Connolly, 2009) and the approach in Bottinga and Weill (1970).

In a first step, we show that it is important to consider 3D models rather than 2D ones, because the magnitudes (e.g., of velocities) can be very different. Next, we used gravity inversions to derive a reasonable density structure, which was subsequently used in a series of forward simulations in which we tested the effect of lithospheric rheology, reservoir connectivity and magma influx on surface velocities. These simulations suggest that observed background uplift rates can be obtained for simulations in which the reservoirs are connected and plasticity is active in the upper crust surrounding the magma reservoirs. Velocity magnitudes obtained in this manner vary between 0.2 and 1.2 cm/year depending on whether plasticity is active or not, on the viscosity of the reservoirs, and on whether the reservoirs are connected, as shown in **Figures 9A,B**.

We perform a comparison of the surface velocities with GPS measurements. Chang et al. (2010) report phases of higher surface uplift rates during a timespan of 1 year between September 2007 and September 2008, representing velocities between 2 and 4 cm/year. To account for these enhanced velocities we considered two additional processes: (i) overpressure at the lower boundary of the domain to simulate magma rising from the mantle plume through the magmatic plumbing system, and (ii) magma transfer from the lower to the upper magma reservoir, by applying a kinematic internal boundary condition between the two reservoirs at the location of the connection. The effect of overpressure appears to have a relatively minor impact on the surface velocities and most likely only contributes to the long term signal at the surface velocities. On the other hand, the prescribed Poiseuille flow between the upper and lower reservoirs has a much bigger effect. Increasing the magma flux between the reservoirs results in large changes of the surface velocities, e.g., 12 cm/year imposed velocity within the connection, which is equivalent to an inflation volume of 0.018 km^3 within only 5 years, nearly doubles the surface uplift velocity to 2.6 cm/year.

An adjoint-based sensitivity analysis is performed to demonstrate that the viscosity parameters of the upper and lower crust are of key importance for the surface velocities. An inversion was performed to better fit the models to both the magnitude and spatial pattern of the recorded uplift during a period of high activity with velocities of up to 4 cm/year (Chang et al., 2010). Results show that this can be fitted with a weakened

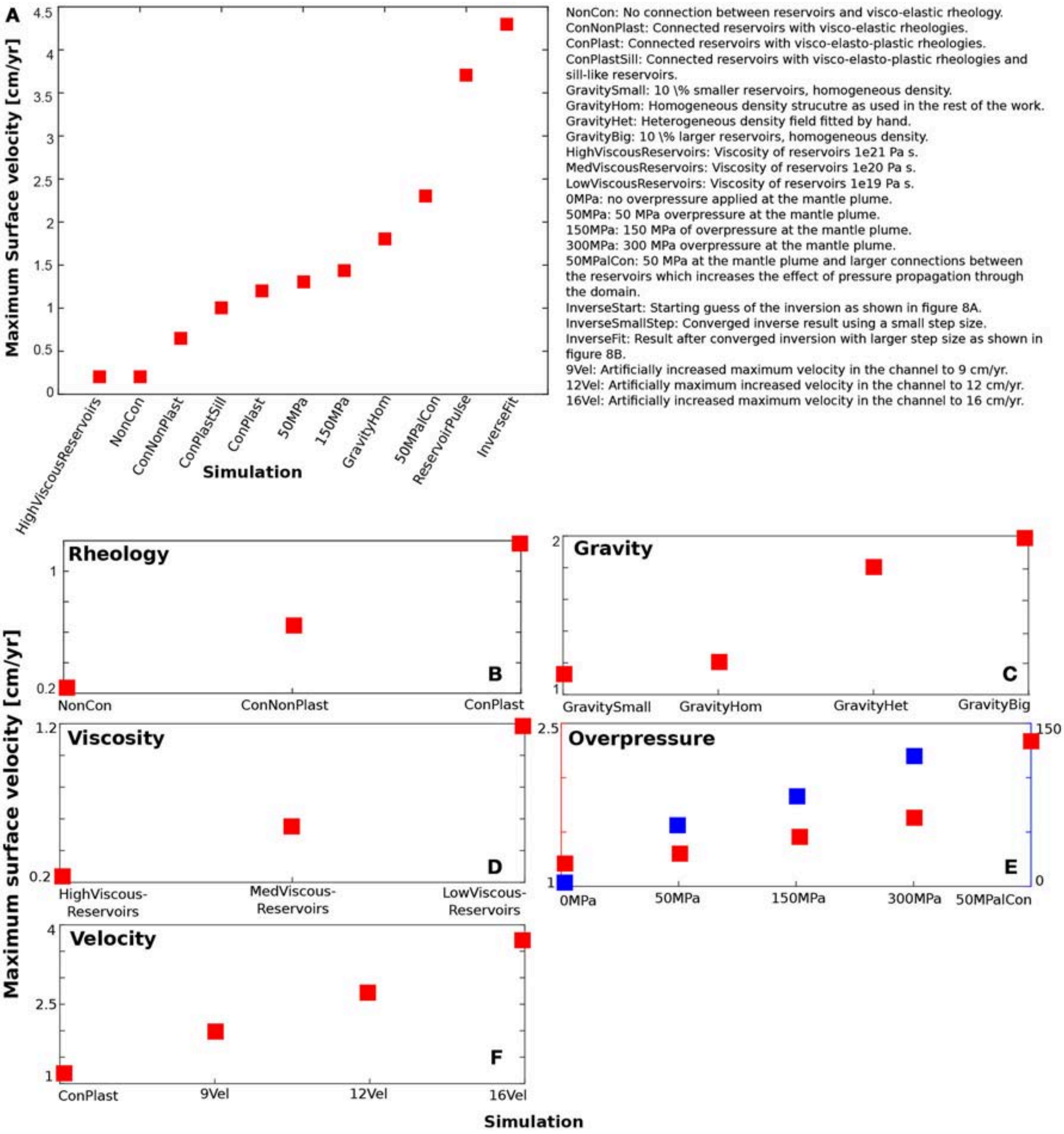

FIGURE 9 | Summary of the impact of the various parameters considered here on the vertical surface velocity. **(A)** Set of representative simulations and the resulting surface velocities. **(B)** Effect of rheology. **(C)** Effect of the different density models on the surface velocity. **(D)** Viscosity of the magma reservoirs. **(E)** Effect of overpressure at the mantle plume. Red squares represent the surface velocity. Blue squares show the maximum z-velocity at the boundary where the overpressure is applied (numbers on the right axis). **(F)** Effect of kinematic internal boundary condition between the reservoirs simulating inflation and deflation between the upper and lower reservoirs, respectively. The largest effect on the vertical surface velocity is caused by changing the kinematic boundary condition.

crust. Yet, changing the viscosity structure of the whole crust affects the long term uplift signal as well, while a short term period of enhanced uplift is more likely caused by a smaller scale magmatic pulse in the upper crust. In future work, it would thus be interesting to take the temporal evolution of the surface uplift signal into account (for example from INSAR data) as it may allow unraveling both the long term uplift, and the emplacement of a smaller scale magma pulses in a rheologically realistic lithosphere.

AUTHOR CONTRIBUTIONS

GR created the manuscript, created the Perple_X phase diagrams, temporarily implemented the gravity computation and the phase diagram feedback into LaMEM and performed all simulations presented in this work. BK proposed the main idea and helped in all aspects of this work. AP is the main developer of LaMEM and helped with implementation issues. TB supported processing the raw gravity data, implementing the gravity solver into LaMEM and helped with interpreting inversion results. All authors contributed to the writing and statements made in this work.

FUNDING

GR received funding from the University of Mainz.

ACKNOWLEDGMENTS

Parts of this research were conducted using the supercomputer Mogon and/or advisory services offered by Johannes Gutenberg University Mainz (https://hpc.uni-mainz.de/), which is a member of the AHRP (Alliance for High Performance Computing in Rhineland Palatinate, www.ahrp.info) and the Gauss Alliance e.V. The authors gratefully acknowledge the computing time granted on the supercomputer MOGON I and MOGON II at Johannes Gutenberg University Mainz (https://hpc.uni-mainz.de/).

SUPPLEMENTARY MATERIAL

The Supplementary Material for this article can be found online at: https://www.frontiersin.org/articles/10.3389/feart.2018.00117/full#supplementary-material

REFERENCES

Angiboust, S., Wolf, S., Burov, E., Agard, P., and Yamato, P. (2012). Effect of fluid circulation on subduction interface tectonic processes: Insights from thermo-mechanical numerical modelling. *Earth Planet. Sci. Lett.* 357, 238–248. doi: 10.1016/j.epsl.2012.09.012

Annen, C. (2011). Implications of incremental emplacement of magma bodies for magma differentiation, thermal aureole dimensions and plutonism–volcanism relationships. *Tectonophysics* 500, 3–10. doi: 10.1016/j.tecto.2009.04.010

Annen, C., and Sparks, R. S. J. (2002). Effects of repetitive emplacement of basaltic intrusions on thermal evolution and melt generation in the crust. *Earth Planet. Sci. Lett.* 203, 937–955. doi: 10.1016/S0012-821X(02)00929-9

Ayachit, U. (2015). *The Paraview Guide: A Parallel Visualization Application*. Kitware.

Balay, S., Abhyankar, S., Adams, M. F., Brown, J., Brune, P., Buschelman, K., et al. (2016). *PETSc Users Manual*. Technical Report ANL-95/11-Revision 3.7, Argonne National Laboratory.

Battaglia, M., and Segall, P. (2004). The interpretation of gravity changes and crustal deformation in active volcanic areas. *Geodet. Geophys. Eff. Assoc. Seismic Volcanic Hazards* 16, 1453–1467. doi: 10.1007/978-3-0348-7897-5_10

Baumann, C., Gerya, T. V., and Connolly, J. A. (2010). Numerical modelling of spontaneous slab breakoff dynamics during continental collision. *Geol. Soc. Lond. Spec. Publ.* 332, 99–114. doi: 10.1144/SP332.7

Baumann, T. S., and Bauville, A. (2016). "geomio: A tool for geodynamicists to turn 2d cross-sections into 3d geometries," in *EGU General Assembly Conference Abstracts*, Vol 18, 17980.

Baumann, T. S., and Kaus, B. J. (2015). Geodynamic inversion to constrain the non-linear rheology of the lithosphere. *Geophys. J. Int.* 202, 1289–1316. doi: 10.1093/gji/ggv201

Baumann, T. S., Kaus, B. J., and Popov, A. A. (2014). Constraining effective rheology through parallel joint geodynamic inversion. *Tectonophysics* 631, 197–211. doi: 10.1016/j.tecto.2014.04.037

Bottinga, Y., and Weill, D. F. (1970). Densities of liquid silicate systems calculated from partial molar volumes of oxide components. *Am. J. Sci.* 269, 169–182. doi: 10.2475/ajs.269.2.169

Cashman, K. V., Sparks, R. S., and Blundy, J. D. (2017). Vertically extensive and unstable magmatic systems: a unified view of igneous processes. *Science* 355:eaag3055. doi: 10.1126/science.aag3055

Chang, W.-L., Smith, R. B., Farrell, J., and Puskas, C. M. (2010). An extraordinary episode of yellowstone caldera uplift, 2004–2010, from gps and insar observations. *Geophys. Res. Lett.* 37. doi: 10.1029/2010GL045451

Chang, W. L., Smith, R. B., Wicks, C., Farrell, J. M., and Puskas, C. M. (2007). Accelerated uplift and magmatic intrusion of the yellowstone caldera, 2004 to 2006. *Science* 318, 952–956. doi: 10.1126/science.1146842

Christiansen, R. L. (2001). *The Quaternary and Pliocene Yellowstone Plateau Volcanic Field of Wyoming, Idaho, and Montana.* Technical report, U.S. Geological Survey.

Colón, D., Bindeman, I., and Gerya, T. (2018). Thermomechanical modeling of the formation of a multilevel, crustal-scale magmatic system by the yellowstone plume. *Geophys. Res. Lett.* 45, 3873–3879. doi: 10.1029/2018GL077090

Connolly, J. (2009). The geodynamic equation of state: what and how. *Geochem. Geophys. Geosyst.* 10. doi: 10.1029/2009GC002540

Crameri, F., Schmeling, H., Golabek, G., Duretz, T., Orendt, R., Buiter, S., et al. (2012). A comparison of numerical surface topography calculations in geodynamic modelling: an evaluation of the 'sticky air' method. *Geophys. J. Int.* 189, 38–54. doi: 10.1111/j.1365-246X.2012.05388.x

Currenti, G., Bonaccorso, A., Del Negro, C., Scandura, D., and Boschi, E. (2010). Elasto-plastic modeling of volcano ground deformation. *Earth Planet. Sci. Lett.* 296, 311–318. doi: 10.1016/j.epsl.2010.05.013

Davis, P., Hastie, L., and Stacey, F. (1974). Stresses within an active volcano—with particular reference to kilauea. *Tectonophysics* 22, 355–362. doi: 10.1016/0040-1951(74)90091-2

Degruyter, W., and Huber, C. (2014). A model for eruption frequency of upper crustal silicic magma chambers. *Earth Planet. Sci. Lett.* 403, 117–130. doi: 10.1016/j.epsl.2014.06.047

Del Negro, C., Currenti, G., and Scandura, D. (2009). Temperature-dependent viscoelastic modeling of ground deformation: application to etna volcano during the 1993–1997 inflation period. *Phys. Earth Planet. Inter.* 172, 299–309. doi: 10.1016/j.pepi.2008.10.019

DeNosaquo, K. R., Smith, R. B., and Lowry, A. R. (2009). Density and lithospheric strength models of the yellowstone–snake river plain volcanic system from gravity and heat flow data. *J. Volcanol. Geothermal Res.* 188, 108–127. doi: 10.1016/j.jvolgeores.2009.08.006

Drucker, D. C., and Prager, W. (1952). Soil mechanics and plastic analysis or limit design. *Q. Appl. Math.* 10, 157–165. doi: 10.1090/qam/48291

Duretz, T., May, D. A., Gerya, T. V., and Tackley, P. J. (2011). Discretization errors and free surface stabilization in the finite difference and marker-in-cell method for applied geodynamics: a numerical study. *Geochem. Geophys. Geosyst.* 12, 244–256. doi: 10.1029/2011GC003567

Fournier, R. O. (1989). Geochemistry and dynamics of the yellowstone national park hydrothermal system. *Ann. Rev. Earth Planet. Sci.* 17, 13–53. doi: 10.1146/annurev.ea.17.050189.000305

Gerbault, M., Cappa, F., and Hassani, R. (2012). Elasto-plastic and hydromechanical models of failure around an infinitely long magma chamber. *Geochem. Geophys. Geosyst.* 13. doi: 10.1029/2011GC003917

Gerya, T. V., and Yuen, D. A. (2007). Robust characteristics method for modelling multiphase visco-elasto-plastic thermo-mechanical problems. *Phys. Earth Planet. Inter.* 163, 83–105. doi: 10.1016/j.pepi.2007.04.015

Harlow, F., and Welsh, J. (1965). Numerical calculation of time-dependant viscous incompressible flow of fluid with free surface. *Phys. Fluids* 8, 2182–2189. doi: 10.1063/1.1761178

Hautmann, S., Gottsmann, J., Sparks, R. S. J., Costa, A., Melnik, O., and Voight, B. (2009). Modelling ground deformation caused by oscillating overpressure in a dyke conduit at soufrière hills volcano, montserrat. *Tectonophysics* 471, 87–95. doi: 10.1016/j.tecto.2008.10.021

Hickey, J., and Gottsmann, J. (2014). Benchmarking and developing numerical finite element models of volcanic deformation. *J. Volcanol. Geother. Res.* 280, 126–130. doi: 10.1016/j.jvolgeores.2014.05.011

Holland, T., and Powell, R. (1998). An internally consistent thermodynamic data set for phases of petrological interest. *J. Metamorphic Geol.* 16, 309–343. doi: 10.1111/j.1525-1314.1998.00140.x

Huang, H.-H., Lin, F.-C., Schmandt, B., Farrell, J., Smith, R. B., and Tsai, V. C. (2015). The yellowstone magmatic system from the mantle plume to the upper crust. *Science* 348, 773–776. doi: 10.1126/science.aaa5648

Ismail-Zadeh, A., Korotkii, A., Naimark, B., and Tsepelev, I. (2003). Three-dimensional numerical simulation of the inverse problem of thermal convection. *Comput. Math. Math. Phys.* 43, 581–599. doi: 10.1134/S0965542506120153

Jaxybulatov, K., Shapiro, N., Koulakov, I., Mordret, A., Landès, M., and Sens-Schönfelder, C. (2014). A large magmatic sill complex beneath the toba caldera. *Science* 346, 617–619. doi: 10.1126/science.1258582

Kameyama, M., Yuen, D., and Karato, S. (1999). Thermal-mechanical effects of low-temperature plasticity (the peierls mechanism) on the deformation of a viscoelastic shear zone. *Earth Planet. Sci. Lett.* 168, 159–172. doi: 10.1016/S0012-821X(99)00040-0

Karlstrom, L., Paterson, S. R., and Jellinek, A. M. (2017). A reverse energy cascade for crustal magma transport. *Nat. Geosci.* 20:177. doi: 10.1130/abs/2017AM-298728

Kaus, B., Popov, A., Baumann, T., Pusok, A., Bauville, A., Fernandez, N., et al. (2016). Forward and inverse modeling of lithospheric deformation on geological timescales. in *NIC Proceedings*, Vol. 48, eds K. Binder, M. Müller, M. Kremer, and A. Schnurpfeil. 299–307.

Kaus, B. J., Mühlhaus, H., and May, D. A. (2010). A stabilization algorithm for geodynamic numerical simulations with a free surface. *Phys. Earth Planet. Inter.* 181, 12–20. doi: 10.1016/j.pepi.2010.04.007

Kjartansson, E., and Gronvold, K. (1983). Location of a magma reservoir beneath hekla volcano, iceland. *Nature* 301, 139. doi: 10.1038/301139a0

Koptev, A., Burov, E., Calais, E., Leroy, S., Gerya, T., Guillou-Frottier, L., et al. (2016). Contrasted continental rifting via plume-craton interaction: applications to central east african rift. *Geosci. Front.* 7, 221–236. doi: 10.1016/j.gsf.2015.11.002

Koptev, A., Burov, E., Gerya, T., Le Pourhiet, L., Leroy, S., Calais, E., et al. (in press). Plume-induced continental rifting and break-up in ultra-slow extension context: Insights from 3d numerical modeling. *Tectonophysics.* doi: 10.1016/j.tecto.2017.03.025

Lanari, R., Lundgren, P., and Sansosti, E. (1998). Dynamic deformation of etna volcano observed by satellite radar interferometry. *Geophys. Res. Lett.* 25, 1541–1544. doi: 10.1029/98GL00642

Manconi, A., Walter, T. R., Manzo, M., Zeni, G., Tizzani, P., Sansosti, E., et al. (2010). On the effects of 3-d mechanical heterogeneities at campi flegrei caldera, southern italy. *J. Geophys. Res. Solid Earth* 115. doi: 10.1029/2009JB007099

Mogi, K. (1958). Relations between the eruptions of various volcanoes and the deformations of the ground surfaces around them. *Earthquake Res. Inst.* 36, 99–134.

Morgan, L. A. (2007). *Integrated Geoscience Studies in the Greater Yellowstone Area-Volcanic, Tectonic, and Hydrothermal Processes in the Yellowstone Geoecosystem*. Number 1717. Geological Survey (US).

Paulatto, M., Annen, C., Henstock, T. J., Kiddle, E., Minshull, T. A., Sparks, R., et al. (2012). Magma chamber properties from integrated seismic tomography and thermal modeling at montserrat. *Geochem. Geophy. Geosyst.* 13. doi: 10.1029/2011GC003892

Plouff, D. (1976). Gravity and magnetic fields of polygonal prisms and application to magnetic terrain corrections. *Geophysics* 41, 727–741. doi: 10.1190/1.1440645

Ranalli, G. (1995). *Rheology of the Earth*. Springer.

Ratnaswamy, V., Stadler, G., and Gurnis, M. (2015). Adjoint-based estimation of plate coupling in a non-linear mantle flow model: theory and examples. *Geophys. J. Int.* 202, 768–786. doi: 10.1093/gji/ggv166

Reid, M. E. (2004). Massive collapse of volcano edifices triggered by hydrothermal pressurization. *Geology* 32, 373–376. doi: 10.1130/G20300.1

Reuber, G. S., Popov, A. A., and Kaus, B. J. (in press). Deriving scaling laws in geodynamics using adjoint gradients. *Tectonophysics.* doi: 10.1016/j.tecto.2017.07.017

Rudnick, R., and Gao, S. (2003). Composition of the continental crust. *Treat. Geochem.* 3:659. doi: 10.1016/B0-08-043751-6/03016-4

Saad, Y. (1993). A flexible inner-outer preconditioned gmres algorithm. *SIAM J. Sci. Comput.* 14, 461–469. doi: 10.1137/0914028

Smith, R. B., and Braile, L. W. (1994). The yellowstone hotspot. *J. Volcanol. Geother. Res.* 61, 121–187. doi: 10.1016/0377-0273(94)90002-7

Smith, R. B., Jordan, M., Steinberger, B., Puskas, C. M., Farrell, J., Waite, G. P., et al. (2009). Geodynamics of the yellowstone hotspot and mantle plume: seismic and gps imaging, kinematics, and mantle flow. *J. Volcanol. Geother. Res.* 188, 26–56. doi: 10.1016/j.jvolgeores.2009.08.020

Tackley, P. J. (2008). Modelling compressible mantle convection with large viscosity contrasts in a three-dimensional spherical shell using the yin-yang grid. *Phys. Earth Planet. Inter.* 171, 7–18. doi: 10.1016/j.pepi.2008.08.005

Trasatti, E., Giunchi, C., and Bonafede, M. (2003). Effects of topography and rheological layering on ground deformation in volcanic regions. *J. Volcanol. Geother. Res.* 122, 89–110. doi: 10.1016/S0377-0273(02)00473-0

Turcotte, D. L., and Schubert, G. (2014). *Geodynamics*. Cambridge University Press.

Vargas, C. A., Koulakov, I., Jaupart, C., Gladkov, V., Gomez, E., El Khrepy, S., et al. (2017). Breathing of the nevado del ruiz volcano reservoir, colombia, inferred from repeated seismic tomography. *Sci. Rep.* 7:46094. doi: 10.1038/srep46094

Vasco, D., Puskas, C., Smith, R., and Meertens, C. (2007). Crustal deformation and source models of the yellowstone volcanic field from geodetic data. *J. Geophys. Res. Solid Earth* 112. doi: 10.1029/2006JB004641

Waite, G. P., and Smith, R. B. (2004). Seismotectonics and stress field of the yellowstone volcanic plateau from earthquake first-motions and other indicators. *J. Geophys. Res. Solid Earth* 109. doi: 10.1029/2003JB002675

Conflict of Interest Statement: The authors declare that the research was conducted in the absence of any commercial or financial relationships that could be construed as a potential conflict of interest.

Advantages of publishing in Frontiers

OPEN ACCESS
Articles are free to read
for greatest visibility
and readership

FAST PUBLICATION
Around 90 days
from submission
to decision

HIGH QUALITY PEER-REVIEW
Rigorous, collaborative,
and constructive
peer-review

TRANSPARENT PEER-REVIEW
Editors and reviewers
acknowledged by name
on published articles

Frontiers
Avenue du Tribunal-Fédéral 34
1005 Lausanne | Switzerland

Visit us: www.frontiersin.org
Contact us: info@frontiersin.org | +41 21 510 17 00

REPRODUCIBILITY OF RESEARCH
Support open data
and methods to enhance
research reproducibility

DIGITAL PUBLISHING
Articles designed
for optimal readership
across devices

FOLLOW US
@frontiersin

IMPACT METRICS
Advanced article metrics
track visibility across
digital media

EXTENSIVE PROMOTION
Marketing
and promotion
of impactful research

LOOP RESEARCH NETWORK
Our network
increases your
article's readership